Star Formation and Disk Stability in Nearby Galaxies

Elizabeth Naluminsa

October 2018

A Thesis presented in fulfillment of the requirements for the degree of
Doctor of Philosophy
in the Department of Astronomy
UNIVERSITY OF CAPE TOWN

Supervisors:
Prof. Thomas Jarrett *
Dr. Edward Elson †

* Department of Astronomy, University of Cape Town
† Department of Physics and Astronomy, University of the Western Cape

Abstract

Observations of apparent cutoffs in star formation in the disks of galaxies as well as apparent thresholds in empirical laws of star formation have led many workers in the field to seek out the drivers and regulators of star formation in galaxies. Although the intricate details of these drivers are yet to be untangled, one of the main theories put forward is the existence of a gravitational stability threshold, controlled by the balance between the pressure-forces and gravity in a galactic disk to determine where gas collapses to form stars. Studies on this have mainly focused on the radial variation of the gravitational stability parameter and how it relates to the radial variations in the star formation activity. In this study, we look at the two dimensional structure of this parameter across the disks of star forming galaxies and compare it with the two dimensional structure of the star formation activity. The gravitational stability of the disks was derived using two different models. (i) The thin gas-disk model (single-fluid disk criterion, Q_g) was derived for each galaxy in our sample. We use atomic gas for the majority of the sample and we use molecular gas whenever available. (ii) A two-fluid disk criterion which models a galaxy disk with gas and stars as two distinct fluids each with single-fluid instabilities and together having the combined two-fluid instabilities (Q_T). Both models were compared to maps of star formation rate. Data from the Westerbork survey of HI in Irregular and SPiral galaxies (WHISP) were used to trace the properties of the gas disk, while data from the Wide-field Infrared Survey Explorer (WISE) were used to derive the stellar disk and star formation properties.

In the case of the single-fluid thin gas-disk model, we find that the star forming disks show typical values of 3 - 15, much higher than the theoretical threshold value of 1. The high values can be attributed to low HI gas densities ($\Sigma_{\rm HI}$) in the central regions, although the general structure in the maps traces the local density enhancements. However, the structural variations in Q_g do not correlate with local variations in the surface density of the star formation rate, except in 25% of the sample, which are late type and have high gas fractions relative to the rest of the sample. This result confirms previous findings of 1D studies that the single-fluid criterion is better suited for late type galaxies. This is because the low stellar surface densities coupled with high gas fractions make the thin gas disk approximation yield a close description of late types. In addition to the above, we find that the values of Q_g along the edges of the star forming disks are generally lower than those inside the disk. In about half the sample, the values on the edges are found

to be roughly constant with an overall average of 4.0, which is four times higher than the theoretical threshold but in agreement with previous studies of the radial variation of Q_g. Incorporating the stellar disk (the two-fluid disk criterion) leads to lower stability for all the disks in the sample, which is consistent with the increased gravity budget of the disks. Nevertheless, the two-fluid consideration does not render the disks unstable. In fact, we see that 80% of the galaxies in the sample have $Q_T \approx 2$ or higher. The Q_T values vary only slightly, yielding flat maps consistent with previous studies of the azimuthally-averaged Q_T parameter. The overall average value of Q_T is 2.5 both inside the star forming disks and at the edges. This is in agreement with previous studies which showed that the critical value of the two-fluid disk criterion lies between 2 - 3.

In spite of the mostly flat featureless Q_T disks, four galaxies had some variations in Q_T across their disks which mapped lower stability values to local regions of enhanced star formation. It is interesting to note that these galaxies also had lower Q_g values matching the locally enhanced SF regions, although the Q_T maps had lower stability values and more extended patches. All four galaxies are late types. This confirms previous findings that the single-fluid disk criterion may be a reliable predictor of star formation in late type galaxies. This is because the stellar surface density in late types is low, and if coupled with a high gas fraction as is the case for these four galaxies, the gas-disk predictions will be close to the predictions for a disk of gas+stars.

Additionally, as part of characterization of our sample, we have also studied the scaling relations between atomic gas and star formation rate. We found general correlation between the the star formation rate and HI surface densities on sub-kpc scales, defined by a non-linear power law relationship with index varying between 1.6 - 3.8.

Acknowledgements

First and foremost, I thank the Almighty God for His gift of life and strength without which I never would have been able to begin or finish this journey.

I thank my supervisors Prof. Thomas Jarrett and Dr. Edward Elson for their guidance throughout this work. Their enthusiasm and support for the project has been phenomenal and is very much appreciated. Thank you for diligently pursuing the progress of this project, reviewing every bit of the writing, and most of all growing me to become a better scientist.

My sincere appreciation to Prof. Michelle Cluver, Dr. Bradley Frank and Dr. Maria Kapala for technical help and useful discussions around my work and their encouragement throughout my doctoral study. Great thanks to Dr. Iniyan Natarajan for helping with the proof reading of this thesis.

I'm grateful for the time spent with my writing circle organised by Dr. Kate Le Roux, as their detailed constructive critiques did a lot to improve my writing.

I thank Pastor Beatrice Katshunga and Mrs. Nelisa Mnyasane for their motherly love, encouragement and counselling throughout this journey.

Heartfelt thanks to friends that have supported me in various ways; Dr. Doreen Agaba, Ms. Andiswa Mfengu, Ms. Nosipho Bele, Mrs. Florence Wegoye, Ms. Dora Rubombora, Mrs. Roslyn Daniels, Mrs. Nicky Walker, Dr. Matamba Tshimangadzo, Mr. Ghislain Ntengu, Mr. and Mrs. Katungi.
Thanks to my office-mates Samuel Legodi, Brenda Namumba, Mokhine Motsoaledi, Narges Hatamkani, Nikki Pekeur and Hannes Breytenbach for the camaraderie all through the rough postgraduate years. I'm grateful for friends who were my spiritual family in Cape Town; Mr. and Mrs. Kalala, Ms. Juliet Naggawa, Ms. Zama Jonga, the Ekinga and Mnyasane families. You made cape town a home away from home for me.

I'm eternally grateful to and for my family; My father, Mr. James Mabaale, my brothers, Mr. Herbert Kaweesa and Mr. Yosia Sekiremba and my sisters Mrs. Olga Sekiremba and Mrs. Allen Kaweesa for carrying me through their love and prayers, encouragement, financial support, sanity checks, advice, wisdom, name it. You have been my saving grace and I thank the heavens for throwing you into my basket. Look, we have made it!

My mother, Mrs. Zeulia Nyanjura-Mabaale (RIP), to whom this work is dedicated, was a source of inspiration through her silent lessons in perseverance, trust and hope, right up to her last breath. Were it not for her inspiration, the temptation to quit when the journey

became tough might have gotten the better of me.

My dream to pursue Astronomy formed long before there ever was such a possibility in my country. Were it not for the enthusiastic support of my lecturers Dr. Edward Jurua and Dr. Simon Katrini Anguma when I eventually joined university, the dream could have remained but only a dream. Thanks to the National Astrophysics and Space Science Programme (NASSP) organizers for making it possible to kick-start my journey into Astronomy by sponsoring my Honours and Masters studies.

This thesis has been funded by the National Research Foundation (NRF) via the South African Research Chair Initiative (SARChI) bursary program.

For Mom

Plagiarism Declaration

I, Elizabeth Naluminsa, know the meaning of plagiarism and declare that all of the work in this document, save for that which is properly acknowledged, is my own.

Signed by candidate

Contents

List of Figures

List of Tables

Chapter 1

Introduction

1.1 Background

Hydrogen gas is the most abundant element in the universe and provides the raw fuel for star formation. This fuel is either already existing as bound material within the galaxies (the interstellar medium, ISM) or is accreted from a galaxy's environment, which could be the intergalactic medium between galaxies or simply another galaxy's gas being stripped away.
Hydrogen mostly exists in its atomic form. The detection of the 21cm (HI) emission line of atomic Hydrogen by Ewen & Purcell (1951) and van de Hulst (1951) marked the long overdue birth of Radio Astronomy. Prior to this, continuum radiation was being detected from the Milky Way, however, the detection of line emission meant that the distribution and kinematics of the atomic Hydrogen gas in the universe could now be mapped. Furthermore, the HI distribution extends beyond the distribution of stars in a galaxy's disk (for example see Figure 1.1) and is instrumental in tracing the gravitational potential of galaxies (e.g. Bosma 1981, Sofue & Rubin 2001, de Blok et al. 2008, Swaters et al. 2009). The molecular form of Hydrogen gas (H_2) is the most abundant molecule, but its observation poses major challenges. Due to its lack of a permanent electric dipole moment, the molecule can not radiate at its rotational frequency, and any emission lines from transitions between its energy levels are either weak or only possible at temperatures higher than typical temperatures inhabited by interstellar H_2 (Leroy et al. 2009, Bolatto et al. 2013). However, H_2 distribution can be traced indirectly by CO (Lebrun et al. 1983). This opened the way for both the atomic and molecular components of the ISM to be studied, giving a more complete view of the ISM.

Accurate mapping of the distribution and kinematics of HI in galaxies is done using radio interferometry. Radio interferometer telescopes consist of arrays of several ($N \geq 2$) single-dish telescopes in order to increase the resolution of the telescope. A single dish telescope of diameter d has angular resolution $\theta \approx \lambda/d$, where λ is the wavelength of the light being observed. Given the long wavelengths of radio waves, the resolution of a radio telescope

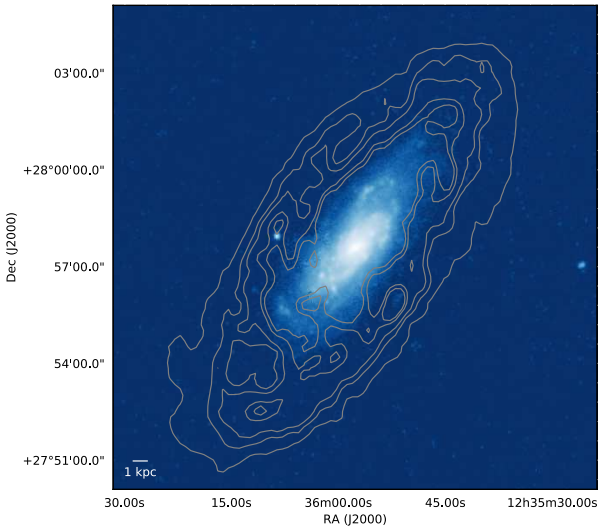

Figure 1.1: Distribution of neutral atomic hydrogen (contours) and stars (image) in the spiral galaxy NGC4559. Contour levels are 0.03, 0.06, 0.08, 0.12 and 0.14 Jy km/s. The HI gas in galaxies typically extends well beyond the disk of stars and is used to trace the gravitational potential of galaxies. The data used to make this image come from the Wide-field Infrared Survey Explorer 3.4 μm imaging (Wright et al. 2010, Jarrett et al. 2013) and the westerbork Synthesis Radio Telescope survey of HI in Irregular and SPiral galaxies (Kamphuis et al. 1996, van der Hulst et al. 2001).

is limited by the size of the dish. The largest single-dish radio telescopes are: The Five-hundred-meter Aperture Spherical Telescope (Nan et al. 2011) and The Arecibo telescope which have diameters $d \approx 500$ m and $d \approx 300$ m respectively. Observing the 21 cm line on these significantly large dishes yields angular resolutions on the order of arcminutes. In an interferometer, the effective diameter is equal to the longest baseline (distance D) between the dishes, thus having the resolution of a single dish with diameter D. For example, the Westerbork Synthesis Radio Telescope (WSRT), an array of 14 dishes with $d = 25$ m and a maximum baseline of $D = 3$ km, has a native angular resolution on the order of $10''$.
The Westerbork survey of HI in Irregular and SPiral galaxies (WHISP, Kamphuis et al. 1996, van der Hulst et al. 2001), was the first homogeneous mapping of HI in a large sample of galaxies (375) using radio interferometry. WHISP increased the size of homogeneously reduced HI observational data by an order of magnitude. The HI Nearby Galaxy Survey (THINGS, Walter et al. 2008) has so far achieved the highest spatial ($6''$) and spectral (≤ 5.2 km/s) resolutions for HI observations albeit with a much smaller sample of 34 galaxies. The Faint Irregular Galaxies GMRT Survey (FIGGS) on the Giant Metrewave Radio Telescope (Begum et al. 2008) carried out HI observations of the lowest mass and faintest

dwarf galaxies resulting in a sample of 65 dwarf irregular galaxies. Other surveys include the Westerbork Hydrogen Accretion in LOcal GAlaxies Survey (HALOGAS, Heald et al. 2011) which mapped gas accretion signatures in spiral galaxies and the Local Volume HI Survey (LVHIS, Koribalski et al. 2018) whose long-term aim is to map HI gas in all galaxies in the Local Volume, within a radius of 10 Mpc about the Local Group. Future surveys on state-of-the-art telescopes, e.g. the Meer Karoo Array Telescope (MeerKAT, Booth et al. 2009, Booth & Jonas 2012), the Australian Square Kilometre Array Pathfinder (ASKAP, Johnston et al. 2008) and the APERture Tile In Focus (APERTIF, Verheijen et al. 2008) system on the WSRT, will enable HI observations in very wide Field of View (FoVs) and combine high resolution with high sensitivity surpassing current Radio telescopes. Such surveys include the MeerKAT HI Observations of Nearby Galactic Objects - Observing Southern Emitters (MHONGOOSE, de Blok et al. 2016), the MeerKAT International GHz Tiered Extragalactic Exploration (MIGHTEE, Taylor & Jarvis 2016), the Widefield ASKAP L-Band Legacy All-Sky Blind Survey (WALLABY, Koribalski & Staveley-Smith 2009, Duffy et al. 2012), the Evolutionary Map of the Universe survey (EMU, Norris et al. 2011) and the APERTIF Westerbork Northern Sky HI Survey (WNSHS, Verheijen et al. 2010).
Surveys of the molecular Hydrogen in the ISM have also been made, most notably, the Five Colleges Radio Astronomy Observatory (FCRAO) Extragalactic CO Survey (Young et al. 1995) which covered a sample of 300 galaxies, the Berkeley Illinois Maryland Association Survey Of Nearby Galaxies (BIMA-SONG, Helfer et al. 2003) which mapped CO in 44 galaxies at $6''$ resolution. The BIMA-SONG was the first systematic survey of CO with spatial resolution scales of Giant Molecular Clouds. Most recently, the HEterodyne Receiver Array CO Line Extragalactic Survey (HERACLES, Leroy et al. 2009) made the first full-disk mapping of CO across the entire optical disk for 48 galaxies while the ATLAS 3D project carried out a single dish survey of CO in 260 early type galaxies (Young et al. 2011) and an interferometric CO survey on 30 galaxies (Alatalo et al. 2013). A major challenge facing the use of CO as a tracer for H_2 is the variability of the CO - H_2 conversion factor, which has been shown to change in different environments depending on metallicity (e.g. Bolatto et al. 2013).

One of the results of mapping gas in galaxies has been the ability to study scaling relations between the star formation and ISM properties of galaxies. Such empirical relations provide critical constraints in models of galaxy evolution (e.g. Davis et al. 1985, Boissier & Prantzos 1999, Firmani & Avila-Reese 2000, Lia et al. 2002, Hatton et al. 2003, Springel et al. 2005, Klypin et al. 2011, Schaye et al. 2015, Li et al. 2017, Davé et al. 2017).

1.2 Star Formation

The importance of star formation in galaxy evolution can not be overstated and is the driving force behind a multitude of efforts to study and understand the underlying physics and properties of star formation in galaxies. Star formation (SF) not only results in the consumption of gas in galaxies, but also to the production of heavy elements and enriching of the

ISM with these elements. Stellar winds and supernovae also inject energy into the ISM and strong outflows can result into heavy elements being added into the galaxy's environment (e.g. de Blok et al. 2015). In observations, the SF is studied by tracing young hot stars using observable properties called star formation rate (SFR) indicators. SFR indicators span the entire electromagnetic spectrum, some more effective than others. A summary of the most commonly used indicators is given below, based on the reviews of Kennicutt (1998a), Kennicutt & Evans (2012), and Calzetti (2013).

Direct emission from hot young stars ($\leq$ 100 Myr) (Hao et al. 2011) is observed in the far ultraviolet wavelengths (1250 Å - 2500 Å). For nearby galaxies at redshifts $\leq$ 0.5, the FUV indicator is only observable in space (Kennicutt 1998a). Several FUV observations have been done with space telescopes in the past, for example on the Hubble Space Telescope (e.g. Meurer et al. 1995, Maoz et al. 1996) and most recently using the Galaxy Evolution Explorer satellite (GALEX, Martin et al. 2005). At optical wavelengths, the most widely used indicator is the Hydrogen recombination line at λ6563 Å (H_α) due to excitation of the Hydrogen atoms by ionizing UV radiation from young stars. Examples of major surveys that have been done using H_α include the Gassendi H_α survey of SPirals (GHASP, Garrido et al. 2002, Epinat et al. 2008) and the Isaac Newton Telescope Photometric H_α Survey of the Northern Galactic Plane (IPHAS, Drew et al. 2005). The Oxygen emission line [OII] λ3727 Å and the H_β(4861 Å) Hydrogen recombination line also trace SFR but given large related uncertainties and dust attenuation, they are not as widely used as the H_α indicator. Dust grains surrounding star forming regions absorb UV photons from these regions and re-emit at infrared wavelengths. Infrared SFR indicators thus trace light that has been re-processed by dust.

SFR calibration in the IR is done by tracing dust heated by young stellar populations using either the total infrared luminosity (L_{TIR}) across the wavelength range 5 - 1000 μm, or monochromatic indicators. Successful missions in monochromatic infrared bands include the 12 μm, 25 μm, 60 μm and 100 μm bands of the Infrared Astronomical Satellite (Neugebauer et al. 1984), the 7 μm and 15 μm bands of the Infrared Space Observatory (Kessler et al. 2003), the 8 μm, 24 μm and 70 μm bands of the Spitzer Space Telescope (SST, Werner et al. 2004), the Herschel Space Telescope's 70 μm band (Pilbratt et al. 2010), and the Wide-field Infrared Survey Explorer (WISE) 11.6 μm (W3) and 22.8 μm (W4) bands (Wright et al. 2010, Jarrett et al. 2013). It has also become common practice to combine FUV/optical and IR indicators to form the so-called hybrid indicators in order to account for both dust-obscured and unobscured star formation. For example, the $L_{H_\alpha+24\mu m}$ (Kennicutt et al. 2007, Calzetti et al. 2007, Bolatto et al. 2011, Jameson et al. 2016) and $L_{FUV+24\mu m}$ (Bigiel et al. 2008, Salmi et al. 2012, Williams et al. 2018). This is because emission at UV and optical wavelengths is susceptible to attenuation due to dust absorption, hence they suffer dust-obscuration which is not a limitation for the IR-based SFR indicators. The $\sim$ 24 μm band is widely used because it does not trace stellar continuum, which peaks at shorter IR wavelengths, or dust heated by older stellar populations,

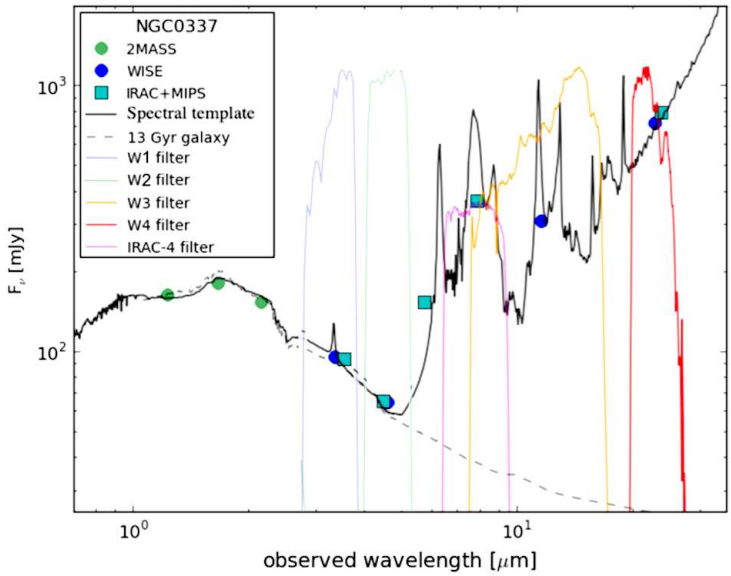

Figure 1.2: Figure from Cluver et al. (2017) showing the WISE spectral response function superimposed on the infrared spectral energy distribution of a star-forming late-type spiral galaxy NGC 337. The yellow curve illustrates the 11.6 μm (W3) band which spans several emission features namely; PAH emission at 7.7 μm and 8.5 μm, silicate absorption at 10 μm, PAH emission at 11.3 μm and Neon nebular emission lines 12.8 μm [Ne II] and 15.6 μm [Ne III]. Warm dust continuum was found to be the dominant contributor to W3 flux, over the PAH and nebular emission lines, with an average contribution of 34% from all PAHs and specifically 7.5% from the 11.3 μm PAH feature (Cluver et al. 2017).

which peaks at longer wavelengths, (Calzetti 2013, Cluver et al. 2017). The indicator used in this study is the WISE 11.6 μm band, and we give a brief review of it below based on the recent work of Cluver et al. (2017).

The WISE 11.6 μm (W3) and 22.8 μm (W4) bands are ISM tracing bands that are well suited as SFR indicators (Jarrett et al. 2013, Cluver et al. 2017). While the W4 band is dominated by warm dust continuum just like the 24 μm band of the SST, the W3 band (11.6 μm) is wide and canvasses several sources of emission, (See Figure 1.2). Centered on the Polycyclic Aromatic Hydrocarbon (PAH) emission feature at 11.3 μm, W3 also encompasses PAH features at 7.7 μm and 8.5 μm, nebular emission lines of Neon, [Ne II] and [Ne III] at 12.8 μm and 15.6 μm as well as a silicate absorption feature at 10 μm (Cluver et al. 2017). However, in spite of all the emission features in the W3, the dominant flux source in this band is continuum from warm dust grains (Cluver et al. 2017). Furthermore, Cluver et al. (2017) also showed that the W3 band's ability to sample a range of excitation sources was well depicted by the tight correlation between the 11.6 μm luminosity and the total infrared luminosity (L_{TIR}). The W3 emission may also trace the central HI in some galaxies, as has been shown for the spiral galaxy M83 (Jarrett et al. 2013) (see Figure 1.3).

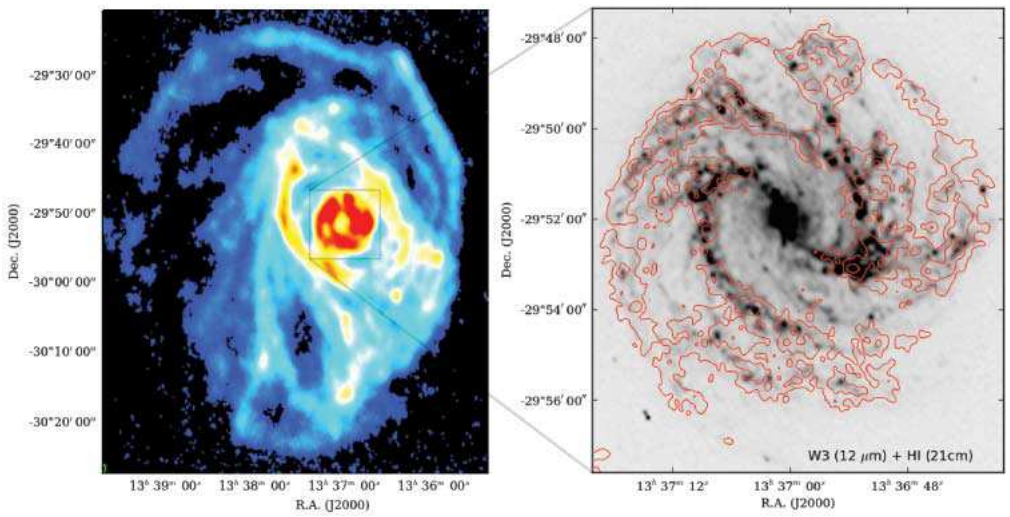

Figure 1.3: This figure from Jarrett et al. (2013) shows the HI distribution of the spiral galaxy M83 and the WISE 11.6 μm emission which traces star formation (7″ resolution). The left panel shows the HI intensity map, while the right panel shows a grayscale 11.6 μm map of the central region overlaid with contours of the HI (contour levels 0.1, 0.27, 0.43 and 0.6 Jy/beam km/s) in the same region. The HI data were a combination of data from the Australian Telescope Compact Array (∼10″ resolution) and the Parkes Observatory 64 m radio telescope. This figure shows the possibility of the 11.6 μm flux to trace the high column density HI in the central regions of galaxies.

1.2.1 Star Formation Laws

The treatment of star formation rates and efficiencies is critical to models of galaxy evolution. Several models of SF are used in galaxy formation simulations, the most common of these being the Kennicutt-Schmidt (KS) law (Kennicutt 1989; 1998b). Schmidt (1959) parametrized the relationship between star formation and interstellar gas in a galaxy as a power law;

$$SFR \;=\; a\rho_g^n, \tag{1.1}$$

where ρ_g is the total gas volume-density, a a proportionality constant and n the power law index (with $1 \leq n \leq 2$). Given the complexity of measuring the three-dimensional size scales of galaxies, Kennicutt (1989) proposed a modified Schmidt law based on observable quantities rather than volume densities. The KS law thus defines a power-law relationship between the global average surface densities of gas and star formation rate in galaxies, and is given by

$$\Sigma_{\rm SFR} \;=\; {\rm A}\Sigma_{\rm g}^{\rm N}, \tag{1.2}$$

where $\Sigma_{\rm SFR}$ is the star formation rate surface density (in $M_\odot$ yr^{-1} kpc^{-2}), $\Sigma_{\rm g}$ is the gas surface density (in $M_\odot$ pc^{-2}) and A is a constant of proportionality. Kennicutt (1989) and Kennicutt (1998b) found index N = 1.4±0.15. However, over the years, different studies have found varying values of N. Most notably, it has been shown that the value of N is

closer to 1.0 when the surface density of molecular Hydrogen gas (as traced by CO) is used instead of the total gas surface density, especially in molecule-rich ISM conditions such as the central regions of spiral galaxies or in molecule-rich spiral galaxies (e.g. Wong & Blitz 2002, Bigiel et al. 2008, Leroy et al. 2013, Dessauges-Zavadsky et al. 2014). Studies such as Boissier et al. (2003), Bigiel et al. (2008), Schruba et al. (2011), Calzetti et al. (2018) have also shown that there is, at best, a nonlinear power law relationship between $\Sigma_{\mathrm{HI+H_2}}$ and Σ_{SFR} with a higher index N $\approx$ 2.0. This is attributed to the weak relationship between Σ_{HI} and Σ_{SFR} because stars form from collapsing clouds of molecular Hydrogen. Still, the atomic gas does have a connection to the SFR and it has been shown that reduction in the amount of HI in galactic disks will suppress the SF (Rownd & Young 1999, Bekki et al. 2002, Fumagalli & Gavazzi 2008) because HI is the fundamental fuel for star formation, and H_2 is formed from cold HI clouds. Wang (1990) and Wong & Blitz (2002) suggested that the KS law may in fact be a combination of two laws, the first governing the conversion of HI into H_2, and the second defining the collapse of H_2 into stars. More recently, there has also been renewed interest in the volumetric Schmidt-type star formation law which considers the volume-densities of the gas and SFR (Krumholz et al. 2012, Evans et al. 2014). Indeed Krumholz et al. (2012) showed that a simple power law between the volume-densities of SFR and gas matches observed data from small scale clouds of mass 10^3 $M_\odot$ to global scales of galaxies with mass 10^{11} $M_\odot$. In spite of the complexities involved in deriving three-dimensional scale measures of galaxies, volume-densities are more physically meaningful and representative of the conditions averaged over by line-of-sight measurements Bacchini et al. (2018). However, there is evidence to support that the global average SFR correlates with the mass of HI in a galaxy's disk, as has been shown by different studies, e.g. Cluver et al. 2010, Michałowski et al. 2015 and as later shown for WHISP galaxies in this thesis.

In addition to studying the global KS law, authors in the field are also studying the KS law at resolved scales within individual galaxies (Heyer et al. 2004, Kennicutt et al. 2007, Bigiel et al. 2008, Liu et al. 2011, Kim et al. 2013, Roychowdhury et al. 2015, Calzetti et al. 2018). In these sub-galactic scale studies, it has been found that the KS law breaks down at scales of 100 pc, which is about the size of giant molecular clouds (GMCs), the sites of star formation by gravitational collapse. In fact, Williams et al. (2018) showed that the index N increases at progressively smaller physical scales until the KS relationship completely breaks down at GMC scales, regardless of whether atomic gas, molecular gas, or total gas is considered. Inside the GMC complexes, H_2 over-dense sub-regions collapse under their own gravity until temperatures at the cores are adequate for hydrogen fusion such that protostars are born (Williams et al. 2000). The break down of the KS law at these scales has been partly attributed to migration of the stellar cores from their parent GMCs or ionization of the surrounding neutral Hydrogen by UV radiation coming from the young stars. On larger scales (kpc and global) as well, observations have shown that the KS law becomes steep, implying a possible break down, in HI-dominated regions such as the low gas density ($\leq$10 $M_\odot$ pc^{-2}) environments in the outer radii of spirals and in dwarf galaxies (Kennicutt 1989, Bigiel et al. 2010, Dessauges-Zavadsky et al.

2014, López-Sánchez et al. 2018). This led studies to actively investigate the theory of SF thresholds in more depth (Kennicutt 1989, van der Hulst et al. 1993, Hunter et al. 1998, Martin & Kennicutt Jr. 2001, Boissier et al. 2003, Schaye 2004, de Blok & Walter 2006, Leroy et al. 2008, Romeo & Falstad 2013, Romeo & Mogotsi 2017, Marchuk 2018).

1.2.2 Star Formation Thresholds

Star formation happens via collapse of dense cores of molecular clouds. The first attempt to describe the initial conditions preceding the collapse of a gas cloud was done by Jeans (1902). The Jeans criterion defines the minimum size for a spherical gas cloud of mean density ρ to be stable against gravitational collapse (the Jeans length) as;

$$\lambda_J \;=\; \left(\frac{\pi\sigma^2}{G\rho}\right)^{0.5}, \tag{1.3}$$

where σ is the velocity dispersion of the particles inside the cloud and G is the gravitational constant. The Jeans criterion provided valuable insights into the importance of thermal motions and gas density in gravitational stability. However, it neglected the role of rotation and turbulence. Chandrasekhar (1955) and Bel & Schatzman (1958) derived generalizations for the Jeans criterion to account for rotation, albeit for systems that were ideally infinite along the axis of rotation. Adaptation of the Jeans criterion to disk-like systems (representative of a typical galaxy) was first attempted by Safronov (1960).

Following the work of Safronov (1960) on the gravitational stability of thin disk-like systems, Toomre (1964) defined a criterion for the susceptibility of a thin disk of stars to large scale gravitational instabilities. The Toomre criterion (also referred to as the single-fluid disk stability criterion) considers the stabilizing effects of differential rotation and gas dispersion (see for example Figure 1.5) against changes in the gravitational potential energy due to radial perturbations in the system, and is defined as

$$Q \;=\; \frac{C_s\kappa}{3.36G\Sigma} \;<\; 1, \tag{1.4}$$

where C_s is the sound speed in the disk medium, Σ the surface density of the disk and κ is the epicyclic frequency, defined thus: When a particle in a circular orbit is displaced radially, it will move into an elliptical orbit such that its distance from the center of the orbit oscillates about its original mean orbital distance (see Figure 1.4). The frequency of these oscillations is the epicyclic frequency and is given by;

$$\kappa \;=\; \left[2\left(\frac{\mathrm{V_r^2}}{\mathrm{r^2}} \;+\; \frac{\mathrm{V_r}}{\mathrm{r}}\frac{\mathrm{dV_r}}{\mathrm{dr}}\right)\right]^{0.5}, \tag{1.5}$$

where $\mathrm{V_r}$ is the rotational velocity of the particle and r is its mean orbital distance.

The existence of gas density thresholds to star formation in galaxies was first investigated by Spitzer (1968) and Quirk (1972). Later authors have used the Safronov -Toomre criterion

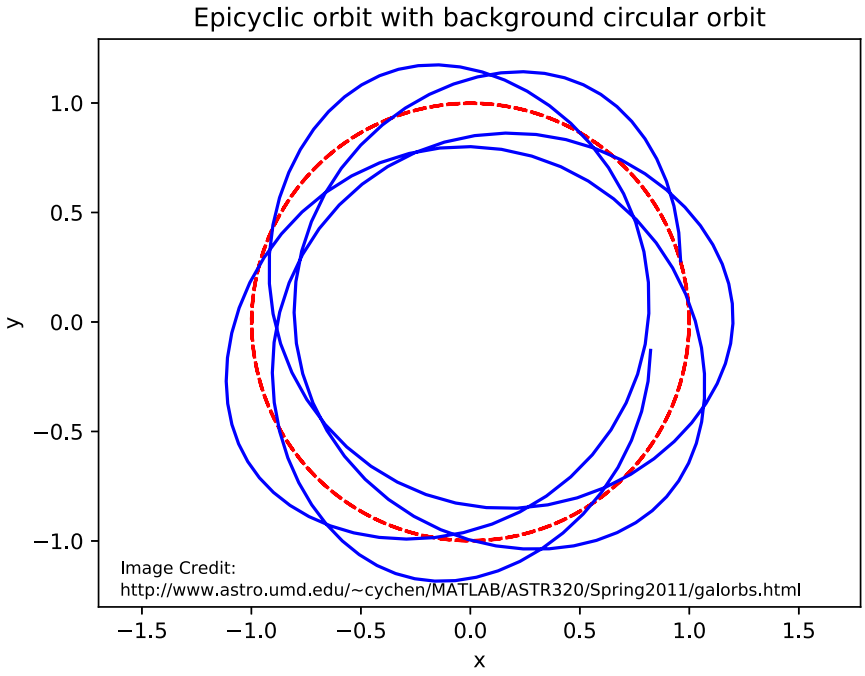

Figure 1.4: Illustration of epicyclic orbits. A particle in a circular orbit about a center of mass will begin to define elliptical orbits (epicycles) when displaced by a radial force. In elliptical orbit, the distance of the particle oscillates about its mean unperturbed orbital distance. The frequency of these oscillations is called the epicyclic frequency (κ).

to study the stability of galactic disks in relation with observed star formation thresholds. The seminal study of Kennicutt (1989) adapted the Toomre criterion to gas disks as

$$Q \;=\; \frac{\sigma_g \kappa}{\pi G \Sigma_g} \;<\; 1, \tag{1.6}$$

where σ_g is the velocity dispersion of the gas, κ is the epicyclic frequency and Σ_g is the gas surface density. In neutral equilibrium the gravitational pull (denominator) is in balance with the pressure forces (numerator) and Q=1 such that the critical density above which gravitational instabilities form in the gas disk is defined as;

$$\Sigma_c \;=\; \alpha \frac{\sigma_g \kappa}{\pi G}, \tag{1.7}$$

where α is a constant that allows for deviation of a real galactic disk from the ideal theoretical thin gas disk for which $\alpha = 1$. From his sample of star-forming galaxies, Kennicutt (1989) defined $\alpha = 1/Q$ at the observed threshold radius of star formation.

The ability of the simple Toomre Q criterion to predict thresholds for large scale star formation was shown in external galaxies (Kennicutt 1989, van der Hulst et al. 1993, Martin & Kennicutt Jr. 2001) and the Milky Way(Boissier et al. 2003). However, several authors have questioned

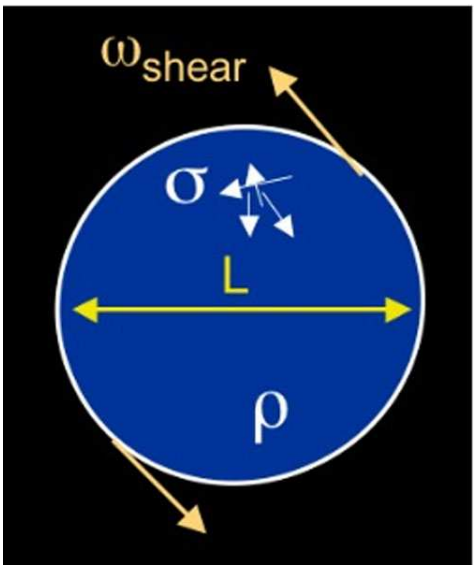

Figure 1.5: Illustration of the factors at play in the Toomre criterion. The action of the velocity dispersion (σ) and the rotation which provides shear prevent the growth of instabilities within the fluid. Short wavelength perturbations are stabilized by the σ while long wavelength perturbations are stabilized by the shear. If the pressure forces are inadequate to stabilize the perturbation, the gas becomes susceptible to gravitational collapse due to growth of instabilities. Image Credit: https://ned.ipac.caltech.edu/level5/March11/Bournaud/Bournaud2.html

its applicability, for example, citing that instead the star formation thresholds are more dependent on other instabilities such as due to spiral density waves (Hunter et al. 1998), or citing the existence of large scale star formation despite the sub-critical gas densities in the inner disks of some galaxies as proof that the $\Sigma_g > \Sigma_c$ is not a necessary condition for star formation, (Thornley & Wilson 1995, Wong & Blitz 2002, Leroy et al. 2008).
The single-fluid thin disk consideration assumes that the collapse of gas is solely driven by instabilities in the gas disk, with no reference to the stars present in a galaxy's disk (see Figure 1.6). However, Jog & Solomon (1984a) showed that in fact the existence of two-fluid instabilities in a galactic disk can cause instabilities in the individual component fluids (i.e. the stars and gas treated as two different fluids with different velocity dispersions).

Jog & Solomon (1984b) studied the dynamics of a two-fluid system of gas and stars to determine the response of the system to perturbations that arise from the interaction between the two component fluids. They found that even when each individual fluid is stable by itself, the interactions of the two fluids can lead to two-fluid instabilities in the system. The growth of the perturbations is governed by the fluid dispersion velocities, their surface densities and the wavenumber of the perturbation. They went on to show that once the two-fluid instabilities are formed they can induce the formation of single-fluid instabilities in the gas by amplification of the gas density locally, concluding that the instability of a two-fluid system can precede star formation in that way. The condition for growth of two-fluid

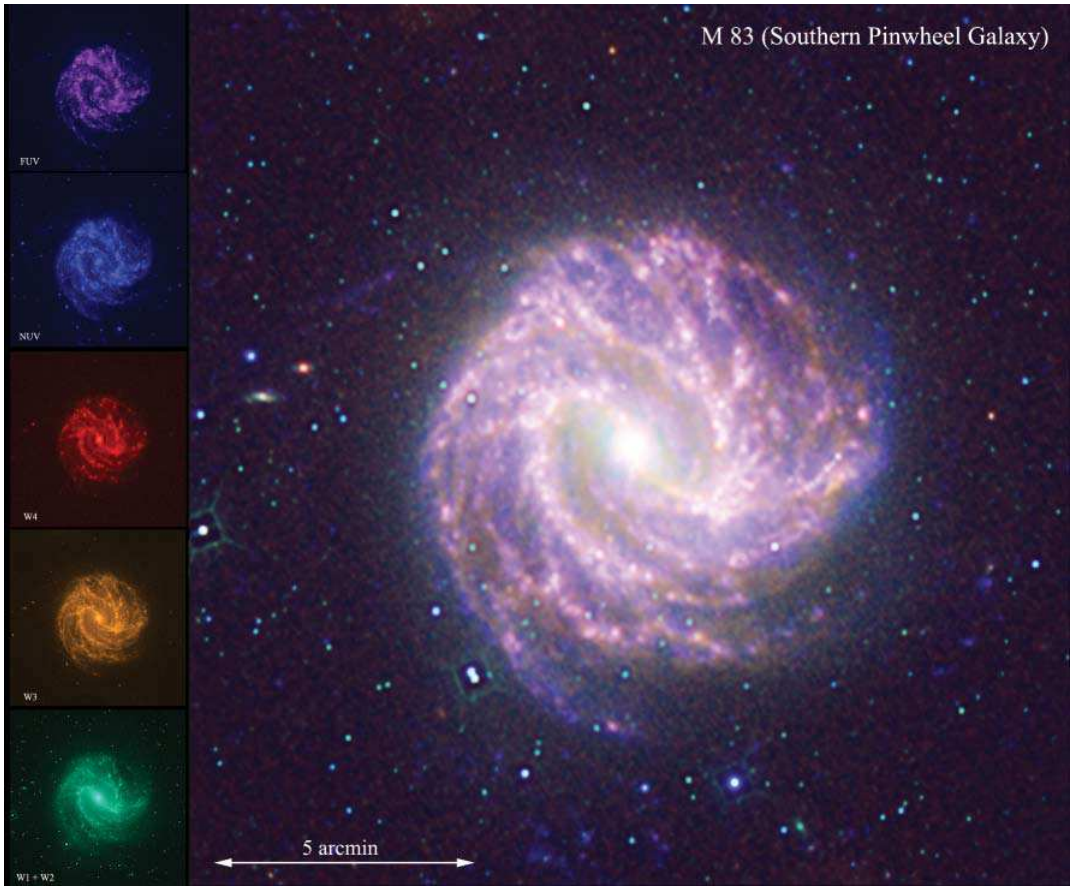

Figure 1.6: This composite image of the spiral galaxy M83 from Jarrett et al. (2013) illustrates the stellar component of this galaxy. The image is a composite of the inset images obtained at different windows of the electromagnetic spectrum; the far ultraviolet (FUV), the near ultraviolet (NUV), the WISE 22.8 μm (W4), WISE 11.6 μm (W3) and a combination of the WISE 3.4 μm and 4.6 μm bands (W1+W2). The first four windows trace the young stellar population while the W1 and W2 trace the older stellar population. A typical galaxy disk contains both stars and gas. The approximation of a gas-only disk in studies of gravitational instability overlooks the contribution of the stars to the gravity budget of a typical galaxy's disk.

instabilities in a two-fluid disk was defined as;

$$\frac{2\pi G k \Sigma_{*,o}}{\kappa^2 + k^2\sigma_*^2} \; + \; \frac{2\pi G k \Sigma_{g,o}}{\kappa^2 + k^2\sigma_g^2} \; > \; 1, \tag{1.8}$$

where κ is the epicyclic frequency of the fluid particles, k is the wavenumber of the fastest growing (and hence most unstable) perturbation, σ_*, σ_g are the velocity dispersions of the stars and gas respectively, and Σ_*, Σ_g are their unperturbed surface densities.
Rafikov (2001) studied the gravitational perturbations in multicomponent disks, treating the stellar component as collisionless and came to similar results as Jog & Solomon (1984b), reformulating the two-fluid instability criterion as;

$$\frac{1}{Q_T} \; = \; \frac{2}{Q_*}\frac{q}{1+q^2} \; + \; \frac{2}{Q_g}R\frac{q}{1+q^2R^2} \; > \; 1, \tag{1.9}$$

where Q_* and Q_g are the single-fluid Toomre stability parameters for a disk of stars and gas separately, $R = \sigma_g/\sigma_*$, and $q \; = \; k\sigma_* \; /\kappa$. *The Rafikov formulation of the two-fluid instability criterion (Equation 1.9) was used to study the star formation thresholds for a chosen sample of galaxies in this thesis.*
A different formulation for the two-fluid instabilities was proposed by Wang & Silk (1994) as;

$$\frac{1}{Q_{WS}} \; = \; \frac{1}{Q_*} \; + \; \frac{1}{Q_g} \; > \; 1, \tag{1.10}$$

such that the critical density for instabilities to form is,

$$\Sigma_c \; = \; \frac{\kappa\sigma_g}{\pi G}\left(1 \; + \; \frac{\Sigma_*\sigma_g}{\Sigma_g\sigma_*}\right)^{-1}. \tag{1.11}$$

Owing to its simplicity, the Wang and Silk formulation has been used by several authors to study disk stability thresholds to star formation (for example Martin & Kennicutt Jr. 2001, Boissier et al. 2003, Elmegreen 2011, Wong et al. 2016). However, it has also been criticized for being an over-simplistic approximation of the dynamics in a disk of two interacting fluids (Jog 1996). It was also shown to yield lower values of the two-fluid stability parameter by Romeo & Wiegert (2011) who improved on it by adding corrections to account for finite thickness of the disk (which increases the stability of the component fluids) and the combined effect of the velocity dispersions of the two fluids. We do not use the Wang & Silk formula in this study, but we do compare our results with results from other studies that made use of it.

1.3 Thesis Aims

1.3.1 Problem Statement

The fundamental goal of astrophysical studies is a better understanding of the origins and evolution of our universe. Both theoretical and observational works are geared towards constructing a solid picture of the processes involved in the formation of cosmic structures. This involves pursuing accurate models of galaxy formation and evolution. Galaxy evolution itself is hinged on the process of star fomation which results in the consumption of gas and chemical enrichment of the ISM (Boissier & Prantzos 1999), therefore both chemical and physical evolution models are governed by the scaling relations and properties of SF in galaxies (e.g. Boissier & Prantzos 1999, Lia et al. 2002, Davé et al. 2017).

The standard model of the universe is the lambda cold dark matter (ΛCDM) framework, in which the universe is made up of 70.1% dark energy, 25.1% dark matter, and only 4.8% visible matter (DES Collaboration et al. 2017). Within this framework, dark matter clumps in the early universe form halos which attract baryons into their potential wells, creating the stage for formation of galaxies in these halos. A major success of this construction is its ability to account for the large scale structure distribution of galaxies (Davis et al. 1985, Somerville & Davé 2015, Bullock & Boylan-Kolchin 2017). However, the model faces challenges at smaller scales such as over-estimation of the number of low-mass galaxies and dwarf satellite galaxies (Bullock & Boylan-Kolchin 2017), under-estimation of the number of dwarf ellipticals in dense environments (Kroupa et al. 2010), the 'missing baryons problem' where the fraction of baryons in the universe is observed to be less than what is predicted, and the famous 'cusp-core problem' where ΛCDM predicts a steep rise in the central density of dark matter halos (cusp) contrary to observations which show a constant density (core) (Flores & Primack 1994, Navarro et al. 1996). Energy feedback into the ISM is usually invoked to reconcile models with observations (Davé et al. 2017). However, critical factors such as ISM structure, SF and feedback (e.g. from stellar winds, supernovae and Active Galactic nuclei) are not resolved in cosmological simulations and are hence modeled using sub-grid recipes (Springel et al. 2005, Somerville & Davé 2015), the parameters of which may be adjusted to match a given observation.

Therefore, despite its importance, SF is one of the least understood processes in galaxy evolution owing to several reasons, not least of which is that the processes that regulate SF vary from small scales (collapse of self-gravitating gas clumps) to large galaxy-wide scales (gas accretion or expulsion) and may interact with each other in ways that are not yet fully understood (Kennicutt & Evans 2012). The Toomre gravitational stability criterion has been used extensively to predict collapse of gas preceding SF. Since the basic Toomre criterion only considers a single-fluid (gas) disk, other studies have attempted to study a modified stability criterion which accounts for the co-existence of the gaseous and stellar components within a real galactic disk - hence the two-fluid disk criterion. The formulation of Wang & Silk (1994) (Equation 1.10) is the most commonly used two-fluid disk criterion

because of its simplicity, although as described above, it oversimplifies the interaction between the stellar and gaseous disks. The Rafikov (2001) formulation (Equation 1.9) is less often used because it requires derivation of the wavenumber of perturbations in the two-fluid system. However, it has a more robust description of the kinematics of a two-fluid system (Leroy et al. 2008, Marchuk 2018).

Two facts stand out from the literature:

1. A majority of the studies, for both the single-fluid and two-fluid approximations, have investigated the radial variation of the stability parameters (e.g. Kennicutt 1989, Thornley & Wilson 1995, Wong & Blitz 2002, Martin & Kennicutt Jr. 2001, Boissier et al. 2003, Leroy et al. 2008), and only a few have considered the two-dimensional variation (e.g. Marchuk 2018). Studies of the radial variations of the parameters have not come to a consensus on whether or not the single-fluid disk criterion is applicable to large scale SF, but there is a general understanding that it ought to apply in dwarf galaxies where the gas fractions are high. On the other hand, studies of the radial variation of the two-fluid parameter generally agree that it presents a sufficient but not necessary threshold for the onset of star formation. On studying the two-dimensional variation of the two-fluid disk stability parameter, Marchuk (2018) found that it adequately predicts the location of star forming regions in NGC 628. Furthermore, they showed that azimuthal averaging (use of radial profiles) returns stable disks and they hence advocate for the use of 2D maps in such analyses due to the clumpy nature of star forming gas.
2. With exception to Leroy et al. (2008) and Marchuk (2018), most of the studies that investigate the two-fluid parameter have preferred the Wang & Silk (1994) formulation.

The motivation for this thesis is, therefore, borne out of the need to contribute to the study of the 2D variation of gravitational stability parameters, and the use of the Rafikov (2001) formulation in derivations of two-fluid disk instabilities in galaxies. The gas distribution as traced by HI *will be compared to the distribution of star formation as traced by the MIR emission.*

1.3.2 Goal

The goal of this thesis is to study the gravitational stability of star forming disks and compare how well the Toomre stability parameter and the two-fluid stability parameter predict the MIR emission from star forming regions.

1.3.3 Strategy

To achieve the goal of this thesis, five measurable objectives were pursued;

1. Use data from the WHISP survey to derive HI data products with as minimum noise as possible. Carried out on the WSRT, WHISP presents a state of the art data-set with good spatial resolution (30″) and sensitivity (100 mJy) that is suitable for studies of star formation, and large enough for statistics.

2. Use the derived HI data products and available IR derived properties to study scaling relations between the global HI properties and star forming properties of the galaxies. Additionally, investigate the relationship between the surface densities of star formation rate and HI gas on both global and resolved scales.

3. Define a sub-sample suitable for a resolved study of the individual disks and derive the Toomre stability parameter of the atomic gas disk for this sub-sample using the surface density, velocity dispersion and rotation curve of HI. CO are available for only three galaxies in our sample, and so their Toomre parameters are derived using their total gas surface densities ($\Sigma_{\rm HI+H_2}$).

4. Derive the two-fluid stability parameter for a disk of gas+stars, utilizing the atomic gas surface density, $\Sigma_{\rm HI}$ (or total gas $\Sigma_{\rm HI+H_2}$ where applicable) and stellar surface density (Σ_*) derived from WISE 3.4 μm imaging of the stellar disks for the same sample of galaxies.

5. Generate maps of the star formation rate surface density using the WISE 11.6 μm imaging, and investigate how well the gravitational stability parameter and measured gas surface density can predict the star formation rate. Some open questions that are tackled include: (a) How well does the Toomre parameter for an atomic gas disk predict the location of the SF as traced by the mid-infrared emission? (b) What is the difference between a Toomre parameter based on $\Sigma_{\rm HI}$ and one based on $\Sigma_{\rm HI+H_2}$? (b) How well does the two-fluid-disk stability parameter predict star formation in galaxy disks, both on large scales and locally? (d) Do the predictions of the Toomre parameter echo the predictions of the two-fluid parameter on resolved scales? (e) Are the gravitational stability criteria necessary conditions for occurrence of star formation in galactic disks?

1.4 Thesis Outline

Chapter 2 presents descriptions of the WHISP and WISE data that were used in this study, and detailed descriptions of how HI data products were derived. An atlas of the generated data products is given in Appendix A. The global properties of the HI disks, their star formation properties and scaling relations are presented in Chapter 3 and compared to similar samples in the literature. In Chapter 4, we describe the derivation of the gravitational stability models and star formation rate surface densities. In the same chapter, we present an analysis and discussion of the results in line with the guiding questions stated above. Note that the WISE data and CO data had to first be fit to the resolution and astrometric grid of the WHISP data; Details of this process for the CO data are given in Chapter 4 while the details for the WISE data are given in Appendix B. Chapter 5 presents a summary of the discussions, concluding remarks and an outline of possible future work.

Chapter 2

Data and Measurements

This study makes use of HI line observations to trace the gas component of the galaxies and uses infrared imaging to study the stellar mass as well as star formation properties. The data are obtained from two main surveys, namely the WHISP survey and the WISE survey.

2.1 The WHISP survey

The Westerbork survey of HI in Irregular and Spiral galaxies (WHISP, Kamphuis et al. (1996), van der Hulst et al. (2001)) was a project carried out using the Westerbork Synthesis Radio Telescope (WSRT) to map the distribution and kinematics of atomic Hydrogen in a large sample of nearby galaxies. A synthesis telescope utilizes the technique of interferometry by combining signals from several individual telescopes to produce images of high angular resolution equivalent to that of a single dish telescope with an aperture equal in diameter to the maximum baseline between the antennas. The first survey of its size on a synthesis telescope, WHISP imaged a total of 400 galaxies thus availing a rich sample of uniformly reduced data that spans a wide range of morphologies (lenticulars to early-type and late-type spirals as well as late-type dwarfs, see Figure 2.1), masses and environments (van der Hulst et al. 2001, Swaters 1999, hereafter S99). It hence presents researchers with a database that is well-suited for detailed studies of individual galaxies as well as statistical studies of galaxy properties such as the distribution, dynamics and kinematics of HI.

The WHISP sample was derived from the Uppsala General Catalogue (Nilson 1973) for all galaxies whose optical B band diameters are larger than $1.5'$, dec $> 20°$, and HI flux densities higher than 100 mJy in the Third Reference catalogue of Bright Galaxies (RC3, de Vaucouleurs et al. 1991). These were mainly observed in 12 hour observations at the WSRT full resolution of 14" x 14"/$\sin\delta$ (Swaters et al. 2002) and velocity resolutions of 2.1 km s^{-1} (with 127 channels), 4.1 km s^{-1} (with 127 channels), or 16 km s^{-1} (with 63 channels) depending on whether the known global profile width at W_{20} (20% the maximum intensity) was less than 100 km s^{-1}, between 100 km s^{-1} and 300 km s^{-1} or greater than

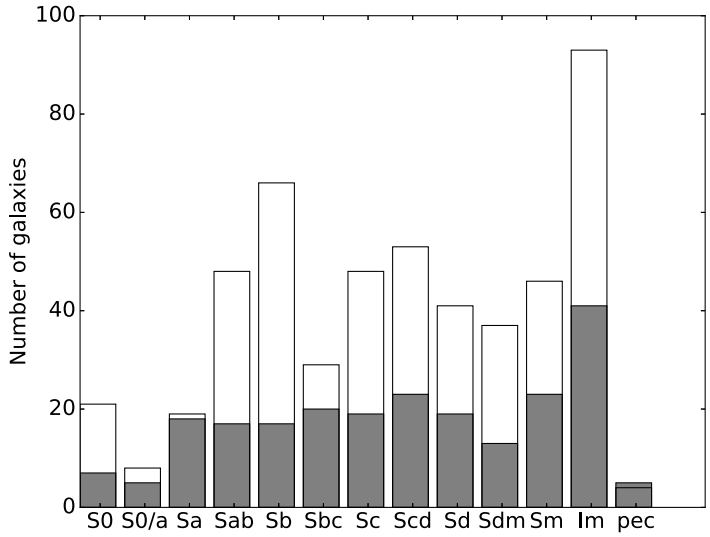

Figure 2.1: Distribution by morphology of the WHISP sample. The main sample used in this study (shaded area, 228 galaxies) fairly represents the entire WHISP sample (background unshaded histogram). The morphologies were obtained from the Third Reference of Bright Galaxies (RC3.9, de Vaucouleurs et al. 1991) via the NASA/IPAC Extragalactic Database (NED)*.

300 km s^{-1} respectively.

The WHISP reduction pipeline, detailed by Swaters et al. (2002), yields HI data cubes and moment maps at three resolutions; 14" x 14"/$\sin\delta$, 30"x 30" and at 60"x 60". A natural weighting taper type that uses all available data points was employed to Fourier transform the UV data to the image plane (Noordermeer et al. 2005). The HI intensity and velocity field maps of the spiral galaxy UGC7766 at the three WHISP resolutions are shown in Figures 2.2 and 2.3. These data are publicly available through the WHISP database.

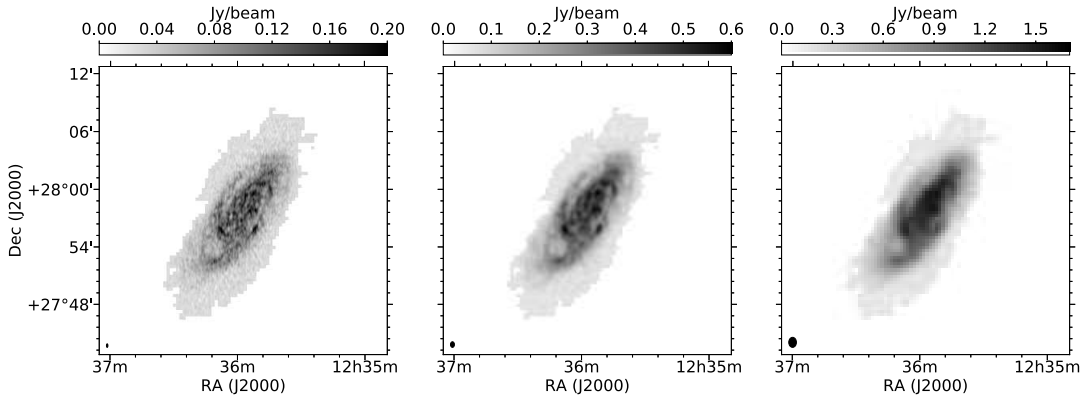

Figure 2.2: Three sets of data at three resolutions are provided via the WHISP database. Shown here, UGC7766 at the full resolution 14" x 14" $/\sin\delta$ (a), $30''$ (b), and $60''$ (c). Filled circles in the lower left corner of each panel show the corresponding beam sizes.

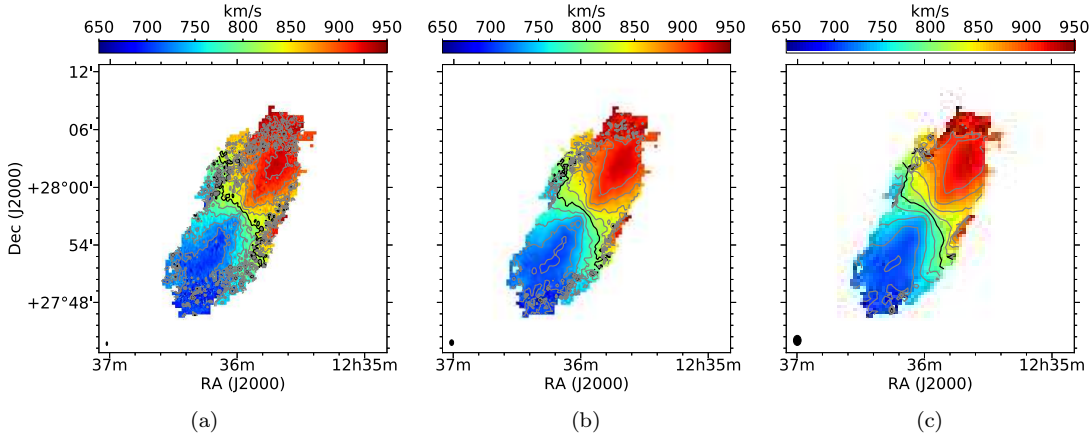

Figure 2.3: WHISP Velocity field maps of UGC7766 at the three WHISP resolutions as in Figure 2.2 above. The iso-velocity contours are spaced by 25 km s^{-1}, and the black contour marks the systemic velocity at 806.2 km s^{-1}.

2.2 The WISE Survey

The Wide-field Infrared Survey Explorer was a NASA funded mission that mapped point sources in the entire sky sensitive to point sources above 0.08, 0.11, 1 and 6 mJy in four infrared bands at 3.4μm,, 4.6μm, 11.6μm and 22.8μm (Wright et al. 2010). The four WISE bands are referred to as W1, W2, W3 and W4. The W1 and W2 bands trace the stellar component of galaxies while the W3 and W4 bands pick up line and continuum emission from the Polycyclic Aromatic Hydrocarbons and warm dust.

The WISE All-Sky Data release atlas (Cutri & et al. 2012) may be used for accessing WISE images and photometry. The WISE survey was targeted at point sources and hence

the calibration of the data was optimized for the detection of point sources. This involved interpolation and co-adding of multiple single exposure images which is not ideal for extended sources as the images get smeared out (Jarrett et al. 2012).
Jarrett et al. (2012; 2013) hence developed the WISE Enhanced Resolution Galaxy Atlas (WERGA), by enhancing the resolution of the All-sky Data Atlas from 8.4″, 9.2″, 11.4″ and 18.6″ to the WISE native resolution of 5.9″, 6.5″, 7.0″ and 12.4″ in the respective WISE bands.

The WERGA lists extended sources in the WISE field (which is all-Sky) thus enabling resolved studies of nearby galaxies in four infrared bands. Figure 2.4 illustrates the galaxy UGC7766 in all the four WISE bands, showing the sensitivity of the WISE bands to different galaxy components. We use W1 and W3 data in this thesis to investigate the star formation properties of WHISP galaxies. The W3 band was chosen over W4 because of its higher sensitivity (Cluver et al. 2014; 2017, see Table 2.7 here).

WISE data that include imaging, photometric measurements and derived properties, such as global star formation rates and stellar masses for all the galaxies were supplied by Jarrett et al. (2017).
Notable photometric parameters that are used in this thesis are;

1. $R_{\rm iso}$, the semi major axis of a 1σ isophote in the W1 image.
2. b/a, the axial ratio of this isophote.
3. pa, the position angle and,
4. $\Delta{\rm mag}_1$, $\Delta{\rm mag}_3$, the magnitude errors in the W1 and W3 bands.

The first three parameters are used in chapter 4 to define an elliptical region that demarcates the stellar disk, in which calculations of the enclosed stellar mass and star formation rates are made, while the magnitude errors are used to determine the signal to noise ratio of the observations (SNR = $1.0856/\Delta$mag). Conversion from magnitudes to flux is done using the flux zero points as below;

$$f_\nu(Jy) \;=\; f_o \;\times\; 10^{-W_\nu/2.5}, \tag{2.1}$$

where W_ν is the magnitude in a given WISE band, and f_o is the flux zero point in that band. The zero points are shown in Table 2.1 while Table 2.6, obtained from Jarrett et al. (2017), is a summary of the WISE properties of the sample.

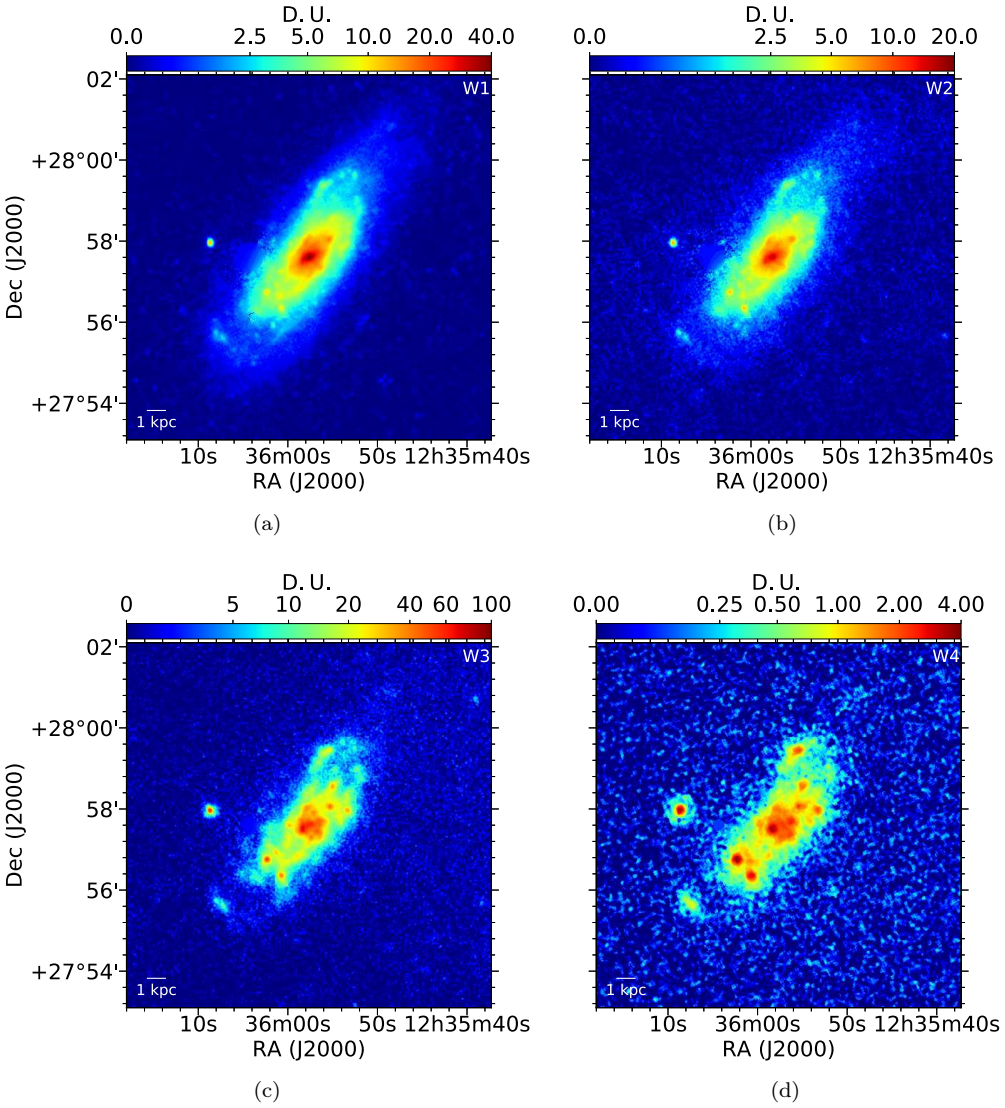

Figure 2.4: WISE images of UGC7766 in W1, W2, W3 and W4. Note that the sensitivity is different in each band, and each panel has been displayed using a different color scale. W1 and W2 trace the stellar disk component while W3 and W4 trace the star formation. The color-bar units (D.U. - Data Unit) are intensity units in the figures.

Table 2.1: WISE flux zero points (Wright et al. 2010).

Band	λ μm	f_o Jy
W1	3.6	306.681
W2	4.6	170.663
W3	11.6	29.045
W4	22.8	8.284

2.3 Neutral Hydrogen Data products and Measurements

The WHISP survey provides both data cubes and moment maps. However, new moment maps are generated here in order to foster more robust measurements of the global properties, and HI density maps which are used to generate the gas stability models in Chapter 4. In this section, I describe the sample selection and the methods that were employed to derive the HI data products.

2.3.1 The Sample

The sample used in this study was chosen from the WHISP 30″ resolution data which have higher sensitivity to low HI column density structures than the full resolution (14" x 14" /sin δ) data. Also, given the distance range 5 Mpc - 30 Mpc, where 70% of the sample falls (see Figure 2.5), the angular resolution of 30″ enables investigation of physical scales ∼1 kpc. Such spatial resolution enables us to study the physics of star forming disks without going down to sub-GMC scales where the Kennicutt-Schmidt star formation law is likely to break down due to offsets between the ionized gas tracing young stars and the neutral or molecular Hydrogen tracing the ISM (see for example Sheth et al. 2002, Bigiel et al. 2008, Onodera et al. 2010, Liu et al. 2011, Kim et al. 2013).

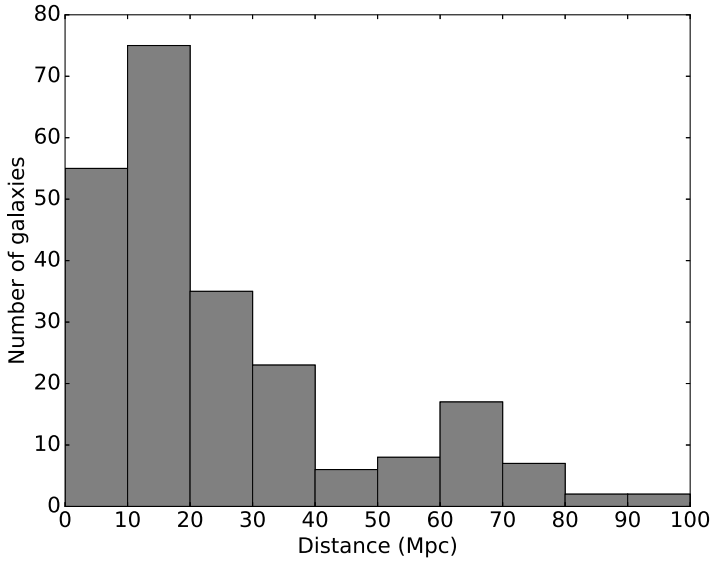

Figure 2.5: Distance distribution of the main sample used in this study. For these 228 galaxies, new data products have been generated (current chapter) and global HI properties derived (Chapter 3.1).

The cubes are generally centered on a main galaxy and any other galaxies within the field of view are included in the same data cube. These other galaxies that populate the field

of view, some of which may be satellite galaxies, are generally small and faint. Therefore, for the main sample of this study, only central galaxies in the cubes or 'included-galaxies' which are comparable in spatial extent to the central galaxy are chosen. Galaxies in close interactions (close enough for the interaction to be seen in the infrared images) or mergers were excluded. Poor data and non-detections were also excluded. These data were checked by eye to ensure there was no disturbance on the target's IR flux by bright foreground stars. Wherever the masking or subtraction of these stars adversely compromised the disk of the galaxy, that target was dropped from the sample. Figure 2.6 illustrates how this was achieved.

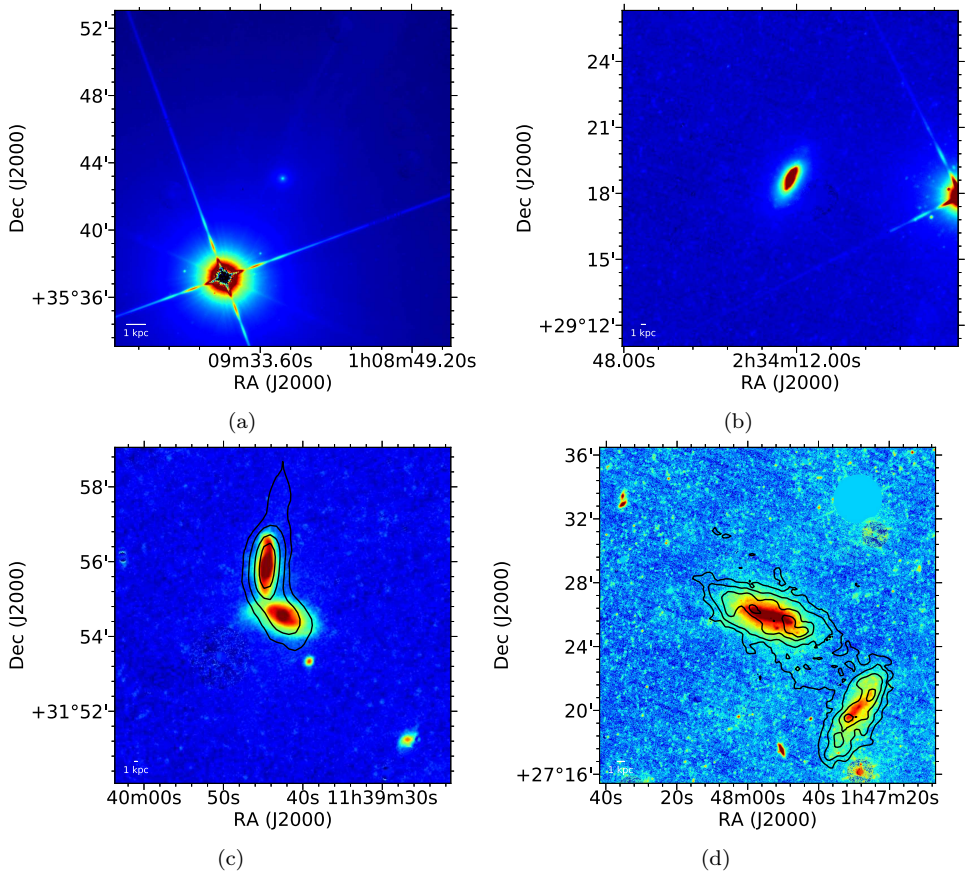

Figure 2.6: Top panels - WISE W1 images with foreground stars; Galaxies where the image flux was dominated by a foreground star (a) were dropped from the sample, unlike images where a bright foreground star did not dominate the flux (b). Bottom panels - W1 images of interacting galaxies. Black contours trace the HI distribution at levels of 0.032 Jy km s^{-1}, 0.081 Jy km s^{-1} , 0.16 Jy km s^{-1} and 0.24 Jy km s^{-1}; Wherever the interaction was close enough to be picked up in the infrared, such targets were dropped from the sample. Panel (c) shows one such example (UGC6621/UGC6623), while panel (d) shows a case where the infrared stellar disks are well separated (UGC1256/UGC1249).

Imposing these criteria resulted in a sample of 228 galaxies which are used as the main sample in this thesis. Since the resultant sample of galaxies was determined purely by data-related conditions, it is not biased by morphology and can be taken as a fair representation of the original sample. The morphological properties of this sample are plotted in Figure 2.5 against the properties of the complete WHISP sample presented by van der Hulst et al. (2001). Table 2.4 lists the WHISP observational properties of the data in this sample while Table 2.6 lists the WISE photometry.

To study the global star formation properties, every galaxy that was detected in the W3 band was chosen. This yielded a sub-sample of 180 galaxies. The Kennicutt-Schmidt relation was investigated on galaxy scales and a "resolved" study was done where pixel by pixel comparisons were made between the HI gas density and the IR star formation rates for a few well resolved galaxies. Details of this study are shown in Chapter 3. Table 2.7 lists the detection properties of this sample in W1, W2 and W3.

A significant portion of this study was dedicated to investigating the star formation threshold and thus requires good spatial resolution. A sub-sample of 35 galaxies was hence derived for the study of star formation thresholds. The 35 were taken from the above sample of 180 for galaxies having HI major axis greater than 10 beams, physical pixel size less than 1 kpc and inclinations between 35°-70° in order to obtain robust rotation curves (Begeman 1987, Spekkens & Sellwood 2007). The size and inclination properties of these galaxies are shown in Table 2.8.

2.3.2 HI intensity maps

CLEANed 30″ resolution data cubes were obtained from the public database of the WHISP* survey. Each data cube consists of several RA-DEC images of a galaxy at consecutive velocities that cover the entire velocity range of that galaxy. These cubes were corrected for primary beam attenuation using the MIRIAD† task *linmos*. Further processing was done to remove low level noise as well as high noise peaks found at the same position as a galaxy, but at a different frequency. A description of this process is given below.

First, the cubes were smoothed to twice their resolution using a Gaussian kernel whose size is determined by the input and desired output beam size. The beam was assumed to be Gaussian; The convolution of a Gaussian function with a Gaussian kernel (standard deviations σ_1 and σ_2, respectively) results in a Gaussian function with a standard deviation of $\sigma_3 = \sqrt{\sigma_1^2 + \sigma_2^2}$. Hence, the kernel size that was required to smooth the 30″ cubes down to 60″ was obtained by,

*https://www.astro.rug.nl/∼whisp/
†http://www.atnf.csiro.au/computing/software/miriad/

$$\sigma_2 = \sqrt{(\sigma_3^2 - \sigma_1^2)}, \tag{2.2}$$

which, for $\sigma_3 = 2\sigma_1$, gives

$$\sigma_2 = \sqrt{3 \times \sigma_1^2}. \tag{2.3}$$

The noise in the original cubes followed a Gaussian distribution, and after smoothing, it remained Gaussian in all cases. The standard deviation, σ was calculated, and a noise clip applied to the smoothed cubes such that all pixel values below 2σ were masked with zeros and those above this threshold were masked with ones. This mask was then applied to the original $30''$ cube. The importance of making a mask from the smoothed cubes is that the smoothing procedure increases the signal to noise ratio such that the low level emission, especially at the galaxy edges, is not clipped as noise. Figure 2.7 illustrates the result of this sigma-clipping process on the data cube of UGC1913. The top and middle panels show channel maps from the original data cube and the Gaussian - smoothed data cube, respectively. The bottom panels show the same channel maps after application of the sigma-clipped mask to the original data cube.

The sigma-clipping rids the data of faint noise. However, there are high noise pixels that survived the 2σ noise clip in the smoothed data cube which can result in exaggeration of the flux in individual line profiles. To remove this noise, a further step (the multi-channel peak criterion) was taken where line profiles through each pixel position were inspected. Any peak that was detected in three or more channels was considered to be galaxy flux, otherwise it was flagged as noise and masked out. Figure 2.8 shows examples of line profiles (also from the data cube of UGC1913) showing this process. From the resulting cube, the HI intensity map was obtained by summing up the intensities from all the channels containing emission. This same cube was used in deriving the global profiles.

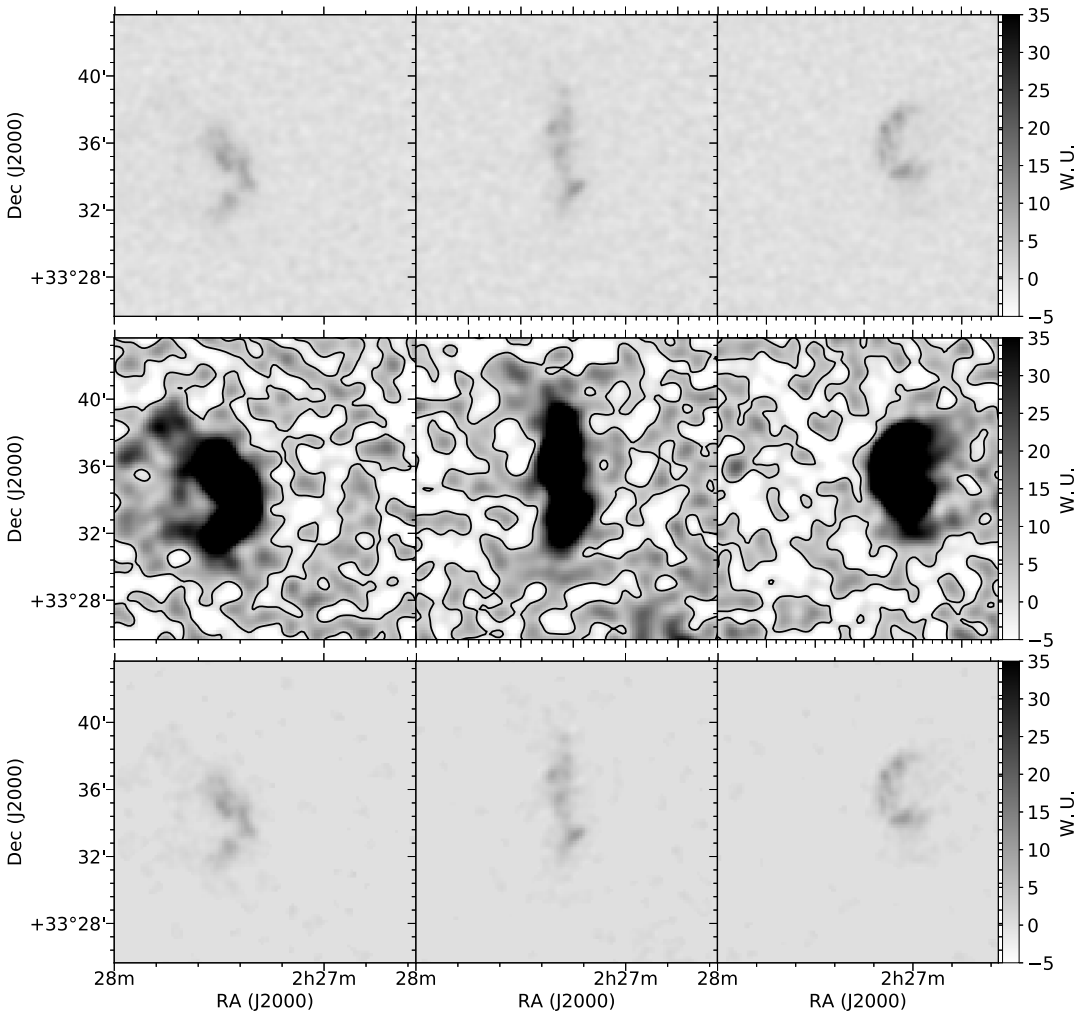

Figure 2.7: Three channel maps from UGC1913 illustrating the sigma-clipping process. The top panels are the channel maps from the original 30″ data cube, while the middle panels show the corresponding maps from the smoothed cube. The contours in the middle panels show the 2σ level. A 2σ noise clip was applied on the smoothed cube and the resulting mask laid on the original cube. The bottom panels show these channel maps after masking the noise. This step cleaned out most of the low level noise.

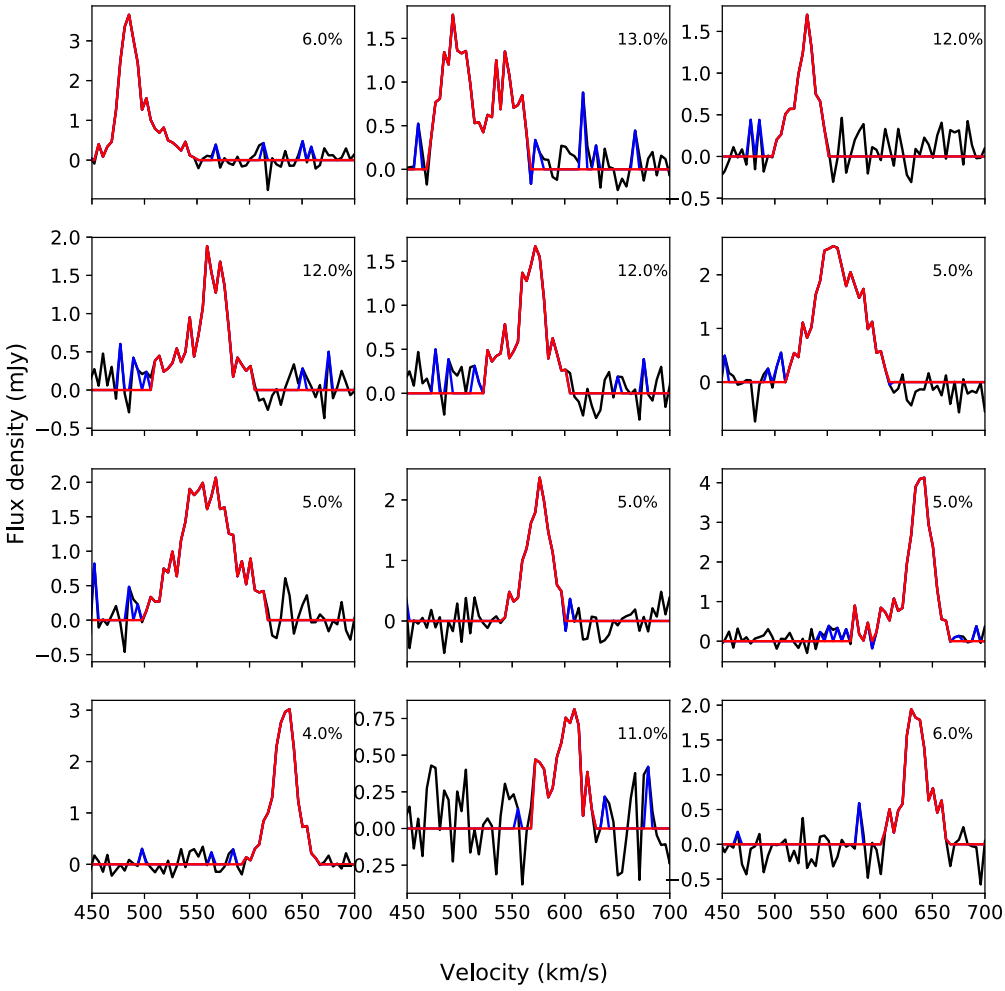

Figure 2.8: Line profiles at different pixel positions, drawn from the data cube of UGC1913, to illustrate the multi-channel-peak criterion. The black shows profiles from the original cube. The blue shows profiles from the sigma clipped cube which survived the 2σ clipping. The percentage contribution of the blue noise peaks to the total profile flux is shown in the upper right corner of each panel. These were removed by using the multi-channel-peak criterion whose resulting profiles are shown in red.

This multi-channel peak criterion is very strict and may lead to the masking of real galaxy emission. To check its efficiency, the procedure was carried out on three model galaxies with different noise levels. The models were generated using the *galmod* task in the Groningen Image Processing System (GIPSY) * (van der Hulst et al. 1992, Vogelaar & Terlouw 2001). Rotation curves and orientation parameters of actual galaxies were used to model the kinematics of these three synthetic galaxies. The actual galaxies used were; UGC5918 (for Target X1) - a dwarf galaxy with a rising rotation curve, UGC4305 (for Target X2) - a dwarf galaxy with a flat outer rotation curve, and UGC7766 (for Target X3) - a spiral galaxy with a flat outer rotation curve. In *galmod*, the models were chosen to have different surface densities, representative of the range of surface densities in the sample with a mean of 3.6±1.1 $M_\odot$ pc^{-2} such that in their order they had surface densities 2.5 $M_\odot$ pc^{-2}, 3.6 $M_\odot$ pc^{-2} and 4.7 $M_\odot$ pc^{-2}. The parameters used are listed in Table 2.2. The GIPSY task *smooth* was used to smooth the model cubes to a resolution of 30″ x 30″ to match the resolution of the sample. The total 'pure' flux in each cube was recorded. Noise was added to the model cubes using the noise statistics of the sample where the average noise across all cubes is 0.68±0.39 W.U. (Westerbork Units). So the noise added to targets X1, X2 and X3 was 0.68 W.U., 1.08 W.U., and 1.47 W.U. respectively, to cover two standard deviations from the average noise. Since 1 W.U. = 5 mJy/beam, that is , 3.5 mJy/beam, 5.5 mJy/beam and 7.5 mJy/beam. The total flux in each cube at this stage was also recorded. The added noise was meant to mimic the typical noise found in the cubes, and at this stage the 2σ noise clipping and multi-channel-peak criterion were applied in order to retrieve the galaxy flux. Note that when removing noise, we attempt to remove as much noise as possible, and to lose as little real emission as possible in the cube, keeping in mind that the real emission is the flux in the model cubes before noise was added. So it is possible that some real galaxy emission is flagged as noise and some noise retained as real flux (Noordermeer et al. 2005). After the noise removal, the total flux in each cube was again recorded. The global profiles of the cubes before and after addition of noise, after sigma clipping, and after the peak removal are shown for all three models in Figures 2.9 - 2.11 while the summed total fluxes are listed in Table 2.3. We see that indeed some galaxy emission, especially at the low and high velocity end, is lost but also that most of the noise that was retained in the sigma clipped cube is removed. In the three model cubes the flux retained in the final product is 101% (implying that some noise is retained) for X1, 98% for X2 and 101% for X3 (also indicating retained noise). In the first model, the lost galaxy emission at the edges of the global profile is more than compensated for by retained noise while in the third case the galaxy emission is retained as well as some noise. From these three examples, we see that the multi-channel-peak criterion, indeed may flag some true galaxy flux as noise, but is also robust at removing a lot of the noise that is left by the sigma clipping while retaining a decent amount of the galaxy flux, as is well illustrated by the global profiles for target X1, (which had the lowest HI surface density). Figure 2.12 shows intensity maps for UGC1913, with and without using the multi-channel-peak criterion.

*https://www.astro.rug.nl/ gipsy/

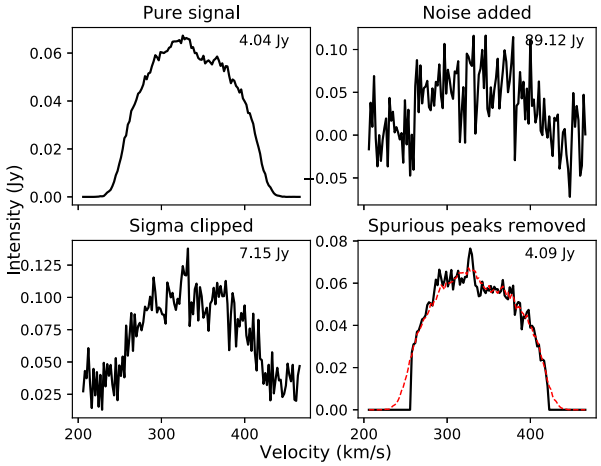

Figure 2.9: Global profiles of a model galaxy (Target X1, see parameters in Table 2.2). From top left to bottom right: Initial synthetic galaxy with no noise added, same galaxy with Gaussian noise added to it, profile after sigma clipping, and finally after removing spurious peaks. The numbers in the upper right show the total flux in the emission containing channels. The negative noise in the upper right panel was not added to the total flux calculation.

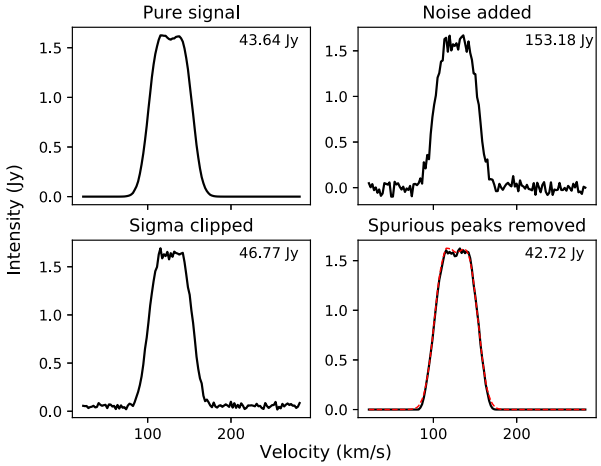

Figure 2.10: Global profiles of model galaxy, target X2 (see parameters in Table 2.2). From top left to bottom right: Initial synthetic galaxy with no noise added, same galaxy with Gaussian noise added to it, profile after sigma clipping, and finally after removing spurious peaks. The numbers in the upper right show the total flux in the emission containing channels. The negative noise in the upper right panel was not added to the total flux calculation.

Table 2.2: **Parameters for the model galaxies:** These three models were generated using the *galmod* task in GIPSY. The rotation curves and orientation parameters were drawn from three actual galaxies which are indicated in column (7) of the table. The HI surface densities were chosen to represent the average surface density in the sample, 3.6±1.1 $M_\odot$ pc^{-2}. Column densities were derived from the surface densities (1 $M_\odot$ pc^{-2} = 1.248×10^{20} cm^{-2}, Brinks (2006)). Description: Col (1) - Name of the model galaxy. Col (2) - Average HI surface density. Col (3) - Column density. Cols (4)-(6) - Systemic velocity, inclination and position angle, all adapted from actual galaxies in column (7). The position angle is measured anti-clockwise from north to the receeding side of the the major axis (de Blok et al. 2008). The literature source of the rotation curves is shown in column (8), with vE11 for van Eymeren et al. (2011) and S99 for Swaters (1999).

Target	Σ_{HI}	N_{HI}	V_{sys}	inc	PA	Kinematics	Source
	$M_\odot$ pc^{-2}	$\times 10^{20}$ cm^{-2}	kms^{-1}	deg	deg		
(1)	(2)	(3)	(4)	(5)	(6)	(7)	(8)
X1	2.5	3.12	338	46	239	UGC5918	S99
X2	3.6	4.49	142	40	172	UGC4305	S99
X3	4.7	5.86	806	67	323	UGC7766	vE11

Table 2.3: **Total flux in the model galaxy cubes:** This table lists the total flux in each model cube at different stages. Col (1) - Name of the model galaxy. Col (2) - True emission from the galaxy. This was calculated before adding noise to the cube. This is the true flux that the noise removal procedures are trying to recover. Col (3) - Total flux in the noisy cube after adding noise to the channels. Note that in this column, only the positive noise was considered when summing up the flux. Col (4) - Total flux after noise-clipping at the 2σ level. The sigma-clipped fluxes are too high by several Jy because of noise peaks that are missed by the sigma clipping. Col (5) - Total flux in the final cube, after removal of the high noise peaks using the multi-channel-peak criterion. Note that the peak-clipped fluxes are still too high by a few mJy, due to added flux from a few remaining noise peaks.

Target	Pure flux	Noise added flux	Sigma clipped flux	Peak clipped flux
	Jy	Jy	Jy	Jy
(1)	(2)	(3)	(4)	(5)
X1	4.04	89.12	7.15	4.09
X2	43.64	152.18	46.77	42.72
X3	135.25	317.06	140.92	136.49

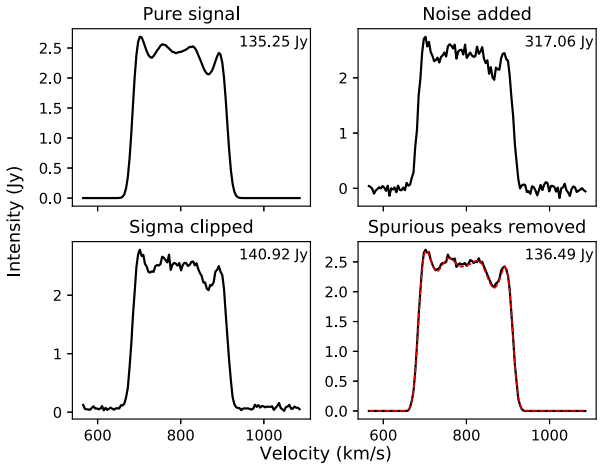

Figure 2.11: Global profiles of model galaxy, target X3 (see parameters in Table 2.2). From top left to bottom right: Initial synthetic galaxy with no noise added, same galaxy with Gaussian noise added to it, profile after sigma clipping, and finally after removing spurious peaks. The numbers in the upper right show the total flux in the emission containing channels. The negative noise in the upper right panel was not added to the total flux calculation.

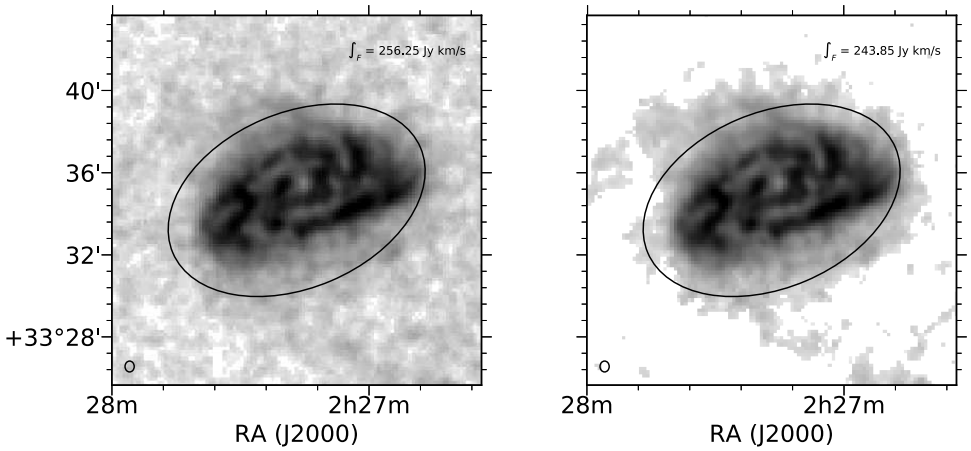

(a) (b)

Figure 2.12: HI intensity maps of the late type spiral galaxy UGC1913. Panel (a) shows the result of adding up the emission in the sigma clipped cube, while (b) shows the result when the same cube is further processed using the multi-peak criterion described in text. The extra step gets rid of sharp noise peaks which may be spatially coincident with the galaxy but separated in velocity space. The flux in the region enclosed by the black ellipse is shown in the upper right corner of each image. The beam size ($\sim 30'' \times \sim 30''$) is shown in the lower left corner of each panel. An atlas of integrated HI distribution maps for the entire sample is given in Appendix A.1.

2.3.3 HI global profiles

Global profiles were extracted from the noise-free 30″ cubes using the *mbspect* task in MIRIAD. Figure 2.13 shows the global profile of a late type galaxy UGC6840. Global profiles show the distribution of the HI flux within a galaxy as a function of radial velocity. To obtain the width of the profile, the peak flux was obtained and the 50% level of that peak calculated. This 50% level was then located on either side of the global profile and the separation between the two points measured. This is the W_{50} linewidth. Likewise, the W_{20} linewidth was obtained. For both linewidths, the central velocity midway between the two points on either side of the global profile was obtained. The magenta and black horizontal lines in Figure 2.13 indicate the 20% and 50% peak flux levels for UGC6840 while the vertical lines mark the corresponding midpoints. These two midpoints were used to calculate the systemic velocity as below,

$$V_{sys} = 0.5 \times (C_{50} + C_{20}), \tag{2.4}$$

where C_{50} and C_{20} are the midpoints of the profile at the 50% and 20% peak flux levels.

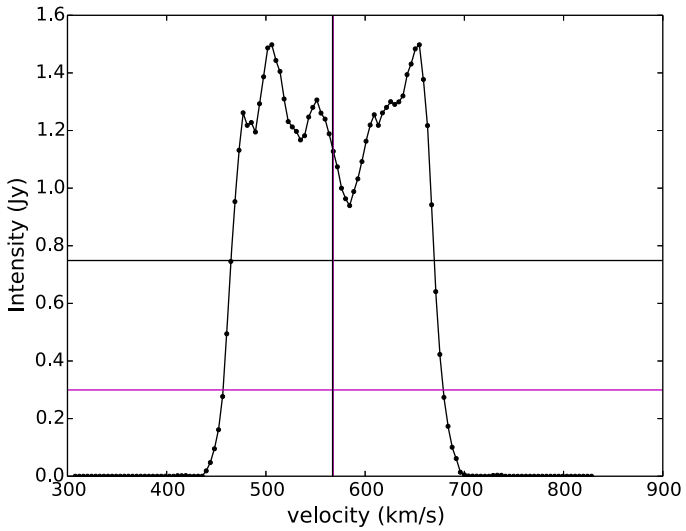

Figure 2.13: HI global profile of UGC1913. The horizontal lines indicate the 20%(magenta) and 50%(black) levels of the peak flux. The vertical lines are the corresponding profile centers based on these levels. The systemic velocity was derived as the average of these two points.

The HI linewidths were corrected for instrumental broadening following the method of (Verheijen 1997)(hereafter V97). The method of V97 assumes that the two edges of a global profile form a Gaussian (which they called the true Gaussian distribution of the profile) with

a dispersion σ_o defined as

$$\sigma_o \;=\; \frac{W_{20_o}}{\sqrt{8\ln(5)}} \;=\; \frac{W_{50_o}}{\sqrt{8\ln(2)}}, \tag{2.5}$$

where W_{20_o} and W_{50_o} are the full widths of the Gaussian at 20% and 50% maximum intensity. This intrinsic profile is broadened by a near-Gaussian function of dispersion σ_R and whose full width at half maximum is the instrumental resolution, R, such that

$$\sigma_R \;=\; \frac{R}{\sqrt{8\ln(2)}}. \tag{2.6}$$

This would then result in the observed Gaussian being a convolution of the two functions, with a dispersion

$$\sigma_c \;=\; \sqrt{\sigma_o^2 + \sigma_R^2}. \tag{2.7}$$

As in Equation 2.5, the full width at 20% maximum of this observed Gaussian is given by

$$\begin{aligned} W_{20_c} \;&=\; \sqrt{8\ln(5)}\,\sqrt{\sigma_o^2 + \sigma_R^2} \\ W_{20_c} \;&=\; \sqrt{8\ln(5)}\,\sqrt{\sigma_o^2 + \tfrac{R^2}{8\ln(2)}}, \end{aligned} \tag{2.8}$$

hence the broadening factor is the difference between the observed (2.8) and true widths (2.5),

$$\delta W_{20} \;=\; W_{20_c} \;-\; W_{20_o} \;=\; \sqrt{8\ln(5)}\,\sqrt{\sigma_o^2 + \frac{R^2}{8\ln(2)}} \;-\; \sigma_o\sqrt{8\ln(5)}. \tag{2.9}$$

Likewise for the full width at 50% maximum,

$$\begin{aligned} W_{50_c} \;&=\; \sqrt{8\ln(2)}\,\sqrt{\sigma_o^2 + \sigma_R^2} \\ W_{50_c} \;&=\; \sqrt{8\ln(2)}\,\sqrt{\sigma_o^2 + \tfrac{R^2}{8\ln(2)}} \\ \delta W_{50} \;&=\; \sqrt{8\ln(2)}\,\sqrt{\sigma_o^2 + \tfrac{R^2}{8\ln(2)}} \;-\; \sigma_o\sqrt{8\ln(2)}. \end{aligned} \tag{2.10}$$

V97 took the dispersion of the true Gaussian (σ_o) to be entirely due to random motions in the gas with dispersion velocity of 10 km/s. The factors $\sigma_o\sqrt{8\ln(5)}$ and $\sigma_o\sqrt{8\ln(2)}$ then reduce to 35.8 km/s and 23.5 km/s. To correct the line widths for instrumental broadening, the broadening factor is subtracted from the observed width as,

$$\begin{aligned} \mathrm{W}'_{20} \;&=\; \mathrm{W}_{20} - 35.8\left[\sqrt{1 \;+\; \left(\tfrac{\mathrm{R}}{23.5}\right)^2} \;-\; 1\right] \\ \mathrm{W}'_{50} \;&=\; \mathrm{W}_{50} - 23.5\left[\sqrt{1 \;+\; \left(\tfrac{\mathrm{R}}{23.5}\right)^2} \;-\; 1\right], \end{aligned} \tag{2.11}$$

where R is the instrumental resolution in units of km/s, W_{20} and W_{50} are the observed

linewidths, while W'_{20} and W'_{50} are the corrected linewidths which are essentially W_{20_o} and W_{50_o} from Equation 2.5.

2.3.4 HI mass

The total HI flux was obtained by summing up all the flux in the global profile. The total flux was used to calculate the HI mass as,

$$M_{HI}(M_\odot) \;=\; (1+z)\; 2.36\times10^5 \times D^2(\mathrm{Mpc}) \times \int S_\nu \; dv \; (\mathrm{Jykm\; s^{-1}}), \qquad (2.12)$$

where D is the distance, and $\int S_\nu$ dv is the total HI flux integrated over the global profile. The factor of (1+z) in this equation reduces to unity at low redshifts. Figure 2.14 shows comparisons of the masses derived in this study with masses derived by two other studies that used WHISP data. These are Swaters (1999)(hereafter S99) and Noordermeer et al. (2005)(hereafter N05), with whom we had 60 and 52 galaxies in common, respectively. The masses were compared after synchronizing the distances across the samples (see Table 2.5 for adopted distances). The masses in this study are systematically lower than those of S99, which is expected because they did not carry out the extra noise handling by the multi-channel-peak criterion hence having higher fluxes, while N05 employed the multi-channel-peak criterion when generating their data products which explains why their mass estimates are in general agreement with those here. The total flux and mass as well as linewidths and systemic velocities for all galaxies in the sample are listed in Table 2.5.

Distances

The distances used in this study were obtained from two sources: the Cosmic Flows catalog (CF2) (Tully et al. 2013) via the Extragalactic Distance Database (EDD)* (Tully et al. 2009) and the NASA/IPAC Extragalactic Database (NED)†. The NED distances are estimates from redshift-derived radial velocities (V = cz) corrected for peculiar flows due to the influence of the Virgo cluster, the Great Attractor and the Shapley supercluster (Mould et al. 2000). The distances on the EDD are based on different surveys, namely, The 2Micron All Sky Survey Extended Source Catalog (2MASX, Jarrett et al. 2000), The Catalog of Neigbouring Galaxies (Karachentsev et al. 2004), and the 2MASS V8k catalog (Huchra et al. 2005), as well as independent distance derivations from archival data by Tully et al. (2009).These sources had varying methods of deriving their distances, and hence the EDD distances are weighted averages of several methods; the Cepheid period-luminosity relation (C), Tip of the Red Giant Branch method (TRGB), Supernovae type 1a (SNIa), Tully-Fisher relation (TFR) method and the Fundamental plane (FP) method. The Cepheids method and FP method get the highest and lowest weights respectively. When

*http://edd.ifa.hawaii.edu/
†https://ned.ipac.caltech.edu/

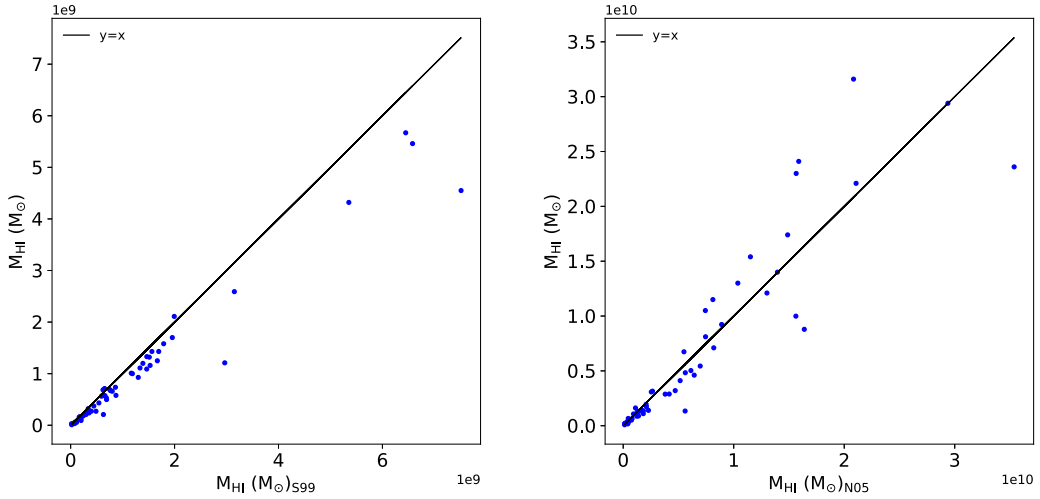

(a) (b)

Figure 2.14: Comparison of mass estimates from the literature with this study. S99 ((a), horizontal axis) retrieved higher fluxes from the WHISP cubes because they did not carry out the multi-peak criterion noise removal, which N05 ((b), horizontal axis) carried out and hence their fluxes are in agreement with ours. Note that the masses of both S99 and N05 were re-derived from their fluxes using the distance estimates adopted here. In both plots, the y axis represents mass estimates from the current study. There were 52 and 60 galaxies in common with N05 and S99 respectively.

obtaining distances from the EDD, we took only distances with estimates from the first four methods. Those galaxies that were not listed on EDD or had only FP-based estimates were obtained from the NED Mould flow estimates. Since the distance estimates given in the EDD are scaled by a value of H_0=74.4 ± 3.0 km s^{-1}Mpc^{-1}, the Mould flow parameters were set to match the same cosmological parameters (H_0=74.4 ± 5.0 km s^{-1}Mpc^{-1}, with Ω_m=0.27 and Ω_Λ=0.73). Table 2.5 lists the adopted distances while Figure 2.5 shows the distance distribution of the sample. A sanity check was done to look for any systematic differences between the two databases. There were 116 galaxies for which we could get both CF2 and NED distance estimates. The differences between the two sets of distance estimates were plotted as a function of the CF2 distances. Figure 2.15 below illustrates our findings. Overall we see no systematic offsets, but rather evenly distributed differences, with a standard deviation of 4 Mpc and 9 outliers (labelled on plot) which were not used in calculation of the standard deviation.

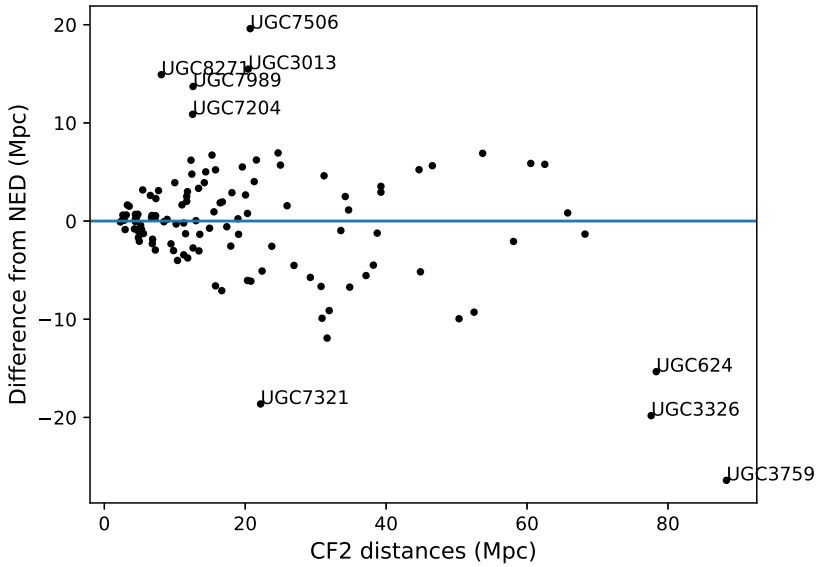

Figure 2.15: A comparison of distances from the CF2 and NED databases. On the vertical axis, the residuals between NED distance and CF2 distance, while the horizontal axis shows the CF2 distance. The residuals do not show any systematic offsets, but are evenly distributed about zero, with a few outliers as is expected of any realistic distribution.

2.3.5 Radial profiles

Surface density maps of HI were calculated from the total intensity maps via standard conversions. The HI column density was first derived:

$$\mathrm{N_{HI}(cm^{-2})} \;=\; 1.823\times10^{18}\times\frac{\sum_\nu \mathrm{S}_\nu}{1.65\times10^{-3}\times\Delta\alpha\Delta\delta}\times\Delta\mathrm{V}, \tag{2.13}$$

(Brinks 2006), where $\Delta\alpha$ and $\Delta\delta$ are the major and minor axes of the synthesized beam, ΔV is the velocity resolution in km s^{-1}, and $\sum_\nu \mathrm{S}_\nu$ is the integrated HI in mJy/beam. The factor in the denominator converts the intensity map into a brightness temperature map. A linear conversion was applied to the column density map to obtain surface density,

$$\Sigma_{\mathrm{HI}}(\mathrm{M_\odot\ pc^{-2}}) \;=\; \frac{\mathrm{N_{HI}}}{1.248\times10^{20}}, \tag{2.14}$$

(Brinks 2006). To get radial profiles, the MIRIAD task *ellint* was used. For each galaxy, a map of the HI surface density was used as input and the task divides the image into elliptical annuli, returning the average HI density in each annulus. This results in an average density for each radius bin. The size of the width of the annuli was left at the default 10″ of *ellint* which for the data used here is the width of a pixel. This width, in spite of being very narrow and leading to a smoothing out of the radial profiles due to beam smearing, will

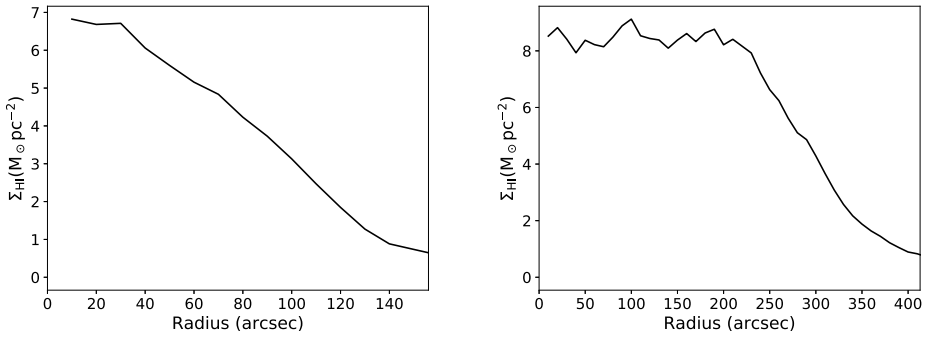

(a) (b)

Figure 2.16: Radial profiles of HI surface density for UGC10445 (a) and UGC1913 (b), generated using the task *ellint* in MIRIAD.

still yield profiles that are a general representation of the radial extent and shape of the HI distribution in the disks. The NIR-derived PA and axial ratio (for inclination) in Table 2.6 were used as orientation parameters for the annuli. The centers of the annuli were set to the galaxy RA and DEC (J2000) in the data cube headers. Figure 2.16 shows radial profiles for UGC10445 and UGC1913. The rest of the radial profiles are shown in Appendix A.1 (lower left panels).

2.3.6 Velocity fields

Velocity field maps were obtained by fitting third order Gauss-Hermite polynomials to the line of sight profiles in the original data cubes. Note that the noise corrected cubes were not used here because the noise properties were needed for the purpose of making robust fits. However, the HI intensity maps derived in Section 2.3.2 were used as masks so as not to include the low signal to noise pixels in the final velocity maps.

Gauss-Hermite polynomials were first used by van der Marel & Franx (1993) who showed that the line profiles of elliptical galaxies could be described by breaking down the profile into orthogonal functions to account for both symmetric and asymmetric deviations from a pure Gaussian profile. This was done by summing the Gauss-Hermite polynomials up to the fourth term;

$$\phi(\mathrm{x}) \;=\; \mathrm{a}\mathrm{e}^{-\mathrm{y}^2/2}\left[1 \;+\; \frac{\mathrm{h}_3}{\sqrt{3}}(2\mathrm{y}^3 \;-\; 3\mathrm{y}) \;+\; \frac{\mathrm{h}_4}{\sqrt{24}}(4\mathrm{y}^4 \;-\; 12\mathrm{y}^2 \;+\; 3)\right], \tag{2.15}$$

where $\mathrm{y} = (\mathrm{x} - \mu)/\mathrm{c}$. The terms h_3 and h_4 are measures of skewness and flatness of the distribution, while the first term represents a pure Gaussian distribution of amplitude a, mean μ and dispersion c.

The choice of the third order sum was due to its robustness in fitting both high and low signal to noise peaks as pointed out by de Blok et al. (2008). Also, several authors have found that

fitting the third order polynomial is sufficient to recover the typical radial velocity in a profile (e.g. Noordermeer et al. 2005, de Blok et al. 2008, Ianjamasimanana et al. 2012).
To do the fitting, one needs reasonable initial estimates to the parameters in Equation 2.15. For h_3, an initial value of 0.4 was used, while the estimates for the Gaussian terms (a, μ and c) were obtained by deriving maps of the peak intensity and the first and second moments respectively at each pixel position. The moment maps were derived from the data cube using the standard centroid method as

$$\mu_1 = \frac{\sum_i (S_i\ V_i)}{\sum_i S_i} \tag{2.16}$$

$$\mu_2 = \sqrt{\frac{\sum_i [S_i\ (V_i - \mu_1)^2]}{\sum_i S_i}}, \tag{2.17}$$

where μ_1 is the first moment of the profile, S_i and V_i are the integrated intensity and velocity of the i^{th} channel in the data cube respectively.
Figure 2.17 illustrates the h_3 fit on profiles from an early type galaxy UGC10445 showing that the function is able to fit both symmetric and asymmetric profiles which are prevalent in the central regions. The velocity map of UGC10445 is shown in Figure 2.18 along with that of UGC1913. The maps for the rest of the sample are shown in Appendix A.1 (upper right panels).

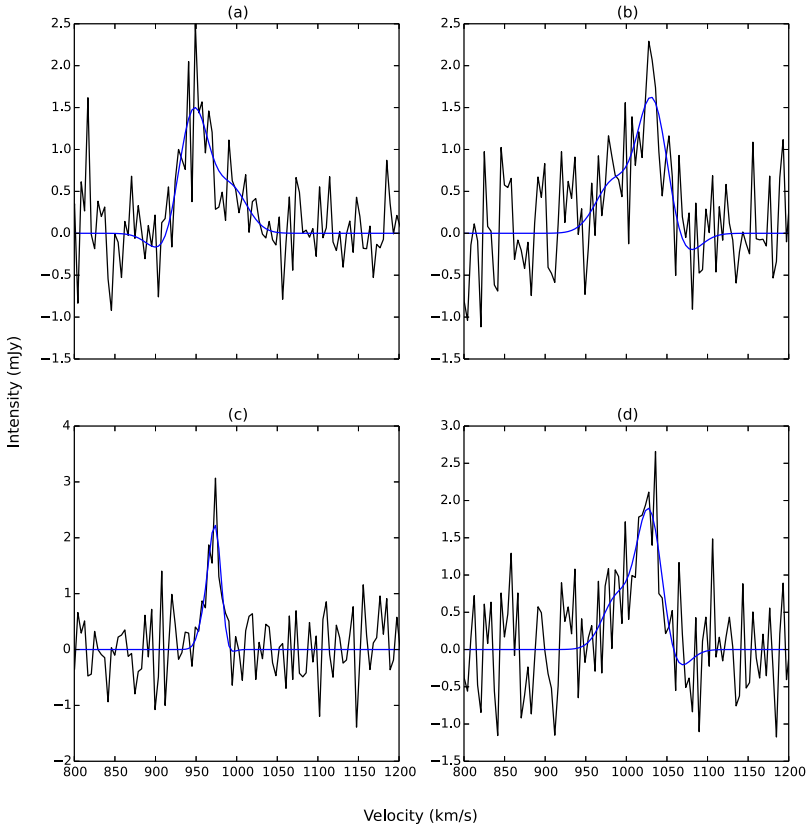

Figure 2.17: Line of sight velocity profiles from UGC10445 at positions: (α, δ)=a($16^{\rm h}33^{\rm m}46^{\rm s}.8, 28°59'16''.9$), b($16^{\rm h}33^{\rm m}50^{\rm s}.6, 28°58'56''.9$), c($16^{\rm h}33^{\rm m}48^{\rm s}.3, 29°00'26''.9$) and d($16^{\rm h}33^{\rm m}50^{\rm s}.6, 28°59'6''.9$). The line profile is shown by the black line while the blue line is the Gauss-Hermite h_3 fit to the profile. The shapes of line profiles varies, with some skewed and others close to Gaussian, but the h_3 fits were found to adequately fit both cases.

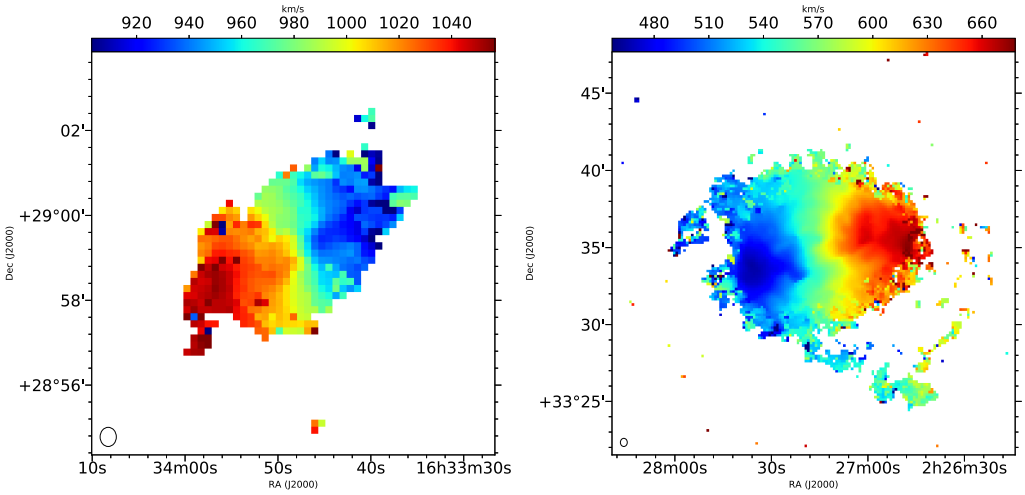

(a) (b)

Figure 2.18: Gauss-Hermite velocity fields for UGC10445 (a) and UGC1913 (b). The WHISP beam of $\sim 30'' \times \sim 30''$ is shown in the lower left corner of each panel. For some cubes, the beam was elliptical with a major axis greater than $30''$ as seen in (a). The maps were obtained by fitting third order Gauss-Hermite polynomials to the line profiles. Quality filters were applied to the fits to flag profiles with SNR less than 4, and profiles with width less than the velocity resolution of the cube.

2.4 Tables

Table 2.4: **Observational parameters of HI data from the WHISP survey**. Notes on columns: col (2,3): RA(2000) and Dec(2000), cols (4-6):Beam resolution (major and minor axis) and position angle. This study makes use of the WHISP data at resolution 30" x 30". Where the header information does not include exact resolution we use exactly 30".x30" and position angle 0. col (7):Average noise in cubes before primary beam correction. col (8): Number of velocity channels, dependent on the WHISP flux density category(< 100mJy, 100mJy $-$ 300mJy, > 300mJy). col (9): Velocity resolution of the cube.

Name	R.A.	Dec	B_{maj}	B_{min}	BPA	Noise	Channels	ΔV
	deg	deg	$''$	$''$	deg	mJy beam^{-1}		km s^{-1}
(1)	(2)	(3)	(4)	(5)	(6)	(7)	(8)	(9)
UGC89	2.4725	25.9238	35.91	23.91	0	0.72	127	8.4
UGC192	5.0723	59.3038	30.81	30.48	90	7.14	127	2.1
UGC232	6.1612	33.2562	40.66	30.93	0	0.88	127	8.4
UGC485	11.7845	30.3409	28.48	24.01	0	1.75	63	16.8
UGC528	13.018	47.5505	30.0	30.0	0	4.26	127	4.1
UGC624	15.1517	30.669	43.84	32.93	0	0.63	127	8.4
UGC625	15.2309	47.682	28.33	28.32	0	1.96	63	16.6
UGC655	16.0052	41.8429	31.87	26.08	0	4.15	127	4.1
UGC690	16.8865	39.4001	29.98	25.17	0	1.79	63	16.8
UGC731	17.6833	49.6022	30.0	30.0	0	4.3	127	4.1
UGC798	18.7995	30.1948	29.07	26.69	0	0.84	115	8.4
UGC1013	21.5907	34.703	30.35	23.93	0	1.72	63	16.8
UGC1256	26.9772	27.4328	30.0	30.0	0	2.15	63	16.5
UGC1281	27.3833	32.5897	30.0	30.0	0	4.79	127	4.1
UGC1437	29.4258	35.9161	30.54	23.88	0	2.04	63	16.8
UGC1501	30.3205	28.8373	34.89	26.61	0	3.6	127	4.1
UGC1541	30.8664	38.1169	41.49	33.26	0	0.84	127	8.4
UGC1633	32.1855	38.7772	32.34	24.29	0	1.7	63	16.7
UGC1810	35.3696	39.3757	29.93	25.32	0	1.6	63	16.9
UGC1856	36.1316	31.6153	26.14	23.25	0	4.19	127	4.2
UGC1886	36.502	39.4709	29.55	24.51	0	1.66	63	16.8
UGC1913	36.8203	33.5792	31.75	26.82	0	2.25	127	4.1
UGC2023	38.3258	33.4911	30.0	30.0	0	5.67	127	2.1
UGC2034	38.429	40.5281	30.0	30.0	0	5.6	127	2.1
UGC2045	38.5558	29.3113	44.86	32.99	0	0.78	127	8.3
UGC2053	38.6221	29.7498	30.0	30.0	0	5.36	127	2.1
UGC2080	39.1162	38.9699	30.0	30.0	0	4.11	127	4.1
UGC2082	39.0673	25.4238	26.99	25.42	0	4.27	127	4.1
UGC2141	39.8121	30.1514	37.5	19.91	0	4.2	127	4.1

Table 2.4 – *Continued from previous page*

Name	R.A.	Dec	B_{maj}	B_{min}	BPA	Noise	Channels	ΔV
	deg	deg	$''$	$''$	deg	mJy beam^{-1}		km s^{-1}
(1)	(2)	(3)	(4)	(5)	(6)	(7)	(8)	(9)
UGC2183	40.7013	28.5742	42.18	30.07	0	0.82	127	8.3
UGC2193	40.875	37.3413	27.18	24.18	0	6.9	127	2.1
UGC2455	44.9263	25.2378	30.0	30.0	0	5.84	127	2.1
UGC2459	45.1532	49.044	29.18	28.25	90	2.15	63	16.6
UGC2487	45.4265	35.2058	44.26	34.27	0	0.99	127	8.4
UGC2503	45.8948	46.3864	29.11	25.87	0	2.23	63	16.6
UGC2800	55.0102	71.4059	27.09	26.97	0	4.3	127	4.1
UGC2855	57.0864	70.1329	30.0	30.0	0	1.87	63	16.6
UGC2916	60.6411	71.7059	36.1	25.27	0	0.65	127	8.4
UGC2941	60.9333	22.1591	51.39	31.51	0	1.58	127	4.2
UGC3013	65.8629	75.2956	33.15	23.56	0	1.88	63	16.6
UGC3137	71.5708	76.4189	30.0	30.0	0	4.21	127	4.1
UGC3205	74.062	30.0524	35.96	26.4	0	0.57	127	8.3
UGC3326	84.9046	77.3125	29.7	23.01	0	1.56	63	16.7
UGC3334	85.5194	69.3784	29.27	29.27	90	1.65	63	16.7
UGC3354	86.8259	56.1124	36.18	33.96	0	0.64	127	8.3
UGC3371	89.1608	75.3161	30.0	30.0	0	4.33	127	4.1
UGC3382	89.9489	62.158	30.24	29.33	0	0.81	127	4.2
UGC3384	90.4042	73.1167	34.53	32.62	0	8.0	127	2.1
UGC3407	92.2837	42.0852	29.15	28.51	90	0.64	115	8.3
UGC3546	102.5361	60.8458	35.59	32.48	0	0.65	127	8.3
UGC3574	103.2935	57.1778	30.0	30.0	0	4.2	127	4.1
UGC3580	103.8786	69.5631	27.13	26.9	0	3.39	127	4.1
UGC3642	106.0846	64.0203	30.05	25.65	0	0.82	127	8.4
UGC3698	107.3281	44.3801	27.96	24.93	0	3.21	127	4.1
UGC3711	107.5566	44.4573	30.0	30.0	0	4.02	127	4.1
UGC3734	108.1194	47.1667	27.19	26.83	0	4.09	127	4.1
UGC3740	111.8098	85.7546	30.0	30.0	0	4.93	127	4.2
UGC3759	109.0154	64.7089	28.57	28.56	0	1.73	63	16.7
UGC3817	110.6853	45.1085	30.0	30.0	0	5.69	127	2.1
UGC3826	111.1162	61.6939	32.46	26.2	0	5.76	127	2.1
UGC3965	115.3254	34.2322	31.6	25.09	0	2.13	127	2.1
UGC3966	115.3583	40.1122	30.0	30.0	0	7.39	127	2.1
UGC3993	118.9332	84.9264	30.67	30.44	0	0.94	127	4.2
UGC4036	117.9781	73.0157	28.61	28.41	0	3.96	127	4.2
UGC4165	120.4717	50.7371	28.43	28.19	0	3.97	127	4.1
UGC4173	121.8004	80.125	30.0	30.0	0	7.55	127	2.1

Table 2.4 – *Continued from previous page*

Name	R.A.	Dec	B_{maj}	B_{min}	BPA	Noise	Channels	ΔV
	deg	deg	$''$	$''$	deg	mJy beam^{-1}		km s^{-1}
(1)	(2)	(3)	(4)	(5)	(6)	(7)	(8)	(9)
UGC4256	122.5632	33.9566	32.95	19.6	0	3.61	127	4.2
UGC4273	123.2413	36.2546	32.2	25.24	0	2.41	63	16.6
UGC4278	123.4955	45.7421	29.67	29.67	90	4.66	127	4.1
UGC4284	123.6672	49.0617	28.98	28.98	0	2.56	127	4.1
UGC4305	124.7708	70.72	30.0	30.0	0	7.48	127	2.1
UGC4325	124.8355	50.0096	30.0	30.0	0	4.26	127	4.1
UGC4458	128.0471	22.5606	41.71	23.87	0	0.72	127	8.4
UGC4483	129.2625	69.7753	35.48	29.78	90	7.47	127	2.1
UGC4499	129.4228	51.6524	30.0	30.0	0	4.32	127	4.1
UGC4543	130.841	45.736	28.82	28.33	67	6.3	127	2.1
UGC4605	132.2995	60.2211	32.23	28.48	0	0.74	127	8.3
UGC4666	133.8946	58.7344	26.6	26.2	0	0.77	115	8.3
UGC4806	137.3905	33.1235	35.74	30.09	0	1.94	63	16.6
UGC4838	138.0605	44.9548	28.02	27.74	0	4.38	127	4.2
UGC5060	142.5707	29.54	42.36	32.63	0	0.93	127	4.1
UGC5079	143.0421	21.5008	27.25	25.98	0	1.87	127	4.1
UGC5251	147.1502	33.4215	31.52	24.15	0	5.08	127	4.1
UGC5253	147.5926	72.2786	30.0	30.0	0	1.74	63	16.6
UGC5272	147.5933	31.4878	30.0	30.0	0	6.77	127	2.1
UGC5351	149.5878	32.3699	31.82	30.66	0	0.81	115	8.3
UGC5414	150.989	40.7569	30.0	30.0	0	6.33	127	2.1
UGC5452	151.7981	33.0274	28.6	26.99	0	3.3	127	4.1
UGC5459	152.042	53.0835	30.07	29.56	0	5.0	127	4.1
UGC5532	154.2235	73.4008	27.97	26.94	0	1.97	63	16.7
UGC5557	154.5702	41.4241	27.37	24.69	0	4.69	127	4.1
UGC5589	155.4483	56.9304	28.17	28.13	0	4.45	127	4.1
UGC5685	157.3331	29.4918	28.3	26.8	0	2.12	63	16.6
UGC5717	158.1452	65.0411	30.98	28.93	0	5.33	127	4.1
UGC5721	158.072	27.6688	38.79	29.05	19	5.62	127	4.1
UGC5786	159.6911	53.5034	30.71	29.85	0	1.6	63	16.6
UGC5789	159.7894	41.6867	29.13	29.12	0	3.99	127	4.1
UGC5829	160.6746	34.4489	30.0	30.0	0	7.77	127	2.1
UGC5840	160.8798	24.9222	27.84	26.34	0	3.14	127	4.1
UGC5846	161.1229	60.3678	30.0	30.0	0	5.77	127	2.1
UGC5906	162.0507	28.6018	36.16	26.14	0	1.22	127	4.1
UGC5909	162.1034	34.7114	30.94	26.99	0	4.49	127	4.1
UGC5918	162.4021	65.5306	31.97	29.67	90	5.96	127	2.1

Table 2.4 – *Continued from previous page*

Name	R.A.	Dec	B_{maj}	B_{min}	BPA	Noise	Channels	ΔV
	deg	deg	$''$	$''$	deg	mJy beam^{-1}		km s^{-1}
(1)	(2)	(3)	(4)	(5)	(6)	(7)	(8)	(9)
UGC5960	162.8364	32.7664	34.11	24.68	0	1.35	127	4.1
UGC5997	163.4786	73.6904	32.05	31.81	0	4.59	127	4.1
UGC6001	163.2838	33.9104	31.41	24.92	0	0.99	127	4.1
UGC6118	165.7967	27.9725	35.92	26.28	0	0.78	127	8.3
UGC6126	165.9307	28.8872	36.29	30.34	0	3.34	127	4.1
UGC6161	166.705	43.7233	32.8	31.97	0	3.3	127	4.1
UGC6225	167.879	55.6741	29.85	26.49	0	2.03	63	16.5
UGC6251	168.3589	53.5951	29.69	29.26	0	6.67	127	2.1
UGC6263	168.5454	48.3185	28.39	28.38	0	1.82	63	16.6
UGC6283	168.9667	41.591	29.77	29.63	90	3.93	127	4.1
UGC6446	171.6686	53.7467	29.67	29.67	90	4.17	127	4.1
UGC6537	173.338	47.0292	30.0	30.0	0	4.23	127	4.1
UGC6713	176.104	48.8352	28.93	28.84	0	2.45	127	4.1
UGC6742	176.4858	50.1998	33.14	28.94	0	0.77	127	4.1
UGC6778	177.1591	48.7108	30.0	30.0	0	4.21	127	4.1
UGC6786	177.2894	27.022	44.37	31.51	0	0.81	127	8.3
UGC6787	177.314	56.0844	31.87	29.67	0	0.68	127	8.3
UGC6813	177.6623	55.3539	27.09	26.94	0	6.63	127	2.1
UGC6817	177.7208	38.8803	28.13	26.04	0	6.65	127	2.1
UGC6833	177.9417	38.0151	30.1	26.95	0	4.39	127	4.1
UGC6840	178.0292	52.108	27.01	27.01	0	1.75	127	4.1
UGC6884	178.7446	58.4936	29.69	29.21	0	3.99	127	4.2
UGC6921	179.1755	48.3339	24.98	24.1	0	2.22	127	4.1
UGC6930	179.3223	49.2831	29.63	27.37	0	2.6	127	4.1
UGC6964	179.6579	47.2615	28.46	28.21	0	2.41	127	4.1
UGC7030	180.79	44.5313	29.54	29.03	0	3.12	127	4.1
UGC7047	181.0033	52.5883	30.0	30.0	0	5.62	127	2.1
UGC7075	181.3446	50.3529	29.7	29.69	0	3.47	127	4.1
UGC7089	181.4906	43.1433	32.15	30.71	0	4.17	127	4.1
UGC7095	181.5352	49.5827	27.78	27.67	0	1.71	63	16.6
UGC7125	182.1764	36.8028	29.7	28.3	0	4.65	127	4.1
UGC7151	182.4942	46.4572	31.29	30.23	0	4.7	127	4.1
UGC7166	182.6358	39.4057	32.39	27.99	0	3.64	127	4.1
UGC7183	182.7682	50.4847	35.43	24.92	0	1.96	63	16.5
UGC7199	183.0382	36.1692	31.7	30.92	0	6.76	127	2.1
UGC7204	183.0894	29.2071	29.35	23.65	0	4.11	127	4.1
UGC7222	183.3203	43.6986	24.81	24.53	0	2.67	127	4.1

Table 2.4 – *Continued from previous page*

Name	R.A.	Dec	B_{maj}	B_{min}	BPA	Noise	Channels	ΔV
	deg	deg	$''$	$''$	deg	mJy beam^{-1}		km s^{-1}
(1)	(2)	(3)	(4)	(5)	(6)	(7)	(8)	(9)
UGC7232	183.4365	36.634	32.07	28.94	0	6.31	127	2.1
UGC7256	183.7711	33.1973	42.55	31.58	0	1.92	127	4.1
UGC7261	183.8102	20.6586	32.82	29.89	0	4.9	127	4.1
UGC7321	184.3917	22.5401	29.16	25.7	0	4.76	127	4.1
UGC7323	184.3758	45.6193	30.85	30.83	0	4.39	127	4.1
UGC7399	185.1588	46.2917	32.27	31.14	0	4.53	127	4.1
UGC7408	185.3125	45.8113	32.34	31.17	0	7.47	127	2.1
UGC7483	186.0465	31.5219	29.94	26.39	0	4.51	127	4.1
UGC7489	186.1508	39.383	32.9	24.93	0	5.09	127	4.1
UGC7490	186.1054	70.3336	30.0	30.0	0	5.64	127	2.1
UGC7506	186.2999	54.5062	36.53	35.98	90	1.02	127	4.2
UGC7524	186.4536	33.5469	30.79	28.3	0	3.06	127	4.1
UGC7559	186.7715	37.1426	33.77	28.74	0	6.07	127	2.1
UGC7592	187.0462	44.0936	30.0	30.0	0	4.5	127	4.1
UGC7603	187.1838	22.8204	33.44	29.14	0	4.89	127	4.1
UGC7690	188.112	42.7041	32.04	31.21	0	6.21	127	2.1
UGC7704	188.2783	32.0916	49.93	29.78	0	1.03	127	4.1
UGC7766	188.9902	27.96	35.19	24.5	0	2.33	127	4.1
UGC7831	189.9974	61.6092	34.14	25.05	0	4.64	127	4.1
UGC7853	190.3869	41.1508	33.81	30.2	0	3.55	127	4.1
UGC7866	190.5629	38.5033	29.79	26.65	0	5.77	127	2.1
UGC7971	192.0953	51.1647	30.0	30.0	0	7.07	127	2.1
UGC7989	192.6107	25.5008	28.36	25.46	0	1.32	63	16.6
UGC8146	195.5337	58.7013	28.98	28.52	0	4.15	127	4.1
UGC8188	196.4564	37.6049	30.0	30.0	0	6.17	127	2.1
UGC8201	196.6035	67.7069	31.91	31.51	0	6.75	127	2.1
UGC8246	197.5185	34.1812	31.15	27.68	0	4.14	127	4.1
UGC8271	197.8801	36.2821	44.9	30.88	0	0.82	127	4.1
UGC8286	198.0525	44.0412	28.44	27.28	90	2.94	127	4.1
UGC8331	198.8763	47.4989	31.81	31.45	0	5.09	127	2.1
UGC8396	200.3528	38.5376	31.57	28.66	0	4.19	127	4.1
UGC8490	202.4021	58.4187	30.0	30.0	0	2.96	127	4.1
UGC8508	202.685	54.91	30.11	29.43	0	7.05	127	2.1
UGC8550	203.5118	47.9154	32.65	31.24	0	5.69	127	4.1
UGC8651	204.9743	40.7391	32.75	27.94	0	6.92	127	2.1
UGC8683	205.6355	39.6585	30.0	30.0	0	5.57	127	2.1
UGC8709	206.5986	43.8723	29.89	28.15	90	1.9	63	16.6

Table 2.4 – *Continued from previous page*

Name	R.A.	Dec	B_{maj}	B_{min}	BPA	Noise	Channels	ΔV
	deg	deg	$''$	$''$	deg	mJy beam^{-1}		km s^{-1}
(1)	(2)	(3)	(4)	(5)	(6)	(7)	(8)	(9)
UGC8711	206.6028	46.1071	28.43	27.96	90	1.87	63	16.6
UGC8805	208.3243	33.4908	35.14	25.88	0	5.44	127	4.2
UGC8837	208.6907	53.9008	30.0	30.0	0	3.24	127	2.1
UGC8863	209.0695	47.2357	33.24	28.74	0	0.7	127	8.3
UGC9018	211.3887	54.4611	31.43	28.32	0	4.7	127	2.1
UGC9128	213.9855	23.0553	52.92	33.19	0	7.4	127	2.1
UGC9211	215.634	45.3839	30.0	30.0	0	4.2	127	4.1
UGC9242	216.3376	39.5396	29.74	24.98	0	4.04	127	4.1
UGC9366	218.1952	49.4579	30.94	25.78	0	1.84	63	16.6
UGC9431	219.548	46.6382	28.47	28.21	0	1.82	63	16.6
UGC9644	224.893	27.1163	35.98	26.06	0	1.26	127	4.2
UGC9649	224.4405	71.6823	28.99	28.99	0	4.51	127	4.1
UGC9753	227.4447	57.0002	30.0	30.0	0	4.18	127	4.1
UGC9797	228.8472	55.5174	30.0	30.0	0	2.23	63	16.7
UGC9805	229.1801	55.4093	29.16	28.95	0	1.58	63	16.7
UGC9858	231.6728	40.5645	32.57	26.23	0	2.26	63	16.6
UGC9969	234.9045	59.3319	27.78	27.59	90	1.91	63	16.6
UGC9992	235.4494	67.2542	29.75	29.57	0	7.15	127	2.1
UGC10310	244.0765	47.0464	30.0	30.0	0	4.12	127	4.1
UGC10359	245.2423	65.3906	30.0	30.0	0	4.26	127	4.1
UGC10445	248.4484	28.9848	27.09	22.94	0	5.93	127	4.1
UGC10470	248.1633	78.1982	34.49	34.14	0	4.37	127	4.1
UGC10564	251.5916	70.3588	30.0	30.0	0	4.25	127	4.1
UGC11124	271.8646	35.5633	30.24	23.79	0	4.25	127	4.1
UGC11218	274.9434	74.5684	30.7	25.28	0	2.02	63	16.6
UGC11269	277.6658	67.987	34.82	31.36	0	0.69	127	8.3
UGC11283	278.469	49.2786	27.17	26.96	0	4.39	127	4.2
UGC11429	290.2392	43.1325	29.12	29.11	0	1.62	63	16.8
UGC11466	295.7448	45.2982	31.39	28.02	0	4.87	127	4.1
UGC11496	298.2585	67.665	28.42	28.22	0	4.42	127	4.2
UGC11670	315.8899	29.8975	37.34	23.64	0	0.79	127	8.3
UGC11852	328.9971	27.8984	36.23	26.56	0	0.88	127	8.4
UGC11861	329.1	73.2607	30.0	30.0	0	4.39	127	4.1
UGC11864	329.4782	42.3062	35.7	28.49	0	2.71	127	4.2
UGC11891	330.8912	43.7492	30.0	30.0	0	4.25	127	4.1
UGC11909	331.5674	47.2512	31.1	30.75	0	4.7	127	4.1
UGC11914	331.9683	31.3593	36.59	21.36	0	0.77	127	8.3

Table 2.4 – *Continued from previous page*

Name	R.A.	Dec	B_{maj}	B_{min}	BPA	Noise	Channels	ΔV
	deg	deg	$''$	$''$	deg	mJy beam^{-1}		km s^{-1}
(1)	(2)	(3)	(4)	(5)	(6)	(7)	(8)	(9)
UGC11951	333.1255	45.3285	26.98	26.98	0	4.11	127	4.1
UGC11994	335.2213	33.2953	30.21	23.87	0	1.7	63	16.8
UGC12043	336.9605	29.096	37.82	24.55	0	1.28	127	4.1
UGC12060	337.6416	33.8197	30.0	30.0	0	3.94	127	4.1
UGC12082	338.5451	32.8605	29.03	28.52	0	5.56	127	2.1
UGC12212	342.6264	29.1384	31.37	23.94	0	5.56	127	2.1
UGC12276	344.6356	35.8024	33.1	26.83	0	0.88	127	4.2
UGC12554	350.5274	40.8454	29.35	28.98	90	2.67	127	2.1
UGC12632	352.4945	40.9902	28.46	26.93	0	4.02	127	4.1
UGC12693	353.9318	32.3851	31.77	23.74	0	3.99	127	4.2
UGC12713	354.5614	30.7092	31.87	24.8	0	1.13	127	4.1
UGC12732	355.1661	26.2364	30.0	30.0	0	4.21	127	4.1
UGC12754	355.9765	26.0756	30.0	30.0	0	4.32	127	4.1
UGC12808	357.7665	20.1504	55.96	31.9	0	0.81	127	8.4

Table 2.5: **HI global properties.** Col 2: Systemic velocity. Col 3-4: Global profile linewidths at the 20% and 50% levels. Col 5: HI radius measured at $1 M_{\odot} pc^{-2}$. Col 6-7: Integrated HI flux and total HI mass. Col 8: Relative log uncertainty on mass. Col 9-10: Distance in Mpc and associated uncertainty. Col 11: The literature source of the distances, with NED for Mould flow model estimates from the NED database and CF2 for Cosmic flow database.

Name	V_{sys}	W_{20}	W_{50}	R_{HI}	$\int$ Sdv	M_{HI}	e(M_{HI})	D	e(D)	Ref
	km s^{-1}	km s^{-1}	km s^{-1}	$''$	Jy km s^{-1}	log($M_{\odot}$)	Mpc	Mpc		
(1)	(2)	(3)	(4)	(5)	(6)	(7)	(8)	(9)	(10)	(11)
UGC89	4509.8	425.2	371.9	82	6.8	9.66	0.17	53.7	10.7	CF2
UGC192	−366.4	69.7	52.1	403	241.0	7.49	0.05	0.7	0.0	CF2
UGC232	4779.1	272.8	252.4	100	8.3	9.91	0.06	64.2	4.5	NED
UGC485	5167.4	370.0	349.5	105	14.8	10.22	0.06	69.2	4.8	NED
UGC528	661.7	129.2	82.2	100	13.7	8.6	0.06	11.1	0.8	NED
UGC624	4709.6	543.4	509.1	121	21.8	10.5	0.17	78.3	15.7	CF2
UGC625	2630.7	348.0	328.6	174	37.3	9.93	0.17	31.2	6.2	CF2
UGC655	801.3	127.3	115.5	155	20.1	8.92	0.06	13.2	0.9	NED
UGC690	5788.5	315.3	297.7	69	3.6	9.71	0.06	77.6	5.4	NED
UGC731	618.7	143.4	129.6	188	44.4	9.12	0.06	11.3	0.8	NED

Table 2.5 – *Continued from previous page*

Name	V_{sys}	W_{20}	W_{50}	R_{HI}	$\int$ Sdv	M_{HI}	e(M_{HI})	D	e(D)	Ref
	km s^{-1}	km s^{-1}	km s^{-1}	$''$	Jy km s^{-1}	log($M_\odot$)	Mpc	Mpc		
(1)	(2)	(3)	(4)	(5)	(6)	(7)	(8)	(9)	(10)	(11)
UGC798	4833.2	212.2	192.5	67	3.0	9.46	0.06	64.4	4.5	NED
UGC1013	5121.4	521.9	487.0	102	4.7	9.64	0.17	62.5	12.5	CF2
UGC1256	351.0	267.2	117.1	520	242.6	9.47	0.09	7.2	0.7	CF2
UGC1281	129.3	133.0	120.4	197	32.7	8.33	0.09	5.3	0.5	CF2
UGC1437	4832.1	333.9	303.9	107	13.8	10.13	0.06	64.5	4.5	NED
UGC1501	224.5	119.7	99.5	237	63.7	8.6	0.08	5.2	0.5	CF2
UGC1541	5559.7	429.9	358.8	100	9.9	10.11	0.06	74.4	5.2	NED
UGC1633	4191.1	451.8	438.9	106	12.3	9.99	0.17	58.1	11.6	CF2
UGC1810	7535.0	411.5	304.1	97	6.3	10.17	0.06	99.6	7.0	NED
UGC1856	4737.0	269.7	253.7	129	24.8	10.36	0.06	62.9	4.4	NED
UGC1886	4788.4	485.3	466.0	132	14.8	10.16	0.06	64.1	4.5	NED
UGC1913	567.5	221.3	204.4	393	264.6	9.7	0.06	8.9	0.6	CF2
UGC2023	574.1	46.1	32.3	127	12.8	8.43	0.06	9.5	0.7	NED
UGC2034	550.9	46.9	34.7	172	29.5	8.82	0.06	9.7	0.7	NED
UGC2045	1497.4	333.4	288.3	129	27.6	9.21	0.17	15.8	3.2	CF2
UGC2053	995.3	69.3	53.5	112	11.3	8.76	0.06	14.7	1.0	NED
UGC2080	876.3	130.8	116.6	369	115.4	9.7	0.06	13.6	1.0	NED
UGC2082	732.9	203.3	190.0	190	35.1	9.17	0.17	13.4	2.7	CF2
UGC2141	1009.8	232.2	195.1	128	29.4	9.15	0.06	14.2	1.0	NED
UGC2183	1531.6	287.4	262.5	185	46.5	10.02	0.17	30.9	6.2	CF2
UGC2193	490.7	36.1	25.8	237	32.2	8.77	0.06	8.8	0.6	NED
UGC2455	400.8	103.3	63.6	176	51.4	8.7	0.06	6.4	0.4	NED
UGC2459	2474.4	329.8	313.8	164	34.8	10.08	0.17	38.2	7.6	CF2
UGC2487	4921.2	454.5	428.6	187	24.1	10.38	0.06	65.0	4.5	NED
UGC2503	2397.0	459.1	438.0	179	22.9	9.78	0.17	33.6	6.7	CF2
UGC2800	1191.2	219.3	208.4	172	24.5	9.32	0.17	19.0	3.8	CF2
UGC2855	1199.6	423.7	382.0	198	73.5	9.56	0.17	14.4	2.9	CF2
UGC2916	4491.1	352.0	329.7	112	24.2	10.34	0.06	62.2	4.4	NED
UGC2941	6169.5	152.0	117.5	99	14.5	10.36	0.06	82.1	5.8	NED
UGC3013	2444.2	331.4	309.5	206	27.9	9.44	0.17	20.4	4.1	CF2
UGC3137	978.8	239.3	228.3	213	47.9	9.75	0.17	22.4	4.5	CF2
UGC3205	3566.5	426.3	411.3	127	17.0	9.97	0.06	48.0	3.4	NED
UGC3326	4060.5	516.5	498.0	110	8.1	10.06	0.17	77.6	15.5	CF2
UGC3334	3921.7	671.0	615.9	183	59.2	10.62	0.06	54.9	3.8	NED
UGC3354	3060.0	413.7	392.1	132	23.6	10.19	0.17	52.5	10.5	CF2
UGC3371	796.9	139.1	128.4	181	26.7	9.16	0.06	15.1	1.1	NED
UGC3382	4461.4	201.8	191.1	79	4.5	9.61	0.06	62.0	4.3	NED

Table 2.5 – *Continued from previous page*

Name	V_{sys}	W_{20}	W_{50}	R_{HI}	$\int$ Sdv	M_{HI}	e(M_{HI})	D	e(D)	Ref
	km s^{-1}	km s^{-1}	km s^{-1}	$''$	Jy km s^{-1}	log($M_\odot$)	Mpc	Mpc		
(1)	(2)	(3)	(4)	(5)	(6)	(7)	(8)	(9)	(10)	(11)
UGC3384	1074.6	77.4	70.3	127	20.7	9.23	0.06	18.6	1.3	NED
UGC3407	3580.1	299.5	284.4	53	1.9	9.04	0.06	49.6	3.5	NED
UGC3546	1825.6	359.3	340.6	146	16.7	9.49	0.06	28.0	2.0	NED
UGC3574	1437.9	157.5	141.1	172	38.6	9.56	0.17	20.0	4.0	CF2
UGC3580	1203.3	236.8	220.9	176	30.0	9.46	0.06	20.2	1.4	NED
UGC3642	4483.6	458.6	435.1	169	25.5	10.37	0.06	62.7	4.4	NED
UGC3698	429.2	44.4	35.3	64	3.1	7.97	0.09	11.3	1.1	CF2
UGC3711	423.6	162.0	144.6	135	28.1	8.97	0.09	11.8	1.2	CF2
UGC3734	982.3	154.1	141.4	136	14.1	8.95	0.06	16.3	1.1	NED
UGC3740	2386.0	156.2	97.9	99	14.8	9.67	0.06	36.4	2.6	NED
UGC3759	4378.6	432.2	417.3	77	6.2	10.06	0.17	88.3	17.7	CF2
UGC3817	420.9	44.1	32.1	99	8.3	8.11	0.06	8.1	0.6	NED
UGC3826	1716.4	53.0	48.1	114	3.3	8.76	0.06	27.0	1.9	NED
UGC3965	4656.1	88.5	69.8	112	10.0	10.0	0.06	65.0	4.5	NED
UGC3966	353.9	80.7	71.5	92	8.2	8.32	0.09	10.4	1.0	CF2
UGC3993	4325.5	200.6	189.0	87	6.0	9.74	0.06	61.8	4.3	NED
UGC4036	3439.5	121.5	110.1	84	5.2	9.39	0.07	44.7	3.6	CF2
UGC4165	503.6	115.0	101.2	138	27.0	8.77	0.06	9.6	0.7	NED
UGC4173	844.8	77.3	61.4	259	33.7	9.32	0.06	16.3	1.1	NED
UGC4256	5197.1	179.9	158.3	78	6.7	9.93	0.06	73.3	5.1	NED
UGC4273	2477.6	315.6	296.0	125	16.9	9.67	0.17	34.2	6.8	CF2
UGC4278	551.3	191.2	170.7	202	45.4	9.23	0.17	12.6	2.5	CF2
UGC4284	539.5	213.8	193.1	334	147.6	9.67	0.08	11.5	1.0	CF2
UGC4305	141.6	66.6	53.4	423	271.3	8.84	0.05	3.3	0.2	CF2
UGC4325	517.3	141.8	131.7	152	27.4	8.83	0.17	10.2	2.0	CF2
UGC4458	4723.8	273.0	230.9	120	11.4	10.08	0.06	67.1	4.7	NED
UGC4483	151.0	46.8	30.4	132	13.1	7.58	0.07	3.5	0.3	CF2
UGC4499	680.6	127.8	116.3	162	25.8	9.0	0.06	12.9	0.9	NED
UGC4543	1942.5	119.3	107.5	146	20.6	9.66	0.06	30.6	2.1	NED
UGC4605	1369.8	421.7	383.3	271	58.4	10.15	0.17	31.9	6.4	CF2
UGC4666	867.3	301.0	284.6	160	21.7	9.13	0.06	16.3	1.1	NED
UGC4806	1969.5	350.2	326.1	158	40.4	9.78	0.17	25.0	5.0	CF2
UGC4838	2605.3	186.1	167.8	147	26.3	9.99	0.06	39.8	2.8	NED
UGC5060	1716.4	153.9	66.6	81	5.9	9.03	0.06	27.7	1.9	NED
UGC5079	535.7	383.9	365.8	451	178.8	9.58	0.17	9.5	1.9	CF2
UGC5251	1460.9	290.6	265.4	244	73.6	9.82	0.17	19.6	3.9	CF2
UGC5253	1313.7	318.1	300.2	270	71.1	9.94	0.06	22.9	1.6	NED

Table 2.5 – *Continued from previous page*

Name	V_{sys}	W_{20}	W_{50}	R_{HI}	$\int$ Sdv	M_{HI}	e(M_{HI})	D	e(D)	Ref
	km s^{-1}	km s^{-1}	km s^{-1}	$''$	Jy km s^{-1}	log($M_\odot$)	Mpc	Mpc		
(1)	(2)	(3)	(4)	(5)	(6)	(7)	(8)	(9)	(10)	(11)
UGC5272	512.5	92.5	76.7	106	14.5	8.26	0.06	7.3	0.5	NED
UGC5351	1489.6	275.2	159.9	70	5.9	8.95	0.06	25.2	1.8	NED
UGC5414	602.8	113.8	99.0	141	23.9	8.76	0.06	10.1	0.7	NED
UGC5452	1365.4	221.7	204.2	112	17.5	9.55	0.17	29.2	5.8	CF2
UGC5459	1109.0	277.7	262.0	172	45.4	9.65	0.06	20.3	1.4	NED
UGC5532	2789.3	406.1	380.1	138	16.8	9.79	0.08	39.3	3.5	CF2
UGC5557	583.4	135.1	124.4	267	67.2	9.19	0.06	9.9	0.7	NED
UGC5589	1171.1	180.0	146.1	138	24.9	9.28	0.17	18.1	3.6	CF2
UGC5685	1348.2	411.4	396.8	185	35.2	9.9	0.17	30.8	6.2	CF2
UGC5717	1674.9	243.5	226.4	187	31.3	9.95	0.17	34.8	7.0	CF2
UGC5721	546.1	171.1	154.6	190	68.2	8.85	0.06	6.6	0.5	NED
UGC5786	998.5	223.3	166.3	191	62.4	9.72	0.06	18.8	1.3	NED
UGC5789	726.2	213.1	193.9	259	76.7	9.49	0.08	13.0	1.2	CF2
UGC5829	636.2	86.6	68.7	218	49.0	9.0	0.06	9.3	0.6	NED
UGC5840	613.9	170.8	154.1	327	127.6	9.46	0.09	9.8	1.0	CF2
UGC5846	1011.4	57.7	45.2	119	13.2	9.06	0.06	19.3	1.4	NED
UGC5906	1606.8	118.0	110.6	49	1.7	8.51	0.06	28.0	2.0	NED
UGC5909	1648.3	132.4	57.9	163	43.2	9.91	0.06	28.3	2.0	NED
UGC5918	336.6	75.0	61.7	132	16.3	8.38	0.06	7.9	0.6	NED
UGC5960	660.2	177.3	152.9	113	24.2	9.15	0.12	15.8	2.2	CF2
UGC5997	1274.0	295.2	282.5	207	52.9	9.96	0.17	26.9	5.4	CF2
UGC6001	1724.9	139.9	119.3	48	2.4	8.71	0.06	29.7	2.1	NED
UGC6118	1553.4	206.0	188.0	95	7.1	9.1	0.06	27.3	1.9	NED
UGC6126	722.7	199.0	181.9	198	58.9	9.59	0.17	16.7	3.3	CF2
UGC6161	772.0	132.6	104.7	152	26.7	8.93	0.17	11.7	2.3	CF2
UGC6225	711.7	325.9	303.0	283	142.3	9.53	0.17	10.0	2.0	CF2
UGC6251	942.2	54.7	44.4	98	9.4	8.86	0.06	18.0	1.3	NED
UGC6263	2125.5	349.7	321.6	135	21.9	9.8	0.06	35.0	2.5	NED
UGC6283	734.8	208.7	196.6	187	47.6	9.24	0.06	12.4	0.9	NED
UGC6446	632.3	144.2	130.0	173	34.5	9.12	0.06	12.7	0.9	NED
UGC6537	842.3	278.9	255.1	231	79.0	9.52	0.17	13.4	2.7	CF2
UGC6713	909.5	104.0	89.1	129	14.7	9.03	0.06	17.6	1.2	NED
UGC6742	764.6	131.1	90.4	69	5.6	8.26	0.17	11.8	2.4	CF2
UGC6778	949.9	307.5	269.1	245	73.2	9.79	0.06	19.0	1.3	NED
UGC6786	1799.6	429.4	414.8	164	35.4	10.06	0.17	37.2	7.4	CF2
UGC6787	1183.6	479.1	466.3	252	47.4	9.75	0.06	22.3	1.6	NED
UGC6813	951.8	42.7	37.7	102	6.6	8.74	0.06	18.8	1.3	NED

Table 2.5 – *Continued from previous page*

Name	V_{sys}	W_{20}	W_{50}	R_{HI}	$\int$ Sdv	M_{HI}	e(M_{HI})	D	e(D)	Ref
	km s^{-1}	km s^{-1}	km s^{-1}	$''$	Jy km s^{-1}	log($M_\odot$)	Mpc	Mpc		
(1)	(2)	(3)	(4)	(5)	(6)	(7)	(8)	(9)	(10)	(11)
UGC6817	248.7	43.9	27.1	171	19.6	7.5	0.07	2.6	0.2	CF2
UGC6833	938.1	160.8	151.0	156	24.8	8.96	0.17	12.4	2.5	CF2
UGC6840	1032.3	201.3	139.1	209	55.9	9.74	0.06	20.4	1.4	NED
UGC6884	3174.6	133.3	108.6	109	14.0	9.89	0.06	48.7	3.4	NED
UGC6921	960.5	197.4	134.7	67	5.7	8.58	0.17	16.8	3.4	CF2
UGC6930	779.7	134.6	118.6	179	40.3	9.34	0.06	15.2	1.1	NED
UGC6964	904.9	281.5	266.5	162	36.6	9.5	0.17	19.0	3.8	CF2
UGC7030	694.6	261.7	238.4	155	33.5	8.98	0.17	11.0	2.2	CF2
UGC7047	194.5	75.0	54.6	159	30.7	8.15	0.09	4.4	0.4	CF2
UGC7075	732.1	279.5	265.2	112	16.6	9.23	0.17	20.8	4.2	CF2
UGC7089	767.0	153.7	57.6	120	18.1	8.76	0.17	11.7	2.3	CF2
UGC7095	1056.2	391.4	372.2	205	33.9	9.52	0.17	20.3	4.1	CF2
UGC7125	1074.8	158.1	139.8	172	40.3	9.64	0.06	21.3	1.5	NED
UGC7151	265.9	169.4	157.1	199	51.4	8.75	0.08	6.8	0.6	CF2
UGC7166	1012.7	133.0	113.7	333	55.5	9.7	0.06	19.6	1.4	NED
UGC7183	769.9	415.9	386.1	278	102.5	9.89	0.17	18.0	3.6	CF2
UGC7199	166.5	35.1	22.1	69	4.4	6.96	0.07	3.0	0.2	CF2
UGC7204	1101.4	172.0	154.4	187	32.9	9.09	0.17	12.5	2.5	CF2
UGC7222	940.5	256.8	232.4	177	40.1	9.41	0.17	16.4	3.3	CF2
UGC7232	231.2	73.6	51.2	114	17.3	7.51	0.09	2.8	0.3	CF2
UGC7256	1098.7	312.5	226.0	241	57.2	9.5	0.12	15.3	2.1	CF2
UGC7261	861.8	95.1	81.4	175	31.4	9.16	0.06	13.9	1.0	NED
UGC7321	423.0	231.0	217.2	205	35.2	9.61	0.17	22.2	4.4	CF2
UGC7323	514.3	135.3	120.1	178	42.2	8.47	0.17	5.4	1.1	CF2
UGC7399	533.9	187.5	163.1	156	38.0	8.87	0.06	9.1	0.6	NED
UGC7408	462.0	26.2	18.2	83	4.5	7.75	0.09	7.3	0.7	CF2
UGC7483	1270.4	207.2	193.8	117	17.2	9.42	0.06	25.5	1.8	NED
UGC7489	1036.0	72.5	40.4	40	1.6	8.23	0.06	20.9	1.5	NED
UGC7490	462.1	64.4	59.3	108	9.7	8.43	0.06	10.9	0.8	NED
UGC7506	2523.8	159.9	103.7	60	3.7	8.57	0.17	20.7	4.1	CF2
UGC7524	338.2	131.7	115.9	486	295.6	9.2	0.09	4.8	0.5	CF2
UGC7559	216.6	74.7	61.8	170	28.5	8.22	0.09	5.0	0.5	CF2
UGC7592	196.4	135.5	95.9	407	280.1	9.08	0.09	4.3	0.4	CF2
UGC7603	647.2	144.0	130.0	179	39.1	8.64	0.17	6.8	1.4	CF2
UGC7690	531.9	96.0	84.0	126	20.7	8.57	0.06	8.7	0.6	NED
UGC7704	947.2	89.1	59.5	77	9.5	8.82	0.06	17.2	1.2	NED
UGC7766	806.1	251.8	239.4	497	298.5	9.58	0.17	7.3	1.5	CF2

Table 2.5 – *Continued from previous page*

Name	V_{sys}	W_{20}	W_{50}	R_{HI}	$\int$ Sdv	M_{HI}	e(M_{HI})	D	e(D)	Ref
	km s^{-1}	km s^{-1}	km s^{-1}	$''$	Jy km s^{-1}	log($M_\odot$)	Mpc	Mpc		
(1)	(2)	(3)	(4)	(5)	(6)	(7)	(8)	(9)	(10)	(11)
UGC7831	153.3	173.8	141.5	129	33.0	8.38	0.09	5.6	0.6	CF2
UGC7853	571.5	147.5	107.6	230	94.9	9.22	0.06	8.6	0.6	NED
UGC7866	352.2	57.8	46.8	145	16.9	7.92	0.09	4.6	0.5	CF2
UGC7971	470.3	69.3	53.9	110	15.5	8.19	0.09	6.5	0.6	CF2
UGC7989	1204.8	407.2	382.4	361	85.6	9.51	0.07	12.6	1.0	CF2
UGC8146	676.9	174.2	160.3	169	29.6	9.46	0.17	20.3	4.1	CF2
UGC8188	298.1	47.7	33.8	188	44.7	8.31	0.05	4.4	0.3	CF2
UGC8201	21.3	53.9	38.3	155	23.7	8.12	0.09	4.8	0.5	CF2
UGC8246	821.9	148.7	132.7	124	12.5	8.82	0.17	14.9	3.0	CF2
UGC8271	1145.8	165.5	78.2	108	14.9	8.36	0.17	8.1	1.6	CF2
UGC8286	423.0	189.2	177.9	230	50.3	8.73	0.08	6.7	0.6	CF2
UGC8331	271.6	61.0	42.3	102	12.7	7.76	0.09	4.4	0.4	CF2
UGC8396	962.8	166.8	146.6	89	11.3	8.99	0.06	19.1	1.3	NED
UGC8490	204.3	129.1	113.2	335	129.5	8.84	0.08	4.8	0.4	CF2
UGC8508	70.2	61.8	50.0	88	11.8	7.29	0.07	2.6	0.2	CF2
UGC8550	375.0	136.1	121.8	167	26.3	8.51	0.06	7.2	0.5	NED
UGC8651	220.2	52.4	42.4	118	10.9	7.4	0.07	3.1	0.2	CF2
UGC8683	638.6	34.9	26.8	89	6.0	8.32	0.06	12.1	0.8	NED
UGC8709	2409.4	409.5	385.8	195	46.7	10.24	0.06	39.9	2.8	NED
UGC8711	1518.0	326.2	305.9	147	32.7	9.56	0.17	21.6	4.3	CF2
UGC8805	2392.8	123.7	89.8	51	3.7	9.13	0.06	39.2	2.8	NED
UGC8837	144.5	110.1	65.9	152	23.0	8.45	0.09	7.2	0.7	CF2
UGC8863	1798.1	383.0	358.6	164	13.6	9.29	0.17	24.7	4.9	CF2
UGC9018	311.4	66.4	55.0	121	17.8	8.28	0.09	6.8	0.7	CF2
UGC9128	175.4	47.5	33.6	120	24.3	7.47	0.07	2.3	0.2	CF2
UGC9211	695.7	108.0	98.4	170	24.1	9.08	0.06	14.5	1.0	NED
UGC9242	1449.9	209.3	192.9	152	19.5	9.49	0.17	25.9	5.2	CF2
UGC9366	2124.9	456.4	430.3	135	24.9	9.85	0.17	34.7	6.9	CF2
UGC9431	2241.9	345.4	329.8	144	20.9	9.87	0.17	38.7	7.8	CF2
UGC9644	6612.1	124.7	111.5	61	3.1	9.85	0.06	97.8	6.8	NED
UGC9649	448.7	166.0	154.2	180	30.6	8.96	0.06	11.2	0.8	NED
UGC9753	758.0	281.2	269.5	155	23.6	9.23	0.17	17.4	3.5	CF2
UGC9797	3362.7	353.9	334.1	200	40.1	10.31	0.17	46.6	9.3	CF2
UGC9805	3300.5	660.2	626.6	97	14.2	9.94	0.06	51.1	3.6	NED
UGC9858	2617.4	378.6	351.0	181	41.7	10.18	0.17	39.3	7.8	CF2
UGC9969	2515.2	539.1	513.0	183	22.4	10.13	0.17	50.4	10.1	CF2
UGC9992	430.6	46.6	36.5	103	8.0	8.38	0.09	11.3	1.1	CF2

Table 2.5 – *Continued from previous page*

Name	V_{sys}	W_{20}	W_{50}	R_{HI}	$\int$ Sdv	M_{HI}	$e(M_{HI})$	D	e(D)	Ref
	km s^{-1}	km s^{-1}	km s^{-1}	$''$	Jy km s^{-1}	log($M_\odot$)	Mpc	Mpc		
(1)	(2)	(3)	(4)	(5)	(6)	(7)	(8)	(9)	(10)	(11)
UGC10310	726.6	99.8	88.4	140	18.2	9.05	0.06	16.1	1.1	NED
UGC10359	907.9	218.7	201.6	288	92.5	9.88	0.06	18.6	1.3	NED
UGC10445	979.7	153.6	128.3	136	21.1	9.7	0.17	31.6	6.3	CF2
UGC10470	1353.3	194.1	168.1	246	66.3	9.95	0.06	23.9	1.7	NED
UGC10564	1129.0	168.8	153.2	174	34.6	9.66	0.17	23.8	4.8	CF2
UGC11124	1599.8	156.8	137.2	115	14.4	9.43	0.06	28.2	2.0	NED
UGC11218	1483.7	345.3	324.1	143	28.8	9.49	0.17	21.3	4.3	CF2
UGC11269	2566.1	406.8	332.7	161	36.6	10.24	0.17	44.9	9.0	CF2
UGC11283	1946.9	198.2	161.2	89	12.1	9.47	0.06	32.1	2.2	NED
UGC11429	4599.0	514.0	497.0	101	9.1	10.0	0.17	68.2	13.6	CF2
UGC11466	818.5	244.9	182.0	119	29.9	9.23	0.17	15.6	3.1	CF2
UGC11496	2107.9	128.7	118.3	74	4.5	9.06	0.06	33.1	2.3	NED
UGC11670	756.0	335.4	318.2	168	25.6	9.12	0.06	14.8	1.0	NED
UGC11852	5766.5	315.1	288.4	144	19.6	10.47	0.06	79.8	5.6	NED
UGC11861	1468.2	256.7	235.3	177	39.8	9.74	0.06	24.1	1.7	NED
UGC11864	4296.4	161.4	149.7	108	13.4	10.05	0.06	59.9	4.2	NED
UGC11891	447.0	149.0	130.6	256	79.4	9.05	0.17	7.7	1.5	CF2
UGC11909	1094.1	243.5	225.3	203	61.3	9.34	0.17	12.3	2.5	CF2
UGC11914	945.2	315.8	304.8	109	10.6	8.81	0.06	16.1	1.1	NED
UGC11951	1095.7	214.2	201.0	109	18.3	8.94	0.17	14.2	2.8	CF2
UGC11994	4828.2	423.3	410.3	82	5.3	9.73	0.17	65.8	13.2	CF2
UGC12043	989.8	187.5	176.1	145	19.9	9.11	0.06	16.5	1.2	NED
UGC12060	869.9	121.3	109.2	171	23.1	9.1	0.06	15.1	1.1	NED
UGC12082	789.9	80.1	68.8	171	22.7	9.01	0.06	13.9	1.0	NED
UGC12212	911.2	107.3	96.7	120	12.1	8.79	0.06	14.7	1.0	NED
UGC12276	5587.9	128.1	104.3	69	3.5	9.68	0.06	76.3	5.3	NED
UGC12554	368.8	250.5	236.2	456	290.8	9.69	0.09	8.4	0.8	CF2
UGC12632	402.0	120.4	107.1	291	57.3	9.04	0.06	9.0	0.6	NED
UGC12693	4899.5	234.5	220.4	103	8.8	9.88	0.17	60.5	12.1	CF2
UGC12713	270.7	144.4	102.2	85	7.5	7.94	0.06	7.0	0.5	NED
UGC12732	728.5	129.8	115.9	290	73.2	9.41	0.06	12.2	0.9	NED
UGC12754	776.1	203.9	188.6	155	40.8	9.25	0.17	13.6	2.7	CF2
UGC12808	4157.1	360.7	313.8	82	12.3	9.96	0.06	56.1	3.9	NED

Table 2.6: **Photometric parameters of Infrared data from WISE**
Note: Cols (2-3) - Axial ratio and position angle of the stellar disk, measured in the W1 band. Col (4) - Semi major axis of the 1σ isophote in W1. Cols (5-10) W1, W3 and W4 Vega magnitudes, with corresponding magnitude errors which were used to calculate the signal to noise ratio in the respective bands. The SNR in W3 was used to define a sample threshold for sample B described in text. Cols (11-12) - W1-W2 and W2-W3 color indices. Col (13) - Morphologies

Name	b/a	pa	$R1_{iso}$	mag_1	Δmag_1	mag_3	Δmag_3	mag_4	Δmag_4	W1W2	W2W3	Morph
		deg	$''$	mag	mag	mag	mag	mag	mag	mag	mag	
(1)	(2)	(3)	(4)	(5)	(6)	(7)	(8)	(9)	(10)	(11)	(12)	(13)
UGC89	0.65	169.3	100.03	8.568	0.011	4.807	0.012	2.366	0.012	0.132	3.63	Sa
UGC192	0.87	125.8	440.03	5.113	0.011	2.321	0.012	−0.322	0.012	0.08	2.712	Im
UGC232	0.62	10.3	58.55	10.479	0.012	7.076	0.013	4.341	0.015	0.101	3.338	Sa
UGC485	0.23	179.3	84.1	10.505	0.012	7.574	0.016	6.158	0.056	0.072	2.883	Scd
UGC528	0.97	173.2	122.95	7.437	0.011	3.419	0.011	1.412	0.012	0.179	3.839	Sb
UGC624	0.52	109.2	109.12	8.942	0.011	5.431	0.012	3.778	0.015	0.1	3.445	Sab
UGC625	0.33	152.3	134.55	9.111	0.011	5.505	0.012	3.752	0.018	0.124	3.482	Sbc
UGC655	0.82	130.4	58.62	11.461	0.014	10.988	0.092	10.125	0.776	0.015	0.569	Sm
UGC690	0.72	93.9	69.02	10.218	0.012	7.026	0.014	5.401	0.034	0.073	3.146	Scd
UGC731	0.56	68.5	88.97	11.613	0.015	13.404	0.228	11.628	1.539	0.117	null	Im
UGC798	0.66	39.9	55.16	10.774	0.012	7.772	0.016	5.91	0.038	0.061	2.976	Sa
UGC1013	0.35	59.4	134.92	9.002	0.011	6.862	0.016	5.515	0.059	0.021	2.141	Sb
UGC1256	0.35	71.0	271.91	8.283	0.011	5.687	0.012	3.625	0.018	0.053	2.628	Scd
UGC1281	0.18	41.0	155.75	10.776	0.012	10.06	0.202	7.166	0.191	0.119	0.666	Sdm
UGC1437	0.69	120.8	98.87	8.959	0.011	5.113	0.012	3.295	0.014	0.181	3.683	Sbc
UGC1501	0.24	179.9	219.91	9.618	0.012	9.146	0.147	6.059	0.112	0.026	0.589	Sdm
UGC1541	0.69	69.4	89.11	9.437	0.011	7.36	0.016	6.008	0.06	0.013	2.101	Sa
UGC1633	0.46	111.1	94.11	9.09	0.011	5.609	0.012	3.909	0.024	0.094	3.387	Sc

Table 2.6 – *Continued from previous page*

Name	b/a	pa	$R1_{iso}$	mag_1	Δmag_1	mag_3	Δmag_3	mag_4	Δmag_4	W1W2	W2W3	Morph
		deg	$''$	mag	mag	mag	mag	mag	mag	mag	mag	
(1)	(2)	(3)	(4)	(5)	(6)	(7)	(8)	(9)	(10)	(11)	(12)	(13)
UGC1810	0.65	54.3	94.51	9.634	0.012	7.171	0.02	5.624	0.085	0.013	2.494	Sb
UGC1856	0.2	120.6	97.34	11.394	0.015	8.161	0.029	5.94	0.089	−0.188	3.421	Sd
UGC1886	0.54	40.0	111.57	9.302	0.012	7.219	0.025	5.666	0.102	0.011	2.104	Sbc
UGC1913	0.5	110.1	311.71	7.57	0.011	4.386	0.013	2.453	0.021	0.053	3.131	Sd
UGC2023	0.76	153.8	91.19	11.029	0.013	13.784	0.628	9.52	0.489	0.132	null	Im
UGC2034	0.94	129.1	67.55	11.157	0.014	17.651	51.405	9.441	0.495	−0.002	null	Im
UGC2045	0.54	149.1	183.07	7.415	0.011	3.169	0.011	1.05	0.012	0.222	4.049	Sab
UGC2053	0.46	33.9	54.0	12.963	0.021	16.563	6.367	10.097	0.656	0.276	null	Im
UGC2080	0.9	126.5	185.42	8.158	0.011	5.272	0.014	3.877	0.034	0.014	2.903	Scd
UGC2082	0.22	133.0	147.81	9.858	0.012	7.583	0.023	5.992	0.112	0.024	2.289	Scd
UGC2141	0.44	19.7	123.66	9.109	0.011	5.733	0.013	3.354	0.017	0.134	3.274	S0/a
UGC2183	0.59	157.9	113.78	8.737	0.011	5.201	0.012	3.16	0.015	0.109	3.461	Sa
UGC2193	0.96	73.1	138.38	8.497	0.011	5.261	0.013	3.527	0.022	0.056	3.256	Sc
UGC2455	0.8	48.6	124.68	8.792	0.011	5.65	0.016	2.873	0.017	0.156	3.013	Im
UGC2459	0.32	60.9	100.17	9.701	0.012	6.796	0.037	4.978	0.034	0.15	2.784	Sdm
UGC2487	0.84	62.7	128.77	8.357	0.011	6.798	0.048	5.845	0.156	−0.024	1.628	S0
UGC2503	0.69	28.7	156.41	7.583	0.011	5.788	0.038	3.966	0.033	−0.006	1.82	Sb
UGC2800	0.4	106.2	93.38	10.37	0.012	11.932	0.672	7.017	0.092	0.051	null	Im
UGC2855	0.49	106.6	180.56	6.861	0.011	2.846	0.013	0.727	0.012	0.214	3.802	Sc
UGC2916	0.94	114.9	63.29	9.674	0.012	6.4	0.023	4.644	0.023	0.105	3.186	Sab
UGC2941	0.91	37.6	67.93	9.228	0.012	5.655	0.017	3.16	0.014	0.149	3.444	Sab
UGC3013	0.64	26.4	192.02	7.816	0.011	4.547	0.016	2.195	0.012	0.1	3.202	Sb

Table 2.6 – *Continued from previous page*

Name	b/a	pa	$R1_{iso}$	mag_1	Δmag_1	mag_3	Δmag_3	mag_4	Δmag_4	W1W2	W2W3	Morph
		deg	$''$	mag	mag	mag	mag	mag	mag	mag	mag	
(1)	(2)	(3)	(4)	(5)	(6)	(7)	(8)	(9)	(10)	(11)	(12)	(13)
UGC3137	0.22	75.2	140.53	10.307	0.012	7.983	0.231	5.744	0.068	0.074	2.304	Sb
UGC3205	0.46	45.1	80.12	9.324	0.012	7.251	0.052	5.587	0.045	0.054	2.031	Sab
UGC3326	0.19	65.7	150.79	9.223	0.011	6.541	0.039	4.688	0.026	0.127	2.575	Scd
UGC3334	0.77	79.6	207.9	7.425	0.011	4.123	0.028	2.472	0.017	0.085	3.248	Sc
UGC3354	0.35	164.8	121.33	9.014	0.011	5.681	0.022	3.785	0.022	0.18	3.175	Sab
UGC3371	0.71	144.2	95.46	11.431	0.015	14.921	7.83	10.912	1.282	−0.062	null	Im
UGC3382	0.94	178.4	58.38	9.646	0.012	7.618	0.037	6.419	0.074	0.005	2.04	Sa
UGC3384	0.9	139.2	29.29	12.926	0.021	null	null	12.265	7.053	−0.049	null	Sm
UGC3407	0.74	176.5	49.39	9.845	0.012	7.37	0.02	4.201	0.015	0.038	2.456	Sa
UGC3546	0.62	50.3	131.24	8.143	0.011	4.712	0.012	2.031	0.012	0.303	3.136	Sa
UGC3574	0.88	45.3	123.7	9.735	0.012	7.049	0.02	5.22	0.057	−0.077	3.034	Scd
UGC3580	0.51	5.9	113.89	9.702	0.012	6.389	0.138	4.478	0.1	0.066	3.309	pec
UGC3642	0.78	158.0	120.9	9.08	0.011	7.35	0.025	5.935	0.188	−0.029	1.835	S0
UGC3698	0.6	1.6	38.65	12.648	0.018	19.96	null	null	null	−0.081	null	Im
UGC3711	0.66	105.8	87.37	9.913	0.012	7.184	0.015	4.247	0.017	0.113	2.664	Im
UGC3734	0.89	156.5	124.26	8.867	0.012	6.568	0.019	5.158	0.08	−0.023	2.394	Sc
UGC3740	1.0	17.9	148.76	8.194	0.011	4.044	0.014	1.831	0.012	0.224	3.994	Sc
UGC3759	0.61	7.1	81.65	9.197	0.011	5.909	0.012	4.247	0.019	0.062	3.253	Sb
UGC3817	0.89	176.0	27.74	13.888	0.038	null	null	null	null	null	null	Im
UGC3826	0.82	160.5	113.0	10.171	0.012	7.58	0.032	5.828	0.115	−0.082	2.835	Sd
UGC3965	0.77	161.6	47.36	10.437	0.012	7.549	0.018	5.793	0.049	0.03	2.898	Sab
UGC3966	1.0	5.1	27.15	13.784	0.041	14.82	2.046	12.853	12.371	null	null	Im

Table 2.6 – *Continued from previous page*

Name	b/a	pa	$R1_{iso}$	mag_1	Δmag_1	mag_3	Δmag_3	mag_4	Δmag_4	W1W2	W2W3	Morph
		deg	″	mag	mag	mag	mag	mag	mag	mag	mag	
(1)	(2)	(3)	(4)	(5)	(6)	(7)	(8)	(9)	(10)	(11)	(12)	(13)
UGC3993	0.87	17.6	64.61	10.078	0.012	9.022	0.074	7.903	0.176	−0.022	1.105	S0
UGC4036	0.9	50.6	76.31	9.363	0.011	6.296	0.014	4.608	0.033	0.034	3.059	Sb
UGC4165	0.91	140.9	128.57	8.947	0.075	5.995	0.013	4.084	0.025	0.129	2.847	Sd
UGC4173	0.44	131.6	64.65	12.894	0.019	14.182	0.56	10.457	0.61	0.009	null	Im
UGC4256	0.81	7.1	68.32	9.271	0.011	5.063	0.012	2.891	0.014	0.195	4.013	Sc
UGC4273	0.48	46.1	100.83	9.173	0.011	5.766	0.013	3.748	0.02	0.08	3.347	Sb
UGC4278	0.14	172.3	168.85	10.443	0.012	8.447	0.044	6.156	0.096	−0.008	2.087	Sd
UGC4284	0.55	167.2	172.97	9.231	0.012	6.778	0.016	4.406	0.028	−0.048	2.61	Scd
UGC4305	0.71	33.3	183.47	9.446	0.012	7.479	0.065	4.144	0.059	0.175	1.793	Im
UGC4325	0.56	52.5	123.03	10.127	0.012	13.367	0.396	9.723	0.465	−0.058	null	Sm
UGC4458	0.92	137.7	100.49	9.023	0.012	6.377	0.018	4.884	0.067	0.04	2.653	Sa
UGC4483	0.39	173.9	42.29	13.585	0.028	11.742	0.366	8.293	0.299	0.073	2.071	Im
UGC4499	0.59	167.8	80.37	11.246	0.014	11.409	0.133	9.369	0.384	0.033	null	Sdm
UGC4543	0.59	0.6	66.93	11.655	0.015	11.806	0.157	9.764	0.487	−0.108	0.421	Sdm
UGC4605	0.24	64.1	162.1	8.347	0.011	6.901	0.017	5.469	0.064	0.002	1.455	Sab
UGC4666	0.68	47.1	127.55	8.221	0.011	5.863	0.014	4.748	0.057	0.035	2.33	pec
UGC4806	0.29	146.6	135.72	9.169	0.011	5.846	0.013	4.043	0.024	0.108	3.235	Sc
UGC4838	0.99	85.1	105.25	8.788	0.011	5.056	0.012	3.367	0.015	0.053	3.732	Sc
UGC5060	0.81	159.3	50.2	9.989	0.012	6.089	0.013	3.134	0.014	0.102	3.798	S0/a
UGC5079	0.49	21.5	388.99	5.671	0.011	2.065	0.011	0.094	0.012	0.091	3.515	Sbc
UGC5251	0.29	78.1	177.05	9.123	0.012	5.464	0.012	3.418	0.017	0.139	3.572	Sbc
UGC5253	0.78	7.1	270.71	7.094	0.011	4.083	0.012	2.549	0.016	0.05	3.016	Sab

Table 2.6 – *Continued from previous page*

Name	b/a	pa	$R1_{iso}$	mag_1	Δmag_1	mag_3	Δmag_3	mag_4	Δmag_4	W1W2	W2W3	Morph
		deg	$''$	mag	mag	mag	mag	mag	mag	mag	mag	
(1)	(2)	(3)	(4)	(5)	(6)	(7)	(8)	(9)	(10)	(11)	(12)	(13)
UGC5272	0.37	109.6	55.74	12.648	0.021	10.524	0.213	7.593	0.259	0.238	1.968	Im
UGC5351	0.54	101.9	87.15	8.608	0.011	4.584	0.012	2.48	0.013	0.188	3.836	Sab
UGC5414	0.53	25.5	117.68	10.796	0.013	14.535	0.946	9.61	0.353	−0.073	null	Im
UGC5452	0.39	40.5	66.18	11.219	0.013	8.518	0.033	6.274	0.074	−0.007	2.828	Sbc
UGC5459	0.33	132.1	140.18	9.371	0.012	6.043	0.013	3.969	0.021	0.132	3.215	Sc
UGC5532	0.84	158.9	214.54	7.095	0.011	3.869	0.011	2.188	0.013	0.09	3.165	Sbc
UGC5557	0.93	106.7	227.06	6.987	0.011	3.563	0.012	1.845	0.014	0.076	3.38	Scd
UGC5589	0.52	30.5	99.31	10.277	0.012	7.525	0.023	5.188	0.046	−0.001	2.836	Scd
UGC5685	0.3	45.1	158.05	8.769	0.011	6.303	0.016	4.812	0.057	−0.022	2.488	Sbc
UGC5717	0.56	19.2	92.22	9.86	0.012	6.454	0.012	4.791	0.023	0.041	3.423	Sbc
UGC5721	0.64	95.1	64.66	10.573	0.012	8.233	0.023	5.524	0.038	0.101	2.282	Sd
UGC5786	0.66	157.8	151.89	8.033	0.011	3.529	0.011	0.577	0.012	0.267	4.237	pec
UGC5789	0.58	39.8	198.05	9.041	0.012	7.12	0.018	5.436	0.055	0.016	2.003	Scd
UGC5829	0.79	25.2	87.46	11.445	0.016	11.727	0.661	13.283	28.354	−0.116	0.851	Im
UGC5840	0.89	1.4	238.54	7.07	0.011	3.825	0.012	2.061	0.014	0.058	3.235	Sbc
UGC5846	0.67	108.1	44.67	13.36	0.03	13.688	0.503	9.894	0.554	0.013	null	Im
UGC5906	0.95	29.2	63.75	9.651	0.012	7.205	0.014	5.485	0.034	0.014	2.455	Sa
UGC5909	0.86	54.3	73.12	9.881	0.012	6.293	0.014	4.43	0.03	0.047	3.577	Sd
UGC5918	1.0	17.6	27.73	14.087	0.038	15.987	4.204	11.532	1.353	−0.131	null	Im
UGC5960	0.55	2.8	67.78	10.366	0.012	7.659	0.021	5.156	0.035	0.034	2.722	S0
UGC5997	0.4	74.1	126.47	9.406	0.011	6.164	0.013	4.529	0.025	0.043	3.237	Sbc
UGC6001	0.91	45.2	35.17	10.572	0.012	6.39	0.013	4.411	0.02	0.18	4.002	Sa

Table 2.6 – *Continued from previous page*

Name	b/a	pa	$R1_{iso}$	mag_1	Δmag_1	mag_3	Δmag_3	mag_4	Δmag_4	W1W2	W2W3	Morph
		deg	″	mag	mag	mag	mag	mag	mag	mag	mag	
(1)	(2)	(3)	(4)	(5)	(6)	(7)	(8)	(9)	(10)	(11)	(12)	(13)
UGC6118	0.86	157.9	121.67	7.868	0.011	3.79	0.011	0.999	0.012	0.284	3.794	Sab
UGC6126	0.2	162.9	129.62	10.571	0.012	8.063	0.023	5.747	0.045	0.074	2.519	Sm
UGC6161	0.44	53.1	78.44	11.683	0.015	10.884	0.093	8.18	0.151	0.042	0.943	Sdm
UGC6225	0.35	79.9	302.67	6.677	0.011	2.844	0.011	0.756	0.012	0.17	3.663	Scd
UGC6251	0.85	62.1	33.44	13.114	0.022	14.751	1.296	10.011	0.617	−0.062	null	Sm
UGC6263	0.77	122.0	105.14	8.187	0.011	4.524	0.012	2.657	0.014	0.1	3.563	Sb
UGC6283	0.5	5.5	90.55	9.974	0.012	7.068	0.016	4.559	0.024	0.078	2.886	Sa
UGC6446	0.72	30.4	78.22	11.317	0.014	13.418	0.386	null	null	−0.044	null	Sd
UGC6537	0.63	19.1	217.01	7.519	0.011	4.221	0.012	2.473	0.014	0.087	3.227	Sc
UGC6713	0.94	69.6	49.24	11.994	0.015	12.577	0.204	null	null	0.119	null	Sm
UGC6742	0.68	21.9	54.54	10.482	0.012	7.231	0.014	4.877	0.022	0.079	3.21	S0
UGC6778	0.64	170.3	194.62	7.565	0.011	3.575	0.011	1.777	0.012	0.164	3.85	Sc
UGC6786	0.56	2.2	146.04	8.47	0.011	6.276	0.015	4.893	0.056	0.006	2.225	S0
UGC6787	0.64	108.6	231.06	7.484	0.011	5.889	0.016	4.725	0.074	−0.004	1.641	Sab
UGC6813	0.8	68.1	98.58	10.204	0.012	7.233	0.021	5.392	0.065	−0.024	3.124	Sd
UGC6817	0.6	31.9	83.81	12.011	0.019	10.246	0.345	7.618	0.597	0.107	1.658	Im
UGC6833	0.69	33.6	128.33	9.647	0.012	7.408	0.03	5.662	0.106	−0.129	2.531	Sc
UGC6840	0.36	83.3	88.11	11.863	0.015	10.16	0.051	8.31	0.172	0.05	1.943	Sm
UGC6884	0.94	0.7	93.14	8.991	0.011	5.474	0.012	3.796	0.019	0.09	3.449	Sbc
UGC6921	0.81	63.4	69.17	9.835	0.011	6.437	0.012	4.563	0.019	0.083	3.344	Sm
UGC6930	0.73	31.3	137.96	9.584	0.012	6.631	0.015	4.864	0.039	−0.032	3.077	Sd
UGC6964	0.19	64.8	176.13	9.102	0.011	5.716	0.012	3.843	0.02	0.109	3.277	Sd

Table 2.6 – *Continued from previous page*

Name	b/a	pa	$R1_{iso}$	mag_1	Δmag_1	mag_3	Δmag_3	mag_4	Δmag_4	W1W2	W2W3	Morph
		deg	$''$	mag	mag	mag	mag	mag	mag	mag	mag	
(1)	(2)	(3)	(4)	(5)	(6)	(7)	(8)	(9)	(10)	(11)	(12)	(13)
UGC7030	0.88	115.3	200.82	7.199	0.011	3.399	0.011	1.349	0.012	0.357	3.462	Sbc
UGC7047	0.66	34.6	105.47	10.217	0.012	9.087	0.074	6.61	0.143	−0.133	1.483	Im
UGC7075	0.33	75.2	103.06	8.826	0.011	4.867	0.011	2.902	0.012	0.173	3.787	Sc
UGC7089	0.24	35.1	130.48	10.682	0.012	9.194	0.038	7.415	0.135	−0.031	1.574	Sdm
UGC7095	0.35	167.4	194.39	7.719	0.011	4.31	0.011	2.368	0.012	0.093	3.327	Sbc
UGC7125	0.33	82.7	102.58	11.386	0.014	13.682	0.463	10.627	0.895	0.064	null	Sm
UGC7151	0.24	102.4	224.55	9.081	0.012	7.179	0.016	5.009	0.03	0.058	1.905	Scd
UGC7166	0.68	142.6	295.35	6.681	0.011	3.091	0.011	0.552	0.011	null	2.845	Sab
UGC7183	0.21	66.5	298.81	7.087	0.011	3.34	0.011	1.619	0.012	0.162	3.584	Sb
UGC7199	0.77	16.4	77.16	10.785	0.012	9.742	0.129	8.069	0.519	−0.086	1.292	Im
UGC7204	0.22	135.6	128.1	10.998	0.012	9.781	0.124	7.244	0.231	0.108	1.227	Sd
UGC7222	0.2	165.9	167.29	9.533	0.012	6.766	0.014	5.078	0.033	0.075	2.746	Scd
UGC7232	0.66	33.1	89.39	10.604	0.012	9.518	0.111	7.023	0.213	−0.015	1.256	Im
UGC7256	0.9	2.0	161.59	7.274	0.011	6.332	0.013	5.15	0.045	−0.011	0.972	S0
UGC7261	0.56	127.1	137.08	10.189	0.012	7.212	0.04	4.556	0.063	0.047	2.93	Sdm
UGC7321	0.12	81.6	169.26	10.5	0.012	8.113	0.034	6.35	0.119	0.06	2.376	Sd
UGC7323	0.82	11.9	221.79	8.538	0.012	6.35	0.02	4.678	0.069	0.044	2.289	Sdm
UGC7399	0.85	146.6	68.73	10.452	0.012	7.528	0.019	5.407	0.044	0.075	2.918	Sdm
UGC7408	0.79	106.3	72.26	11.528	0.015	11.66	0.724	8.184	0.568	0.082	null	Im
UGC7483	0.24	105.0	167.69	10.083	0.012	7.615	0.016	6.018	0.051	0.095	2.476	Sc
UGC7489	0.99	171.0	93.8	8.646	0.011	5.201	0.012	2.855	0.012	0.099	3.366	Sa
UGC7490	0.92	140.3	98.97	10.418	0.012	12.755	0.242	11.774	2.833	−0.062	null	Sm

Table 2.6 – *Continued from previous page*

Name	b/a	pa	$R1_{iso}$	mag_1	Δmag_1	mag_3	Δmag_3	mag_4	Δmag_4	W1W2	W2W3	Morph
		deg	″	mag	mag	mag	mag	mag	mag	mag	mag	
(1)	(2)	(3)	(4)	(5)	(6)	(7)	(8)	(9)	(10)	(11)	(12)	(13)
UGC7506	0.85	87.1	48.07	10.278	0.012	6.282	0.012	4.07	0.015	0.155	3.841	Sa
UGC7524	0.81	126.5	414.72	7.731	0.012	5.485	0.03	3.019	0.056	−0.044	2.291	Sm
UGC7559	0.54	160.7	72.21	12.383	0.019	10.86	0.239	7.994	0.327	0.206	1.792	Im
UGC7592	0.62	63.4	280.65	7.003	0.011	3.438	0.011	0.962	0.012	0.15	3.446	Im
UGC7603	0.39	16.2	100.02	10.41	0.012	8.605	0.054	6.213	0.111	−0.027	1.91	Sd
UGC7690	0.81	0.5	71.64	10.618	0.012	8.697	0.054	6.328	0.114	0.034	1.962	Im
UGC7704	1.0	7.9	28.32	12.033	0.013	8.709	0.037	5.307	0.031	0.18	3.144	Im
UGC7766	0.38	149.5	297.59	7.389	0.011	4.097	0.012	2.171	0.016	0.154	3.138	Scd
UGC7831	0.53	117.3	243.31	7.421	0.011	4.196	0.011	2.215	0.012	0.111	3.141	Sc
UGC7853	0.68	8.9	169.24	8.219	0.011	5.138	0.012	3.284	0.02	0.086	3.027	Sm
UGC7866	0.55	155.8	83.8	11.773	0.016	10.442	0.204	7.643	0.293	0.136	1.547	Im
UGC7971	0.75	41.9	77.47	11.543	0.014	10.728	0.245	8.105	0.42	0.016	1.114	Sm
UGC7989	0.63	40.0	386.33	6.086	0.011	3.991	0.012	2.615	0.023	−0.02	2.156	Sab
UGC8146	0.22	30.9	107.17	11.445	0.012	9.493	0.058	7.477	0.172	−0.04	2.09	Sd
UGC8188	0.94	109.3	184.24	9.32	0.012	7.691	0.052	5.565	0.138	0.035	1.832	Sm
UGC8201	0.52	98.2	114.65	11.125	0.014	15.413	22.258	8.729	1.558	−0.018	null	Im
UGC8246	0.22	88.0	88.74	11.841	0.014	10.437	0.068	8.021	0.138	0.103	1.424	Scd
UGC8271	0.49	103.3	65.24	9.844	0.012	6.343	0.012	4.116	0.015	0.136	3.384	S0/a
UGC8286	0.16	27.0	208.07	9.644	0.012	7.799	0.025	5.669	0.062	−0.012	1.954	Scd
UGC8331	0.39	133.9	78.02	12.324	0.016	10.409	0.153	8.091	0.351	0.174	1.983	Im
UGC8396	0.5	130.6	70.88	10.957	0.012	8.478	0.021	5.422	0.035	0.126	2.437	Sd
UGC8490	0.62	174.4	159.39	9.169	0.012	6.623	0.019	4.209	0.033	0.077	2.528	Sm

Table 2.6 – *Continued from previous page*

Name	b/a	pa	$R1_{iso}$	mag_1	Δmag_1	mag_3	Δmag_3	mag_4	Δmag_4	W1W2	W2W3	Morph
		deg	$''$	mag	mag	mag	mag	mag	mag	mag	mag	
(1)	(2)	(3)	(4)	(5)	(6)	(7)	(8)	(9)	(10)	(11)	(12)	(13)
UGC8508	0.69	110.1	60.3	11.828	0.014	10.408	0.171	9.263	1.161	0.033	1.498	Im
UGC8550	0.26	168.2	100.68	11.132	0.012	9.453	0.067	7.134	0.153	0.047	1.7	Sd
UGC8651	0.52	65.6	75.87	12.299	0.017	11.671	0.425	8.847	0.6	0.1	0.766	Im
UGC8683	0.63	131.4	58.75	12.569	0.019	14.589	0.922	10.783	0.983	−0.016	null	Im
UGC8709	0.36	146.1	164.92	8.654	0.011	5.45	0.012	3.733	0.017	0.081	3.159	Sc
UGC8711	0.24	151.7	175.57	8.668	0.011	5.372	0.012	3.656	0.016	0.114	3.196	Sbc
UGC8805	0.82	123.9	84.25	9.24	0.011	5.071	0.012	2.429	0.012	0.594	3.576	Sab
UGC8837	0.3	22.7	161.32	10.931	0.013	15.454	1.789	11.591	1.678	−0.04	null	Im
UGC8863	0.54	25.9	187.57	8.064	0.011	6.569	0.013	5.186	0.036	0.002	1.515	Sa
UGC9018	0.88	77.1	49.52	11.941	0.014	10.042	0.106	7.095	0.137	0.078	1.917	Sm
UGC9128	0.48	67.6	55.84	12.907	0.022	12.137	0.556	null	null	−0.093	1.173	Im
UGC9211	0.7	154.1	39.86	12.446	0.015	13.679	0.419	null	null	0.163	null	Im
UGC9242	0.1	71.2	167.03	11.251	0.012	9.181	0.045	7.087	0.124	0.001	2.16	Sd
UGC9366	0.52	44.6	153.69	7.703	0.011	3.818	0.011	1.892	0.012	0.156	3.729	Sbc
UGC9431	0.27	82.3	107.16	9.641	0.011	6.356	0.012	4.701	0.023	0.105	3.193	Scd
UGC9644	0.99	40.0	42.71	10.945	0.012	7.758	0.016	5.179	0.022	0.077	3.131	Sab
UGC9649	0.62	46.1	119.81	9.627	0.012	7.33	0.024	5.806	0.102	−0.021	2.318	Sb
UGC9753	0.4	4.1	152.27	8.465	0.011	5.116	0.012	3.334	0.015	0.076	3.272	Sbc
UGC9797	0.83	132.2	138.15	8.818	0.011	5.357	0.012	3.351	0.017	0.048	3.412	Sb
UGC9805	0.69	157.5	120.45	7.937	0.011	4.792	0.012	3.087	0.014	0.141	3.004	Sb
UGC9858	0.29	72.9	168.06	9.527	0.011	6.525	0.012	4.774	0.019	0.059	3.01	Sbc
UGC9969	0.5	15.4	176.69	7.997	0.011	5.209	0.012	3.591	0.018	0.045	2.751	Sb

Table 2.6 – *Continued from previous page*

Name	b/a	pa	$R1_{iso}$	mag_1	Δmag_1	mag_3	Δmag_3	mag_4	Δmag_4	W1W2	W2W3	Morph
		deg	″	mag	mag	mag	mag	mag	mag	mag	mag	
(1)	(2)	(3)	(4)	(5)	(6)	(7)	(8)	(9)	(10)	(11)	(12)	(13)
UGC9992	0.58	153.7	57.62	12.585	0.016	13.068	0.219	12.047	1.983	0.124	null	Im
UGC10310	0.6	22.1	87.42	11.349	0.013	9.571	0.06	7.119	0.121	0.036	1.911	Sm
UGC10359	0.83	80.1	168.71	9.079	0.012	6.116	0.013	4.295	0.022	0.126	2.925	Scd
UGC10445	0.79	136.6	74.98	10.789	0.012	8.259	0.1	6.145	0.107	0.036	2.568	Scd
UGC10470	0.75	159.0	147.17	8.254	0.011	4.273	0.011	1.635	0.012	0.175	3.806	Sbc
UGC10564	0.4	152.3	91.58	11.32	0.012	9.276	0.055	7.024	0.134	0.026	2.072	Sd
UGC11124	0.93	155.1	77.41	10.347	0.012	11.266	0.51	5.75	0.056	0.051	null	Scd
UGC11218	0.57	37.7	154.73	7.756	0.011	3.9	0.012	1.985	0.012	0.162	3.701	Sc
UGC11269	0.67	94.0	154.52	8.885	0.011	5.922	0.011	3.716	0.012	0.091	2.891	pec
UGC11283	0.67	179.5	69.5	10.806	0.012	7.645	0.015	5.237	0.023	0.099	3.13	Sdm
UGC11429	0.57	26.7	102.83	8.806	0.011	6.007	0.012	4.424	0.025	0.041	2.776	Sb
UGC11466	0.67	32.3	80.06	8.983	0.011	5.069	0.011	2.724	0.012	0.214	3.699	Sm
UGC11496	1.0	162.6	48.59	11.298	0.015	9.708	0.034	8.039	0.132	0.075	1.549	Sm
UGC11670	0.34	164.6	216.71	7.468	0.136	5.467	0.013	4.119	0.036	0.034	2.004	Sa
UGC11852	0.65	8.3	52.5	10.395	0.012	7.151	0.014	4.777	0.021	0.112	3.153	Sa
UGC11861	0.63	37.9	147.14	8.557	0.011	4.851	0.012	3.079	0.016	0.132	3.574	Sdm
UGC11864	0.65	164.0	71.79	10.667	0.013	7.54	0.019	5.646	0.052	0.056	3.125	Sdm
UGC11891	0.6	115.0	139.03	9.52	0.012	6.861	0.022	4.584	0.044	0.104	2.597	Im
UGC11909	0.24	0.5	107.15	9.303	0.012	5.812	0.012	3.746	0.015	0.122	3.368	pec
UGC11914	0.89	104.2	280.06	6.463	0.011	4.358	0.012	2.864	0.014	0.003	2.13	Sab
UGC11951	0.45	83.4	74.65	9.665	0.012	6.244	0.013	3.853	0.017	0.151	3.27	Sa
UGC11994	0.17	119.9	83.9	9.852	0.011	6.724	0.013	5.096	0.026	0.111	3.017	Sbc

Table 2.6 – *Continued from previous page*

Name	b/a	pa	$R1_{iso}$	mag_1	Δmag_1	mag_3	Δmag_3	mag_4	Δmag_4	W1W2	W2W3	Morph
		deg	$''$	mag	mag	mag	mag	mag	mag	mag	mag	
(1)	(2)	(3)	(4)	(5)	(6)	(7)	(8)	(9)	(10)	(11)	(12)	(13)
UGC12043	0.45	99.4	60.0	10.713	0.012	8.574	0.023	6.414	0.059	0.039	2.127	S0/a
UGC12060	0.37	149.5	104.91	11.448	0.015	10.345	0.198	7.753	0.352	−0.054	1.446	Im
UGC12082	0.6	9.4	88.59	11.485	0.015	13.452	0.369	10.063	0.564	0.058	null	Sm
UGC12212	0.61	117.3	46.57	12.702	0.02	13.719	0.536	10.321	0.845	0.02	null	Sm
UGC12276	0.68	88.8	59.79	10.262	0.012	7.831	0.021	6.44	0.091	−0.001	2.456	Sa
UGC12554	0.28	167.8	263.81	8.274	0.011	5.386	0.013	3.401	0.023	0.064	2.88	Sc
UGC12632	0.37	20.8	165.13	10.918	0.014	15.118	1.173	12.693	3.933	0.13	null	Sm
UGC12693	0.26	4.0	45.01	12.851	0.016	10.808	0.081	8.447	0.195	0.107	2.032	Scd
UGC12713	0.6	63.9	42.16	12.074	0.015	13.897	0.569	10.123	0.642	0.093	null	S0/a
UGC12732	0.76	39.6	84.97	11.026	0.014	9.526	0.211	7.25	0.502	0.226	1.274	Sm
UGC12754	0.66	172.3	171.15	8.622	0.012	5.601	0.014	3.7	0.03	0.138	2.912	Scd
UGC12808	0.95	144.7	90.84	8.626	0.011	5.12	0.012	2.979	0.013	0.111	3.416	Sb

Table 2.7: **Derived properties of the WISE data** (Jarrett et al. 2017)
Note: Cols(2-4) - The signal to noise ratios in the W1, W3 and W4 bands. Cols (5-7) - Fluxes in the W1, W3 and W4. The W1 fluxes were corrected for non stellar sources of radiation and the W3 and W4 fluxes corrected for the stellar continuum by Cluver et al. (2017). Cols(8-9) - Stellar masses and associated (relative logarithmic) errors. Cols (10-13) - Star formation rates from the respective bands and corresponding errors.

Name	SNR_{W1}	SNR_{W3}	SNR_{W4}	W1	W3	W4	$\log(M_*)$	$e(M_*)$	$\log(SFR_{W3})$	$e(SFR_{W3})$	$\log(SFR_{W4})$	$e(SFR_{W4})$
				mJy	mJy	mJy	$M_\odot$	$M_\odot$	$M_\odot$ yr^{-1}	$M_\odot$ yr^{-1}	$M_\odot$ yr^{-1}	$M_\odot$ yr^{-1}
(1)	(2)	(3)	(4)	(5)	(6)	(7)	(8)	(9)	(10)	(11)	(12)	(13)
UGC89	98.7	90.5	90.5	110.4	327.7	904.1	10.78	0.1	1.03	0.15	1.17	0.17
UGC192	98.7	90.5	90.5	2790.7	3110.0	10 600.7	8.6	0.1	−1.4	0.15	−1.26	0.17
UGC232	90.5	83.5	83.5	18.7	40.8	149.9	10.26	0.1	0.37	0.15	0.6	0.17
UGC485	90.5	67.8	67.8	18.4	25.9	32.5	10.41	0.1	0.25	0.15	0.05	0.17
UGC528	98.7	98.7	98.7	320.3	1202.3	2128.3	9.77	0.1	0.32	0.15	0.26	0.17
UGC624	98.7	90.5	90.5	76.6	186.6	261.9	11.05	0.1	1.1	0.15	0.97	0.17
UGC625	98.7	90.5	90.5	67.8	174.3	256.6	10.13	0.1	0.37	0.15	0.24	0.17
UGC690	90.5	77.5	77.5	23.7	41.7	58.6	10.62	0.1	0.52	0.15	0.37	0.17
UGC798	90.5	67.8	67.8	14.4	21.6	36.2	10.27	0.1	0.13	0.15	0.04	0.17
UGC1013	98.7	67.8	67.8	73.8	41.8	52.3	11.07	0.1	0.36	0.15	0.16	0.17
UGC1256	98.7	90.5	90.5	146.5	158.4	305.8	9.38	0.1	−0.79	0.15	−0.86	0.17
UGC1437	98.7	90.5	90.5	76.4	245.1	374.8	10.67	0.1	1.06	0.15	0.96	0.17
UGC1541	98.7	67.8	67.8	48.9	27.2	36.7	11.06	0.1	0.33	0.15	0.16	0.17
UGC1633	98.7	90.5	90.5	67.9	152.9	216.0	10.75	0.1	0.8	0.15	0.66	0.17
UGC1810	90.5	54.3	54.3	39.7	36.3	57.3	11.21	0.1	0.66	0.15	0.56	0.17
UGC1856	72.4	37.4	37.4	8.1	16.1	41.1	10.27	0.12	0.0	0.15	0.07	0.17
UGC1886	90.5	43.4	43.4	55.7	33.7	40.0	11.0	0.1	0.29	0.15	0.07	0.17
UGC1913	98.7	83.5	83.5	283.6	469.1	790.0	9.73	0.1	−0.21	0.15	−0.31	0.17

Table 2.7 – *Continued from previous page*

Name	SNR_{W1}	SNR_{W3}	SNR_{W4}	W1	W3	W4	$\log(M_*)$	$e(M_*)$	$\log(SFR_{W3})$	$e(SFR_{W3})$	$\log(SFR_{W4})$	$e(SFR_{W4})$
				mJy	mJy	mJy	$M_\odot$	$M_\odot$	$M_\odot\ yr^{-1}$	$M_\odot\ yr^{-1}$	$M_\odot\ yr^{-1}$	$M_\odot\ yr^{-1}$
(1)	(2)	(3)	(4)	(5)	(6)	(7)	(8)	(9)	(10)	(11)	(12)	(13)
UGC2045	98.7	98.7	98.7	327.9	1549.3	3152.2	10.04	0.1	0.68	0.15	0.69	0.17
UGC2080	98.7	77.5	77.5	165.2	254.4	272.0	10.09	0.1	−0.12	0.15	−0.4	0.17
UGC2082	90.5	47.2	47.2	34.5	25.2	30.1	9.37	0.1	−1.01	0.15	−1.28	0.17
UGC2141	98.7	83.5	83.5	68.3	141.2	372.5	9.41	0.1	−0.31	0.15	−0.24	0.17
UGC2183	98.7	90.5	90.5	95.9	232.5	437.8	10.32	0.1	0.47	0.15	0.44	0.17
UGC2193	98.7	83.5	83.5	120.3	226.5	330.4	9.46	0.1	−0.49	0.15	−0.66	0.17
UGC2455	98.7	67.8	67.8	91.6	154.6	575.8	8.81	0.1	−0.88	0.15	−0.7	0.17
UGC2459	90.5	29.3	29.3	39.4	53.4	87.9	10.02	0.1	0.07	0.15	−0.03	0.17
UGC2487	98.7	22.6	22.6	133.5	44.1	34.0	11.48	0.1	0.41	0.15	0.02	0.17
UGC2503	98.7	28.6	28.6	277.4	112.2	187.1	11.16	0.1	0.26	0.15	0.17	0.17
UGC2855	98.7	83.5	83.5	544.6	2154.4	4025.4	10.18	0.1	0.74	0.15	0.71	0.17
UGC2916	90.5	47.2	47.2	39.8	75.4	116.5	10.57	0.1	0.58	0.15	0.47	0.17
UGC2941	90.5	63.9	63.9	58.9	148.5	451.2	10.84	0.1	1.05	0.15	1.23	0.17
UGC3013	98.7	67.8	67.8	226.6	691.3	1149.0	10.36	0.1	0.57	0.15	0.5	0.17
UGC3137	90.5	4.7	4.7	22.8	15.5	40.4	9.51	0.1	−0.8	0.17	−0.76	0.19
UGC3205	90.5	20.9	20.9	55.2	30.4	54.6	10.62	0.1	0.03	0.15	−0.03	0.17
UGC3326	98.7	27.8	27.8	59.5	68.9	111.1	10.89	0.1	0.71	0.15	0.63	0.17
UGC3334	98.7	38.8	38.8	314.2	678.5	829.0	11.38	0.1	1.32	0.15	1.15	0.17
UGC3354	98.7	49.4	49.4	72.3	144.7	245.7	10.43	0.1	0.7	0.15	0.63	0.17
UGC3382	90.5	29.3	29.3	40.8	37.1	18.6	10.84	0.1	0.3	0.16	−0.26	0.18
UGC3407	90.5	54.3	54.3	34.2	28.3	165.4	10.47	0.1	0.03	0.15	0.43	0.17
UGC3546	98.7	90.5	90.5	166.5	354.9	1224.0	10.24	0.1	0.56	0.15	0.77	0.17

Table 2.7 – *Continued from previous page*

Name	SNR_{W1}	SNR_{W3}	SNR_{W4}	W1	W3	W4	$\log(M_*)$	$e(M_*)$	$\log(SFR_{W3})$	$e(SFR_{W3})$	$\log(SFR_{W4})$	$e(SFR_{W4})$
				mJy	mJy	mJy	$M_\odot$	$M_\odot$	$M_\odot\ yr^{-1}$	$M_\odot\ yr^{-1}$	$M_\odot\ yr^{-1}$	$M_\odot\ yr^{-1}$
(1)	(2)	(3)	(4)	(5)	(6)	(7)	(8)	(9)	(10)	(11)	(12)	(13)
UGC3574	90.5	54.3	54.3	38.9	45.9	85.7	9.96	0.1	−0.48	0.15	−0.55	0.17
UGC3580	90.5	7.9	7.9	39.8	87.7	138.2	9.68	0.1	−0.22	0.16	−0.35	0.18
UGC3642	98.7	43.4	43.4	68.8	63.6	33.2	11.16	0.1	0.52	0.15	−0.02	0.17
UGC3711	90.5	72.4	72.4	32.8	37.2	171.2	9.01	0.1	−0.96	0.15	−0.69	0.17
UGC3734	90.5	57.1	57.1	86.1	65.9	77.5	10.06	0.1	−0.49	0.15	−0.75	0.17
UGC3740	98.7	77.5	77.5	157.9	687.8	1528.5	10.45	0.1	1.01	0.15	1.07	0.17
UGC3759	98.7	90.5	90.5	59.9	112.8	161.2	11.16	0.1	1.0	0.15	0.88	0.17
UGC3826	90.5	33.9	33.9	26.0	34.0	43.3	10.04	0.1	−0.36	0.15	−0.58	0.17
UGC3965	90.5	60.3	60.3	19.7	27.0	44.1	10.49	0.1	0.22	0.15	0.12	0.17
UGC3993	90.5	14.7	14.7	27.4	4.3	4.8	10.74	0.1	−0.52	0.16	−0.8	0.18
UGC4036	98.7	77.5	77.5	53.5	82.9	127.3	10.59	0.1	0.36	0.15	0.24	0.17
UGC4165	14.5	83.5	83.5	79.6	141.1	207.3	9.18	0.34	−0.61	0.15	−0.78	0.17
UGC4256	98.7	90.5	90.5	56.9	260.5	565.3	10.61	0.1	1.18	0.15	1.23	0.17
UGC4273	98.7	83.5	83.5	63.5	138.2	261.6	10.26	0.1	0.35	0.15	0.32	0.17
UGC4278	90.5	24.7	24.7	20.1	12.7	30.5	9.16	0.1	−1.32	0.15	−1.33	0.18
UGC4284	90.5	67.8	67.8	61.5	64.7	188.3	9.67	0.1	−0.77	0.15	−0.67	0.17
UGC4305	90.5	16.7	16.7	51.6	21.5	170.3	7.93	0.1	−2.15	0.12	−1.72	0.18
UGC4458	90.5	60.3	60.3	72.3	74.5	94.8	11.08	0.1	0.63	0.15	0.45	0.17
UGC4543	72.4	6.9	6.9	6.5	1.7	nan	9.55	0.12	−1.41	0.17	nf	nan
UGC4605	98.7	63.9	63.9	137.3	31.7	53.3	10.79	0.1	−0.26	0.15	−0.37	0.17
UGC4666	98.7	77.5	77.5	156.3	120.2	108.8	10.17	0.1	−0.26	0.15	−0.62	0.17
UGC4806	98.7	83.5	83.5	64.5	126.8	203.3	9.97	0.1	0.08	0.15	−0.03	0.17

Table 2.7 – *Continued from previous page*

Name	SNR_{W1}	SNR_{W3}	SNR_{W4}	W1	W3	W4	$\log(M_*)$	$e(M_*)$	$\log(SFR_{W3})$	$e(SFR_{W3})$	$\log(SFR_{W4})$	$e(SFR_{W4})$
				mJy	mJy	mJy	$M_\odot$	$M_\odot$	$M_\odot$ yr^{-1}	$M_\odot$ yr^{-1}	$M_\odot$ yr^{-1}	$M_\odot$ yr^{-1}
(1)	(2)	(3)	(4)	(5)	(6)	(7)	(8)	(9)	(10)	(11)	(12)	(13)
UGC4838	98.7	90.5	90.5	91.3	283.9	356.7	10.65	0.1	0.74	0.15	0.56	0.17
UGC5060	90.5	83.5	83.5	30.3	103.5	441.5	9.74	0.1	0.08	0.15	0.36	0.17
UGC5079	98.7	98.7	98.7	1625.8	4125.9	7247.9	10.57	0.1	0.67	0.15	0.62	0.17
UGC5251	90.5	90.5	90.5	68.1	193.1	359.9	9.7	0.1	0.06	0.15	0.0	0.17
UGC5253	98.7	90.5	90.5	440.7	653.4	787.7	10.87	0.1	0.64	0.15	0.44	0.17
UGC5351	98.7	90.5	90.5	108.4	406.6	811.0	10.0	0.1	0.53	0.15	0.52	0.17
UGC5452	83.5	32.9	32.9	9.8	11.5	27.9	9.58	0.1	−0.72	0.15	−0.69	0.17
UGC5459	90.5	83.5	83.5	54.0	107.7	213.4	9.64	0.1	−0.14	0.15	−0.18	0.17
UGC5532	98.7	98.7	98.7	434.0	765.3	1069.9	11.24	0.1	1.11	0.15	0.99	0.17
UGC5557	98.7	90.5	90.5	484.3	1040.5	1479.2	10.13	0.1	0.18	0.15	0.02	0.17
UGC5589	90.5	47.2	47.2	23.3	29.3	81.8	9.5	0.1	−0.73	0.15	−0.65	0.17
UGC5685	98.7	67.8	67.8	93.3	79.6	109.5	10.65	0.1	0.06	0.15	−0.11	0.17
UGC5717	90.5	90.5	90.5	34.0	73.2	101.2	10.14	0.1	0.12	0.15	−0.04	0.17
UGC5721	90.5	47.2	47.2	17.8	18.0	55.0	8.28	0.1	−1.68	0.14	−1.6	0.17
UGC5786	98.7	98.7	98.7	185.4	1103.3	4628.9	9.94	0.1	0.69	0.15	0.98	0.17
UGC5789	90.5	60.3	60.3	73.3	73.2	135.9	9.69	0.1	−0.63	0.15	−0.71	0.17
UGC5840	98.7	90.5	90.5	448.2	867.0	1283.1	10.12	0.1	0.1	0.15	−0.04	0.17
UGC5906	90.5	77.5	77.5	41.3	33.8	56.7	10.11	0.1	−0.34	0.15	−0.45	0.17
UGC5909	90.5	77.5	77.5	33.4	87.3	138.5	9.94	0.1	0.03	0.15	−0.08	0.17
UGC5960	90.5	51.7	51.7	21.6	24.1	78.1	9.28	0.1	−0.91	0.15	−0.77	0.17
UGC5997	98.7	83.5	83.5	51.9	94.5	126.5	10.1	0.1	0.03	0.15	−0.16	0.17
UGC6001	90.5	83.5	83.5	17.7	78.6	139.7	9.34	0.1	0.03	0.15	−0.04	0.17

Table 2.7 – *Continued from previous page*

Name	SNR_{W1}	SNR_{W3}	SNR_{W4}	W1	W3	W4	$\log(M_*)$	$e(M_*)$	$\log(SFR_{W3})$	$e(SFR_{W3})$	$\log(SFR_{W4})$	$e(SFR_{W4})$
				mJy	mJy	mJy	$M_\odot$	$M_\odot$	$M_\odot\ yr^{-1}$	$M_\odot\ yr^{-1}$	$M_\odot\ yr^{-1}$	$M_\odot\ yr^{-1}$
(1)	(2)	(3)	(4)	(5)	(6)	(7)	(8)	(9)	(10)	(11)	(12)	(13)
UGC6118	98.7	98.7	98.7	213.8	863.5	3157.4	10.33	0.1	0.88	0.15	1.13	0.17
UGC6126	90.5	47.2	47.2	18.0	18.0	49.9	9.15	0.1	−0.97	0.15	−0.91	0.17
UGC6161	72.4	11.7	11.7	6.4	2.3	5.5	8.48	0.12	−2.05	0.14	−2.05	0.19
UGC6225	98.7	98.7	98.7	634.9	2034.2	3965.0	10.0	0.1	0.44	0.15	0.42	0.17
UGC6263	98.7	90.5	90.5	158.6	428.2	692.8	10.66	0.1	0.8	0.15	0.72	0.17
UGC6283	90.5	67.8	67.8	31.0	41.7	116.8	9.11	0.1	−0.88	0.15	−0.8	0.17
UGC6537	98.7	90.5	90.5	297.6	581.5	826.2	10.14	0.1	0.19	0.15	0.03	0.17
UGC6713	72.4	5.3	5.3	4.8	0.3	nan	8.51	0.12	−2.52	0.14	nf	nan
UGC6742	90.5	77.5	77.5	19.3	36.8	86.8	8.84	0.1	−0.97	0.15	−0.96	0.17
UGC6778	98.7	98.7	98.7	289.3	1068.0	1531.8	10.25	0.1	0.69	0.15	0.55	0.17
UGC6786	98.7	72.4	72.4	122.3	76.6	96.3	10.87	0.1	0.19	0.15	−0.01	0.17
UGC6787	98.7	67.8	67.8	307.7	94.9	103.8	10.84	0.1	−0.12	0.15	−0.39	0.17
UGC6813	90.5	51.7	51.7	26.2	38.6	65.9	9.64	0.1	−0.59	0.15	−0.7	0.17
UGC6833	90.5	36.2	36.2	42.0	28.8	46.4	9.57	0.1	−1.02	0.15	−1.17	0.17
UGC6840	72.4	21.3	21.3	5.4	4.2	4.5	8.87	0.12	−1.38	0.15	−1.7	0.17
UGC6884	98.7	90.5	90.5	74.8	177.7	251.0	10.65	0.1	0.72	0.15	0.58	0.17
UGC6921	98.7	90.5	90.5	35.2	75.1	116.7	9.42	0.1	−0.42	0.15	−0.57	0.17
UGC6930	90.5	72.4	72.4	43.7	61.9	92.6	9.66	0.1	−0.57	0.15	−0.74	0.17
UGC6964	98.7	90.5	90.5	70.1	142.9	238.0	9.77	0.1	−0.08	0.15	−0.18	0.17
UGC7030	98.7	98.7	98.7	400.4	1251.1	2328.8	9.81	0.1	0.33	0.15	0.29	0.17
UGC7047	90.5	14.7	14.7	15.2	4.6	23.0	8.23	0.11	−2.52	0.14	−2.3	0.17
UGC7075	98.7	98.7	98.7	88.8	319.8	544.5	9.76	0.1	0.29	0.15	0.22	0.17

Table 2.7 – *Continued from previous page*

Name	SNR_{W1}	SNR_{W3}	SNR_{W4}	W1	W3	W4	$\log(M_*)$	$e(M_*)$	$\log(SFR_{W3})$	$e(SFR_{W3})$	$\log(SFR_{W4})$	$e(SFR_{W4})$
				mJy	mJy	mJy	$M_\odot$	$M_\odot$	$M_\odot$ yr^{-1}	$M_\odot$ yr^{-1}	$M_\odot$ yr^{-1}	$M_\odot$ yr^{-1}
(1)	(2)	(3)	(4)	(5)	(6)	(7)	(8)	(9)	(10)	(11)	(12)	(13)
UGC7089	90.5	28.6	28.6	16.1	3.7	7.9	9.06	0.1	−1.85	0.16	−1.92	0.18
UGC7095	98.7	98.7	98.7	247.3	539.6	872.8	10.41	0.1	0.48	0.15	0.38	0.17
UGC7151	90.5	67.8	67.8	70.2	35.0	92.6	9.0	0.1	−1.41	0.16	−1.38	0.18
UGC7166	98.7	98.7	98.7	648.6	1605.6	4838.6	10.52	0.1	0.86	0.15	1.03	0.17
UGC7183	98.7	98.7	98.7	443.5	1287.5	1788.5	10.38	0.1	0.71	0.15	0.57	0.17
UGC7204	90.5	8.8	8.8	12.1	2.0	10.2	8.64	0.1	−2.05	0.14	−1.77	0.18
UGC7222	90.5	77.5	77.5	46.5	58.7	82.8	9.54	0.1	−0.53	0.15	−0.72	0.17
UGC7232	90.5	9.8	9.8	17.8	2.4	13.0	7.83	0.1	−3.0	0.0	−3.0	0.43
UGC7256	98.7	83.5	83.5	373.3	40.8	45.6	10.61	0.1	−0.73	0.15	−1.01	0.17
UGC7261	90.5	27.1	27.1	25.3	38.8	132.2	9.19	0.11	−0.82	0.15	−0.67	0.17
UGC7321	90.5	31.9	31.9	19.3	16.7	27.1	9.45	0.1	−0.79	0.15	−0.92	0.17
UGC7323	90.5	54.3	54.3	115.7	82.9	111.3	9.06	0.1	−1.24	0.15	−1.47	0.17
UGC7399	90.5	57.1	57.1	19.9	29.0	63.4	8.65	0.1	−1.25	0.15	−1.29	0.17
UGC7483	90.5	67.8	67.8	28.0	28.1	40.2	9.71	0.1	−0.48	0.15	−0.66	0.17
UGC7489	98.7	90.5	90.5	105.6	228.5	579.2	10.05	0.1	0.17	0.15	0.24	0.17
UGC7506	90.5	90.5	90.5	23.4	85.8	188.3	9.23	0.1	−0.21	0.15	−0.21	0.17
UGC7524	90.5	36.2	36.2	243.8	161.4	480.9	9.49	0.1	−1.09	0.16	−1.0	0.17
UGC7592	98.7	98.7	98.7	489.5	1206.0	3372.3	9.2	0.1	−0.41	0.15	−0.32	0.17
UGC7603	90.5	20.1	20.1	20.6	10.8	24.2	8.69	0.1	−1.85	0.16	−1.89	0.17
UGC7690	90.5	20.1	20.1	17.1	9.1	29.2	8.67	0.1	−1.72	0.16	−1.64	0.17
UGC7704	83.5	29.3	29.3	4.7	9.5	61.4	8.31	0.11	−1.19	0.15	−0.8	0.17
UGC7766	98.7	90.5	90.5	334.1	634.1	1130.4	9.5	0.1	−0.24	0.15	−0.33	0.17

Table 2.7 – *Continued from previous page*

Name	SNR_{W1}	SNR_{W3}	SNR_{W4}	W1	W3	W4	$\log(M_*)$	$e(M_*)$	$\log(SFR_{W3})$	$e(SFR_{W3})$	$\log(SFR_{W4})$	$e(SFR_{W4})$
				mJy	mJy	mJy	$M_\odot$	$M_\odot$	$M_\odot\ yr^{-1}$	$M_\odot\ yr^{-1}$	$M_\odot\ yr^{-1}$	$M_\odot\ yr^{-1}$
(1)	(2)	(3)	(4)	(5)	(6)	(7)	(8)	(9)	(10)	(11)	(12)	(13)
UGC7831	98.7	98.7	98.7	324.4	571.8	1035.5	9.36	0.1	−0.49	0.15	−0.58	0.17
UGC7853	98.7	90.5	90.5	155.4	246.7	403.0	9.48	0.1	−0.48	0.15	−0.6	0.17
UGC7989	98.7	90.5	90.5	1113.9	614.6	676.2	10.94	0.1	0.16	0.15	−0.1	0.17
UGC8146	90.5	18.7	18.7	8.2	3.8	10.8	9.28	0.1	−1.41	0.16	−1.36	0.18
UGC8188	90.5	20.9	20.9	56.4	20.7	53.5	8.59	0.1	−1.92	0.14	−1.92	0.18
UGC8246	77.5	16.0	16.0	5.6	3.1	12.7	8.47	0.11	−1.72	0.16	−1.54	0.18
UGC8271	90.5	90.5	90.5	34.8	80.4	179.7	8.64	0.1	−0.95	0.15	−0.97	0.17
UGC8286	90.5	43.4	43.4	41.8	19.0	50.9	8.94	0.1	−1.64	0.15	−1.62	0.16
UGC8396	90.5	51.7	51.7	12.6	14.2	59.0	8.98	0.1	−0.96	0.15	−0.73	0.17
UGC8490	90.5	57.1	57.1	64.8	63.5	185.8	8.61	0.1	−1.44	0.14	−1.38	0.18
UGC8550	90.5	16.2	16.2	10.6	4.1	10.8	8.25	0.1	−2.15	0.12	−2.15	0.19
UGC8709	98.7	90.5	90.5	103.2	181.7	269.9	10.65	0.1	0.58	0.15	0.45	0.17
UGC8711	98.7	90.5	90.5	103.3	195.1	284.5	10.03	0.1	0.13	0.15	−0.01	0.17
UGC8805	98.7	90.5	90.5	60.5	266.9	857.3	10.1	0.1	0.71	0.15	0.9	0.17
UGC8863	98.7	83.5	83.5	178.7	59.4	67.1	10.68	0.1	−0.22	0.15	−0.48	0.17
UGC9018	77.5	10.2	10.2	5.0	3.2	13.3	7.8	0.11	−2.3	0.17	−2.15	0.19
UGC9242	90.5	24.1	24.1	9.5	5.2	13.0	9.45	0.1	−1.11	0.15	−1.09	0.17
UGC9366	98.7	98.7	98.7	247.6	818.7	1402.2	10.69	0.1	1.04	0.15	0.99	0.17
UGC9431	98.7	90.5	90.5	41.6	77.9	109.5	10.17	0.1	0.23	0.15	0.07	0.17
UGC9644	90.5	67.8	67.8	11.9	21.2	70.4	10.5	0.1	0.44	0.15	0.63	0.17
UGC9649	90.5	45.2	45.2	42.6	30.3	34.4	9.42	0.1	−1.08	0.15	−1.37	0.17
UGC9753	98.7	90.5	90.5	124.8	241.6	363.1	10.02	0.1	0.05	0.15	−0.09	0.17

Table 2.7 – *Continued from previous page*

Name	SNR_{W1}	SNR_{W3}	SNR_{W4}	W1	W3	W4	$\log(M_*)$	$e(M_*)$	$\log(SFR_{W3})$	$e(SFR_{W3})$	$\log(SFR_{W4})$	$e(SFR_{W4})$
				mJy	mJy	mJy	$M_\odot$	$M_\odot$	$M_\odot$ yr^{-1}	$M_\odot$ yr^{-1}	$M_\odot$ yr^{-1}	$M_\odot$ yr^{-1}
(1)	(2)	(3)	(4)	(5)	(6)	(7)	(8)	(9)	(10)	(11)	(12)	(13)
UGC9797	98.7	90.5	90.5	86.9	201.6	371.4	10.73	0.1	0.73	0.15	0.7	0.17
UGC9805	98.7	90.5	90.5	198.2	317.9	456.2	10.99	0.1	0.98	0.15	0.86	0.17
UGC9858	98.7	90.5	90.5	46.2	66.4	101.2	10.34	0.1	0.18	0.15	0.05	0.17
UGC9969	98.7	90.5	90.5	187.1	218.0	301.5	11.21	0.1	0.82	0.15	0.68	0.17
UGC10310	83.5	18.1	18.1	8.8	3.6	12.4	8.9	0.11	−1.62	0.14	−1.49	0.18
UGC10359	90.5	83.5	83.5	70.8	109.5	162.2	9.71	0.1	−0.2	0.15	−0.35	0.17
UGC10445	90.5	10.9	10.9	14.5	12.7	28.6	9.71	0.1	−0.62	0.15	−0.62	0.17
UGC10470	98.7	98.7	98.7	149.8	545.6	1751.0	10.12	0.1	0.6	0.15	0.79	0.17
UGC10564	90.5	19.7	19.7	8.9	5.1	12.3	9.27	0.1	−1.18	0.16	−1.18	0.17
UGC11218	98.7	90.5	90.5	238.5	776.5	1301.0	10.24	0.1	0.65	0.15	0.58	0.17
UGC11269	98.7	98.7	98.7	82.4	115.4	264.3	10.63	0.1	0.49	0.15	0.54	0.17
UGC11283	90.5	72.4	72.4	14.4	25.0	69.8	9.56	0.1	−0.35	0.15	−0.26	0.17
UGC11429	98.7	90.5	90.5	87.8	100.1	138.7	11.16	0.1	0.76	0.15	0.61	0.17
UGC11466	98.7	98.7	98.7	77.4	260.6	640.6	9.4	0.1	−0.01	0.15	0.05	0.17
UGC11496	72.4	31.9	31.9	9.1	3.9	8.3	9.45	0.11	−1.04	0.15	−1.08	0.17
UGC11670	8.0	83.5	83.5	73.1	201.5	200.3	9.72	0.11	−0.14	0.15	−0.45	0.17
UGC11852	90.5	77.5	77.5	19.8	37.1	102.6	10.36	0.1	0.5	0.15	0.62	0.17
UGC11861	98.7	90.5	90.5	113.4	346.5	519.8	10.12	0.1	0.44	0.15	0.31	0.17
UGC11864	83.5	57.1	57.1	15.7	29.1	52.8	10.17	0.1	0.19	0.15	0.13	0.17
UGC11891	90.5	49.4	49.4	46.9	45.6	114.4	8.81	0.1	−1.21	0.15	−1.19	0.17
UGC11909	90.5	90.5	90.5	57.5	135.9	262.0	9.26	0.1	−0.43	0.15	−0.49	0.17
UGC11914	98.7	90.5	90.5	793.0	468.5	525.2	10.95	0.1	0.24	0.15	0.0	0.17

Table 2.7 – *Continued from previous page*

Name	SNR_{W1}	SNR_{W3}	SNR_{W4}	W1	W3	W4	$\log(M_*)$	$e(M_*)$	$\log(SFR_{W3})$	$e(SFR_{W3})$	$\log(SFR_{W4})$	$e(SFR_{W4})$
				mJy	mJy	mJy	$M_\odot$	$M_\odot$	$M_\odot\ yr^{-1}$	$M_\odot\ yr^{-1}$	$M_\odot\ yr^{-1}$	$M_\odot\ yr^{-1}$
(1)	(2)	(3)	(4)	(5)	(6)	(7)	(8)	(9)	(10)	(11)	(12)	(13)
UGC11951	90.5	83.5	83.5	41.3	87.5	229.4	9.18	0.1	−0.49	0.15	−0.43	0.17
UGC11994	98.7	83.5	83.5	33.5	53.6	78.2	10.53	0.1	0.49	0.15	0.36	0.17
UGC12043	90.5	47.2	47.2	15.7	9.6	25.4	9.17	0.1	−1.22	0.15	−1.18	0.17
UGC12276	90.5	51.7	51.7	22.8	18.4	19.5	10.78	0.1	0.2	0.15	−0.08	0.17
UGC12554	98.7	83.5	83.5	147.7	203.7	390.4	9.49	0.1	−0.57	0.15	−0.63	0.17
UGC12693	67.8	13.4	13.4	2.1	2.8	3.0	9.26	0.12	−0.69	0.16	−1.0	0.18
UGC12754	90.5	77.5	77.5	105.5	158.7	253.3	9.63	0.1	−0.3	0.15	−0.43	0.17
UGC12808	98.7	90.5	90.5	105.2	240.0	521.5	10.9	0.1	0.94	0.15	0.98	0.17

Table 2.8: **Properties of sub sample used to study star formation thresholds**. Note: Col (2-3)-Inclination based on the WISE photometry and associated error (a 5% relative error was assumed on the inclinations), col (4)- Number of beams across the HI diameter at $1M_{\odot}pc^{-2}$, col (5) Spatial resolution per $10''$ pixel in the HI data, col (6)-Morphology.

Name	Incl	e(incl)	Beams	Res	Morph
	deg	deg		pc	
(1)	(2)	(3)	(4)	(5)	(6)
UGC1256	62.2	3.1	35.0	348	Scd
UGC1913	49.4	2.5	26.0	431	Sd
UGC2455	37.2	1.9	12.0	310	Im
UGC2855	60.4	3.0	13.0	697	Sc
UGC4284	49.1	2.5	22.0	558	Scd
UGC4666	47.9	2.4	11.0	790	pec
UGC5079	60.7	3.0	30.0	458	Sbc
UGC5459	68.8	3.4	11.0	984	Sc
UGC5721	50.2	2.5	13.0	322	Sd
UGC5786	48.7	2.4	13.0	911	pec
UGC5789	63.6	3.2	17.0	630	Scd
UGC6161	63.6	3.2	10.0	566	Sdm
UGC6225	69.6	3.5	19.0	484	Scd
UGC6283	58.1	2.9	12.0	603	Sa
UGC6537	51.2	2.6	15.0	648	Sc
UGC6778	49.6	2.5	16.0	921	Sc
UGC6833	46.2	2.3	10.0	602	Sc
UGC7047	48.7	2.4	11.0	212	Im
UGC7095	69.5	3.5	14.0	985	Sbc
UGC7166	50.7	2.5	22.0	950	Sab
UGC7261	55.2	2.8	12.0	673	Sdm
UGC7323	44.2	2.2	12.0	264	Sdm
UGC7524	35.9	1.8	32.0	230	Sm
UGC7592	51.8	2.6	27.0	207	Im
UGC7603	67.2	3.4	12.0	332	Sd
UGC7766	68.4	3.4	33.0	354	Scd
UGC7853	47.2	2.4	15.0	417	Sm
UGC7989	53.8	2.7	24.0	610	Sab
UGC8490	51.1	2.6	22.0	230	Sm
UGC9649	52.7	2.6	12.0	544	Sb
UGC9753	66.3	3.3	10.0	842	Sbc
UGC11670	70.0	3.5	11.0	717	Sa
UGC11891	52.0	2.6	17.0	372	Im

Chapter 3

Global Properties

As detailed in Chapter 2, the sample in this study was derived from the WHISP survey sample. A total of 228 galaxies was obtained following the criteria outlined that chapter. The first objective of this study was to derive new HI data products such HI intensity maps and velocity fields for all 228 (see Chapter 2). Two sub-samples were subsequently drawn from this main sample to pursue the other two objectives of this study, namely, (i) to study the relationship between atomic gas and star formation rate as traced by NIR emission and (ii) to investigate how well the gravitational stability of disks predicts the NIR - derived star formation properties on resolved, kpc scales.

In this chapter I present the global properties for both HI emission line data (WHISP) and infrared (WISE) data of the galaxies in the sample and place them in the context of properties of the more complete samples of Verheijen & Sancisi (2001) and Cluver et al. (2017). The chapter is divided into two main sections: (1) The global HI properties section, which presents the structural properties and distribution of the HI as well as the sample distributions of gas mass and the mass-to-light ratio as functions of the 3.6μm stellar luminosity. (2) The star formation properties section, which presents a sub sample of the main sample consisting of galaxies that are detected in W3 (11.6 μm) which is sensitive to the heating of the interstellar medium by star formation. This second section examines the galaxy main sequence relation and the Kennicutt-Schmidt relation in light of several studies in the literature.

3.1 Global HI Properties

The global HI properties were derived for the full sample of 228 galaxies in this study. In particular, we examined the HI mass-size relation and the HI mass-luminosity relation.

3.1.1 HI mass - size relation

The HI masses of galaxies and their HI diameters are known to be tightly correlated. We defined HI diameters from the surface density profiles at the radius where the density equals 1 $M_\odot$ pc^{-2} (in keeping with literature), while the HI masses were obtained by integrating the global profiles. In one galaxy, UGC3826, the surface density was $\leq$ 1 $M_\odot$ pc^{-2} at all radii, and so this galaxy was not used when deriving the mass-size relation. This relation has been found by several observers to hold across three and five orders of magnitude in diameter and mass respectively (Wang et al. 2016), for morphologies ranging from early-type spirals to dwarfs and irregulars (Broeils & Rhee 1997, Verheijen & Sancisi 2001, Swaters et al. 2002, Noordermeer et al. 2005, Martinsson 2011, Wang et al. 2014, Ponomareva et al. 2016). The relations found by the different authors have slopes of 1.84±0.12 in log space. Such a power law relates the approximate square of the diameter against the mass, giving an estimated average surface density for HI across galaxy disks. That this relation is found consistent for samples across all morphologies and in different environments implies that *the* HI *disks regulate themselves to a constant average surface density* (Verheijen & Sancisi 2001, Noordermeer et al. 2005). Swaters et al. (2002) and Noordermeer et al. (2005) derived this relation for 73 dwarf irregulars and 68 early-type spirals respectively in the WHISP sample. Here we present this relation for 228 WHISP galaxies, spanning from early-type spirals to dwarf irregulars and find the relation to be in agreement with previous studies within the errors. We find the tight relation below:

$$\log \mathrm{M_{HI}} \;=\; (1.95 \pm 0.03) \log \mathrm{D_{HI}} \;+\; (6.5 \pm 0.04), \tag{3.1}$$

which has a dex error of 3% on the slope, 4% on the intercept and a vertical scatter of 0.14 about the best-fit line. The relation for our sample is in particularly good agreement with the relations of Broeils & Rhee (1997) and Wang et al. (2016) who had slopes of 1.96±0.04 and 1.98±0.01 respectively, and whose samples were complete comprising of all morphological types from early-type spirals to dwarfs as did our sample. Our slope is steeper than other studies by Verheijen & Sancisi (2001), Swaters et al. (2002), Noordermeer et al. (2005), Ponomareva et al. (2016) mostly because their samples were less complete, consisting only of either spirals or dwarfs. Note that the Wang et al. (2016) study included 100 WHISP galaxies in their sample of 549.

The average HI surface density can be calculated from the disk surface area and HI mass as

$$\begin{aligned} \langle \sigma_{\mathrm{HI}} \rangle &= \tfrac{M_{\mathrm{HI}}}{\pi R_{\mathrm{HI}}^2}, \\ \Rightarrow \langle \sigma_{\mathrm{HI}} \rangle &= \tfrac{4 M_{\mathrm{HI}}}{\pi D_{\mathrm{HI}}^2}, \end{aligned} \tag{3.2}$$

where $\pi \mathrm{R_{HI}^2}$ is the surface area of the disk and $\mathrm{D_{HI}} = 2\mathrm{R_{HI}}$. From Equation 3.1, we have,

$$\begin{aligned} \log \mathrm{M_{HI}} \;&\sim\; 2 \log \mathrm{D_{HI}} \;+\; 6.5, \\ \Rightarrow \tfrac{M_{\mathrm{HI}}}{D_{\mathrm{HI}}^2} \;&\simeq\; 10^{6.5}. \end{aligned} \tag{3.3}$$

Combining Equations 3.2 and 3.3 for our sample gives $\langle \sigma_{\rm HI} \rangle = 3.6$ $M_\odot$ pc^{-2}. This is a characteristic surface density within the HI radius and is consistent with the mean density of the HI calculated within the stellar disk, 3.57 ± 1.06 $M_\odot$ pc^{-2}. However, $\sigma_{\rm HI}$ is not equivalent to the global average surface density (Wang et al. 2016) because the HI diameter, $D_{\rm HI}$, is a definition of the diameter within which most of the HI flux lies but does not enclose the entire HI disk (Cayatte et al. 1994, Broeils & Rhee 1997, Wang et al. 2016). Figure 3.1 is a plot of the data, overlaid with the relations of Broeils & Rhee (1997), Verheijen & Sancisi (2001) and Wang et al. (2016). Late-type dwarfs such as UGC192 (IC10) populate the low mass end of the relation while early-type spirals such as UGC9797 (NGC5905) are found at the high mass end. Exceptions exist such as an early-type at the low mass end which is the case for UGC12713, a dwarf spheroidal. However, this is in keeping with the correlation that the smaller HI disks contain lower HI masses regardless of morphological type.

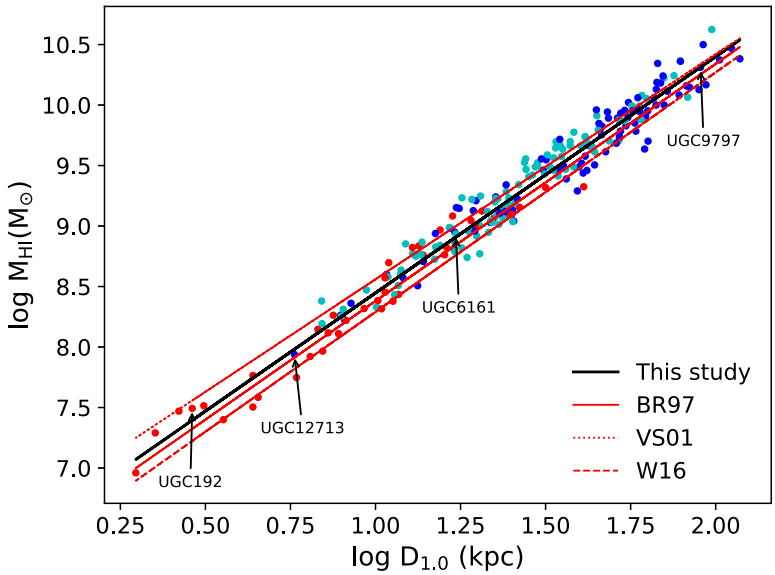

Figure 3.1: HI mass versus HI diameter for all galaxies in our sample. The data points are color coded by the morphology of the galaxies such that the blue represents early-type spirals, cyan represents late-type spirals (Sc - Sm) and the red are the late-type dwarfs. A fit to the data is shown by the black solid line. The relations of Broeils & Rhee (1997) (BR97), Verheijen & Sancisi (2001) (VS01) and Wang et al. (2016) (W16) are shown as solid, dotted and dashed red lines. For clarity, the BR97 and W16 relations were given vertical offsets of -0.1 dex and -0.2 dex respectively. The HI diameters were defined at the 1 $M_\odot$ pc^{-2} level of the radial profiles while HI masses were determined from the total flux in the global profiles. The mass-size relation of HI disks is an indicator of a constant average HI surface density.

Because it holds for all morphologies, several orders of HI mass and diameter, and in both cluster and field environments, this relation provides useful constraints on models of galaxy formation since it implies that all galaxies regulate their HI disks at a constant average

surface density regardless of whether gas is accreted externally, consumed during the star formation process or removed via gas stripping or quenching (Wang et al. 2016)

3.1.2 HI mass vs Luminosity

The relationships between the HI mass and stellar disk properties of luminosity and surface brightness represent the scaling relations between the ISM which is a reservoir of fuel for star formation and the galaxy's underlying baryonic mass in the form of the old stellar population. The HI mass derived here is the mass enclosed within the stellar disk, defined by a 1σ isophote in the W1 image (Jarrett et al. 2013). This gives us a direct comparison between the atomic gas reservoir for star formation spatially co-located with the stellar disk.

Figure 3.2 illustrates the relationships between the HI mass and stellar disk magnitude and surface brightness. The plots are also color-coded according to morphological type such that blue points show early-type spirals, cyan shows late-type spirals while red points show late-type dwarfs and irregulars. The color-coding pattern follows from the infrared color index (W1-W2) of the different morphological types, in that the early-types have 'bluer' colors while the late-types have 'redder' colors (Cluver et al. 2014). The 'r' labels in the plots are the correlation coefficients while 'σ' denotes the vertical scatter about the least squares fits to the data (solid line). All the plots show strong correlation coefficients between the properties. This is in agreement with the complete (although smaller) sample of Verheijen & Sancisi (2001), as well as the sample of Ponomareva et al. (2016), although the Ponomareva et al. (2016) study found a weaker correlation (0.64) between the M_{HI} and stellar luminosity. Note that our relations derived for the atomic gas enclosed within the stellar disk follow the same trend as those from previous studies that used integrated properties over the entire HI disk. However, there is clearly less scatter in the relation between M_{HI} and M_{W1}, as would be expected, because we are comparing spatially co-located properties in the stellar disk (See Figure 3.3 for comparison with plots where the HI is integrated over the entire disk) . From a morphological point of view, the late-type dwarfs have lower luminosities (intrinsically fainter) and higher surface brightness than the earlier type spirals. The intrinsic brightness decreases across the Hubble sequence from early-type spirals to late-type dwarfs.We also see that the enclosed HI mass decreases from early-types towards late-types while on the other hand the gas-star fraction increases towards the late-types. Indicated in each plot are the locations of four galaxies mentioned in the previous section. Right away we see that UGC192 (IC10, a blue compact dwarf) is behaving like an outlier. In the bottom panels, it shows much lower gas fraction (M_{HI}/M_*) than the rest of the dwarfs and is tending toward the spiral regime in luminosity and surface brightness. This is because (i) the quantities presented here are calculated within the W1 stellar disk, while this galaxy has been shown to have a significant amount of its HI gas in an extended stream beyond the main disk (Wilcots & Miller 1998) and (ii) this galaxy is a star burst dwarf irregular galaxy exhibiting high star formation rates like the spirals and producing more energy than a regular dwarf, hence its high infrared luminosity. On the other hand we

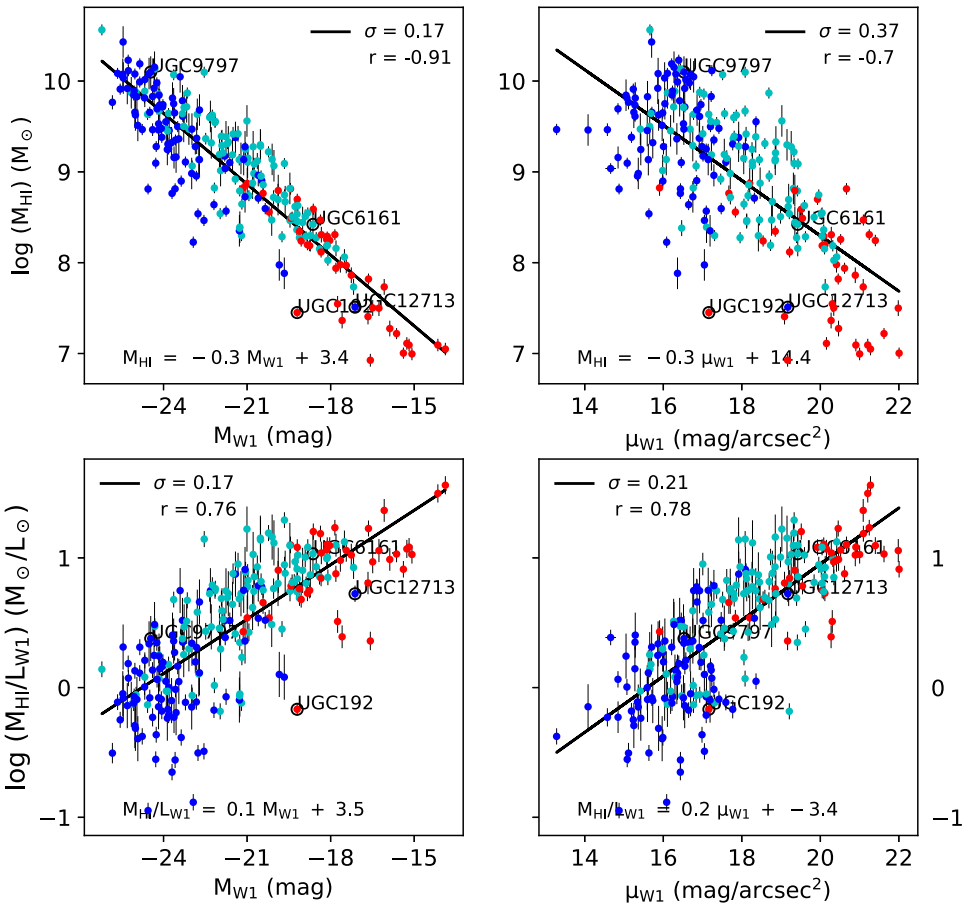

Figure 3.2: Plots of HI mass (upper panels) and HI mass-to-light ratio (lower panels) versus 3.4 μm absolute magnitude (left panels) and surface brightness (right panels). Note that these are 'enclosed quantities' measured within the stellar disks.The plots are color-coded according to morphological type, with the red points showing dwarfs, and the blue and cyan showing early and late-type spirals respectively. The correlation coefficient (r) for each plot and the vertical scatter (σ) about the fitted line are shown in the upper left/right corners of the plots. For most points, the errors on the x axes are smaller than the data points.

have UGC12713 a dwarf spheroidal in a zone populated by late-type dwarfs. This shows that the apparent scaling of these quantities with morphology is not a cause but rather an effect of the underlying scaling relations amongst the quantities themselves and processes such as star formation. We find that galaxies with higher gas factions are intrinsically fainter in W1, i.e. they have lower stellar luminosity, than those with low gas fractions. Roberts (1969) posited that in log-log space, the gas fraction is in fact a color index scale such that smaller

gas fractions indicate bluer color indices, which indeed shows in the lower panels of Figure 3.2 where the early-type spirals, which have bluer color index, populate the low gas fraction part of the plots. The mass luminosity scaling relations in our sample are in agreement with those of Verheijen & Sancisi (2001) taken from the Ursa major galaxy cluster.

In summary, we see that the global HI properties of our galaxy sample are in agreement with other smaller samples and scale as expected. This means that our large sample is a balanced representation of the general galaxy population in terms of the HI content and stellar luminosity.

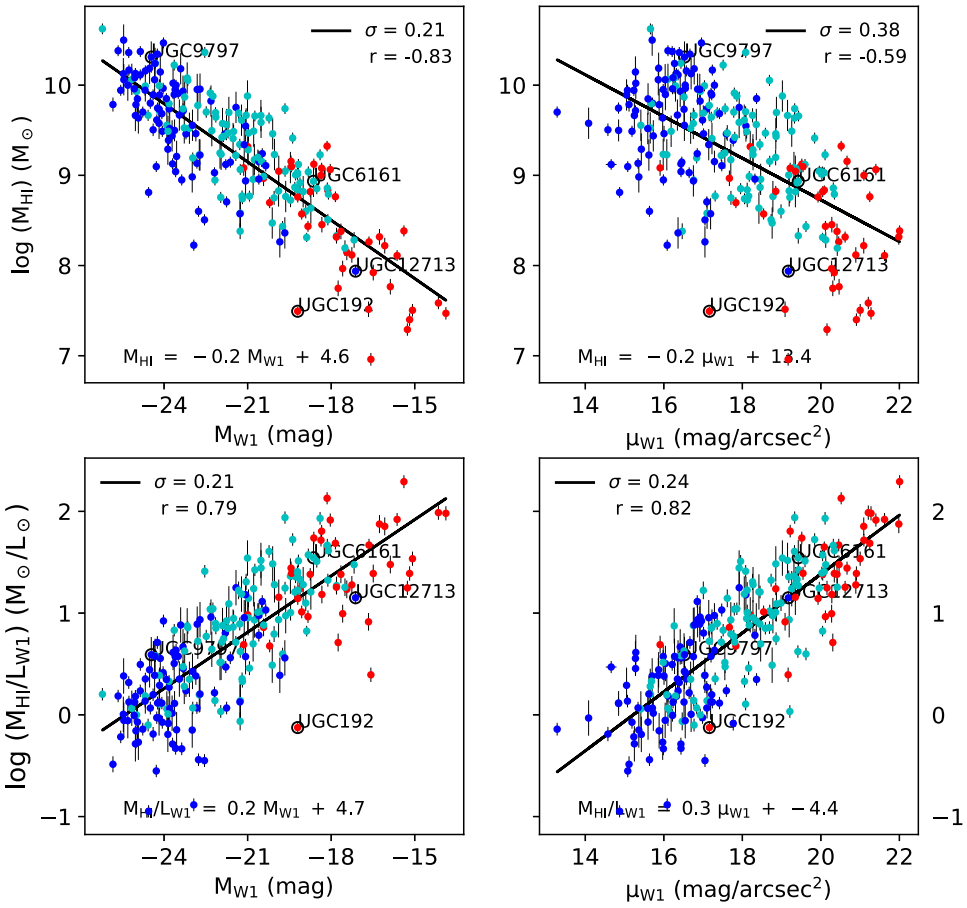

Figure 3.3: This is a plot showing the relations in Figure 3.2 derived for M_{HI} integrated over the entire HI disk. All the labels and colors are the same as in Figure 3.2. Note that when we use the HI enclosed within the stellar disk, we get a tighter correlation between the mass and luminosity because we are comparing spatially co-located properties.

3.2 Star formation properties

The W3 data were used to study the star formation properties of the sample due to its superior sensitivity (1 mJy) over the W4 band (6 mJy). In addition, Cluver et al. (2017) found that W3 is a better tracer of the total infrared luminosity than W4. Of the 228 galaxies in the main sample, 180 galaxies are detected in W3 and their W3 luminosities range from $10^{5.2}$ $L_{\odot}$ to $10^{10.2}$ $L_{\odot}$. None of the 48 undetected galaxies had detections in W4 either. These 180 formed a subsample which was used to study the relations between galaxy star formation rate (SFR) and properties of stellar mass, HI mass and HI surface density. All the quantities used in this section were measured within the W1 stellar disk, defined by a 1σ isophote in the W1 image (Jarrett et al. 2013). We hence refer to enclosed masses and 'global' averaged SFR inside this disk. Therefore the relations discussed here are relations of enclosed quantities. The measurements of SFR and galaxy stellar masses were provided by Jarrett et al. (2017) having corrected for the stellar contribution to the W3 flux according to the correction factor of Cluver et al. (2017). The HI masses and surface density were derived from the HI data products derived in Chapter 2.

3.2.1 The star formation main sequence

The correlation between star formation rate and stellar mass, known as the star formation main sequence (SFMS), is a well established scaling relation in galaxies (Brinchmann et al. 2004, Noeske et al. 2007, Daddi et al. 2007, Rodighiero et al. 2010, Wuyts et al. 2011) with a remarkably tight scatter of 0.2 dex that has been shown to hold over all redshifts up to z=6 (Speagle et al. 2014). The SFMS is an important constraint on the mass assembly histories of galaxies and is widely applied in models of galaxy formation and evolution (e.g., Peng et al. 2010, Leitner 2012, Behroozi et al. 2013, Henriques et al. 2015, Sparre et al. 2015). This relation defines the rate at which galaxies build their mass, with the more massive galaxies assembling their mass earlier on in cosmic history. It thus depicts the star forming histories (SFH) of galaxies in the universe since it compares the instantaneous star formation to past star formation. The scatter in the relation has, in the past, been observed to increase at the high mass end, a feature attributed to the more widely varying SFH among massive galaxies.

We present, in Figure 3.4, the main sequence relation for our sub sample of 180 galaxies. Unlike in the previous section, the plots are now color-coded by the W2-W3 color which is an indicator of morphological type and dust content, such that the galaxies with little to no star formation have bluer (small) W2-W3 colors while actively star forming galaxies have redder colors (Wright et al. 2010, Cluver et al. 2017). In our plot, the specific color-code is as follows; Blue for W2-W3 < 2 which are mainly low star forming lenticulars and dwarf spheroidals (Cluver et al. 2017), cyan for W2-W3< 3.0 which are early-type spirals, orange for W2-W3 < 3.5 which are intermediate spirals, and red for W2-W3 > 3.5 which are late-type disk dominated spirals with higher SFR's.

We see that the galaxies follow a well defined main sequence with a scatter of 0.4 dex. There is an increase in scatter at the high mass end, in agreement with previous studies (e.g Guo et al. 2015, Ilbert et al. 2015, Jarrett et al. 2017, Cluver et al. 2017). Noeske et al. (2007) suggest that this large scatter is partly due to gas exhaustion being more prevalent in high mass systems. Passive evolution as well as processes such as mergers, quenching or gas stripping lead to declining SFRs, eventually leading the affected galaxy to migrate from the main sequence or its current star formation rate being decoupled from its past SFR (Ilbert et al. 2015, Jarrett et al. 2017). On the other hand, having decomposed their sample galaxies into disks and bulges, Guo et al. (2015) suggest that the increased variations in the star formation histories of massive galaxies, which caused the large scatter, are due to the prevalence of central dense structures such as bars and bulges in massive systems. A bulge that is not star forming contributes to the total stellar mass of a galaxy but not to the total star formation, yielding a specific star formation rate ($sSFR = SFR/M_*$) that is lower than that for a disk dominated system of similar mass. The varying masses of the bulges affect the derived sSFR to different extents hence we see scatter in the relation, leaving the disk dominated systems to have more similar SFHs and hence a tighter main sequence relation. This may well be the reason for the clear segregation seen between the different morphological types in Figure 3.4, suggesting different SF main sequences for the different galaxy types. The slope of our SFMS relation (1.11±0.04) agrees with the slope of Cluver et al. (2017) (1.049±0.089, Priv. Comm). The slight offset in SFR is likely because they calculated it for only the disks in their sample, which have higher SFR than dwarfs, resulting in a positive vertical offset. We also compare our relation to the SFMS relation of Parkash et al. (2018). Their stellar-mass-selected sample comprises mostly high stellar-mass ($M_* \geq 10^9$ $M_\odot$) spirals and tends towards the turnover at high-mass, resulting in a shallower relation, whereas our sample extends to lower masses where the relation is steeper.

The sSFR normalizes the SFR by the mass of the galaxies and is plotted against the stellar mass in Figure 3.5. We see that the relation is flat, but turns downward, tending to a negative slope, for the high mass galaxies. This trend, which was also found by Jarrett et al. (2017) and Cluver et al. (2017), shows that even though the low mass galaxies have lower SFRs than the high mass systems, the former are still in an active stage of building their disks while the latter are progressing toward passive or quiescent star forming states (Jarrett et al. 2017). For example UGC7256 (NGC4203) is a lenticular galaxy with ongoing SFR but given its stellar disk of $\sim 10^{10.6}$ $M_\odot$, it has a low sSFR and is no longer actively building its disk. This is also the case for UGC3993 and UGC2487 (NGC1167). These three also have low gas fractions (≤ 0.04). On the other hand UGC3334 (NGC1961) has a considerable bulge to total disk ratio, has one of the highest stellar masses in the sample but also is dusty (W2-W3 = 3.25) with a higher gas fraction (0.15) and relatively higher sSFR. It is possible that even among the high mass systems there can be cases of enhanced star formation even after the galaxy has assembled its mass, for example in the case of merger events. We find, as did Cluver et al. (2017), that it is the more dusty systems (large W2-W3 colors) that have the highest sSFR. UGC5786 (NGC3310) and UGC 6001 (NGC3442) have the

highest sSFR and highest dust content, $(W2 - W3 \geq 4)$. We have plotted the sSFR-M_* relation of Grootes et al. (2013) in Figure 3.5. Their sample-selection was based on NUV detection which is more sensitive to low SFR systems than to dusty systems with high SFRs (Jarrett et al. 2017). Their flatter relation may thus be an indicator that galaxies with similar gas contents have similar sSFRs.

Note that there are few late-type dwarfs in our SFMS sub sample because most of them have a low dust content and lie below the W3 detection threshold. The W1 band is very sensitive and well able to detect these dwarfs, but this is not the case for W3. The histogram in Figure 3.6 shows the stellar mass distribution of these undetected galaxies. Table 3.1 lists specific properties of the galaxies labelled in Figures 3.1 - 3.8 for reference with the plots.

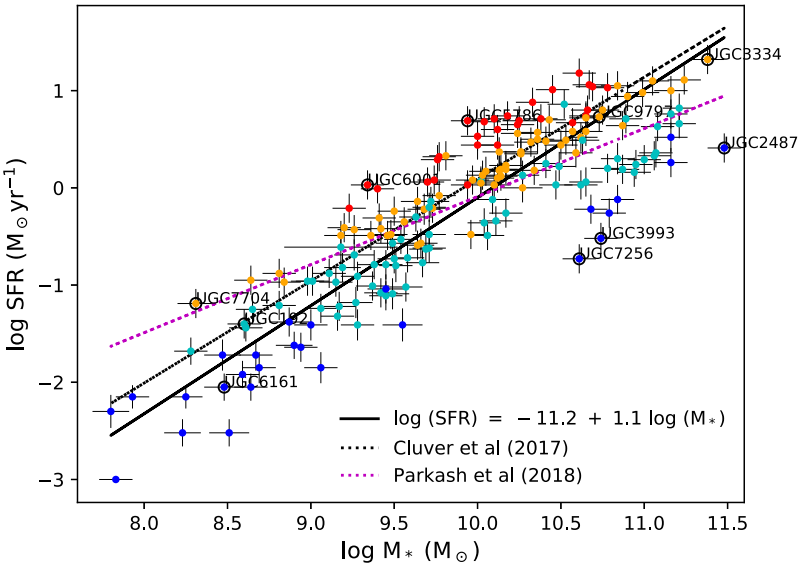

Figure 3.4: Relation between SFR and stellar mass for 180 galaxies detected in W3. The plot is color coded by the W2-W3 color where blue, cyan, orange and red represent W2-W3 ≤ 2, ≤ 3.0, ≤ 3.5 and, ≥ 3.5 respectively. The W2-W3 is an indicator of the dust content but also follows the morphologies such that low star forming early-types have bluer colors while the high star forming intermediate spirals have redder colors (Cluver et al. 2017). The solid black line is a maximum likelihood fit to the data. For a given mass range, the main sequence line marks a separation between early-types and late-types.

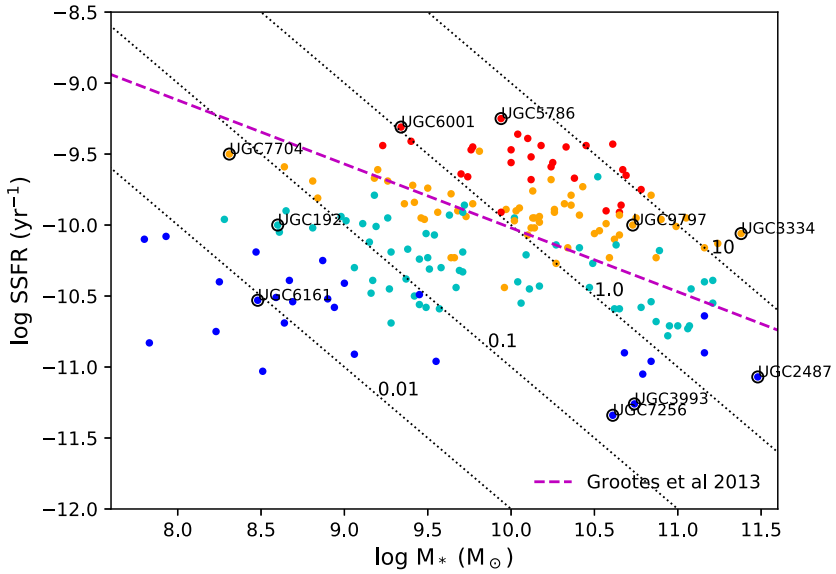

Figure 3.5: Relation between the specific SFR ($sSFR = SFR/M_*$) and stellar mass. The plot is color coded by the W2-W3 color where blue, cyan, orange and red represent W2-W3 ≤ 2, ≤ 3.0, ≤ 3.5 and, ≥ 3.5 respectively. The black dashed diagonal lines represent lines of constant SFR (0.01, 0.1, 1, and 10 $M_\odot yr^{-1}$). The dashed magenta line is the relation of Grootes et al. (2013) whose sample of spirals had $\log M_* \geq 9.6$.

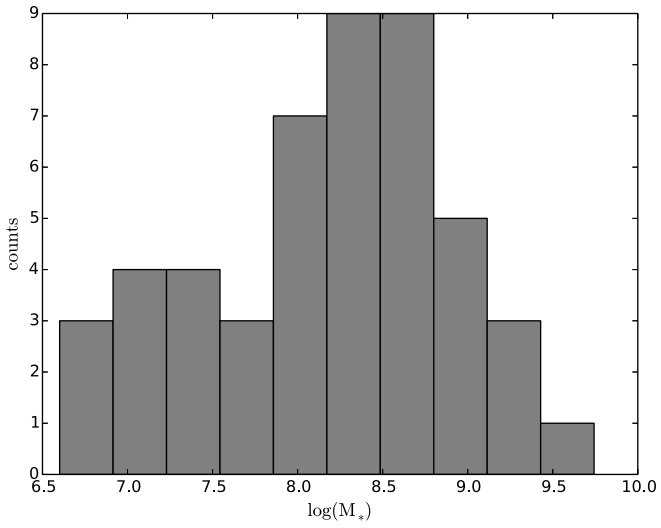

Figure 3.6: A histogram of galaxies in the main sample that were not detected in W3 and are thus not included in the analysis of star formation properties. These galaxies also did not have detections in the W4 band. The majority of them are dwarf galaxies and relatively dust-free, with very low MIR emission that lies below the detection threshold.

Table 3.1: **Specific properties of galaxies labelled in Figure 3.4**: (1) - Name. (2) - stellar mass. (3) - Atomic Hydrogen mass. (4) - Star formation rate as measured from W3 flux calibration. Note that the SFR is integrated over the stellar disk. (5) - Specific star formation rate. (6) - W2 − W3 color index. (7) - Gas fraction, that is, the ratio of HI mass to the stellar mass, both quantities summed up inside the stellar disk. (8) - Morphology.

Name	$\log(M_*)$ $M_\odot$	$\log(M_{\rm HI})$ $M_\odot$	$\log(SFR)$ $M_\odot yr^{-1}$	$\log(sSFR)$ yr^{-1}	W2-W3 mag	$\frac{M_{\rm HI}}{M_*}$	Morph
(1)	(2)	(3)	(4)	(5)	(6)	(7)	(8)
UGC192	8.6	7.45	−1.4	−10.0	2.75	0.07	Im
UGC2487	11.48	10.08	0.41	−11.07	1.83	0.04	S0
UGC3334	11.38	10.56	1.32	−10.06	3.39	0.15	Sc
UGC3993	10.74	9.25	−0.52	−11.26	1.35	0.03	S0
UGC5786	9.94	9.61	0.69	−9.25	4.26	0.47	pec
UGC6001	9.34	8.57	0.03	−9.31	4.03	0.17	Sa
UGC6161	8.48	8.42	−2.05	−10.53	1.8	0.88	Sdm
UGC7256	10.61	9.16	−0.73	−11.34	1.15	0.04	S0
UGC7704	8.31	8.35	−1.19	−9.5	3.25	1.09	Im
UGC9797	10.73	10.1	0.73	−10.0	3.48	0.23	Sb

3.2.2 Star Formation Rate versus Atomic Hydrogen

The Kennicutt-Schmidt relation describes a power law relation between the surface densities of star formation rate and total gas in galaxies with a slope of 1.40±0.15 (Kennicutt 1998b). It has been highlighted by later studies that the apparent correlation between SFR and total gas surface density is very likely due to the tight correlation between Σ_{SFR} and $\Sigma_{\rm H_2}$ and only a loose correlation, if any, with the $\Sigma_{\rm HI}$ (Wong & Blitz 2002, Fumagalli & Gavazzi 2008, Bigiel et al. 2008, Krumholz et al. 2009b, Schruba et al. 2011, Bolatto et al. 2011, Leroy et al. 2013). In fact it would be expected for SFR to be more strongly correlated with the H_2 content than the HI content because cold HI condenses into H_2 (Krumholz et al. 2009a), and it is this molecular gas that is more directly linked to the SF process because stars form out of collapsing molecular clouds (Kennicutt & Evans 2012). Recent work has highlighted the existence of a volumetric star formation law, wherein the SFR and total gas are related via their volume-densities by a power law, for scales ranging from molecular clouds to starburst galaxies (Krumholz et al. 2012, Evans et al. 2014, Sofue 2017, Bacchini et al. 2018). However, in this subsection we focus our investigation on HI gas due to the limitation of having only HI imaging for all our sample. *It is important to note that Bacchini et al. (2018) found 'an unexpected and tight' correlation between the volume densities of SFR and atomic gas, highlighting the important role of the* HI *gas, especially in low-density and low-metallicity environments.* The role of molecular gas in the equation of SF is self-evident. However, we attempt to learn more about the relationship between SFR and atomic gas. The SFR is correlated with the total atomic gas content, the quenching of which leads, in the long run, to suppression of star formation because the atomic gas is needed to cool and form molecular clouds (Fumagalli & Gavazzi 2008, Elmegreen & Hunter 2015).

Figure 3.7 shows the SFR as a function of the atomic gas mass enclosed within the stellar disk. The plot is also color coded by the W2-W3 color. The red points are the most dusty systems (with $\rm W2-W3 \geq\ 4$), while the blue dots are the least dusty systems with $\rm W2-W3 \leq\ 2$, and they represent mostly late-type dwarfs and lenticular galaxies in the sample. Cyan and orange points represent intermediate star forming galaxies. From Figure 3.5 we saw that the more dusty systems have higher sSFR and that less dusty systems have lower sSFR (Cluver et al. 2017). We see a gradual separation in the SFR - MHI plane between the low and the high dust content systems such that the former lie closer to the low gas mass - low SFR end of the relation while the latter tend to dominate the high gas mass - high SFR end. This follows from the availability of molecular gas as fuel for star formation, such that higher gas contents are coupled with high SFRs. Therefore, since dust is associated with active SF (Cluver et al. 2017), it is expected that high gas content systems are equivalent to high dust content systems. Note, however, that there are some high gas mass systems that have low dust contents and low sSFR but relatively high SFR. For example, UGC2487 (NGC1167) has W2-W3 = 1.83 (low dust content), a relatively high SFR (0.41 $\rm M_{\odot} yr^{-1}$) but, despite its high HI mass of $\sim 10^{10.1}$ $\rm M_{\odot}$, it has a very low gas fraction (0.04) and low sSFR ($\sim 10^{-11.1}$ $\rm yr^{-1}$) due to the high stellar mass of $\sim 10^{11.5}$ $\rm M_{\odot}$.

Overlaid on the data in Figure 3.7 are, a best fit line (maximum likelihood fit using the Hyperfit* package), as well as the relations of Cluver et al. (2010) for galaxies in the Spitzer Infrared Nearby Galaxies survey (SINGS†) and Michałowski et al. (2015). These two relations have considerably shallower slopes than the data here which on closer inspection appears to become flatter at $\log \mathrm{SFR} \geq -1$. The sample of Cluver et al. (2010) is dominated by systems with $\log \mathrm{SFR} \geq -1.5$ and it may be that they pick up the flatter end of the relation in their study. Michałowski et al. (2015), on the other hand, have a much wider range spanning five orders of magnitude in both SFR and HI mass, albeit with a higher concentration of systems at the high SFR end. The difference in our sample is that while Cluver et al. (2010) and Michałowski et al. (2015) measure the total HI mass, here we measure the HI mass enclosed within the stellar disk, and thus we are comparing spatially co-located gas and stars.

Figure 3.8 shows, however, that there is no correlation between the surface densities of the two quantities. This is likely due to the limited range of HI surface densities (one magnitude) spanned by our sample. This limitation may partly arise from the tight mass-size relation of spiral galaxies (see Section 3.1.1) whose consistent slope of ~ 2 for a wide variety of samples (Wang et al. 2016) implies a roughly constant characteristic average HI surface density for all star forming galaxies (Verheijen & Sancisi 2001, Noordermeer et al. 2005, Martinsson 2011). The SFR, on the other hand, is not regulated by disk size (or projected surface area) so the Σ_{SFR} spans a wider range of three orders of magnitude.

Note, also, that the entire sample lies either at or below the density threshold at which the SF - gas relation steepens for low gas surface densities (Bigiel et al. 2008). The Σ_{SFR} - Σ_{HI} relation of Bigiel et al. (2008) is shown in Figure 3.9 below showing a steep decline in Σ_{SFR} at HI surface densities below 10 $\mathrm{M}_{\odot}$ pc^{-2}. The global average gas surface densities for all our galaxies fall under this regime.

Several authors have observed a cutoff of the HI surface density signalling a saturation density where the atomic gas converts to molecular gas. For example, Wong & Blitz (2002), Bigiel et al. (2008), and Liu et al. (2011) found a maximum HI surface density of 10 $\mathrm{M}_{\odot}$ pc^{-2} while Kennicutt et al. (2007), and Liu et al. (2015) found a cut-off of 25 $\mathrm{M}_{\odot}$ pc^{-2}. Using theoretical models, Krumholz et al. (2009a), found that HI surface densities of 10 $\mathrm{M}_{\odot}$ pc^{-2} are sufficient to shield molecular regions against photo-dissociation hence forming a physical boundary for the atomic-molecular conversion to occur. It is above these densities that the H_2 regime takes over and forms giant molecular clouds, which are the regions of SF. Therefore, with all our global estimates for Σ_{HI} being below 10 $\mathrm{M}_{\odot}$ pc^{-2}, we can not see a well defined correlation between the globally-averaged surface densities of atomic gas and star formation rate. In the discussion below, we attempt to look for a correlation at local scales in individual galaxies.

*http://hyperfit.icrar.org/

†http://irsa.ipac.caltech.edu/data/SPITZER/SINGS/

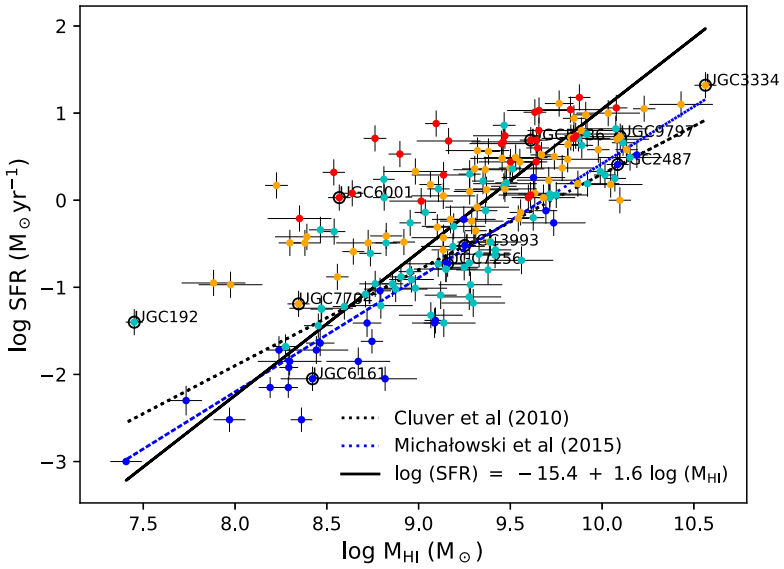

Figure 3.7: Star formation rate versus atomic gas mass for a sub sample of 180 galaxies with a W3 detection. The HI masses were integrated over the stellar disk defined by the 1σ isophote in the W1 images. The plot is color coded by the W2-W3 color where blue, cyan, orange and red represent W2-W3 ≤ 2, ≤ 3.0, ≤ 3.5 and, ≥ 3.5. Our best fit line was obtained using the Hyperfit package which does a maximum likelihood estimation.

In Figures 3.10 and 3.11, the Σ_{SFR} is plotted as a function of $\Sigma_{\rm HI}$ for individual pixels in 33 galaxies with spatial resolution higher than $\sim$1 kpc per pixel. The galaxies have varying spatial resolutions. The upside of this is that it enables one to see the relation at different physical scales.

This "resolved Kennicutt-Schmidt" relation has been studied by several authors for individual galaxies as well as in samples of galaxies, (for example Wong & Blitz 2002, Kennicutt et al. 2007, Bigiel et al. 2008, Onodera et al. 2010, Liu et al. 2011, Yim & van der Hulst 2016). The plots in Figures 3.10 and 3.11 are presented as 2D histograms, such that regions of overlapping data points are given higher intensity and a redder color. We find that a trend between Σ_{SFR} and $\Sigma_{\rm HI}$ emerges at these kpc to sub kpc scales in about 30% of the subsample. We attempt to fit power laws to the plots which visually appear to have a correlation and find that, in agreement with Bigiel et al. (2008), the relationship is typically non-linear and the indices range between 1.6 to 3.8. Note, however, that even though a majority of the plots (90%) have $\Sigma_{\rm HI} \leq 10$ $M_\odot$ pc^{-2}, the saturation point observed for HI by Bigiel et al. (2008) and Wong & Blitz (2002), they still show a trend between these low gas surface densities and the Σ_{SFR}. Only three galaxies (UGC1913, UGC7592, UGC8490) have data points with densities higher than 10 $M_\odot$ pc^{-2}.

Onodera et al. (2010) used CO data to study the molecular KS relation and concluded

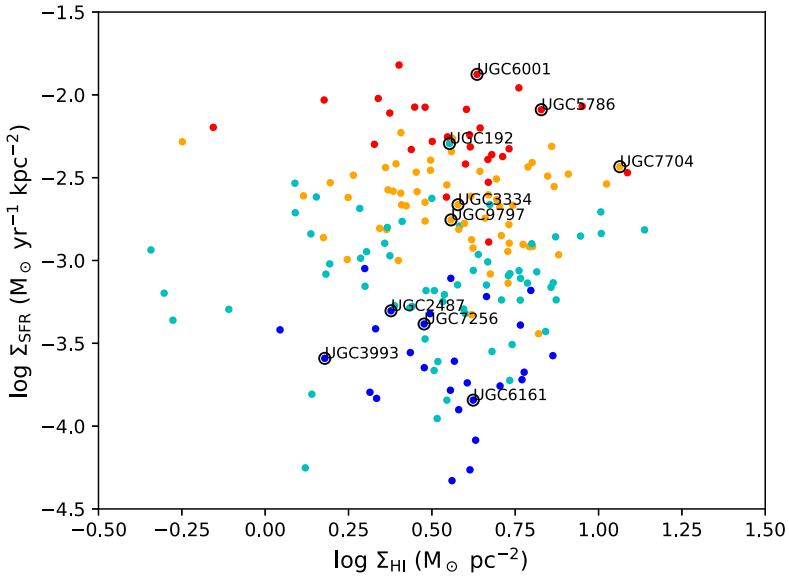

Figure 3.8: Mean star formation rate surface density versus HI surface density for the sub sample. The surface densities were averaged over the stellar disk defined by the 1σ isophote in the W1 images. The plot is color coded by the W2-W3 color where blue, cyan, orange and red represent W2-W3 ≤ 2, ≤ 3.0, ≤ 3.5 and, ≥ 3.5. There is no correlation observed between the $\Sigma_{\rm HI}$ and Σ_{SFR} at these global scales, contrary to the global Kennicutt-Schmidt law (Kennicutt 1998b).

that it only holds at kpc sales and has a scatter that increases with resolution, eventually breaking down at GMC scales. The study of Williams et al. (2018) also showed that the molecular KS law was approximatley linear at 2 kpc scales with an index N = 1.07±0.16 but becomes non linear at 100 pc (GMC scales) indicating a break down. This is said to be a result of migration of the young stellar cores away from their parent gas cores (Leisawitz et al. 1989, Sheth et al. 2002, Louie et al. 2013) and the different stages of GMC evolution that are traced in highly resolved observations (Miura et al. 2010, Egusa et al. 2011). Williams et al. (2018) also found no linear relationship for the $\Sigma_{\rm HI}$ and Σ_{SFR} at either kpc or sub-kpc scales as did Wong & Blitz (2002) and Bigiel et al. (2008) who concluded that the correlation observed for total gas ($\Sigma_{\rm HI+H_2}$) by Kennicutt (1998b) was due to the stronger underlying correlation between $\Sigma_{\rm H_2}$ and Σ_{SFR}. However, we see here that there may be systems in which the atomic KS relation holds at resolved scales. In fact Wyder et al. (2009) found a strong correlation between $\Sigma_{\rm HI}$ and Σ_{SFR} in low surface brightness galaxies, while Yim & van der Hulst (2016) found a tight correlation between $\Sigma_{\rm HI}$ and Σ_{SFR} in the outer regions of quiescent, accreting and interacting galaxies alike. Krumholz (2012) has, analytically, shown that in low metallicity systems, stars may form from the collapse of cool atomic clouds due to the inefficient conversion of HI to H_2 such that atomic Hydrogen clouds cool down to temperatures that are adequate for star formation to occur before they

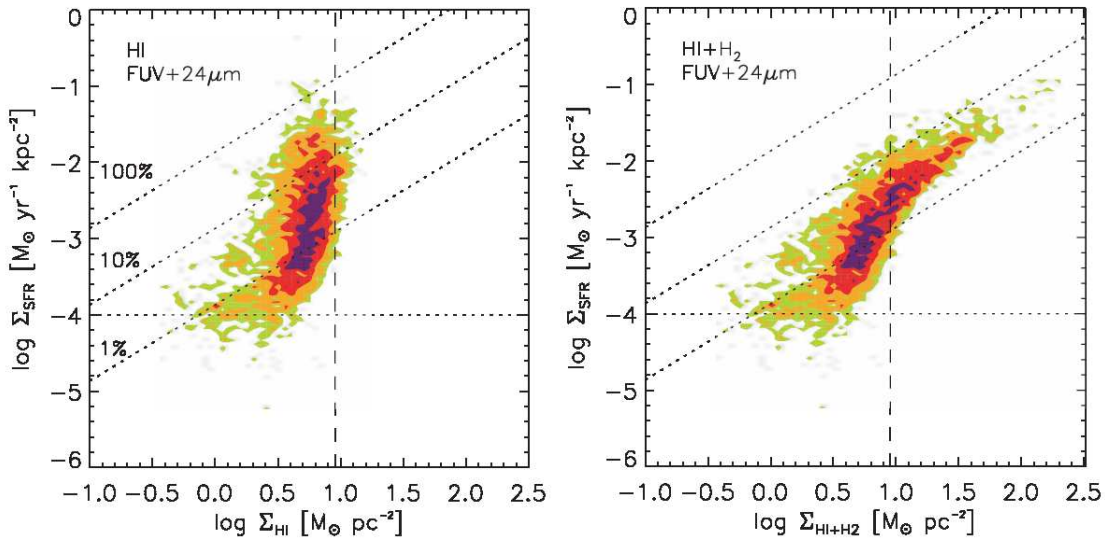

(a) (b)

Figure 3.9: Plots from Bigiel et al. (2008) showing Σ_{SFR} vs $\Sigma_{\rm HI}$ (left panel) and Σ_{SFR} vs $\Sigma_{\rm H_2}$ (right panel) for seven spiral galaxies. The plots are density contours corresponding to the number of independent data points plotted, i.e. green, orange, red and magenta for 1,2,5 and 10 independent data points. In the plot of $\Sigma_{\rm HI}$, a cut off was seen by Bigiel et al. (2008) at 10 $M_\odot$ pc^{-2}, shown by the vertical dotted line and a steep decline in Σ_{SFR} indicating a break down or change in star formation law at these low surface densities. It is in this region 0.25 - 10 $M_\odot$ pc^{-2} that all the average HI surface densities in our sample fall, hence the observed lack of correlation in our sample. The horizontal lines indicate sensitivity limits of the SFR tracer while diagonal lines are lines of constant star formation efficiency.

are converted into molecular clouds. Although metallicities were not derived in this study, this observation points to interesting research deeper into the realm of a possible 'Atomic Kennicutt-Schmidt law'. Such a relation may never be as tight as that for molecular gas surface density, but can prove useful in high density spiral arms where there is photo-dissociation of H_2 into HI by ultraviolet radiation from star forming regions (as in the case of M83 - Tilanus & Allen 1993, or M33 - Heyer et al. 2004) and the HI could be used to trace star formation. Figure 1.3 illustrates the case of M83 using WISE 11.6 μm emission and HI imaging (Jarrett et al. 2013).

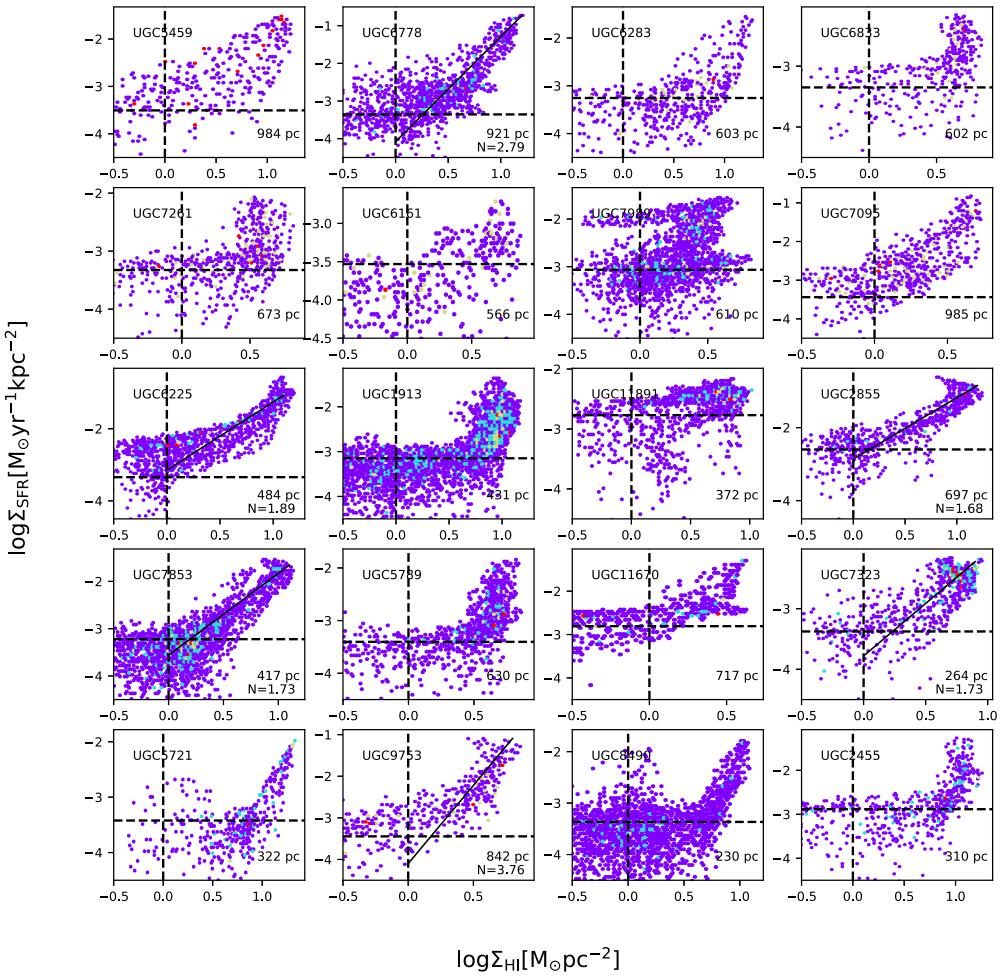

Figure 3.10: Plots of the 'resolved Kennicutt-Schmidt law' for 33 galaxies in our sample of 180 which had spatial resolutions higher than 1 kpc per pixel. Each data point represents a pixel in the 2D maps of Σ_{SFR} and $\Sigma_{\rm HI}$.The resolution (in parsec) per pixel and the fitted power-law index are shown in the lower right corner of each plot. The density contours are such that the regions with the most overlapping points have the highest density (red). In some galaxies, there are not many data points to make a density plot, so we use a regular scatter plot. The horizontal dashed lines mark the noise level in W3 for the respective galaxies, while the vertical dashed lines mark the level $\Sigma_{\rm HI} = 1$ $M_\odot$ pc^{-2}which was used as a constant noise level for all the galaxies. These plots show that there is a possible relationship between the surface densities of SFR and atomic gas at sub-kpc scales, in spite of no correlation seen at global scales. The plots are in order of increasing dust content (W2-W3 color).

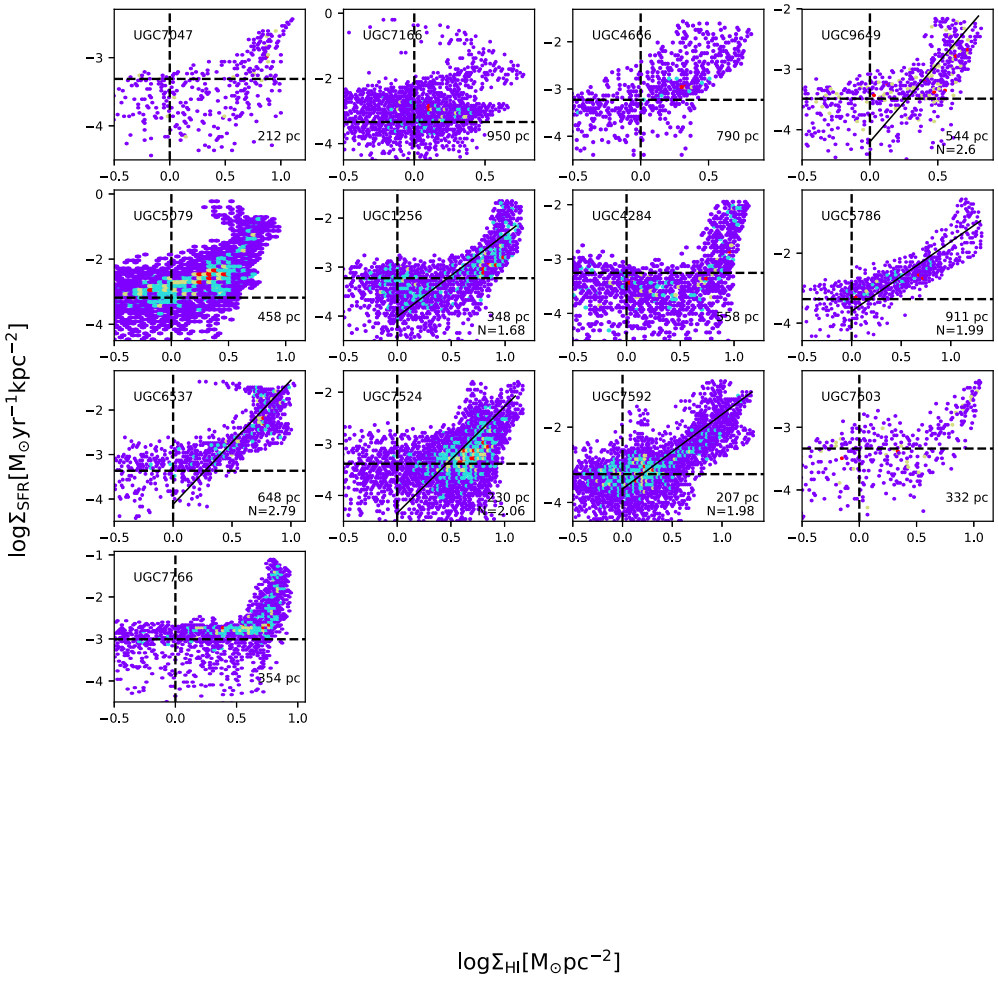

Figure 3.11: Same as Figure 3.10 for the rest of the resolved galaxies. Labels and colors remain the same.

3.3 Summary

In this chapter, we have studied the global properties of HI and star formation in our sample galaxies. The HI global properties were studied for the entire sample of 228 galaxies, while star formation scaling relations were studied for a sub-sample of 180 galaxies which were detected in the WISE 11.6 μm band.
We have found all galaxies to fall on the HI mass-size relation with a slope of 1.95±0.03, and have derived a characteristic mean HI surface density of 3.6 $M_\odot$ pc^{-2}, both in agreement with the literature on studies of other samples. Correlations between the HI mass with stellar luminosity and stellar surface brightness also hold for the entire sample. The HI mass is negatively correlated with the stellar luminosity and stellar surface brightness while the mass-to-light ratio is positively correlated with the same. But the correlations with luminosity are tighter than those with stellar surface brightness. Also, the early-type spiral galaxies are found to have higher stellar luminosities and higher HI masses but lower mass-to-light ratios (M_{HI}/L) than late-types. Note that the HI masses and mass-to-light ratios in our study were derived inside the stellar disk. The trends in our relations are the same as in other studies which use integrated properties over the entire HI disk, although we have less scatter in our relations, especially the relation between HI mass and stellar luminosity.

From our main sample of 228, a sub-sample of 180 galaxies with W3 detections was derived to investigate the scaling relations of star formation rate with stellar mass (the star formation main sequence) and atomic Hydrogen (the Kennicutt-Schmidt relation). Our sample defines a main sequence with a slope of 1.1, and an apparent segregation is seen between the higher SFR galaxies (with high dust content) above the main sequence and the low star forming galaxies below the main sequence.
We have found no correlation between the global average surface densities of SFR and atomic gas, and we observe a cut-off in global average Σ_{HI} at 10 $M_\odot$ pc^{-2}, in agreement with previous studies. For 33 resolved galaxies (resolutions $\leq 10''$/pixel), a pixel-by-pixel analysis of the Σ_{SFR} vs Σ_{HI} relation was done, and we found that 30% of them exhibited power-law relation with indices ranging from 1.6 to 3.8. From the pixel-by-pixel analysis, we find a trend that suggests a possible relationship between the atomic gas and star formation rate surface densities. In the next chapter, we investigate the relationship between star formation rates and disk gravitational stability on resolved scales.

Chapter 4

Disk Stability and Star Formation Thresholds

A study of the physical factors controlling star formation thresholds is crucial to understanding the process of star formation and hence evolution of galaxies (Kennicutt 1998b). The star formation rate is highly dependent on the amount of gas present in a galaxy's disk (Michałowski et al. 2015), because cold atomic gas provides the fuel for star formation (Cluver et al. 2010). However, the stability of the gaseous disk against collapse greatly impacts the onset (and regulation) of star formation on both global and local scales. For a purely gaseous galactic disk (an idealized case) without stars, the condition for stability is set by the balance between the self gravity and the rotational and dispersive motions of the gas (Toomre 1964). For such a disk to be stable against gravitational collapse, the Toomre stability parameter, Q_g,

$$Q_g \;=\; \frac{\sigma_g \kappa}{\pi G \Sigma} \tag{4.1}$$

must exceed 1, where σ_g, κ, and Σ are the gas velocity dispersion, epicyclic frequency (a function of the gradient of the rotation curve) and the gas surface density respectively. Equation 4.1 implies that for any region of the disk to undergo star formation, the gas density must be higher than a certain critical value, Σ_c which can be obtained by re-writing Equation 4.1 as

$$\Sigma_c \;=\; \alpha \frac{\sigma \kappa}{\pi G}, \tag{4.2}$$

where α is a constant that allows for deviation of a real galactic disk from the theoretical thin gas disk defined by Kennicutt (1989) as $1/Q_g$ at the edge of the star forming disk and found $\alpha = 0.63$. The relationship between disk stability and star formation is explored in this chapter.

For the gas density, we mainly use atomic gas data from the WHISP survey (see Chapter 2). Molecular gas data were available from the HERACLES survey * for three galaxies in our

*http://www.cv.nrao.edu/ aleroy/HERACLES/Overview.html

sample (UGC1913, UGC7766, UGC7989). For these three, total gas density measurements ($\Sigma_{\rm HI+H_2}$) were used. This presents an opportunity to compare total Hydrogen and atomic Hydrogen gas stability thresholds for star formation. Measurements of Star formation were obtained from WISE W3 (11.6 μm) imaging. The W3 band is an excellent tracer of the Polycyclic Aromatic Hydrocarbons which are excited by UV radiation from star forming regions and re-emit at 11.6 μm (Wu et al. 2005, Tielens 2008, Cluver et al. 2014). Conversion into the respective units was done based on the calibrations by Cluver et al. (2017). The galaxy disks were probed for trends in the stability parameter and a single-fluid stability threshold for star formation discussed in Section 4.2. After studying this single-fluid disk stability model, we also study the stability for a two-fluid disk model that accounts for the co-existence of both stellar and gaseous disks within a galaxy (a more realistic case). In this model the stability of the galaxy disk is determined by the gravity and motions of both the stars and the gas as well as their impact on the dynamics of each other. We use the formulation of Rafikov (2001) to derive the two-fluid disk stability criterion,

$$\frac{1}{Q_T} \;=\; \frac{2}{Q_*}\frac{q}{1+q^2} \;+\; \frac{2}{Q_g}R\frac{q}{1+q^2R^2} \;>\; 1, \tag{4.3}$$

where Q_g is the single-fluid stability condition for a gas disk, $R = \sigma_g/\sigma_*$, σ_* being the stellar velocity dispersion, $q \;=\; k\sigma_* \;/\kappa$ with k denoting the wavelength of maximum perturbation, and Q_* is the single-fluid stability parameter for a purely stellar disk, defined as in Equation 4.1, but with the stellar surface density, Σ_* and stellar dispersion in the place of Σ_g and σ_g. The analysis of the two-fluid disk model is presented in Section 4.3.

The study presented in this chapter is an analysis of spatially resolved disks; As such, a subsample of suitable WHISP galaxies was defined using the following criteria. Intermediate inclination of the disk ($35^\circ \;-\; 70^\circ$, for reliable rotation curves), a large HI disk size (>10 beams along the major axis) to maximize the physical area probed and a physical pixel scale of 1 kpc. Since the WHISP beam is 3 pixels ($30''$) across, and with the galaxies in this sample having pixel scales ranging from ∼200 pc to ∼700 pc, we are looking at resolution elements ranging from ∼600 pc - ∼2.1 kpc.Note that the inclinations used in these criteria were derived from infrared photometry which may be different from those estimated by tilted ring models. A final condition, to remain within the scope of the study, was the availability of rotation curves, preferably from the same data set. A sample of 20 galaxies was thus defined, with WHISP rotation curves (Swaters 1999, van Eymeren et al. 2011) availed by R. Swaters (priv. communication) and J.v. Eymeren (priv. communication). Both authors derived their rotation curves using the GIPSY task *rotcur*. The properties of the sample are presented in Table 4.1, which also indicates the literature source for each rotation curve. Note that no attempt was made to smooth all the disks to a common spatial resolution. Instead, contrasts were drawn across the different resolution scales.
Hence we present an analysis of gravitational stability thresholds for a sample of 20 galaxies using WISE mid- infrared imaging and WHISP atomic gas mapping supplemented by

molecular gas measurements from the HERACLES survey where available. First, we derived maps of star formation rate from the W3 maps and then derived maps of the gravitational stability parameters.

4.1 Star formation rate maps

The single-fluid stability maps were studied together with maps of the W3 SFR surface density. In this subsection, I describe how the SFR maps were derived. The WISE W3 and W4 bands trace PAH molecules and warm dust (respectively) which absorb light from young stars and re-emit it at mid infrared wavelengths (Jarrett et al. 2012; 2013). Since the W3 band is more sensitive than W4, (Jarrett et al. 2013), W3 was used for the derivation of SFR maps in this study. The WISE images have a resolution of $\sim 7''$ and a re-sampled pixel scale of $1''$ per pixel. Therefore, they were first smoothed to the beam resolution ($\sim 30''$) and astrometric grid ($10''$ per pixel) of the WHISP data. The details of this process, as well as accompanying image atlases, are given in Appendix B. The calibration of W3 imaging into SFR for resolved galaxies (Cluver et al. 2017) is given by ;

$$\log(\mathrm{SFR}) \;=\; (-7.76 \pm 0.15) \;+\; (0.889 \pm 0.018)\, \log(\nu \mathrm{L}_{\nu}) \tag{4.4}$$

where νL_{ν} is the spectral luminosity in $\mathrm{L}_{\odot}$.
To arrive at the spectral luminosity, the W3 magnitude was converted into flux (f_{ν}) using the W3 flux zero point. The equations used were;

$$W3 \;=\; Zp_3 \;-\; 2.5 \log(\mathrm{DU}), \tag{4.5}$$

$$\mathrm{f}_{\nu}(\mathrm{Wm}^{-2}\mathrm{Hz}^{-1}) \;=\; \mathrm{f}_{\mathrm{o}} \;\times\; 10^{-W3/2.5} \;\times\; 10^{-26}, \tag{4.6}$$

$$\nu \mathrm{L}_{\nu}(\mathrm{L}_{\odot}) \;=\; \frac{\nu_{\mathrm{w3}} \;\times\; 4\pi \mathrm{D}^2 \;\times\; \mathrm{f}_{\nu}}{3.846 \;\times\; 10^{26}} \tag{4.7}$$

where DU is the W3 image in data units, *W3* is the W3 magnitude in the Vega system, Zp_3 is the instrumental zeropoint of the W3 band, while $\mathrm{f}_{\mathrm{o}} = 29.0448$Jy is the W3 flux zeropoint (Wright et al. 2010), ν_{w3} the mid-band frequency of the W3 band, and D is the distance in meters.

Maps of the SFR surface density (see Figures 4.2 and 4.3) were obtained by dividing the SFR maps by the physical pixel area in units of kpc^2. The pixel area is defined as

$$\mathrm{A} \;=\; [\theta \times \mathrm{D(kpc)}]^2, \tag{4.8}$$

where θ is the pixel scale in radians.

All analyses were carried out within the star forming disk. The edge of this disk was defined as the isophote at 18.8 mag/arcsec^2 (8.7714×10^{-4}mJy) which roughly corresponds

to the 5σ noise level in the W3 maps (See Table 4.2). Five of the 20 galaxies did not fit into this range and an isophote of 17.5 mag/arcsec^2 (2.2033×10^{-3}mJy) was used which also corresponds to the 5σ level. One galaxy (UGC2855) was much brighter than the rest and its own 5σ level at 16.5 mag/arcsec^2 (5.0474×10^{-3}mJy) was used to define the star forming disk. The isophote is shown as a black contour on all the maps of SFR and gravitational stability parameter in this chapter.

To crosscheck the reliability of the SFR maps, global SFRs were calculated from the total flux from f_ν in Equation 4.6 and compared with global values from Jarrett et al. (2017) (Figure 4.1). Note that the W3 band suffers contamination by emission from evolved stars, (Cluver et al. 2014), and the SFR calibration relation has considerable scatter because of this (Jarrett et al. 2013). The W4 band does not suffer from these contaminants, but the superior sensitivity of the W3 band and the fact that it traces the interstellar medium (ISM) make it a more reliable calibrator of mid-infrared SFRs than W4 (Cluver et al. 2014; 2017).

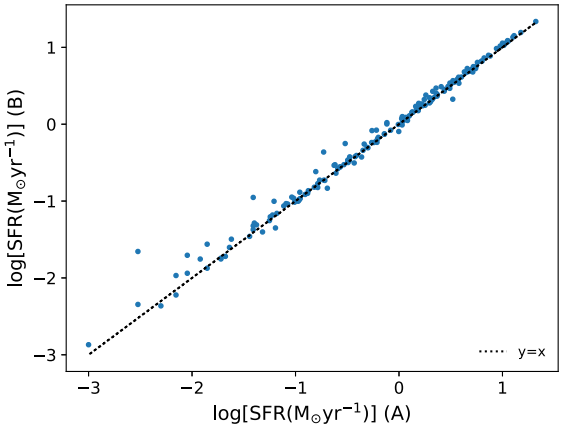

Figure 4.1: Comparison of star formation rates. Global average SFRs from the method described in Section 4.1 above (method B on the y axis) were compared to global average values (A) provided by Jarrett et al. (2017) who used native resolution and $1''$ pixel imaging for photometric measurements. In both cases, summation of total flux was within the stellar disk, defined by the W1 1σ isophote. Also note that SFR values were obtained only for galaxies that had a detection in the W3 band. The measurements on both axes used the same distances. There is good agreement with a few outliers, implying that the SFR maps derived above were reliable.

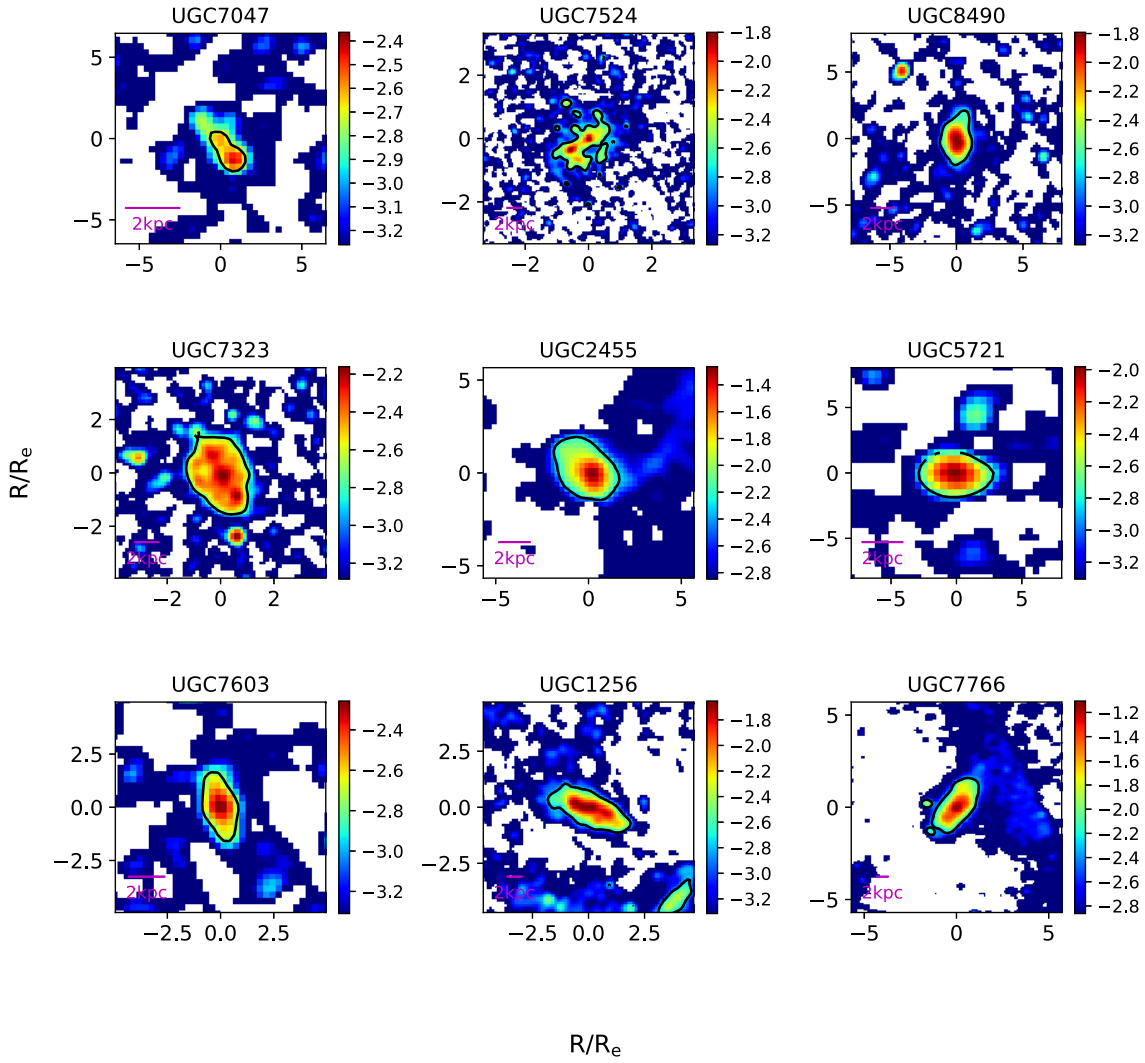

Figure 4.2: Maps of the SFR surface density (log Σ_{SFR} [$M_\odot$ yr^{-1} kpc^{-2}]). These were derived from the WISE W3 images which were first matched to the resolution (30″) and astrometric grid (10″ per pixel) of the WHISP HI imaging. The smoothing and re-gridding process is detailed in Appendix B . Black contours mark the edge of the 'star forming disk' defined by an isophote in surface brightness which roughly matches the 5σ (in most cases, $\sim$ 18.8mag arcsec^{-2}) level in the W3 maps (see Column 2 of Table 4.2). The SF in UGC11891 is patchy, hence the scattered contours.

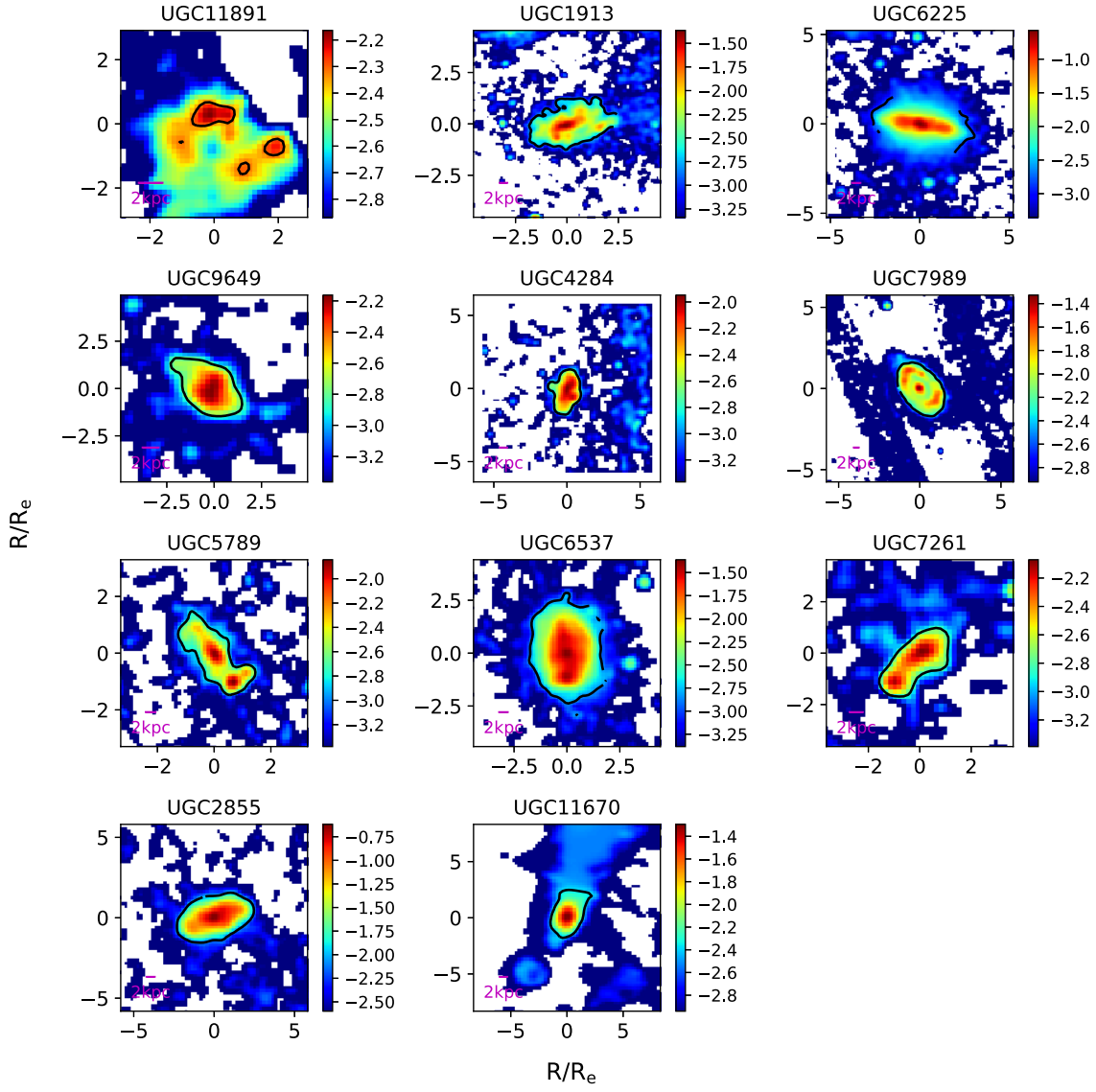

Figure 4.3: Maps of the SFR surface density (log Σ_{SFR} [$M_\odot$ yr^{-1} kpc^{-2}]). These were derived from the WISE W3 images which were first matched to the resolution (30″) and astrometric grid (10″ per pixel) of the WHISP HI imaging. The smoothing and re-gridding process is detailed in Appendix B . Black contours mark the edge of the 'star forming disk' defined by an isophote in surface brightness which roughly matches the 5σ (in most cases, $\sim$ 18.8mag arcsec^{-2}) level in the W3 maps (see Column 2 of Table 4.2).

4.2 The Single-fluid stability criterion

In this section, we examine the relationship between the Single-fluid stability parameter and the MIR emission. First, details are given (in Section 4.2.1) for the methods of derivation of the gas velocity dispersion, rotation curves (and epicyclic frequency) and the gas surface densities, whose maps are used to derive the maps of Q_g for the different galaxies according to Equation 4.1. The following investigations were then carried out:

i) Is there an atomic gas threshold for star formation in this sample of galaxies? First, the Q_g maps were probed for apparent thresholds. Constant Q_g values at the edges of the star forming disks $Q_g \leq 1$ in regions of high SFR can indicate thresholds, while constant Q_g values in the disks are evidence for self-regulated star formation (Silk 1997).

ii) Is the Q_g a necessary condition for the onset of star formation? The existence of high star formation rates in regions with high Q_g (i.e. stable against collapse) would show that Q_g does not predict or determine SF. However a relationship between these two properties can be sought since each of them is closely related to the gas surface density. The results and discussion for these two analyses are presented in Section 4.2.2.

4.2.1 Methodology

To carry out this analysis, 2D maps of the variables in Equation 4.1 were derived and used to obtain a map of the Q_g for each galaxy.

Gas surface density

Gas surface density represents the self gravity of the gas in Equation 4.1. The data used in this study were taken from the WHISP survey. Now, it is known that the gas most closely linked to the star forming process is the molecular gas (e.g. Wong & Blitz 2002, Bigiel et al. 2008). However, we would like to find out how to harness the immense HI data available from surveys to study star formation in the absence of data from molecular gas surveys. Nonetheless, three of the galaxies in the subsample studied in this chapter have been observed in CO by the HERACLES survey (Leroy et al. 2009), and their H_2 surface densities were combined with HI surface densities to obtain a total gas surface density.

HI surface density: Surface density maps of HI were calculated from the total intensity maps via standard conversions. The HI column density is derived as,

$$\mathrm{N_{HI}(cm^{-2})} \;=\; 1.823 \times 10^{18} \times \frac{\sum_\nu \mathrm{S}_\nu}{1.65 \times 10^{-3} \times \Delta\alpha\Delta\delta} \times \Delta\mathrm{V}, \tag{4.9}$$

where $\Delta\alpha$ and $\Delta\delta$ are the major and minor axes of the telescope beam, ΔV is the velocity resolution in km s^{-1}, and $\sum_\nu \mathrm{S}_\nu$ is the HI intensity map in mJy/beam. The factor in the

denominator converts the intensity map into a brightness temperature map.
A linear conversion is applied to the column density map to obtain surface density,

$$\Sigma_{\rm HI}({\rm M}_\odot\ {\rm pc}^{-2}) \ = \ \frac{{\rm N}_{\rm HI}}{1.248\times10^{20}}\ \cos i\ . \tag{4.10}$$

Most of the galaxies studied in this chapter did not have CO data, so $\Sigma_{\rm HI}$ was used as the gas surface density. A factor of 1.36 was applied to the HI surface densities to account for the presence of Helium (Leroy et al. 2008).

H_2 surface density: For three galaxies, CO data were available in the public database of the HERACLES survey. The BIMA SONG survey was also considered, although no cross matches were found beyond these three. Data were not sourced from other surveys because this would introduce inhomogeneities that would add complexity to a comparative study. Also, the HERACLES was favored over other surveys due to the advantages it had, namely, sampling of the full optical disk, and a combination of high sensitivity with high spatial resolution (Leroy et al. 2009). The CO maps have a resolution of $13''$ with a $2''$/pixel sampling.
These maps were degraded to the HI resolution and fit onto the astrometric grid of the HI data (30" and 10" per pixel, respectively) before conversion to H_2 surface densities.
We follow the method of Leroy et al. (2008) who, for their HERACLES data, use a CO - H_2 conversion factor $X_{\rm CO} = 2\times10^{20}{\rm cm}^{-2}$ and a line ratio $I_{\rm CO}(2\rightarrow1) = 0.8I_{\rm CO}(1\rightarrow0)$. This gives the surface density of H_2 as,

$$\Sigma_{\rm H_2}({\rm M}_\odot{\rm pc}^{-2}) \ = \ 5.5\cos{\rm i}\ I_{\rm CO}(2\rightarrow1)({\rm K\ km\ s}^{-1}), \tag{4.11}$$

where $I_{\rm CO}$ is the CO surface brightness and $\cos i$ corrects for inclination. This conversion also includes a factor of 1.36 to correct for the presence of Helium molecules.
After deriving the $\Sigma_{\rm H_2}$, the total gas surface density maps were obtained by adding the HI and H_2 surface densities. For the rest of the sample galaxies, Σ_g implies $\Sigma_{\rm HI}$.

Note: The CO - H_2 conversion factor, $X_{\rm CO}$, has been shown to vary with different aspects of a galaxy such as metallicity, radiation field and molecular gas content (e.g. Leroy et al. 2008, Bolatto et al. 2013). The variation of $X_{\rm CO}$ is such that it can also vary radially within the same galaxy (e.g. **?**). Attempts at calibrating $X_{\rm CO}$ in other galaxies besides the Milky way (e.g. Bolatto et al. 2013) return values similar to the Milky way value ($2\times10^{20}{\rm cm}^{-2}$) but with large scatter. As such, the CO - H_2 conversion factor is a considerable source of systematic uncertainty in studies involving $\Sigma_{\rm H_2}$.

Velocity Dispersion

The derivation of the gas velocity dispersion in galaxies is not a straightforward process. Second moment maps maybe used but these cease to be meaningful measures of dispersions when the line profiles deviate from pure Gaussian profiles (de Blok & Walter 2006). Sev-

eral factors, such as radial inflows (Romeo & Mogotsi 2017), mixture of cold and warm phases of HI (de Blok & Walter 2006, Ianjamasimanana et al. 2012) and projection effects in highly inclined galaxies (Voigtländer et al. 2013), contribute to the exaggeration of linewidths as well as asymmetries and other non-Gaussian behavior in the velocity distribution. To disentangle the two HI phases, high velocity resolution is required (e.g. 2.6 km s^{-1} Ianjamasimanana et al. 2012), which is not the case for 90% of the galaxies studied in this chapter (4.13 km s^{-1}) and hence we could not separate the cold from the warm component. However, the HI dispersion has been seen to remain uniform over the HI dominated regions of disk galaxies. For instance Leroy et al. (2008) (hereafter L08) and Tamburro et al. (2009) derived velocity dispersions of 11±3 km s^{-1} and 10±2 km s^{-1} in the outer regions of disks in their respective samples. In this study, we derived an 'observationally motivated' (Romeo & Mogotsi 2017) value of the gas velocity dispersion, 12 ± 3 kms^{-1}, following the methodology of L08, as described below.

Third-order Gauss-Hermite polynomials were first fit to the line of sight (LOS) velocity profiles in the data cubes to produce 2D maps. Note that this is a map of the totality of all the random motions along a line of sight. A cut-off in amplitude was applied to the line profiles such that only profiles of amplitude greater than 4 times the root mean square noise in the data cube were considered. Furthermore, a cut-off in velocity dispersion was also used such that only those profiles with widths greater than the velocity resolution for the corresponding cube were considered *. The fitted width of the line profile was taken as the velocity dispersion along that LOS. Any dispersions above 35 km s^{-1} were flagged, although these were few and mostly in the centers of highly inclined galaxies (see Figure 4.4). Much as the GH3 does fit for the skeweness of a profile (see Chapter 3), the width of the fitted profile is very close to the width from a Gaussian fit. And indeed for lines that are minimally skewed, especially lines beyond the central region where large radial motions are prevalent, the profiles are well approximated by Gaussians. Figure 4.4 shows the dispersion maps of UGC7766 and UGC1913, while the rest of the maps for the sample are shown in Appendix C.1

Taking the W1 half-light radius as the effective radius, for each dispersion map, all radii within the effective radius were masked out to avoid the bulge where radial motions and projection effects are most pronounced. The median of dispersions at the larger radii was taken as the representative dispersion for that particular galaxy. The mean of all the median values from the different galaxies (12 ± 3 km s^{-1}) was adopted as the average gas velocity dispersion across the disks of all the galaxies studied in this chapter. L08 considered outer disk radii $0.5 - 1r_{25}$ and obtained an average dispersion of 11 ± 3 kms^{-1}. A plot of our median velocity dispersions versus inclination, like their Figure 21, was made and no dependence on inclination was found (see Figure 4.5).

*Note: The galaxies studied in this chapter, had velocity resolutions of 2.1, 4.1, 8.3, and 16.5 kms^{-1}. Four of them had 16.5 kms^{-1} resolution and were left out when calculating the average velocity dispersion.

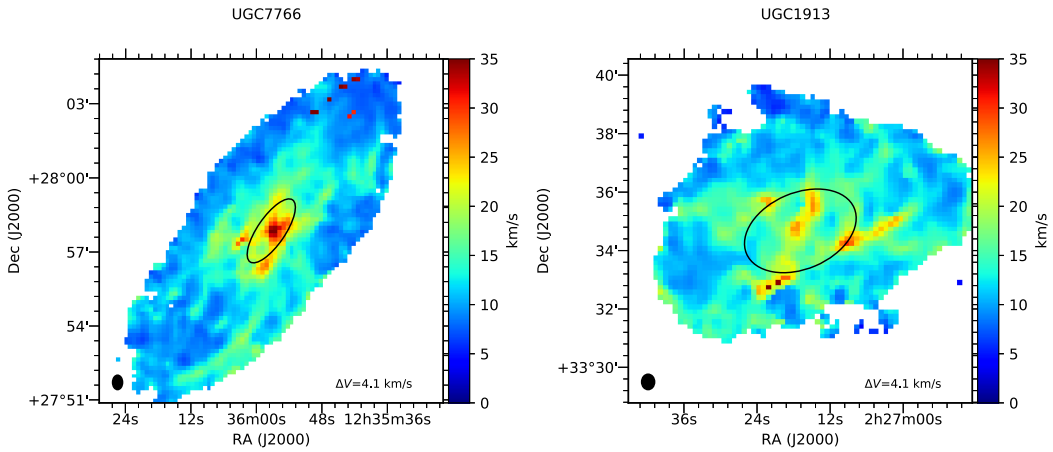

(a) (b)

Figure 4.4: Velocity dispersion maps for UGC7766 (a) and UGC1913. Dispersions were derived by fitting third order Gauss Hermite polynomials to the line profiles (See Chapter 3). The black ellipse marks the effective radius (the radius encompassing half the galaxy's light). Within this region, the dispersions are generally higher than elsewhere in the disk, which is due to various factors such as high velocity clouds, radial inflows in bars and bulges and feedback from star forming regions. The high central velocities are more pronounced in highly inclined galaxies due to projection effects. When determining the average dispersion, values at radii within the effective radius were masked out. Dispersion maps for the rest of the sample are shown in Appendix C.1.

Epicyclic frequency

The epicyclic frequency, κ is the frequency of oscillation of a particle about its orbit, and is related to the orbital angular velocity Ω as,

$$\kappa \;=\; 4\Omega^2 \;+\; \mathrm{r}\frac{\mathrm{d}\Omega^2}{\mathrm{dr}}. \tag{4.12}$$

Since $\Omega \;=\; \mathrm{V_r}/\mathrm{r}$, we have,

$$\kappa \;=\; \left[2\left(\frac{\mathrm{V_r^2}}{\mathrm{r^2}} \;+\; \frac{\mathrm{V_r}}{\mathrm{r}}\frac{\mathrm{dV_r}}{\mathrm{dr}}\right)\right]^{0.5}, \tag{4.13}$$

where r, $\mathrm{V_r}$ and $\frac{\mathrm{dV_r}}{\mathrm{dr}}$ are 2D maps of galactocentric radius, the rotation velocity and the derivative of the rotation curve respectively. Since all these variables are functions of the radius, we first generated maps of the galactocentric radius for all the sample as detailed below.

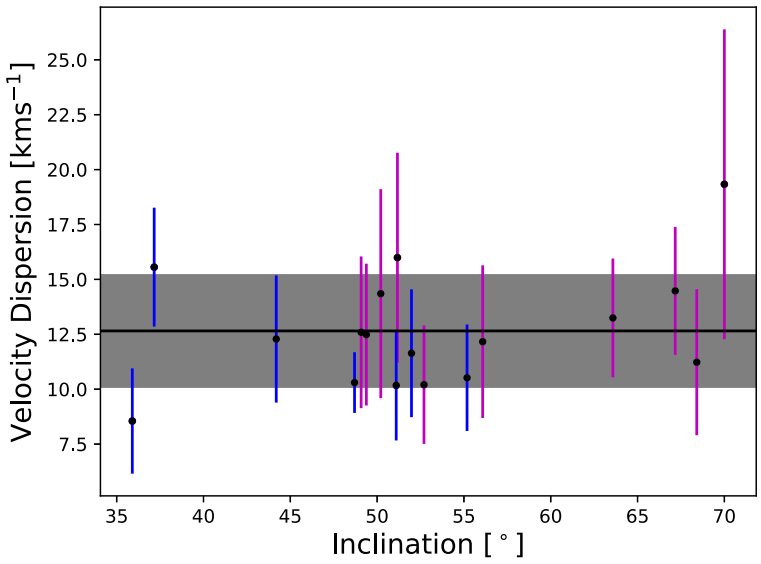

Figure 4.5: Median values of the velocity dispersion maps for the subsample of galaxies that was used to study the star formation thresholds. Error bars show the standard deviation of values within each dispersion map. Radii within the effective radius were masked for each galaxy when calculating these average values. The gray band depicts the 1σ range of the average of the plotted values, $12.6 \pm 2.6 \mathrm{kms}^{-1}$. Magenta points show spiral galaxies (Sa-Sd), while blue points are late type irregular galaxies (Sm-Im).

Calculation of the galactocentric radius: The surface of a galaxy is assumed to be intrinsically spherical and that, due to inclination effects, it takes on an elliptical shape with an orientation determined by the position angle. This implies that the projected distance of a pixel from the center may not represent its true galactocentric radius. To calculate the true radii, the pixel distances (in arcseconds, where pixel scale = $10''$ per pixel) were de-projected through the inclination angle. Taking the y axis as the major axis, the true distance (r) of a pixel (x_i, y_i) from the center (x_o, y_o) is defined by

$$\mathrm{r} = \sqrt{((\Delta \mathrm{x})^2 + (\Delta \mathrm{y})^2)} / \cos(\mathrm{i}), \tag{4.14}$$

$$\text{where,} \tag{4.15}$$

$$\Delta \mathrm{y} = \mathrm{y_i} - \mathrm{y_o}, \tag{4.16}$$

$$\Delta \mathrm{x} = (\mathrm{x_i} - \mathrm{x_o}) \cos(\mathrm{i}), \tag{4.17}$$

$$\tag{4.18}$$

Using the above formalism, a 2D map of the galactocentric radii was produced for each galaxy and then rotated through the position angle using the *Scipy Rotate* * function. The inclination and position angle used to generate the galactocentric radius maps are kinematic

*https://docs.scipy.org/doc/scipy-0.16.1/reference/generated/scipy.ndimage.interpolation.rotate.html

orientation parameters obtained from the work of Swaters (1999) and van Eymeren et al. (2011).
Rotation curves for the respective papers were provided by R. Swaters (priv.communication) and J.v. Eymeren (priv.communication).

Generating maps of rotational velocity: To obtain two-dimensional maps of the rotational velocity, V_r, the rotation curves were parametrized using a functional form and the fitted parameters used to generate a V_r value for every pixel in the galactocentric radius map. The sample comprises an array of rotation curves, some galaxies having rising outer rotation curves, some declining, while others are flat in the outer radii (see Figure 4.6). Because of the various types of rotation curves, the functional form used was the so-called "polyex model" (Giovanelli & Haynes 2002);

$$V_r = V_o \left(1 - e^{-r/l}\right) \left(1 + \frac{\alpha r}{l}\right), \tag{4.19}$$

where V_o is the amplitude of the rotation curve, l is the scale length of the inner rise and α defines the slope of the outer part of the rotation curve. This model can fit for flat, rising or declining outer rotation curves, and is thus well suited to the variety of rotation curves in our sample. As stated by Giovanelli & Haynes (2002), this is an analytic function with parameters that do not have a physical basis in the dynamics of a galactic disk. As such, the parameters returned from the fitting process are sometimes unphysical. The unphysical parameters in turn yield negative κ^2 values. To avoid this, we placed constraints on the fitting process to only return physically reasonable parameters with respect to the rotation curves. This is the reason for the high χ^2 values on the affected fits, (see for example UGC1913, UGC2855 and UGC6225 in Table 4.1). Figure 4.6 shows the literature rotation curves (black) and fitted functional form (red) for all galaxies in the sample, while the fitted parameters and corresponding goodness of fit measures are shown in Table 4.1.

From the rotation velocity function, the maps for the derivative of the rotation curves were derived as

$$\frac{dV_r}{dr} = \frac{\alpha V_o}{l} \left(1 - e^{-r/l}\right) + \frac{V_o e^{-r/l}}{l} \left(1 + \frac{\alpha r}{l}\right) \tag{4.20}$$

The derived maps of epicyclic frequency, gas surface density together with the constant velocity dispersion were used in Equation 4.1 to obtain a map of Q_g for each galaxy. In order to have a dimensionless Q parameter, units of km s^{-1} pc^{-1} were used for the epicyclic frequency and pc $M_\odot^{-1}$ km^2 s^{-2} for the gravitational constant G. Figure 4.7 shows maps of the variables derived for UGC1913. The maps for the rest of the sample are shown in Appendix C.
Note: In using the tilted-ring rotation curves to derive κ, we implicitly used the assumption that $\kappa(\theta, r) = \kappa(r)$, where θ is the position angle in the plane of the galaxy with respect to the major axis. The derivation of $V(\theta, r)$ becomes uncertain beyond a small angular range about the major axis (Begeman 1989), and as pointed out by de Blok & Walter (2006), use of the two-dimensional HI distribution compensates for the limitations of the $\kappa(\theta, r) = \kappa(r)$

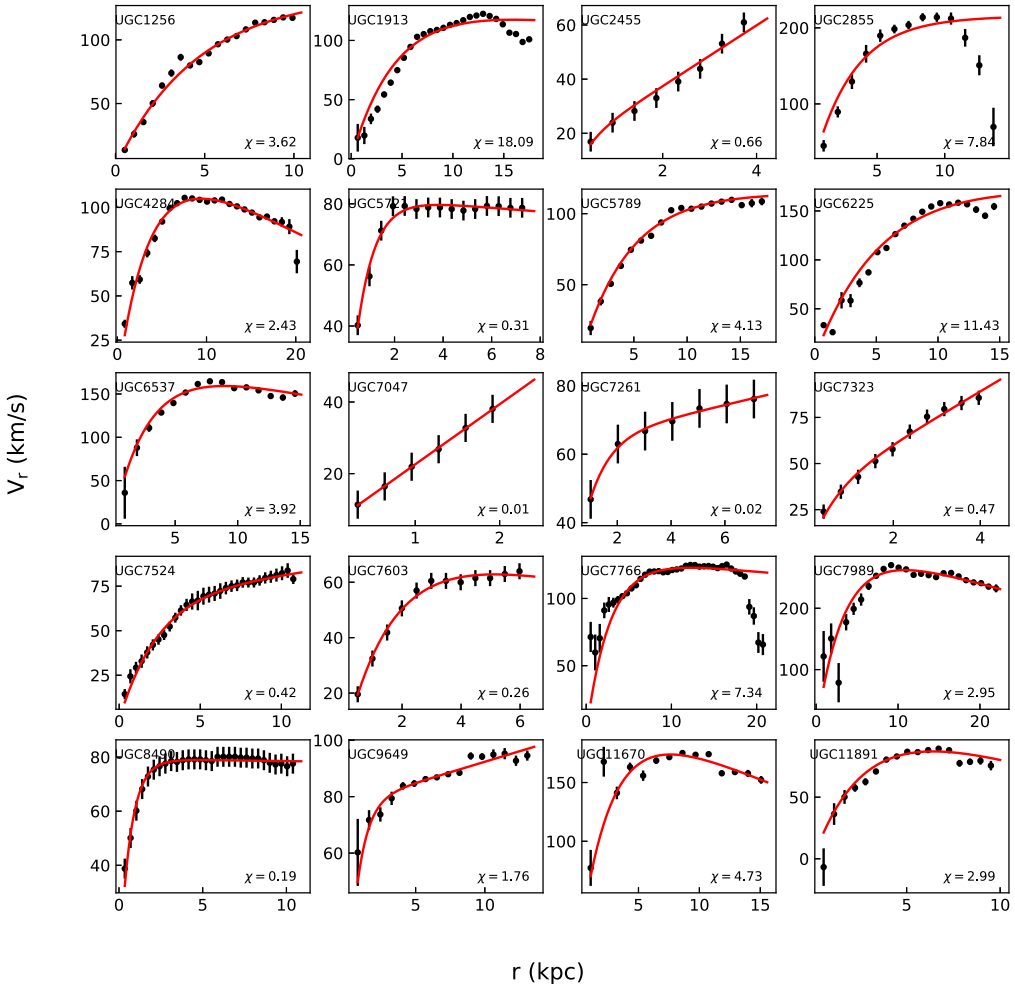

Figure 4.6: The black points are the observed rotation velocities, obtained from Swaters (1999) and van Eymeren et al. (2011) (see Table 4.1). The polyex model functional form (red curve, Equation 4.19, Giovanelli & Haynes 2002) was fit to the observed points in order to derive a 2D map of the galaxy's rotation. The reduced χ^2 value is shown for each fit in the lower left corner of the panels.

assumption because azimuthal variations in the rotation velocity are much smaller than azimuthal variations in the surface density map.

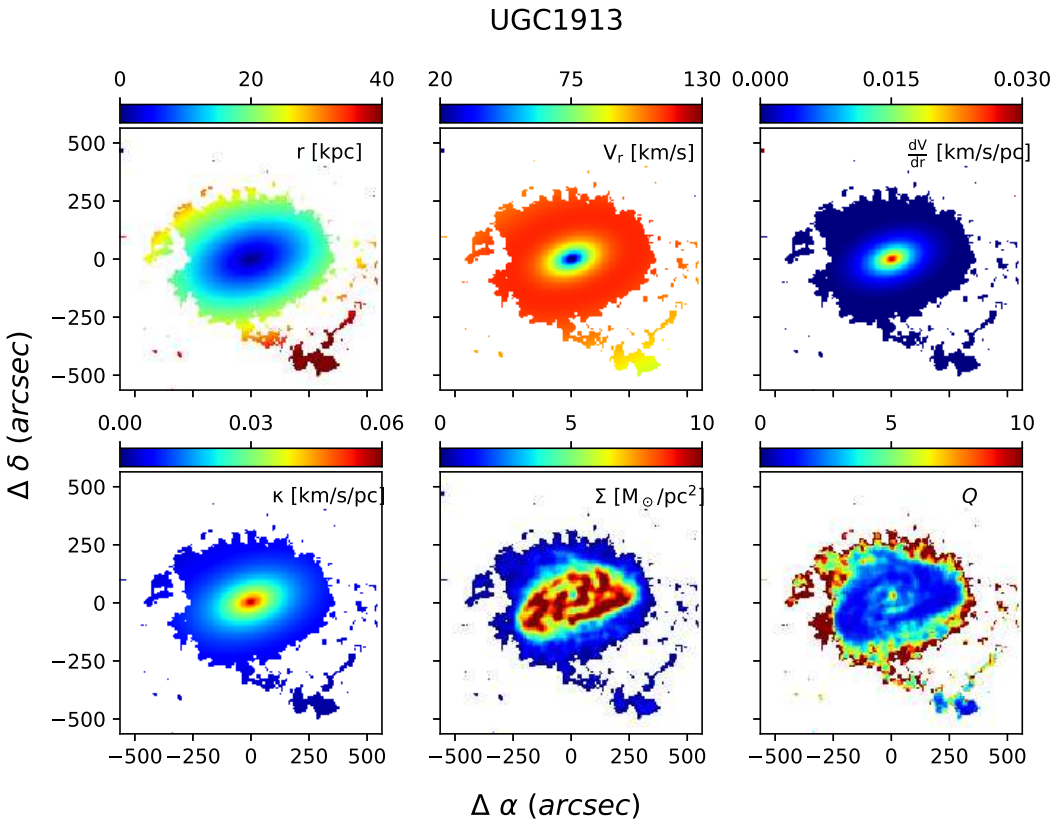

Figure 4.7: Maps from the Single-Fluid methodology for UGC1913. *Top panels* - Galactocentric radius (left), Rotation velocity (middle) and Derivative of the rotation curve (right). *Bottom panels* - Epicyclic frequency (left), Gas surface density (middle) and the Toomre Q parameter (right). The gas surface density map used here is that of total gas ($\Sigma_{\mathrm{HI+H_2}}$). Note that instead of SI units, the units used for the epicyclic frequency were so chosen to return a dimensionless Q parameter.

Table 4.1: **Parameters of sub sample**

Name	incl	pa	beams	res	V_o	l	α	χ^2	source	q
	°	°		pc	km s^{-1}	kpc				
(1)	(2)	(3)	(4)	(5)	(6)	(7)	(8)	(9)	(10)	(11)
UGC1256	71.59	69.44	35	348	129.92	4.37	0.01	3.62	vE	1
UGC1913	53.65	286.63	26	431	133.13	4.43	−0.03	18.09	vE	4
UGC2455	51.0	263.0	12	310	15.00	0.30	0.22	0.66	Sw	2
UGC2855	61.49	111.19	13	697	213.08	2.94	0.00	7.84	vE	3
UGC4284	61.67	169.77	22	558	137.79	3.65	−0.07	2.43	vE	5
UGC5721	61.0	279.0	13	322	82.49	0.74	−0.01	0.31	Sw	2
UGC5789	62.49	35.56	17	630	115.15	4.48	0.00	4.13	vE	1
UGC6225	75.87	256.19	19	484	187.94	5.54	−0.02	11.43	vE	4
UGC6537	49.47	195.65	15	648	190.29	2.85	−0.04	3.92	vE	5
UGC7047	46.0	34.0	11	212	5.80	0.01	0.03	0.01	Sw	2
UGC7261	30.0	262.0	12	673	63.26	0.78	0.02	0.02	Sw	2
UGC7323	47.0	38.0	12	264	33.12	0.50	0.21	0.47	Sw	1
UGC7524	46.0	327.0	32	230	70.30	2.32	0.04	0.42	Sw	1
UGC7603	78.0	197.0	12	332	75.05	1.64	−0.04	0.26	Sw	1
UGC7766	67.31	323.31	33	354	131.26	2.78	−0.01	7.34	vE	5
UGC7989	44.19	32.45	24	610	314.18	3.48	−0.04	2.95	vE	4
UGC8490	50.0	175.0	22	230	79.34	0.66	0.00	0.19	Sw	1
UGC9649	56.56	228.21	12	544	77.52	0.82	0.02	1.76	vE	1
UGC11670	67.34	335.63	11	717	217.13	2.68	−0.05	4.73	vE	2
UGC11891	46.26	115.49	17	372	125.64	2.95	−0.10	2.99	vE	5

Note: (1) - Name. (2-3) - Inclination and position angle (anticlockwise from North to the receding side of the major axis) adapted from the literature for the rotation curves shown in column 10. These orientation parameters were used when constructing the 2-dimensional maps of galactocentric radius in Section 4.2.1. (4) - Number of beams across the HI disk. (5) - Spatial resolution per 10″ pixel in the HI data. The resolution element is 3 pixels across. (6-8) - Parametrization of the rotation curve according to Equation 4.19. (9) - The χ^2 value. The fits were done using the *kmpfit* module of the KAPTEYN[a] package. The polyex model tends to return optimal parameters that are unphysical, resulting in undefined values of the epicyclic frequency. Therefore, the fitting process was constrained to produce physically reasonable parameters, which resulted in high χ^2 values for some galaxies. (10) - Literature reference for the rotation curves: Sw - Swaters (1999), vE - van Eymeren et al. (2011). Note that the actual data were provided by the respective first authors of the two studies. (11) - Quality of the literature rotation curve as determined by the authors, where q=1 is good quality. Note that the definition of q is slightly different betwen Sw and vE. In the former, q depends on the signal to noise ratio of the HI profile, presence of non circular motions and deviation from axial symmetry while the definition of vE is solely dependent on the symmetry between the approaching and receding sides at inner and outer radii.

[a]https://www.astro.rug.nl/software/kapteyn/index.html

4.2.2 The Single-fluid disk MIR Star formation threshold

Figures 4.8 and 4.9 are maps of the Toomre Q parameter while the W3-derived Σ_{SFR} maps are shown in Figures 4.2 and 4.3. High central values of Q_g seen in several galaxies are a result of the central HI depressions in spiral galaxies. The black contours mark the edge of the star forming disk as defined in 4.2.1. Table 4.2 lists the average values of Q_g within the star forming disk and along its edge. The quoted uncertainties represent the standard deviation about the mean value. Right away, it is clear that all of the disks are Toomre-stable, generally having Q_g much higher than 1. Moreover this is in spite of clear existence of star formation in these disks as seen in the Σ_{SFR} maps. Also, from the maps and table, we can see that in side the disks Q_g has large variations by as much as 60% and higher (e.g. see columns 5 and 6 of Table 4.2 for UGC1913, UGC2855, UGC6537, UGC7261). In about half the sample, Q_g varies by less than 30% at the edge of the SF disk. Taking all the galaxies that have constant Q_g (varying by less than 30%)at the threshold, we get an overall average of 4.0.

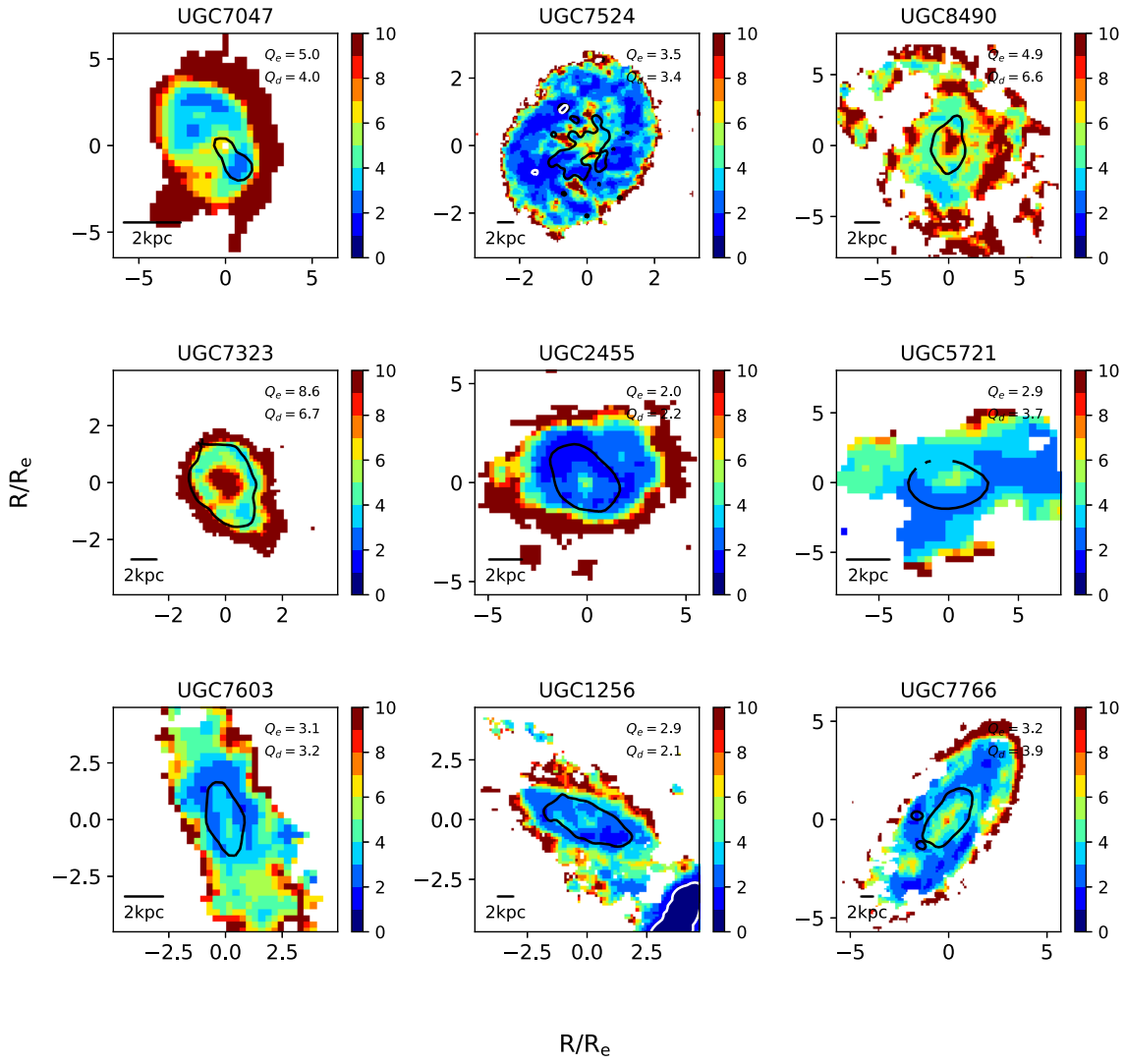

Figure 4.8: Maps of the single-fluid Toomre Q parameter. Black contours mark the edge of the star forming disk defined by an isophote in W3 surface brightness (see Table 4.2). The labels Q_e and Q_d indicate the average values of Q_g along and inside this black contour respectively. White contours mark regions of $Q_T \leq 1$. The Toomre Q parameter maps were derived for a thin gas disk using HI surface densities for the majority of the sample. CO intensity maps were available for three galaxies (UGC1913, UGC7766, UGC7989) from the HERACLES survey, so their H_2 and HI surface densities were combined to obtain the total gas surface density.

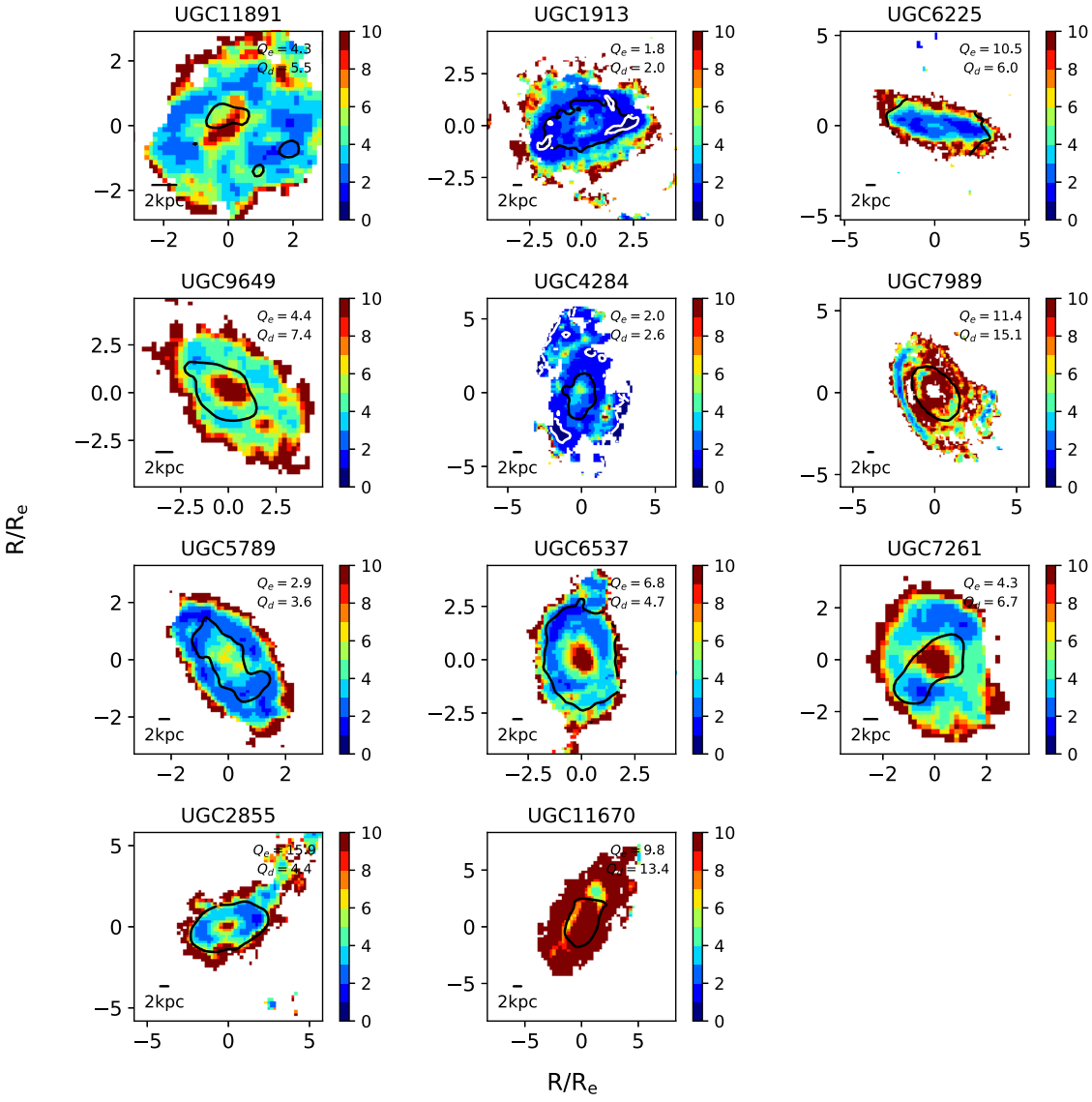

Figure 4.9: same as Figure 4.8. See Section 4.3.2 for comments on the map of UGC6225.

A value of $Q_g = 4.0$ at the SF threshold is more than twice as high as the results of Kennicutt (1989) who found an average value of $\Sigma_c/\Sigma_g = 1.5$ for 15 star forming disks, while Martin & Kennicutt Jr. (2001) obtained 1.4 for a sample of 32 galaxies. However our result is in agreement with the results of Hunter et al. (1998), Boissier et al. (2003), Elson et al. (2012) who also found Q_g to be two to three times higher than the Kennicutt (1989) value. The higher values in our study are mainly because the gas velocity dispersion (σ_g) we used is twice as high as the one used by Kennicutt (1989). As can be seen in Equation 4.1, a

Table 4.2: **Observed single-fluid threshold properties.**

Name	$SB_{5\sigma}$ mag/asec^2	$\langle Q_g \rangle_e$	$\Delta\langle Q_g \rangle_e$	$\langle Q_g \rangle_d$	$\Delta\langle Q_g \rangle_d$	res pc	$\langle \Sigma_g \rangle$ $M_\odot pc^{-2}$
(1)	(2)	(3)	(4)	(5)	(6)	(7)	(8)
UGC7047	18.8	5.0	1.3	4.0	1.6	212	5.8
UGC7524	18.8	3.5	2.1	3.4	2.0	230	4.7
UGC8490	18.8	4.9	1.0	6.6	2.6	230	6.6
UGC7323	18.8	8.6	8.6	6.7	3.8	264	3.8
UGC2455	17.5	2.0	0.1	2.2	0.7	310	8.3
UGC5721	18.8	2.9	0.5	3.7	1.6	322	15.2
UGC7603	18.8	3.1	0.9	3.2	0.7	332	6.8
UGC1256	18.8	2.9	0.7	2.1	1.1	348	5.3
UGC7766	17.5	3.2	0.7	3.9	1.1	354	7.7
UGC11891	17.5	4.3	1.4	5.5	2.3	372	6.4
UGC1913	18.8	1.8	0.6	2.0	1.5	431	10.1
UGC6225	18.8	10.5	8.7	6.0	5.0	484	4.9
UGC9649	18.8	4.4	1.0	7.4	5.4	544	3.9
UGC4284	18.8	2.0	0.5	2.6	0.9	558	7.1
UGC7989	17.5	11.4	5.8	15.1	17.5	610	3.2
UGC5789	18.8	2.9	1.0	3.6	1.2	630	4.5
UGC6537	18.8	6.8	7.3	4.7	4.6	648	4.9
UGC7261	18.8	4.3	1.7	6.7	4.5	673	3.5
UGC2855	16.5	15.9	8.1	4.4	2.8	697	6.4
UGC11670	17.5	9.8	2.6	13.4	6.5	717	1.5

Note: (1) - Name, (2) - W3 surface brightness at the edge of the star forming disk. This surface brightness corresponds roughly to the 5σ level in the W3 image, (3-6) - Value of the stability parameter and corresponding uncertainty at the SF threshold and inside the SF disk, (7) - Physical pixel size. The resolution element is 3 pixels across. (8) - Average gas surface density across the entire stellar disk.

constant σ_g linearly scales Q_g up or down but does not affect the structure in the stability map. Leroy et al. (2008), who used a similar gas dispersion (11 km/s), did not find any evidence in their results for a Q threshold on star formation. Likewise, Thornley & Wilson (1995) failed to determine a Q threshold, although their study did not use a constant σ_g. An implication of the Single-fluid criterion is that the onset of large scale star formation (the SF disk's edge) should be predicted by the Q_g parameter. However, the maps and statistics above do not offer any concrete evidence that connects Q_g to large scale star formation.

On the relevance of Q_g in the SF disks, the results do not conclusively show whether the $Q = 1$ is a necessary condition for SF to occur. All the disks are subcritical (stable) inspite of having star formation occurring in their disks. Even when the gas dispersion value is halved, only four disks in our sample (namely UGC1256, UGC1913, UGC2455 and UGC4284) would be borderline critical (hence only marginally unstable), while the rest remain stable. Sub-critical values of Q_g have been observed by other studies in the disks of star forming galaxies, ranging from irregulars (e.g. Hunter et al. 1998) to dwarfs (e.g. Elson et al. 2012) and spirals (e.g. Leroy et al. 2008). If we considered the K89 threshold value of $Q_g = 1.5$, then, with a lower gas dispersion ($\sigma_g = 6\text{km s}^{-1}$), the four disks above would be Q_g -unstable, six others would be marginally stable, and the remaining 10 galaxies would still have disks that are stable against collapse. Note, the disk averages of Q_g are also hiked by the central high values resulting from the HI depression, so it is tempting to say that the average values at the SF threshold might be lower than the disk averages. However, looking at the SF thresholds (edges of the SF disks), all the galaxies show stable values of Q_g according to the $Q = 1$ criterion, but when the criterion is changed to $Q = 1.5$ and lower gas dispersion are considered, the statistics remain similar to those inside the disks, with five unstable, four marginally stable and 11 stable against collapse.

In a few cases, where the resolution allows us to see some local enhancements in the structure of the SF maps, we can study the local relevance of Q_g to SF. In five galaxies, the values of Q_g happen to be lower for localized regions of high Σ_{SFR}. These are UGC7047 (South West), UGC7524 (South East of the nucleus) , UGC1913 (West), UGC5789 (South West) and UGC7261 (South East). Note that UGC1913 is one of the galaxies for which CO data were available hence a more complete map of the gas surface density ($\Sigma_g = \Sigma_{\text{HI}} + \Sigma_{\text{H}_2}$) was used. The other two for which CO data were available (UGC7766 and UGC7989) do not show any local Q_g - Σ_{SFR} correlations inside the SF disk.

In three other galaxies (UGC7323, UGC1256, UGC6537) where some structure is resolved, there is no such correlation between Q_g and Σ_{SFR}. This, with the generally stable values in the disks shown above, goes to show that the single-fluid criterion is not a necessary condition for SF and thus not applicable to large scale star formation (Thornley & Wilson 1995, Wong & Blitz 2002, Boissier et al. 2003, Leroy et al. 2008). Note, however, that four of the five galaxies mentioned above, (in which the lowest Q values match local high SFR regions), are all late types, two of them being dwarfs (UGC7047, UGC7261) and these have the highest gas fractions in the sample. This observation is in line with the conclusion of

de Blok & Walter (2006) that the single-fluid Q is applicable to dwarfs, although the same result is challenged by the observation that the other dwarfs in our sample do not exhibit similar behaviour. Moreover, we also see low $Q_g$values in the outer regions of UGC7989 ($M_* = 10^{10.76}$ $M_\odot$) well beyond the SF disk and the CO disk. On closer inspection of the SFR density map (Figure 4.3), there appears to be low level star formation in that part of the disk, and the stellar disk encompasses this region. This implies that the Q_g parameter may be able to predict SF even in massive spirals.

From this analysis, we see that *the single-fluid model does not define a Toomre Q threshold that predicts the outer edge of the star forming disk* (atleast for 50% of the sample). Therefore, it can not be applied to large scale star formation. This stability criterion also fails to predict the actual unstable regions, since we see high (stable) Q_g values even where the SF is locally enhanced. The main limitation of this model is that it does not represent typical galaxy disks which consist of both stars and gas. In the next section, we study the two-fluid disk model which accounts for the impact of the stellar disk's gravity on the stability of the gas disk.

4.3 The Two-Fluid stability criterion

In this section, we study the two-fluid disk stability criterion which attempts to account for the existence of both the stellar and gaseous components of a galaxy's disk. We derive the stability parameter Q_T using the formulation of Rafikov (2001) in Section 4.3.1 and analyse the results in 4.3.2.

4.3.1 Methodology

Stellar mass and Stellar surface density

The WISE 3.4μm (W1) band is a reliable measure for the stellar mass of galaxies because it traces the evolved stars, which comprise the bulk of the baryonic mass in galaxies (Meidt et al. 2014). Galaxy stellar masses can be directly obtained from the stellar luminosity using the mass-to-light ratios (Υ_*). This is a simple approach and avoids uncertainties which arise from modelling, for example uncertainties in stellar population synthesis models, uncertainty in the stellar initial mass function, and variations in galaxy star formation histories (McGaugh & Schombert 2014). Bell & de Jong (2001) and Bell et al. (2003) studied the color-Υ_* relation and found that in the Near Infrared, Υ_* varies only slightly with color. Moreover, the Υ_* has a tighter relation with color than with other galaxy properties such as gas fraction and surface brightness. Meidt et al. (2014) also found that a single value for Υ_* can be used to derive stellar masses from the NIR flux corrected for non-stellar contamination. McGaugh & Schombert (2014) tested the population synthesis model of Bell et al. (2003) on a sample of spiral galaxies and found a constant NIR Υ_* produced self consistent results when calculating stellar masses even for optical wavelength bands. Using the linear

conversion of Oh et al. (2008) between NIR Υ_* and MIR Υ_*, McGaugh & Schombert (2014) obtained a NIR (3.6μm) Υ_* of 0.47 $M_\odot/L_\odot$, and they further argue that the assumption of a constant Υ_* in the NIR is necessary for consistency when deriving stellar masses from optical and NIR observations.

In this study, a value of 0.5 $M_\odot/L_\odot$ was adopted for the 3.4μm images from WISE to avoid the complexities involved in trying to model the Υ_* from colors as discussed above. Note that as in the case for the SFR maps, the W1 images were matched to the resolution ($\sim 30''$) and astrometric grid ($10''$ per pixel) of the WHISP data before deriving the stellar mass maps. The details of this process are given in Appendix B.
Standard equations were used to convert W1 flux into luminosity as shown below:

$$m = Zp_1 - 2.5\log(\mathrm{DU}) \quad (4.21)$$

$$M = m - 5\log(\mathrm{D}) + 5 \quad (4.22)$$

$$\mathrm{L}(L_\odot) = 10^{-0.4(M - M_{sun})} \quad (4.23)$$

$$\mathrm{M}_\star(M_\odot) = \Upsilon_*^{[3.4]} \times \mathrm{L} \quad (4.24)$$

where m and M are the apparent and absolute magnitudes in the W1 band, DU is the raw W1 image, Zp_1 is the instrument zero point in the W1 band, D is the distance in parsec, L is the in-band luminosity, $M_{sun} = 3.24$, the absolute magnitude of the sun in the W1 band (Oh et al. 2008, Jarrett et al. 2013) and $\Upsilon_*^{[3.4]} = 0.5\ M_\odot/L_\odot$.

A direct calculation for stellar surface densities was done by dividing through the stellar mass maps by the physical area of a pixel in units of pc^2 after deprojecting the map through the inclination angle i;

$$\Sigma_*[M_\odot pc^{-2}] = (M_* \times \cos(\mathrm{i}))/\mathrm{A}, \quad (4.25)$$

where $\mathrm{A} = [\theta \times \mathrm{D(pc)}]^2$ and θ is the pixel scale in radians. The W1 band is sensitive to light from warm dust, AGB stars and PAH molecules (at 3.3μm), all of which can exaggerate the W1 flux (Meidt et al. 2012). This implies that the stellar masses and surface densities quoted here should be taken as upper boundaries.

Stellar velocity dispersion

The radial stellar velocity dispersions, $\sigma_{*,r}$ were derived following the methods and assumptions of Leroy et al. (2008) which were based on results from previous studies. Assuming hydrostatic equilibrium, van der Kruit (1988) calculated the vertical stellar dispersion for a disk with an isothermal vertical profile as;

$$\sigma_{*,z} = \sqrt{2\pi G \Sigma_* h_*}. \quad (4.26)$$

The stellar scale height, h_z was assumed to remain constant at all radii (as observed by van der Kruit & Searle (1981) in edge-on spirals) and approximated from the average flat-

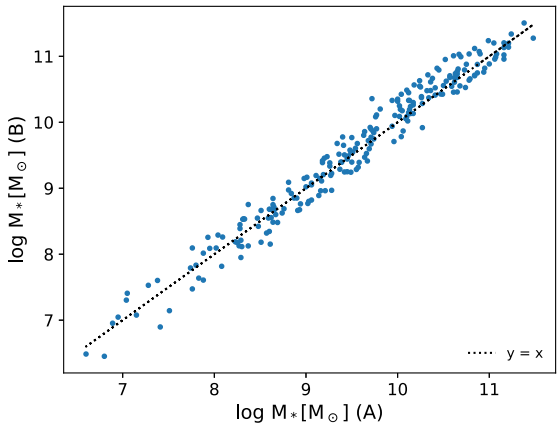

Figure 4.10: Comparison of stellar mass estimates derived from the WISE W1 band. Estimates (A) on the x axis are total stellar mass estimates by Jarrett et al. (2017) who calculated their masses from total W1 flux and the W1 − W2 color which tracks the M/L ratio (Cluver et al. 2014). I obtained estimates (B) on the y axis by deriving maps of stellar mass and then summing up the total mass. In both cases, summation of total flux and total mass were done within the stellar disk, defined by the W1 1σ isophote. The dotted line is a y=x line. The two sets of estimates largely agree, with few outliers which could be because a single M/L ratio is adopted here while Jarrett et al. (2017) use a variable M/L based on WISE colors.

tening ratio of the disk $l_*/h_* = 7.3 \pm 2.2$ (Kregel et al. 2002). Measurements of l_* were obtained from WISE data provided by Jarrett et al. 2017 (priv. communication). Taking after the Leroy et al. (2008) assumption that $\sigma_{*,z} = 0.6\sigma_{*,r}$, this yields,

$$\sigma_{*,r} = 1.67 \times \sqrt{\frac{2\pi G \Sigma_* l_*}{7.3}}. \tag{4.27}$$

Perturbation wavenumber

The stability of a two-fluid system against axisymmetric perturbations depends on the wavelength of the perturbation, $\lambda = 2\pi/k$, where k is the wavenumber (see Equation 4.3). Griv & Gedalin (2012) showed that in spiral galaxies, the fastest growing (hence most unstable) perturbations have wavelength scales of 1 - 4 kpc, while Leroy et al. (2008) found 2 - 5 kpc for their sample of spiral and dwarf galaxies. Jog & Solomon (1984a) analytically showed that two-fluid instabilities in a disk of stars and gas have scales between 2-3 kpc.
To find an appropriate wavelength scale for the galaxies in the sample studied here, a range of scales between 0.5 - 5 kpc (wavenumbers $k = 4\pi, 3\pi, 2\pi, 1.5\pi, \pi, 0.8\pi, 0.6\pi, 0.5\pi, 0.4\pi$) were considered and used to derive maps for the corresponding two-fluid instabilities (Equation 4.3). Figure 4.11 shows these maps for a late type (Sd) spiral galaxy UGC1913 (similar plots for the rest of the sample are shown in Appendix C.3.2). For each galaxy, these maps were azimuthally averaged (using the GIPSY task *ellint*) in order to identify the one with

the lowest Q_T values overall (See Figure 4.12). The 2 kpc scale was found to more closely represent the most unstable scale for all the sample, hence it was chosen as the adequate scale to investigate two-fluid instabilities in our study.

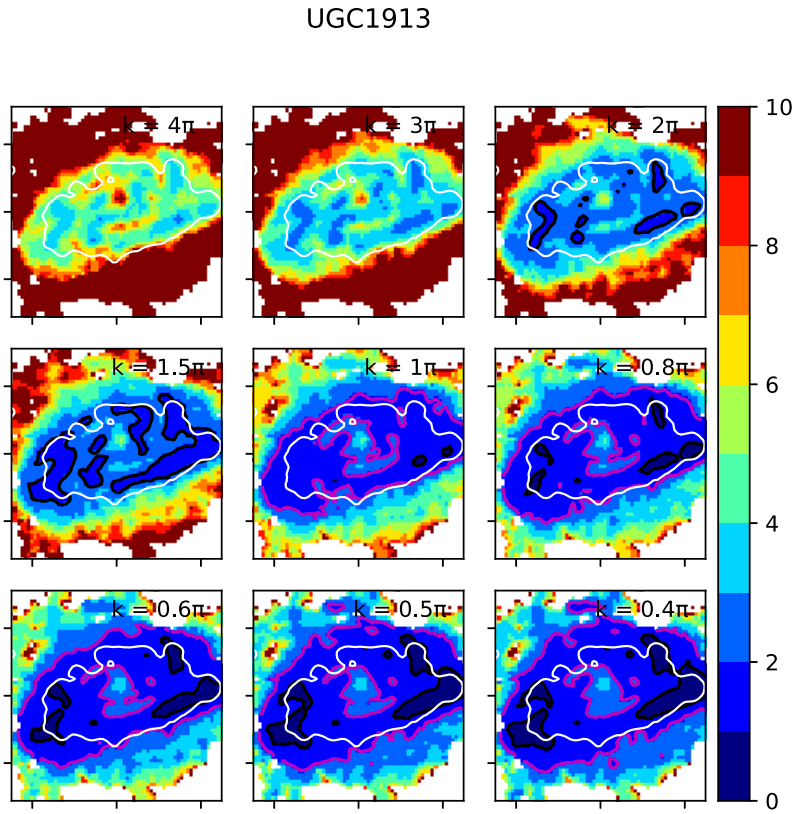

Figure 4.11: Maps of Q_T for a range of wavelength scales to determine the scale of the maximum instability (fastest growing perturbation) for UGC1913. The black contour marks $Q_T = 1.0$, while the magenta contour is at $Q_T = 2.0$. The white contours mark the edge of the SF disk as defined in Section 4.1. Note that for UGC1913 we made use of the total gas density ($\Sigma_{\mathrm{HI+H_2}}$). The wavenumbers in the plots 4π, 3π, 2π, 1.5π, 1π, 0.8π, 0.6π, 0.5π and 0.4π correspond to wavelength scales of 0.5 kpc, 0.66 kpc, 1 kpc, 1.3 kpc, 2 kpc, 2.5 kpc, 3 kpc, 4 kpc and 5 kpc respectively.

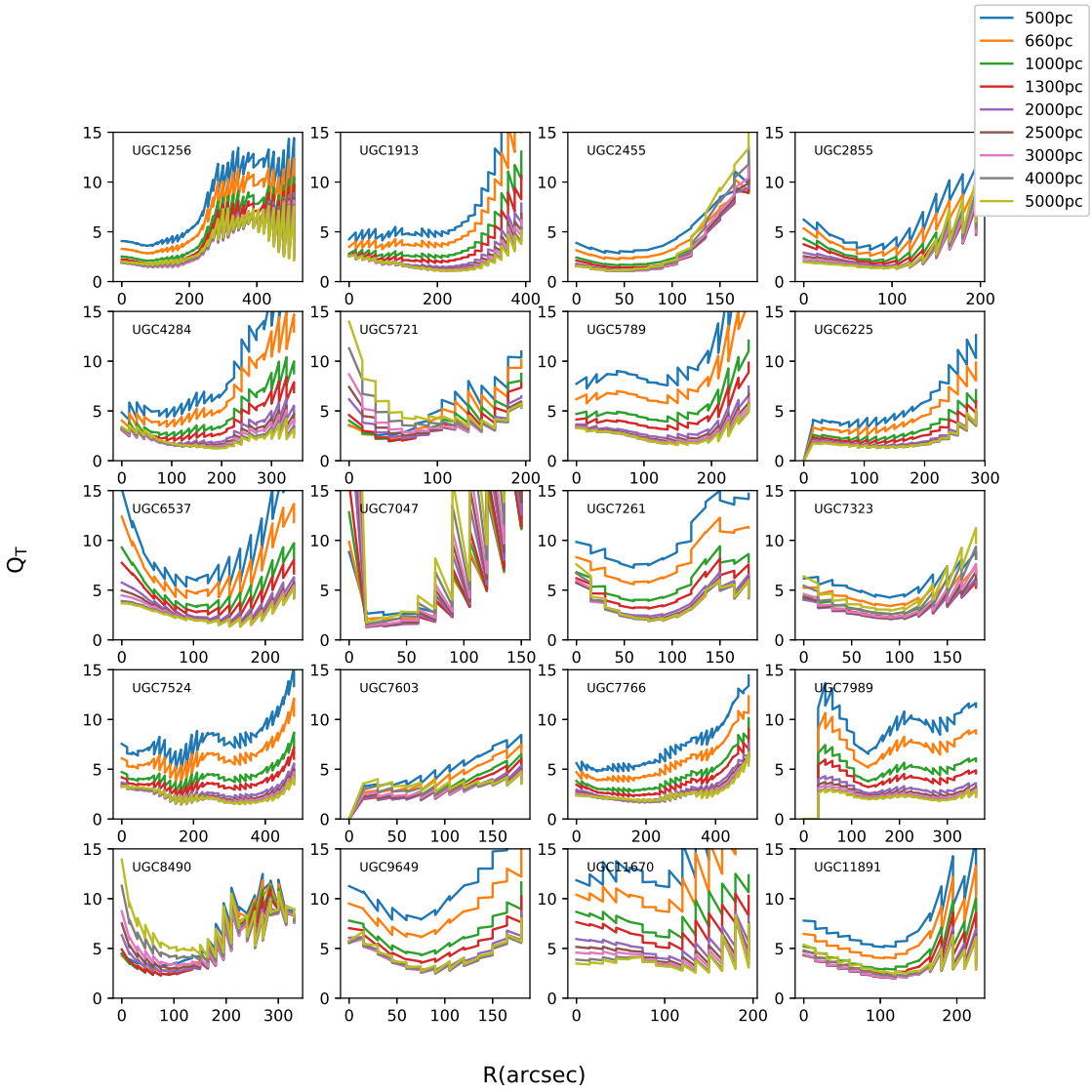

Figure 4.12: Radial profiles of Q_T for varying perturbation wavelength scales. The GIPSY *ellint* task was used to generate these profiles, and we used data within 60° of the major axis to minimize sensitivity to projection effects along the minor axis. The radial profiles were used to determine the scale which yielded the lowest overall Q_T disk for each galaxy. The 2 kpc scale ($k = 1\pi$) most closely represented the least stable scale for the entire sample, and was used to investigate the two-fluid instabilities in this study.

4.3.2 The Two-fluid disk MIR Star formation threshold

Figures 4.13 and 4.14 are maps of the two-fluid instability model for our galaxy sample. The questions below guided the analyses carried out on the Q_T maps.

i) Are the disks unstable according to the two-fluid disk criterion (Equation 4.3)? What

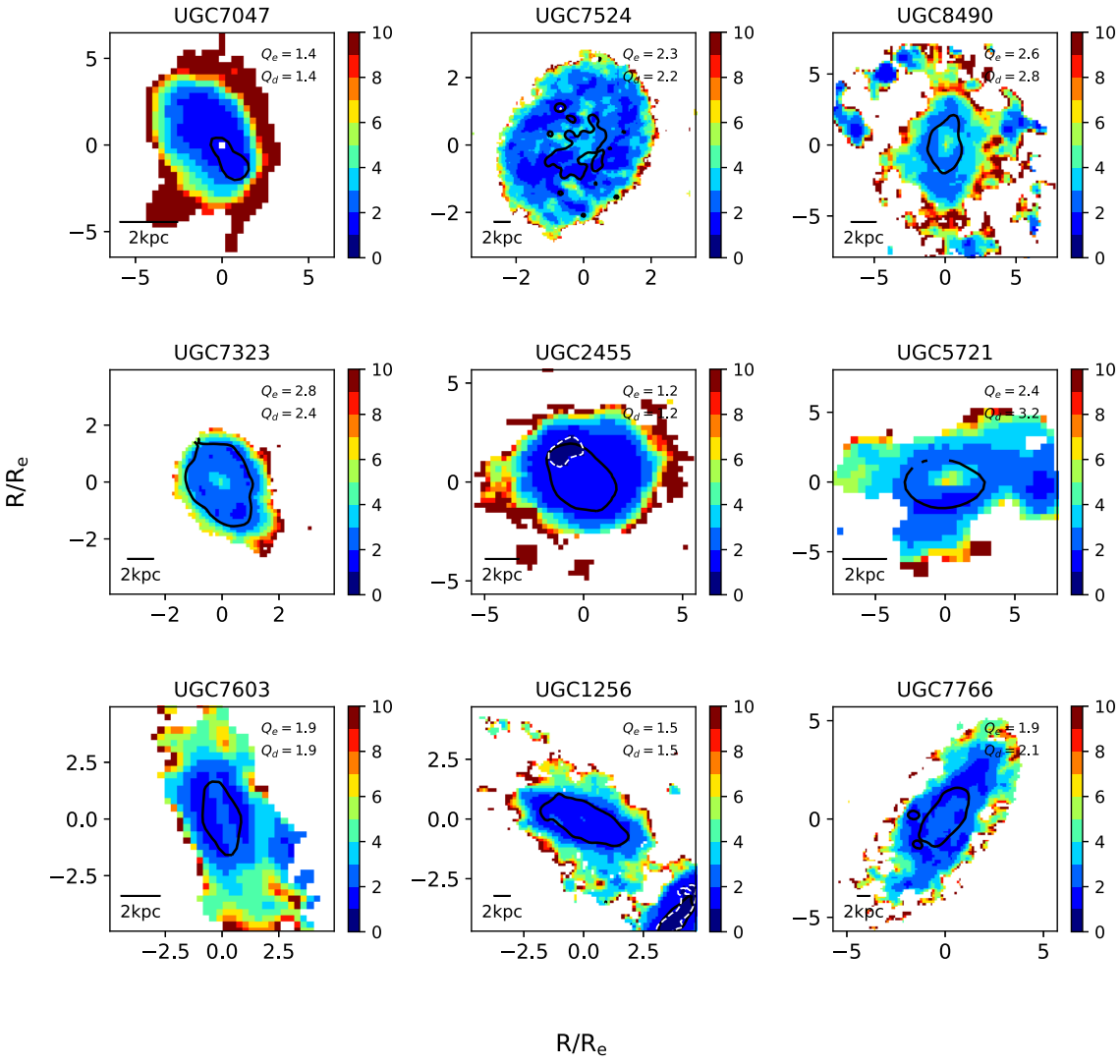

Figure 4.13: Maps of the two-fluid instability parameter (Q_T) derived from the Rafikov (2001) formulation. The sources are listed in order of their spatial resolutions (see Table 4.2). Axes are labeled in units of the effective radius, which is the radius encompassing half of the W1 light. The black contours mark the edge of the star forming disk, as defined in Section 4.1. The labels Q_e and Q_d indicate the average values of Q_T along and inside this black contour respectively. White contours mark regions of $Q_T \leq 1$.

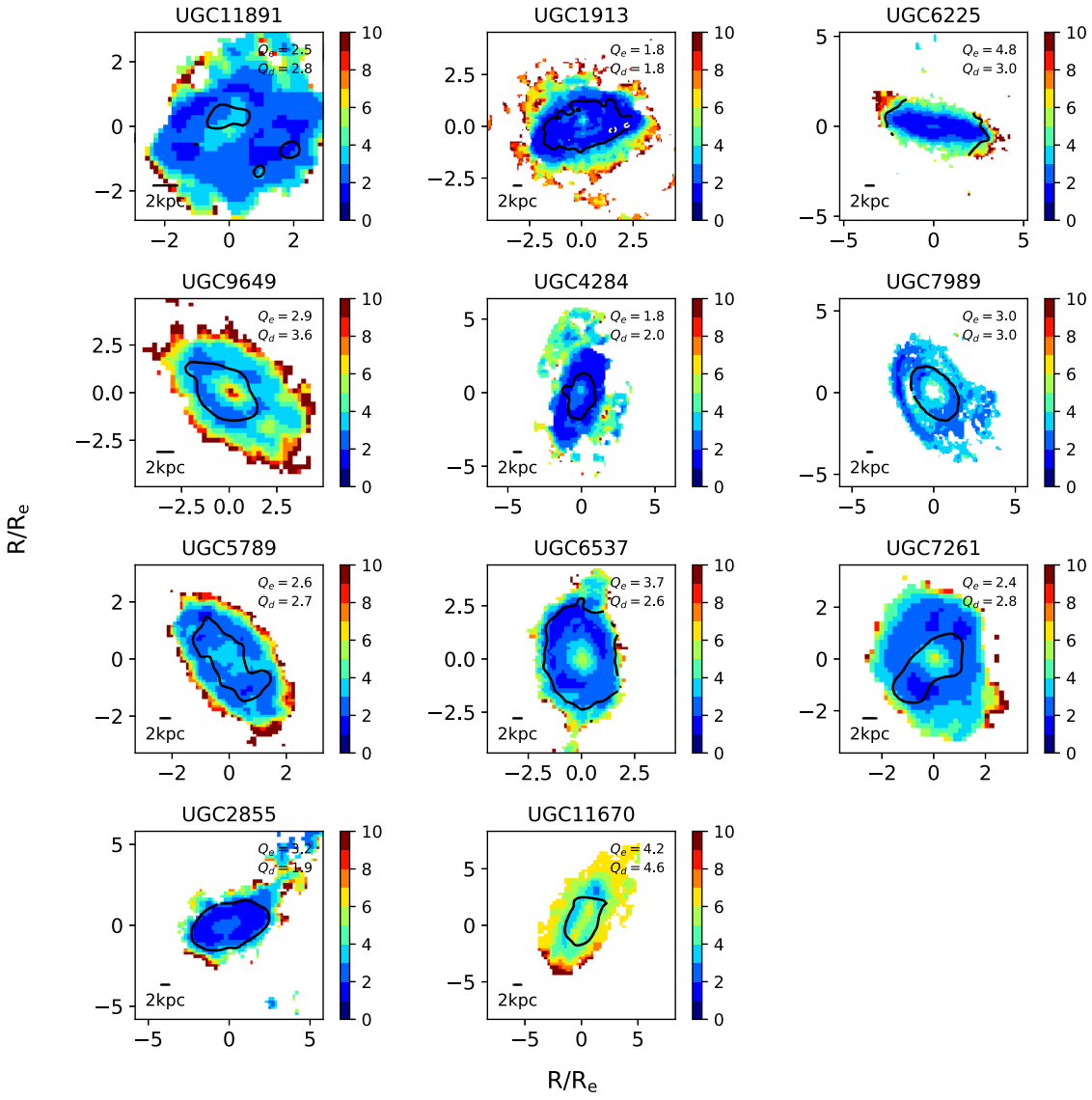

Figure 4.14: Same as Figure 4.13. See Section 4.3.2 for comments on the map of UGC6225.

are the similarities, if any, among the unstable disks and the stable disks, in terms of morphology, mass and gas content? What conclusions can be derived from these?

ii) What are typical values of Q_T in the disks? It has been found by some studies that generally, disks have Q_T above unity and mostly flat (e.g. Leroy et al. 2008, Romeo & Mogotsi 2017), and furthermore that the critical value of Q_T in fact lies around 2- 3 for spirals (Elmegreen 2011) .

iii) Do any local enhancements of SFR correlate spatially with lower values of Q_T? Do the regions of low Q_T match the low Q_g regions? If this is the case, it may mean that Q_g is also a reliable indicator of star forming regions, with a different critical value other than 1.

We see right away that inclusion of the stellar component lowers the gravitational stability of the disks. All galaxies show lower Q_T values than Q_g. This is because of the significant contribution of the stars to the gravity budget of a galaxy disk. However, much as the gravitational stability is considerably lowered, the two-fluid disk model does not necessarily render all the disks unstable because we can see that none of the galaxies have Q_T disks below 1, the theoretical threshold for two-fluid instabilities.

Our results are in agreement with the results of Leroy et al. (2008) who also found that despite lowering the stability of the disks, the two-fluid model did not return unstable disks. Boissier et al. (2003) studied the two-fluid stability criterion for a sample of 16 disk galaxies, and found 14 of them to be unstable, and the other two galaxies were only marginally stable, unlike our results and those of Leroy et al. (2008). The difference arises from the fact that they used the two-fluid disk model of Wang & Silk (1994), whereas this study used the Rafikov (2001) model. The Wang and Silk model has been found to yield lower values of Q_T (Romeo & Wiegert 2011), because it does not account for the effects of the dynamics and kinematics of each individual component (stellar or gaseous) on the stability of the other (Jog 1996).

An isophote in surface brightness (18.8 mag/arcsec^2) defined to correspond to the 5σ level in the W3 images (see Section 4.1 for full description of this isophote) was used to demarcate the edge of the star forming disk (SF disk). Table 4.3 lists the average values of Q_T inside this disk and along its edge. Also shown in the table are the stellar surface density and global average Σ_{SFR}.

The values of Q_T are generally lower inside the SF disk than at the outer radii, showing a correlation between the disk stability and star formation properties, because SFRs are highest inside the SF disk. For some galaxies (for example UGC9649, UGC6537), nuclear values of Q_T are higher than elsewhere in the SF disk, which is due to a combination of low HI densities and high stellar velocity dispersions in the nuclei. Since the stability decreases inside the SF disk without dropping below 1 in all disks, it shows that the value of 1 is not the true Q_T threshold for the onset of large scale SF. Majority of the disks have $\langle Q_T \rangle$ values lying between 1.5 and 3.5. We also see that the Q_T is mostly flat and featureless, in agreement with findings from previous studies that two-fluid stability varies weakly and

lies above unity (e.g. Leroy et al. 2008, Elmegreen 2011, Elson et al. 2012, Griv & Gedalin 2012, Romeo & Mogotsi 2017). In fact Elmegreen (2011) and Griv & Gedalin (2012) assert that the critical value of Q_T is no less than 2. Indeed we see in column 3 of Table 4.3 that for the majority of the sample, Q_T at the edge of the SF disk lies around ~ 2. The overall average of Q_T at the edges is 2.5±0.9, while the overall disk average Q_T (inside the SF disk) is 2.5±0.8.

Table 4.3: **Properties of the two-fluid stability maps**

Name	$SB_{5\sigma}$ mag/asec^2	$\langle Q_T\rangle_e$	$\Delta\langle Q_T\rangle_e$	$\langle Q_T\rangle_d$	$\Delta\langle Q_T\rangle_d$	$\langle\Sigma_*\rangle$ $M_\odot pc^{-2}$	Σ_{SFR} $M_\odot yr^{-1}kpc^{-2}$
(1)	(2)	(3)	(4)	(5)	(6)	(7)	(8)
UGC7047	18.8	1.4	0.1	1.4	0.2	9.7	−3.54
UGC7524	18.8	2.3	0.8	2.2	0.8	6.3	−3.47
UGC8490	18.8	2.6	0.3	2.8	0.8	11.0	−3.1
UGC7323	18.8	2.8	0.8	2.4	0.5	9.3	−3.29
UGC2455	17.5	1.2	0.0	1.2	0.2	25.1	−2.59
UGC5721	18.8	2.4	0.7	3.2	1.7	17.9	−2.86
UGC7603	18.8	1.9	0.4	1.9	0.8	8.9	−3.41
UGC1256	18.8	1.5	0.6	1.5	0.4	10.3	−3.16
UGC7766	17.5	1.9	0.2	2.1	0.3	16.2	−2.8
UGC11891	17.5	2.5	0.5	2.8	0.6	9.2	−3.01
UGC1913	18.8	1.8	0.5	1.8	0.8	16.0	−2.85
UGC6225	18.8	4.8	1.5	3.0	1.4	30.6	−2.38
UGC9649	18.8	2.9	0.4	3.6	1.3	11.8	−3.21
UGC4284	18.8	1.8	0.3	2.0	0.5	10.9	−3.1
UGC7989	17.5	3.0	0.4	3.0	0.6	30.0	−3.05
UGC5789	18.8	2.6	0.8	2.7	0.5	6.0	−3.35
UGC6537	18.8	3.7	1.7	2.6	1.0	27.4	−2.6
UGC7261	18.8	2.4	0.5	2.8	0.9	6.1	−3.24
UGC2855	16.5	3.2	0.6	1.9	0.4	71.8	−1.99
UGC11670	17.5	4.2	0.5	4.6	0.8	32.7	−2.97

Note: (1) - Name, (2) - W3 surface brightness at the edge of the star forming disk. This surface brightness corresponds roughly to a level of 5σ in the W3 image, (3-6)- Mean value of the stability parameter and corresponding uncertainty at the edge and inside of the SF disk, (7) - Average stellar surface density, (8) - Average star formation rate surface density, (9) - Wavenumber of the perturbation.

In some galaxies (UGC7524, UGC1913, UGC5789, UGC7261), Q_T shows some structure, with lower Q_T values matching regions where the local SFR is higher than the rest of the disk. All four galaxies are late types and have HI masses ranging between $10^{9.1}$ $M_\odot$ and $10^{9.7}$ $M_\odot$. We are mindful of the uncertainty introduced into these maps by the sensitivity of the W1 band to the 3.3μm PAH emission from star forming regions. This should be most prevalent in high SFR disks (e.g. nuclear star bursts) such that the SF contribution to the W1 luminosity is significant. The four galaxies mentioned above do not exhibit significantly high SFRs, in fact we see disks with even higher SFRs (e.g. UGC2455, UGC2855, UGC6225, UGC6532, UGC7766) that do not show any similar structure. It can thus be taken that the structure of Q_T in these galaxies is not biased by this limitation on the W1 luminosity. From the

above observations, it is clear that Q_T is consistent with local star forming regions. Note that all of the galaxies with low Q_T structures also had lower Q_g values for some of the same regions of SF (see Section 4.2.2 above). Much as the Q_T model yields lower values than Q_g, these results show that Q_g may also be just as capable of predicting local SF in late types. A net effect of the stellar component thus appears to be a general lowering and flattening (hence a normalization) of the disk stability following the distribution of the stellar surface density.

In future work, the multicomponent disk model of Romeo & Falstad (2013) will be used to treat the cold atomic gas ($\sigma_g = 6\,\mathrm{km\ s^{-1}}$, Ianjamasimanana et al. (2012)) and warm atomic gas ($\sigma_g = 12\,\mathrm{km\ s^{-1}}$, Mogotsi et al. (2016)) separately so as to get a more refined picture of the disk stability parameter. Note that the galaxies with total gas measurement ($\Sigma_{\mathrm{HI+H_2}}$) do not show any special features in the Q_T consideration. This is very likely due to the dominance of the stellar disk contribution in the two-fluid instability model (Romeo & Mogotsi 2017), although we do not rule out the possibility that they may simply not have a significantly high central CO concentration.

Comments on individual galaxies

There are some galaxies that exhibit special features in this analysis. They are presented here with more detailed discussion.

UGC1256 is an interacting galaxy with a companion (UGC1249) to the Southwest. In the Q_g map, the gas in the Southwest is part of the bridge between the two interacting galaxies. Star formation is known to be enhanced in interacting galaxies (Lambas et al. 2003, Di Matteo et al. 2007, Ellison et al. 2013), but UGC1256 does not exhibit SFRs that are much higher than the rest of the sample. This is because UGC1256 is more massive than UGC1249 (van Eymeren et al. 2011) and hence the minor merger process does not significantly affect it. However, the lower Q_g values in the adjoining bridge and in UGC1249 reflect enhanced SF there. In the rest of the (UGC1256) disk, the stability parameter appears to trace the gas density, with high stability($Q_g \geq 10$) in the outskirts. On the other hand, the Two-fluid stability parameter appears to mostly trace the stellar surface density. The bridge between the galaxies does not exhibit lower Q_T values. This is expected if Q_T is dominated by the stellar component, because stripped gas is the main component of the bridge.

UGC1913 is a late type spiral galaxy (Sd). For this galaxy, we used the total gas surface density ($\Sigma_{\mathrm{HI+H_2}}$) when deriving the stability parameters. Inside its disk, we see lower stability values along the arms in both the single-fluid model and the two-fluid model. This galaxy is an example of a HI dominated galaxy (Leroy et al. 2008), and the single-fluid instabilities are not solely driven by the molecular gas. This can be seen in the minimal difference between the Q_g model derived using Σ_{HI} alone and the model where Σ_{HI} and $\Sigma_{\mathrm{H_2}}$

are combined (see Figure 4.15). The other two galaxies with CO measurements (UGC7766 and UGC7989) do not show any special features inside their star forming disks.

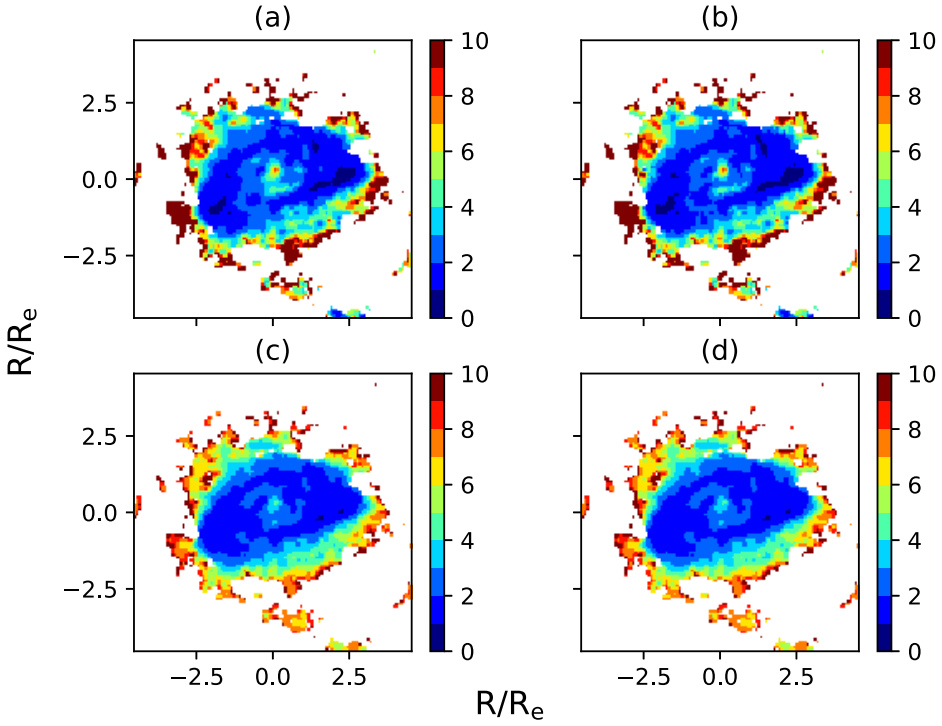

Figure 4.15: *Top panels*: Single-fluid disk stability maps of UGC1913. In (a), only $\Sigma_{\rm HI}$ was used, while in (b) the total gas surface density ($\Sigma_{\rm HI+H_2}$) was used. *Bottom panels*: Two-fluid disk stability maps of the same galaxy with (c) and without (d) $\Sigma_{\rm H_2}$. There is little difference between the maps where $\Sigma_{\rm HI}$ is used and those with $\Sigma_{\rm HI+H_2}$ because the gas disk is dominated by HI (Leroy et al. 2008).

UGC7989 is an Sab type galaxy and has one of the highest average stellar surface densities in the sample. It however has a significant central HI depression (see global profile in Appendix A.1). The Q_T map shows relatively low values in a significant portion of the star forming disk despite a conspicuous deficiency in HI. We also see beyond the defined star forming disk that both the Q_g and Q_T maps have lower values for the outer spiral arm (well beyond the molecular ring) which also has some low-level SF. This galaxy is a good example of the dominance of the stellar component in disk stability. The existence of high SFRs in the HI - deficient nuclear region indicates the presence of star forming molecular gas. A CO map for this galaxy was available, and hence the total gas density was used to derive the stability parameters, however, the Q_g map does not show lower central values, which is likely due to a low level detection of the CO. This is one example of a galaxy where high SNR observations of the molecular gas will be critical for deriving a clearer picture of the

disk stability.

UGC7524 is a magellanic type spiral (Sm). Its spiral structure is seen in both the Q_g and Q_T maps as well as in the SFR map. Radial flows may be present in this galaxy, as shown by kinks in the isovelocity contours in the kinematic map (see Appendix A). This galaxy has some of the lowest Q_g values in the entire sample. However, Q_g is high in the nuclear region where SF is highest (See Figures 4.2 and 4.8) due to relatively lower HI intensity (and hence low gas density) in that region (see global profile in Appendix A.1). Generally, the lowest Q_g values inside the disk of UGC7524 are found along the spiral arms which are regions of active star formation. The Q_T map also shows structure with low values along the spiral arms,and is lowest (and mostly flat) inside the star forming disk where SF is highest. However, note that much as the Q_T disk is generally flatter, the spiral arm values are not necessarily lower than in the Q_g map; In fact, within the spiral arms these two models agree in their predictions. In their study of gravitational instabilities in the large magellanic cloud, Yang et al. (2007) found that the single-fluid model did predict local star forming regions with a $\sim$ 60% accuracy. Our result confirms the findings of Yang et al. (2007) that the single-fluid model can accurately predict star forming regions in magellanic type spirals.

UGC8490 is also a magellanic type spiral with a strong warp in the HI disk (65° in PA and 20° in inclination, Sicotte & Carignan 1997, Swaters 1999). A rotation curve for this galaxy was obtained from Swaters (1999) who used tilted ring analysis. Like UGC7524 above, UGC8490 has lower Q_g and Q_T in the spiral arms. In the case of UGC8490, the spiral arms are further out from the center than UGC7524. This result is also in agreement with the result of Yang et al. (2007).

UGC6225 is an Scd type galaxy with the highest inclination in the sample. It has a thick dust lane and is one of the three galaxies with the highest stellar surface density in the sample. The noise in the W3 image of this galaxy is so low (SNR = 98.7) that the contour marking the approximate edge of the star forming disk at 18.8 mag/arcsec^2 (which is approximately the 5σ noise level) clearly lies beyond the region of high SF. However, for consistency with the rest of the sample, the same contour level was used for UGC6225. This results in high Q_g and Q_T values at the edge and inside the star forming disk, but this galaxy has some of the lowest stability levels in both the single-fluid and two-fluid models.

UGC11670 is an SO/a galaxy. This galaxy has persistently high (stable) values of Q_g and Q_T within and outside the star forming disk. This is due to low gas surface density across its disk. Past studies (e.g. Knapp et al. 1984, Abramova 2012) have suggested that its low gas mass and low surface density which is uncommon to standard lenticulars may be an indicator that this galaxy was previously a late-type spiral that has now exhausted its gas reservoir, resulting in very low levels of star formation.

4.4 Summary

In this chapter, we have investigated the relationship between disk stability and the MIR emission from star forming regions using 2D maps of the two properties. We have found that the single-fluid disk stability model yields values of the stability parameter that are much higher than 1, with typical disk Q_g values ranging between 3 and 15. This is mainly due to the high central Q_g values which are a result of the low HI surface density in the centers. We do find, however, that for the majority (70%) of the sample, Q_g values vary less along the edge than inside of the star forming disk. Half the sample exhibits an apparent threshold for large scale SF, with roughly constant Q_g (varying by less than 30%) along the disk edge. In these galaxies, the overall average Q_g value along the SF disk edge is 4.0 $\pm$ 2.2. We also found that, locally, Q_g does not trace the regions of enhanced star formation, as only five galaxies (UGC1913, UGC5789, UGC7047, UGC7261 and UGC7524) show lower Q_g values for a few regions with locally enhanced SFRs inside the SF disk, while UGC7989 shows low Q_g values for low level SF in outer spiral arms outside the disk. This is either a result of self regulation of the Q_g disks or our working resolution at which we could not resolve all the regions of enhanced SF. Note that of the three galaxies with CO (and hence $\Sigma_{\rm HI+H_2}$)measurements, only one (UGC1913) is among the galaxies with the lowest Q_g disks. In the case of UGC7989, for which we also used $\Sigma_{\rm HI+H_2}$, the regions of low Q_g lie well outside the CO disk.

In the two-fluid disk model, we find that the stability of the disks is greatly lowered but the model does not render the disks unstable. It is also clear that Q_T is a better predictor of SF thresholds as majority of the galaxies have roughly constant Q_T values (varying by less than 25%) at the edge of the SF disk (see Table 4.3). This shows that the two-fluid model is applicable to large scale star formation. We also find that the theoretical value Q_T = 1.0 does not determine the SF threshold, but rather our galaxies have Q_T = 2.5$\pm$0.9 at the edge of the star forming disk and Q_T = 2.5$\pm$0.8 inside the disk. In several galaxies (e.g. UGC5789, UGC7524, UGC7989), we have low values of Q_T occurring beyond the SF disk. This is probably because the W3-defined SF disk does not trace all the SF in the galaxy disks. This highlights the need to investigate other SF tracers that are more extended than the 11.6 μm tracer and to obtain high SNR CO data for the entire sample (see Chapter 5). This will enable us to mark the edge of the CO disks in all the galaxies and to account for the SF in regions beyond this radius.

Chapter 5

Conclusions

We have studied disk stability in a sub-sample of galaxies from the Westerbork survey of HI in Irregular and SPiral galaxies (WHISP, Kamphuis et al. 1996, van der Hulst et al. 2001), with the aim of assessing the connection to star formation thresholds in the mid-infrared (MIR). This study has made use of HI 21cm line emission imaging from WHISP and NIR/MIR imaging (3.4 μm, 11.6 μm) from the Wide-field Infrared Survey Explorer (WISE, Wright et al. 2010), combining two datasets that are well-suited to such a study in terms of uniformity, resolution and sensitivity. New HI data products (intensity maps, velocity maps, global profiles and radial surface density profiles) for 230 WHISP galaxies were derived with minimal noise (Chapter 2) and are presented in Appendix A. The global HI properties of mass, size and mass-to-light scaling relations were also studied and presented in Chapter 3. Note that all the relations studied were for gas and stars within the stellar disk. In that same chapter, star forming properties were studied for a sub-sample of 180 galaxies which had detections in the WISE MIR 11.6 μm band. We investigated the star formation main sequence and the SFR-atomic gas relation at both global and local scales. These scaling relations were also derived within the stellar disk. We have found the following properties to hold in our sample:

- Our sample follows an HI mass-size relation with a slope of 1.95 and an intercept of 6.5 giving a characteristic mean HI surface density of 3.6 $M_\odot$ pc^{-2}. Our result is consistent with earlier results of the HI mass-size relation.
- There exists strong correlations between the stellar luminosity (measured in the WISE 3.4 μm band) and the HI mass as well as the HI mass-to-light ratio ($M_{HI}/L_{3.4\mu m}$).
- Our sample galaxies define a star forming main sequence of slope 1.1, with a clear separation between the high and low star forming galaxies.
- There is a correlation between the SFR and HI mass enclosed within the stellar disk, with a slope of 1.6.

- On global scales, there is no correlation between the surface densities of SFR and HI averaged inside the stellar disk, and the $\Sigma_{\rm HI}$ exhibits a cut-off at 10 $M_\odot$ pc^{-2}.

- On sub-kpc scales, a pixel-by-pixel analysis reveals a trend between Σ_{SFR} and $\Sigma_{\rm HI}$ which, in 30% of the resolved galaxies, follows a power law relationship with index ranging from 1.6 - 3.8. This suggests a possible underlying relationship between atomic gas and SFR at small scales which may be due to the relationship between their small-scale volume densities.

The ultimate goal of this work was to study resolved maps of the gravitational stability parameter and determine how well this predicts the MIR emission from star forming regions in galaxies. This was done for a sub-sample of 20 resolved galaxies. Two models of the gravitational stability parameter were used. First, we constructed stability parameter maps using the single-fluid thin disk model of Toomre (1964). Two-dimensional kinematic maps were generated from the rotation curves of Swaters (1999) and van Eymeren et al. (2011). The HI surface density maps were derived from the HI intensity maps. The second model we derived was the two-fluid disk model which combines a thin gas disk and a thin stellar disk, following the formulation of Rafikov (2001). This involved derivation of the stellar surface density maps from the WISE NIR 3.4 μm images as well as radial stellar velocity dispersions which were inferred from the disk scale lengths and vertical stellar velocity dispersions (van der Kruit 1988, Kregel et al. 2002, Leroy et al. 2008). WISE 11.6 μm surface brightness maps were used to define the edge of the star forming disk at $\sim$ 18.8 mag arcsec^{-2} which corresponds to a $\sim 5\sigma$ noise level. This method is similar to that of Kennicutt (1989) who used the sharp cut-off in the radial star formation rate profile to define the star formation threshold. Our analyses were carried out along the edge and inside of this disk, and we have discussed how well the two stability parameters predict this threshold and local star forming regions within the enclosed disk.

We have found that the single-fluid disk criterion is unable to predict the threshold for large scale SF in spirals and any apparent threshold predictions in dwarfs are not applicable to all the dwarfs in our sample. The applicability of the single-fluid gas disk criterion in dwarfs is dependent on the gas fraction in a given galaxy's disk. As seen in our sample, galaxies with higher gas fractions appear to have an apparent stability threshold in relation to the onset of large scale star formation. Our findings are in agreement with previous studies by Wong & Blitz (2002), Boissier et al. (2003), de Blok & Walter (2006), Leroy et al. (2008). We note, however, that most of our study is based on only the atomic Hydrogen component, which has a much lighter surface density and less contribution to the gravity budget than the molecular Hydrogen. For three of our galaxies we had CO maps from the HERACLES (Leroy et al. 2009), but we did not find significant differences in predictions of their models with $\Sigma_{\rm HI+H_2}$.

We have found that the two-fluid (stars + gas) disk criterion does predict the SF threshold, and can hence be applied to large scale star formation. However, an average threshold value of 2.5$\pm$0.9 instead of the theoretical value of 1 was observed. We conclude that

the critical value of Q_T lies between 1.6 - 3.4, in agreement with Griv & Gedalin (2012), Romeo & Mogotsi (2017). Q_T is indeed a better predictor for large scale star formation than Q_g. However, on smaller scales inside the disks, the predictions of Q_T for star formation are subtly similar to those of Q_g . We see this in four disks that show resolved structure in both Q_g and Q_T (UGC7524, UGC1913, UGC5789, UGC7261), all except one show lower values in both parameters for the same regions of enhanced star formation, but with $Q_T \leq Q_g$. These four galaxies are late type spirals, but it is not conclusive that Q_g and Q_T agree in their predictions for star formation in late type spirals because this is not the case for the other late types in the sample. We note that the Q_T models are dominated by the stellar disk surface density. This is in agreement with Romeo & Mogotsi (2017) who found the stellar disk to be the main driver of instability at kpc scales in their sample of galaxies. It is expected that the stellar disk should dominate the models in the two-fluid disk criterion because of the greater contribution of stars to the gravity budget, especially for earlier-type spirals. In the late-type spirals and dwarfs, however, the gas fractions are higher and the two-fluid instability may not necessarily be driven by the stellar disk. This is witnessed by the agreeing predictions of the Q_g and Q_T inside the disks of the four late-types mentioned above.

In summary, no conclusive evidence has been found for a threshold in Q_g for the onset of large scale star formation. An apparent threshold of $Q_g \leq 4.0$ appears in only 50% of the sample but is clearly not a necessary condition for star formation, as the other 50% show no such threshold and yet have star formation in their disks. On the other other hand, there appears to be a clear Q_T threshold with $\langle Q_T \rangle = 2.5 \pm 0.9$ seen at the edges of the star forming disks, and in agreement with what has been observed in studies of the radial variation of Q_T. This implies that $Q_T \leq 2.5$ may be a sufficient and necessary condition for star formation.

Future prospects

The study presented here has much capacity for growth and improvement. The outlook of future work on this study is as follows:

- Literature rotation curves were used in this thesis, as the generation of rotation curves was not part of the scope of this study. The size of the sample will be increased by generating more rotation curves. This will also enable us to have a more diverse sample that includes isolated galaxies, interacting galaxies, lopsided potentials, barred potentials, field and cluster galaxies. With such a diverse sample, we will be able to study gravitational stability thresholds in the context of environment and varied dynamics of galactic disks.

- We have mostly relied upon the HI surface density to generate models of gravitational stability for a single fluid (gas only) disk and a two-fluid (gas and stars) disk. CO measurements were available for only three of the galaxies and hence for these three

the total gas surface density ($\Sigma_{\rm HI+H_2}$) was used. However, even in these three we did not see any apparent gravitational stability thresholds, which may imply that the H_2 component is not a significant stability driver at the scales probed. However, a larger inventory of CO measurements would enable a more robust comparison of $\Sigma_{\rm HI}$ and $\Sigma_{\rm HI+H_2}$ in the gravitational stability criterion. Therefore, CO measurements will be sought for the rest of the sample for this purpose. Note that the presence of star formation in the HI - deficient (hence high Q_g - high Q_T) nuclei attests to existence of star forming molecular gas in those regions and highlights the importance of using total gas surface density. Likewise, we will also be considering dense molecular gas tracers such as HCN and CHO^+

- We plan to use the multi-component disk model of Romeo & Falstad (2013) to study the contributions of the stellar disk, the atomic Hydrogen and the molecular Hydrogen. Their model allows for several gas components (e.g. multiple phases) and several stellar components to be individually accounted for in order to determine which particular component drives instabilities at particular physical scales.. This will enable us to find out the dominant drivers of stability in our sample of galaxies and, with a larger sample, we may be able to find the dominant drivers of stability in different galaxies as a function of morphology, environment and kinematics.

- We have also used a constant gas velocity dispersion for our models in this thesis. With higher spectral resolution data, we can apply the super-profile technique of Ianjamasimanana et al. (2012) to kinematically separate the cold and warm neutral atomic gas. Since the two components have distinct velocity dispersions and it is the cold gas that is closely associated with SF (de Blok & Walter 2006), this will provide us with more accurate velocity dispersions which are a critical aspect of disk stability.

- Our study is directly connected to the MeerKAT (Meer Karoo Array Telescope) large survey project, the MeerKAT HI Observations of Nearby Galactic Objects - Observing Southern Emitters (MHONGOOSE) survey, whose core goals include studying the relation between atomic gas and star formation. With high sensitivity to low column density HI (3σ sensitivity for 7.5×10^{18} cm^{-2} at a spatial resolution of $30''$, de Blok et al. 2016) and a wide field of view, MHONGOOSE will adequately trace low column density HI gas at the outermost radii of 30 galaxies. This coupled with observations of extended UV disks, the star formation-atomic gas relation will be studied in the outer most edges of galaxies. We intend to apply our study to the MHONGOOSE sample to investigate the relationship between gas stability and star formation in low column density regions. Furthermore, the MeerKAT telescope will be capable of observing HI at spatial resolutions of $5''$, which is equivalent to optical/infrared resolutions. Therefore, high resolution data from the MeerKAT will enable us to conduct our study at smaller physical scales, thus giving a more detailed view of the star formation - disk stability relation.

- Since we have solely used the WISE 11.6 μm as the SFR tracer in our study, we shall also investigate other SF tracers such as high resolution 20 cm radio continuum and the hybrid tracer $L_{FUV+24\mu m}$. This will involve both the use of archival data (for example from GALEX FUV and Spitzer 24 μm data) and applying for telescope time.

Appendices

Appendix A

Atlases of Data Products

A.1 Atlas of HI data products

Description: *Top left*: Integrated HI intensity distribution, derived using the criteria outlined in section 2.3.2. *Top right*: The Velocity field. The thick black contour marks the systemic velocity which is shown in the lower right corner. Δ defines the separation of the contours. *Bottom left*: The Radial HI density profile. The vertical dashed line marks the radius at $\Sigma_{\rm HI} = 1 {\rm M}_{\odot}$ pc^{-2}, which is marked by the horizontal dashed line. However, for galaxies where the density profile is less than $1 {\rm M}_{\odot}$ pc^{-2} at all radii, the vertical line marks the extent of the stellar disk. *Bottom right*: The HI Global profile. The systemic velocity is shown by the dashed vertical line.
The integrated HI maps were used to derive the HI masses and surface density maps. The HI surface density radial profiles were used to determine the HI diameters. The HI flux density global profiles were used to determine the systemic velocity and line widths (W_{50} and W_{20}). The velocity field maps will be used in future work to derive rotation curves.

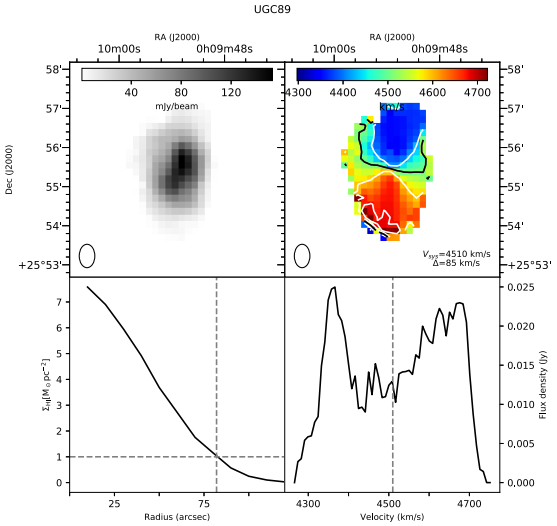
UGC89
RA (J2000)
10m00s
0h09m48s
Dec (J2000)
mJy/beam
km/s
V_{sys}=4510 km/s
Δ=85 km/s
$\Sigma_{HI}[M_\odot pc^{-2}]$
Flux density (Jy)
Radius (arcsec)
Velocity (km/s)

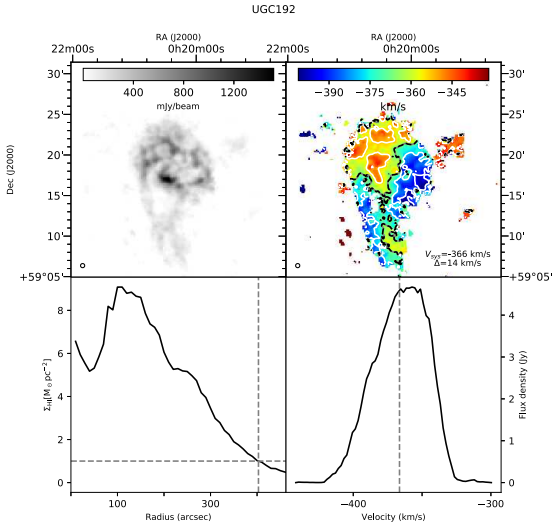
UGC192
RA (J2000)
22m00s
0h20m00s
Dec (J2000)
mJy/beam
km/s
V_{sys}=-366 km/s
Δ=14 km/s
$\Sigma_{HI}[M_\odot pc^{-2}]$
Flux density (Jy)
Radius (arcsec)
Velocity (km/s)

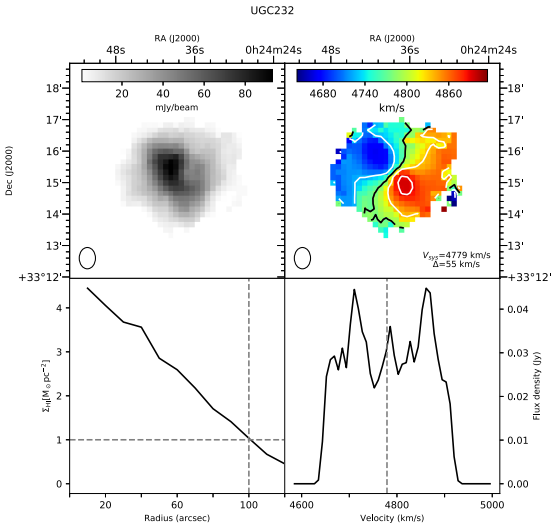
UGC232
RA (J2000)
48s
36s
0h24m24s
Dec (J2000)
mJy/beam
km/s
V_{sys}=4779 km/s
Δ=55 km/s
$\Sigma_{HI}[M_\odot pc^{-2}]$
Flux density (Jy)
Radius (arcsec)
Velocity (km/s)

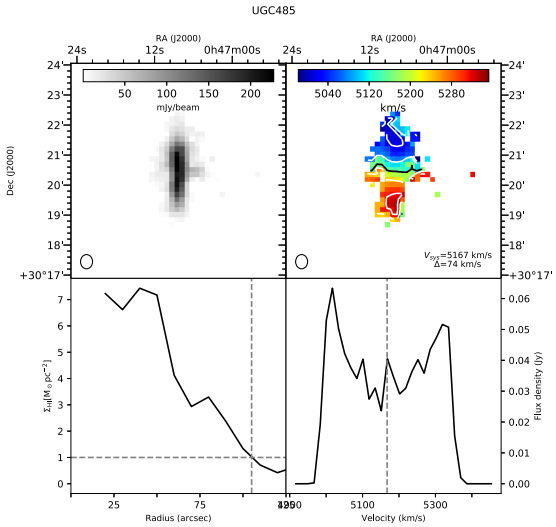
UGC485
RA (J2000)
24s
12s
0h47m00s
Dec (J2000)
mJy/beam
km/s
V_{sys}=5167 km/s
Δ=74 km/s
$\Sigma_{HI}[M_\odot pc^{-2}]$
Flux density (Jy)
Radius (arcsec)
Velocity (km/s)

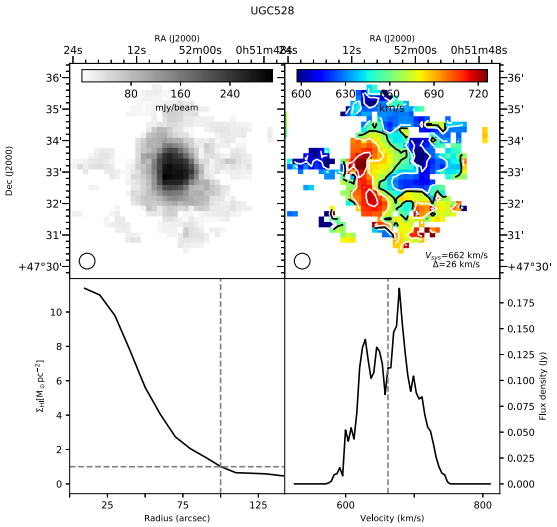
UGC528
RA (J2000)
24s
12s
52m00s
0h51m48s
Dec (J2000)
mJy/beam
km/s
V_{sys}=662 km/s
Δ=26 km/s
$\Sigma_{HI}[M_\odot pc^{-2}]$
Flux density (Jy)
Radius (arcsec)
Velocity (km/s)

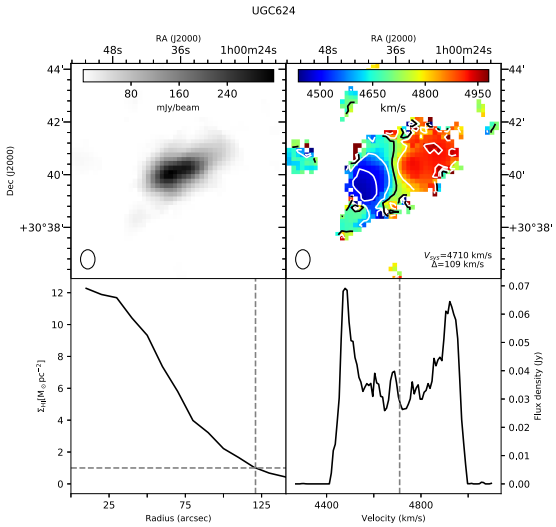
UGC624
RA (J2000)
48s
36s
1h00m24s
Dec (J2000)
mJy/beam
km/s
V_{sys}=4710 km/s
Δ=109 km/s
$\Sigma_{HI}[M_\odot pc^{-2}]$
Flux density (Jy)
Radius (arcsec)
Velocity (km/s)

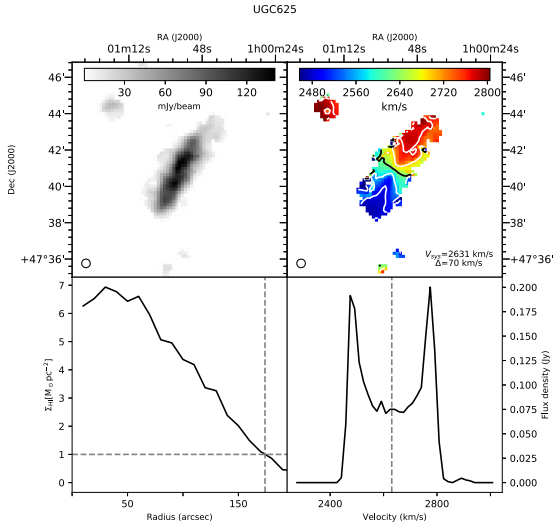
UGC625
RA (J2000)
01m12s
48s
1h00m24s
Dec (J2000)
+47°36'
mJy/beam
km/s
V_{sys}=2631 km/s
Δ=70 km/s
Radius (arcsec)
Velocity (km/s)
Flux density (Jy)

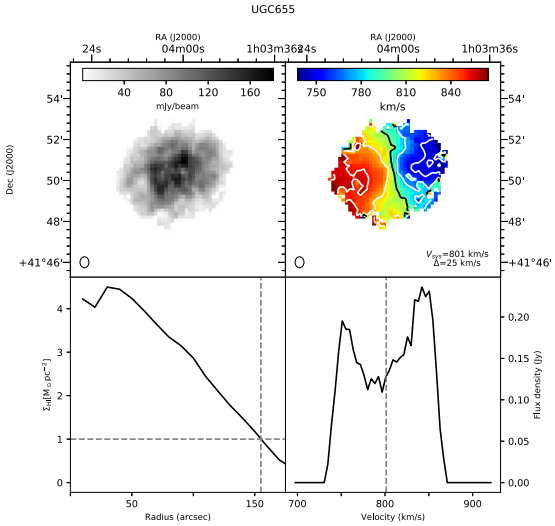
UGC655
RA (J2000)
04m00s
1h03m36s
Dec (J2000)
+41°46'
mJy/beam
km/s
V_{sys}=801 km/s
Δ=25 km/s
Radius (arcsec)
Velocity (km/s)
Flux density (Jy)

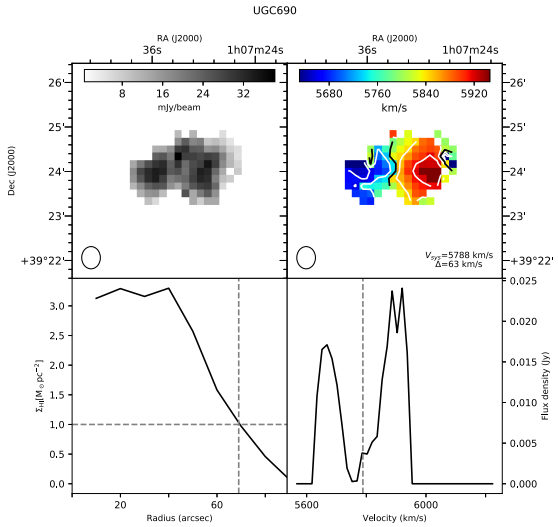
UGC690
RA (J2000)
36s
1h07m24s
Dec (J2000)
+39°22'
mJy/beam
km/s
V_{sys}=5788 km/s
Δ=63 km/s
Radius (arcsec)
Velocity (km/s)
Flux density (Jy)

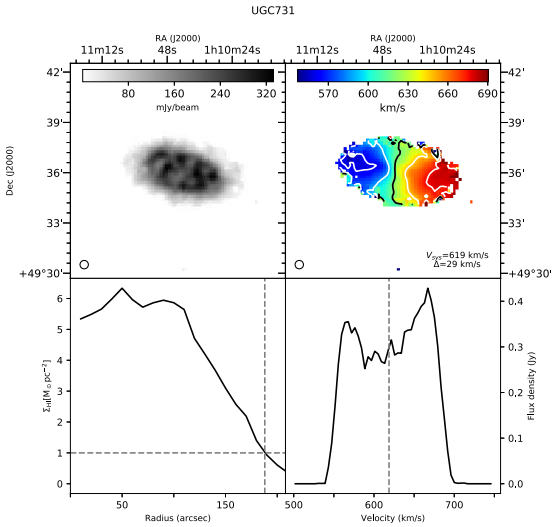
UGC731
RA (J2000)
11m12s
48s
1h10m24s
Dec (J2000)
+49°30'
mJy/beam
km/s
V_{sys}=619 km/s
Δ=29 km/s
Radius (arcsec)
Velocity (km/s)
Flux density (Jy)

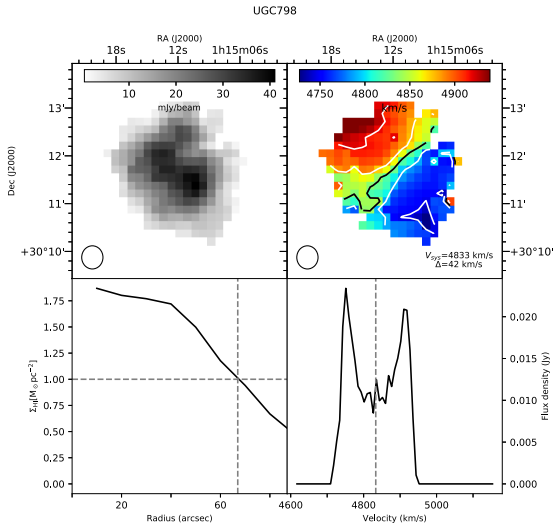
UGC798
RA (J2000)
18s
12s
1h15m06s
Dec (J2000)
+30°10'
mJy/beam
km/s
V_{sys}=4833 km/s
Δ=42 km/s
Radius (arcsec)
Velocity (km/s)
Flux density (Jy)

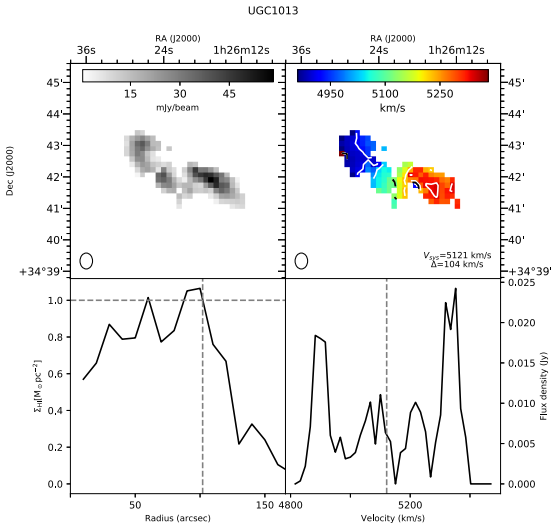
UGC1013
RA (J2000)
36s
24s
1h26m12s
Dec (J2000)
+34°39'
mJy/beam
km/s
V_{sys}=5121 km/s
Δ=104 km/s
Radius (arcsec)
Velocity (km/s)
Flux density (Jy)

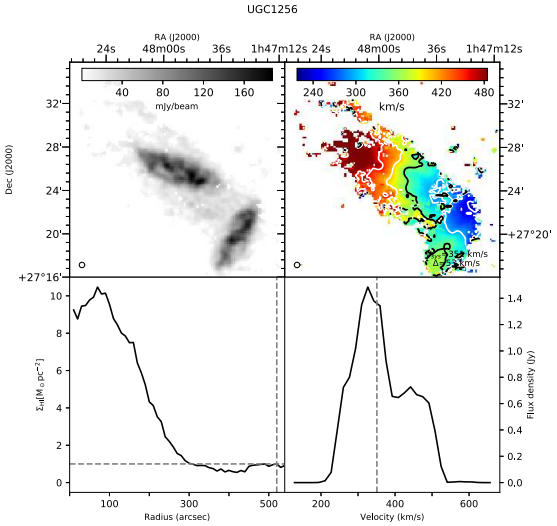
UGC1256
RA (J2000)
Dec (J2000)
mJy/beam
km/s
Radius (arcsec)
Velocity (km/s)
Flux density (Jy)

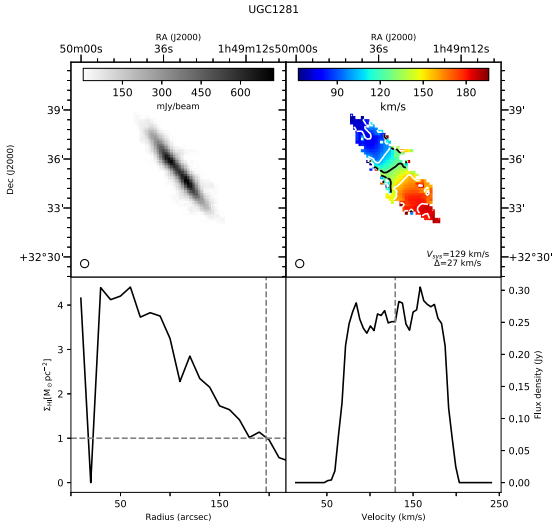
UGC1281
RA (J2000)
Dec (J2000)
mJy/beam
km/s
Radius (arcsec)
Velocity (km/s)
Flux density (Jy)

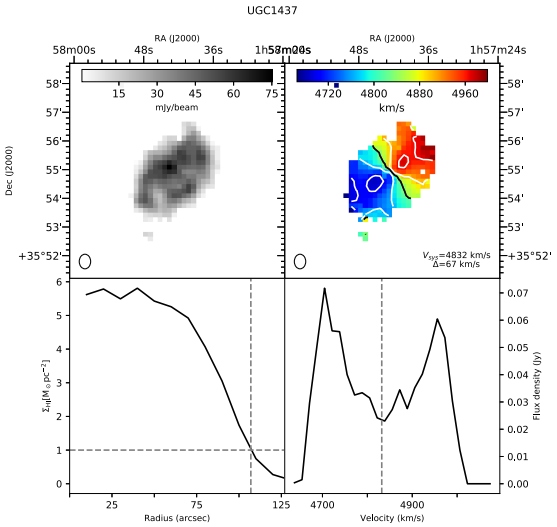
UGC1437
RA (J2000)
Dec (J2000)
mJy/beam
km/s
Radius (arcsec)
Velocity (km/s)
Flux density (Jy)

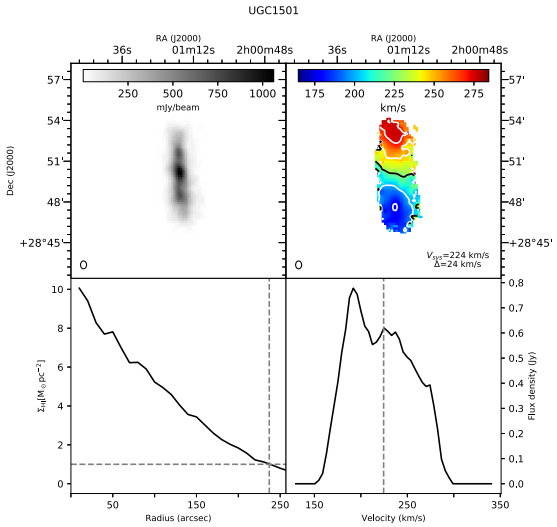
UGC1501
RA (J2000)
Dec (J2000)
mJy/beam
km/s
Radius (arcsec)
Velocity (km/s)
Flux density (Jy)

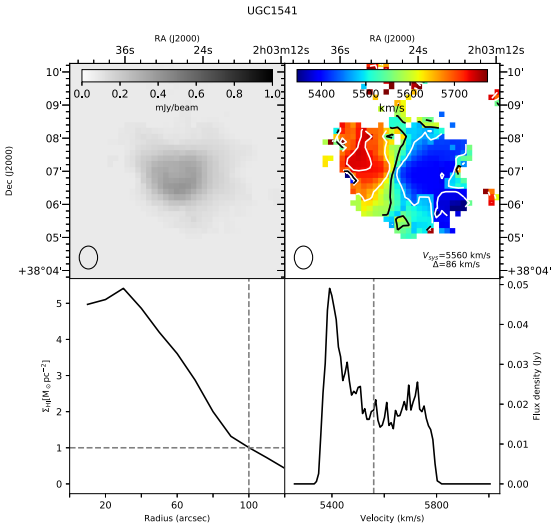
UGC1541
RA (J2000)
Dec (J2000)
mJy/beam
km/s
Radius (arcsec)
Velocity (km/s)
Flux density (Jy)

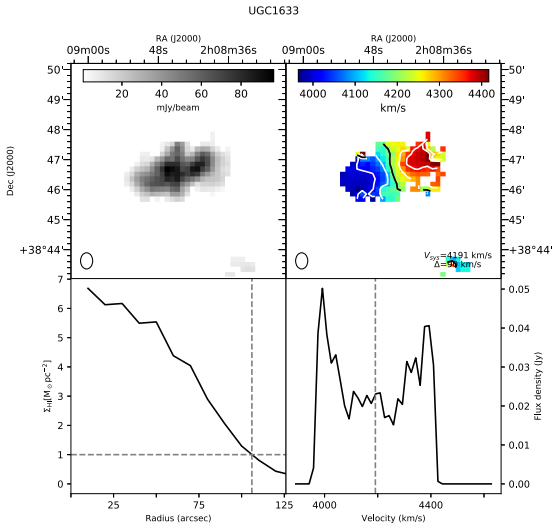
UGC1633
RA (J2000)
Dec (J2000)
mJy/beam
km/s
Radius (arcsec)
Velocity (km/s)
Flux density (Jy)

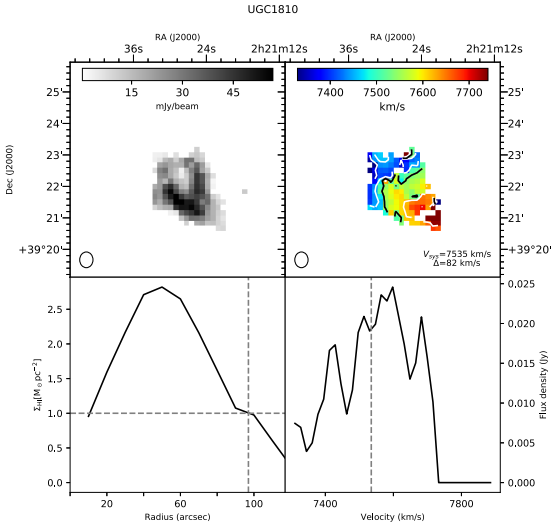
UGC1810
RA (J2000)
Dec (J2000)
mJy/beam
km/s
V_{sys}=7535 km/s
Δ=82 km/s
Σ_{HI}[$M_\odot$ pc^{-2}]
Flux density (Jy)
Radius (arcsec)
Velocity (km/s)

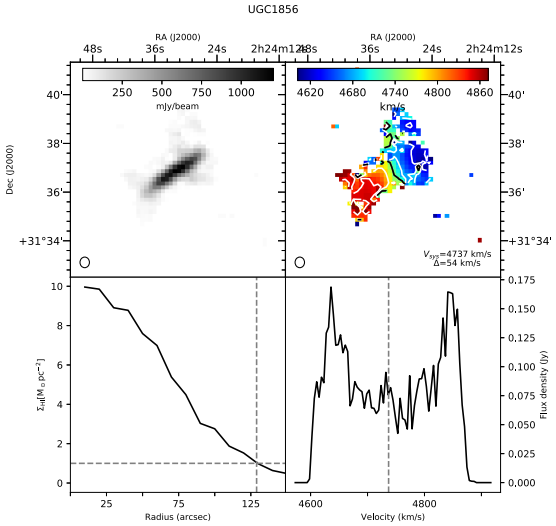
UGC1856
RA (J2000)
Dec (J2000)
mJy/beam
km/s
V_{sys}=4737 km/s
Δ=54 km/s
Σ_{HI}[$M_\odot$ pc^{-2}]
Flux density (Jy)
Radius (arcsec)
Velocity (km/s)

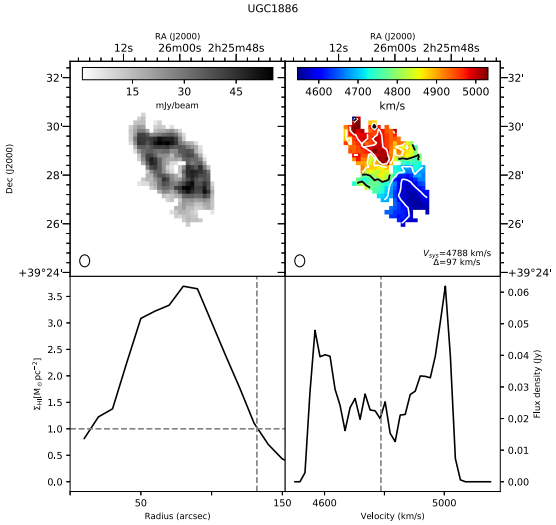
UGC1886
RA (J2000)
Dec (J2000)
mJy/beam
km/s
V_{sys}=4788 km/s
Δ=97 km/s
Σ_{HI}[$M_\odot$ pc^{-2}]
Flux density (Jy)
Radius (arcsec)
Velocity (km/s)

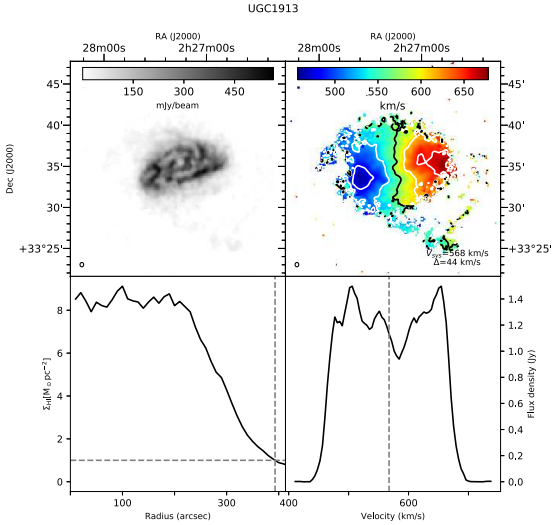
UGC1913
RA (J2000)
Dec (J2000)
mJy/beam
km/s
V_{sys}=568 km/s
Δ=44 km/s
Σ_{HI}[$M_\odot$ pc^{-2}]
Flux density (Jy)
Radius (arcsec)
Velocity (km/s)

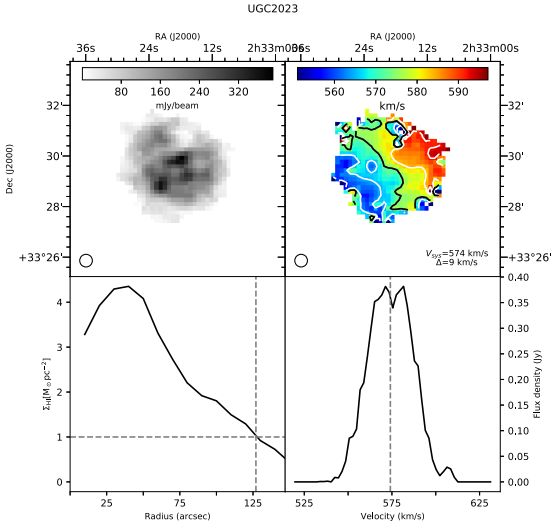
UGC2023
RA (J2000)
Dec (J2000)
mJy/beam
km/s
V_{sys}=574 km/s
Δ=9 km/s
Σ_{HI}[$M_\odot$ pc^{-2}]
Flux density (Jy)
Radius (arcsec)
Velocity (km/s)

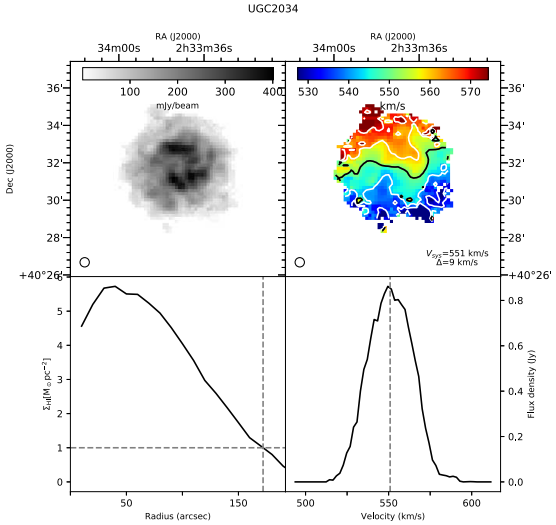
UGC2034
RA (J2000)
Dec (J2000)
mJy/beam
km/s
V_{sys}=551 km/s
Δ=9 km/s
Σ_{HI}[$M_\odot$ pc^{-2}]
Flux density (Jy)
Radius (arcsec)
Velocity (km/s)

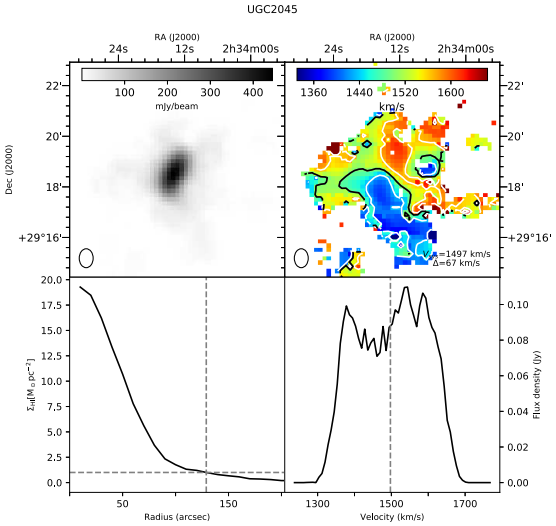
UGC2045
RA (J2000)
Dec (J2000)
mJy/beam
km/s
Radius (arcsec)
Velocity (km/s)
Flux density (Jy)

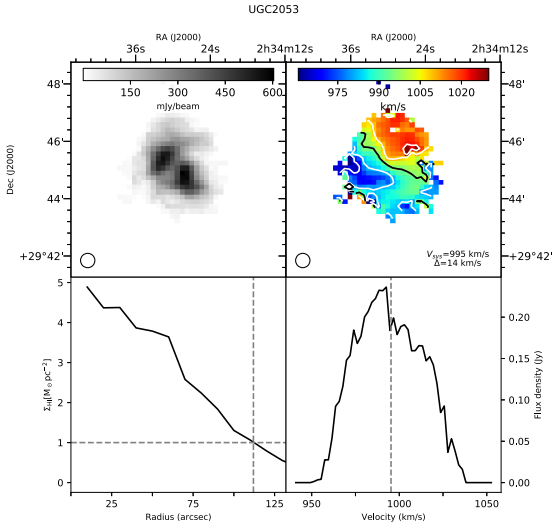
UGC2053
RA (J2000)
Dec (J2000)
mJy/beam
km/s
Radius (arcsec)
Velocity (km/s)
Flux density (Jy)

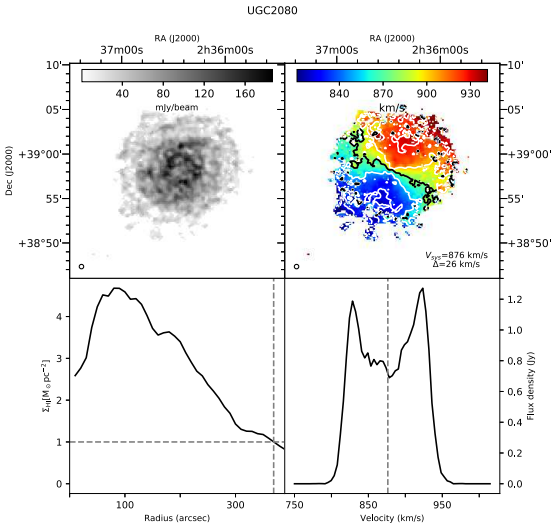
UGC2080
RA (J2000)
Dec (J2000)
mJy/beam
km/s
Radius (arcsec)
Velocity (km/s)
Flux density (Jy)

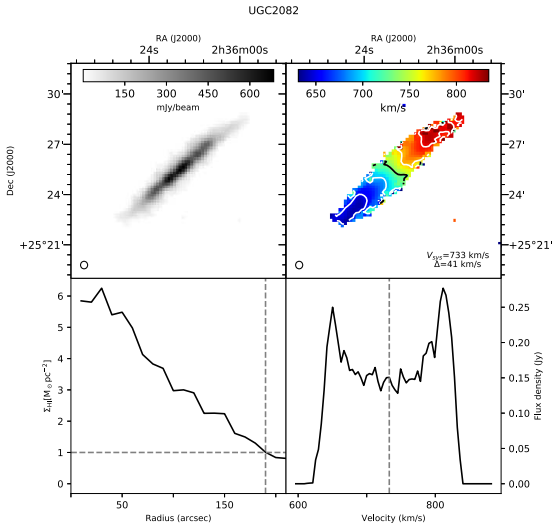
UGC2082
RA (J2000)
Dec (J2000)
mJy/beam
km/s
Radius (arcsec)
Velocity (km/s)
Flux density (Jy)

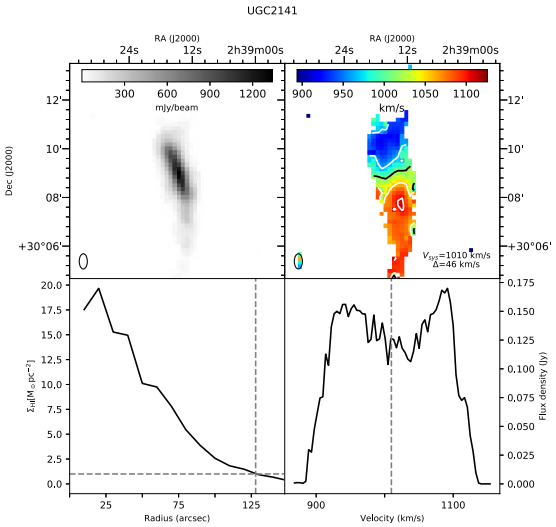
UGC2141
RA (J2000)
Dec (J2000)
mJy/beam
km/s
Radius (arcsec)
Velocity (km/s)
Flux density (Jy)

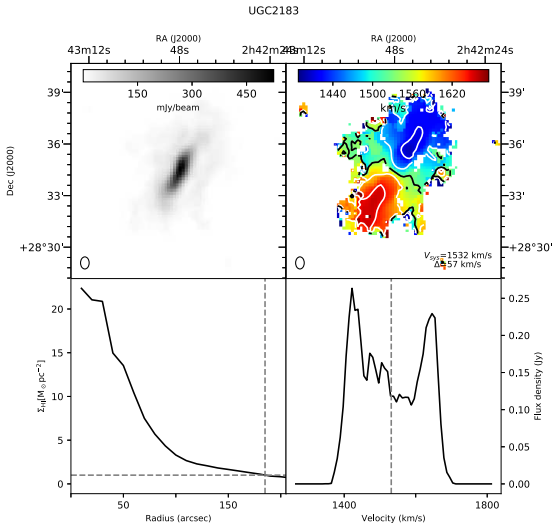
UGC2183
RA (J2000)
Dec (J2000)
mJy/beam
km/s
Radius (arcsec)
Velocity (km/s)
Flux density (Jy)

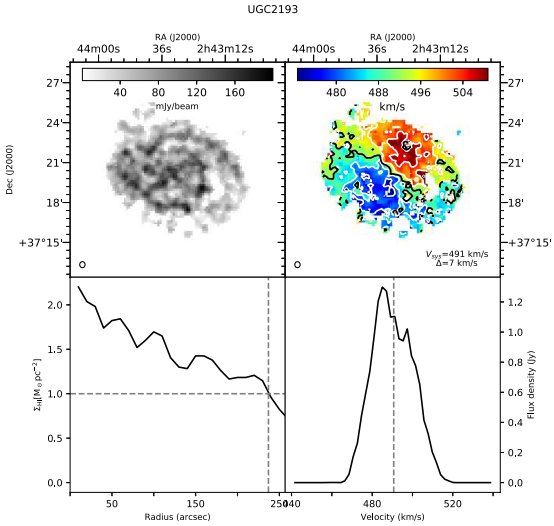
UGC2193
RA (J2000)
Dec (J2000)
mJy/beam
km/s
Radius (arcsec)
Velocity (km/s)
Flux density (Jy)

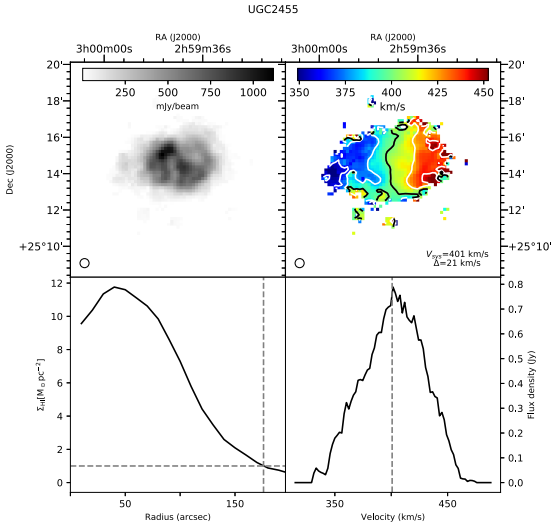
UGC2455
RA (J2000)
Dec (J2000)
mJy/beam
km/s
Radius (arcsec)
Velocity (km/s)
Flux density (Jy)

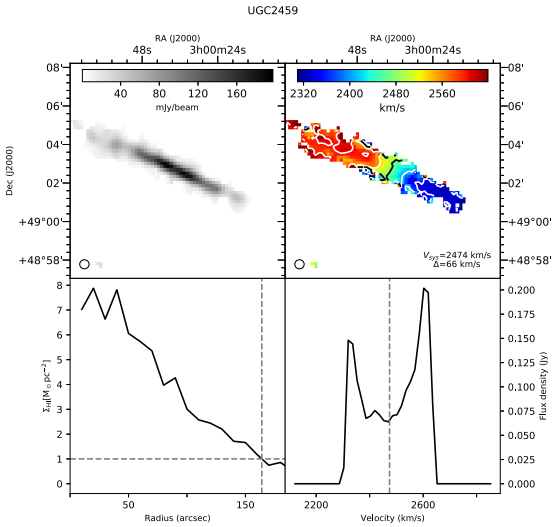
UGC2459
RA (J2000)
Dec (J2000)
mJy/beam
km/s
Radius (arcsec)
Velocity (km/s)
Flux density (Jy)

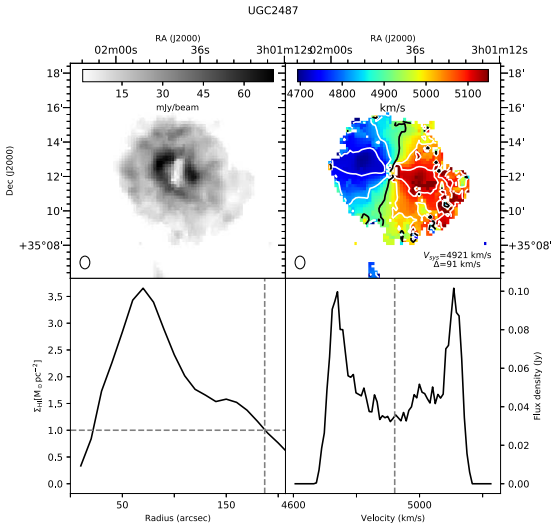
UGC2487
RA (J2000)
Dec (J2000)
mJy/beam
km/s
Radius (arcsec)
Velocity (km/s)
Flux density (Jy)

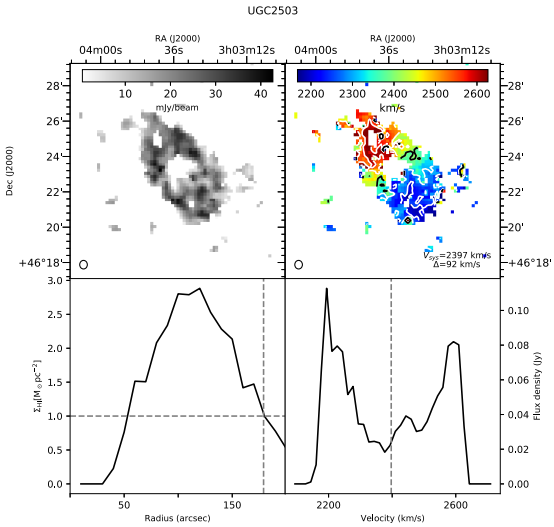
UGC2503
RA (J2000)
Dec (J2000)
mJy/beam
km/s
Radius (arcsec)
Velocity (km/s)
Flux density (Jy)

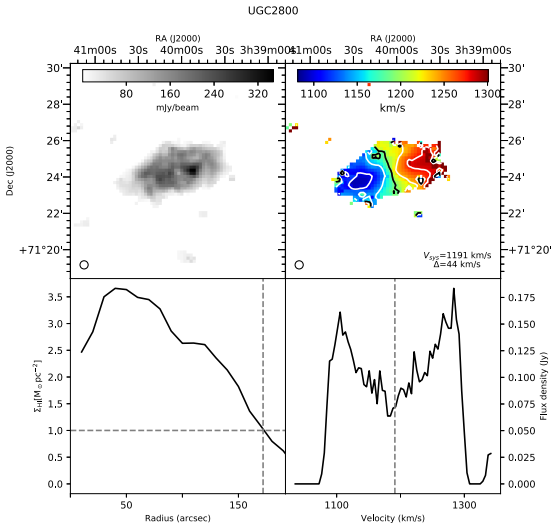
UGC2800
RA (J2000)
Dec (J2000)
mJy/beam
km/s
Radius (arcsec)
Velocity (km/s)
Flux density (Jy)

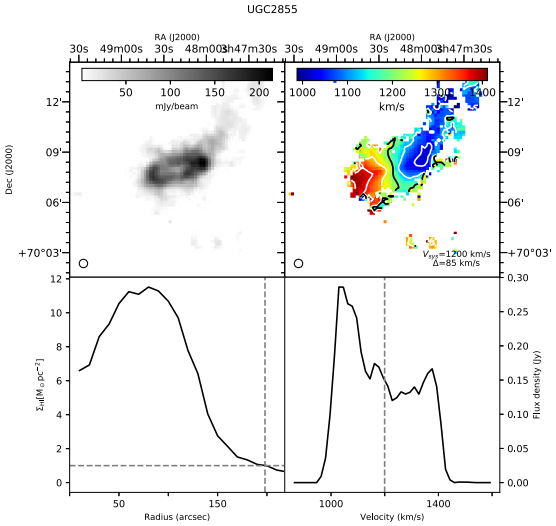
UGC2855
RA (J2000)
Dec (J2000)
mJy/beam
km/s
V_{sys}=1200 km/s
Δ=85 km/s
Radius (arcsec)
Velocity (km/s)
Flux density (Jy)

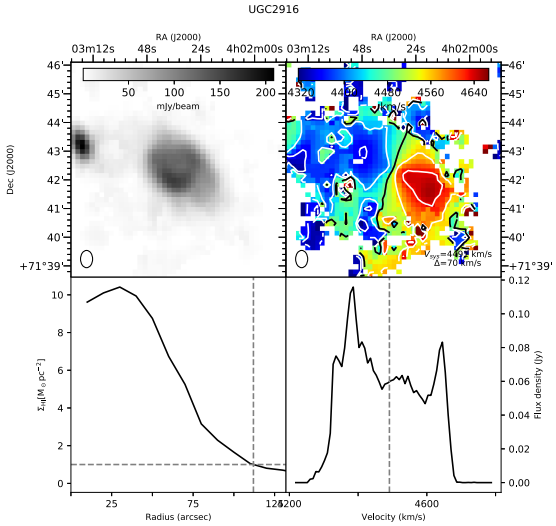
UGC2916
RA (J2000)
Dec (J2000)
mJy/beam
km/s
V_{sys}=4473 km/s
Δ=70 km/s
Radius (arcsec)
Velocity (km/s)
Flux density (Jy)

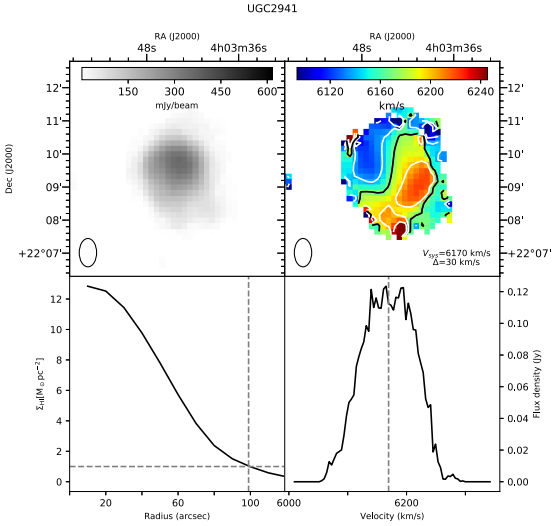
UGC2941
RA (J2000)
Dec (J2000)
mJy/beam
km/s
V_{sys}=6170 km/s
Δ=30 km/s
Radius (arcsec)
Velocity (km/s)
Flux density (Jy)

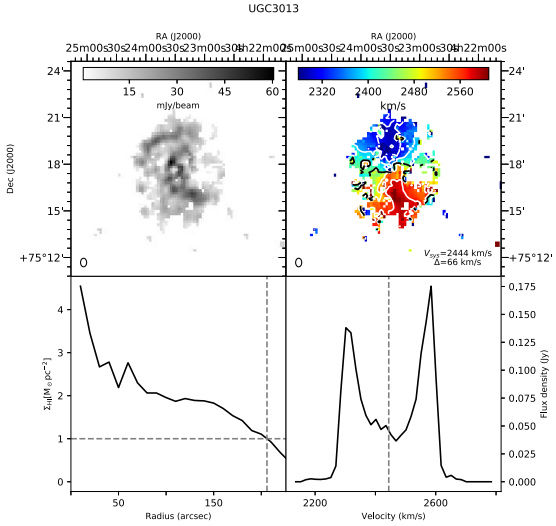
UGC3013
RA (J2000)
Dec (J2000)
mJy/beam
km/s
V_{sys}=2444 km/s
Δ=66 km/s
Radius (arcsec)
Velocity (km/s)
Flux density (Jy)

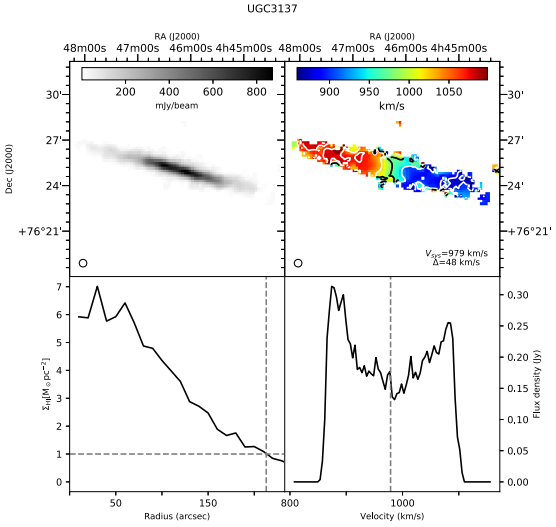
UGC3137
RA (J2000)
Dec (J2000)
mJy/beam
km/s
V_{sys}=979 km/s
Δ=48 km/s
Radius (arcsec)
Velocity (km/s)
Flux density (Jy)

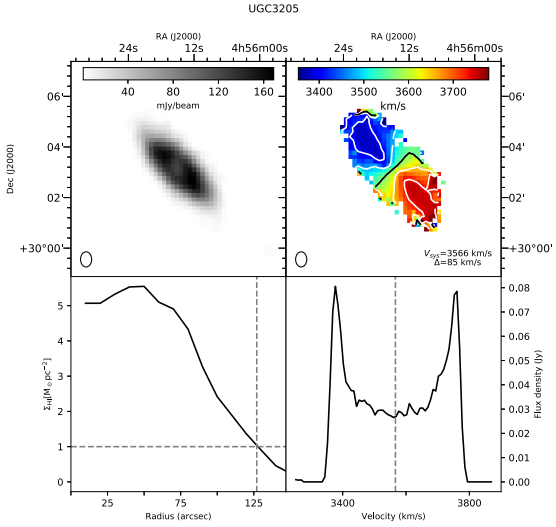
UGC3205
RA (J2000)
Dec (J2000)
mJy/beam
km/s
V_{sys}=3566 km/s
Δ=85 km/s
Radius (arcsec)
Velocity (km/s)
Flux density (Jy)

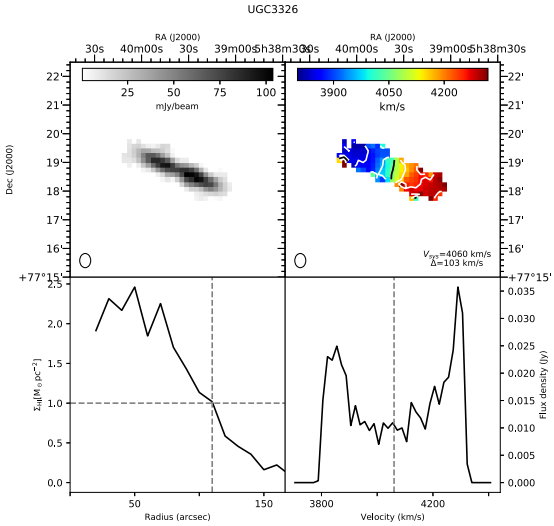
UGC3326
RA (J2000)
Dec (J2000)
mJy/beam
km/s
Radius (arcsec)
Velocity (km/s)
Flux density (Jy)

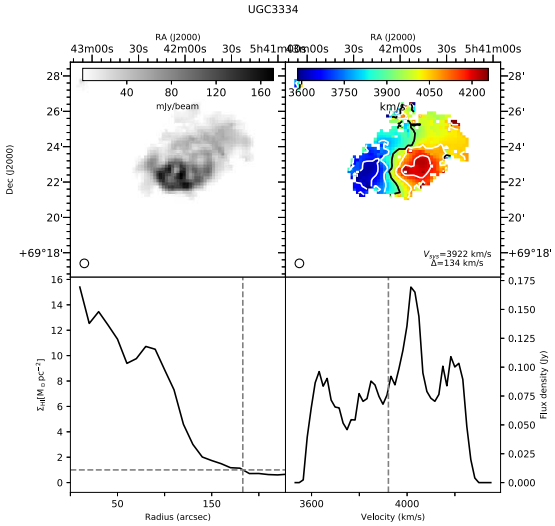
UGC3334
RA (J2000)
Dec (J2000)
mJy/beam
km/s
Radius (arcsec)
Velocity (km/s)
Flux density (Jy)

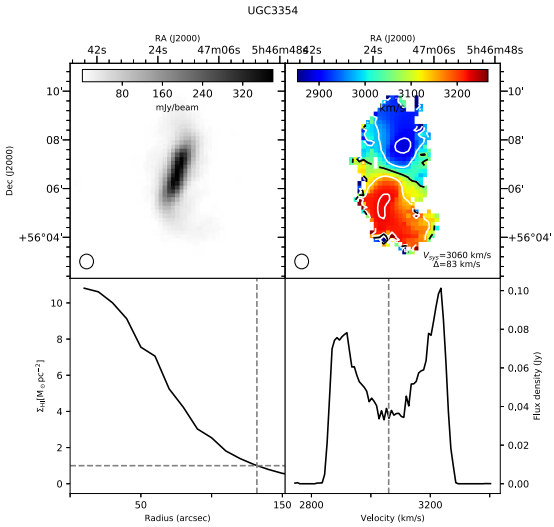
UGC3354
RA (J2000)
Dec (J2000)
mJy/beam
km/s
Radius (arcsec)
Velocity (km/s)
Flux density (Jy)

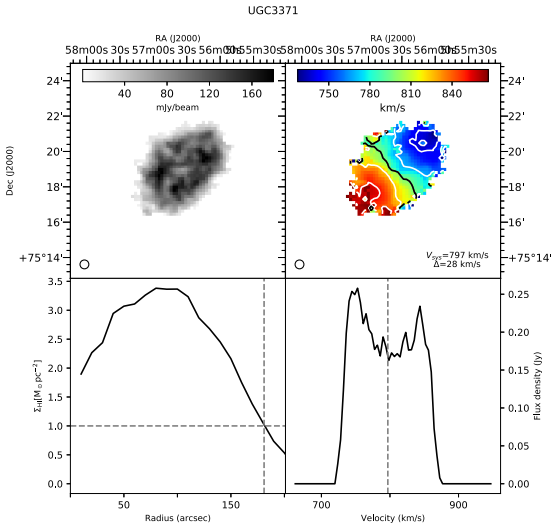
UGC3371
RA (J2000)
Dec (J2000)
mJy/beam
km/s
Radius (arcsec)
Velocity (km/s)
Flux density (Jy)

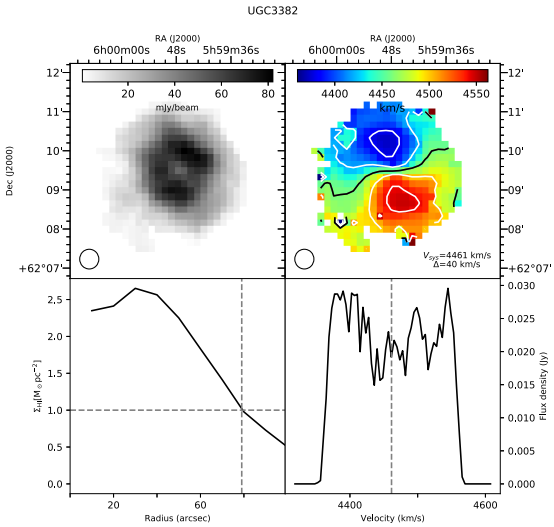
UGC3382
RA (J2000)
Dec (J2000)
mJy/beam
km/s
Radius (arcsec)
Velocity (km/s)
Flux density (Jy)

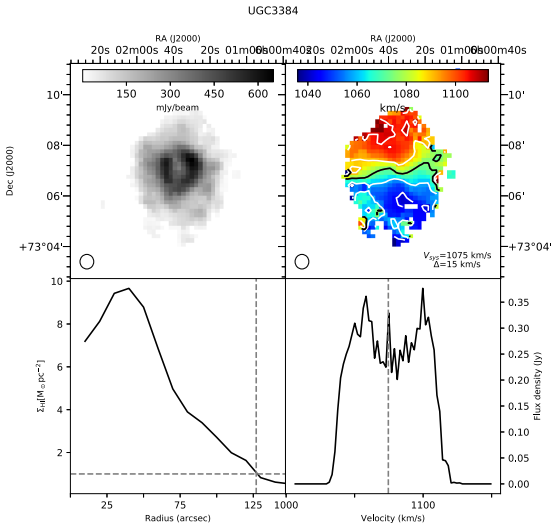
UGC3384
RA (J2000)
Dec (J2000)
mJy/beam
km/s
Radius (arcsec)
Velocity (km/s)
Flux density (Jy)

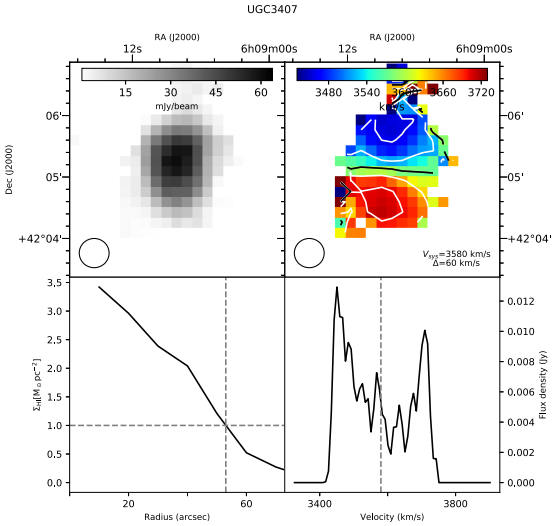
UGC3407
RA (J2000)
Dec (J2000)
mJy/beam
km/s
V_{sys}=3580 km/s
Δ=60 km/s
Radius (arcsec)
Velocity (km/s)
Flux density (Jy)

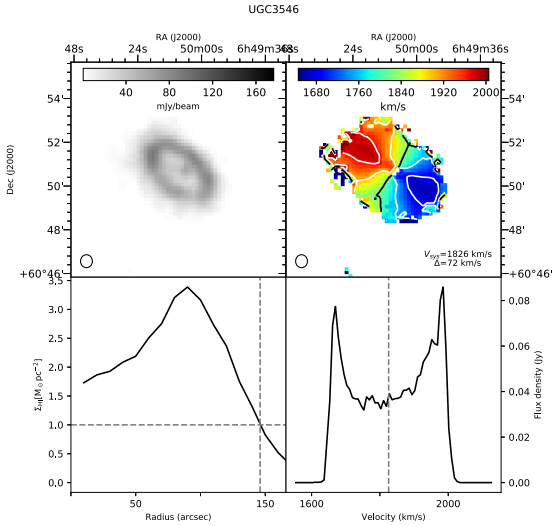
UGC3546
RA (J2000)
Dec (J2000)
mJy/beam
km/s
V_{sys}=1826 km/s
Δ=72 km/s
Radius (arcsec)
Velocity (km/s)
Flux density (Jy)

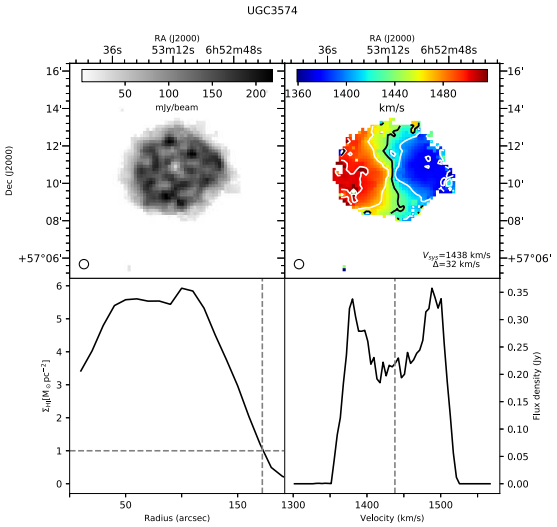
UGC3574
RA (J2000)
Dec (J2000)
mJy/beam
km/s
V_{sys}=1438 km/s
Δ=32 km/s
Radius (arcsec)
Velocity (km/s)
Flux density (Jy)

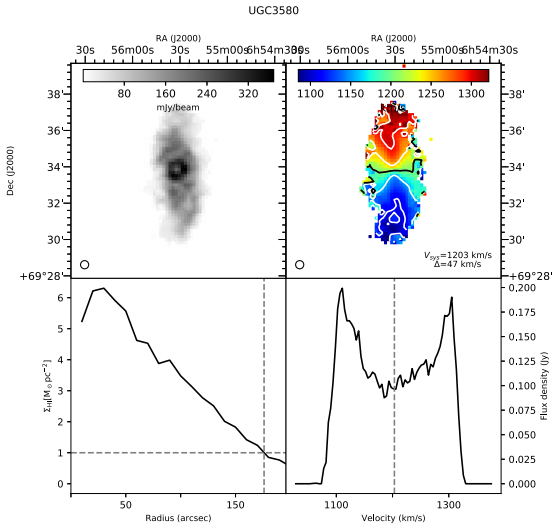
UGC3580
RA (J2000)
Dec (J2000)
mJy/beam
km/s
V_{sys}=1203 km/s
Δ=47 km/s
Radius (arcsec)
Velocity (km/s)
Flux density (Jy)

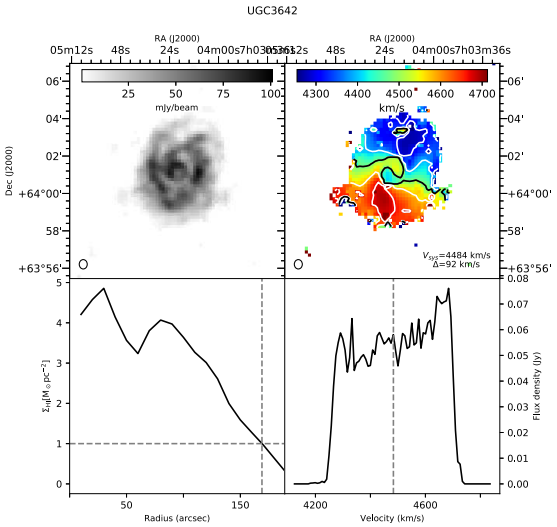
UGC3642
RA (J2000)
Dec (J2000)
mJy/beam
km/s
V_{sys}=4484 km/s
Δ=92 km/s
Radius (arcsec)
Velocity (km/s)
Flux density (Jy)

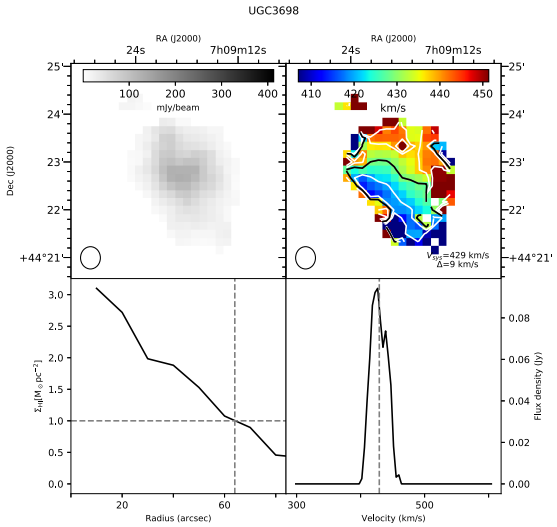
UGC3698
RA (J2000)
Dec (J2000)
mJy/beam
km/s
V_{sys}=429 km/s
Δ=9 km/s
Radius (arcsec)
Velocity (km/s)
Flux density (Jy)

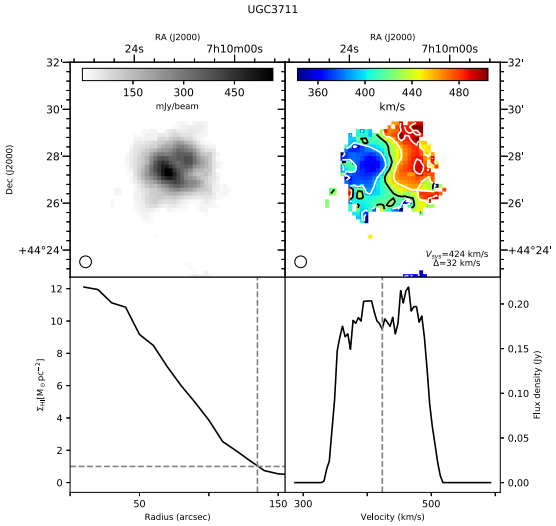
UGC3711
RA (J2000)
Dec (J2000)
mJy/beam
km/s
Radius (arcsec)
Velocity (km/s)
Flux density (Jy)

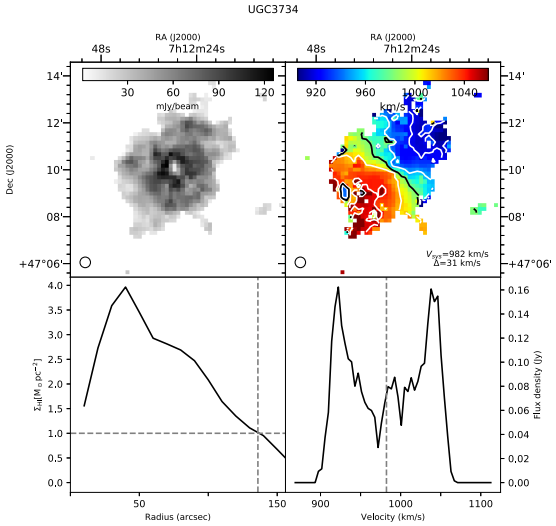
UGC3734
RA (J2000)
Dec (J2000)
mJy/beam
km/s
Radius (arcsec)
Velocity (km/s)
Flux density (Jy)

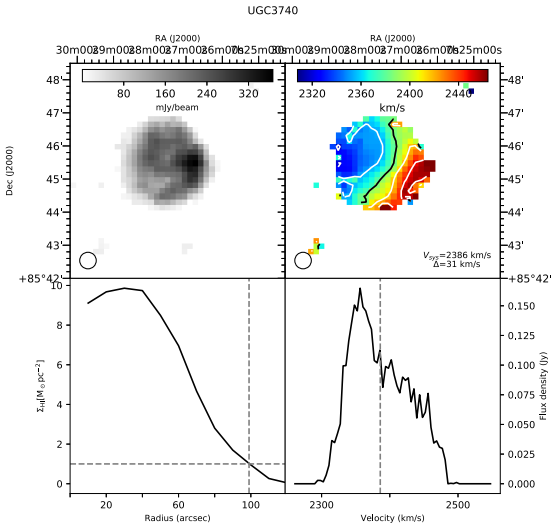
UGC3740
RA (J2000)
Dec (J2000)
mJy/beam
km/s
Radius (arcsec)
Velocity (km/s)
Flux density (Jy)

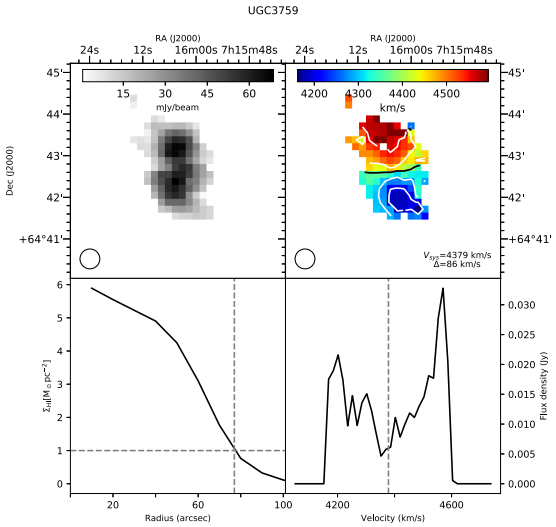
UGC3759
RA (J2000)
Dec (J2000)
mJy/beam
km/s
Radius (arcsec)
Velocity (km/s)
Flux density (Jy)

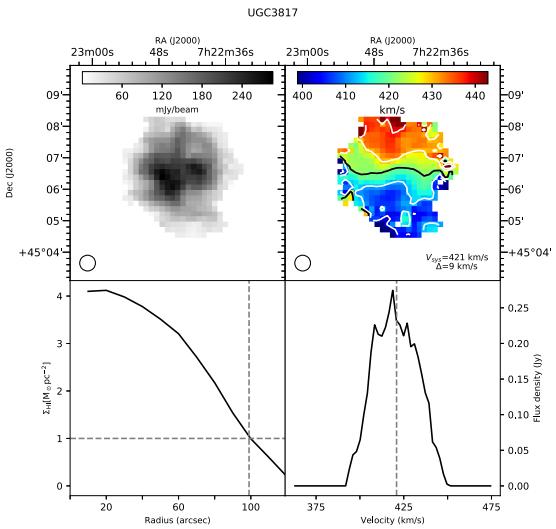
UGC3817
RA (J2000)
Dec (J2000)
mJy/beam
km/s
Radius (arcsec)
Velocity (km/s)
Flux density (Jy)

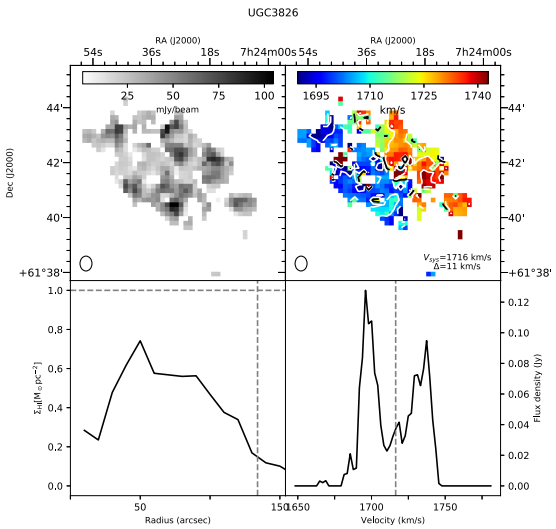
UGC3826
RA (J2000)
Dec (J2000)
mJy/beam
km/s
Radius (arcsec)
Velocity (km/s)
Flux density (Jy)

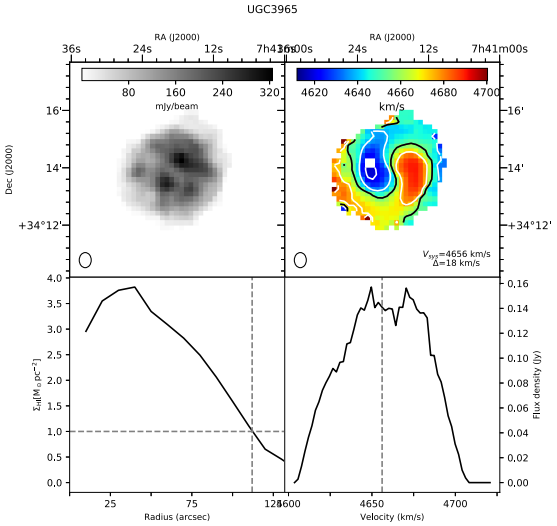
UGC3965
RA (J2000)
Dec (J2000)
mJy/beam
km/s
V_{sys}=4656 km/s
Δ=18 km/s
$\Sigma_{HI}[M_\odot pc^{-2}]$
Flux density (Jy)
Radius (arcsec)
Velocity (km/s)

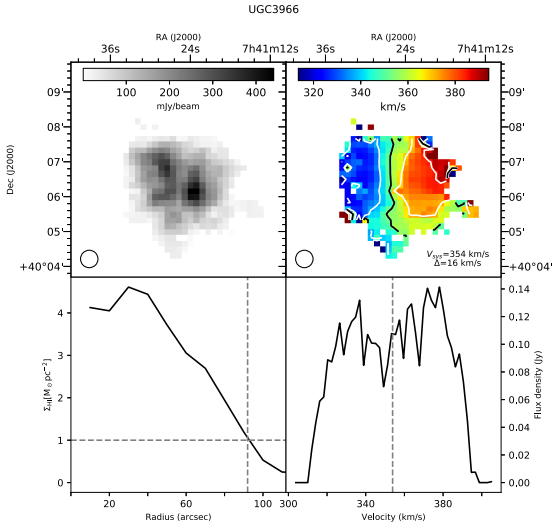
UGC3966
RA (J2000)
Dec (J2000)
mJy/beam
km/s
V_{sys}=354 km/s
Δ=16 km/s
$\Sigma_{HI}[M_\odot pc^{-2}]$
Flux density (Jy)
Radius (arcsec)
Velocity (km/s)

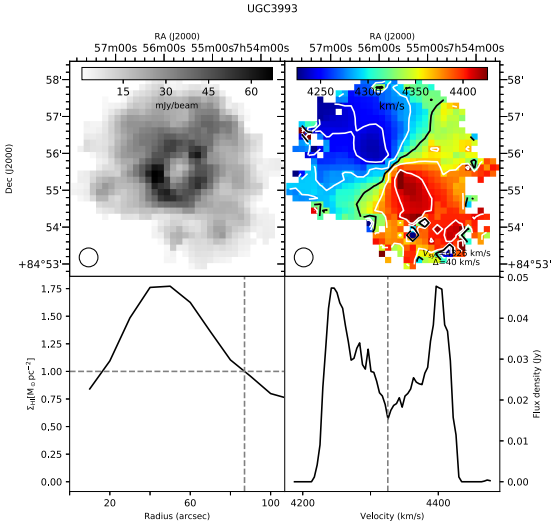
UGC3993
RA (J2000)
Dec (J2000)
mJy/beam
km/s
V_{sys}=4338 km/s
Δ=40 km/s
$\Sigma_{HI}[M_\odot pc^{-2}]$
Flux density (Jy)
Radius (arcsec)
Velocity (km/s)

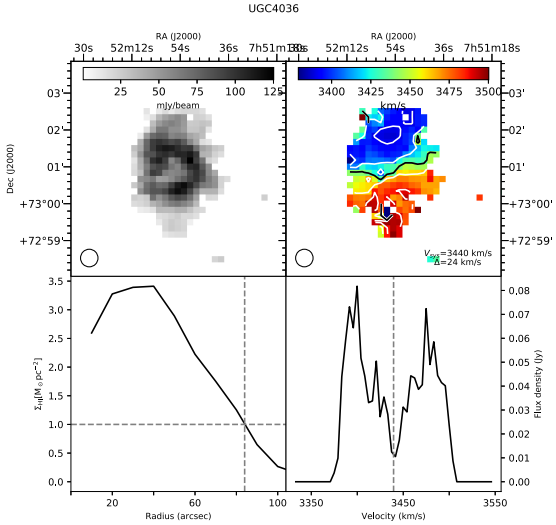
UGC4036
RA (J2000)
Dec (J2000)
mJy/beam
km/s
V_{sys}=3440 km/s
Δ=24 km/s
$\Sigma_{HI}[M_\odot pc^{-2}]$
Flux density (Jy)
Radius (arcsec)
Velocity (km/s)

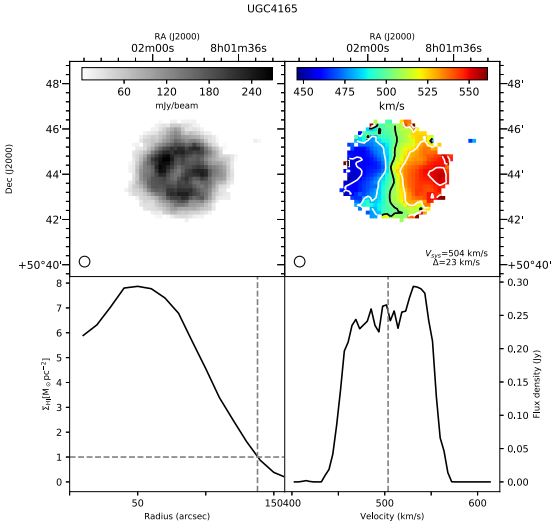
UGC4165
RA (J2000)
Dec (J2000)
mJy/beam
km/s
V_{sys}=504 km/s
Δ=23 km/s
$\Sigma_{HI}[M_\odot pc^{-2}]$
Flux density (Jy)
Radius (arcsec)
Velocity (km/s)

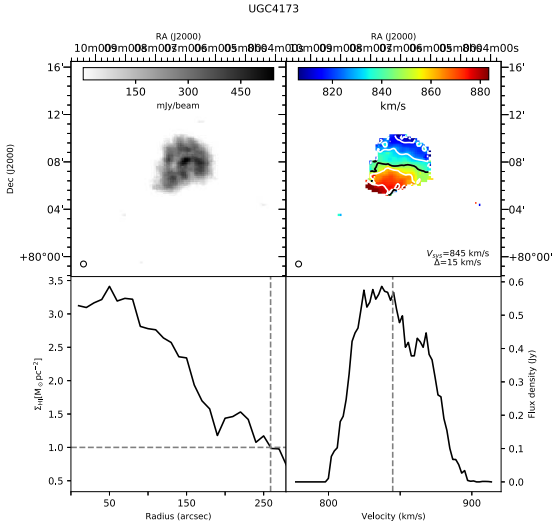
UGC4173
RA (J2000)
Dec (J2000)
mJy/beam
km/s
V_{sys}=845 km/s
Δ=15 km/s
$\Sigma_{HI}[M_\odot pc^{-2}]$
Flux density (Jy)
Radius (arcsec)
Velocity (km/s)

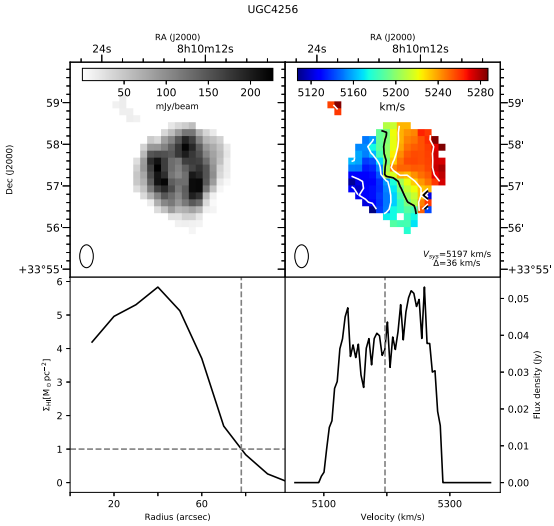
UGC4256
RA (J2000)
Dec (J2000)
mJy/beam
km/s
Radius (arcsec)
Velocity (km/s)
Flux density (Jy)

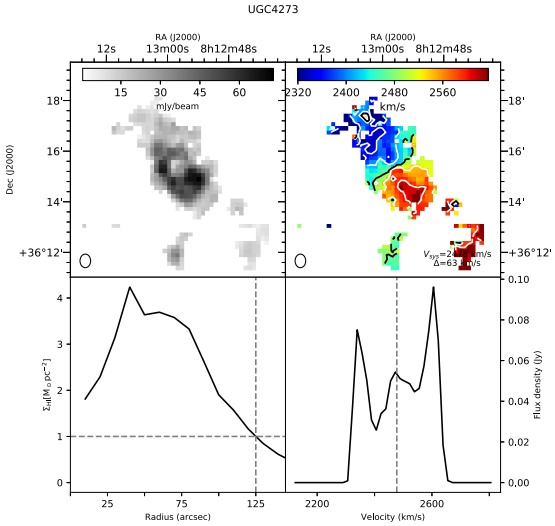
UGC4273
RA (J2000)
Dec (J2000)
mJy/beam
km/s
Radius (arcsec)
Velocity (km/s)
Flux density (Jy)

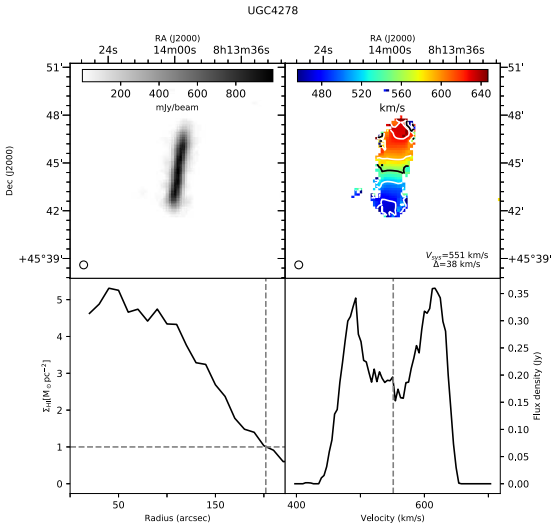
UGC4278
RA (J2000)
Dec (J2000)
mJy/beam
km/s
Radius (arcsec)
Velocity (km/s)
Flux density (Jy)

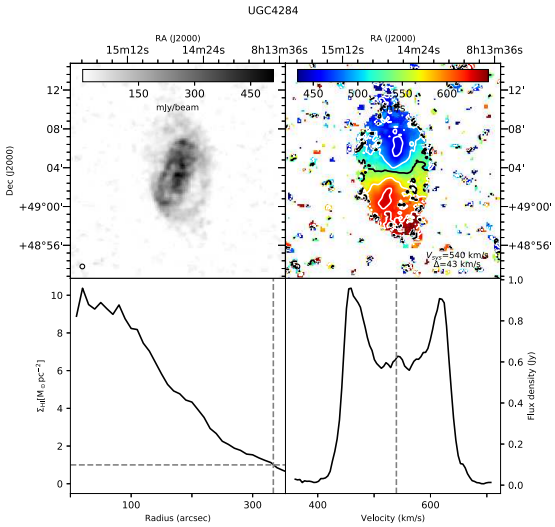
UGC4284
RA (J2000)
Dec (J2000)
mJy/beam
km/s
Radius (arcsec)
Velocity (km/s)
Flux density (Jy)

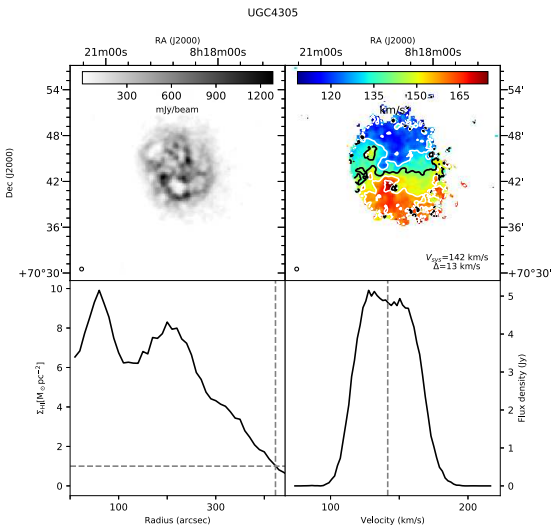
UGC4305
RA (J2000)
Dec (J2000)
mJy/beam
km/s
Radius (arcsec)
Velocity (km/s)
Flux density (Jy)

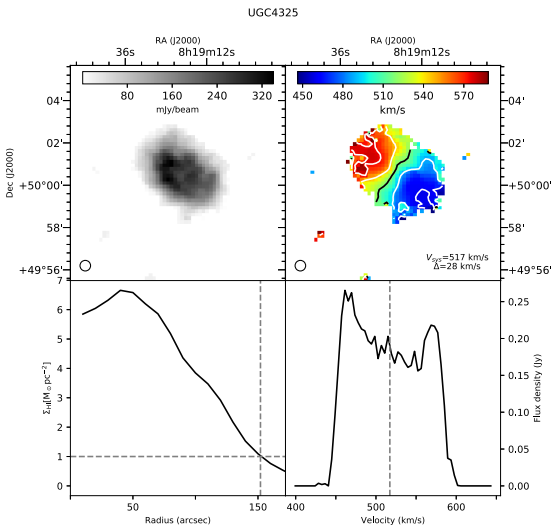
UGC4325
RA (J2000)
Dec (J2000)
mJy/beam
km/s
Radius (arcsec)
Velocity (km/s)
Flux density (Jy)

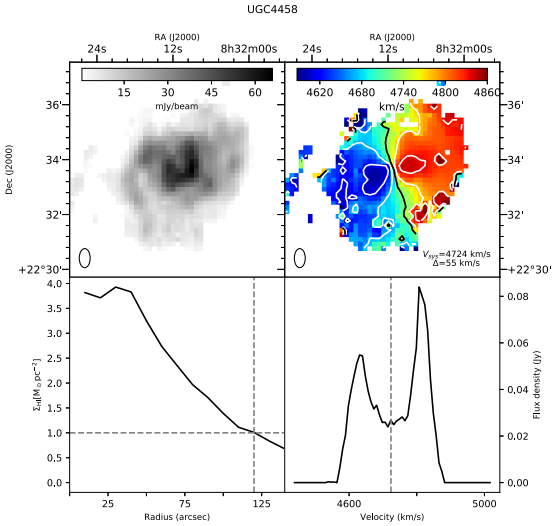
UGC4458
RA (J2000)
Dec (J2000)
mJy/beam
km/s
V_{sys}=4724 km/s
Δ=55 km/s
Radius (arcsec)
Velocity (km/s)
Flux density (Jy)

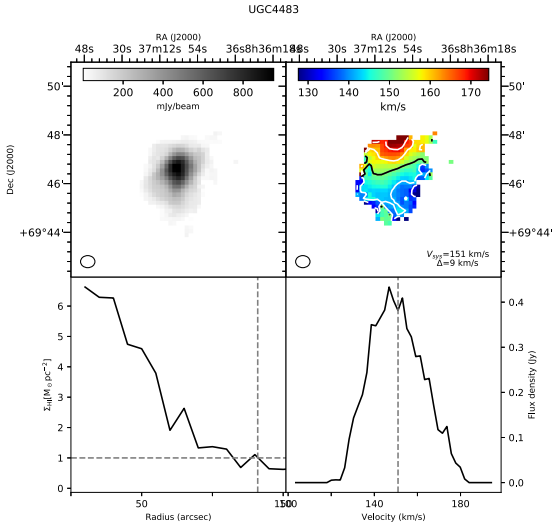
UGC4483
RA (J2000)
Dec (J2000)
mJy/beam
km/s
V_{sys}=151 km/s
Δ=9 km/s
Radius (arcsec)
Velocity (km/s)
Flux density (Jy)

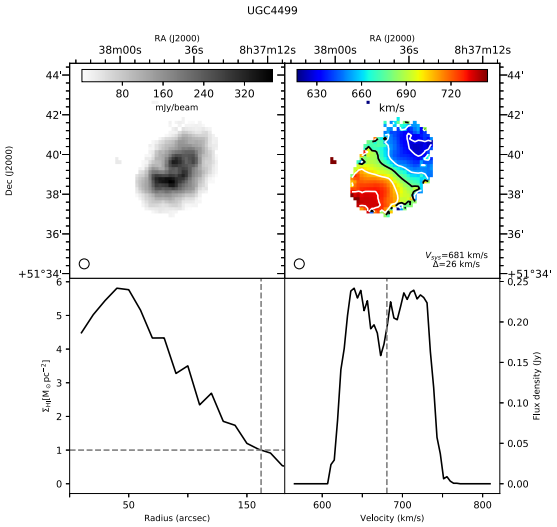
UGC4499
RA (J2000)
Dec (J2000)
mJy/beam
km/s
V_{sys}=681 km/s
Δ=26 km/s
Radius (arcsec)
Velocity (km/s)
Flux density (Jy)

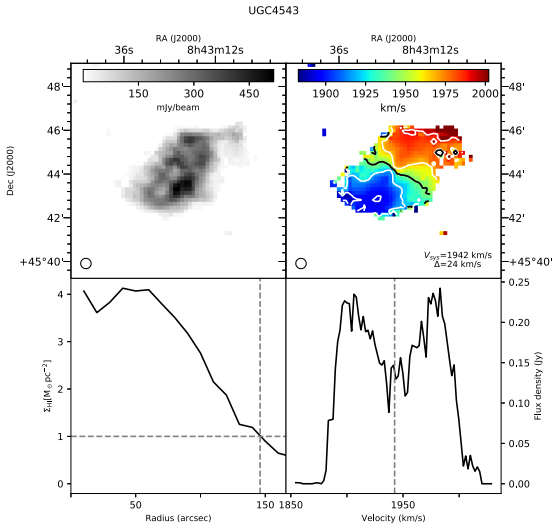
UGC4543
RA (J2000)
Dec (J2000)
mJy/beam
km/s
V_{sys}=1942 km/s
Δ=24 km/s
Radius (arcsec)
Velocity (km/s)
Flux density (Jy)

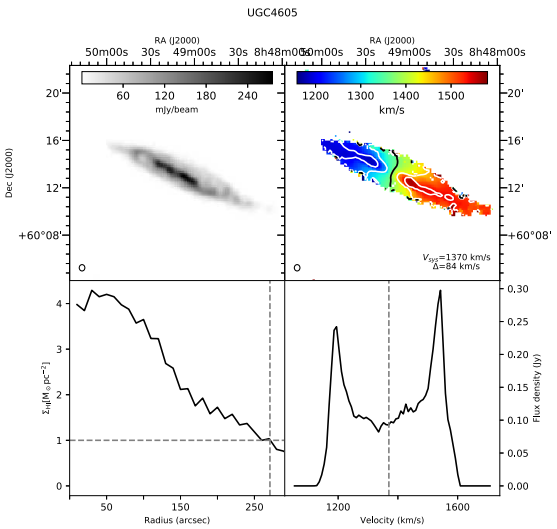
UGC4605
RA (J2000)
Dec (J2000)
mJy/beam
km/s
V_{sys}=1370 km/s
Δ=84 km/s
Radius (arcsec)
Velocity (km/s)
Flux density (Jy)

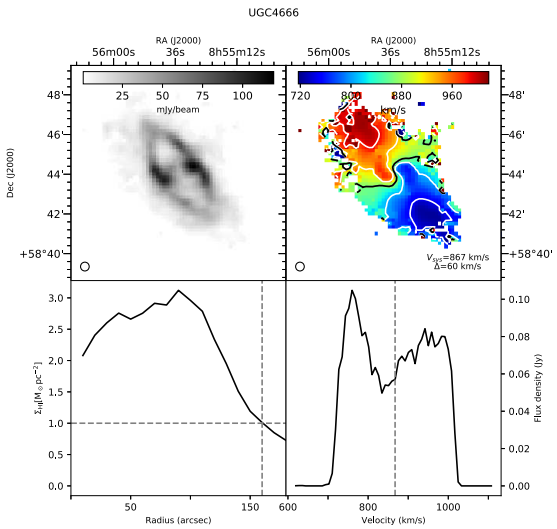
UGC4666
RA (J2000)
Dec (J2000)
mJy/beam
km/s
V_{sys}=867 km/s
Δ=60 km/s
Radius (arcsec)
Velocity (km/s)
Flux density (Jy)

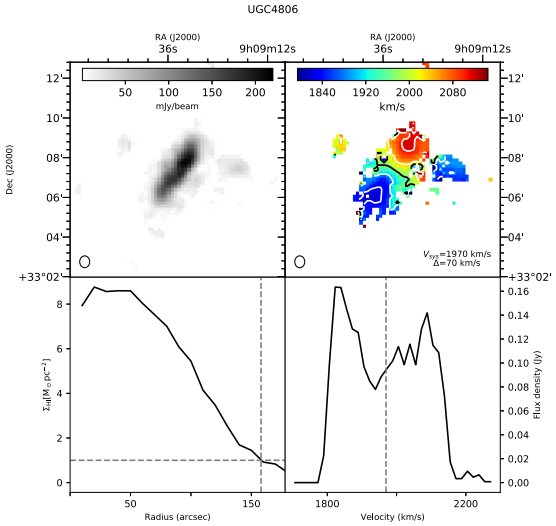
UGC4806
RA (J2000)
Dec (J2000)
mJy/beam
km/s
V_{sys}=1970 km/s
Δ=70 km/s
Radius (arcsec)
Velocity (km/s)
Flux density (Jy)

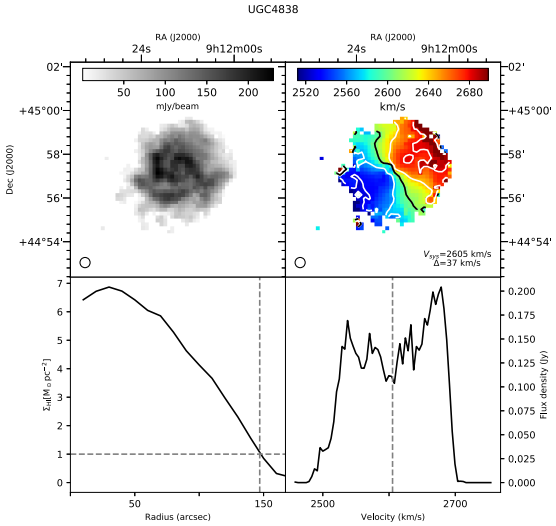
UGC4838
RA (J2000)
Dec (J2000)
mJy/beam
km/s
V_{sys}=2605 km/s
Δ=37 km/s
Radius (arcsec)
Velocity (km/s)
Flux density (Jy)

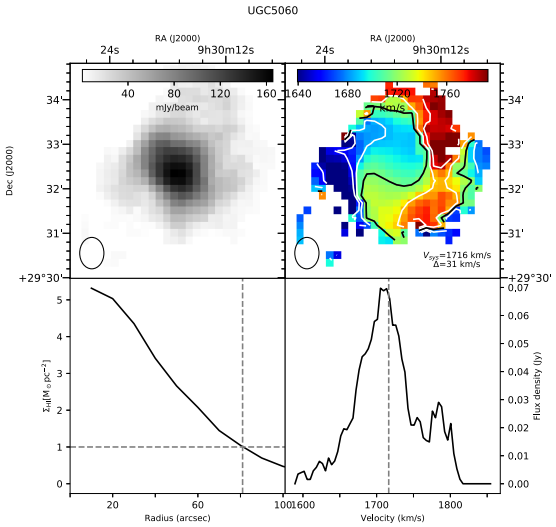
UGC5060
RA (J2000)
Dec (J2000)
mJy/beam
km/s
V_{sys}=1716 km/s
Δ=31 km/s
Radius (arcsec)
Velocity (km/s)
Flux density (Jy)

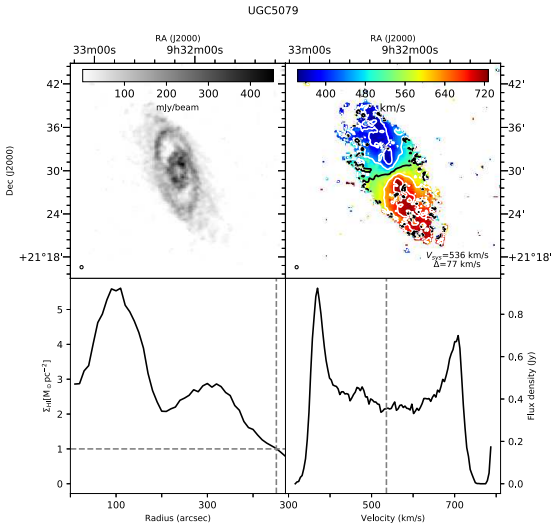
UGC5079
RA (J2000)
Dec (J2000)
mJy/beam
km/s
V_{sys}=536 km/s
Δ=77 km/s
Radius (arcsec)
Velocity (km/s)
Flux density (Jy)

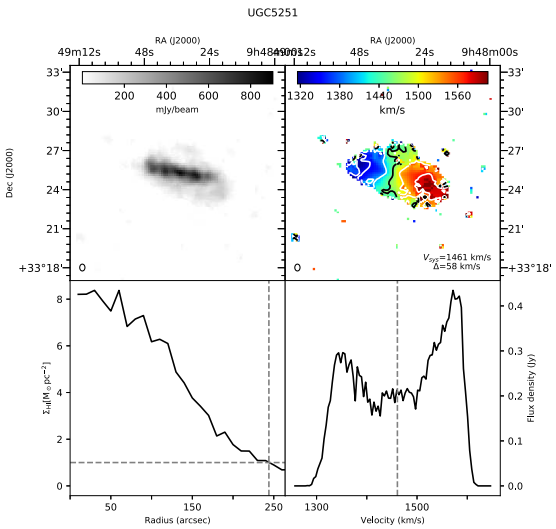
UGC5251
RA (J2000)
Dec (J2000)
mJy/beam
km/s
V_{sys}=1461 km/s
Δ=58 km/s
Radius (arcsec)
Velocity (km/s)
Flux density (Jy)

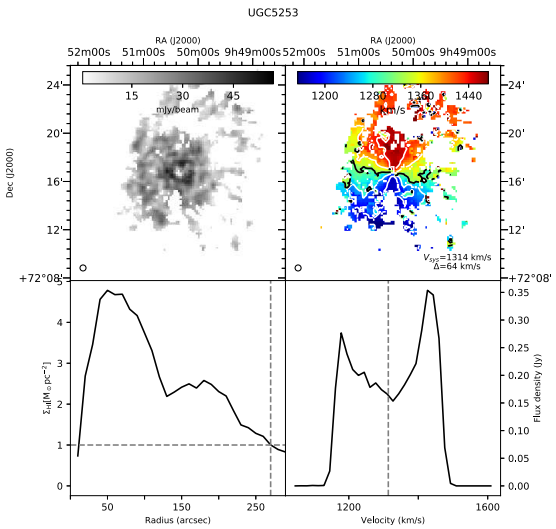
UGC5253
RA (J2000)
Dec (J2000)
mJy/beam
km/s
V_{sys}=1314 km/s
Δ=64 km/s
Radius (arcsec)
Velocity (km/s)
Flux density (Jy)

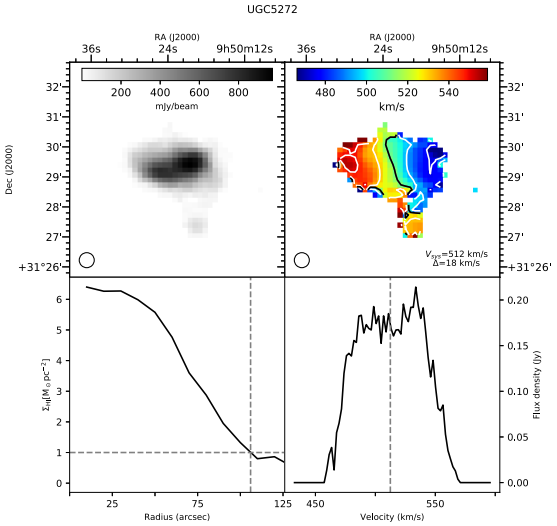
UGC5272
RA (J2000)
Dec (J2000)
mJy/beam
km/s
V_{sys}=512 km/s
Δ=18 km/s
Radius (arcsec)
Velocity (km/s)
Flux density (Jy)

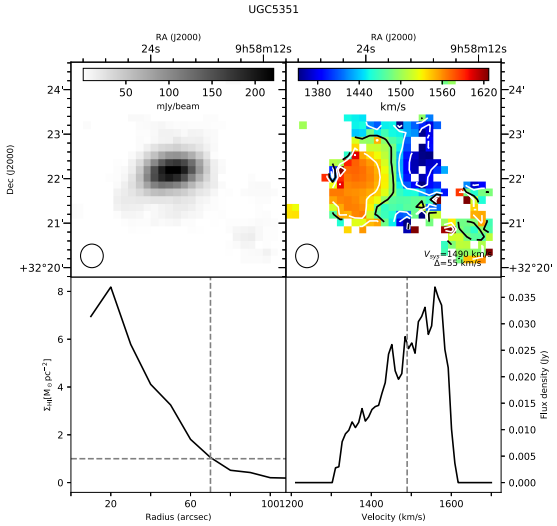
UGC5351
RA (J2000)
Dec (J2000)
mJy/beam
km/s
V_{sys}=1490 km/s
Δ=55 km/s
Radius (arcsec)
Velocity (km/s)
Flux density (Jy)

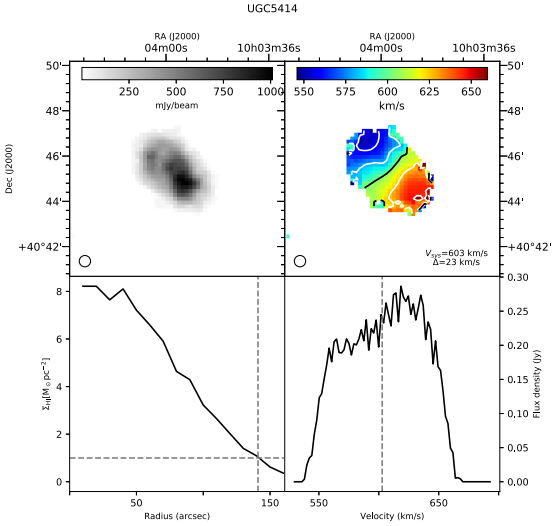
UGC5414
RA (J2000)
Dec (J2000)
mJy/beam
km/s
V_{sys}=603 km/s
Δ=23 km/s
Radius (arcsec)
Velocity (km/s)
Flux density (Jy)

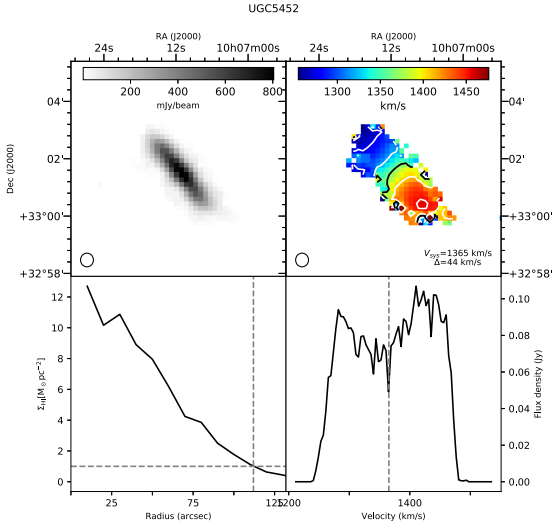
UGC5452
RA (J2000)
Dec (J2000)
mJy/beam
km/s
V_{sys}=1365 km/s
Δ=44 km/s
Radius (arcsec)
Velocity (km/s)
Flux density (Jy)

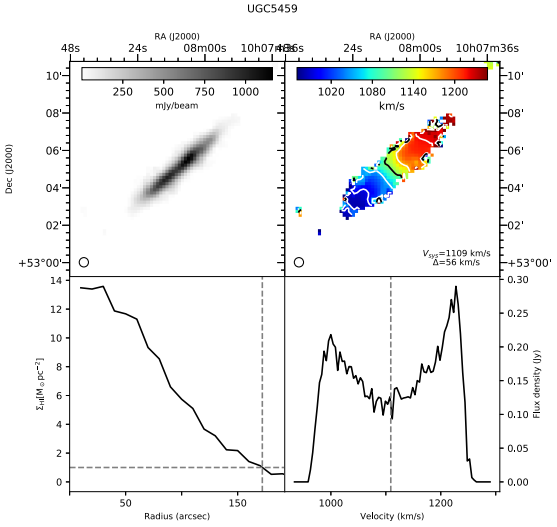
UGC5459
RA (J2000)
Dec (J2000)
mJy/beam
km/s
V_{sys}=1109 km/s
Δ=56 km/s
Radius (arcsec)
Velocity (km/s)
Flux density (Jy)

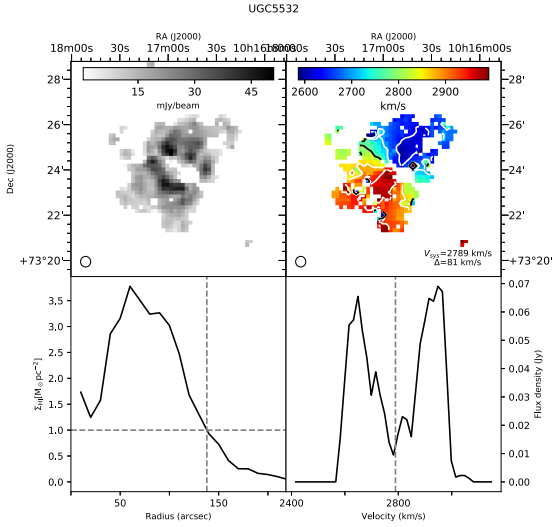
UGC5532
RA (J2000)
Dec (J2000)
mJy/beam
km/s
V_{sys}=2789 km/s
Δ=81 km/s
Radius (arcsec)
Velocity (km/s)
Flux density (Jy)

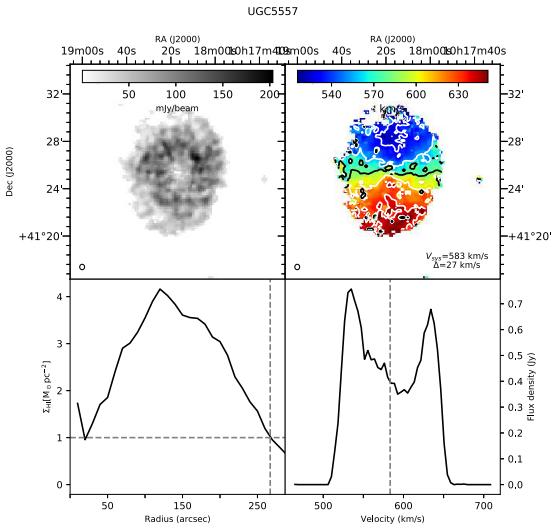
UGC5557
RA (J2000)
Dec (J2000)
mJy/beam
km/s
V_{sys}=583 km/s
Δ=27 km/s
Σ_{HI}[M$_\odot$ pc^{-2}]
Flux density (Jy)
Radius (arcsec)
Velocity (km/s)

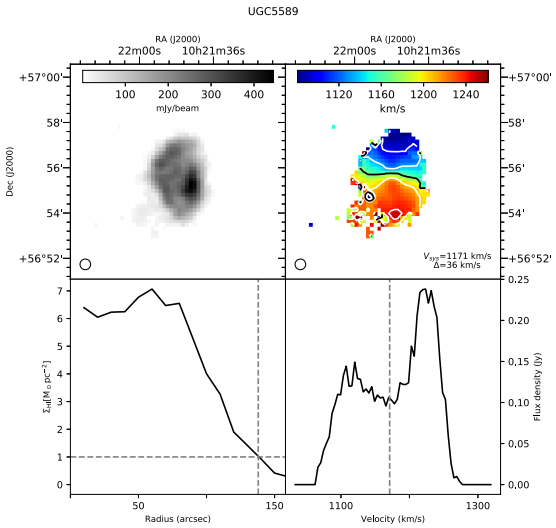
UGC5589
RA (J2000)
Dec (J2000)
mJy/beam
km/s
V_{sys}=1171 km/s
Δ=36 km/s
Σ_{HI}[M$_\odot$ pc^{-2}]
Flux density (Jy)
Radius (arcsec)
Velocity (km/s)

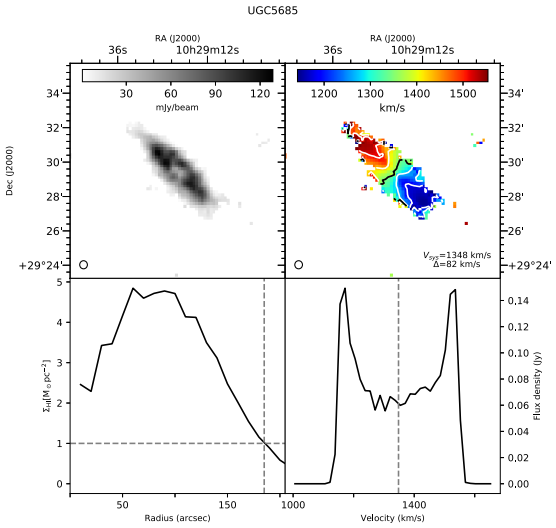
UGC5685
RA (J2000)
Dec (J2000)
mJy/beam
km/s
V_{sys}=1348 km/s
Δ=82 km/s
Σ_{HI}[M$_\odot$ pc^{-2}]
Flux density (Jy)
Radius (arcsec)
Velocity (km/s)

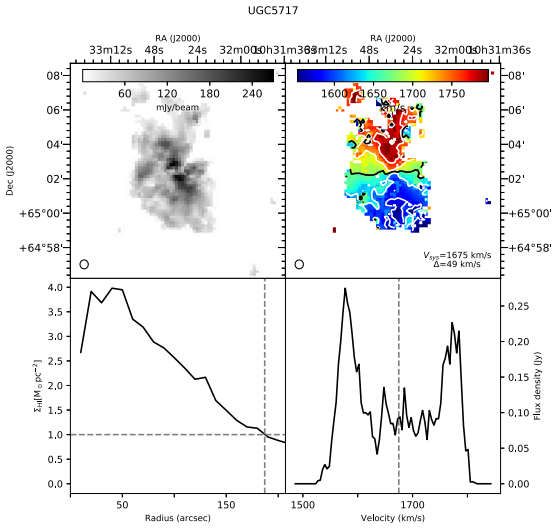
UGC5717
RA (J2000)
Dec (J2000)
mJy/beam
km/s
V_{sys}=1675 km/s
Δ=49 km/s
Σ_{HI}[M$_\odot$ pc^{-2}]
Flux density (Jy)
Radius (arcsec)
Velocity (km/s)

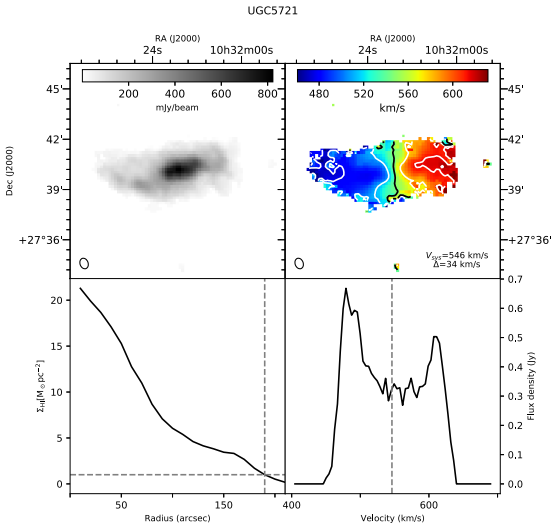
UGC5721
RA (J2000)
Dec (J2000)
mJy/beam
km/s
V_{sys}=546 km/s
Δ=34 km/s
Σ_{HI}[M$_\odot$ pc^{-2}]
Flux density (Jy)
Radius (arcsec)
Velocity (km/s)

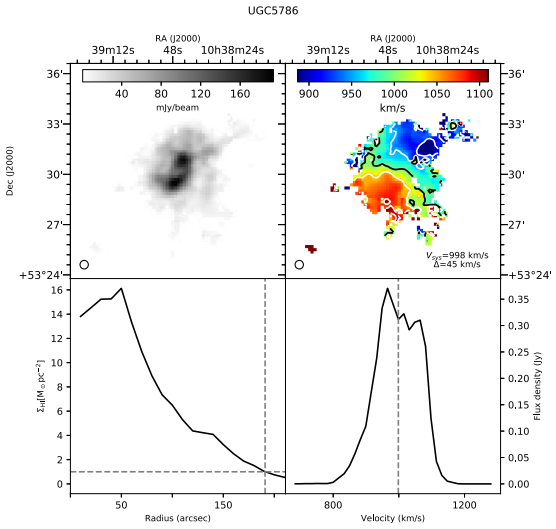
UGC5786
RA (J2000)
Dec (J2000)
mJy/beam
km/s
V_{sys}=998 km/s
Δ=45 km/s
Σ_{HI}[M$_\odot$ pc^{-2}]
Flux density (Jy)
Radius (arcsec)
Velocity (km/s)

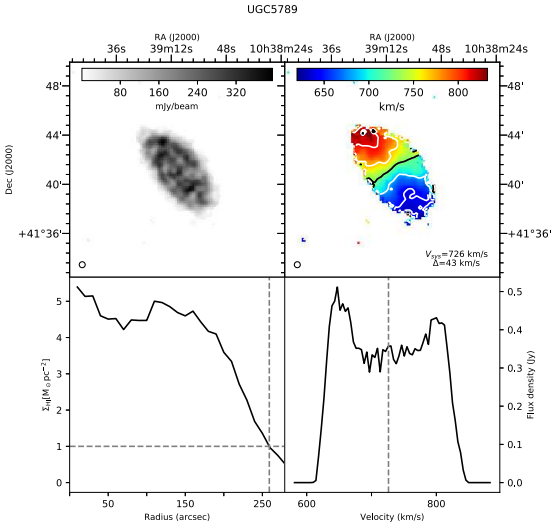
UGC5789
RA (J2000)
Dec (J2000)
mJy/beam
km/s
V_{sys}=726 km/s
Δ=43 km/s
Σ_{HI}[$M_\odot$ pc^{-2}]
Flux density (Jy)
Radius (arcsec)
Velocity (km/s)

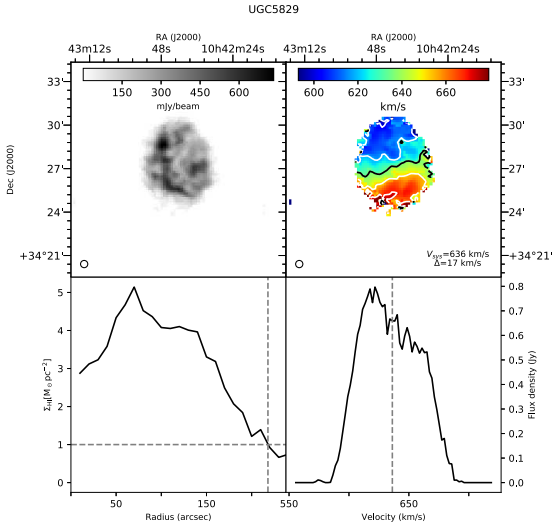
UGC5829
RA (J2000)
Dec (J2000)
mJy/beam
km/s
V_{sys}=636 km/s
Δ=17 km/s
Σ_{HI}[$M_\odot$ pc^{-2}]
Flux density (Jy)
Radius (arcsec)
Velocity (km/s)

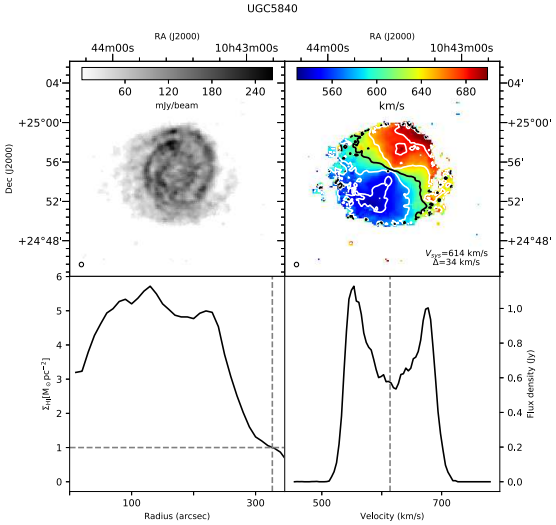
UGC5840
RA (J2000)
Dec (J2000)
mJy/beam
km/s
V_{sys}=614 km/s
Δ=34 km/s
Σ_{HI}[$M_\odot$ pc^{-2}]
Flux density (Jy)
Radius (arcsec)
Velocity (km/s)

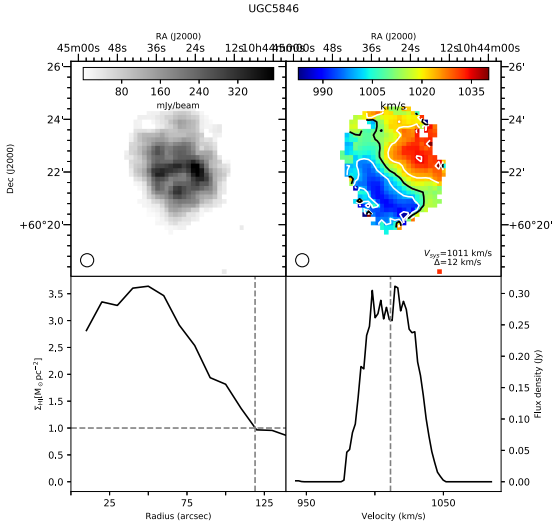
UGC5846
RA (J2000)
Dec (J2000)
mJy/beam
km/s
V_{sys}=1011 km/s
Δ=12 km/s
Σ_{HI}[$M_\odot$ pc^{-2}]
Flux density (Jy)
Radius (arcsec)
Velocity (km/s)

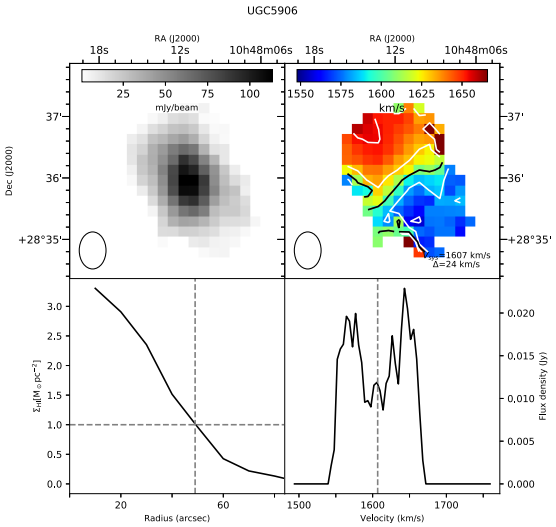
UGC5906
RA (J2000)
Dec (J2000)
mJy/beam
km/s
V_{sys}=1607 km/s
Δ=24 km/s
Σ_{HI}[$M_\odot$ pc^{-2}]
Flux density (Jy)
Radius (arcsec)
Velocity (km/s)

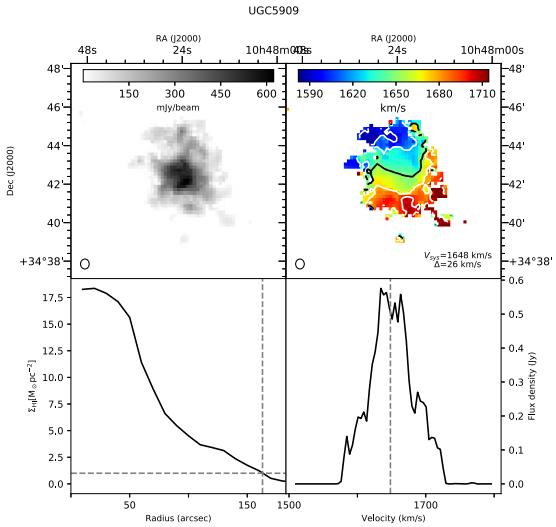
UGC5909
RA (J2000)
Dec (J2000)
mJy/beam
km/s
V_{sys}=1648 km/s
Δ=26 km/s
Σ_{HI}[$M_\odot$ pc^{-2}]
Flux density (Jy)
Radius (arcsec)
Velocity (km/s)

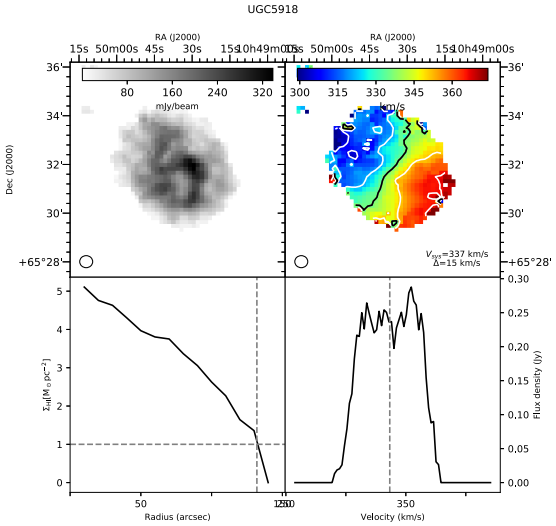
UGC5918
RA (J2000)
Dec (J2000)
mJy/beam
km/s
V_{sys}=337 km/s
Δ=15 km/s
Σ_{HI}[M$_\odot$pc^{-2}]
Flux density (Jy)
Radius (arcsec)
Velocity (km/s)

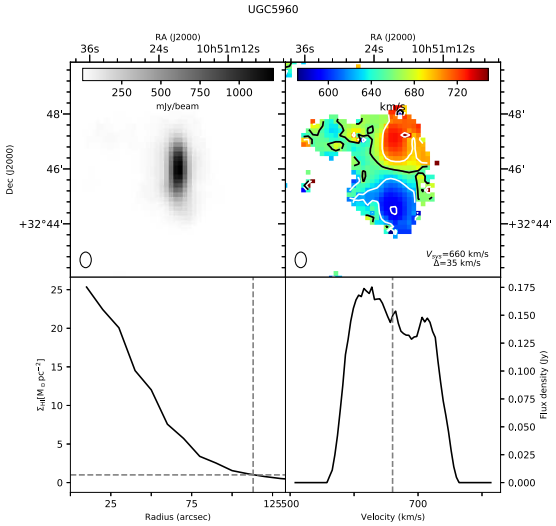
UGC5960
RA (J2000)
Dec (J2000)
mJy/beam
km/s
V_{sys}=660 km/s
Δ=35 km/s
Σ_{HI}[M$_\odot$pc^{-2}]
Flux density (Jy)
Radius (arcsec)
Velocity (km/s)

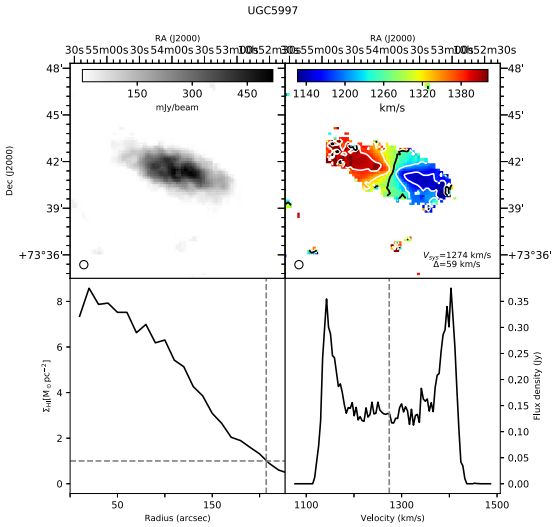
UGC5997
RA (J2000)
Dec (J2000)
mJy/beam
km/s
V_{sys}=1274 km/s
Δ=59 km/s
Σ_{HI}[M$_\odot$pc^{-2}]
Flux density (Jy)
Radius (arcsec)
Velocity (km/s)

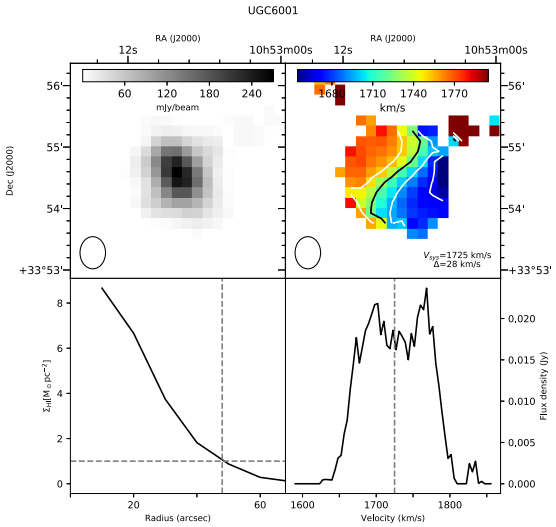
UGC6001
RA (J2000)
Dec (J2000)
mJy/beam
km/s
V_{sys}=1725 km/s
Δ=28 km/s
Σ_{HI}[M$_\odot$pc^{-2}]
Flux density (Jy)
Radius (arcsec)
Velocity (km/s)

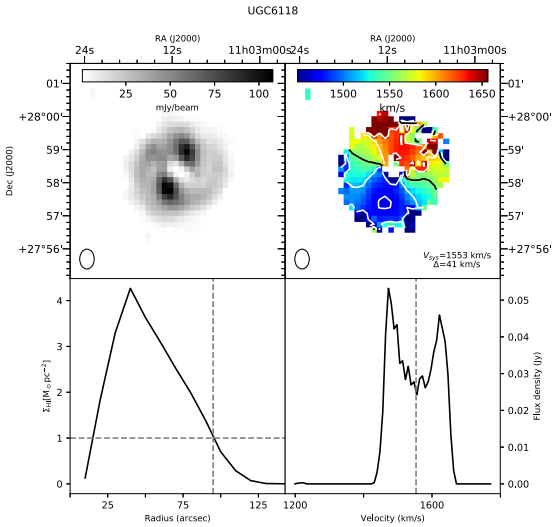
UGC6118
RA (J2000)
Dec (J2000)
mJy/beam
km/s
V_{sys}=1553 km/s
Δ=41 km/s
Σ_{HI}[M$_\odot$pc^{-2}]
Flux density (Jy)
Radius (arcsec)
Velocity (km/s)

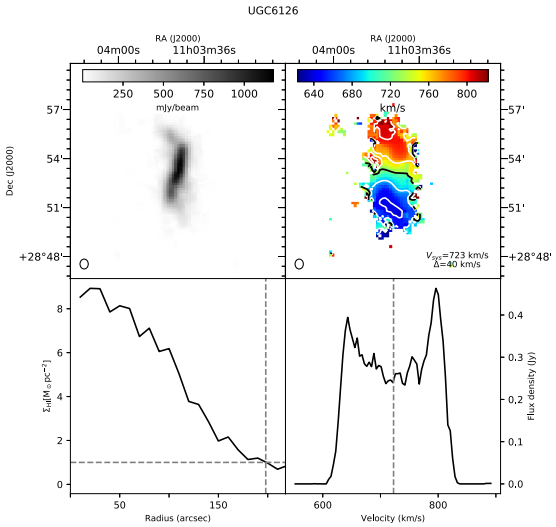
UGC6126
RA (J2000)
Dec (J2000)
mJy/beam
km/s
V_{sys}=723 km/s
Δ=40 km/s
Σ_{HI}[M$_\odot$pc^{-2}]
Flux density (Jy)
Radius (arcsec)
Velocity (km/s)

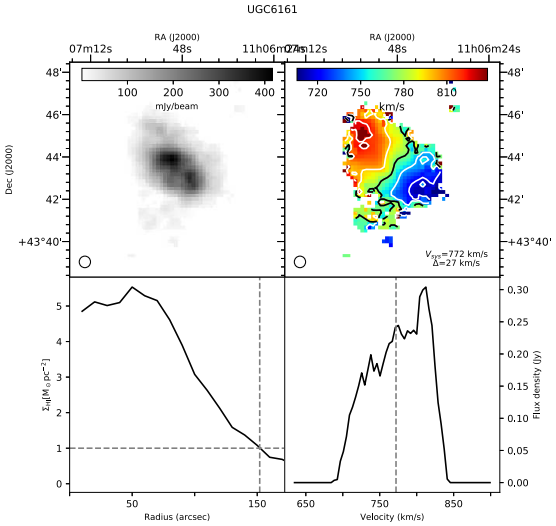
UGC6161
RA (J2000)
Dec (J2000)
mJy/beam
km/s
V_{sys}=772 km/s
Δ=27 km/s
Σ_{HI}[$M_\odot$ pc^{-2}]
Flux density (Jy)
Radius (arcsec)
Velocity (km/s)

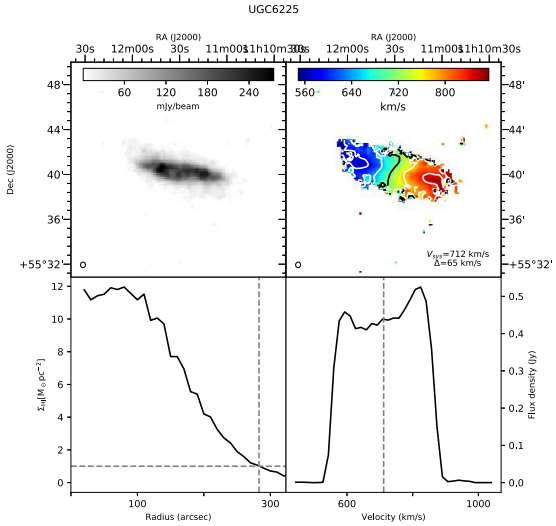
UGC6225
RA (J2000)
Dec (J2000)
mJy/beam
km/s
V_{sys}=712 km/s
Δ=65 km/s
Σ_{HI}[$M_\odot$ pc^{-2}]
Flux density (Jy)
Radius (arcsec)
Velocity (km/s)

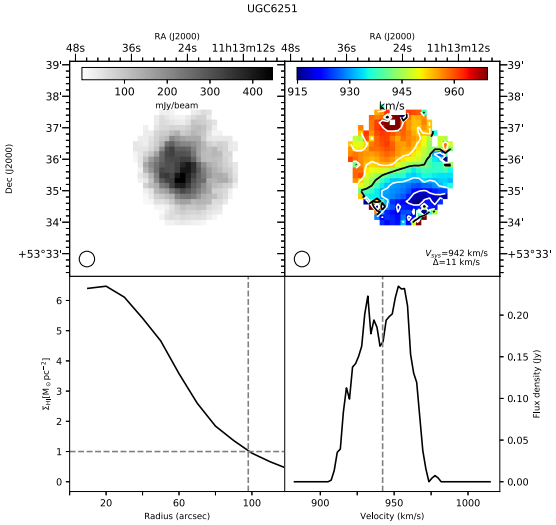
UGC6251
RA (J2000)
Dec (J2000)
mJy/beam
km/s
V_{sys}=942 km/s
Δ=11 km/s
Σ_{HI}[$M_\odot$ pc^{-2}]
Flux density (Jy)
Radius (arcsec)
Velocity (km/s)

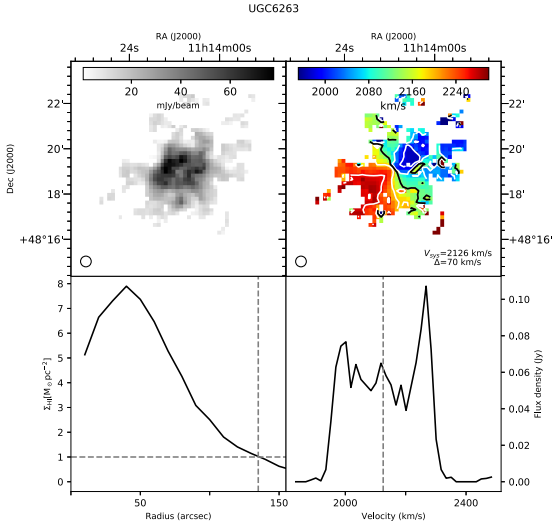
UGC6263
RA (J2000)
Dec (J2000)
mJy/beam
km/s
V_{sys}=2126 km/s
Δ=70 km/s
Σ_{HI}[$M_\odot$ pc^{-2}]
Flux density (Jy)
Radius (arcsec)
Velocity (km/s)

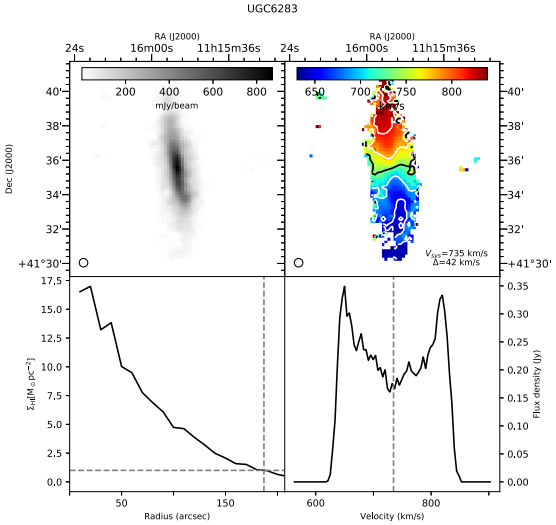
UGC6283
RA (J2000)
Dec (J2000)
mJy/beam
km/s
V_{sys}=735 km/s
Δ=42 km/s
Σ_{HI}[$M_\odot$ pc^{-2}]
Flux density (Jy)
Radius (arcsec)
Velocity (km/s)

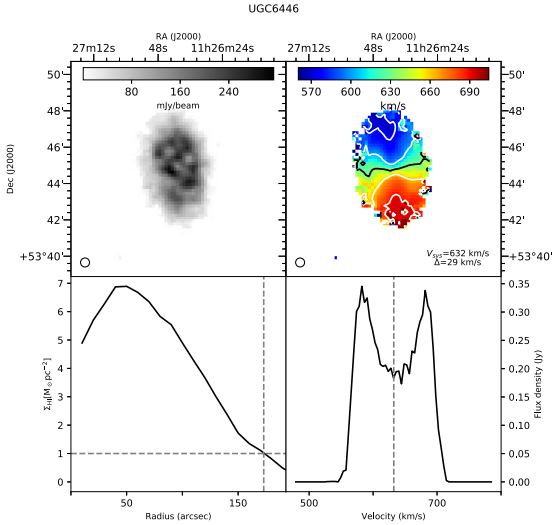
UGC6446
RA (J2000)
Dec (J2000)
mJy/beam
km/s
V_{sys}=632 km/s
Δ=29 km/s
Σ_{HI}[$M_\odot$ pc^{-2}]
Flux density (Jy)
Radius (arcsec)
Velocity (km/s)

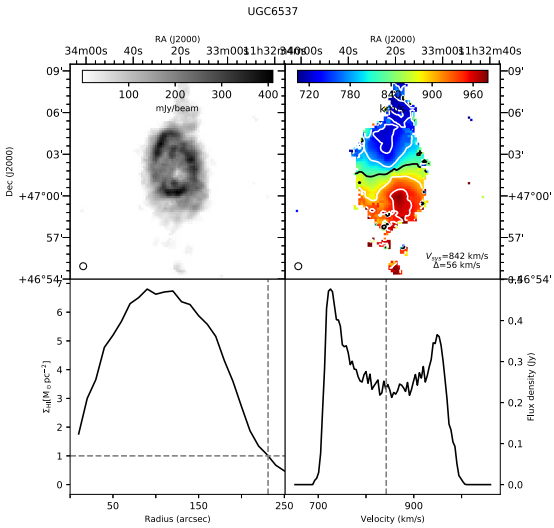
UGC6537
RA (J2000)
Dec (J2000)
mJy/beam
km/s
V_{sys}=842 km/s
Δ=56 km/s
Radius (arcsec)
Velocity (km/s)
Flux density (Jy)

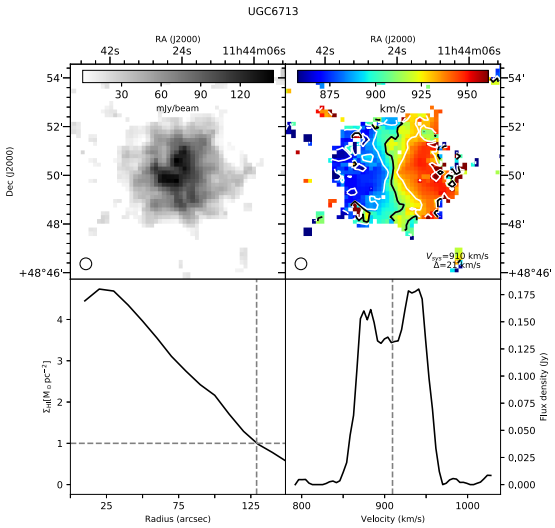
UGC6713
RA (J2000)
Dec (J2000)
mJy/beam
km/s
V_{sys}=910 km/s
Δ=214 km/s
Radius (arcsec)
Velocity (km/s)
Flux density (Jy)

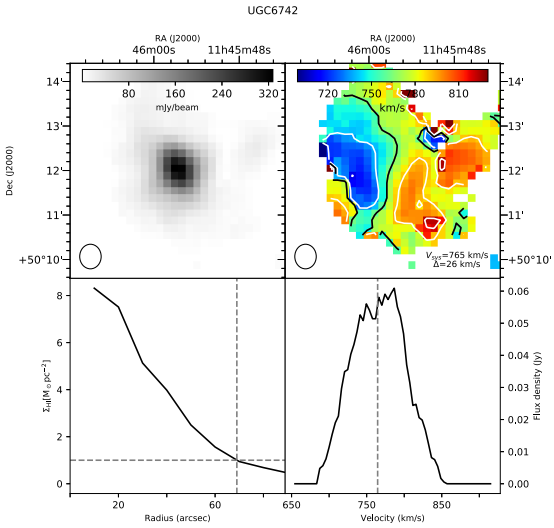
UGC6742
RA (J2000)
Dec (J2000)
mJy/beam
km/s
V_{sys}=765 km/s
Δ=26 km/s
Radius (arcsec)
Velocity (km/s)
Flux density (Jy)

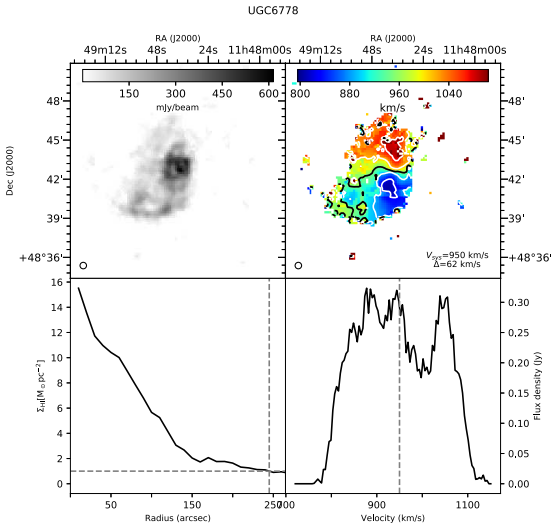
UGC6778
RA (J2000)
Dec (J2000)
mJy/beam
km/s
V_{sys}=950 km/s
Δ=62 km/s
Radius (arcsec)
Velocity (km/s)
Flux density (Jy)

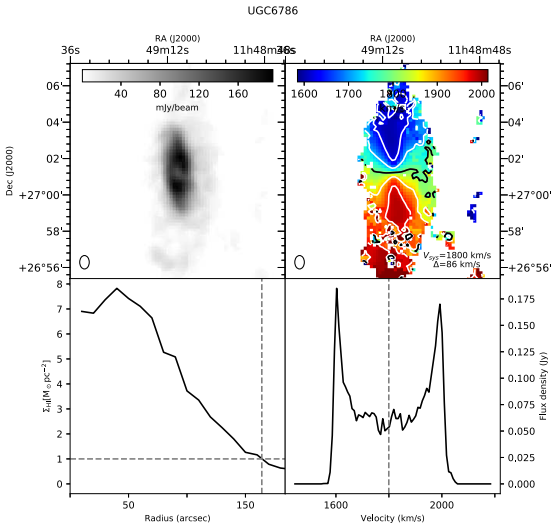
UGC6786
RA (J2000)
Dec (J2000)
mJy/beam
km/s
V_{sys}=1800 km/s
Δ=86 km/s
Radius (arcsec)
Velocity (km/s)
Flux density (Jy)

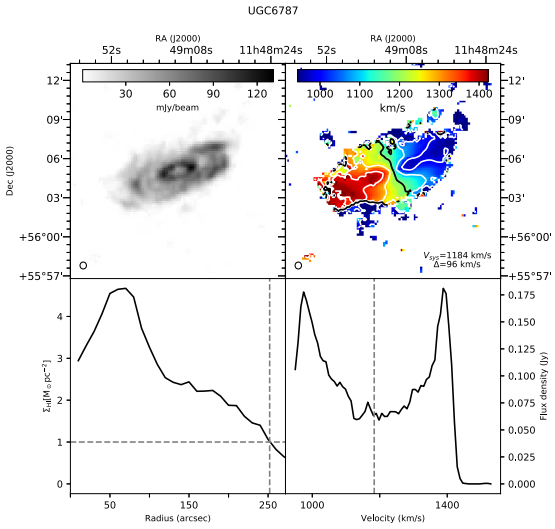
UGC6787
RA (J2000)
Dec (J2000)
mJy/beam
km/s
V_{sys}=1184 km/s
Δ=96 km/s
Radius (arcsec)
Velocity (km/s)
Flux density (Jy)

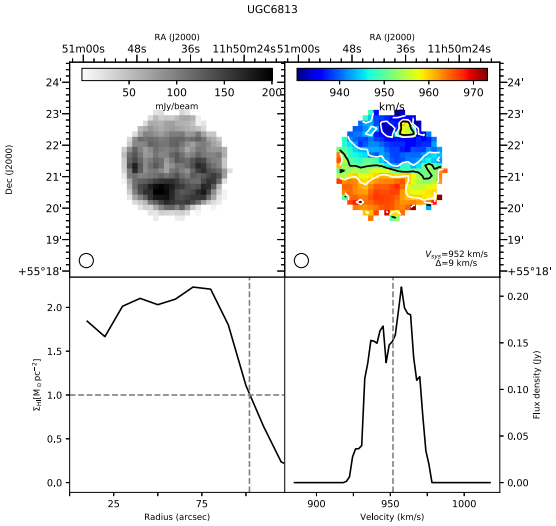
UGC6813
RA (J2000)
Dec (J2000)
mJy/beam
km/s
V_{sys}=952 km/s
Δ=9 km/s
Radius (arcsec)
Velocity (km/s)
Flux density (Jy)

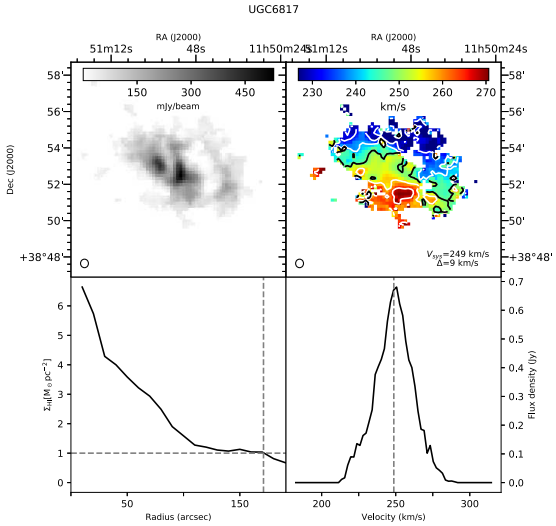
UGC6817
RA (J2000)
Dec (J2000)
mJy/beam
km/s
V_{sys}=249 km/s
Δ=9 km/s
Radius (arcsec)
Velocity (km/s)
Flux density (Jy)

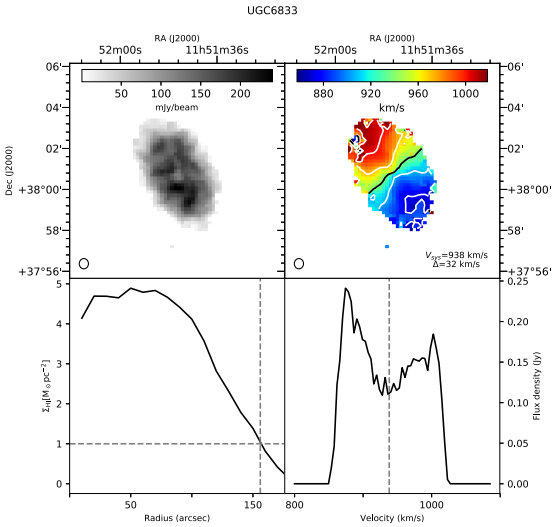
UGC6833
RA (J2000)
Dec (J2000)
mJy/beam
km/s
V_{sys}=938 km/s
Δ=32 km/s
Radius (arcsec)
Velocity (km/s)
Flux density (Jy)

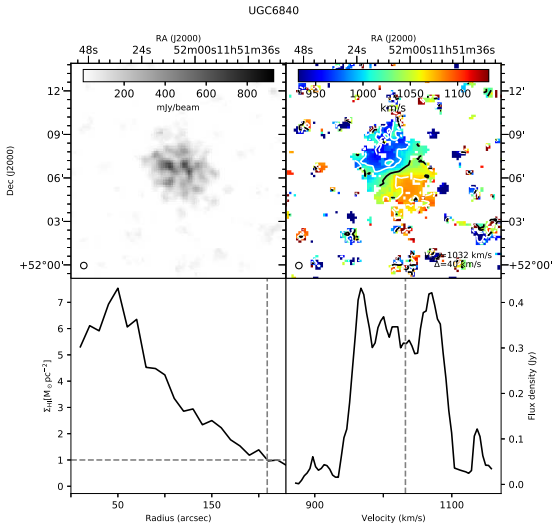
UGC6840
RA (J2000)
Dec (J2000)
mJy/beam
km/s
V_{sys}=1032 km/s
Δ=40 km/s
Radius (arcsec)
Velocity (km/s)
Flux density (Jy)

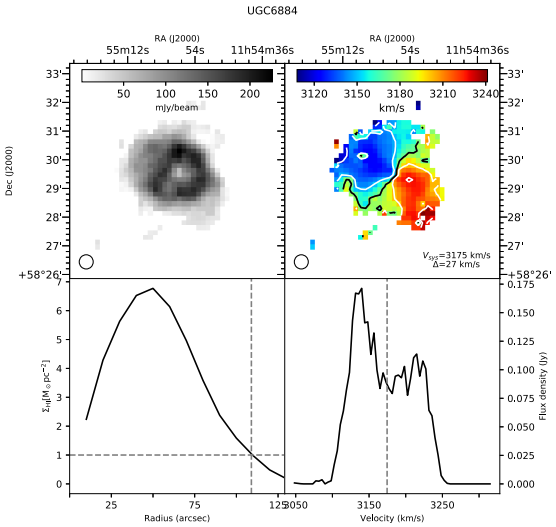
UGC6884
RA (J2000)
Dec (J2000)
mJy/beam
km/s
V_{sys}=3175 km/s
Δ=27 km/s
Radius (arcsec)
Velocity (km/s)
Flux density (Jy)

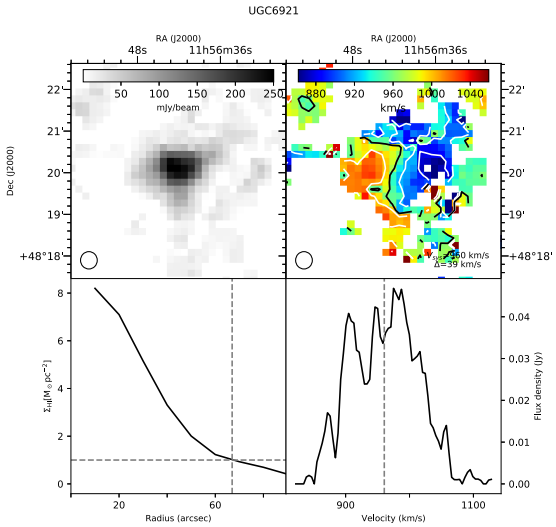
UGC6921
RA (J2000)
Dec (J2000)
mJy/beam
km/s
V_{sys}=960 km/s
Δ=39 km/s
Radius (arcsec)
Velocity (km/s)
Flux density (Jy)

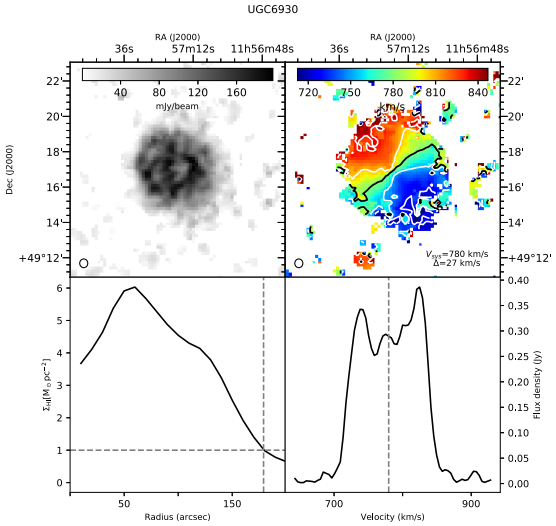
UGC6930
RA (J2000)
Dec (J2000)
mJy/beam
km/s
V_{sys}=780 km/s
Δ=27 km/s
Σ_{HI}[M$_\odot$ pc^{-2}]
Flux density (Jy)
Radius (arcsec)
Velocity (km/s)

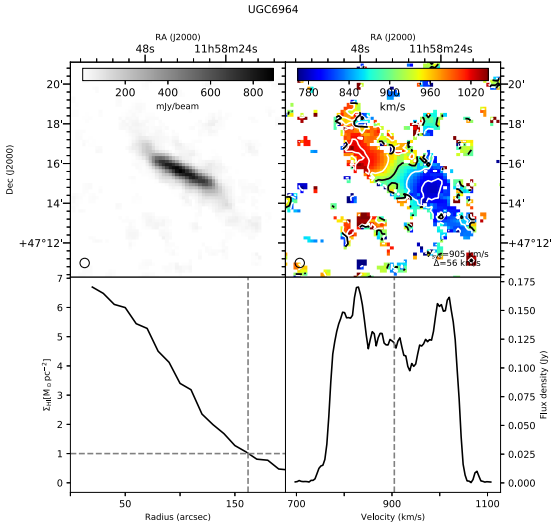
UGC6964
RA (J2000)
Dec (J2000)
mJy/beam
km/s
Σ_{HI}[M$_\odot$ pc^{-2}]
Flux density (Jy)
Radius (arcsec)
Velocity (km/s)

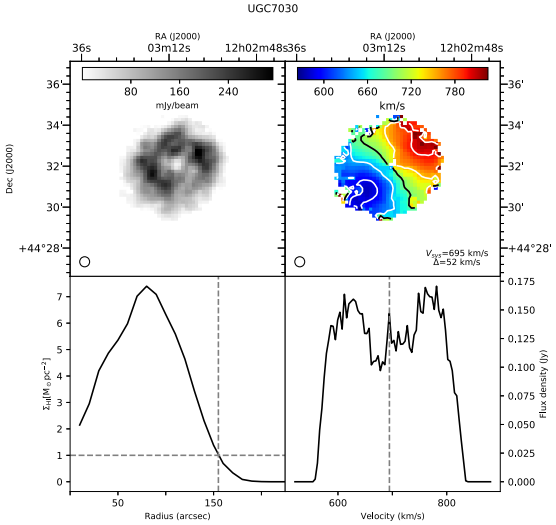
UGC7030
RA (J2000)
Dec (J2000)
mJy/beam
km/s
V_{sys}=695 km/s
Δ=52 km/s
Σ_{HI}[M$_\odot$ pc^{-2}]
Flux density (Jy)
Radius (arcsec)
Velocity (km/s)

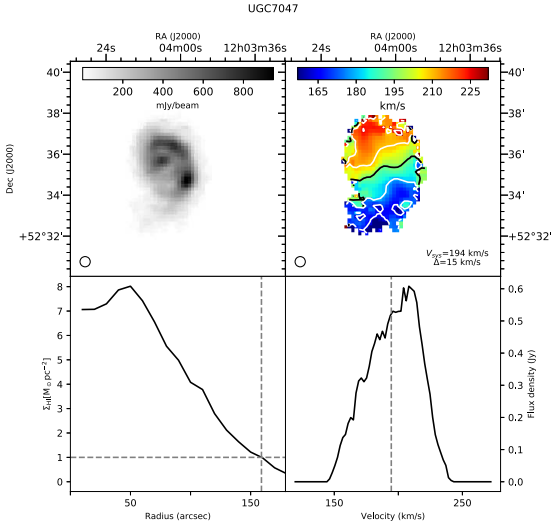
UGC7047
RA (J2000)
Dec (J2000)
mJy/beam
km/s
V_{sys}=194 km/s
Δ=15 km/s
Σ_{HI}[M$_\odot$ pc^{-2}]
Flux density (Jy)
Radius (arcsec)
Velocity (km/s)

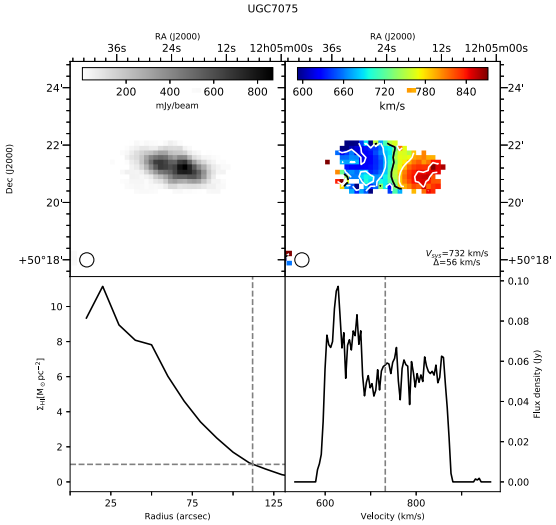
UGC7075
RA (J2000)
Dec (J2000)
mJy/beam
km/s
V_{sys}=732 km/s
Δ=56 km/s
Σ_{HI}[M$_\odot$ pc^{-2}]
Flux density (Jy)
Radius (arcsec)
Velocity (km/s)

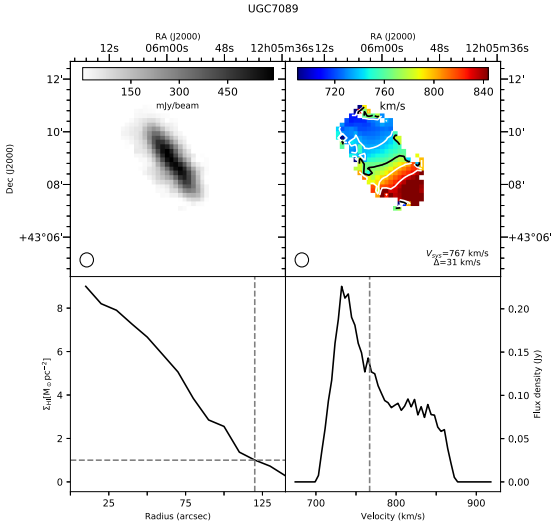
UGC7089
RA (J2000)
Dec (J2000)
mJy/beam
km/s
V_{sys}=767 km/s
Δ=31 km/s
Σ_{HI}[M$_\odot$ pc^{-2}]
Flux density (Jy)
Radius (arcsec)
Velocity (km/s)

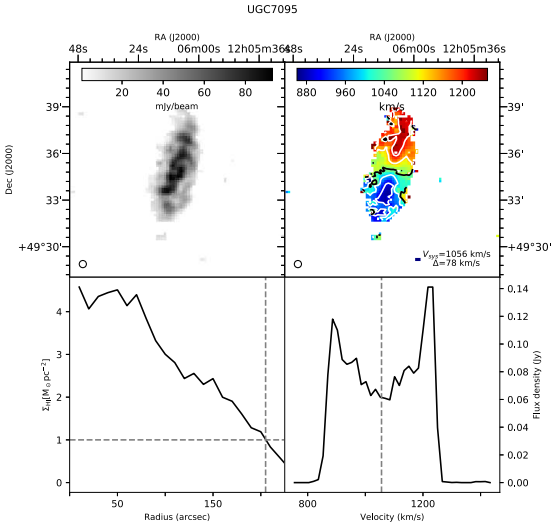
UGC7095
RA (J2000)
Dec (J2000)
mJy/beam
km/s
V_{sys}=1056 km/s
Δ=78 km/s
Σ_{HI}[$M_\odot$ pc^{-2}]
Flux density (Jy)
Radius (arcsec)
Velocity (km/s)

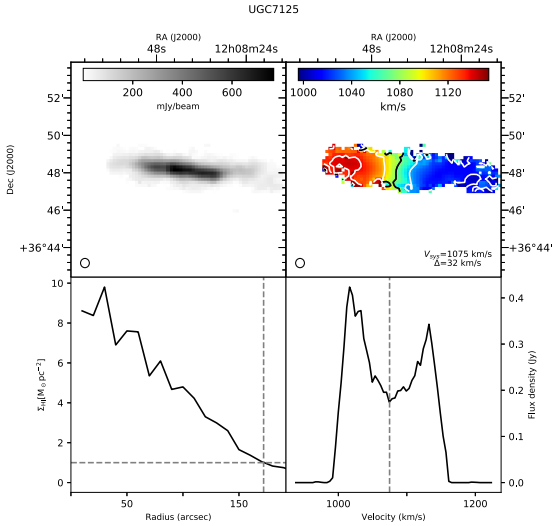
UGC7125
RA (J2000)
Dec (J2000)
mJy/beam
km/s
V_{sys}=1075 km/s
Δ=32 km/s
Σ_{HI}[$M_\odot$ pc^{-2}]
Flux density (Jy)
Radius (arcsec)
Velocity (km/s)

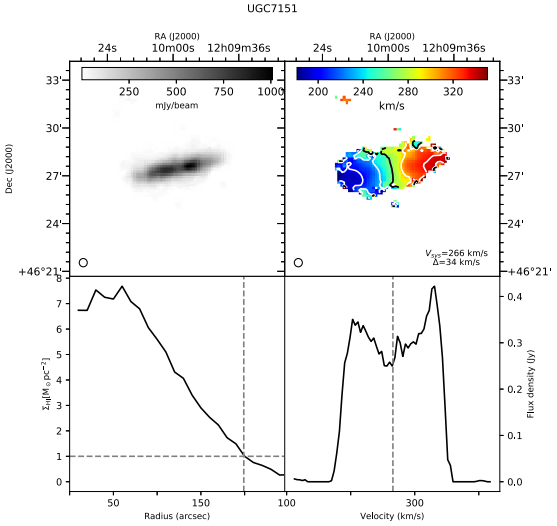
UGC7151
RA (J2000)
Dec (J2000)
mJy/beam
km/s
V_{sys}=266 km/s
Δ=34 km/s
Σ_{HI}[$M_\odot$ pc^{-2}]
Flux density (Jy)
Radius (arcsec)
Velocity (km/s)

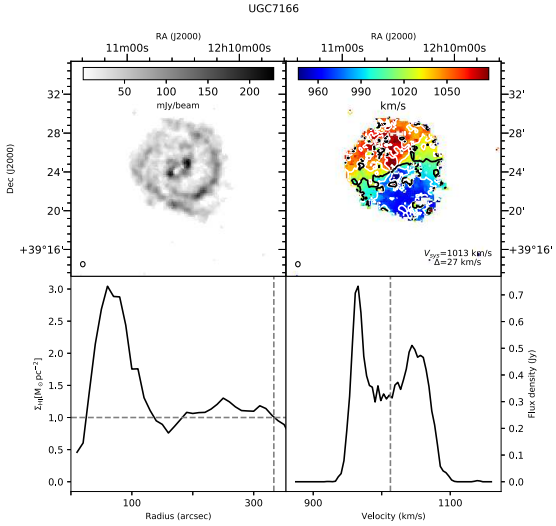
UGC7166
RA (J2000)
Dec (J2000)
mJy/beam
km/s
V_{sys}=1013 km/s
Δ=27 km/s
Σ_{HI}[$M_\odot$ pc^{-2}]
Flux density (Jy)
Radius (arcsec)
Velocity (km/s)

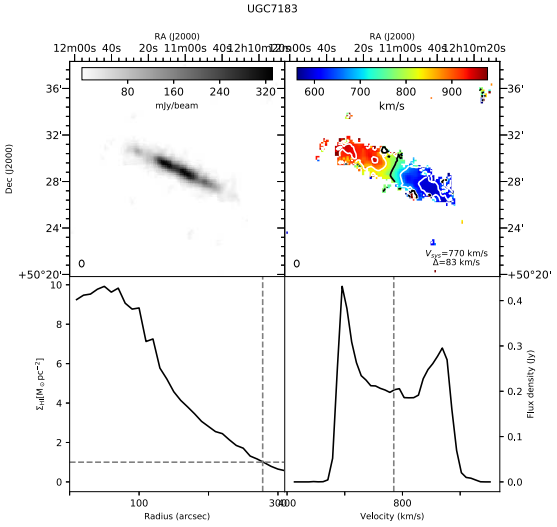
UGC7183
RA (J2000)
Dec (J2000)
mJy/beam
km/s
V_{sys}=770 km/s
Δ=83 km/s
Σ_{HI}[$M_\odot$ pc^{-2}]
Flux density (Jy)
Radius (arcsec)
Velocity (km/s)

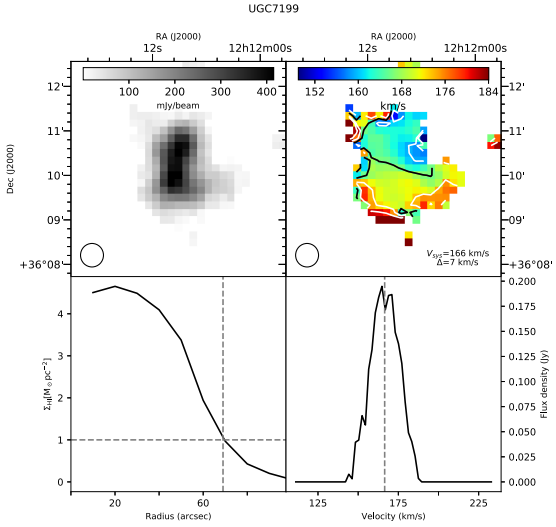
UGC7199
RA (J2000)
Dec (J2000)
mJy/beam
km/s
V_{sys}=166 km/s
Δ=7 km/s
Σ_{HI}[$M_\odot$ pc^{-2}]
Flux density (Jy)
Radius (arcsec)
Velocity (km/s)

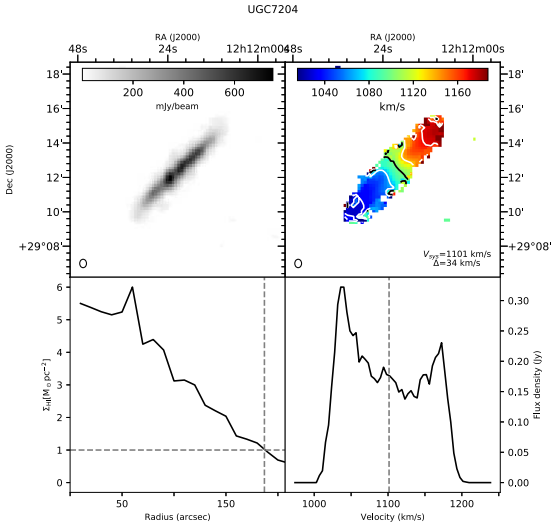
UGC7204
RA (J2000)
Dec (J2000)
mJy/beam
km/s
V_{sys}=1101 km/s
Δ=34 km/s
Radius (arcsec)
Velocity (km/s)
Flux density (Jy)

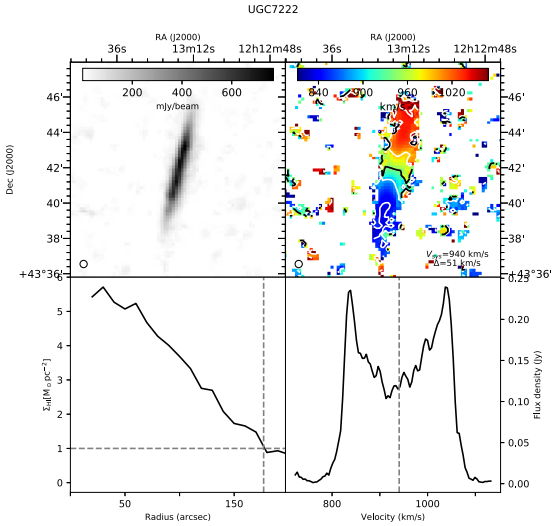
UGC7222
RA (J2000)
Dec (J2000)
mJy/beam
km/s
V_{sys}=940 km/s
Δ=51 km/s
Radius (arcsec)
Velocity (km/s)
Flux density (Jy)

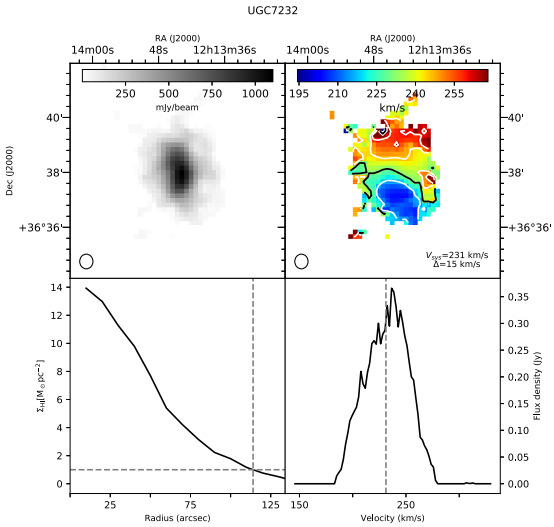
UGC7232
RA (J2000)
Dec (J2000)
mJy/beam
km/s
V_{sys}=231 km/s
Δ=15 km/s
Radius (arcsec)
Velocity (km/s)
Flux density (Jy)

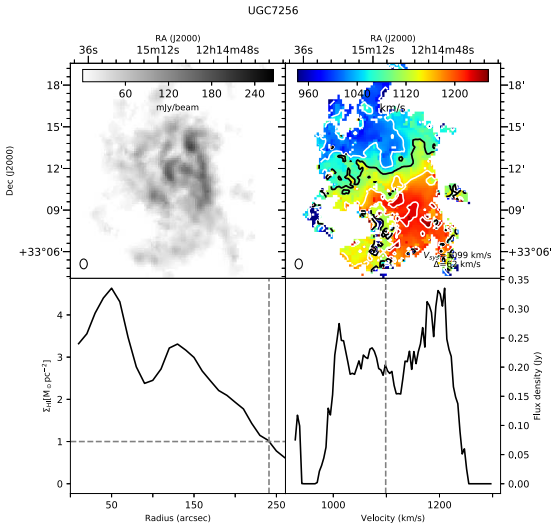
UGC7256
RA (J2000)
Dec (J2000)
mJy/beam
km/s
V_{sys}=1099 km/s
Δ=64 km/s
Radius (arcsec)
Velocity (km/s)
Flux density (Jy)

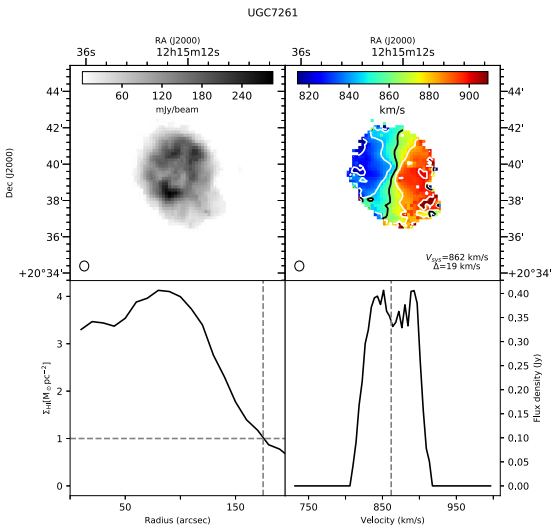
UGC7261
RA (J2000)
Dec (J2000)
mJy/beam
km/s
V_{sys}=862 km/s
Δ=19 km/s
Radius (arcsec)
Velocity (km/s)
Flux density (Jy)

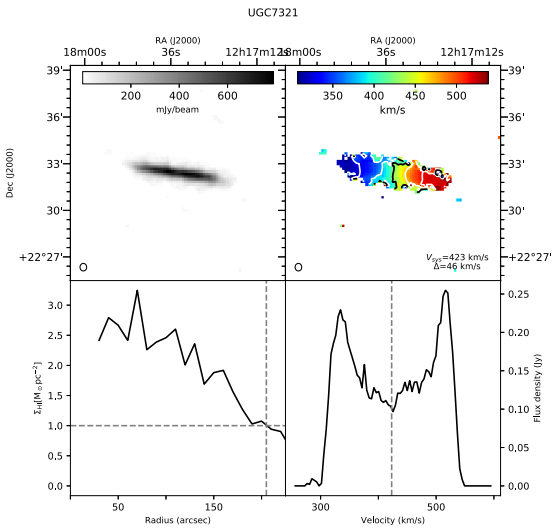
UGC7321
RA (J2000)
Dec (J2000)
mJy/beam
km/s
V_{sys}=423 km/s
Δ=46 km/s
Radius (arcsec)
Velocity (km/s)
Flux density (Jy)

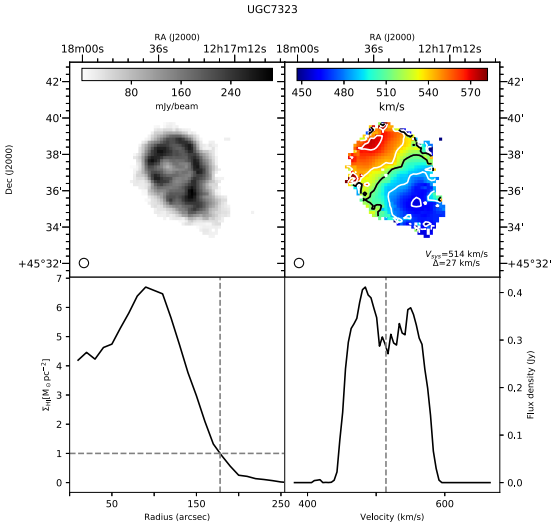
UGC7323
RA (J2000)
Dec (J2000)
mJy/beam
km/s
V_{sys}=514 km/s
Δ=27 km/s
Σ_{HI}[$M_\odot$ pc^{-2}]
Flux density (Jy)
Radius (arcsec)
Velocity (km/s)

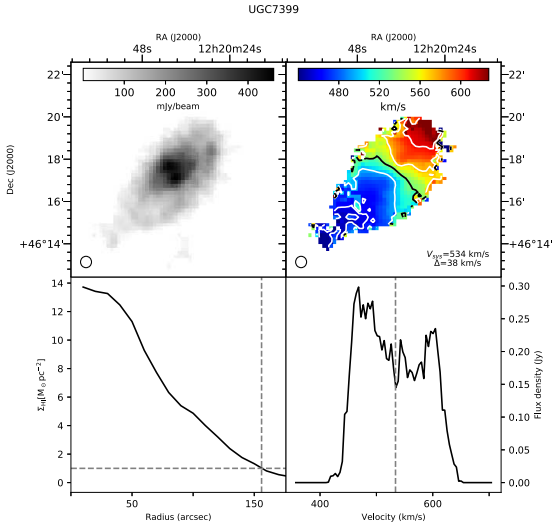
UGC7399
RA (J2000)
Dec (J2000)
mJy/beam
km/s
V_{sys}=534 km/s
Δ=38 km/s
Σ_{HI}[$M_\odot$ pc^{-2}]
Flux density (Jy)
Radius (arcsec)
Velocity (km/s)

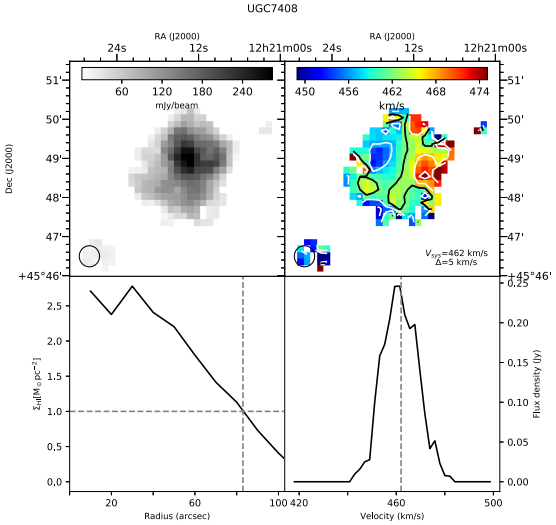
UGC7408
RA (J2000)
Dec (J2000)
mJy/beam
km/s
V_{sys}=462 km/s
Δ=5 km/s
Σ_{HI}[$M_\odot$ pc^{-2}]
Flux density (Jy)
Radius (arcsec)
Velocity (km/s)

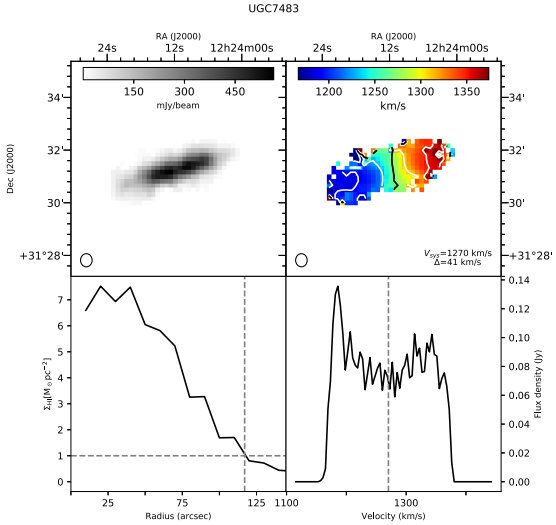
UGC7483
RA (J2000)
Dec (J2000)
mJy/beam
km/s
V_{sys}=1270 km/s
Δ=41 km/s
Σ_{HI}[$M_\odot$ pc^{-2}]
Flux density (Jy)
Radius (arcsec)
Velocity (km/s)

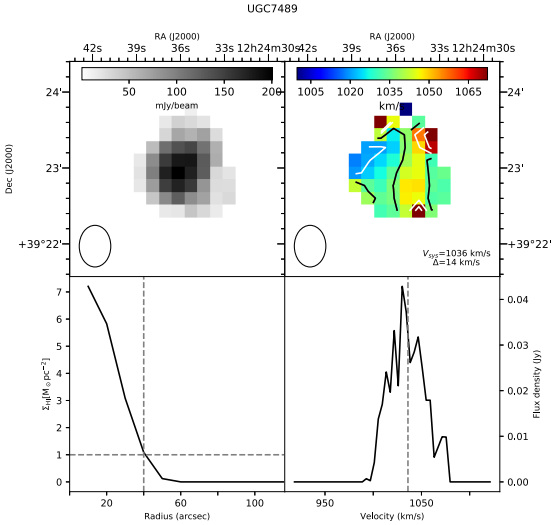
UGC7489
RA (J2000)
Dec (J2000)
mJy/beam
km/s
V_{sys}=1036 km/s
Δ=14 km/s
Σ_{HI}[$M_\odot$ pc^{-2}]
Flux density (Jy)
Radius (arcsec)
Velocity (km/s)

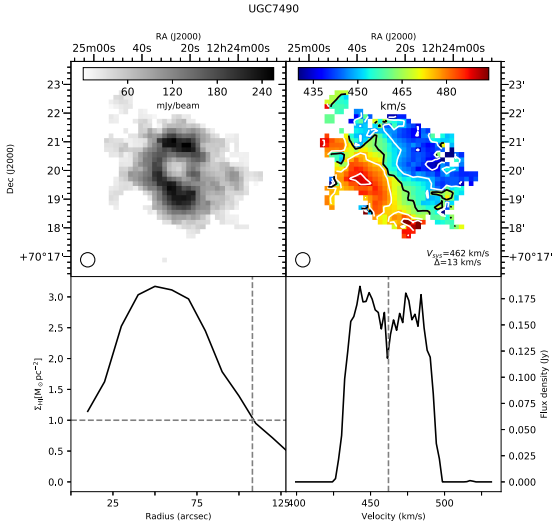
UGC7490
RA (J2000)
Dec (J2000)
mJy/beam
km/s
V_{sys}=462 km/s
Δ=13 km/s
Σ_{HI}[$M_\odot$ pc^{-2}]
Flux density (Jy)
Radius (arcsec)
Velocity (km/s)

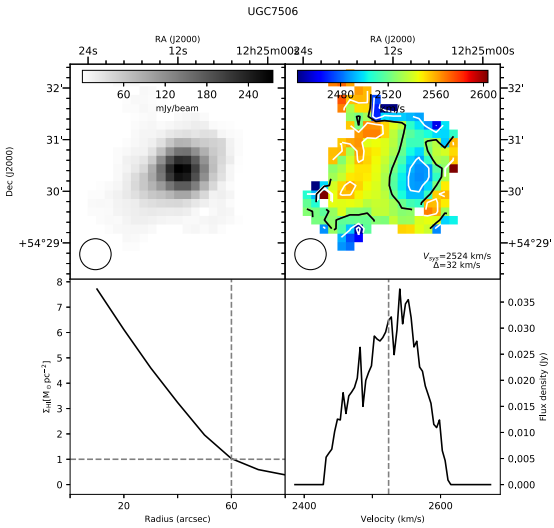
UGC7506
RA (J2000)
Dec (J2000)
mJy/beam
km/s
V_{sys}=2524 km/s
Δ=32 km/s
Σ_{HI}[M$_\odot$ pc^{-2}]
Flux density (Jy)
Radius (arcsec)
Velocity (km/s)

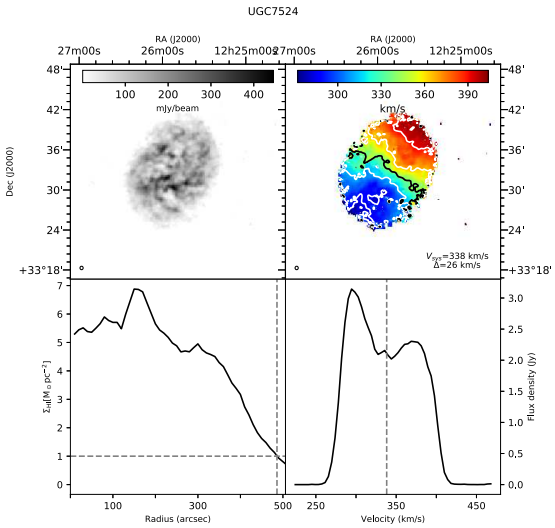
UGC7524
RA (J2000)
Dec (J2000)
mJy/beam
km/s
V_{sys}=338 km/s
Δ=26 km/s
Σ_{HI}[M$_\odot$ pc^{-2}]
Flux density (Jy)
Radius (arcsec)
Velocity (km/s)

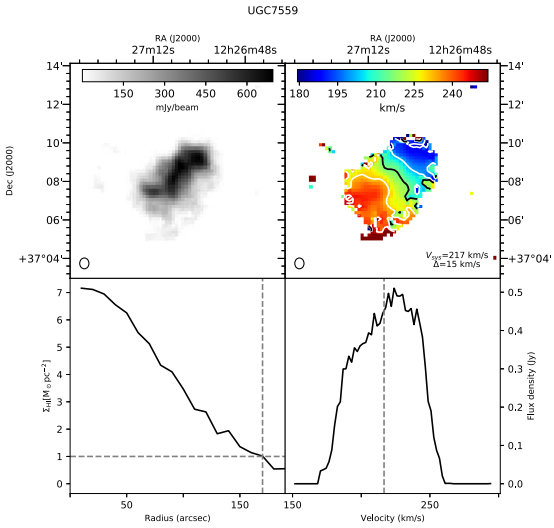
UGC7559
RA (J2000)
Dec (J2000)
mJy/beam
km/s
V_{sys}=217 km/s
Δ=15 km/s
Σ_{HI}[M$_\odot$ pc^{-2}]
Flux density (Jy)
Radius (arcsec)
Velocity (km/s)

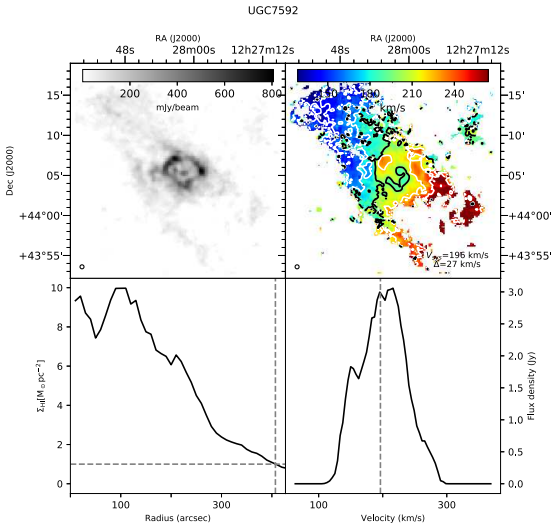
UGC7592
RA (J2000)
Dec (J2000)
mJy/beam
km/s
V_{sys}=196 km/s
Δ=27 km/s
Σ_{HI}[M$_\odot$ pc^{-2}]
Flux density (Jy)
Radius (arcsec)
Velocity (km/s)

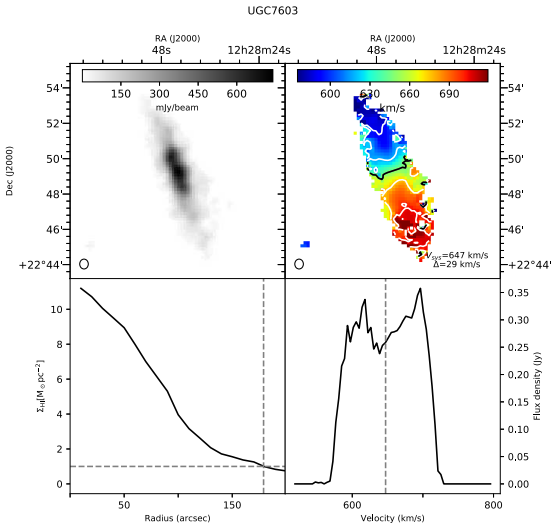
UGC7603
RA (J2000)
Dec (J2000)
mJy/beam
km/s
V_{sys}=647 km/s
Δ=29 km/s
Σ_{HI}[M$_\odot$ pc^{-2}]
Flux density (Jy)
Radius (arcsec)
Velocity (km/s)

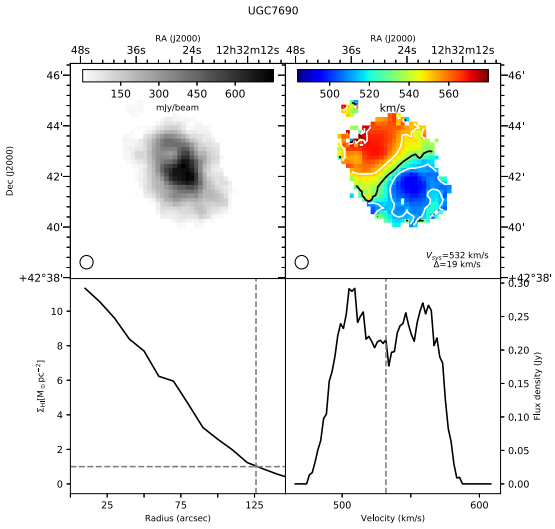
UGC7690
RA (J2000)
Dec (J2000)
mJy/beam
km/s
V_{sys}=532 km/s
Δ=19 km/s
Σ_{HI}[M$_\odot$ pc^{-2}]
Flux density (Jy)
Radius (arcsec)
Velocity (km/s)

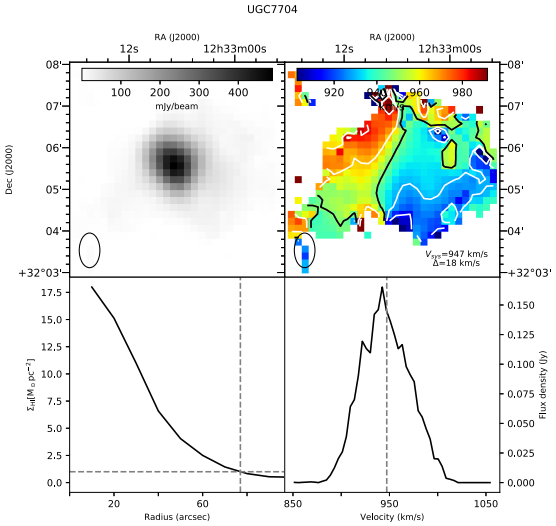
UGC7704
RA (J2000)
Dec (J2000)
mJy/beam
km/s
V_{sys}=947 km/s
Δ=18 km/s
Radius (arcsec)
Velocity (km/s)
Flux density (Jy)

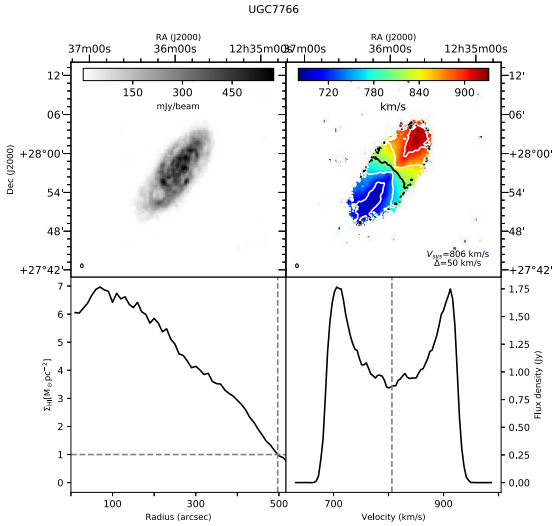
UGC7766
RA (J2000)
Dec (J2000)
mJy/beam
km/s
V_{sys}=806 km/s
Δ=50 km/s
Radius (arcsec)
Velocity (km/s)
Flux density (Jy)

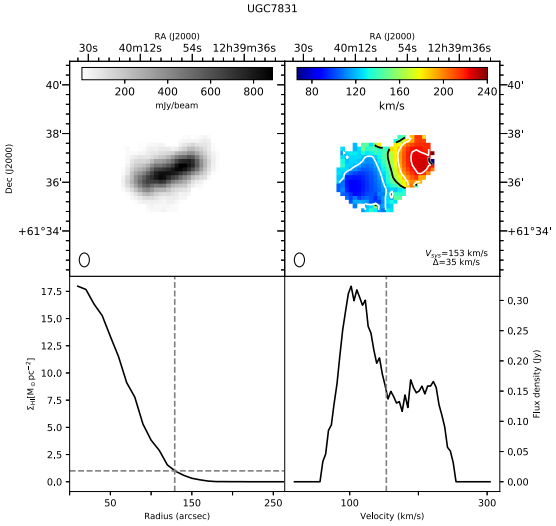
UGC7831
RA (J2000)
Dec (J2000)
mJy/beam
km/s
V_{sys}=153 km/s
Δ=35 km/s
Radius (arcsec)
Velocity (km/s)
Flux density (Jy)

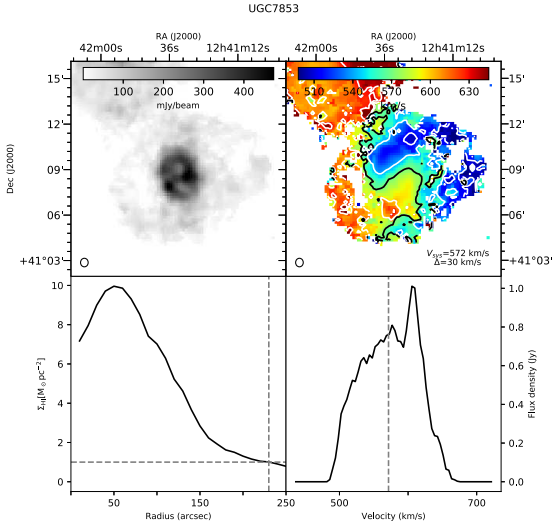
UGC7853
RA (J2000)
Dec (J2000)
mJy/beam
km/s
V_{sys}=572 km/s
Δ=30 km/s
Radius (arcsec)
Velocity (km/s)
Flux density (Jy)

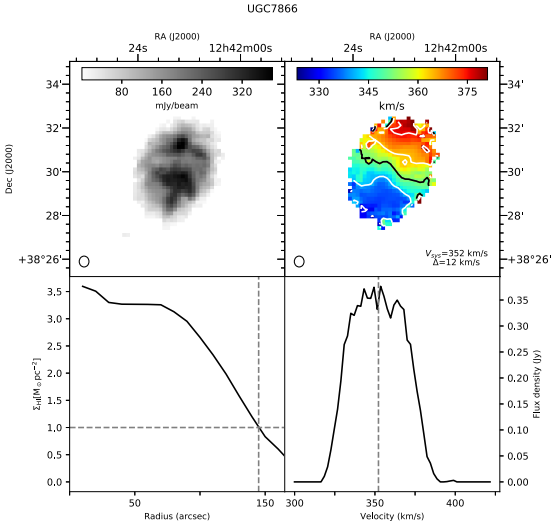
UGC7866
RA (J2000)
Dec (J2000)
mJy/beam
km/s
V_{sys}=352 km/s
Δ=12 km/s
Radius (arcsec)
Velocity (km/s)
Flux density (Jy)

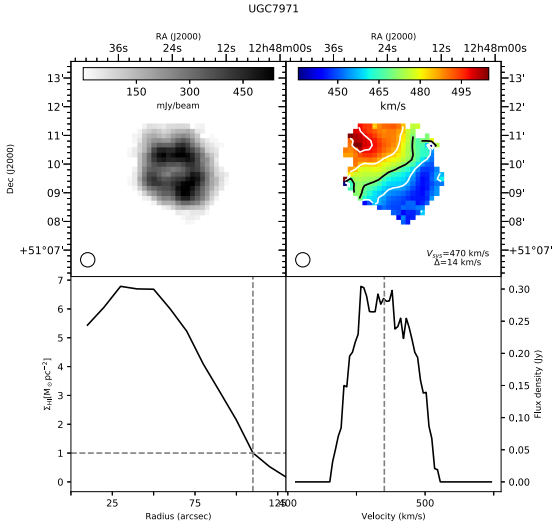
UGC7971
RA (J2000)
Dec (J2000)
mJy/beam
km/s
V_{sys}=470 km/s
Δ=14 km/s
Radius (arcsec)
Velocity (km/s)
Flux density (Jy)

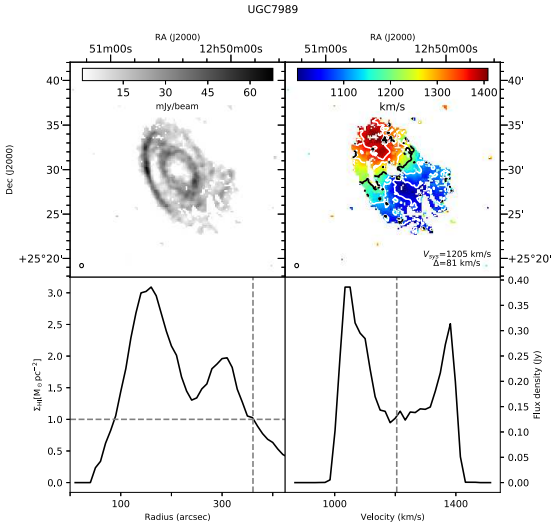
UGC7989
RA (J2000)
Dec (J2000)
mJy/beam
km/s
V_{sys}=1205 km/s
Δ=81 km/s
Radius (arcsec)
Velocity (km/s)
Flux density (Jy)

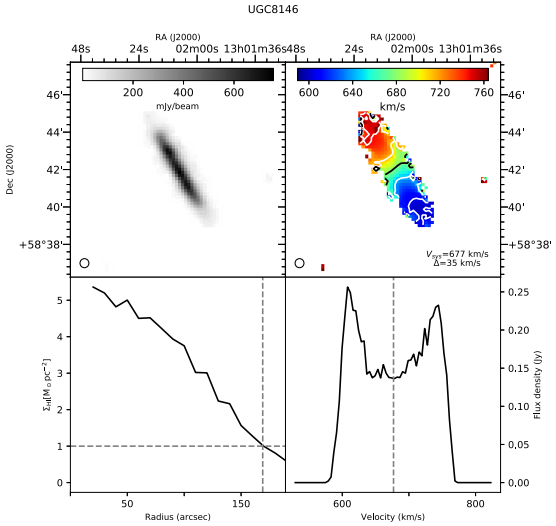
UGC8146
RA (J2000)
Dec (J2000)
mJy/beam
km/s
V_{sys}=677 km/s
Δ=35 km/s
Radius (arcsec)
Velocity (km/s)
Flux density (Jy)

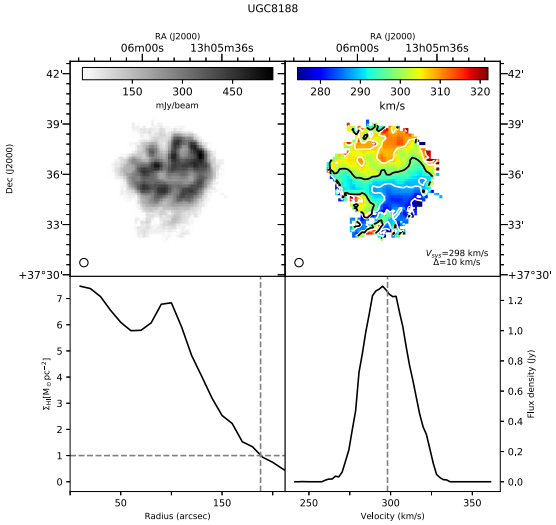
UGC8188
RA (J2000)
Dec (J2000)
mJy/beam
km/s
V_{sys}=298 km/s
Δ=10 km/s
Radius (arcsec)
Velocity (km/s)
Flux density (Jy)

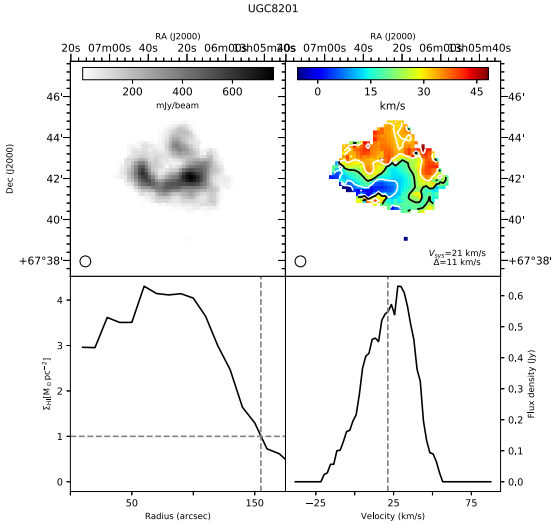
UGC8201
RA (J2000)
Dec (J2000)
mJy/beam
km/s
V_{sys}=21 km/s
Δ=11 km/s
Radius (arcsec)
Velocity (km/s)
Flux density (Jy)

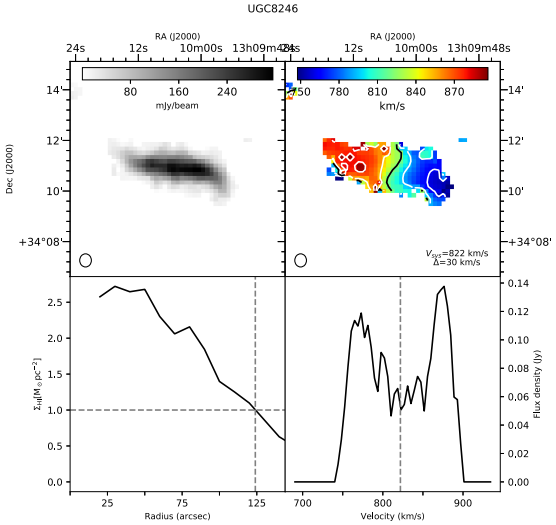
UGC8246
RA (J2000)
Dec (J2000)
mJy/beam
km/s
V_{sys}=822 km/s
Δ=30 km/s
Radius (arcsec)
Velocity (km/s)
Flux density (Jy)

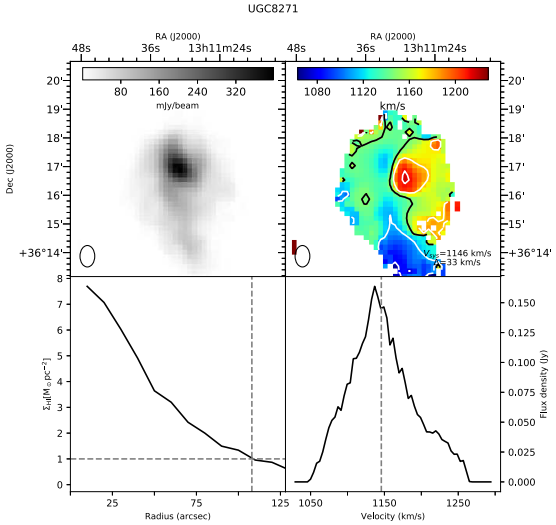
UGC8271
RA (J2000)
Dec (J2000)
mJy/beam
km/s
V_{sys}=1146 km/s
Δ=33 km/s
Radius (arcsec)
Velocity (km/s)
Flux density (Jy)

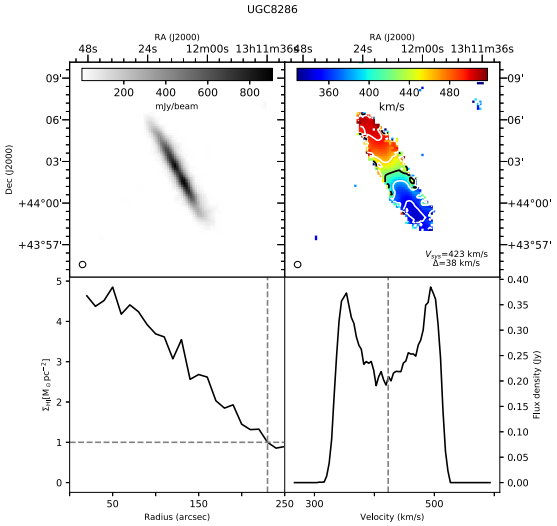
UGC8286
RA (J2000)
Dec (J2000)
mJy/beam
km/s
V_{sys}=423 km/s
Δ=38 km/s
Radius (arcsec)
Velocity (km/s)
Flux density (Jy)

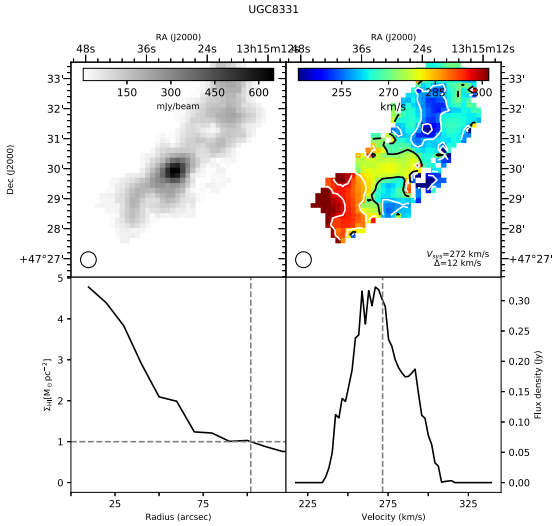
UGC8331
RA (J2000)
Dec (J2000)
mJy/beam
km/s
V_{sys}=272 km/s
Δ=12 km/s
Radius (arcsec)
Velocity (km/s)
Flux density (Jy)

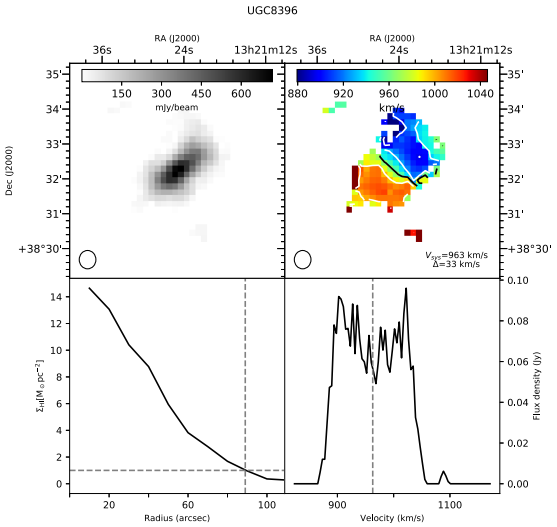
UGC8396
RA (J2000)
Dec (J2000)
mJy/beam
km/s
V_{sys}=963 km/s
Δ=33 km/s
Radius (arcsec)
Velocity (km/s)
Flux density (Jy)

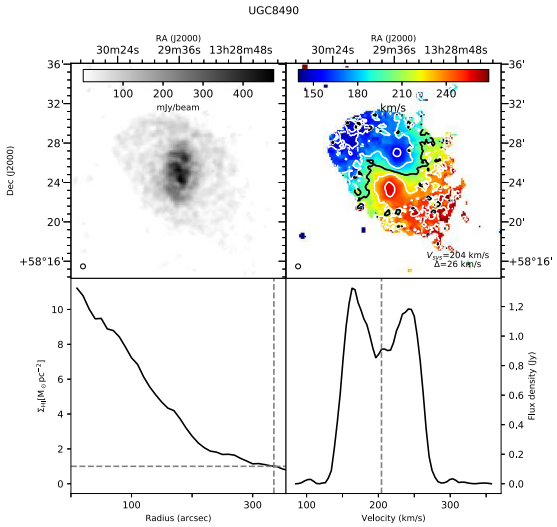
UGC8490
RA (J2000)
Dec (J2000)
mJy/beam
km/s
V_{sys}=204 km/s
Δ=26 km/s
Radius (arcsec)
Velocity (km/s)
Flux density (Jy)

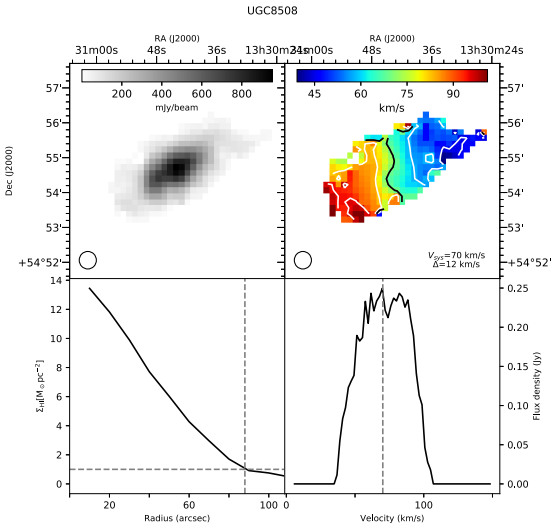
UGC8508
RA (J2000)
Dec (J2000)
mJy/beam
km/s
V_{sys}=70 km/s
Δ=12 km/s
Radius (arcsec)
Velocity (km/s)
Flux density (Jy)

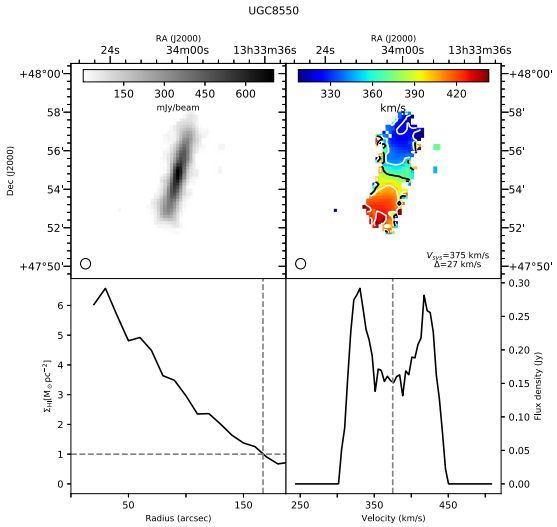
UGC8550
RA (J2000)
Dec (J2000)
mJy/beam
km/s
V_{sys}=375 km/s
Δ=27 km/s
Radius (arcsec)
Velocity (km/s)
Flux density (Jy)

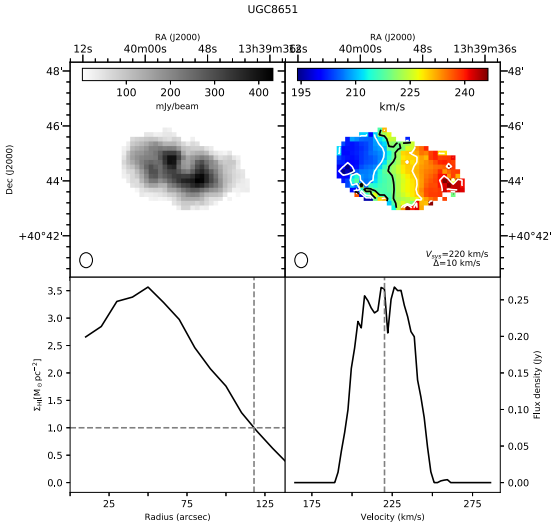
UGC8651
RA (J2000)
Dec (J2000)
mJy/beam
km/s
Radius (arcsec)
Velocity (km/s)
Flux density (Jy)

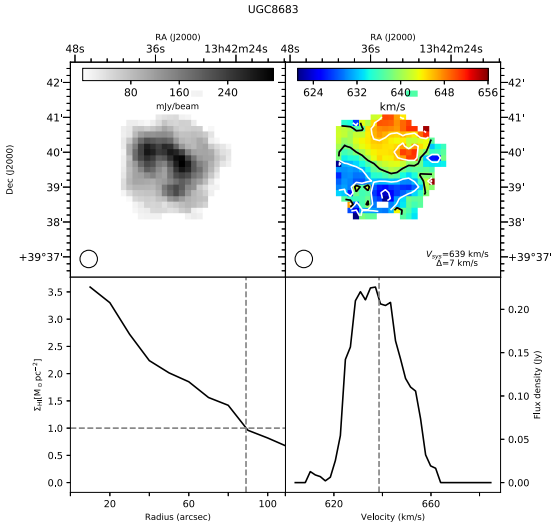
UGC8683
RA (J2000)
Dec (J2000)
mJy/beam
km/s
Radius (arcsec)
Velocity (km/s)
Flux density (Jy)

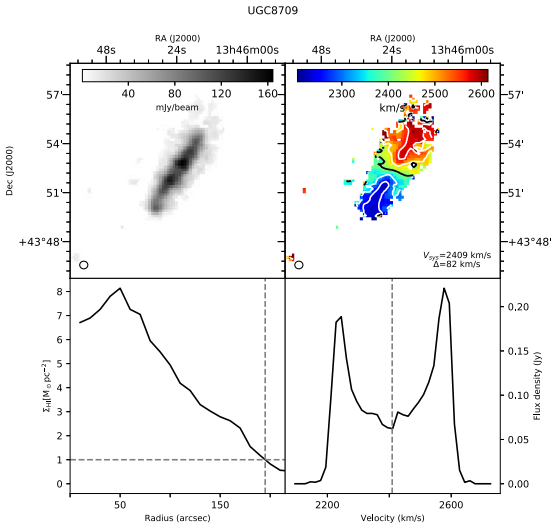
UGC8709
RA (J2000)
Dec (J2000)
mJy/beam
km/s
Radius (arcsec)
Velocity (km/s)
Flux density (Jy)

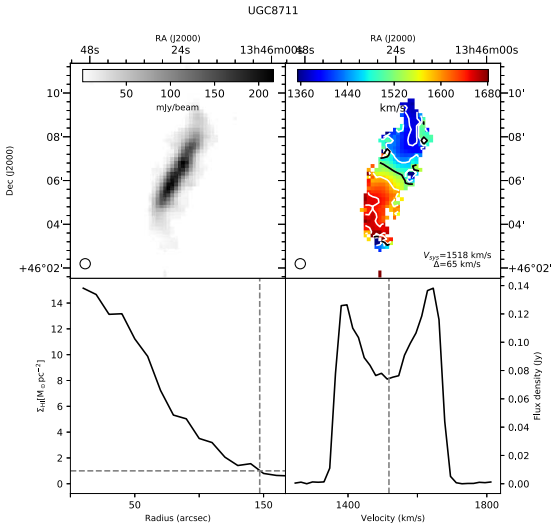
UGC8711
RA (J2000)
Dec (J2000)
mJy/beam
km/s
Radius (arcsec)
Velocity (km/s)
Flux density (Jy)

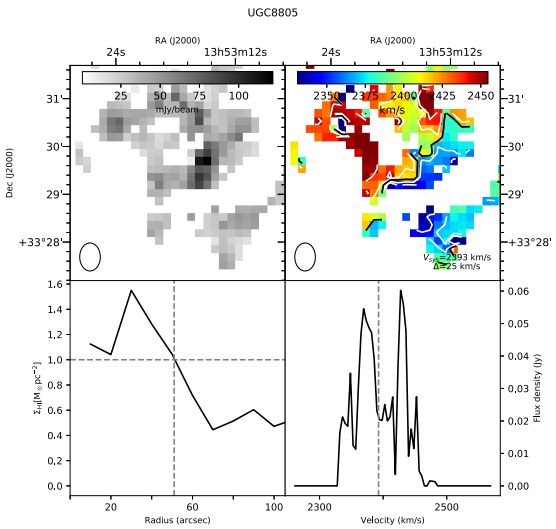
UGC8805
RA (J2000)
Dec (J2000)
mJy/beam
km/s
Radius (arcsec)
Velocity (km/s)
Flux density (Jy)

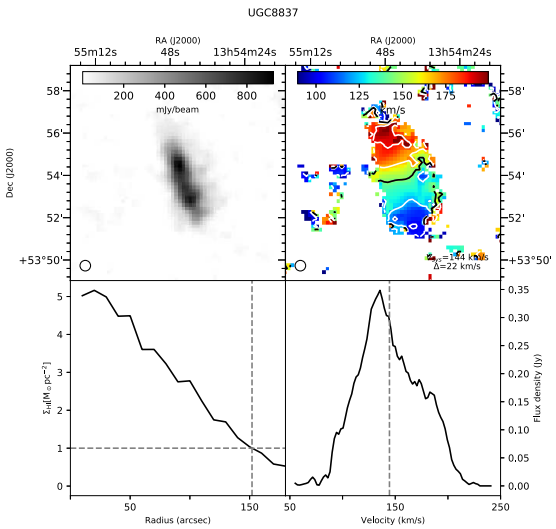
UGC8837
RA (J2000)
Dec (J2000)
mJy/beam
km/s
Radius (arcsec)
Velocity (km/s)
Flux density (Jy)

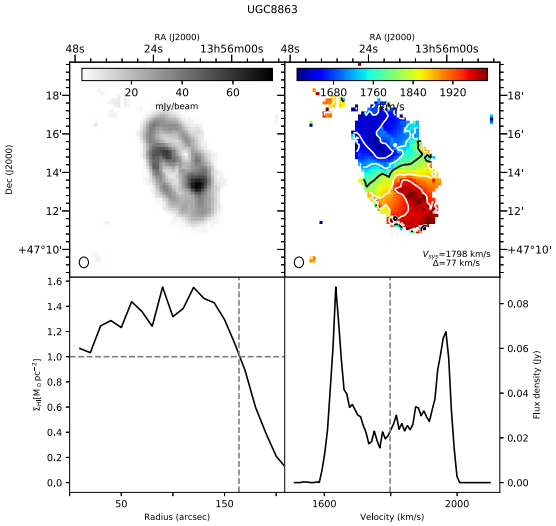
UGC8863
RA (J2000)
Dec (J2000)
mJy/beam
km/s
V_{sys}=1798 km/s
Δ=77 km/s
$\Sigma_{HI}[M_\odot pc^{-2}]$
Flux density (Jy)
Radius (arcsec)
Velocity (km/s)

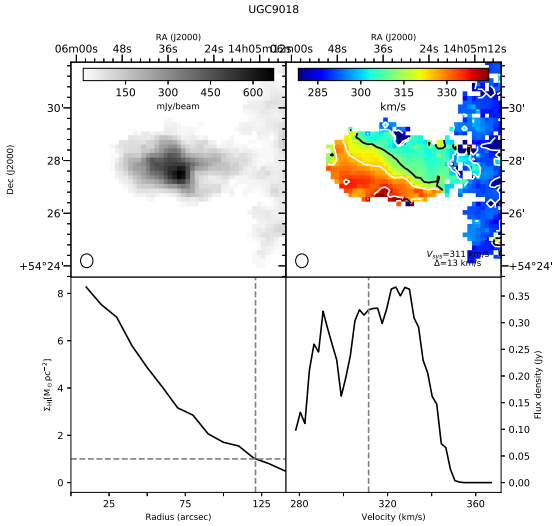
UGC9018
RA (J2000)
Dec (J2000)
mJy/beam
km/s
V_{sys}=311 km/s
Δ=13 km/s
$\Sigma_{HI}[M_\odot pc^{-2}]$
Flux density (Jy)
Radius (arcsec)
Velocity (km/s)

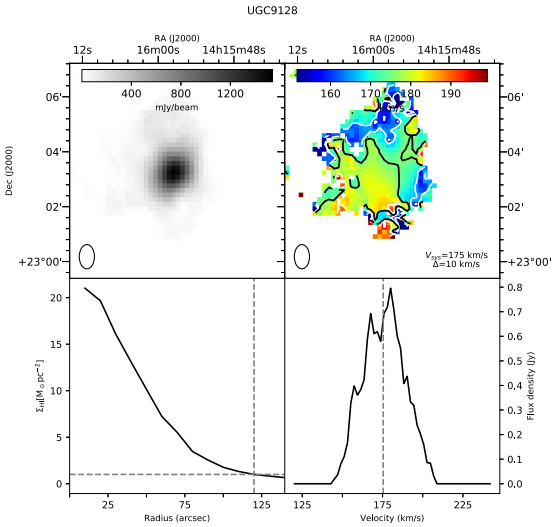
UGC9128
RA (J2000)
Dec (J2000)
mJy/beam
km/s
V_{sys}=175 km/s
Δ=10 km/s
$\Sigma_{HI}[M_\odot pc^{-2}]$
Flux density (Jy)
Radius (arcsec)
Velocity (km/s)

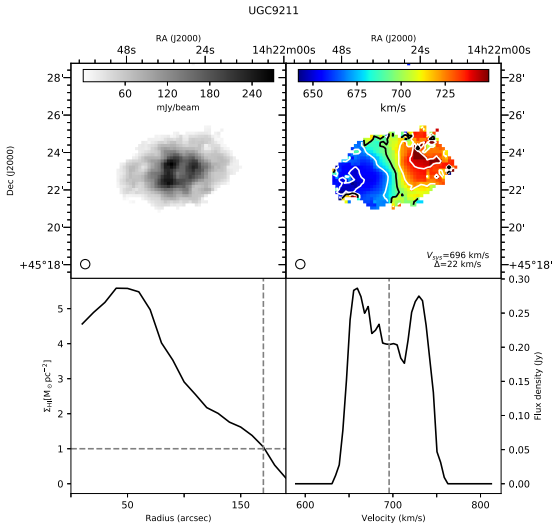
UGC9211
RA (J2000)
Dec (J2000)
mJy/beam
km/s
V_{sys}=696 km/s
Δ=22 km/s
$\Sigma_{HI}[M_\odot pc^{-2}]$
Flux density (Jy)
Radius (arcsec)
Velocity (km/s)

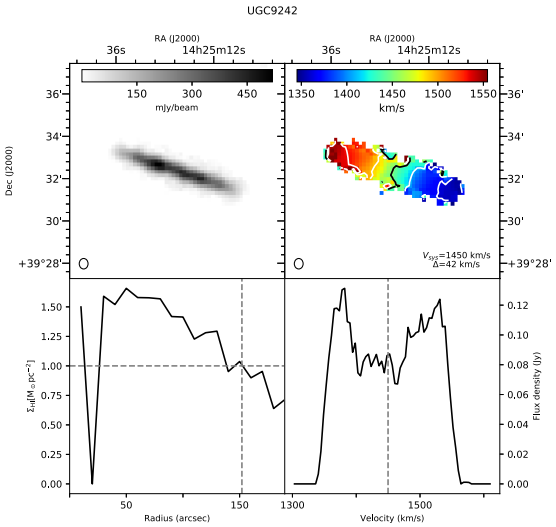
UGC9242
RA (J2000)
Dec (J2000)
mJy/beam
km/s
V_{sys}=1450 km/s
Δ=42 km/s
$\Sigma_{HI}[M_\odot pc^{-2}]$
Flux density (Jy)
Radius (arcsec)
Velocity (km/s)

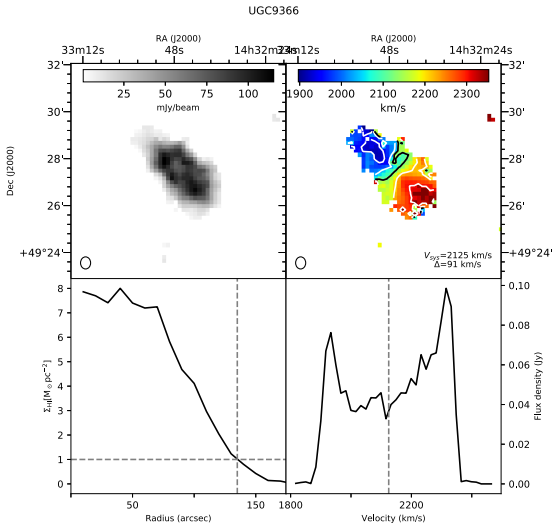
UGC9366
RA (J2000)
Dec (J2000)
mJy/beam
km/s
V_{sys}=2125 km/s
Δ=91 km/s
$\Sigma_{HI}[M_\odot pc^{-2}]$
Flux density (Jy)
Radius (arcsec)
Velocity (km/s)

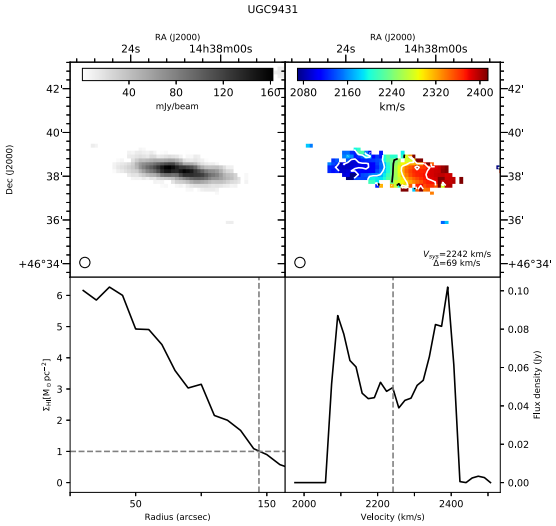
UGC9431
RA (J2000)
Dec (J2000)
mJy/beam
km/s
V_{sys}=2242 km/s
Δ=69 km/s
Radius (arcsec)
Velocity (km/s)
Flux density (Jy)

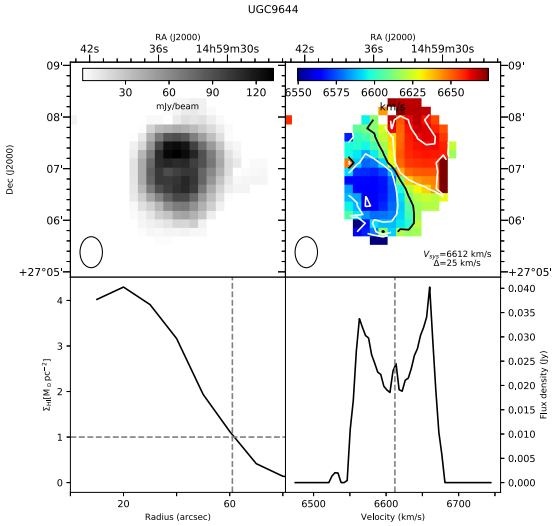
UGC9644
RA (J2000)
Dec (J2000)
mJy/beam
km/s
V_{sys}=6612 km/s
Δ=25 km/s
Radius (arcsec)
Velocity (km/s)
Flux density (Jy)

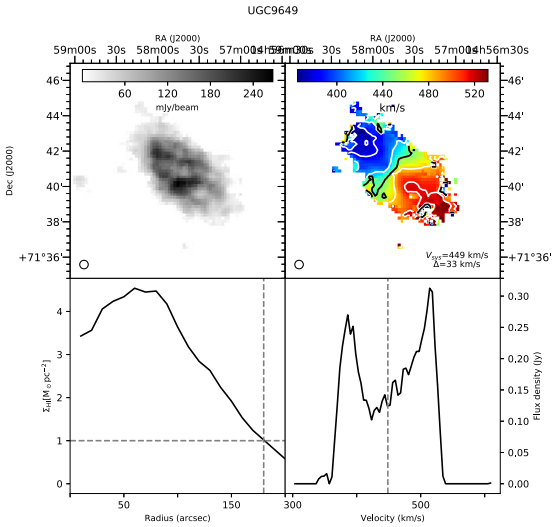
UGC9649
RA (J2000)
Dec (J2000)
mJy/beam
km/s
V_{sys}=449 km/s
Δ=33 km/s
Radius (arcsec)
Velocity (km/s)
Flux density (Jy)

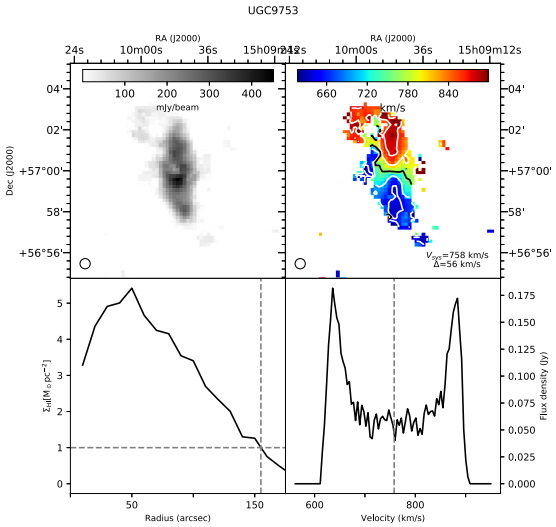
UGC9753
RA (J2000)
Dec (J2000)
mJy/beam
km/s
V_{sys}=758 km/s
Δ=56 km/s
Radius (arcsec)
Velocity (km/s)
Flux density (Jy)

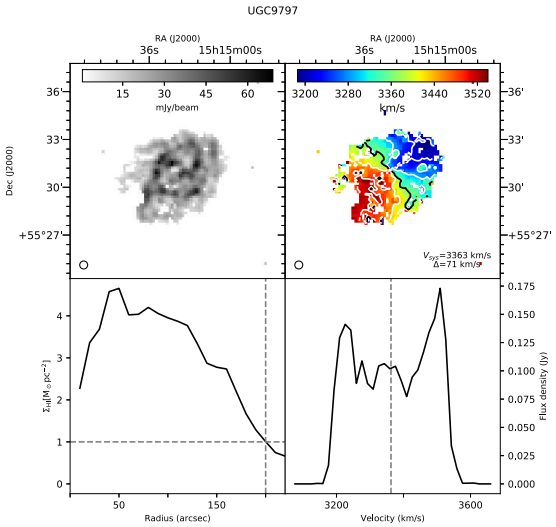
UGC9797
RA (J2000)
Dec (J2000)
mJy/beam
km/s
V_{sys}=3363 km/s
Δ=71 km/s
Radius (arcsec)
Velocity (km/s)
Flux density (Jy)

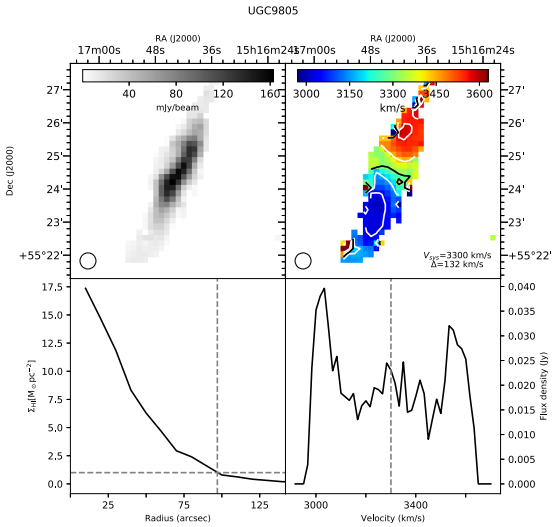
UGC9805
RA (J2000)
Dec (J2000)
mJy/beam
km/s
V_{sys}=3300 km/s
Δ=132 km/s
Radius (arcsec)
Velocity (km/s)
Flux density (Jy)

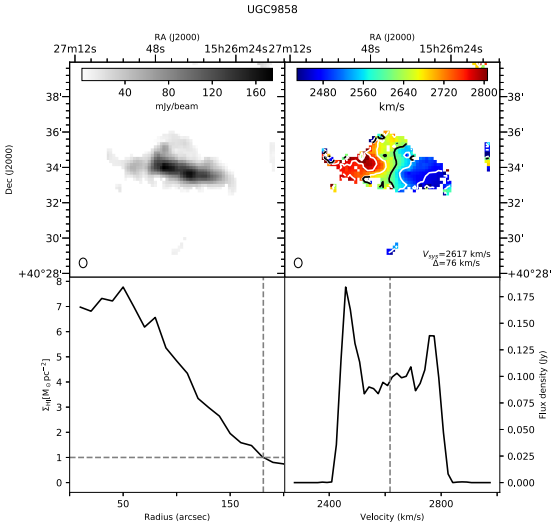
UGC9858
RA (J2000)
Dec (J2000)
mJy/beam
km/s
V_{sys}=2617 km/s
Δ=76 km/s
Σ_{HI}[$M_\odot$ pc^{-2}]
Flux density (Jy)
Radius (arcsec)
Velocity (km/s)

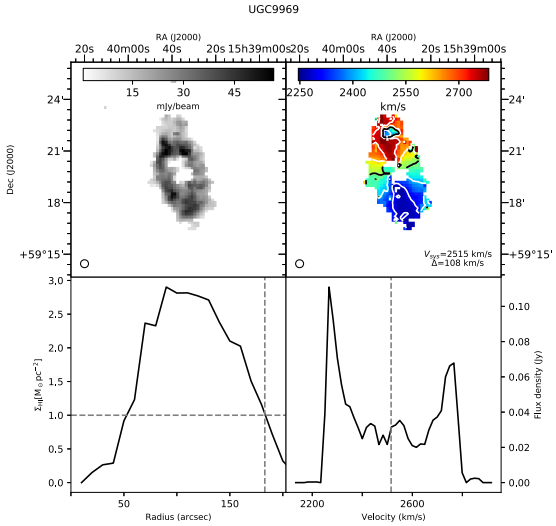
UGC9969
RA (J2000)
Dec (J2000)
mJy/beam
km/s
V_{sys}=2515 km/s
Δ=108 km/s
Σ_{HI}[$M_\odot$ pc^{-2}]
Flux density (Jy)
Radius (arcsec)
Velocity (km/s)

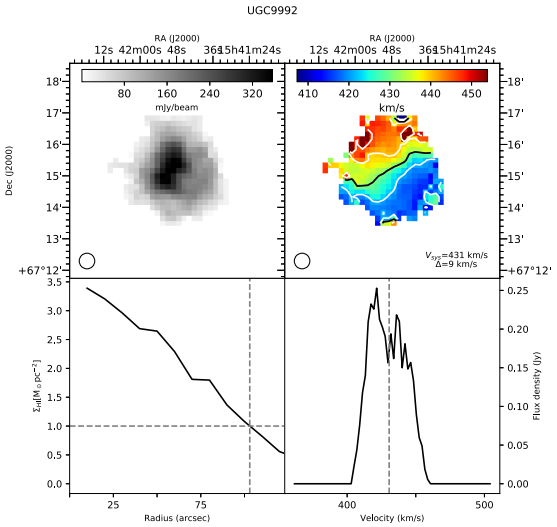
UGC9992
RA (J2000)
Dec (J2000)
mJy/beam
km/s
V_{sys}=431 km/s
Δ=9 km/s
Σ_{HI}[$M_\odot$ pc^{-2}]
Flux density (Jy)
Radius (arcsec)
Velocity (km/s)

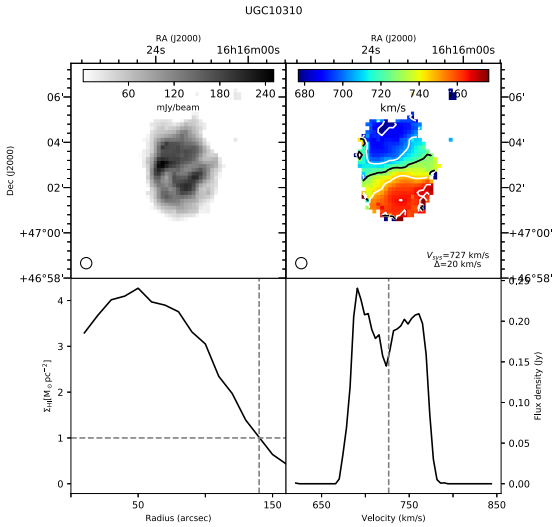
UGC10310
RA (J2000)
Dec (J2000)
mJy/beam
km/s
V_{sys}=727 km/s
Δ=20 km/s
Σ_{HI}[$M_\odot$ pc^{-2}]
Flux density (Jy)
Radius (arcsec)
Velocity (km/s)

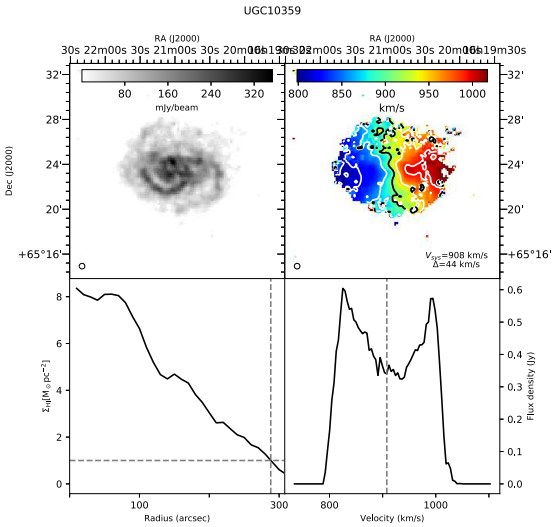
UGC10359
RA (J2000)
Dec (J2000)
mJy/beam
km/s
V_{sys}=908 km/s
Δ=44 km/s
Σ_{HI}[$M_\odot$ pc^{-2}]
Flux density (Jy)
Radius (arcsec)
Velocity (km/s)

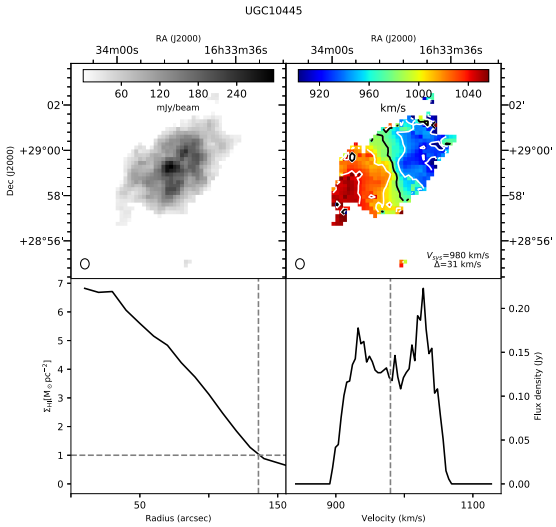
UGC10445
RA (J2000)
Dec (J2000)
mJy/beam
km/s
V_{sys}=980 km/s
Δ=31 km/s
Σ_{HI}[$M_\odot$ pc^{-2}]
Flux density (Jy)
Radius (arcsec)
Velocity (km/s)

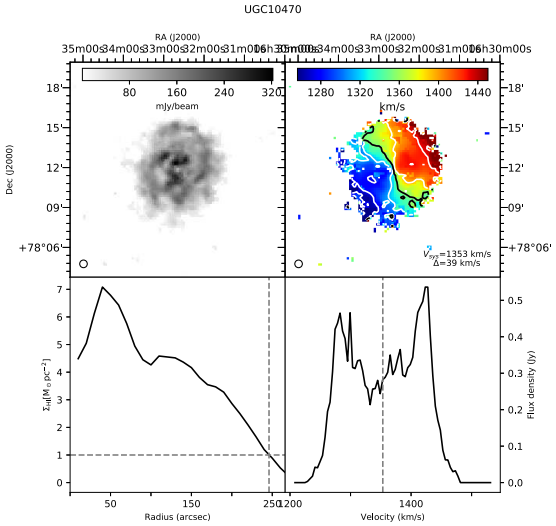
UGC10470
RA (J2000)
Dec (J2000)
mJy/beam
km/s
V_{sys}=1353 km/s
Δ=39 km/s
$\Sigma_{HI}[M_\odot pc^{-2}]$
Flux density (Jy)
Radius (arcsec)
Velocity (km/s)

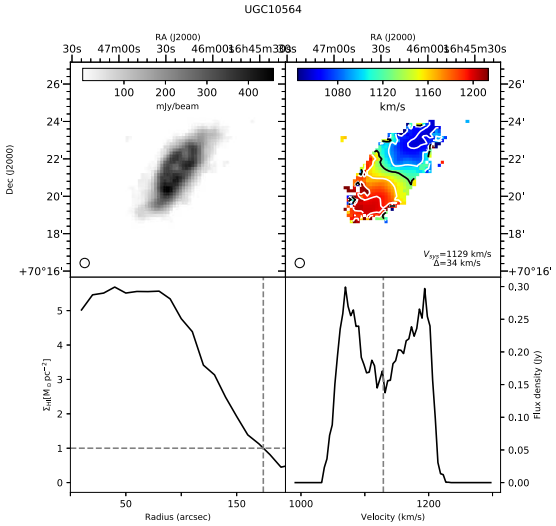
UGC10564
RA (J2000)
Dec (J2000)
mJy/beam
km/s
V_{sys}=1129 km/s
Δ=34 km/s
$\Sigma_{HI}[M_\odot pc^{-2}]$
Flux density (Jy)
Radius (arcsec)
Velocity (km/s)

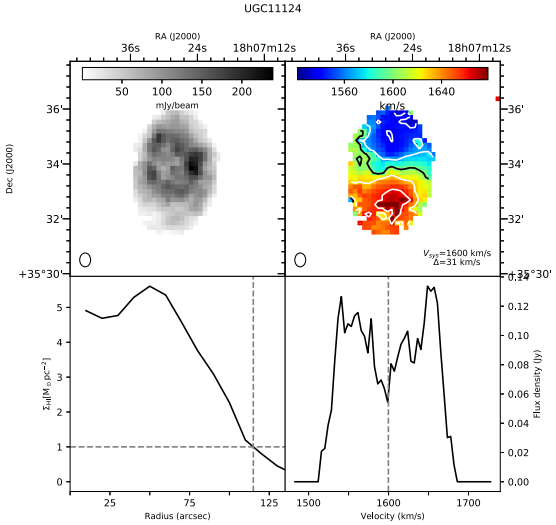
UGC11124
RA (J2000)
Dec (J2000)
mJy/beam
km/s
V_{sys}=1600 km/s
Δ=31 km/s
$\Sigma_{HI}[M_\odot pc^{-2}]$
Flux density (Jy)
Radius (arcsec)
Velocity (km/s)

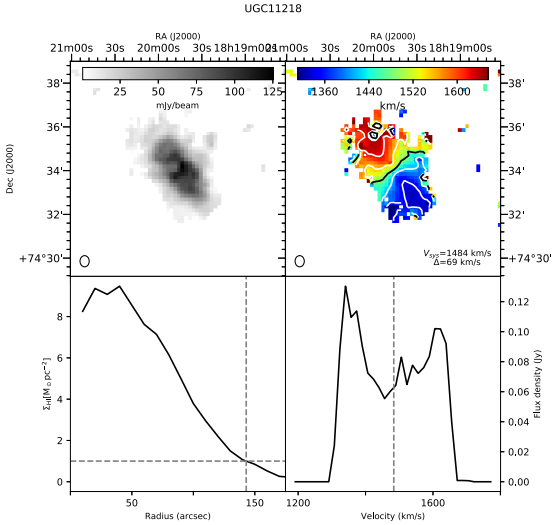
UGC11218
RA (J2000)
Dec (J2000)
mJy/beam
km/s
V_{sys}=1484 km/s
Δ=69 km/s
$\Sigma_{HI}[M_\odot pc^{-2}]$
Flux density (Jy)
Radius (arcsec)
Velocity (km/s)

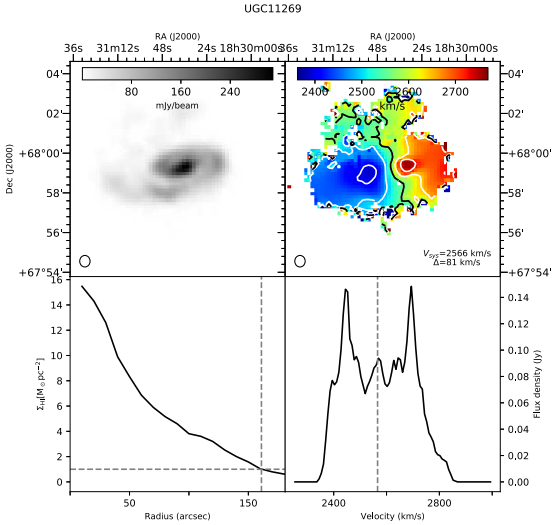
UGC11269
RA (J2000)
Dec (J2000)
mJy/beam
km/s
V_{sys}=2566 km/s
Δ=81 km/s
$\Sigma_{HI}[M_\odot pc^{-2}]$
Flux density (Jy)
Radius (arcsec)
Velocity (km/s)

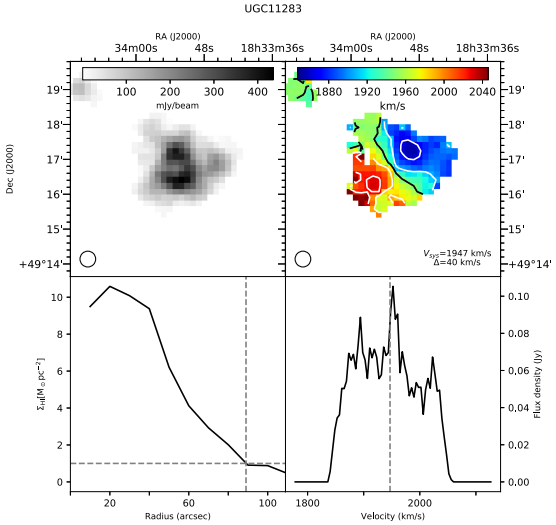
UGC11283
RA (J2000)
Dec (J2000)
mJy/beam
km/s
V_{sys}=1947 km/s
Δ=40 km/s
$\Sigma_{HI}[M_\odot pc^{-2}]$
Flux density (Jy)
Radius (arcsec)
Velocity (km/s)

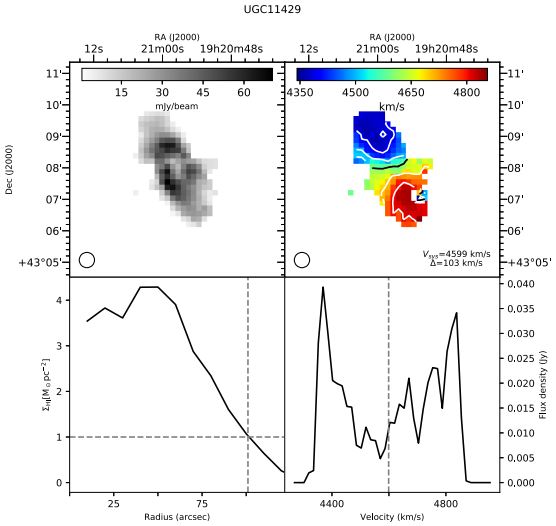
UGC11429
RA (J2000)
Dec (J2000)
mJy/beam
km/s
V_{sys}=4599 km/s
Δ=103 km/s
$\Sigma_{HI}[M_\odot pc^{-2}]$
Flux density (Jy)
Radius (arcsec)
Velocity (km/s)

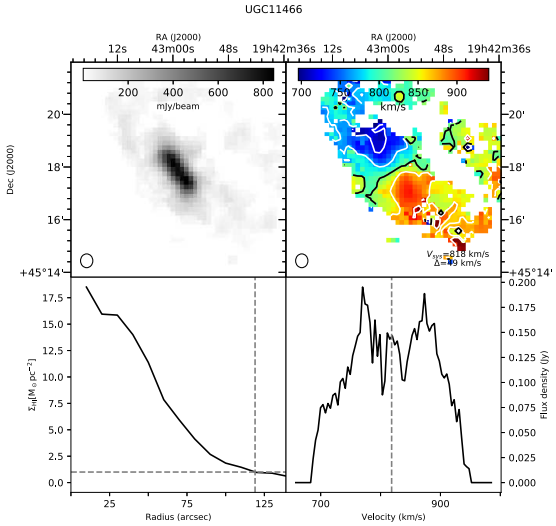
UGC11466
RA (J2000)
Dec (J2000)
mJy/beam
km/s
V_{sys}=818 km/s
Δ=79 km/s
$\Sigma_{HI}[M_\odot pc^{-2}]$
Flux density (Jy)
Radius (arcsec)
Velocity (km/s)

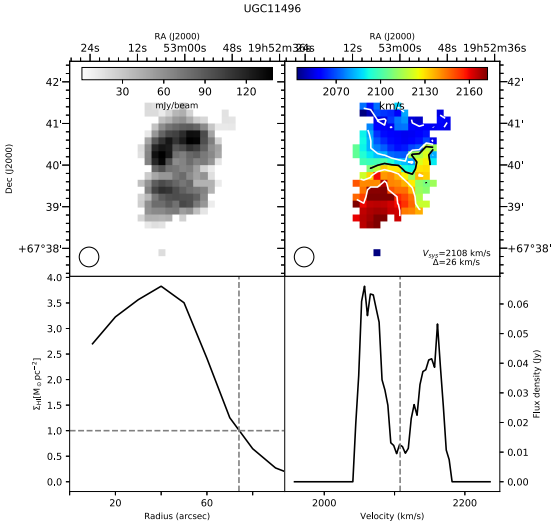
UGC11496
RA (J2000)
Dec (J2000)
mJy/beam
km/s
V_{sys}=2108 km/s
Δ=26 km/s
$\Sigma_{HI}[M_\odot pc^{-2}]$
Flux density (Jy)
Radius (arcsec)
Velocity (km/s)

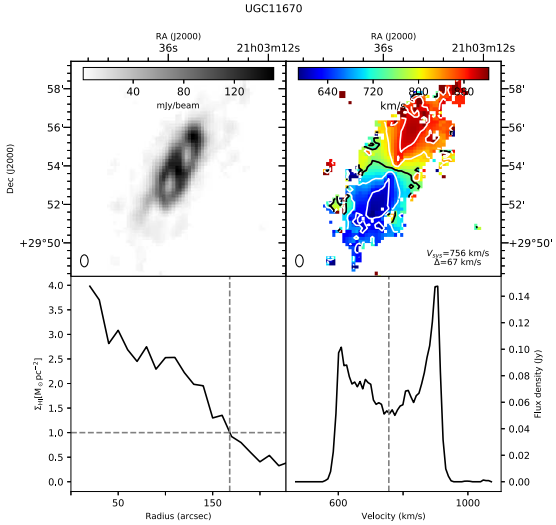
UGC11670
RA (J2000)
Dec (J2000)
mJy/beam
km/s
V_{sys}=756 km/s
Δ=67 km/s
$\Sigma_{HI}[M_\odot pc^{-2}]$
Flux density (Jy)
Radius (arcsec)
Velocity (km/s)

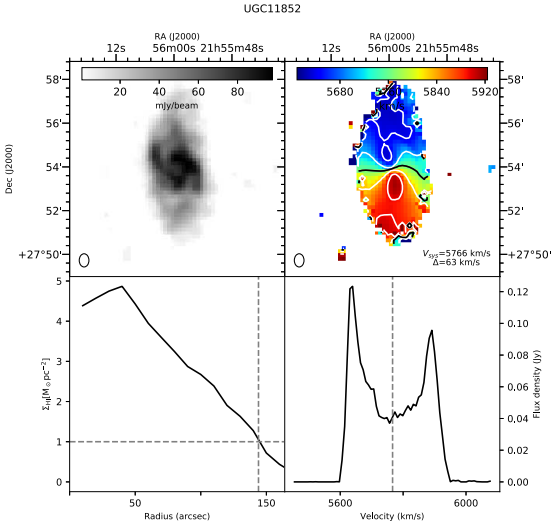
UGC11852
RA (J2000)
Dec (J2000)
mJy/beam
km/s
V_{sys}=5766 km/s
Δ=63 km/s
$\Sigma_{HI}[M_\odot pc^{-2}]$
Flux density (Jy)
Radius (arcsec)
Velocity (km/s)

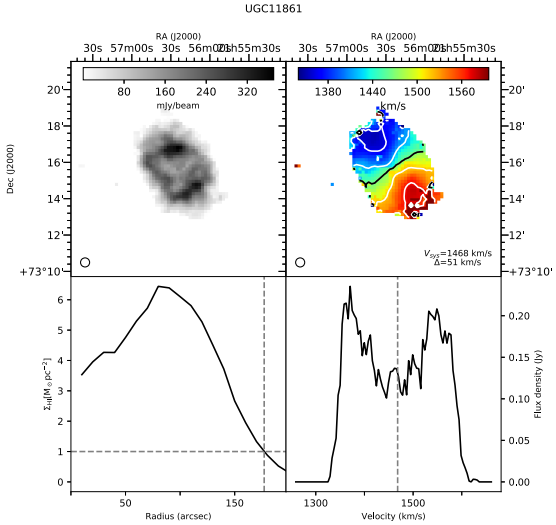
UGC11861
RA (J2000)
Dec (J2000)
mJy/beam
km/s
V_{sys}=1468 km/s
Δ=51 km/s
$\Sigma_{HI}[M_\odot pc^{-2}]$
Flux density (Jy)
Radius (arcsec)
Velocity (km/s)

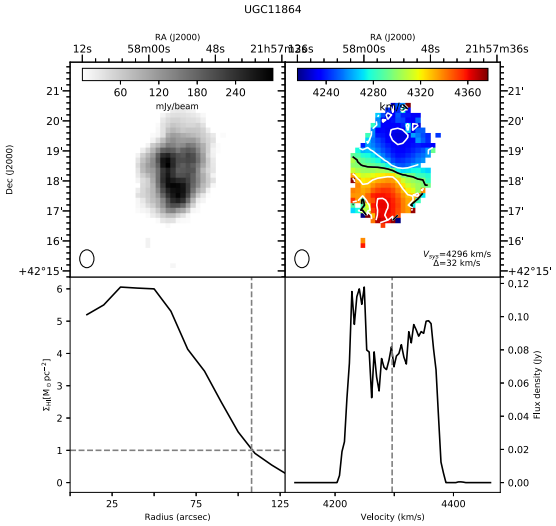
UGC11864
RA (J2000)
Dec (J2000)
mJy/beam
km/s
V_{sys}=4296 km/s
Δ=32 km/s
Radius (arcsec)
Velocity (km/s)
Flux density (Jy)

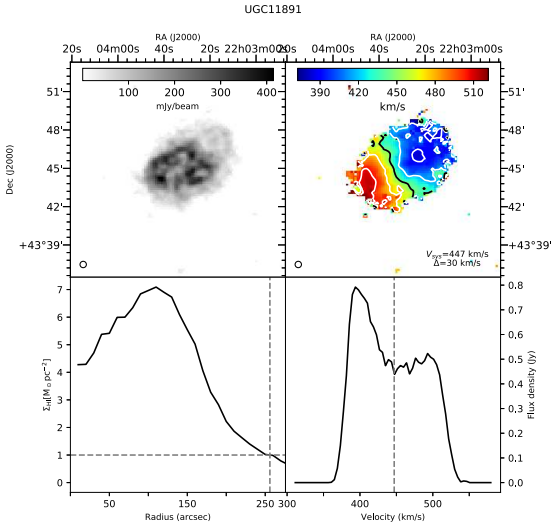
UGC11891
RA (J2000)
Dec (J2000)
mJy/beam
km/s
V_{sys}=447 km/s
Δ=30 km/s
Radius (arcsec)
Velocity (km/s)
Flux density (Jy)

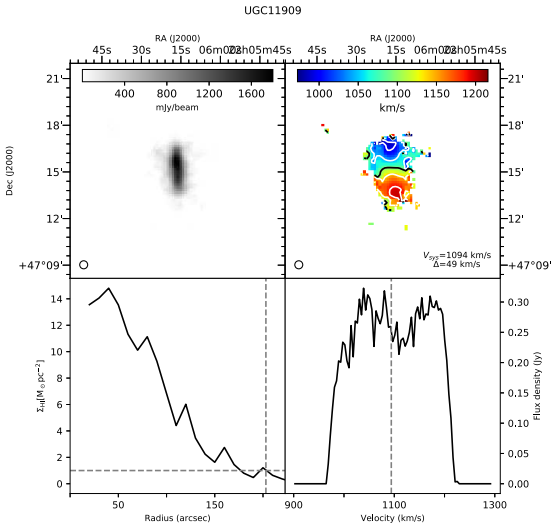
UGC11909
RA (J2000)
Dec (J2000)
mJy/beam
km/s
V_{sys}=1094 km/s
Δ=49 km/s
Radius (arcsec)
Velocity (km/s)
Flux density (Jy)

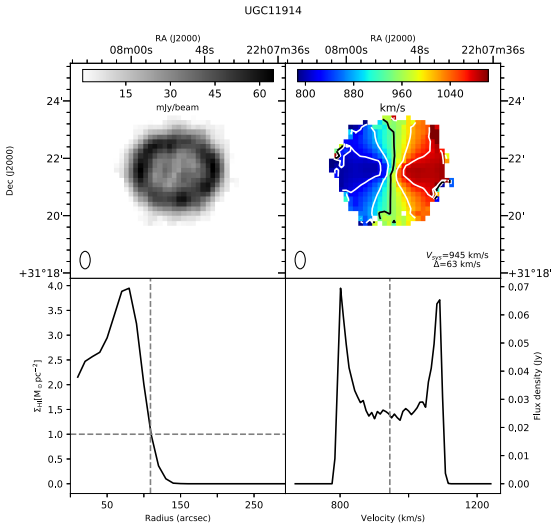
UGC11914
RA (J2000)
Dec (J2000)
mJy/beam
km/s
V_{sys}=945 km/s
Δ=63 km/s
Radius (arcsec)
Velocity (km/s)
Flux density (Jy)

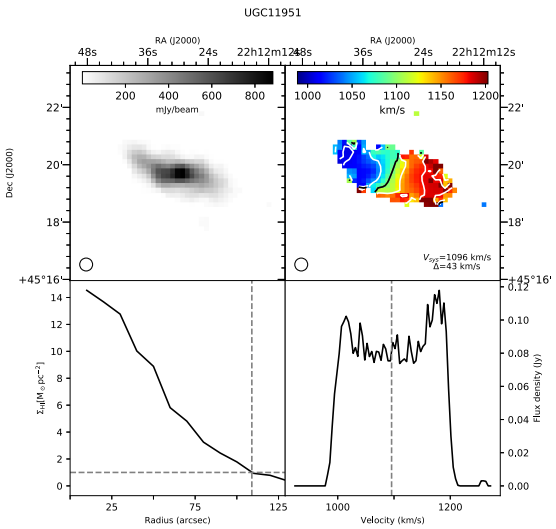
UGC11951
RA (J2000)
Dec (J2000)
mJy/beam
km/s
V_{sys}=1096 km/s
Δ=43 km/s
Radius (arcsec)
Velocity (km/s)
Flux density (Jy)

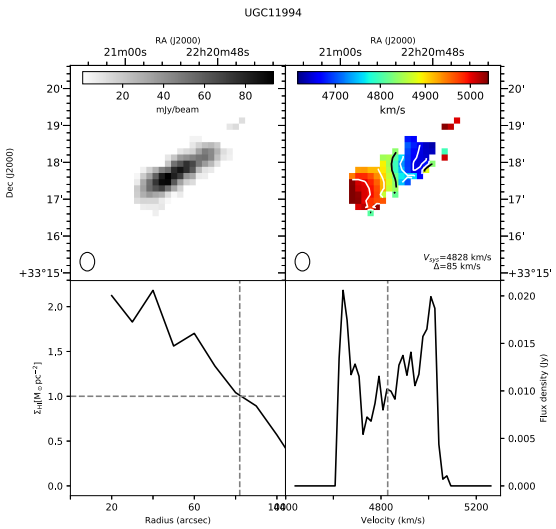
UGC11994
RA (J2000)
Dec (J2000)
mJy/beam
km/s
V_{sys}=4828 km/s
Δ=85 km/s
Radius (arcsec)
Velocity (km/s)
Flux density (Jy)

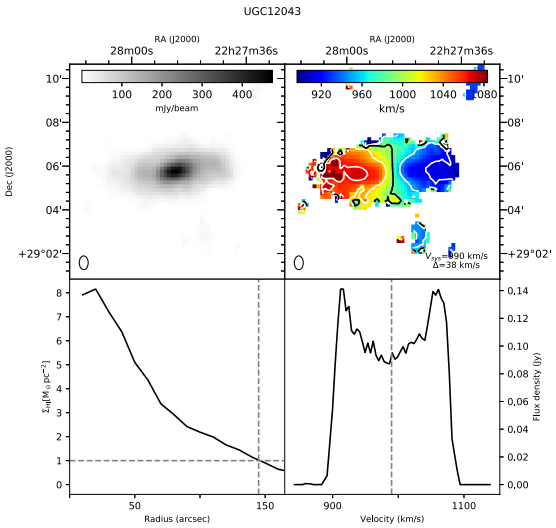
UGC12043
RA (J2000)
28m00s
22h27m36s
mJy/beam
km/s
Dec (J2000)
+29°02'
V_{sys}=990 km/s
Δ=38 km/s
Radius (arcsec)
Velocity (km/s)
Flux density (Jy)

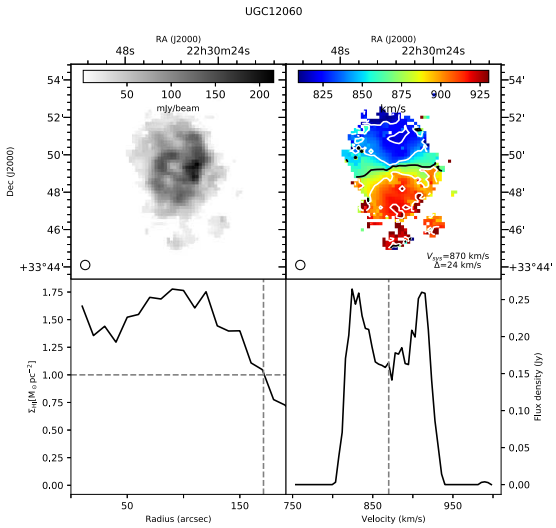
UGC12060
RA (J2000)
48s
22h30m24s
mJy/beam
km/s
Dec (J2000)
+33°44'
V_{sys}=870 km/s
Δ=24 km/s
Radius (arcsec)
Velocity (km/s)
Flux density (Jy)

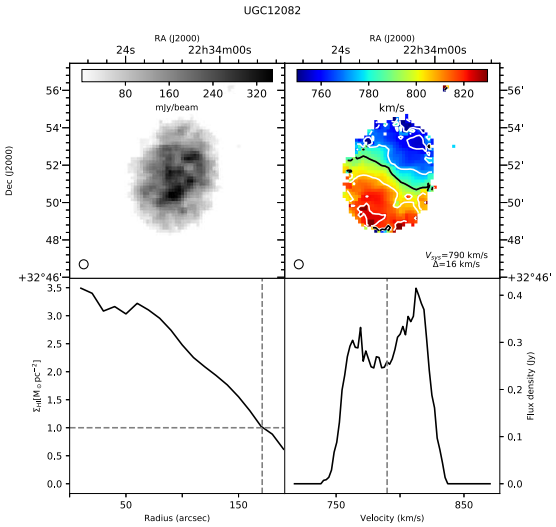
UGC12082
RA (J2000)
24s
22h34m00s
mJy/beam
km/s
Dec (J2000)
+32°46'
V_{sys}=790 km/s
Δ=16 km/s
Radius (arcsec)
Velocity (km/s)
Flux density (Jy)

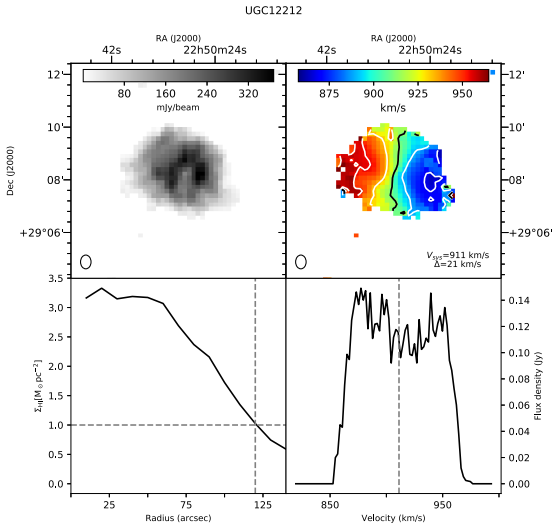
UGC12212
RA (J2000)
42s
22h50m24s
mJy/beam
km/s
Dec (J2000)
+29°06'
V_{sys}=911 km/s
Δ=21 km/s
Radius (arcsec)
Velocity (km/s)
Flux density (Jy)

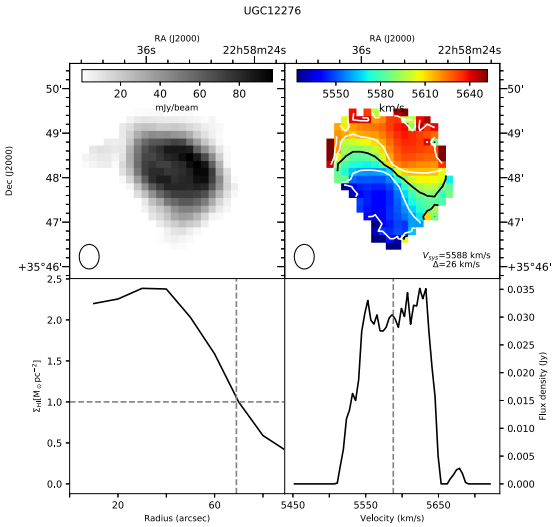
UGC12276
RA (J2000)
36s
22h58m24s
mJy/beam
km/s
Dec (J2000)
+35°46'
V_{sys}=5588 km/s
Δ=26 km/s
Radius (arcsec)
Velocity (km/s)
Flux density (Jy)

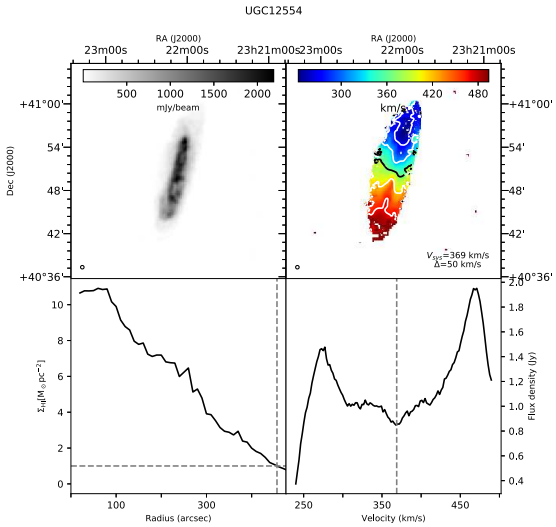
UGC12554
RA (J2000)
23m00s
22m00s
23h21m00s
mJy/beam
km/s
Dec (J2000)
+40°36'
V_{sys}=369 km/s
Δ=50 km/s
Radius (arcsec)
Velocity (km/s)
Flux density (Jy)

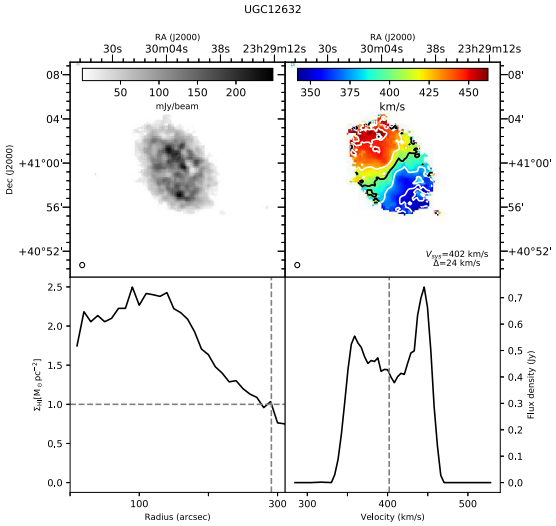
UGC12632
RA (J2000)
Dec (J2000)
mJy/beam
km/s
V_{sys}=402 km/s
Δ=24 km/s
Σ_{HI}[M$_\odot$ pc^{-2}]
Flux density (Jy)
Radius (arcsec)
Velocity (km/s)

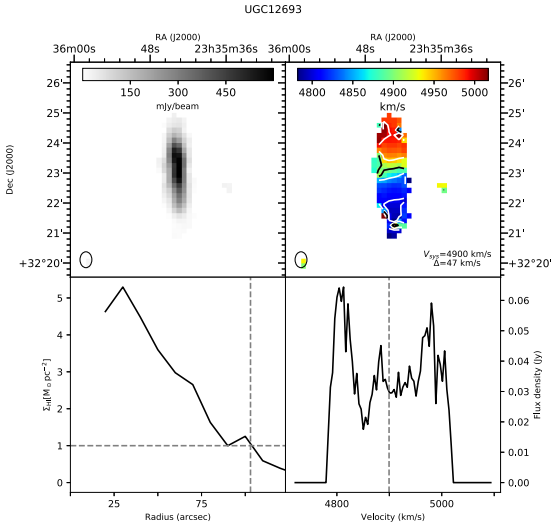
UGC12693
RA (J2000)
Dec (J2000)
mJy/beam
km/s
V_{sys}=4900 km/s
Δ=47 km/s
Σ_{HI}[M$_\odot$ pc^{-2}]
Flux density (Jy)
Radius (arcsec)
Velocity (km/s)

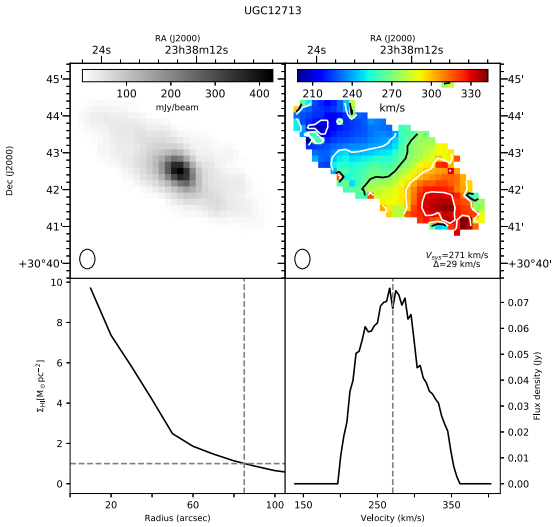
UGC12713
RA (J2000)
Dec (J2000)
mJy/beam
km/s
V_{sys}=271 km/s
Δ=29 km/s
Σ_{HI}[M$_\odot$ pc^{-2}]
Flux density (Jy)
Radius (arcsec)
Velocity (km/s)

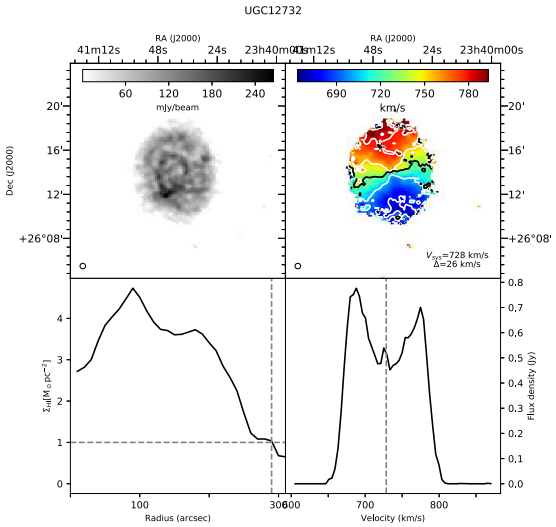
UGC12732
RA (J2000)
Dec (J2000)
mJy/beam
km/s
V_{sys}=728 km/s
Δ=26 km/s
Σ_{HI}[M$_\odot$ pc^{-2}]
Flux density (Jy)
Radius (arcsec)
Velocity (km/s)

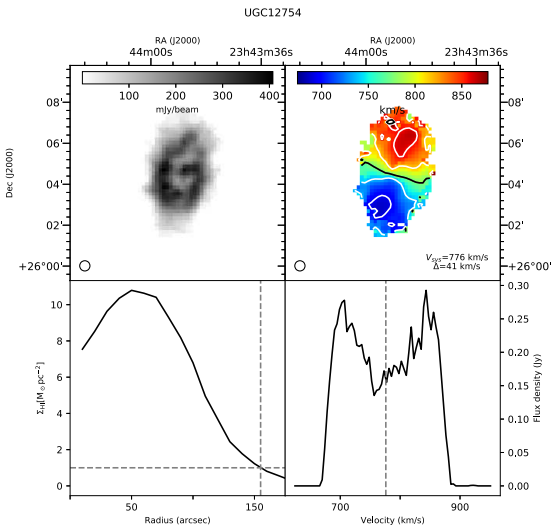
UGC12754
RA (J2000)
Dec (J2000)
mJy/beam
km/s
V_{sys}=776 km/s
Δ=41 km/s
Σ_{HI}[M$_\odot$ pc^{-2}]
Flux density (Jy)
Radius (arcsec)
Velocity (km/s)

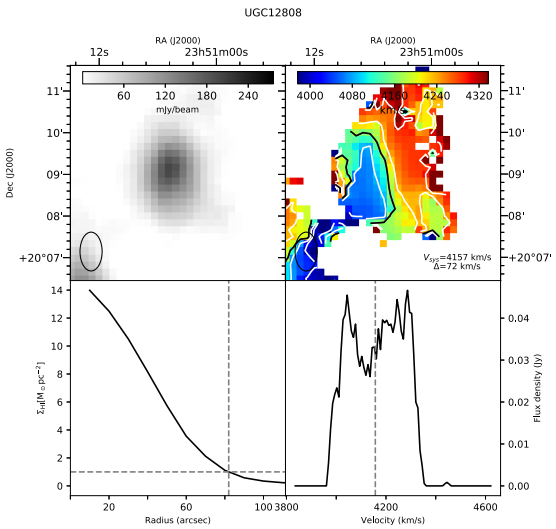
UGC12808
RA (J2000)
Dec (J2000)
mJy/beam
km/s
V_{sys}=4157 km/s
Δ=72 km/s
Σ_{HI}[M$_\odot$ pc^{-2}]
Flux density (Jy)
Radius (arcsec)
Velocity (km/s)

A.2 Atlas of WISE W1 and W3 imaging

Description: WISE imaging data that were used in this study were provided by Jarrett et al. (2017). This atlas contains the W1 (left) and W3 (right) images for our entire sample. Some of the low stellar mass galaxies in the sample are not detected in W3 because of low dust quantities (See Chapter 3.2).

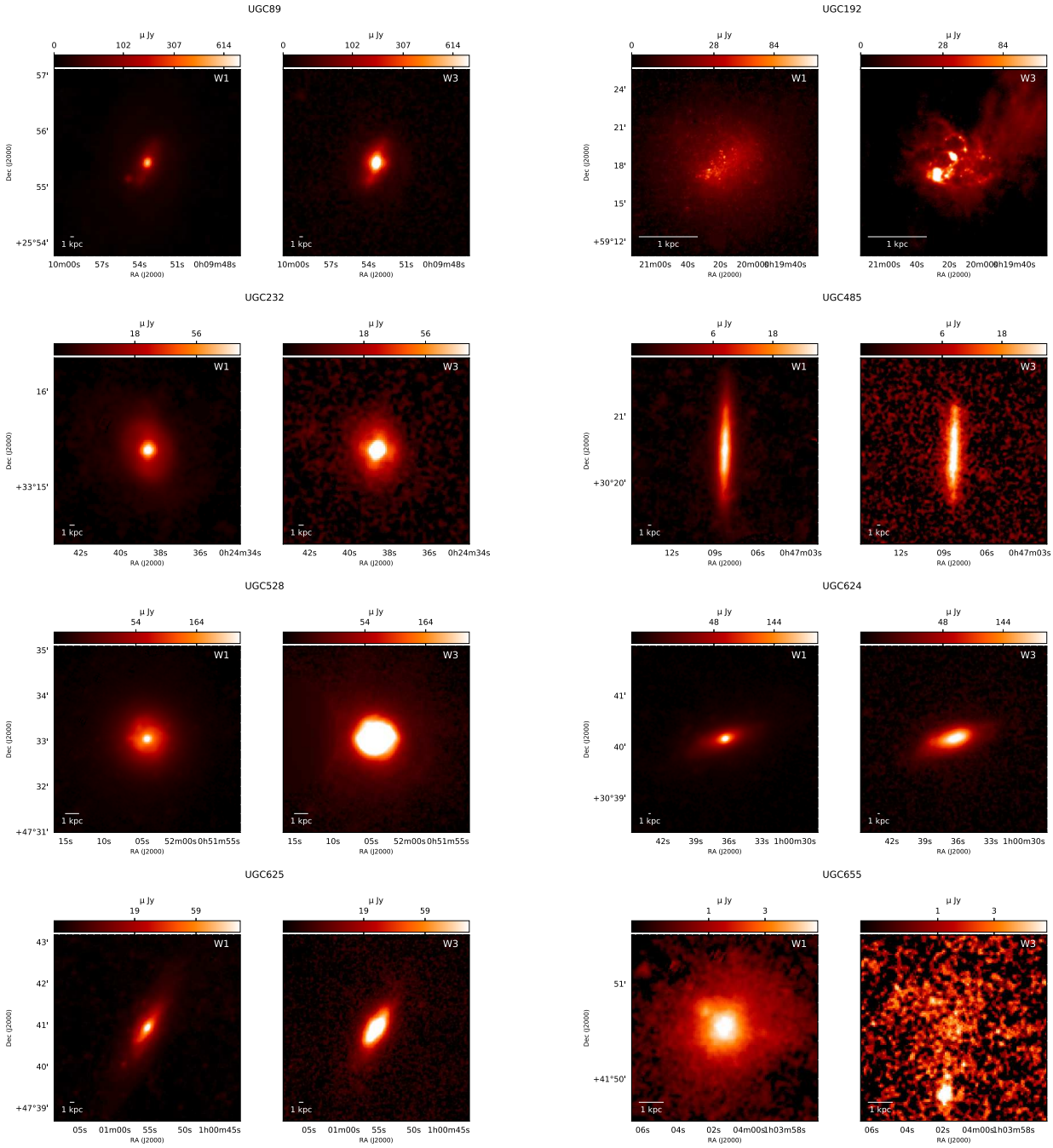
UGC89
UGC192
UGC232
UGC485
UGC528
UGC624
UGC625
UGC655
W1
W3
μ Jy
Dec (J2000)
RA (J2000)
1 kpc

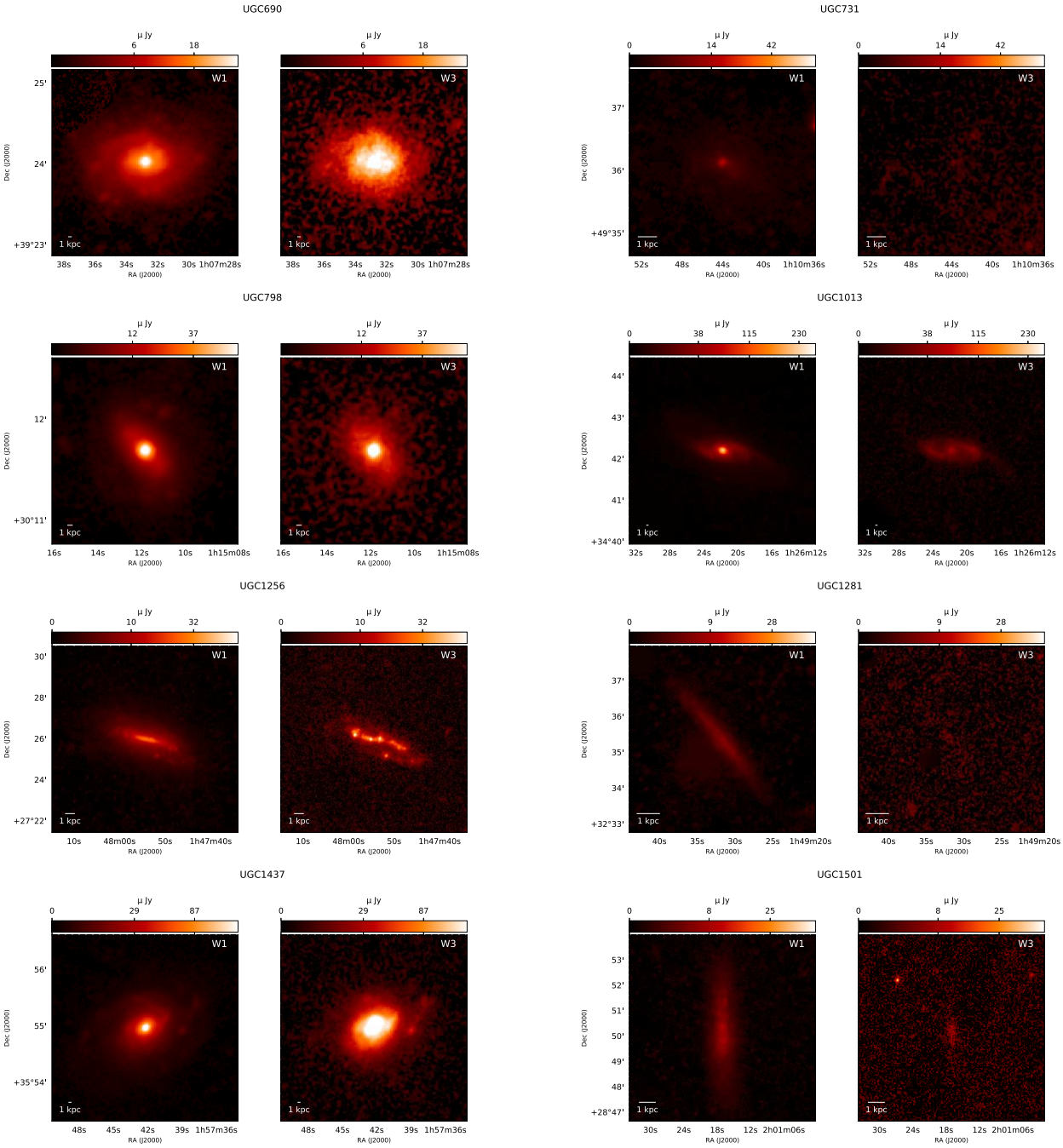
UGC690
UGC731
UGC798
UGC1013
UGC1256
UGC1281
UGC1437
UGC1501
μ Jy
W1
W3
1 kpc
Dec (J2000)
RA (J2000)

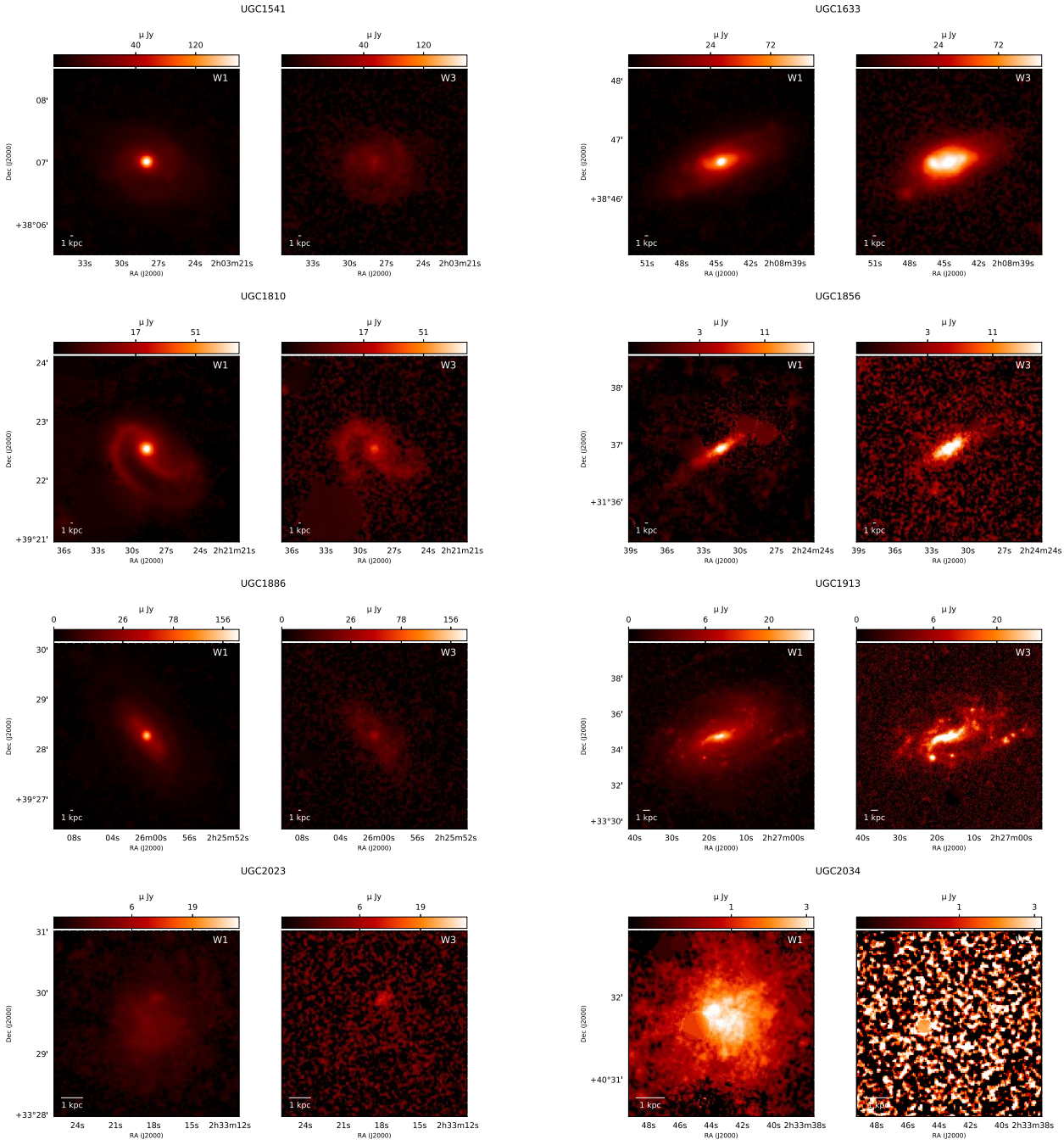
UGC1541
UGC1633
UGC1810
UGC1856
UGC1886
UGC1913
UGC2023
UGC2034
W1
W3
μ Jy
1 kpc
RA (J2000)
Dec (J2000)

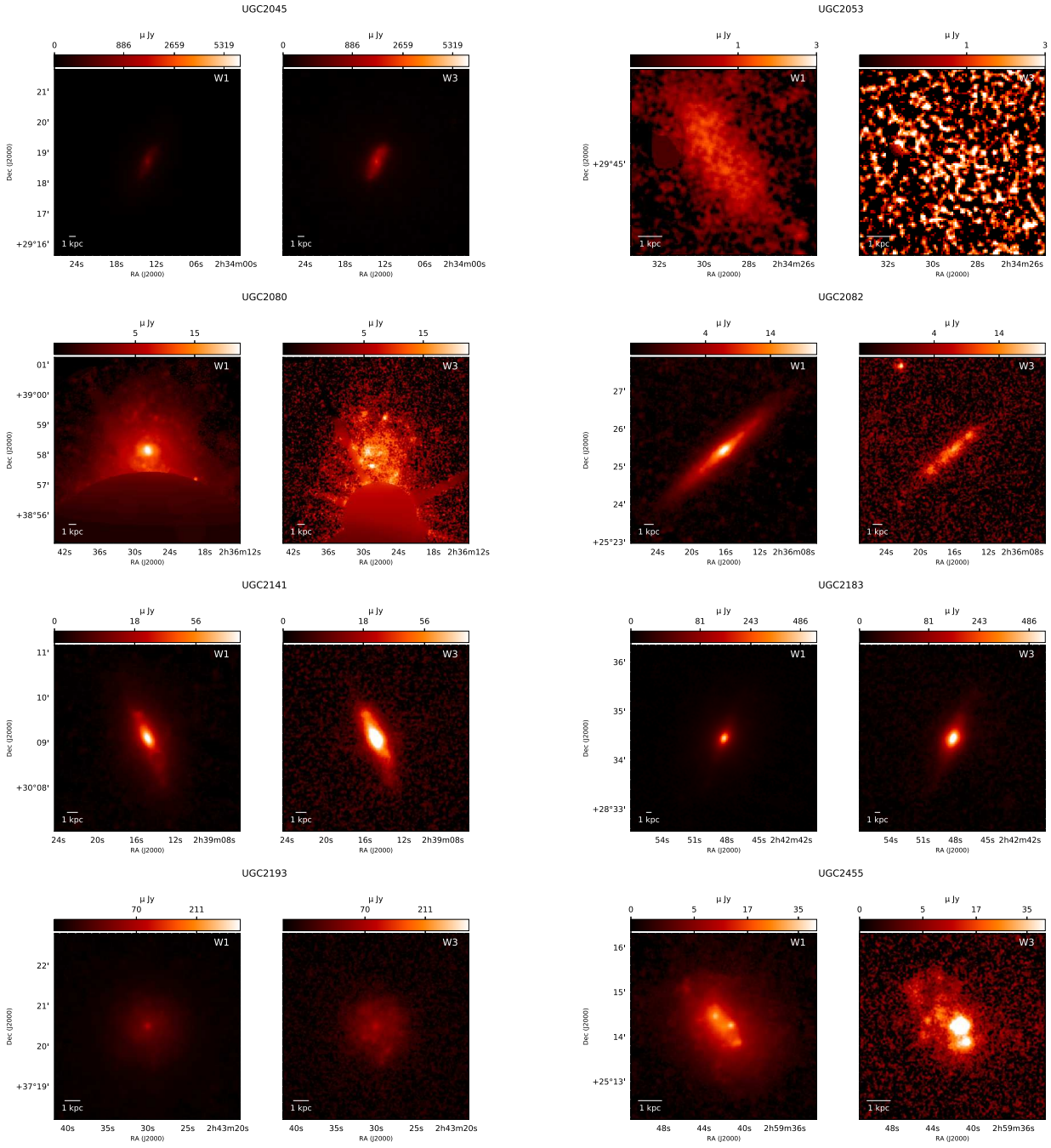
UGC2045
UGC2053
UGC2080
UGC2082
UGC2141
UGC2183
UGC2193
UGC2455
W1
W3
μ Jy
1 kpc
RA (J2000)
Dec (J2000)

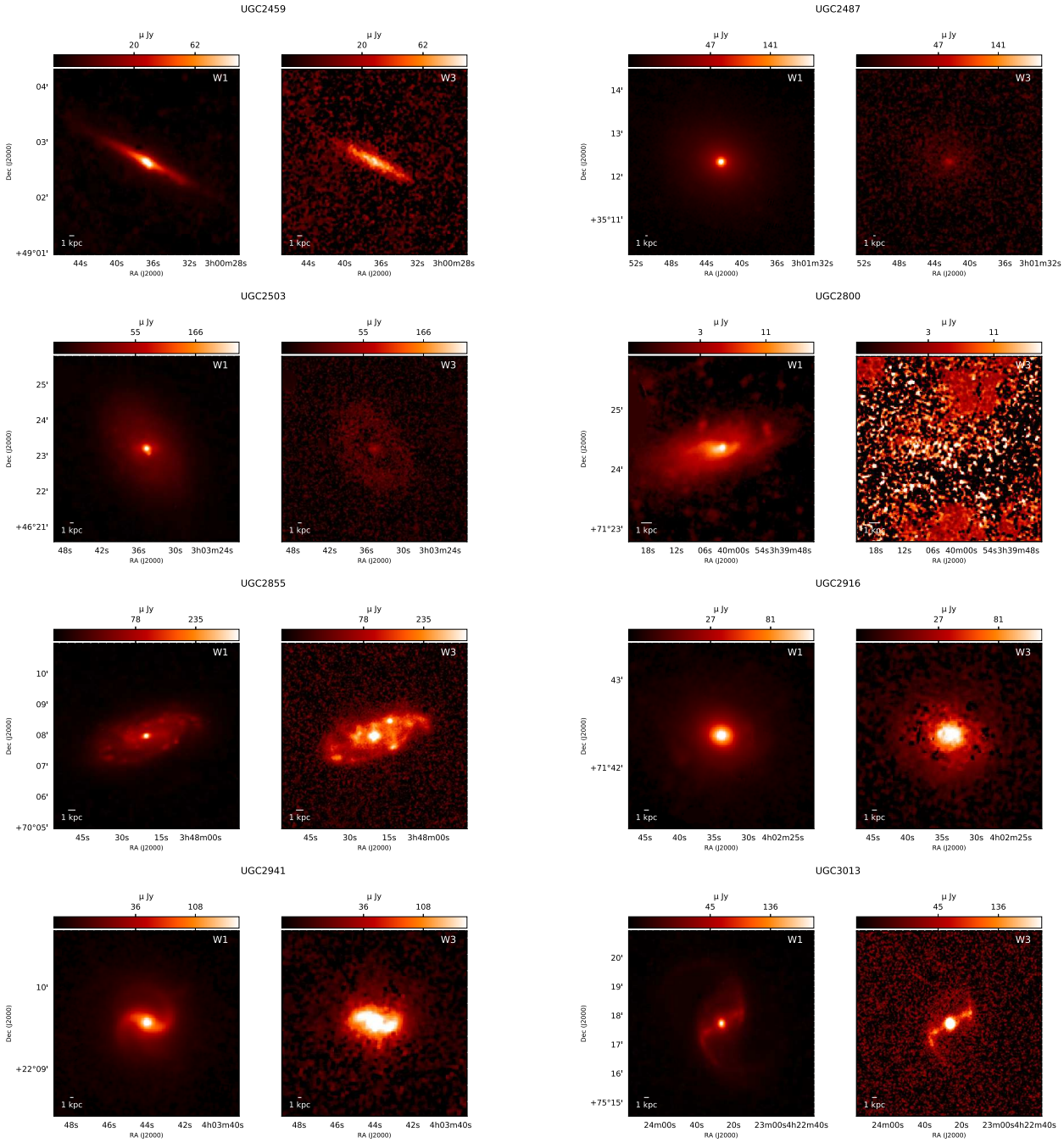
UGC2459
UGC2487
UGC2503
UGC2800
UGC2855
UGC2916
UGC2941
UGC3013
W1
W3
μ Jy
Dec (J2000)
RA (J2000)
1 kpc

UGC3137

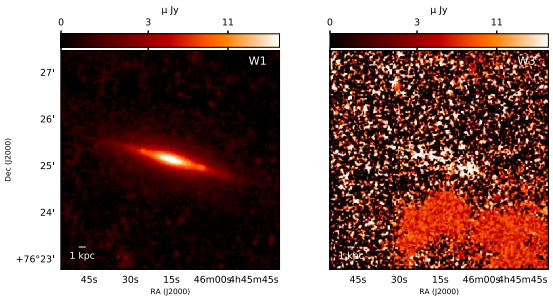

UGC3205

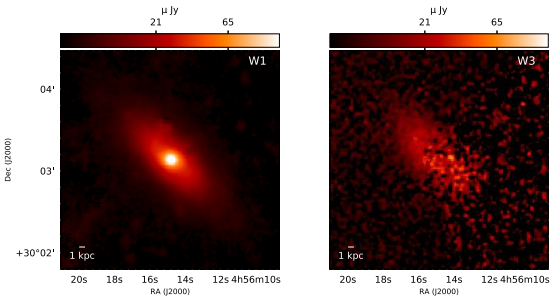

UGC3326

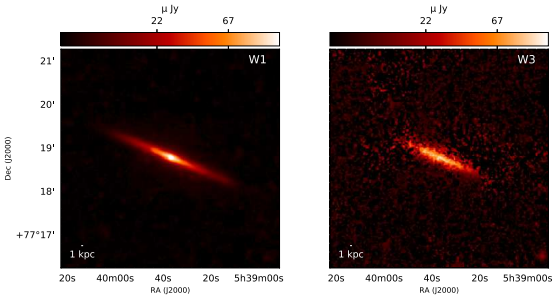

UGC3334

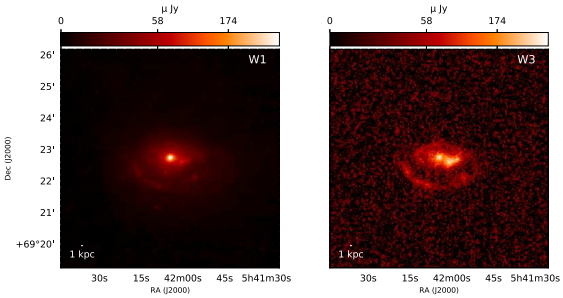

UGC3354

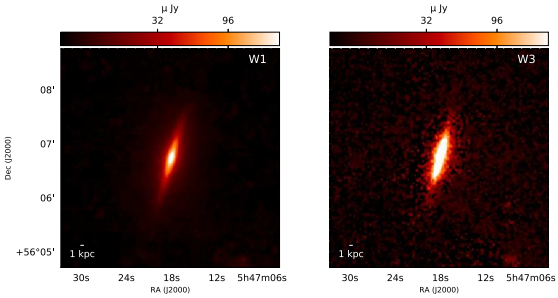

UGC3371

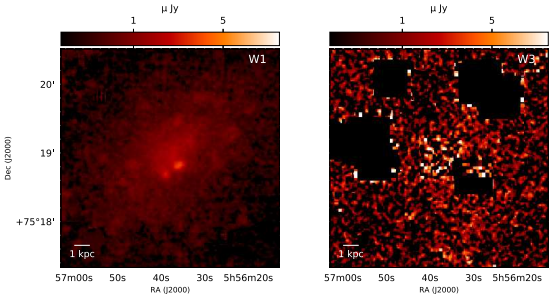

UGC3382

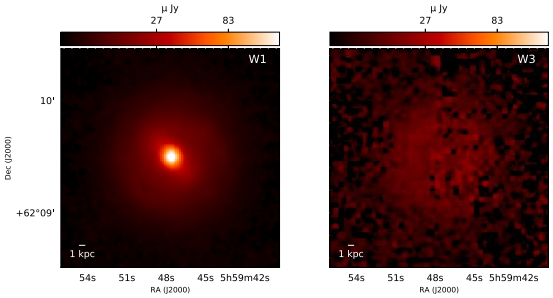

UGC3384

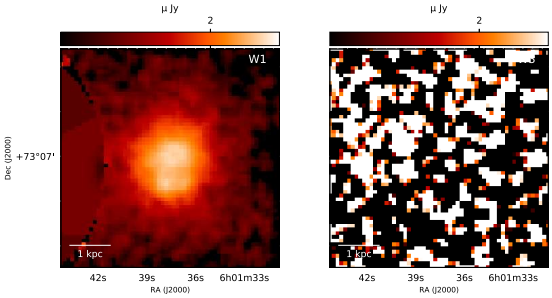

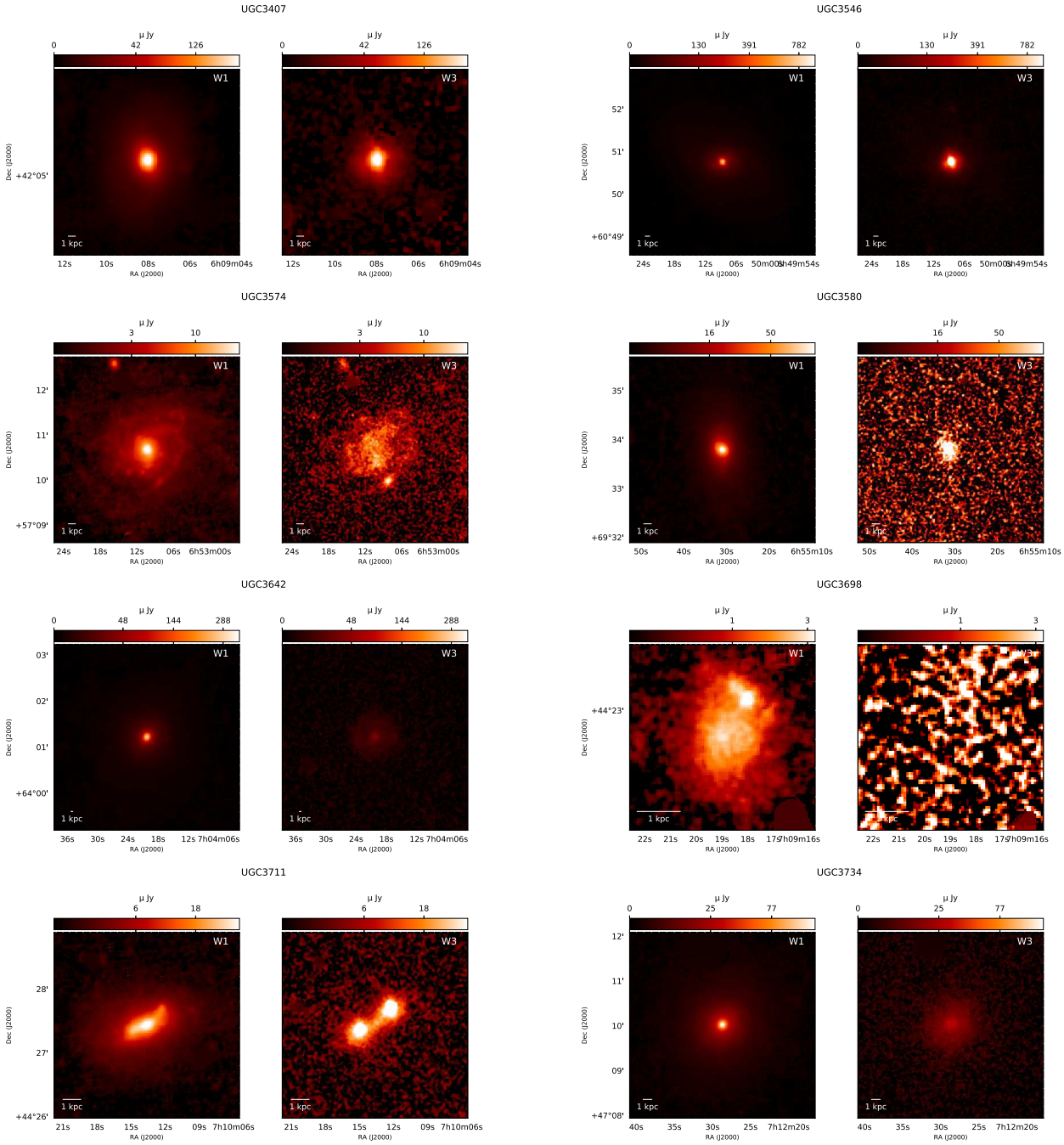
UGC3407
UGC3546
UGC3574
UGC3580
UGC3642
UGC3698
UGC3711
UGC3734
W1
W3
μ Jy
RA (J2000)
Dec (J2000)
1 kpc

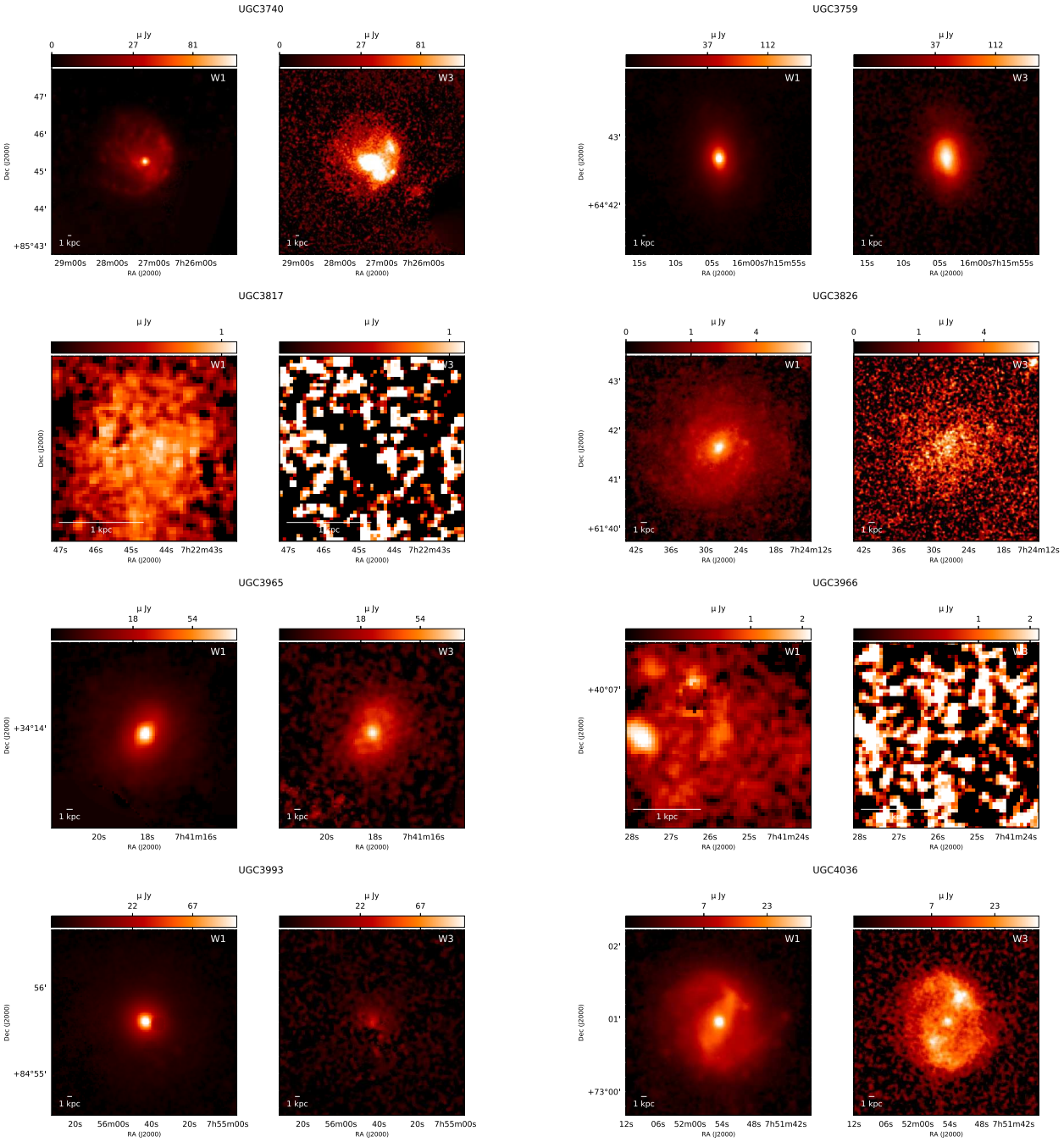
UGC3740
UGC3759
UGC3817
UGC3826
UGC3965
UGC3966
UGC3993
UGC4036
W1
W3
μ Jy
1 kpc
RA (J2000)
Dec (J2000)

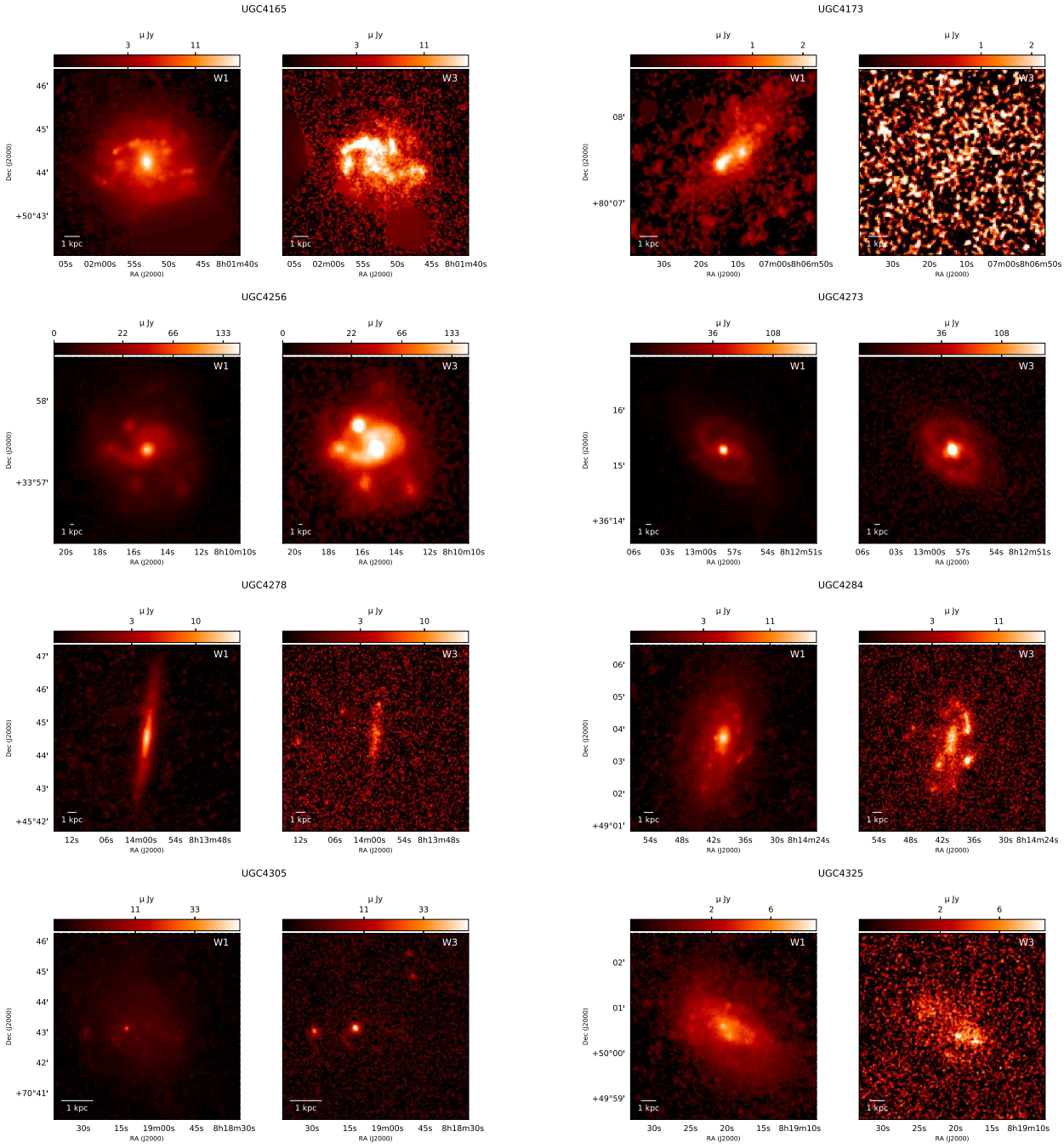
UGC4165
UGC4173
UGC4256
UGC4273
UGC4278
UGC4284
UGC4305
UGC4325
W1
W3
μ Jy
1 kpc
RA (J2000)
Dec (J2000)

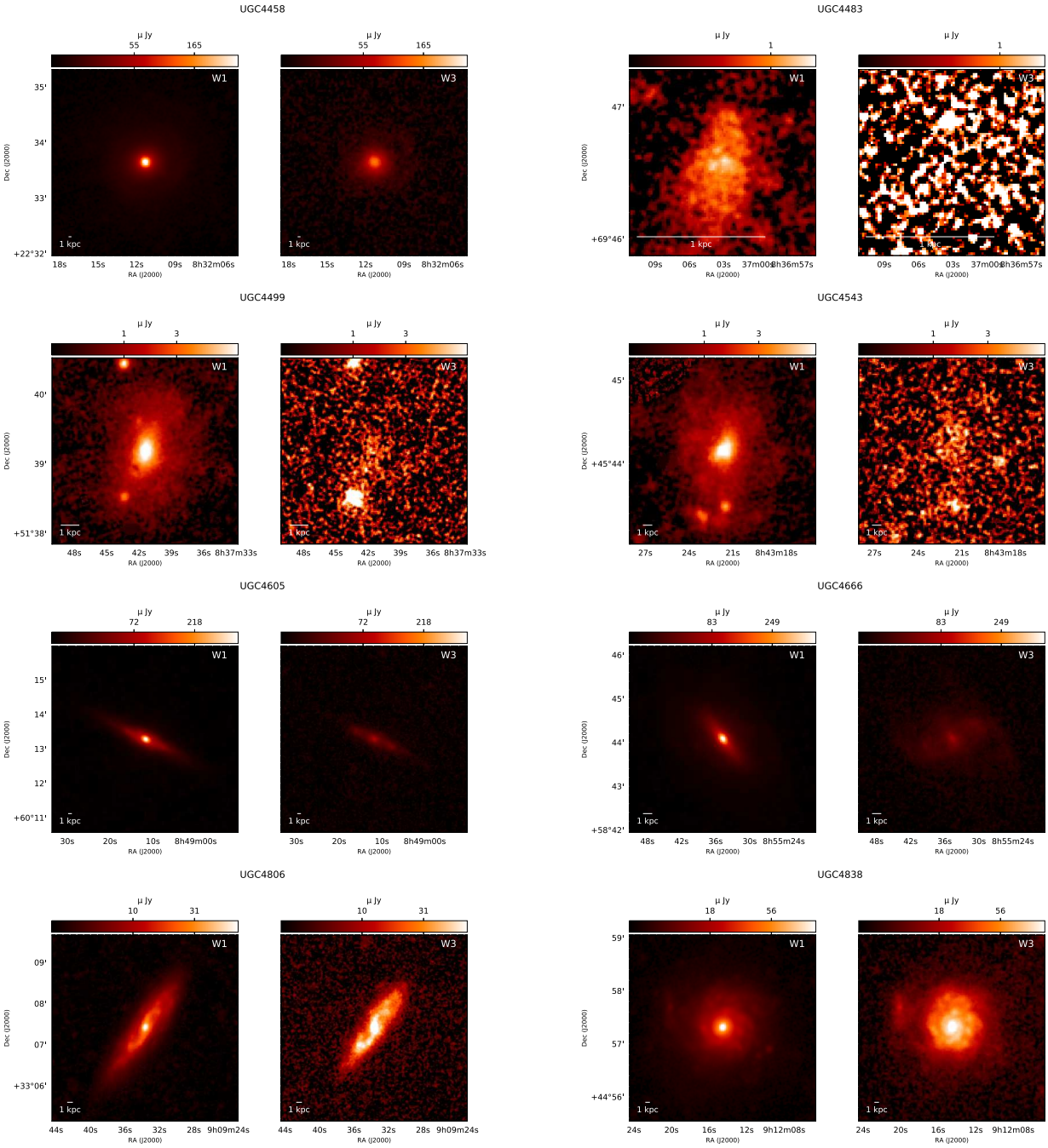
UGC4458
UGC4483
UGC4499
UGC4543
UGC4605
UGC4666
UGC4806
UGC4838
W1
W3
μ Jy
1 kpc
RA (J2000)
Dec (J2000)

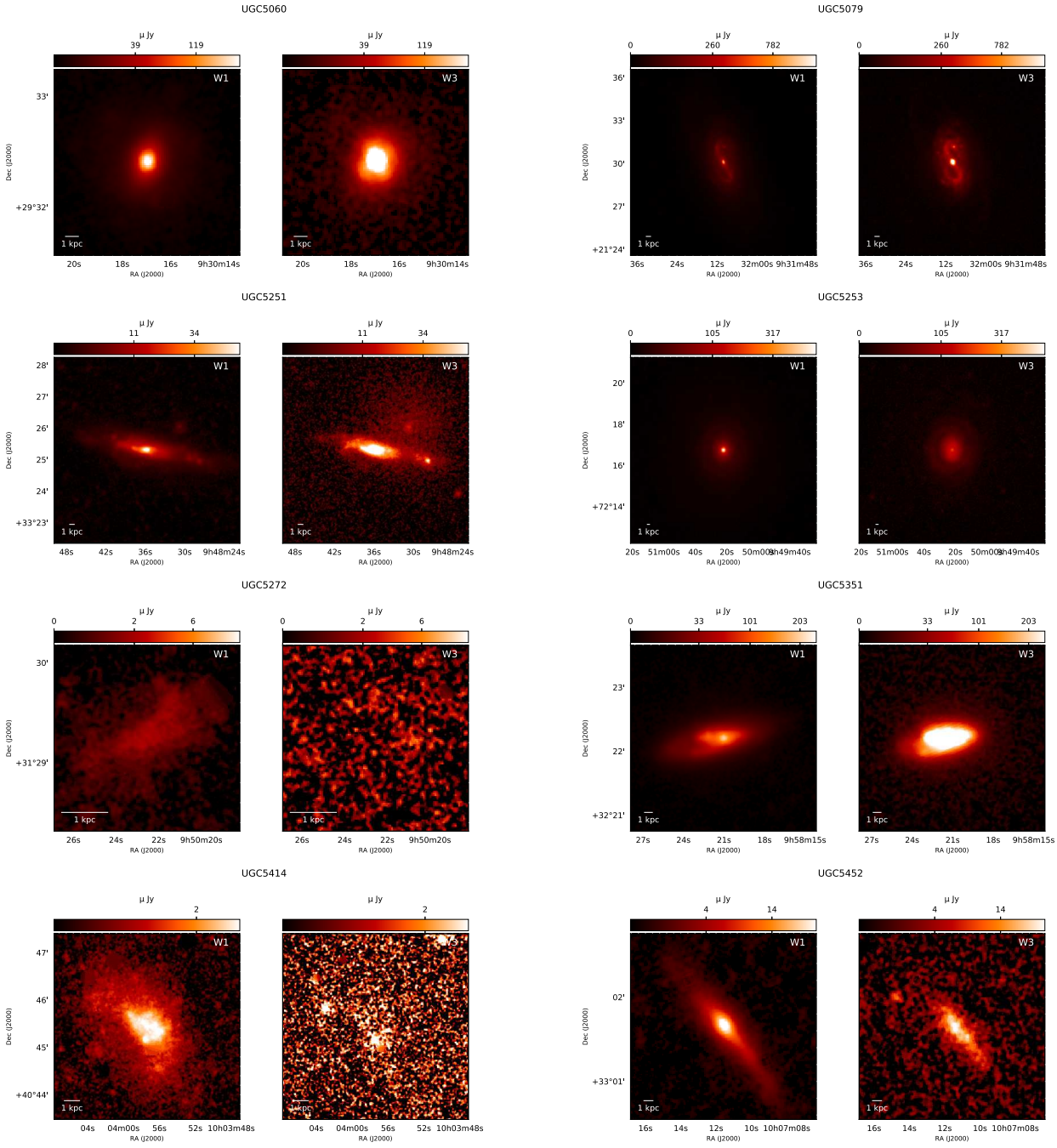
UGC5060
UGC5079
UGC5251
UGC5253
UGC5272
UGC5351
UGC5414
UGC5452
W1
W3
μ Jy
1 kpc
Dec (J2000)
RA (J2000)

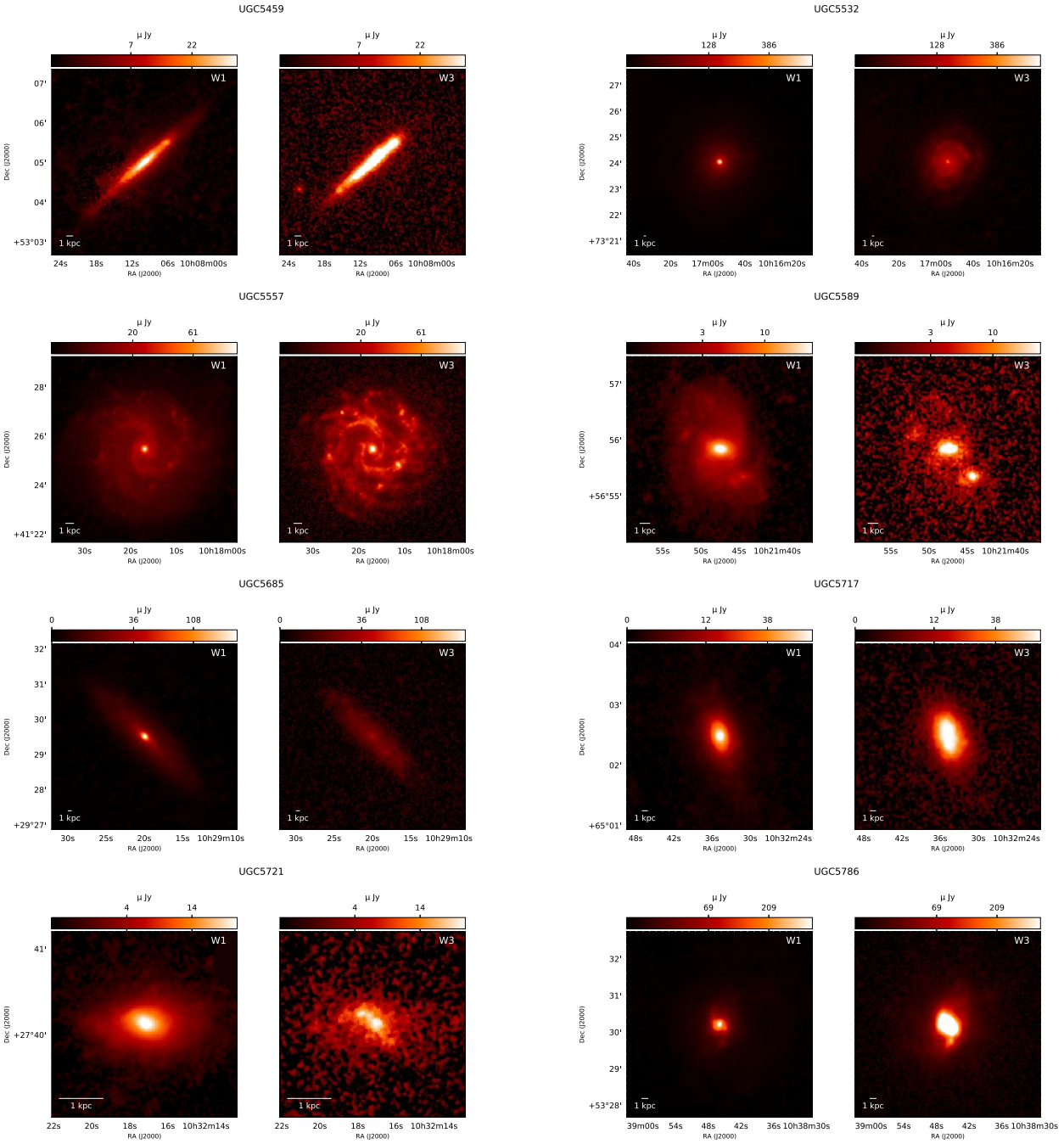
UGC5459
UGC5532
UGC5557
UGC5589
UGC5685
UGC5717
UGC5721
UGC5786
W1
W3
μ Jy
1 kpc
RA (J2000)
Dec (J2000)

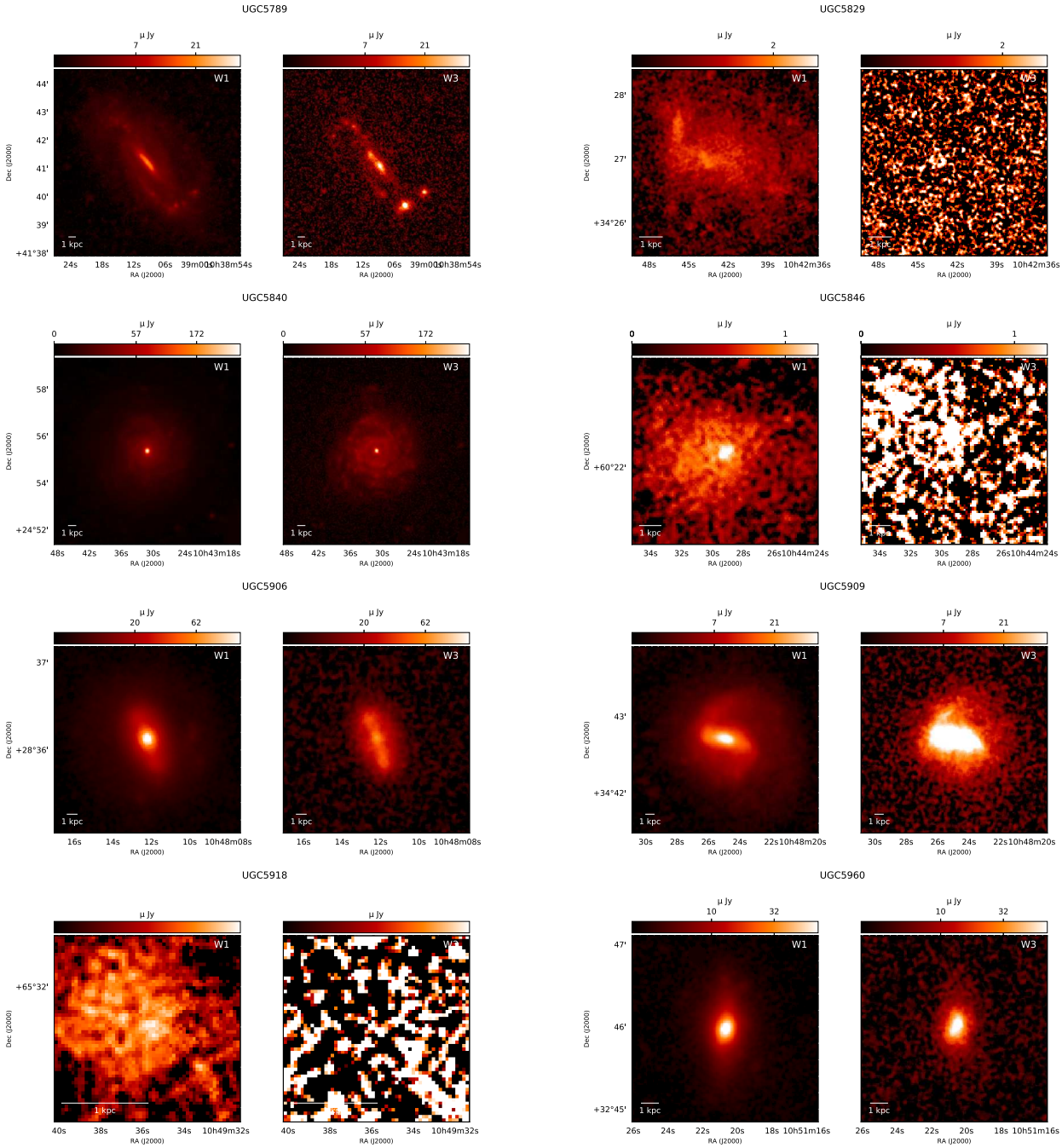
UGC5789
UGC5829
UGC5840
UGC5846
UGC5906
UGC5909
UGC5918
UGC5960
W1
W3
μ Jy
RA (J2000)
Dec (J2000)
1 kpc

UGC5997

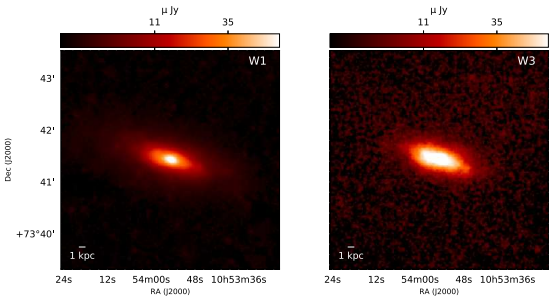

UGC6001

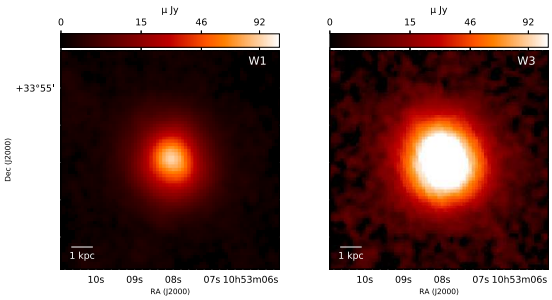

UGC6118

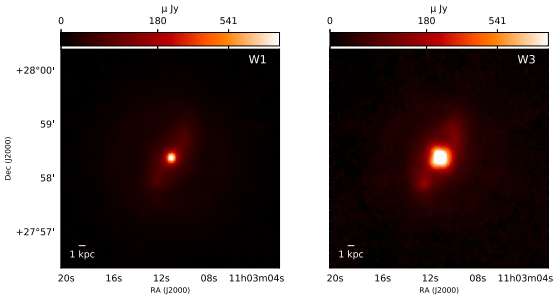

UGC6126

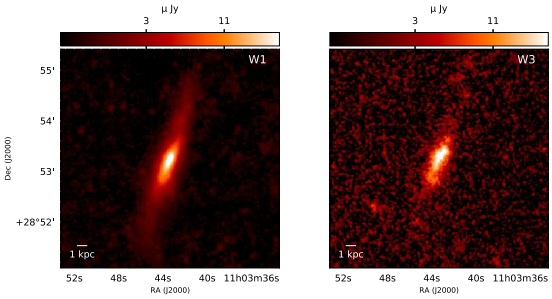

UGC6161

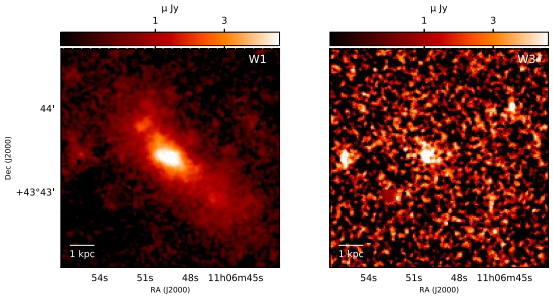

UGC6225

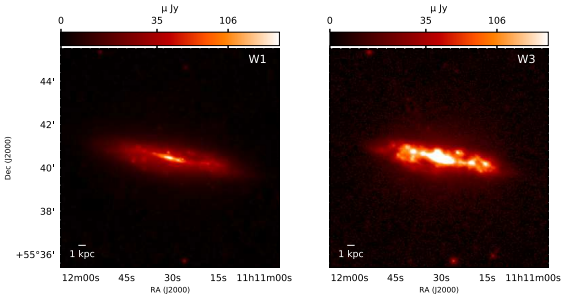

UGC6251

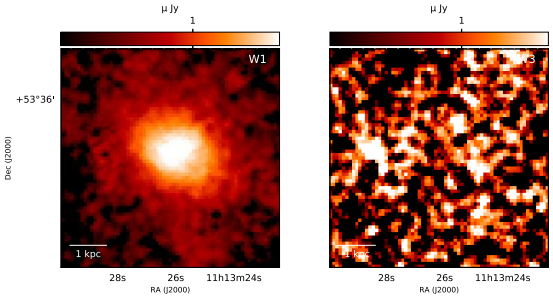

UGC6263

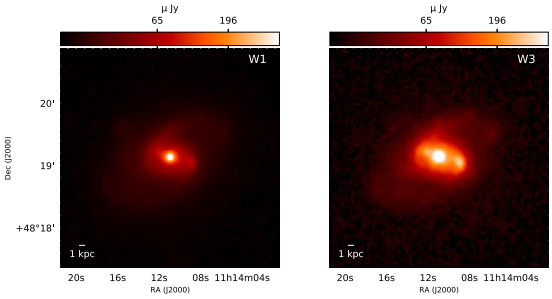

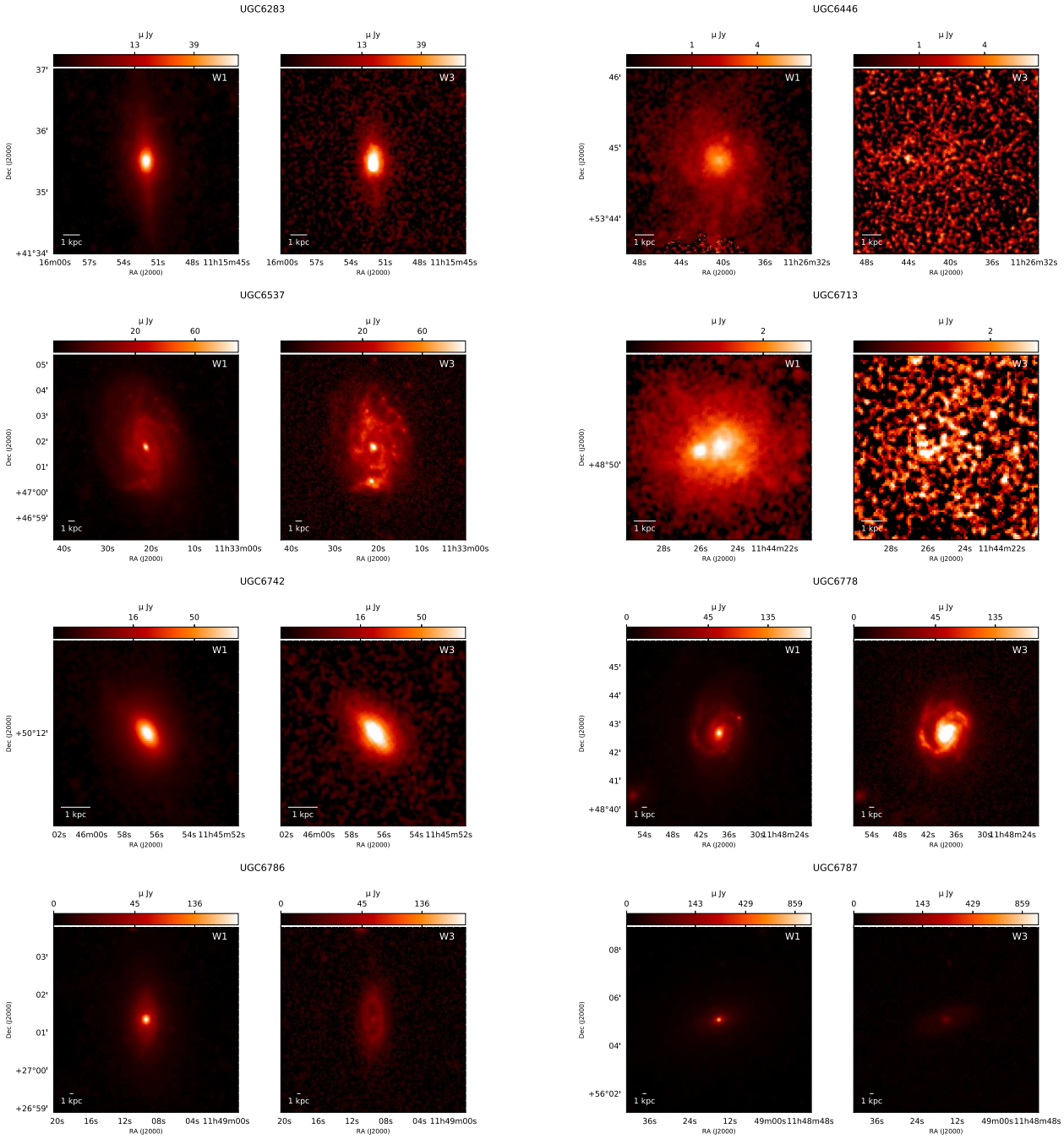
UGC6283
UGC6446
UGC6537
UGC6713
UGC6742
UGC6778
UGC6786
UGC6787
W1
W3
μ Jy
RA (J2000)
Dec (J2000)
1 kpc

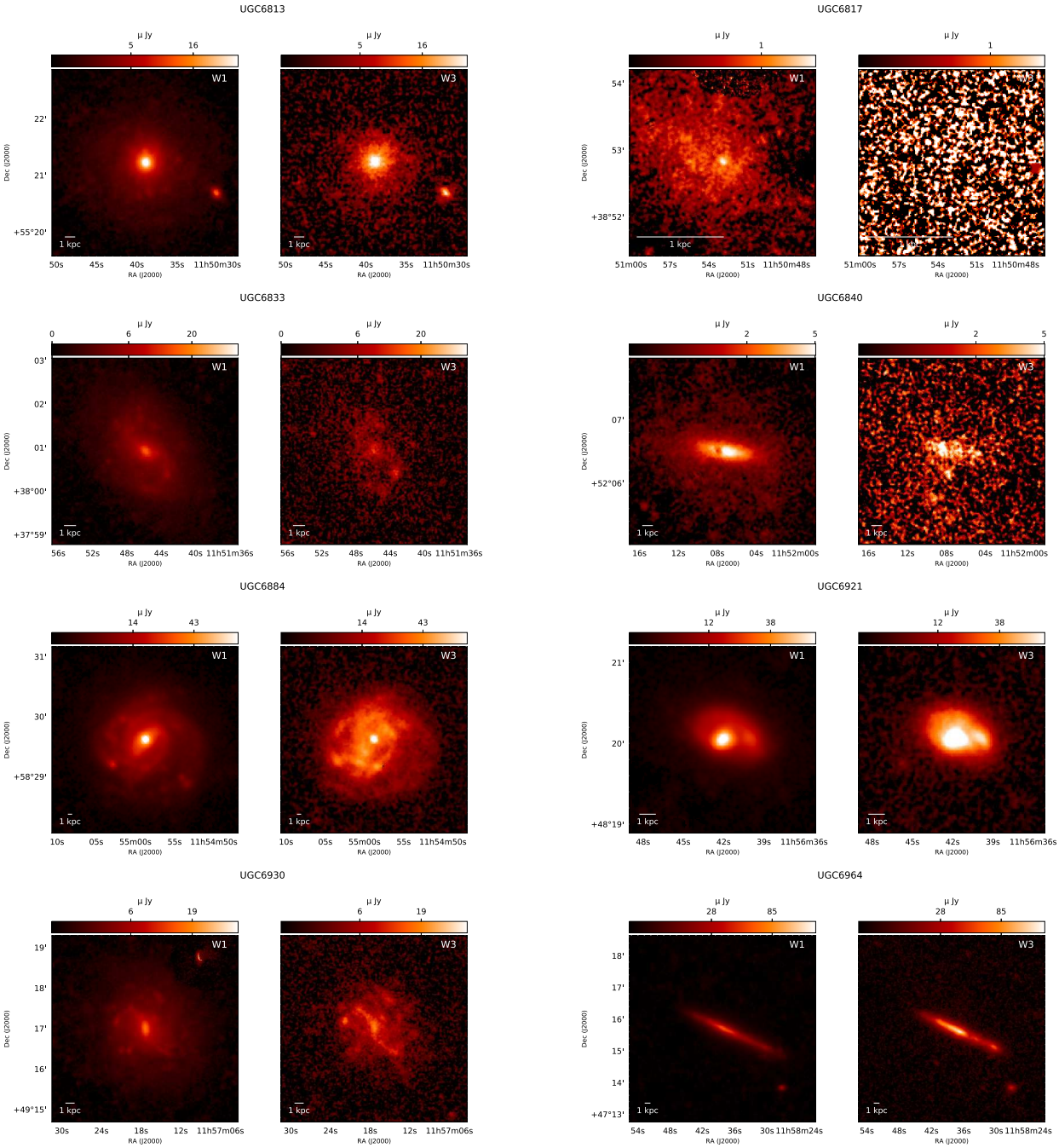
UGC6813
UGC6817
UGC6833
UGC6840
UGC6884
UGC6921
UGC6930
UGC6964
W1
W3
μ Jy
1 kpc
Dec (J2000)
RA (J2000)

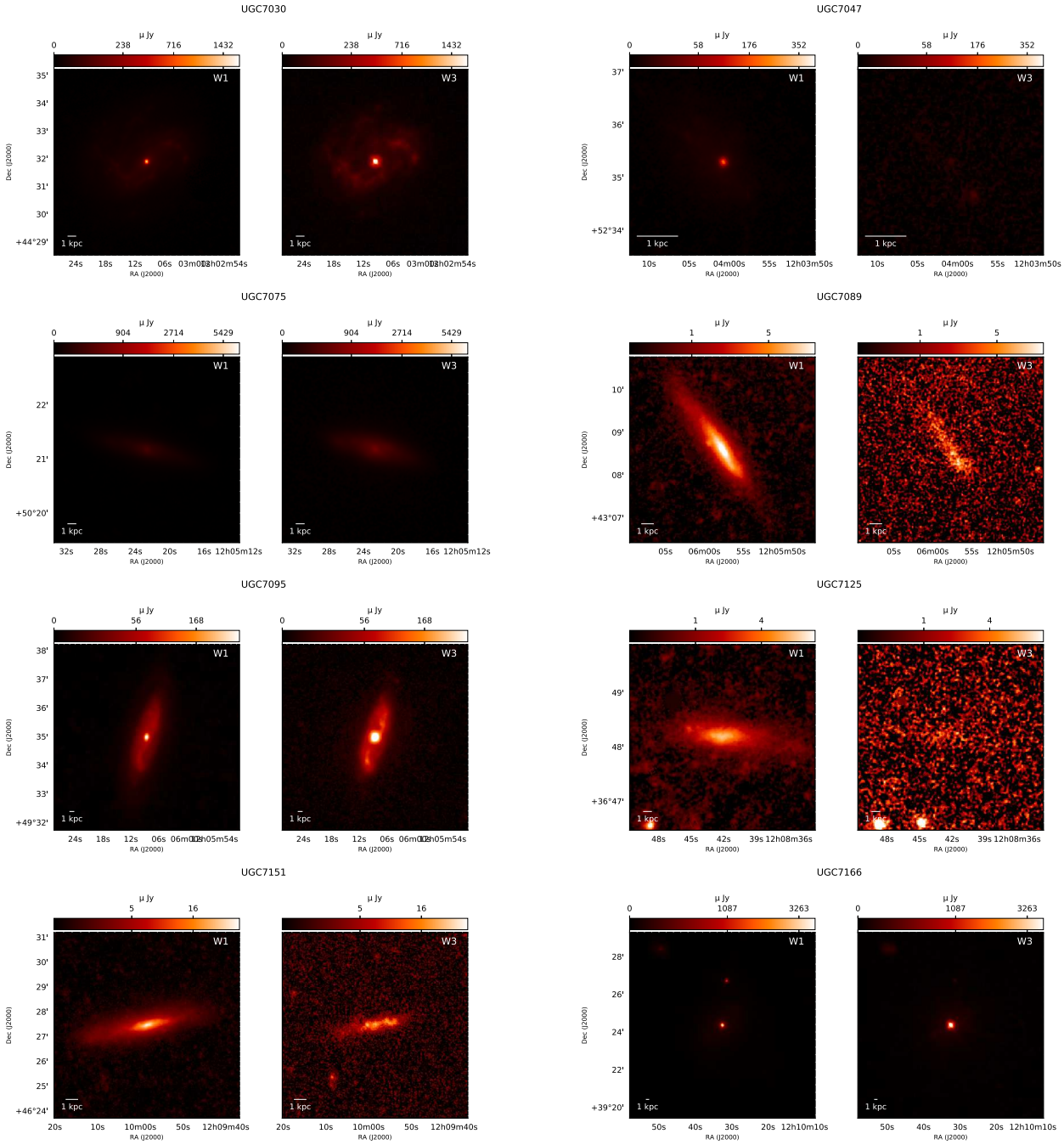
UGC7030
UGC7047
UGC7075
UGC7089
UGC7095
UGC7125
UGC7151
UGC7166
W1
W3
μ Jy
RA (J2000)
Dec (J2000)
1 kpc

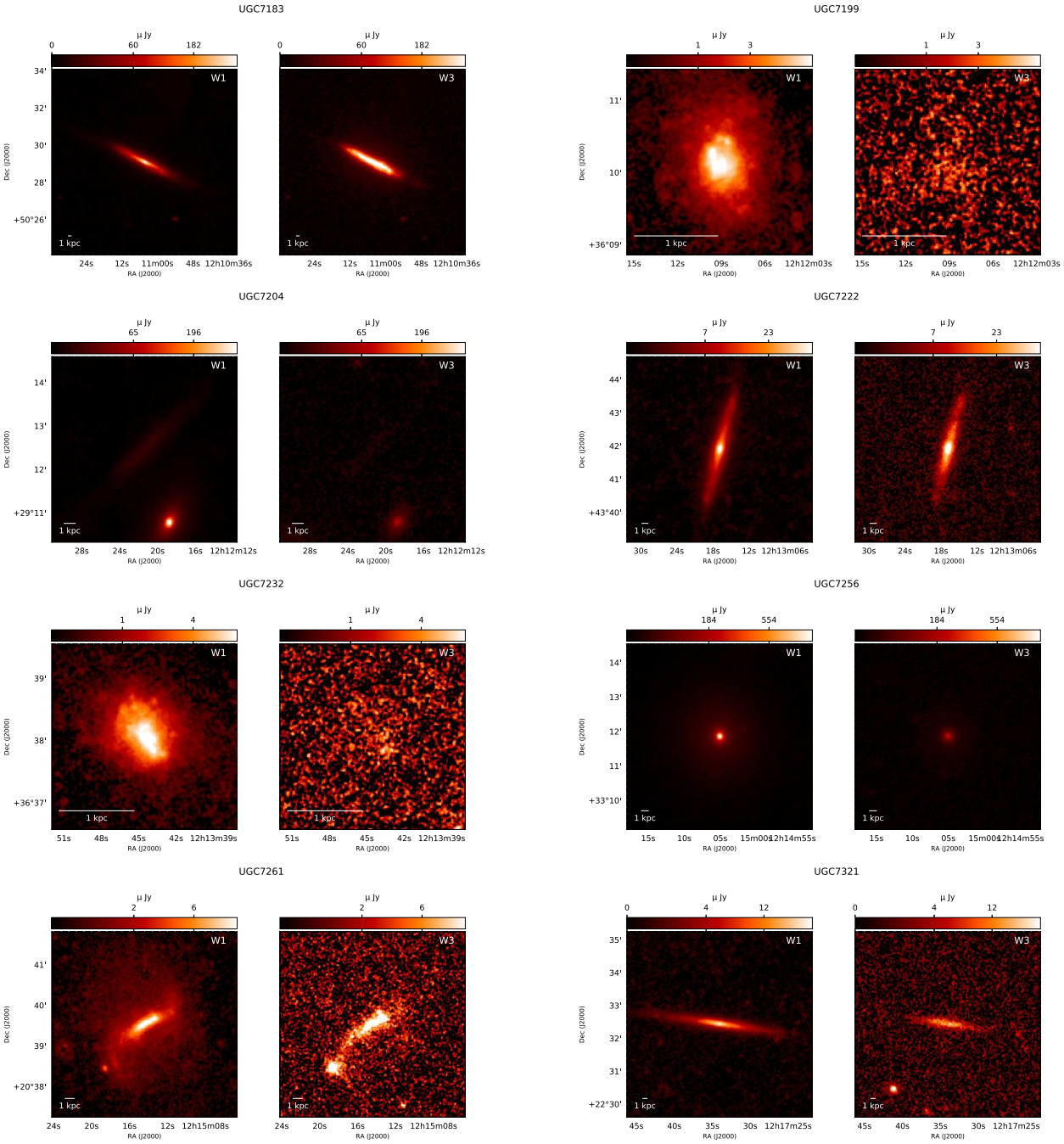
UGC7183
UGC7199
UGC7204
UGC7222
UGC7232
UGC7256
UGC7261
UGC7321
W1
W3
μ Jy
Dec (J2000)
RA (J2000)
1 kpc

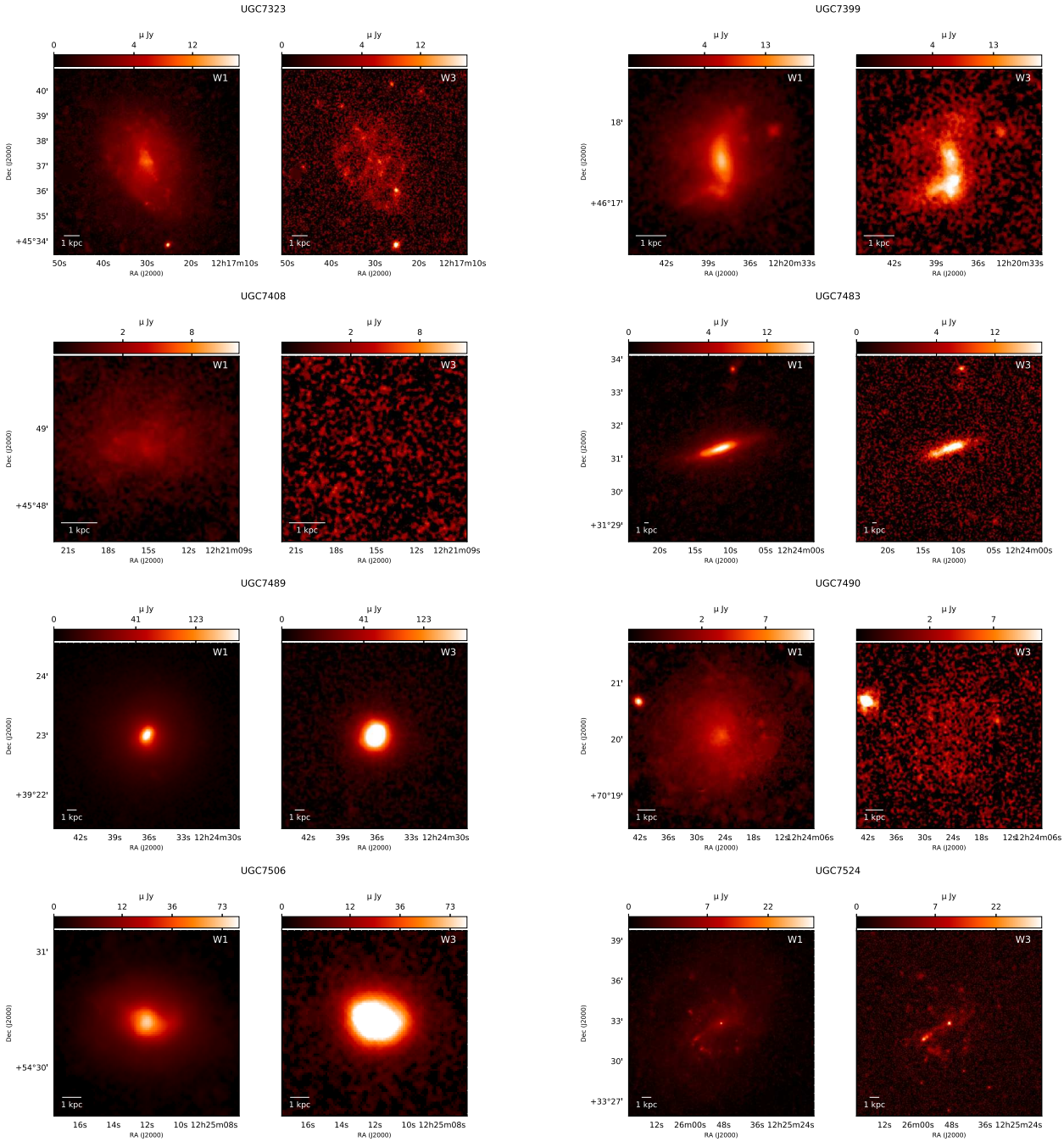
UGC7323
UGC7399
UGC7408
UGC7483
UGC7489
UGC7490
UGC7506
UGC7524
W1
W3
μ Jy
1 kpc
RA (J2000)
Dec (J2000)

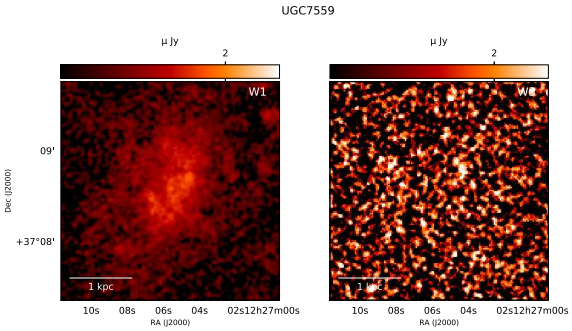
UGC7559
μ Jy
W1
W3
1 kpc
Dec (J2000)
RA (J2000)

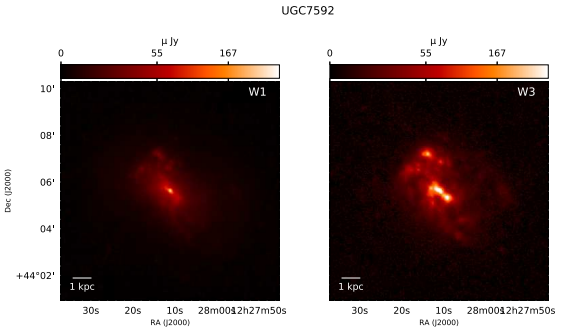
UGC7592
μ Jy
W1
W3
1 kpc
Dec (J2000)
RA (J2000)

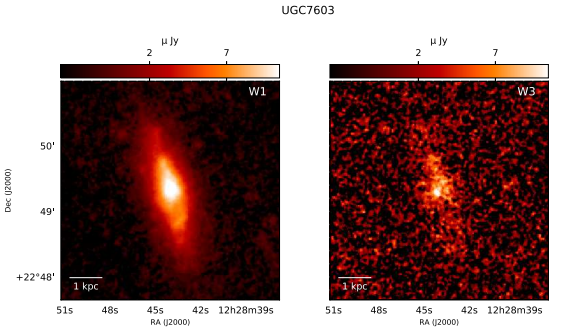
UGC7603
μ Jy
W1
W3
1 kpc
Dec (J2000)
RA (J2000)

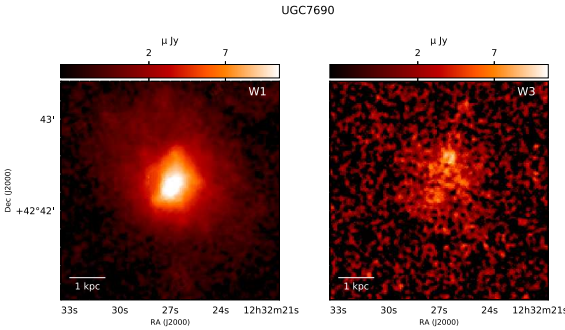
UGC7690
μ Jy
W1
W3
1 kpc
Dec (J2000)
RA (J2000)

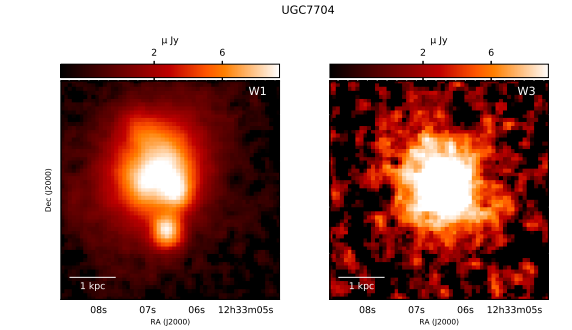
UGC7704
μ Jy
W1
W3
1 kpc
Dec (J2000)
RA (J2000)

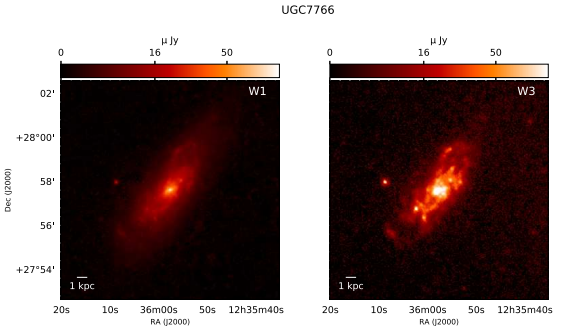
UGC7766
μ Jy
W1
W3
1 kpc
Dec (J2000)
RA (J2000)

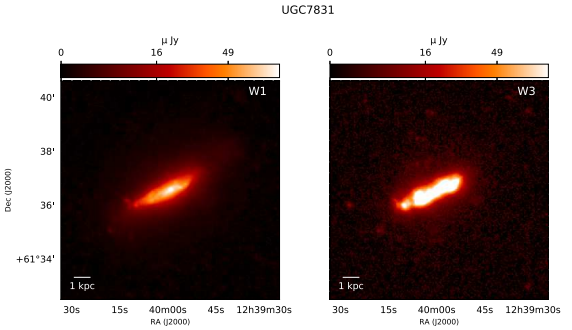
UGC7831
μ Jy
W1
W3
1 kpc
Dec (J2000)
RA (J2000)

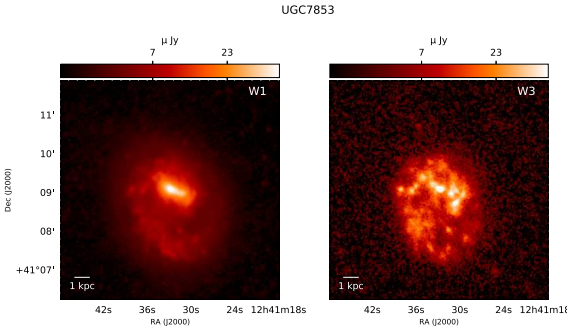
UGC7853
μ Jy
W1
W3
1 kpc
Dec (J2000)
RA (J2000)

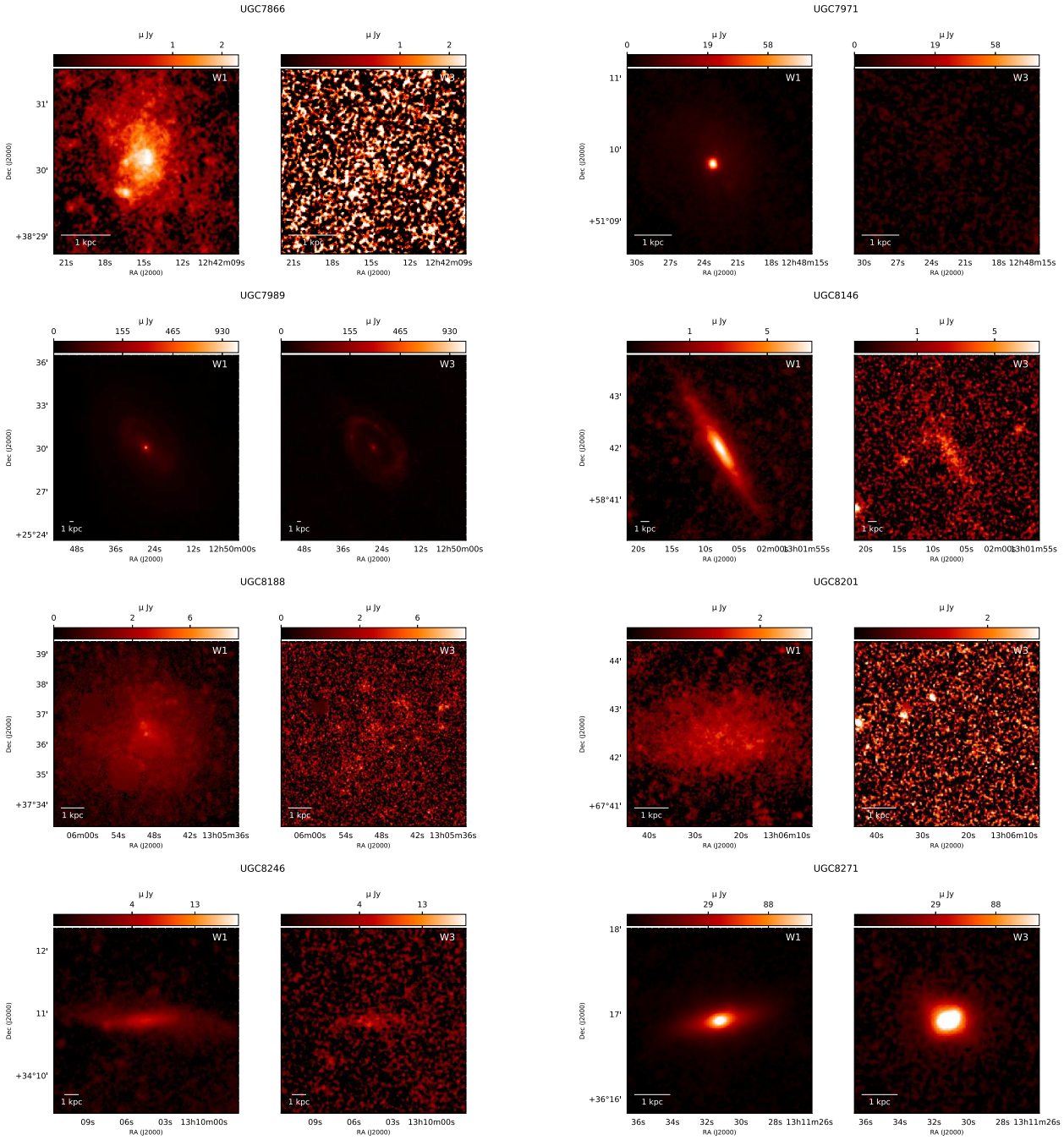
UGC7866
UGC7971
UGC7989
UGC8146
UGC8188
UGC8201
UGC8246
UGC8271
W1
W3
μ Jy
Dec (J2000)
RA (J2000)
1 kpc

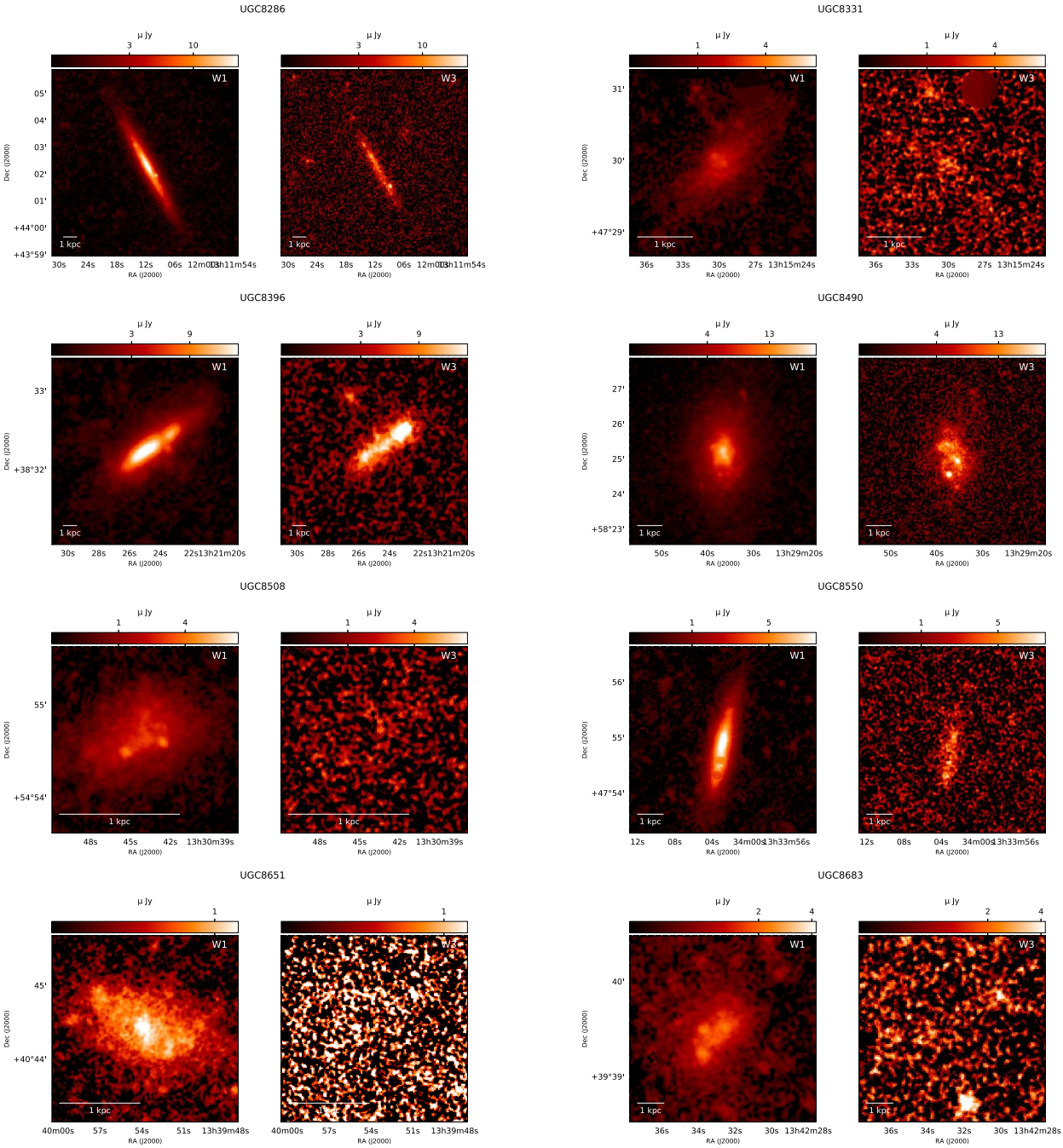
UGC8286
UGC8331
UGC8396
UGC8490
UGC8508
UGC8550
UGC8651
UGC8683
W1
W3
μ Jy
1 kpc
RA (J2000)
Dec (J2000)

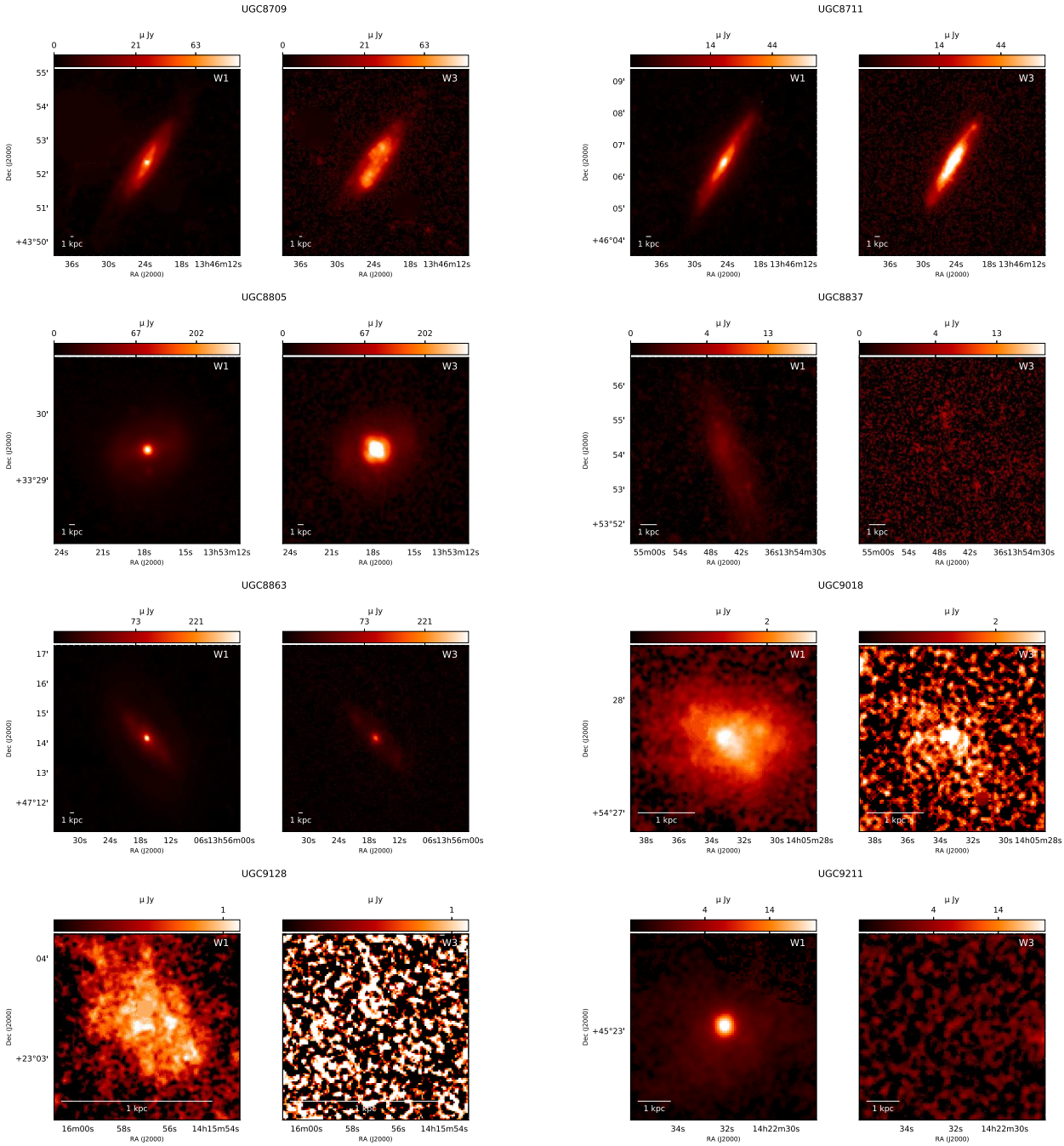
UGC8709
UGC8711
UGC8805
UGC8837
UGC8863
UGC9018
UGC9128
UGC9211
W1
W3
μ Jy
1 kpc
Dec (J2000)
RA (J2000)

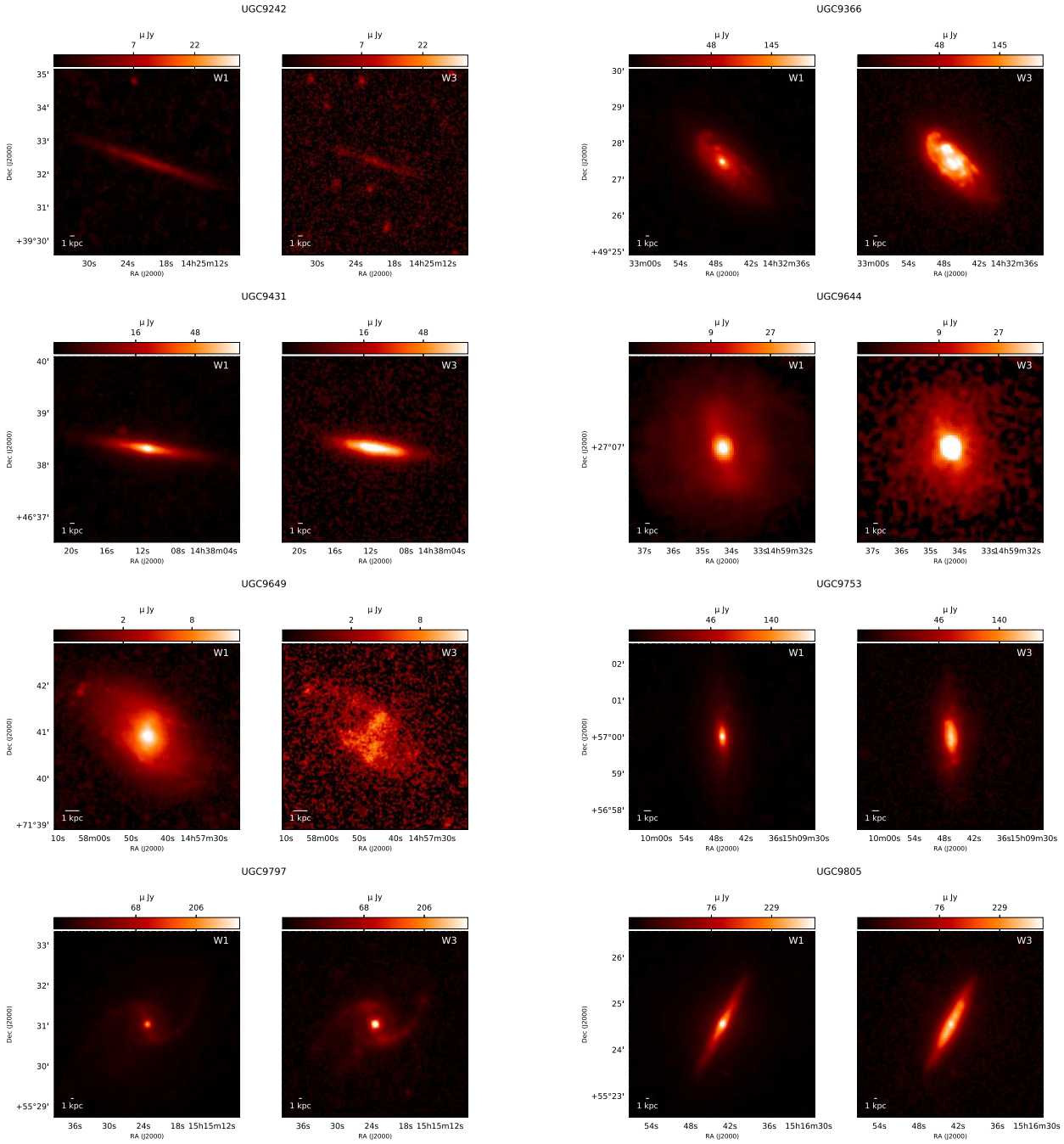
UGC9242
UGC9366
UGC9431
UGC9644
UGC9649
UGC9753
UGC9797
UGC9805
μ Jy
W1
W3
1 kpc
Dec (J2000)
RA (J2000)

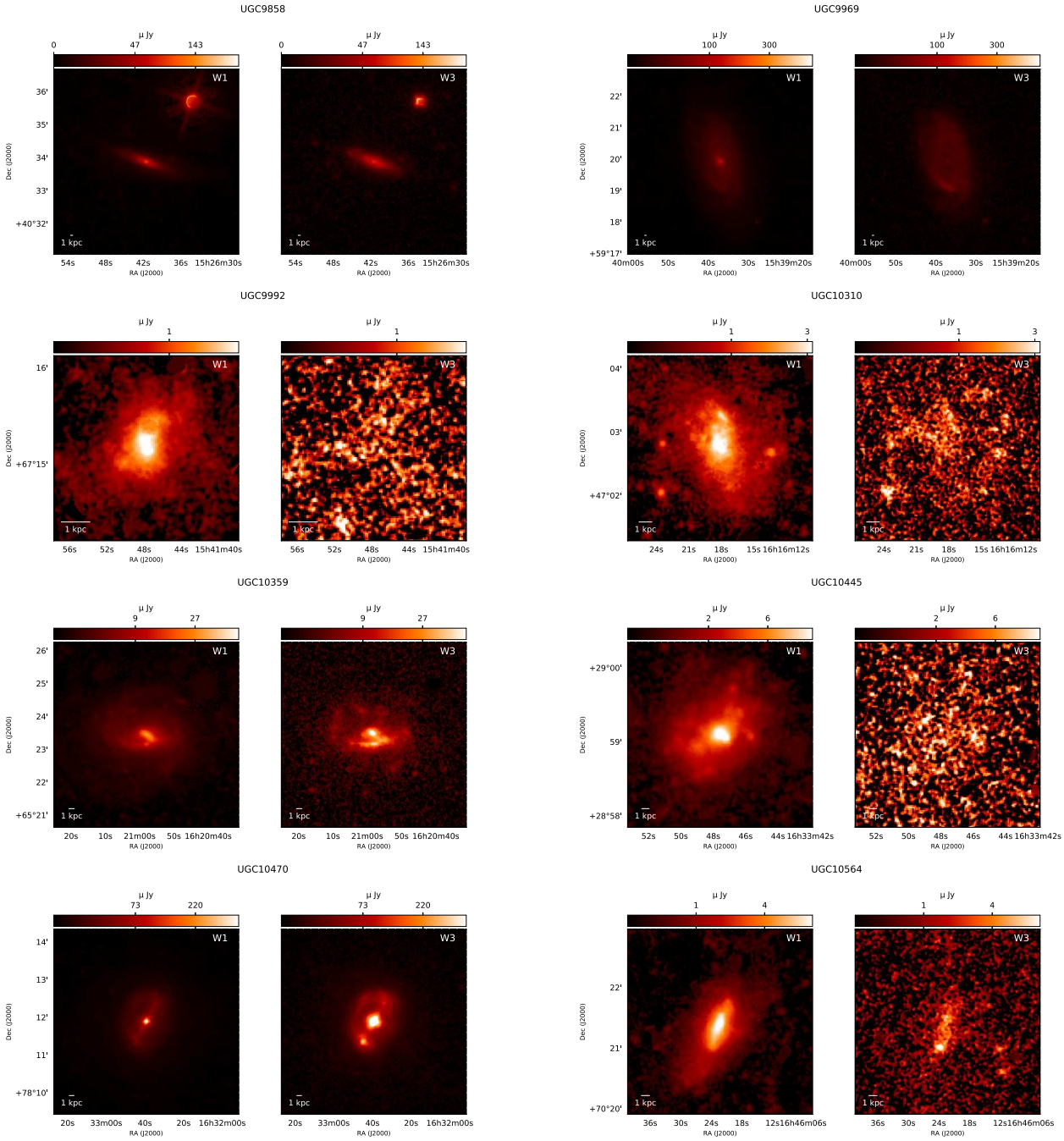
UGC9858
UGC9969
UGC9992
UGC10310
UGC10359
UGC10445
UGC10470
UGC10564
W1
W3
μ Jy
1 kpc
Dec (J2000)
RA (J2000)

UGC11124

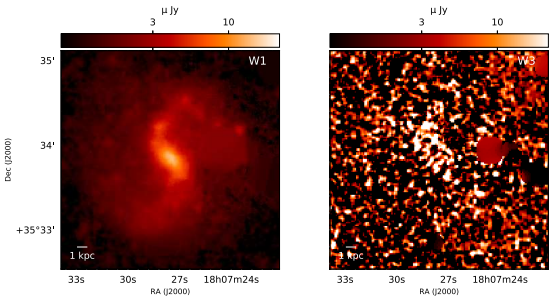

UGC11218

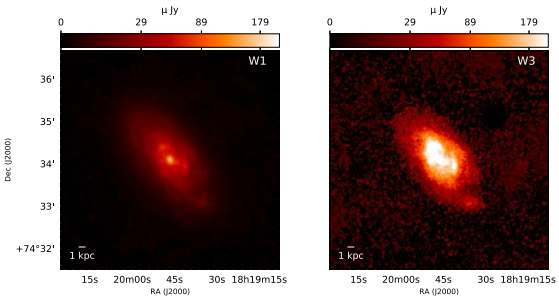

UGC11269

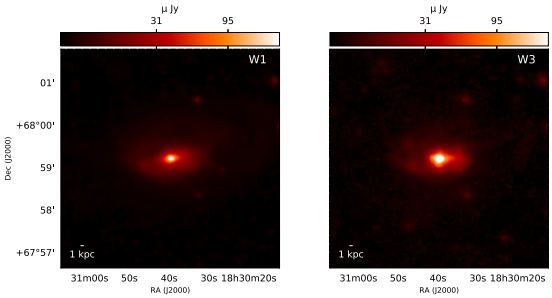

UGC11283

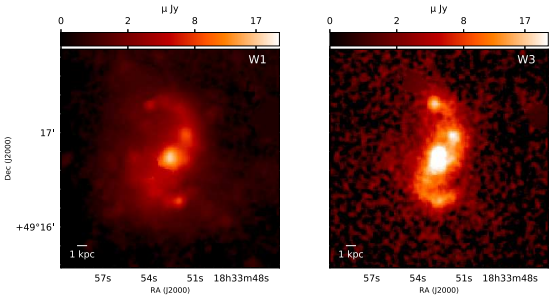

UGC11429

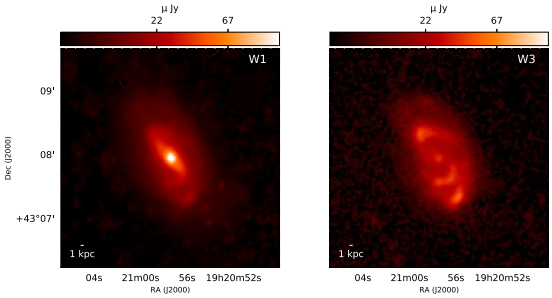

UGC11466

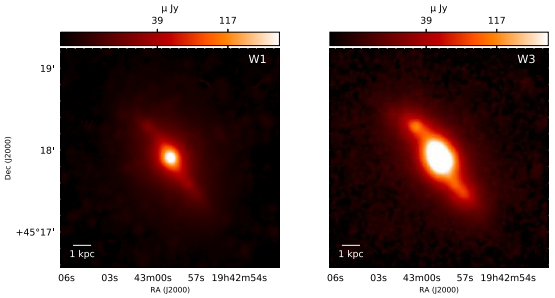

UGC11496

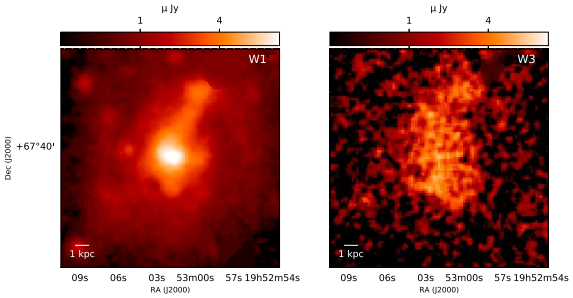

UGC11670

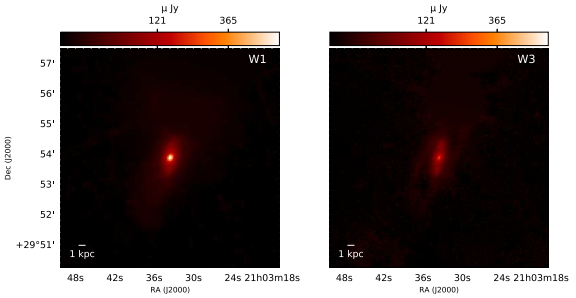

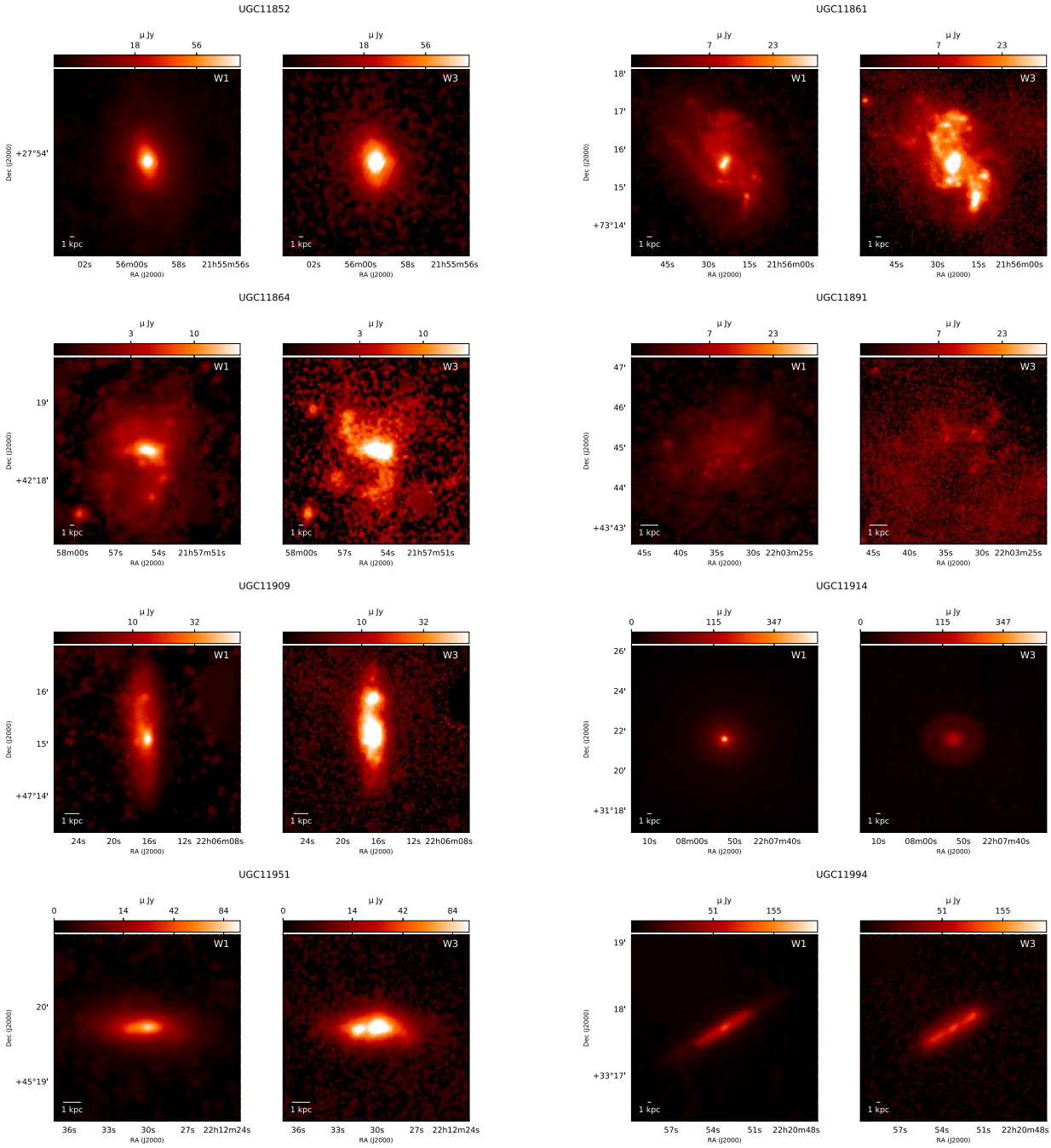
UGC11852
UGC11861
UGC11864
UGC11891
UGC11909
UGC11914
UGC11951
UGC11994
W1
W3
μ Jy
RA (J2000)
Dec (J2000)
1 kpc

UGC12043

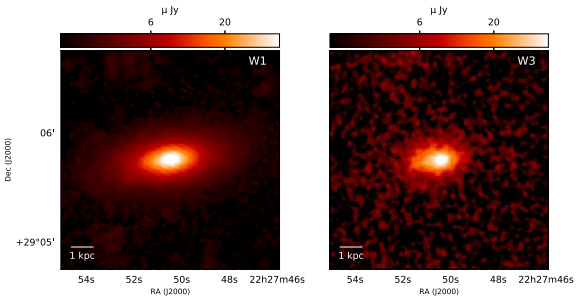

UGC12060

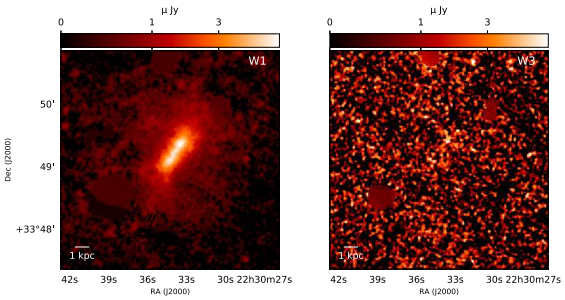

UGC12082

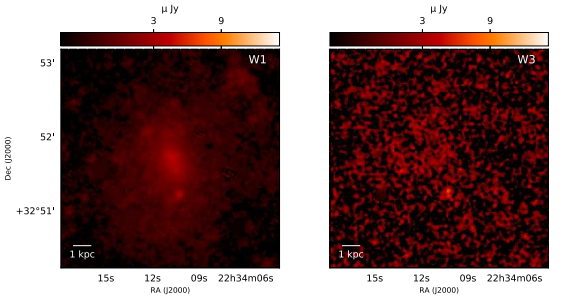

UGC12212

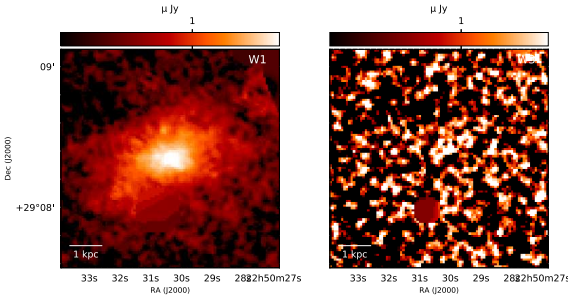

UGC12276

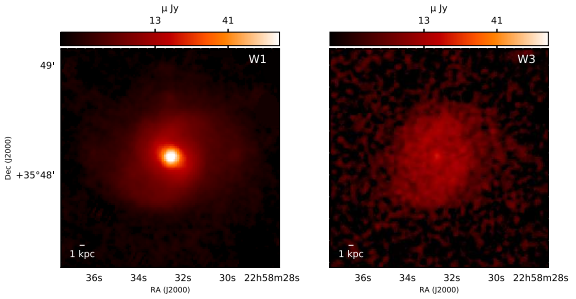

UGC12554

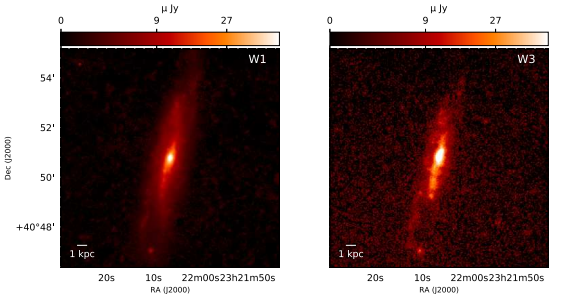

UGC12632

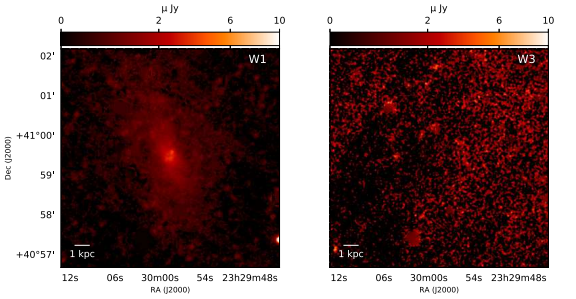

UGC12693

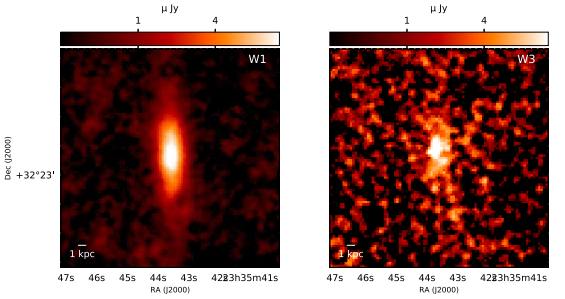

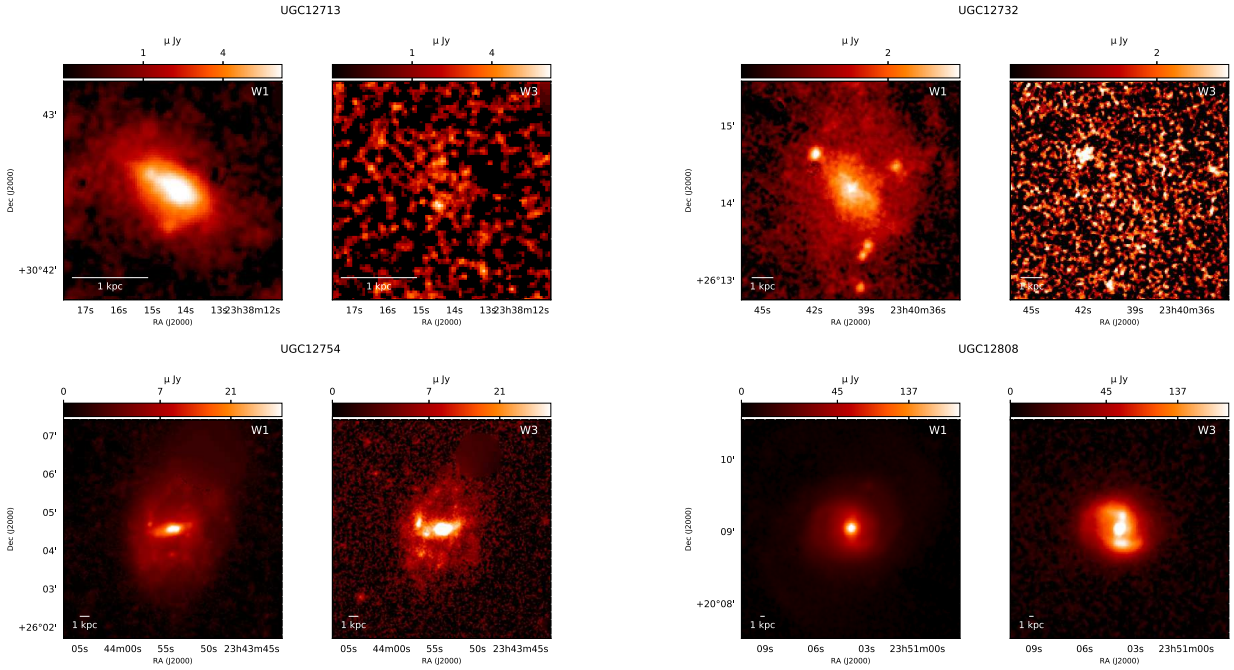
UGC12713
UGC12732
UGC12754
UGC12808
μ Jy
W1
W3
1 kpc
Dec (J2000)
RA (J2000)

Appendix B

Smoothing and Regridding WISE data

B.1 Smoothing and Regridding the WISE data

The HI data products were used together with WISE IR data products, which included maps of star formation rates, stellar mass, as well as their global averages. The global averages were provided by Jarrett et al. (2017), while the maps I derived using standard calibrations from Cluver et al. (2014).

The WISE data have a resolution of $\sim 7''$ and pixel scale of $1''$ per pixel, which is a much higher resolution than the HI data at $\sim 30''$ resolution and $10''$/pixel. Therefore, before deriving products from the WISE data, they were fit to the astrometric grid of the HI data. This was done in two steps using the *gauss* and *blkavg* tasks in the IRAF * software package (Tody 1986). The *gauss* task convolves the image with a Gaussian kernel in order to degrade it to the required resolution ($\sim 30''$). The kernel size was determined by,

$$\sigma_{kernel} = \frac{1}{2.355}\left(\sqrt{\delta^2_{HI} \; - \; \delta^2_{IR}}\right), \tag{B.1}$$

where δ_{HI}, δ_{IR} are the beam resolutions of the WHISP HI and WISE IR data respectively. It is important to note that the resolution of WISE is different in each of the four bands while the resolution of WHISP slightly varies for each target galaxy, hence, a separate kernel was determined for every galaxy in each WISE band.Also, the *gauss* kernel is not normalised, so flux conservation at the smoothing stage was done by normalising the smoothed image and multiplying it by the total flux (in DU) from the original WISE image as follows;

$$I_{sc} \; = \; \frac{I_s}{\Sigma_{I_s}} \times \Sigma_{I_o}, \tag{B.2}$$

*http://iraf.noao.edu/

where I_o, I_s, I_{sc} are the original image, smoothed image, and smoothed image after flux conservation.

After this step, the smoothed image was resampled from $1''$ to $10''$ per pixel .The *blkavg* task casts the flux in several pixels into one pixel by either summing or averaging over them. For these data, the summing option was used, and the number of pixels summed over was set to ten. Since at this stage, the pixels were simply being summed up, the task automatically conserved the total flux in the image. Figure B.1 illustrates the steps of smoothing and resampling for the spiral galaxy UGC7766 in all four WISE bands.

Masks

To enable comparisons on the same physical areas for both HI and IR data, a mask array was defined for each image to demarcate the stellar disk. The masks were determined from the major and minor axis and inclination W1 1σ isophote. The masks were then smoothed to the corresponding resolution of the HI map using the *gauss* task. The smoothing kernel applied on each mask varied according to the resolution of the respective WISE band (see Equation B.1) such that each mask underwent the exact same degradation as its corresponding WISE image. After this the masks were resampled to $10''$/pixel using the *blkavg* task. Figure B.2 shows the masks of UGC7766 (shown in Figure B.1) as they appeared before and after.

The smoothing blurs the edge of the mask, while the regridding increases the value of pixels. To get around this, the half maximum level (arbitrarily chosen) was determined in each mask and used to mark the final mask to apply to the maps of stellar mass and SFR. The black contours in the lower panels of Figure B.2 show the half maximum level of each mask.

W3 noise properties

The WISE data were sky-subtracted to remove background noise before fitting them to the astrometric grid of the WHISP data; however, the processes of degrading the resolution and resampling introduce noise in the sky-subtracted image such that the noise properties of the data have to be calculated again.The resampled data were hence clipped of noise using the robust iterative technique described below.

First, the resampled image was plotted as a histogram to separate the noise "signal" from the true signal (see Figure B.3). The former sits at the center of the histogram and forms a close-to-normal distribution since the majority of the pixels lie in the source-emission-free regions of the image. The source itself lies to the right of that distribution and forms a tail. The median and standard deviation (σ) of the distribution were calculated and the histogram was clipped at -3σ and $+3\sigma$ away from the median. The remaining pixels were plotted again as a histogram and the clipping process repeated until the median of the his-

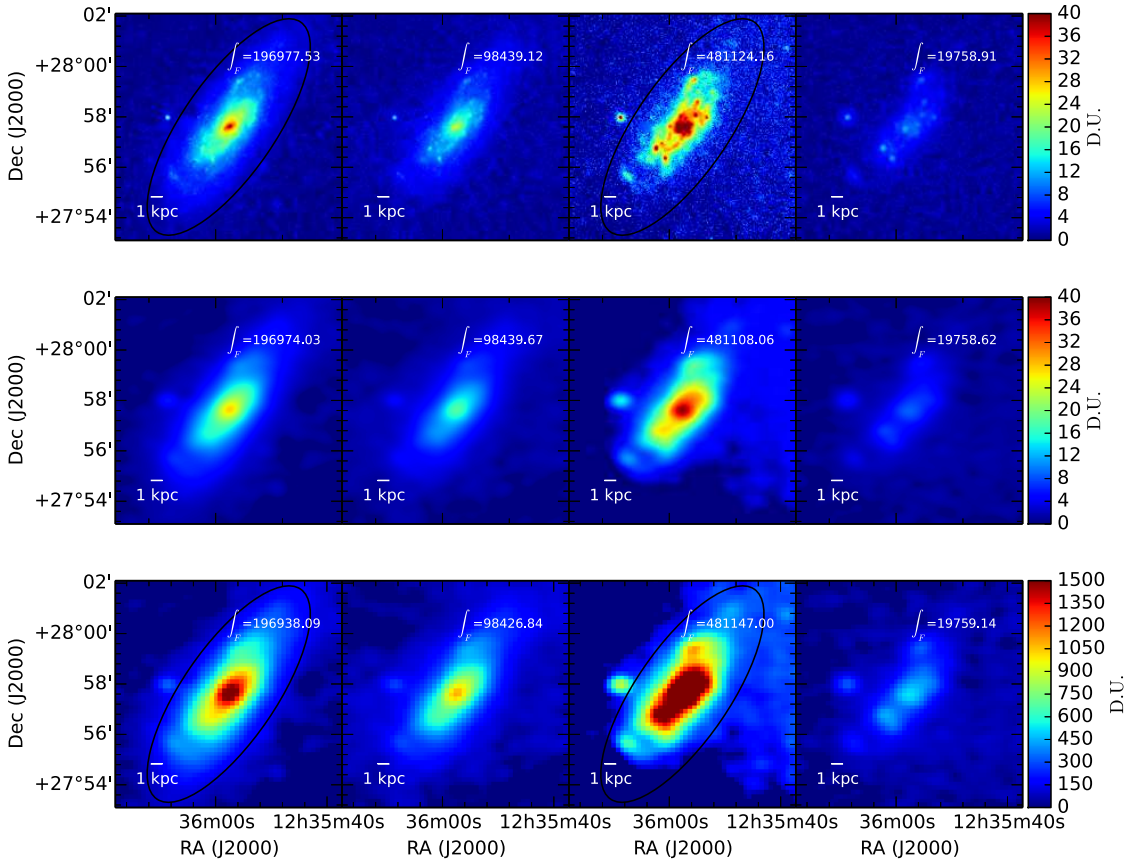

Figure B.1: All WISE images were smoothed and matched to the astrometric grid of the HI data. Shown here, left to right, are W1,W2,W3 and W4 images of UGC7766; the original images (top row), degraded to the HI $\sim 30''$ resolution (middle row) and resampled to $10''$/pixel (bottom row). The $\int_F$ labels in the upper right corners show the total flux in each image. Black contours show the extent of the W1 isophote used to mark the stellar disk.

togram did not change any more. At that point the median is very close to the mean value. The final value of the mean(μ) and standard deviation of the histogram were used to define a noise clip level at $(\mu + 3\sigma)$. This noise level, still in units of DU, was used in two ways.

1 When deriving the global average of SFR , all pixel values in the WISE image below the noise level in W3 were masked out so that they do not contribute to the final SFR

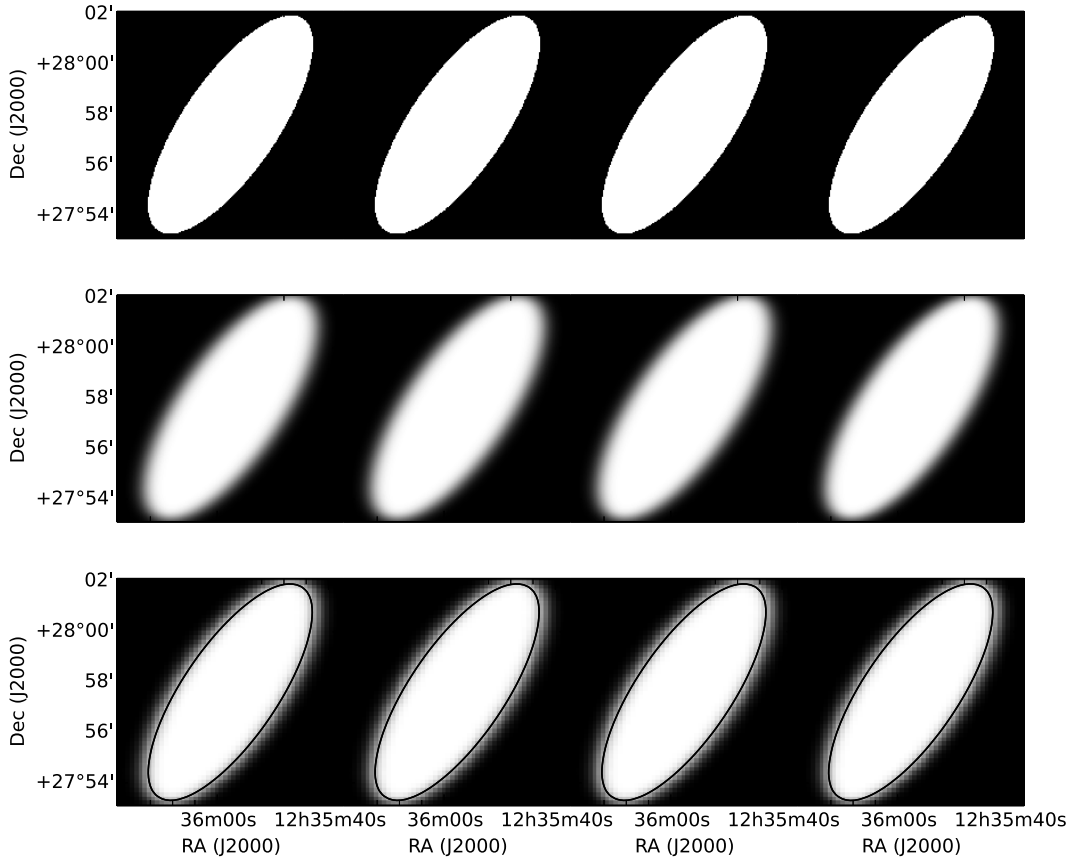

Figure B.2: Isophotal masks for UGC7766. The masks were defined according to the W1 1σ isophote, and smoothed using the same kernel that was used on the different W1, W2, W3 and W4 images (left to right), and then resampled to $10''$/pixel. The black contours show the half-maximum level in the final resampled mask, which was used to mark the edge of the stellar disk. These masks were applied to maps of the HI and IR data products in order to study the same spatial area.

value.

2 When generating maps of the SFR and Σ_{SFR}, the pixels below the noise level were not clipped so as to have a true representation of the noise in the map. However the DU value of the noise level was converted to the units of SFR($M_{\odot}yr^{-1}$) and

$\Sigma_{SFR}(\mathrm{M}_{\odot}\mathrm{yr}^{-1}\mathrm{kpc}^{-2})$, and a red horizontal line in their respective plots indicates this noise level.

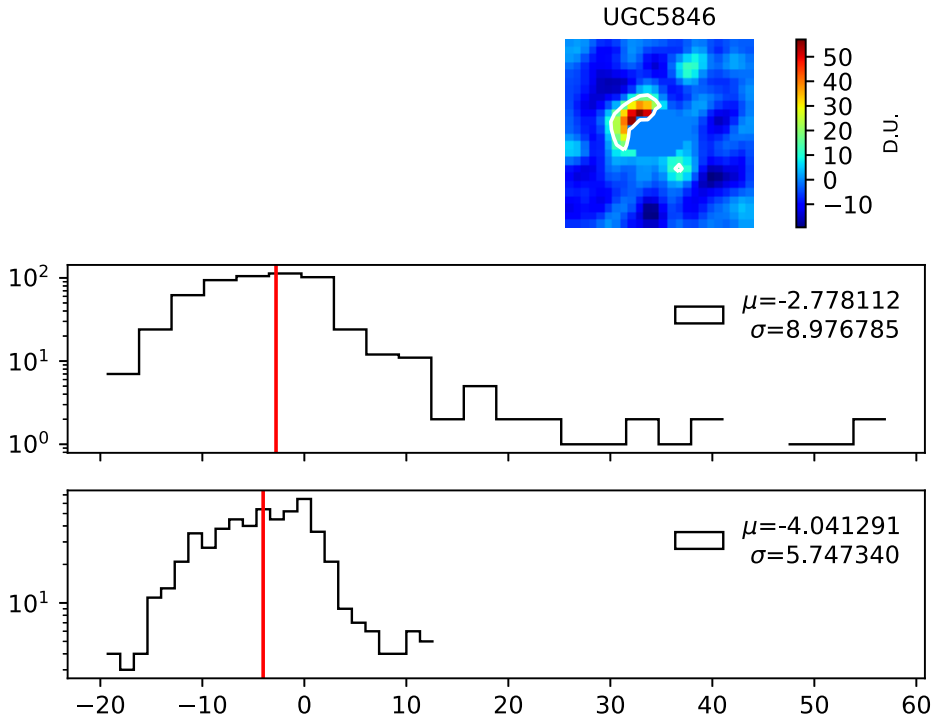

Figure B.3: Derivation of the noise properties of the resampled WISE data. The top histogram shows the average of the entire W3 image of UGC5846 (top panel), while the bottom shows the final average noise after progressively removing the galaxy's flux which forms the tail in the top histogram.

Appendix C

Atlases for the stability chapter

C.1 Velocity dispersion maps

A constant velocity dispersion was derived from the observed velocity dispersion maps which were generated by fitting Gauss-Hermite polynomials to the line profiles in the data cubes. This process is described in Chapter 4.2.1 and the dispersion maps are shown below. Velocity resolutions for this data-set were 2.1 km s^{-1}, 4.1 km s^{-1}, 8.3 km s^{-1} and 16.5 km s^{-1} as shown in the lower right corners of the images. Four galaxies (UGC1256, UGC2855, UGC6225, UGC7989) had velocity resolution of 16.5 km s^{-1} and were left out when deriving the overall average dispersion of the sample. Note that the dispersion maps were derived for the disks defined by the HI intensity maps, and an amplitude cut-off of 4 times the rms noise in the cube was applied. As such, galaxies with significant central HI depressions (UGC6537, UGC7989, UGC9649) had blank values in the centers of their dispersion maps.

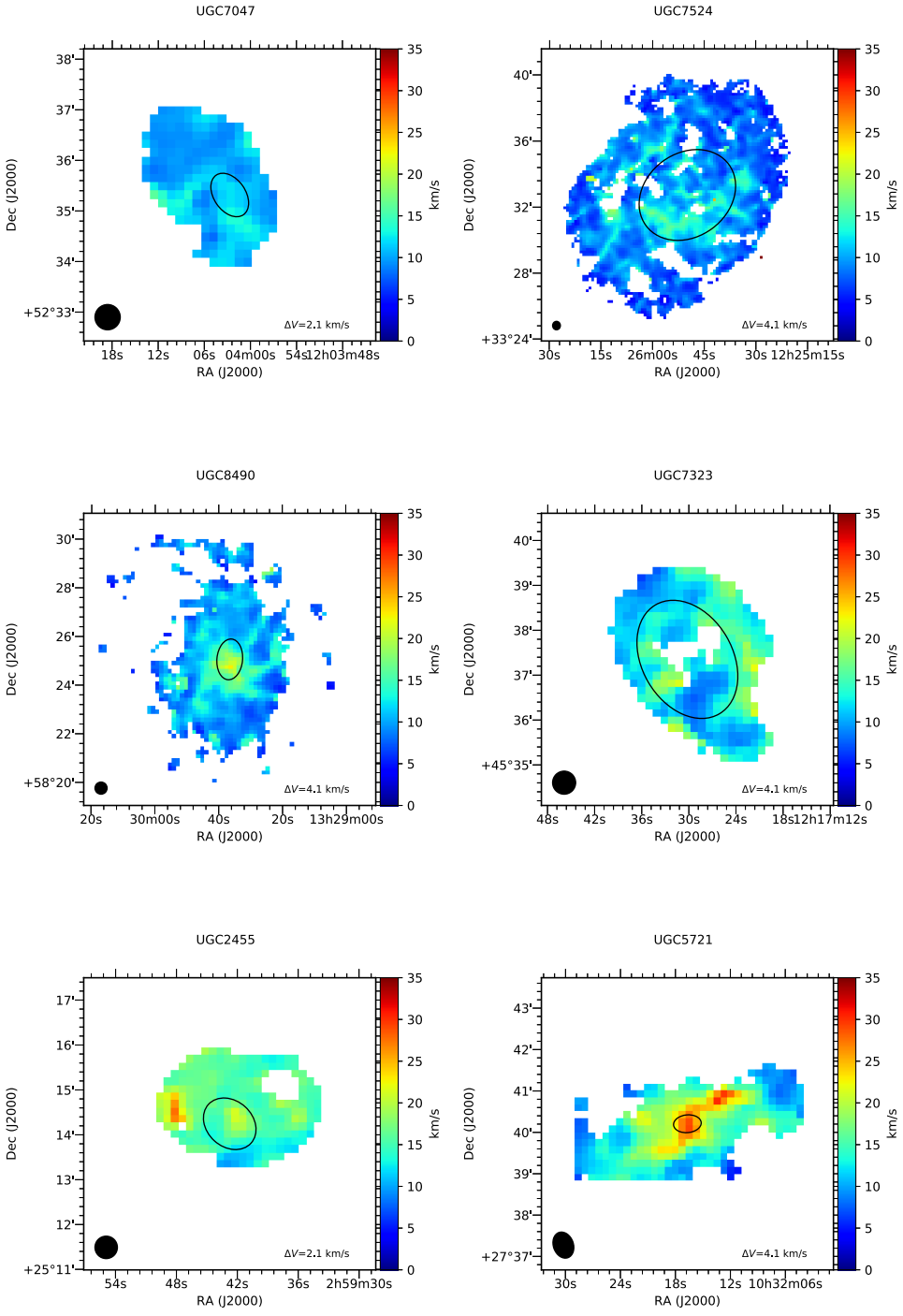

Figure C.1: Velocity dispersion maps for the sub sample defined in Chapter 4. These were derived by fitting Gauss-Hermite polynomials to the line profiles as described in 4.2.1. Fits whose widths were smaller than the velocity resolution of the cube or larger than 35 km s^{-1} were flagged and returned blank values in the dispersion map. The black ellipse marks the effective radius (the radius encompassing half the galaxy's light). Within this region, the dispersions are generally higher than elsewhere in the disk due to various factors such as high velocity clouds, radial inflows in bars and bulges and feedback from star forming regions. The high central velocities are more pronounced in highly inclined galaxies due to projection effects. When determining the average dispersion, values at radii within the effective radius were masked out. The beam size and velocity resolution are shown in the lower left and lower right corners respectively.

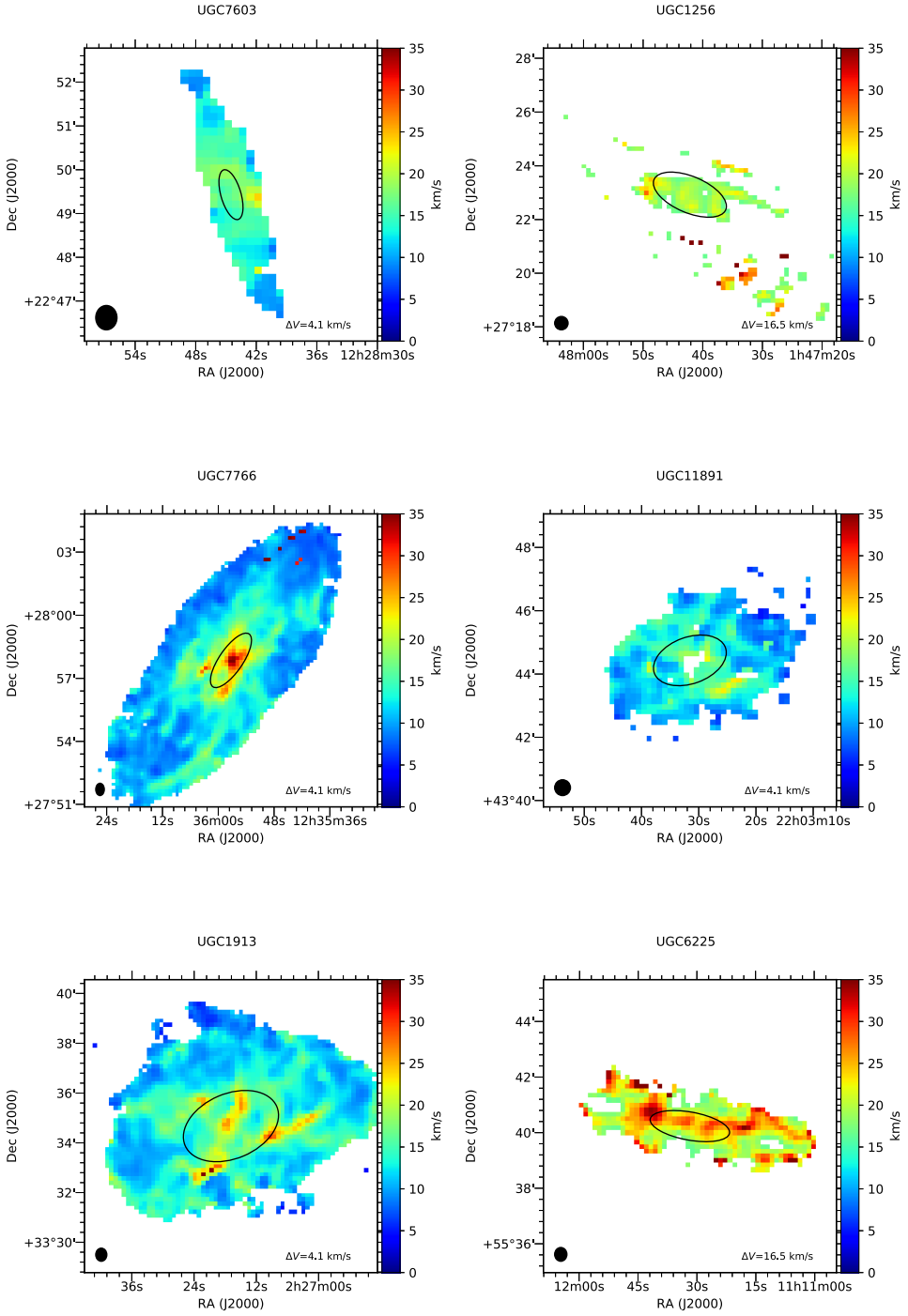

Figure C.2: Same as in Figure C.1

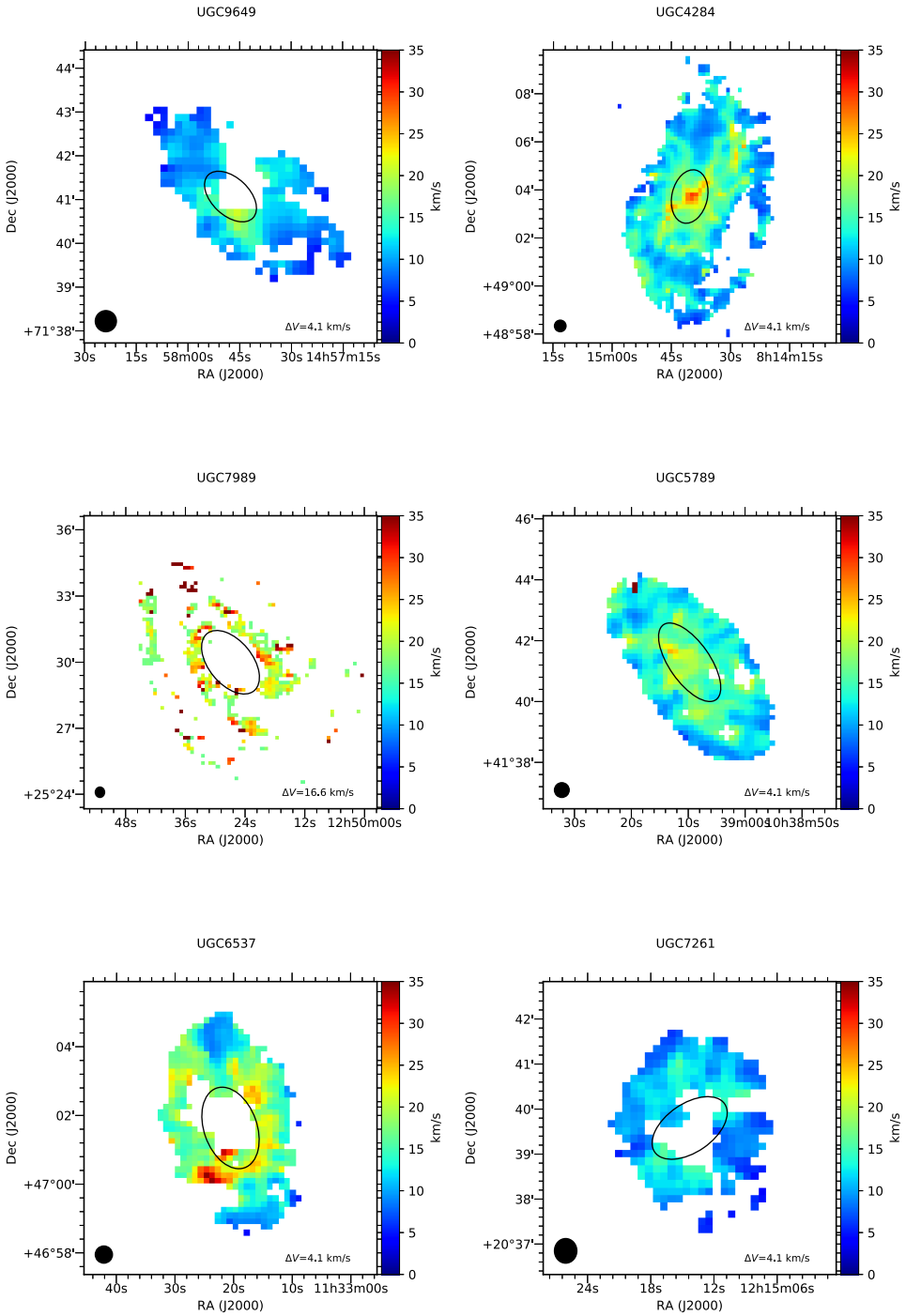

Figure C.3: Same as in Figure C.1

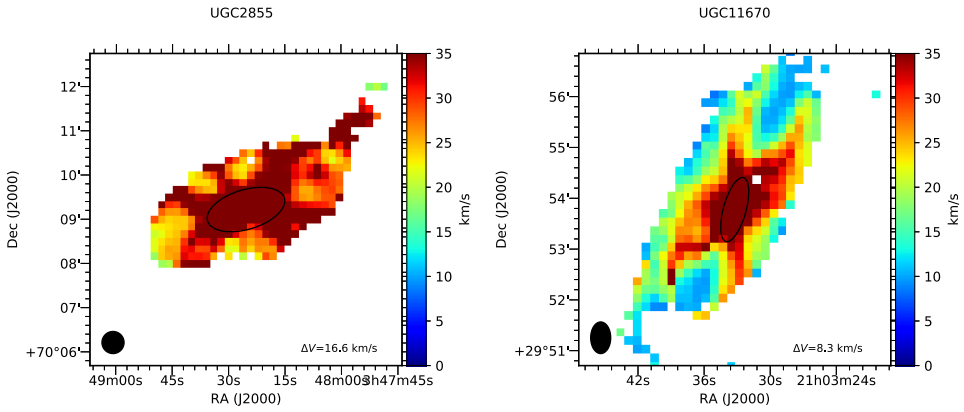

Figure C.4: Same as in Figure C.1

C.2 Validation of the stability parameter methodology

To validate the scripts used in our methods of deriving the stability parameters, we used the published data of NGC0925 from Leroy et al. (2008) (hereafter L08). L08 used data from The HI Nearby Galaxy Survey (THINGS) and the Spitzer Infrared Nearby Galaxies Survey (SINGS).

For the Q_g derivation, the THINGS HI intensity map was obtained from the THINGS public database* while rotation curve parameters (V_o = 136 km s^{-1}, l_o = 6.5 km s^{-1}) and orientation parameters (P.A. = 287°, i = 66°) were obtained from L08. The intensity map was first smoothed to the working resolution of L08 (20″) and then converted into a surface density map according to the L08 equation;

$$\Sigma_{\rm HI}(\rm M \odot\ pc^{-2}) = 0.020 \cos\ i\ I_{21\ cm}(K\ km\ s^{-1}), \tag{C.1}$$

which accounts for inclination and the presence of Helium. A galactocentric map was derived using the orientation parameters and combined with the rotation curve parameters to derive a map of the rotation velocity from which the epicyclic frequency map was derived (Equation 4.13). A constant HI velocity dispersion value of 11 km/s was adopted from L08. The Q_g map was derived according to Equation 4.1 and its radial profile obtained using the GIPSY *ellint* task in rings of 10″ width. Figure C.5 below shows the Q_g radial profile.

For the Q_T derivation, the SINGS 3.6 μm map was obtained from the SINGS public database† and matched to the L08 working resolution of 20″. The 3.6 μm map was then converted into a stellar surface density map using the L08 equation;

$$\Sigma_* = 280\ \cos\ i\ I_{3.6\ \mu m}. \tag{C.2}$$

The stellar velocity dispersion was derived from the stellar surface density according to Equation 4.27. The THINGS and SINGS data were matched in astrometric grid before being combined to derive the two-fluid disk stability parameter according to Equation 4.3. The resulting map of Q_T was azimuthally averaged in rings of 10″ width using the GIPSY *ellint* task, and the resulting radial profile is shown in Figure C.5 below. Note that L08 used the wavenumber that yielded the lowest values of Q_T (Leroy - priv. communication). Comparing Q_T values at wavelength scales of 500 pc - 5 kpc (see Chapter 4.3.1), we found that the lowest Q_T values were from the 5 kpc scale which is also in agreement with the results of L08.

Both profiles replicate the result of L08, with the exception of the nuclear regions in the $Q_T$profile. The slightly higher nuclear values in our Q_T profile are most likely due to contamination of the 3.6 μm flux by emission from nuclear star forming regions. L08 minimized this contamination by using radial profiles of stellar surface density and velocity

*http://www.mpia.de/THINGS/Data.html
†https://irsa.ipac.caltech.edu/data/SPITZER/SINGS/

dispersion, whereas we used the respective two-dimensional maps and hence did not average out the effects of this contamination.

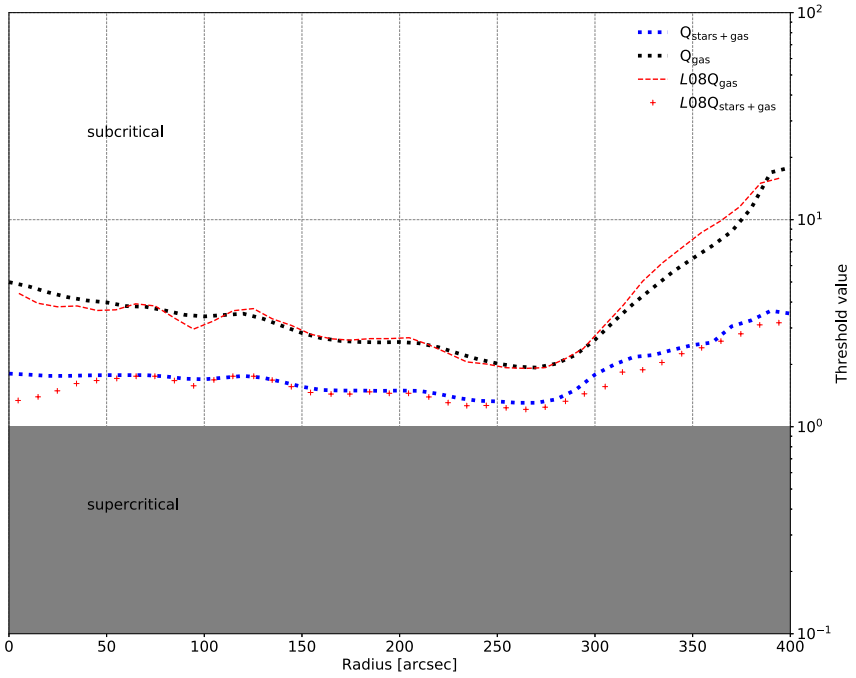

Figure C.5: Radial profiles of Q_g and Q_T for UGC1913 (NGC0925) from the data of Leroy et al. (2008) using the methodology described in Chapter 2. The L08 profiles (overplotted in red) are closely reproduced by our methods (black and blue dots).

C.3 Atlases of derived parameters

C.3.1 Single-fluid disk stability

Maps of variables

Maps of the variables that were generated in the derivation of the single-fluid disk Toomre parameter are presented in Figures C.6 - C.10 below. The Q_g and Q_T maps presented in Chapter 4 were masked using the WISE stellar mass maps so that both Q_g and Q_T maps could show the same physical area. The atlases below were masked using the HI radius and thus show more extended disks. However the analyses in 4 were carried out within the stellar disk.

The panels are arranged as follows: *Top panels* - Galactocentric radius (left), Rotation velocity (middle) and Derivative of the rotation curve (right). *Bottom panels* - Epicyclic

frequency (left), Gas surface density (middle) and the Toomre Q parameter (right). Note that instead of SI units, the units used for the epicyclic frequency were so chosen to return a dimensionless Q parameter. The gas surface density maps used for UGC1913, UGC7766 and UGC7989 are those of total gas ($\Sigma_{\mathrm{HI+H_2}}$).

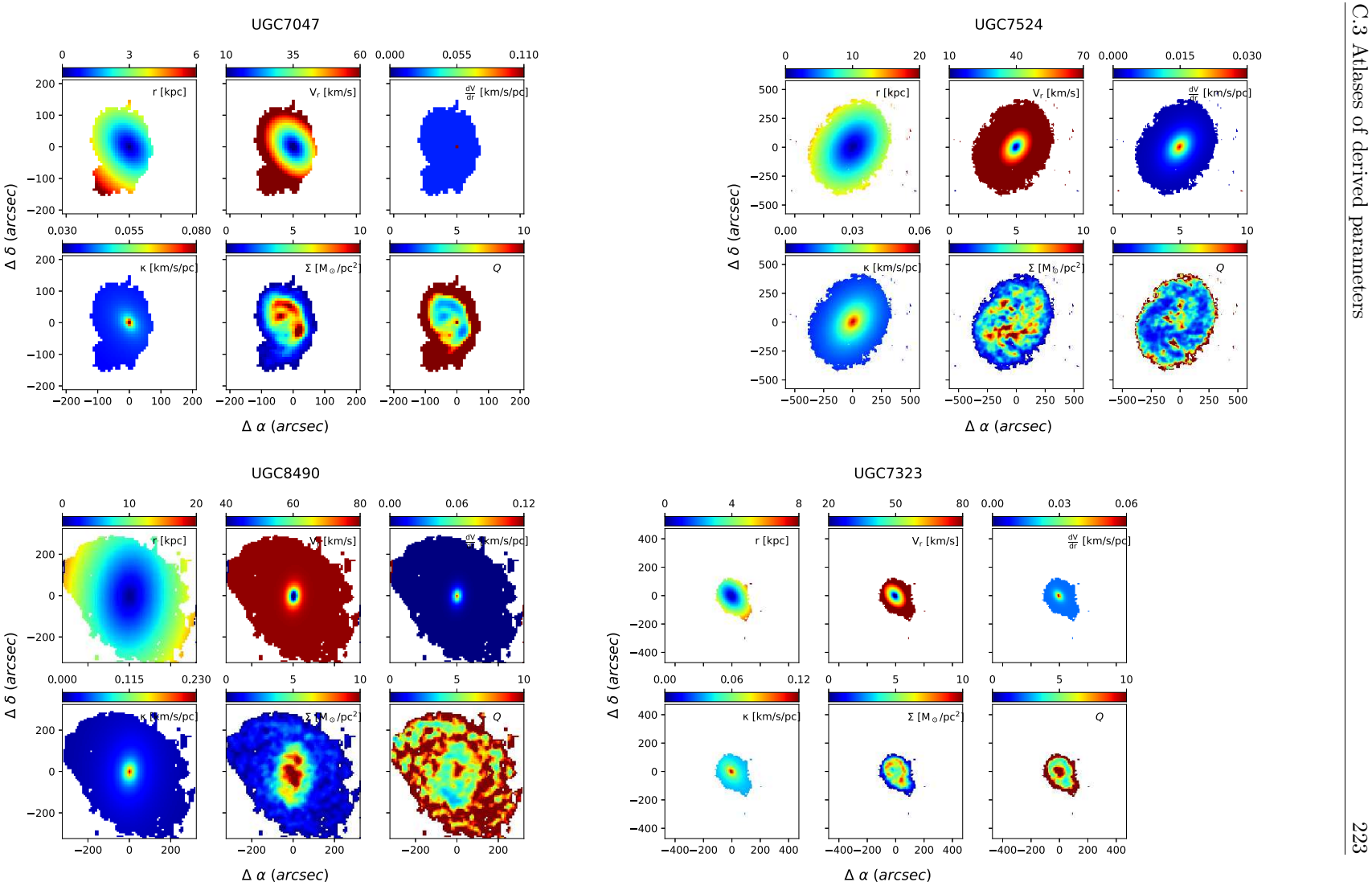

Figure C.6: Single-fluid disk stability derivations

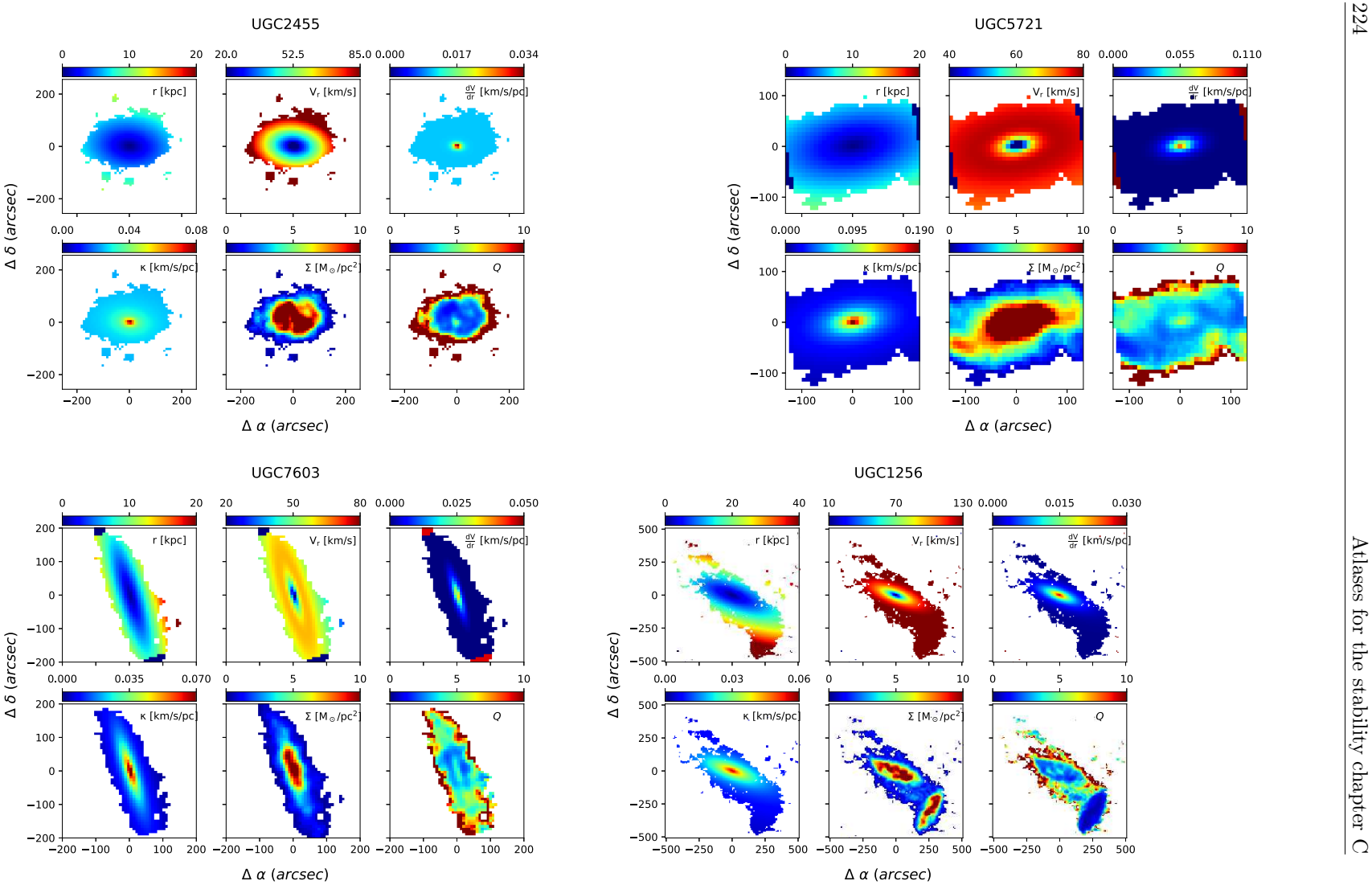

Figure C.7: Single-fluid disk stability derivations

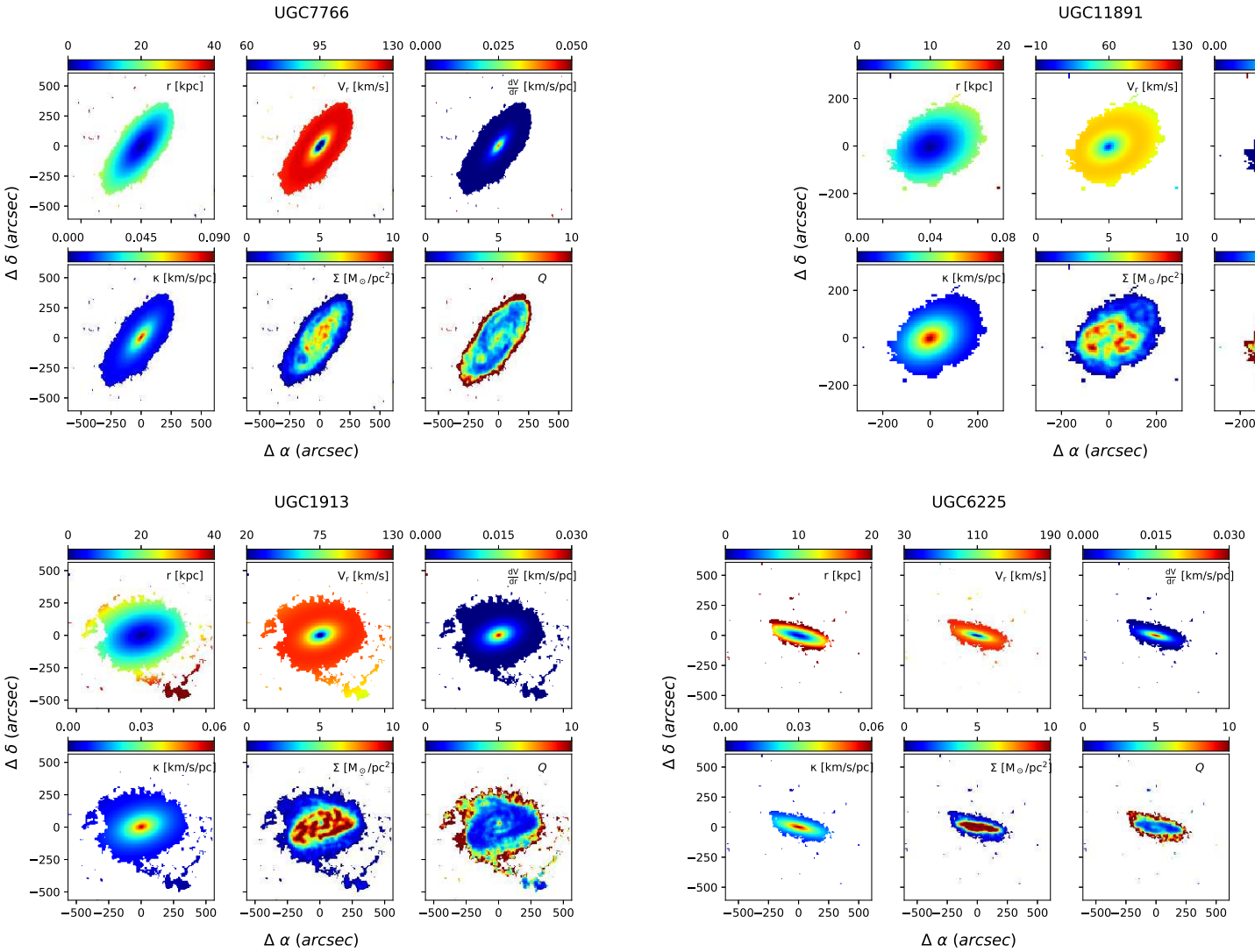

Figure C.8: Single-fluid disk stability derivations

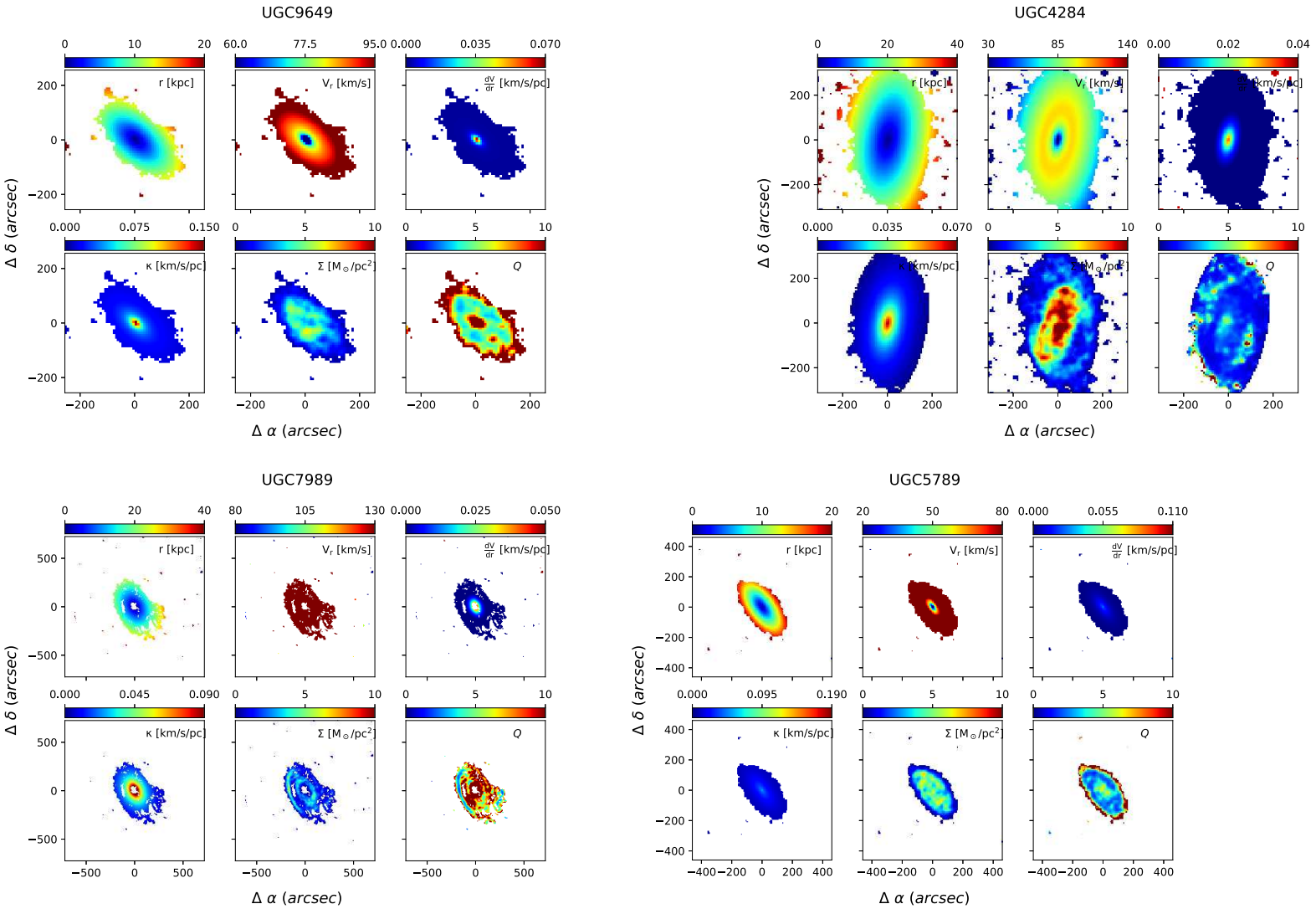

Figure C.9: Single-fluid disk stability derivations

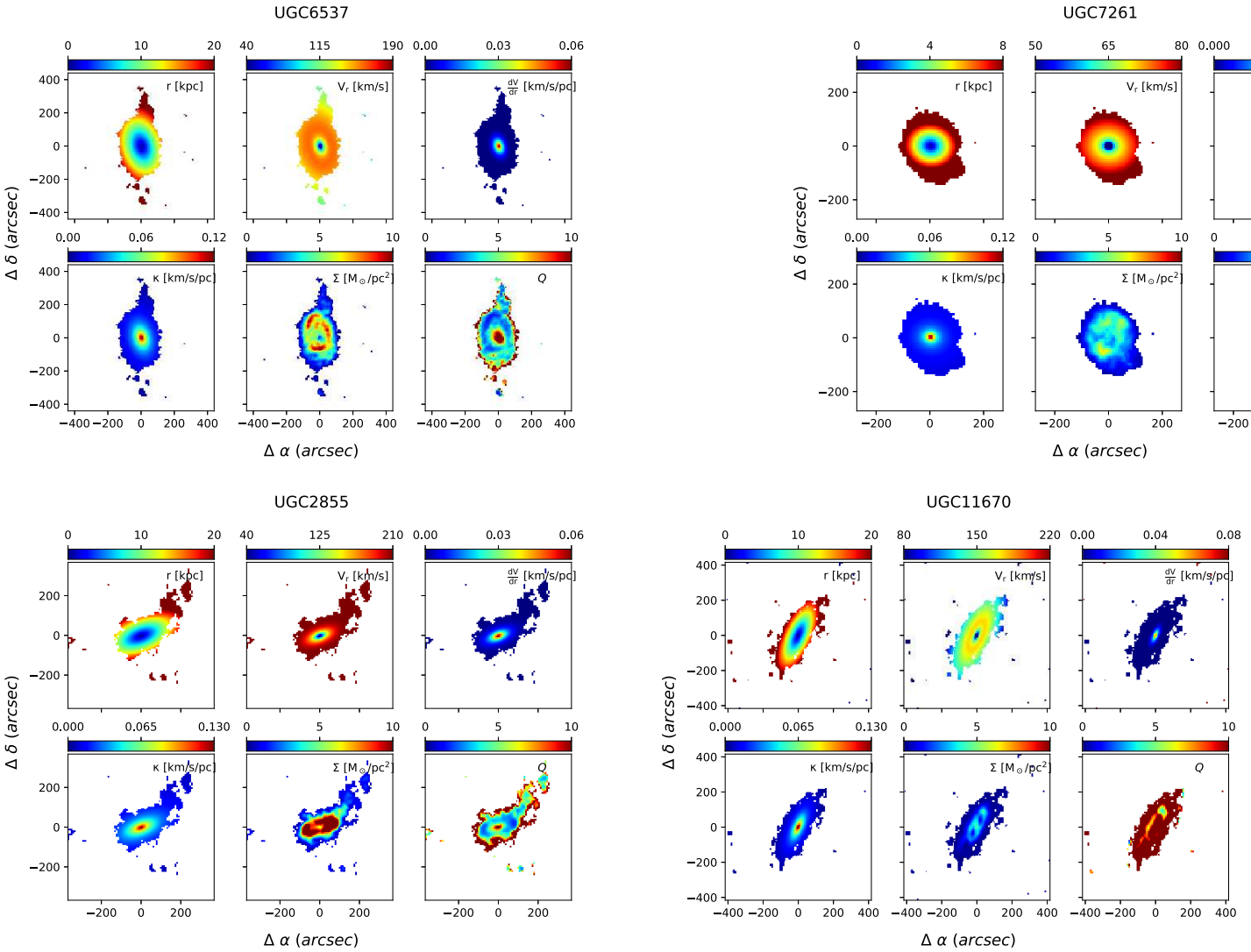

Figure C.10: Single-fluid disk stability derivations

C.3.2 Two-fluid disk stability

Plots for determining the perturbation scales

Deriving the two-fluid instability required determination of the wavenumber for the maximum instability (see Chapter 4.3.1). Plots such as 4.11 were made for all the sample and are shown in Figures C.11 - C.15 below. The black contour marks $Q_T = 1.0$, while the magenta contour is at $Q_T = 2.0$. The white contours mark the edge of the SF disk as defined in Section 4.1. Note that for UGC1913 we made use of the total gas density ($\Sigma_{\mathrm{HI+H_2}}$). The wavenumbers in the plots 4π, 3π, 2π, 1.5π, 1π, 0.8π, 0.6π, 0.5π and 0.4π correspond to wavelength scales of 0.5 kpc, 0.66 kpc, 1 kpc, 1.3 kpc, 2 kpc, 2.5 kpc, 3 kpc, 4 kpc and 5 kpc respectively.

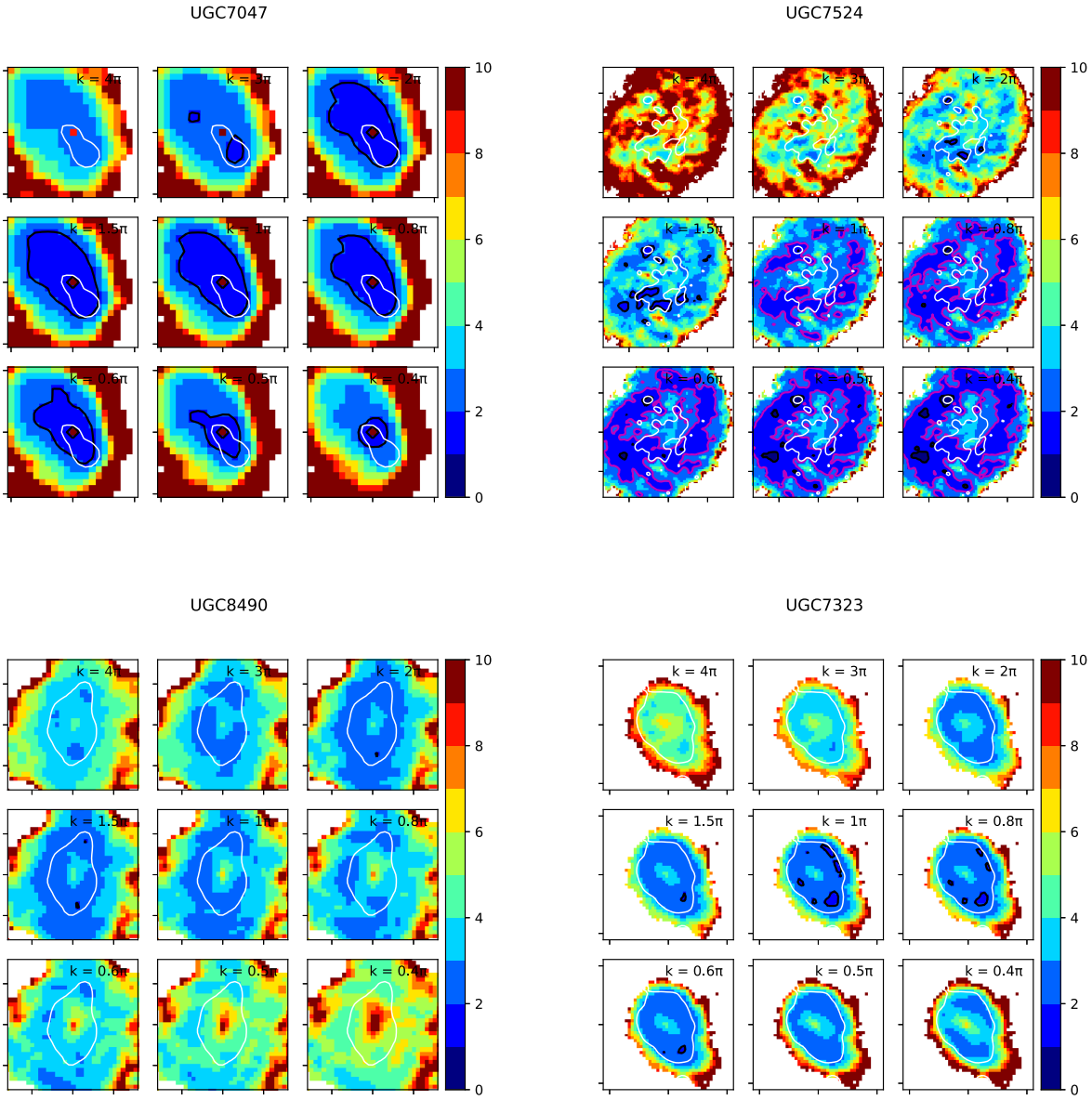

Figure C.11: Determining wavelength of maximum instability

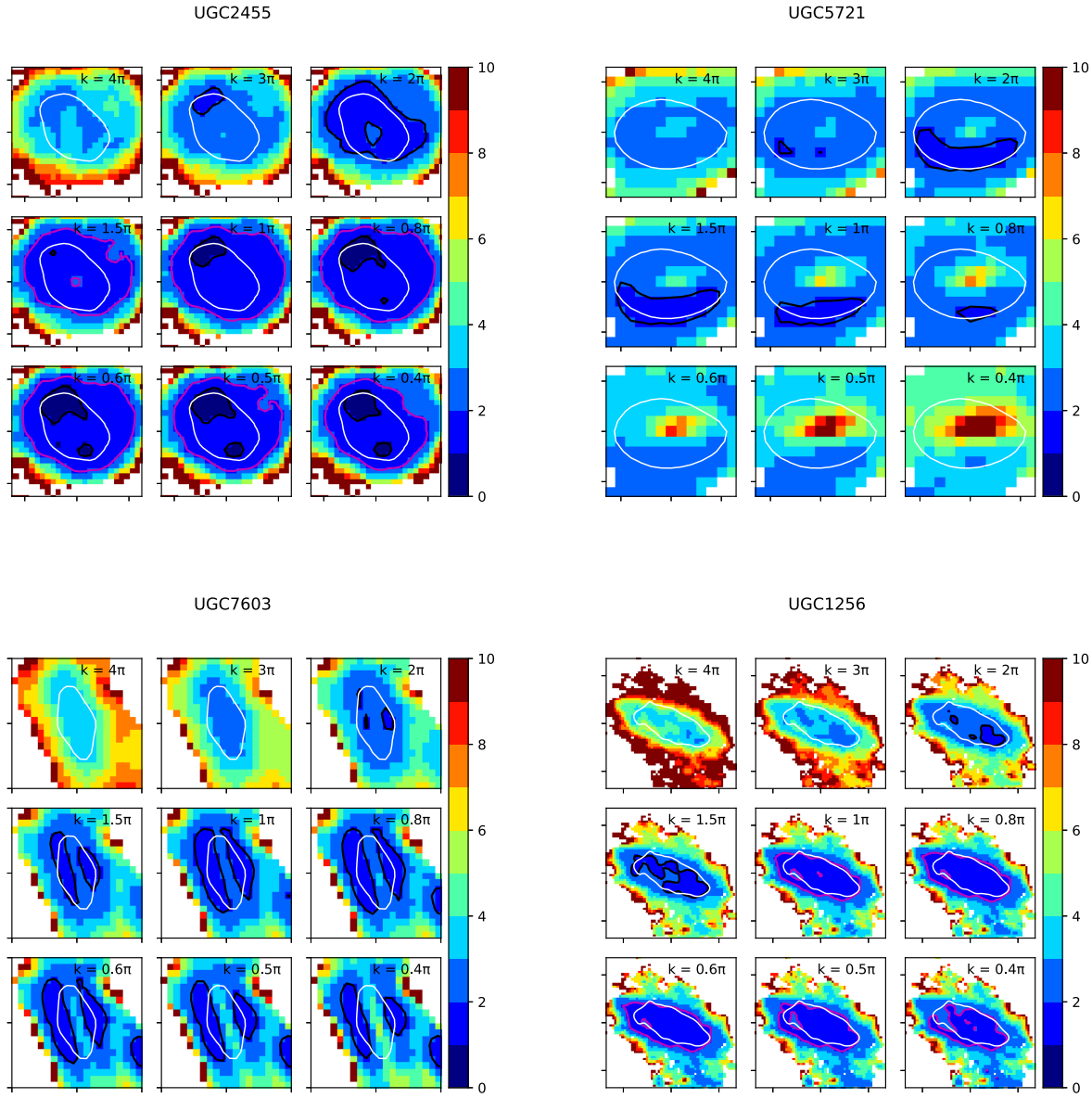

Figure C.12: Determining wavelength of maximum instability

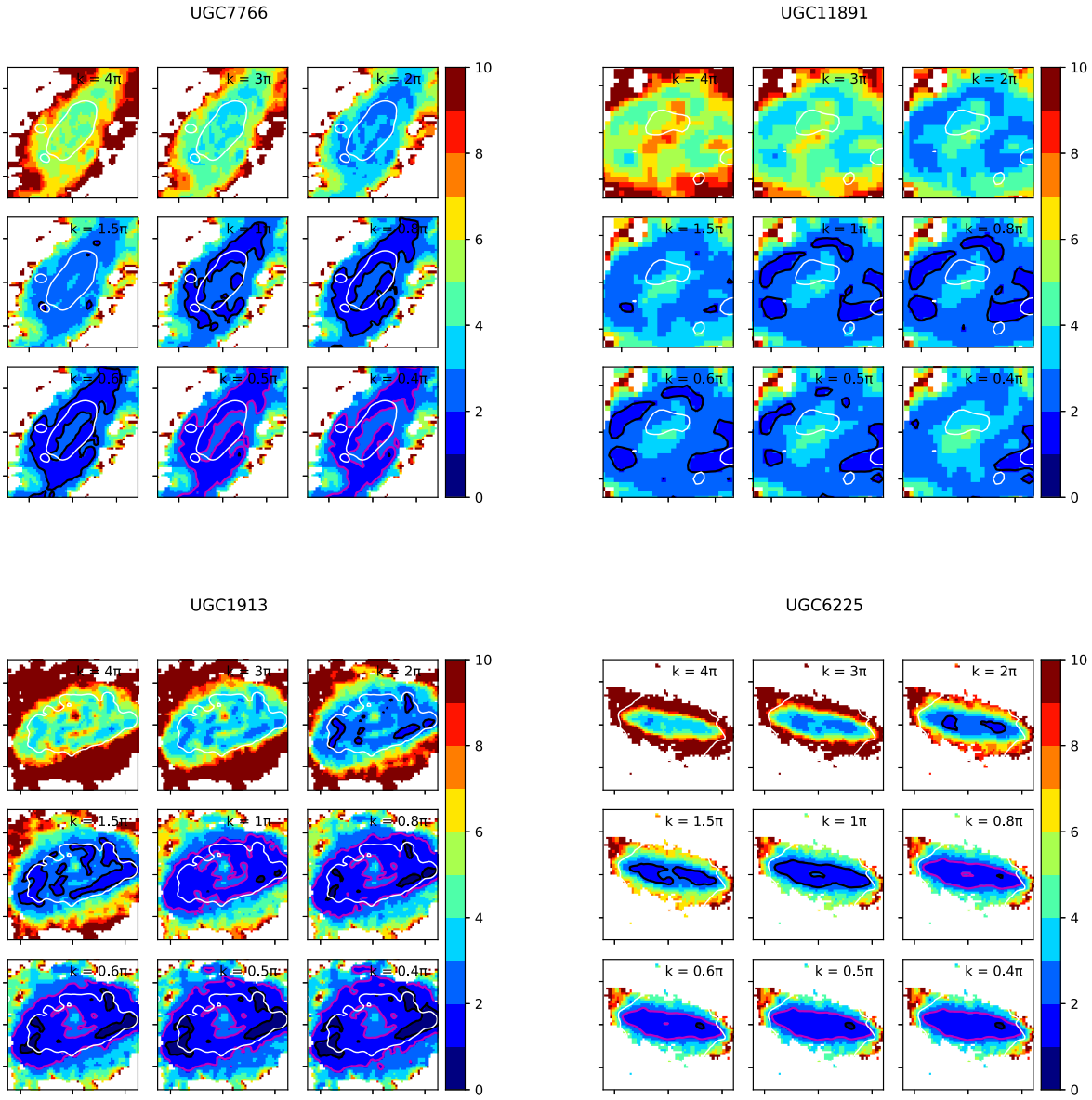

Figure C.13: Determining wavelength of maximum instability

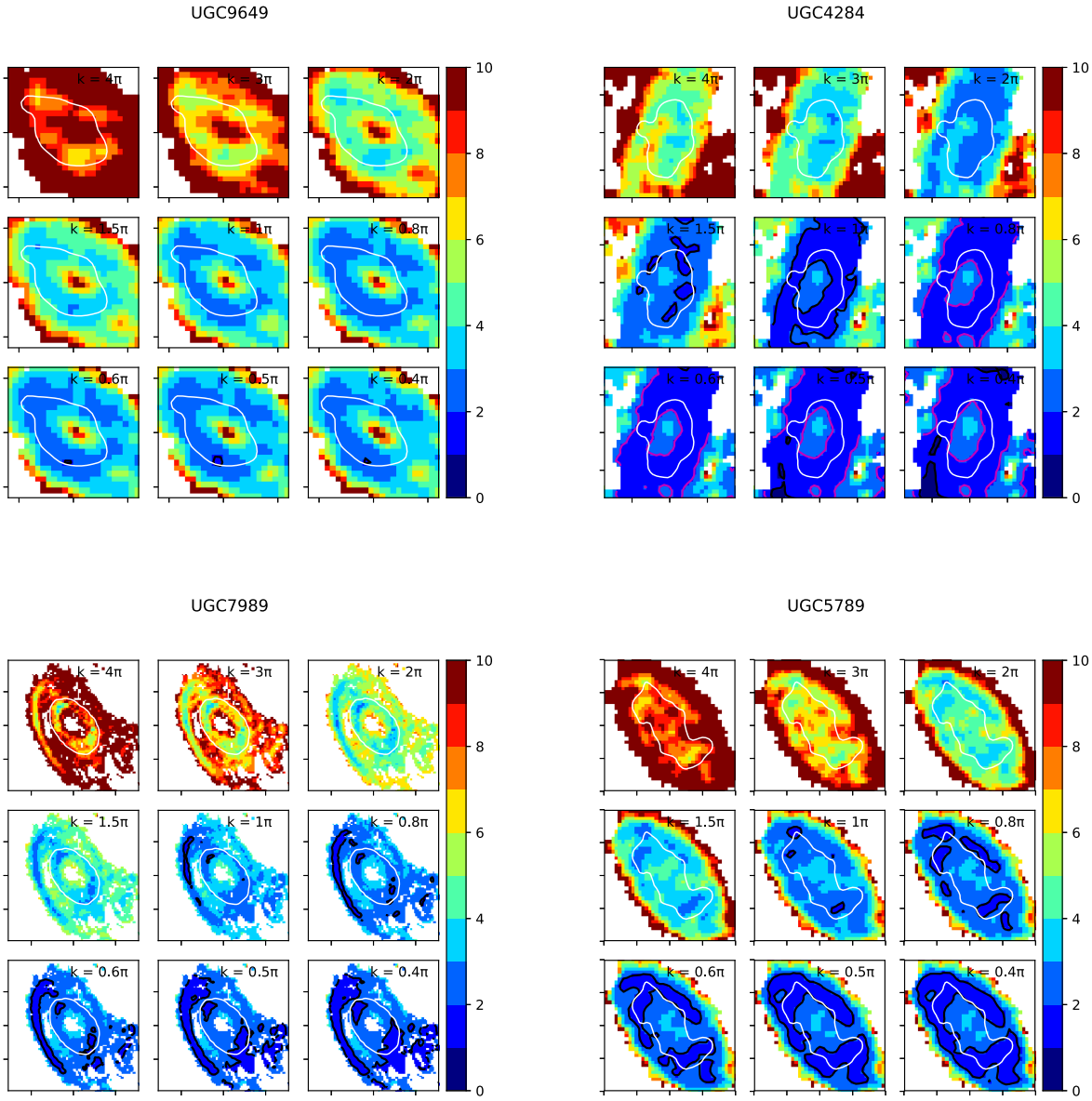

Figure C.14: Determining wavelength of maximum instability

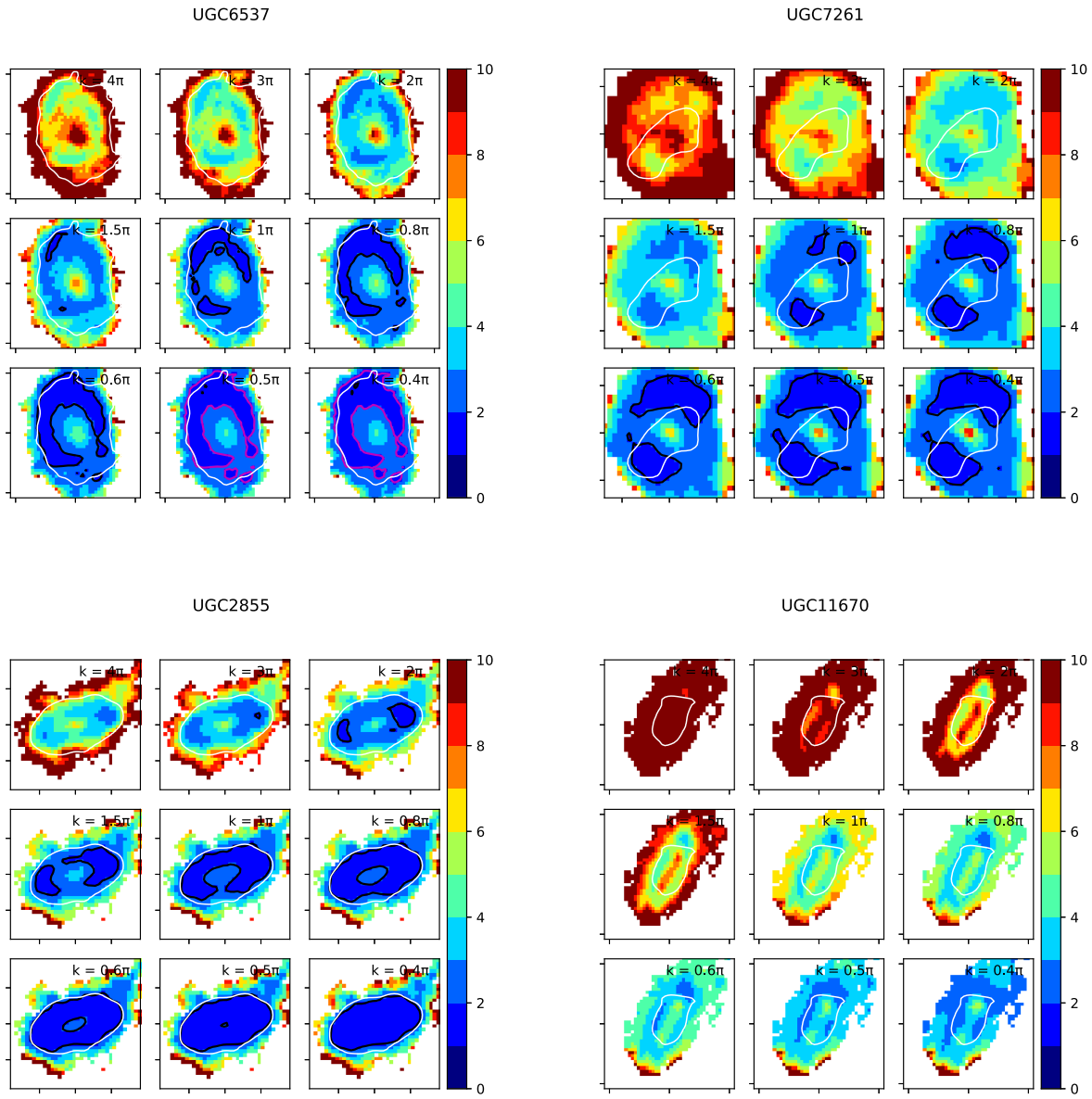

Figure C.15: Determining wavelength of maximum instability

Maps of variables

The variables used in derivation of the two-fluid disk stability parameter were the stellar surface density (Σ_*), stellar radial velocity dispersion (σ_*), and the single-fluid disk parameter for the stellar disk. These are shown in Figures C.16 - C.20 below. These maps were combined according to Equation 4.3 to obtain Q_T.

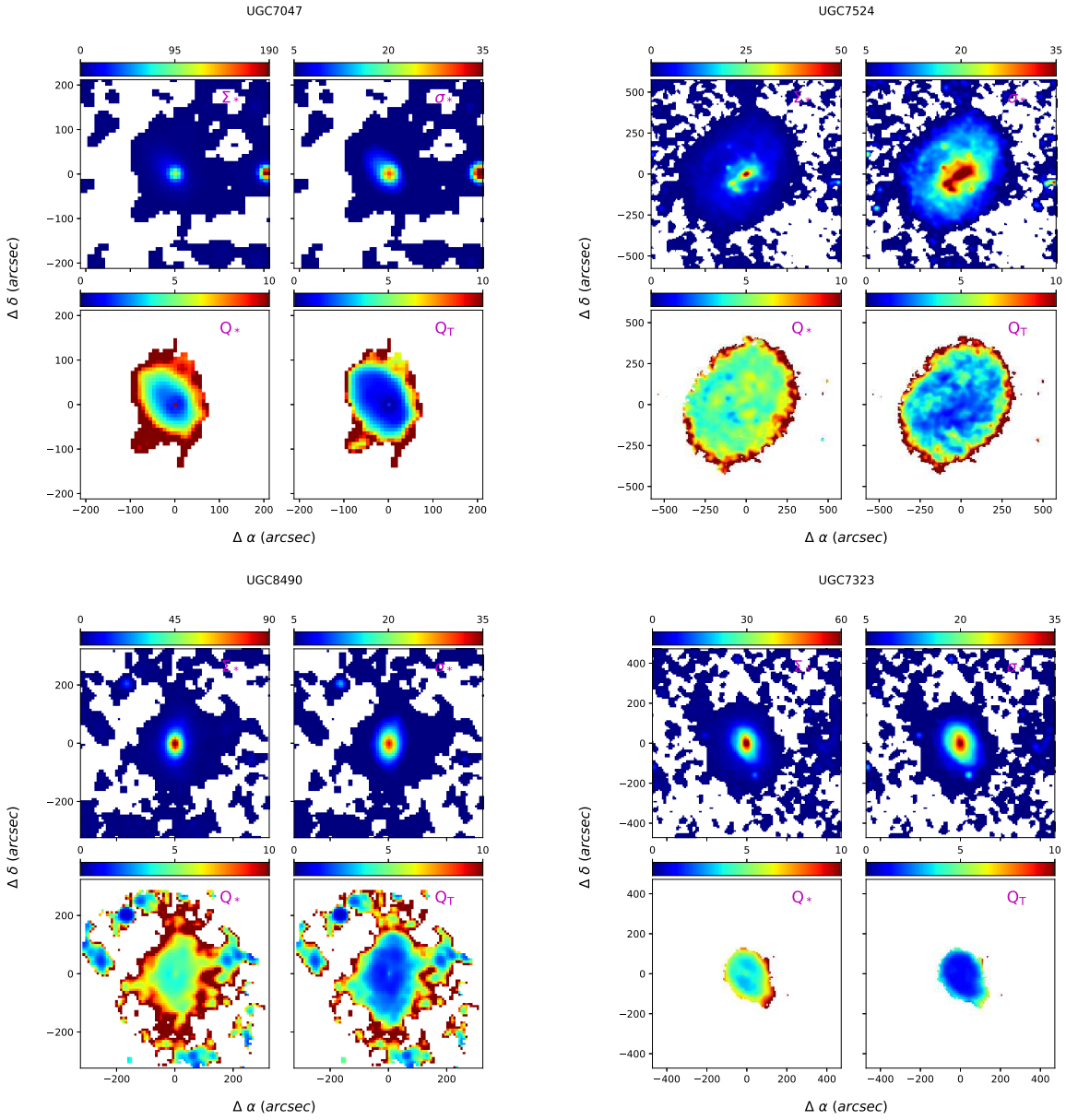

Figure C.16: Two-fluid disk stability derivations

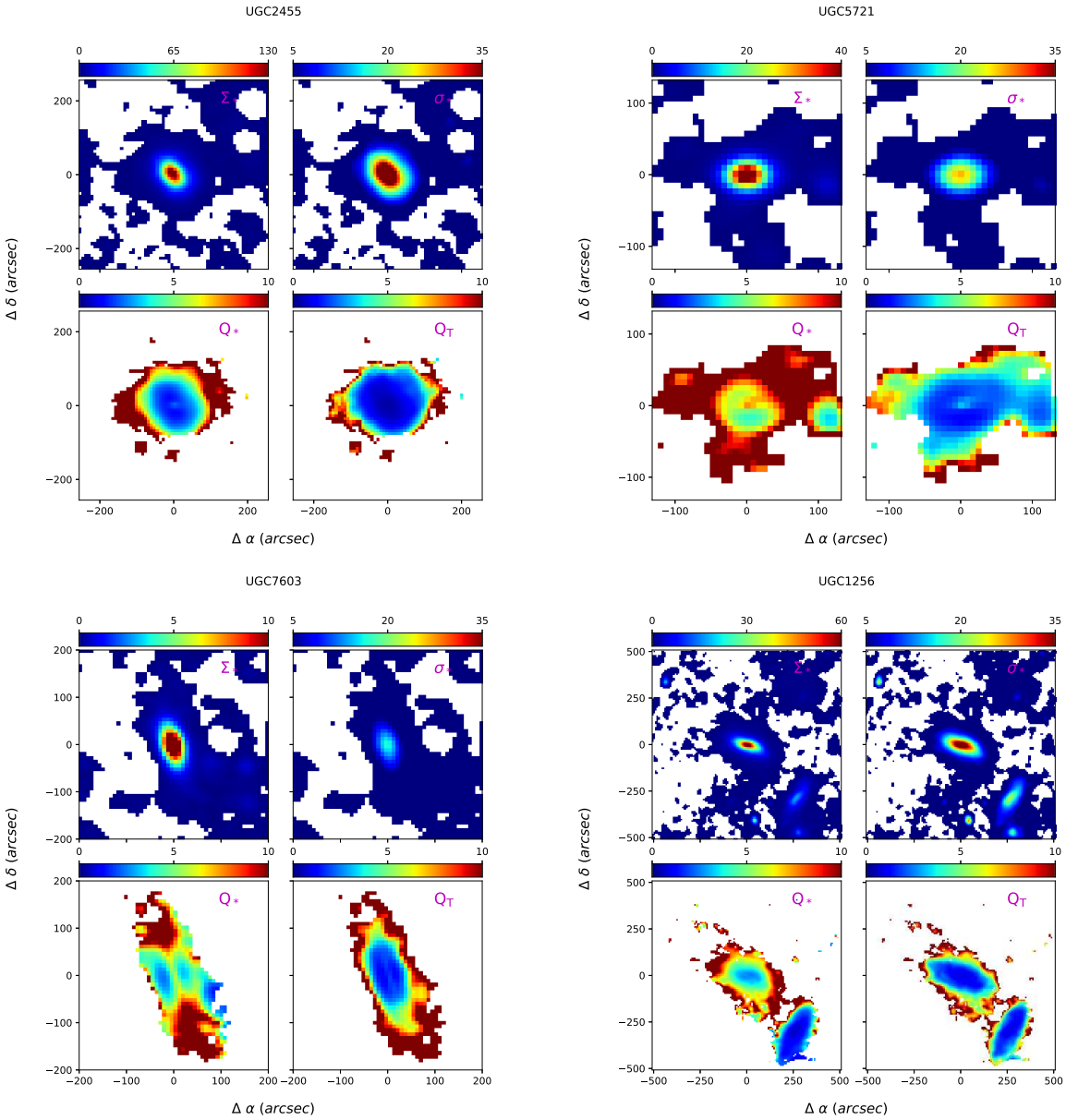

Figure C.17: Two-fluid disk stability derivations

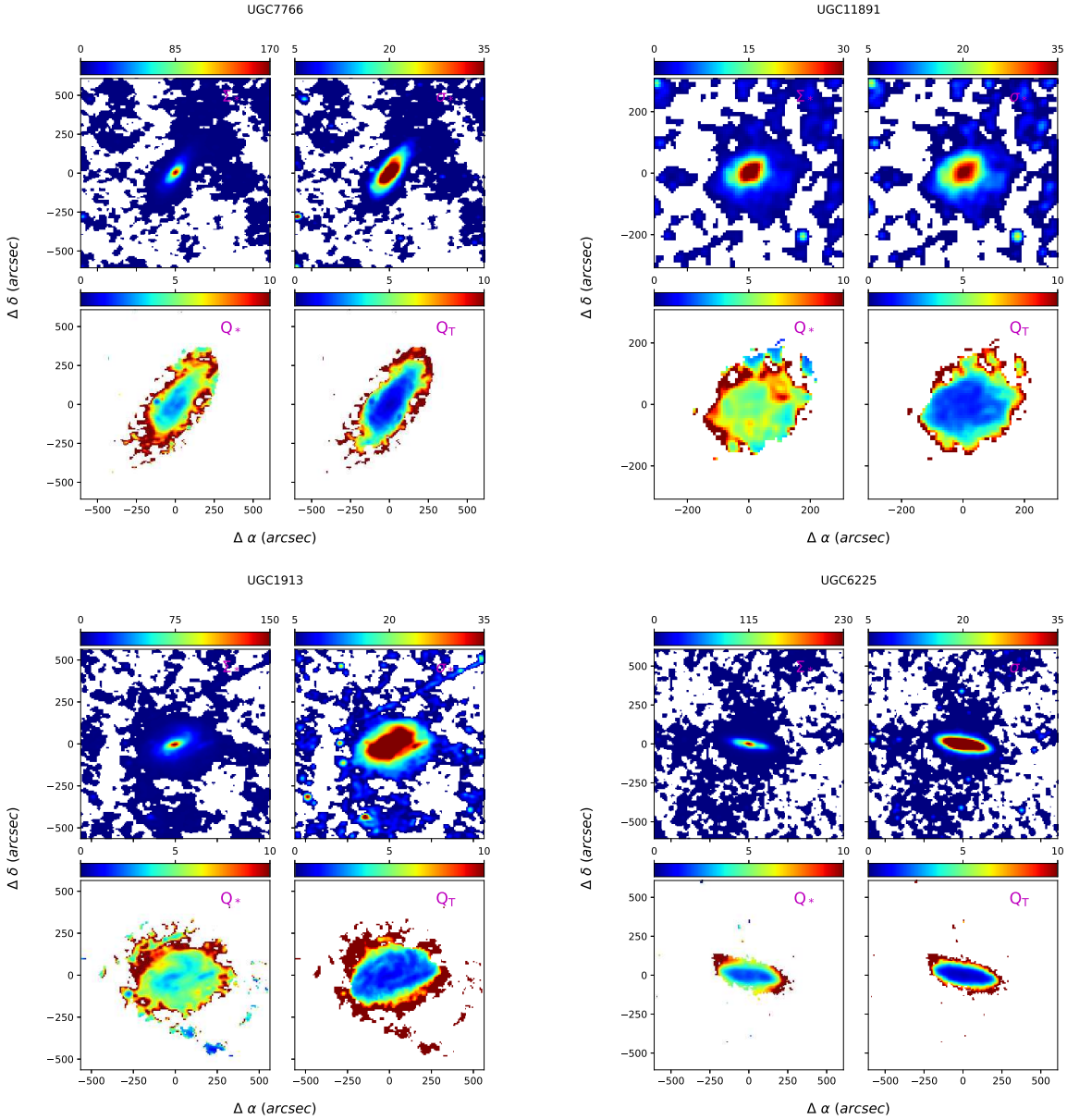

Figure C.18: Two-fluid disk stability derivations

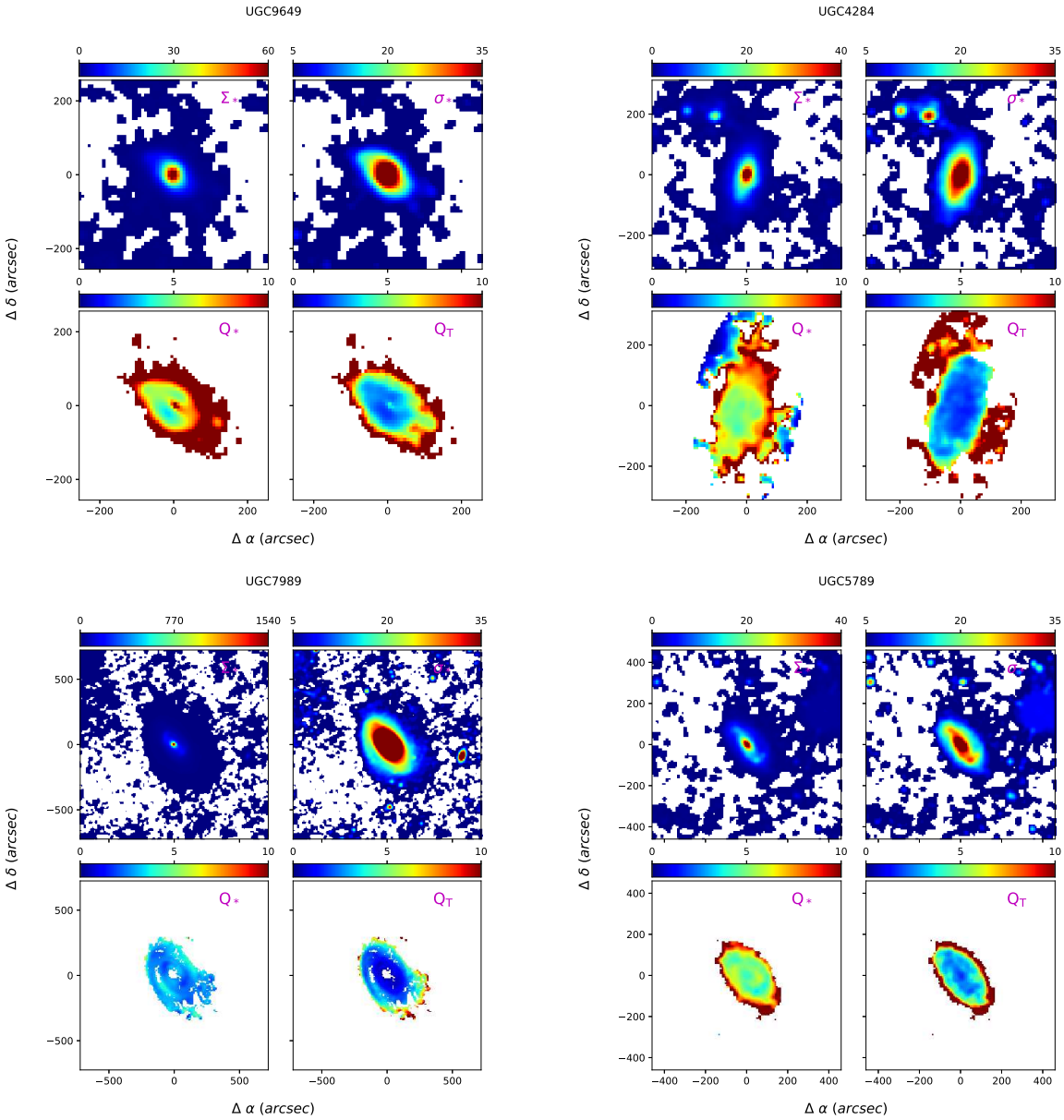

Figure C.19: Two-fluid disk stability derivations

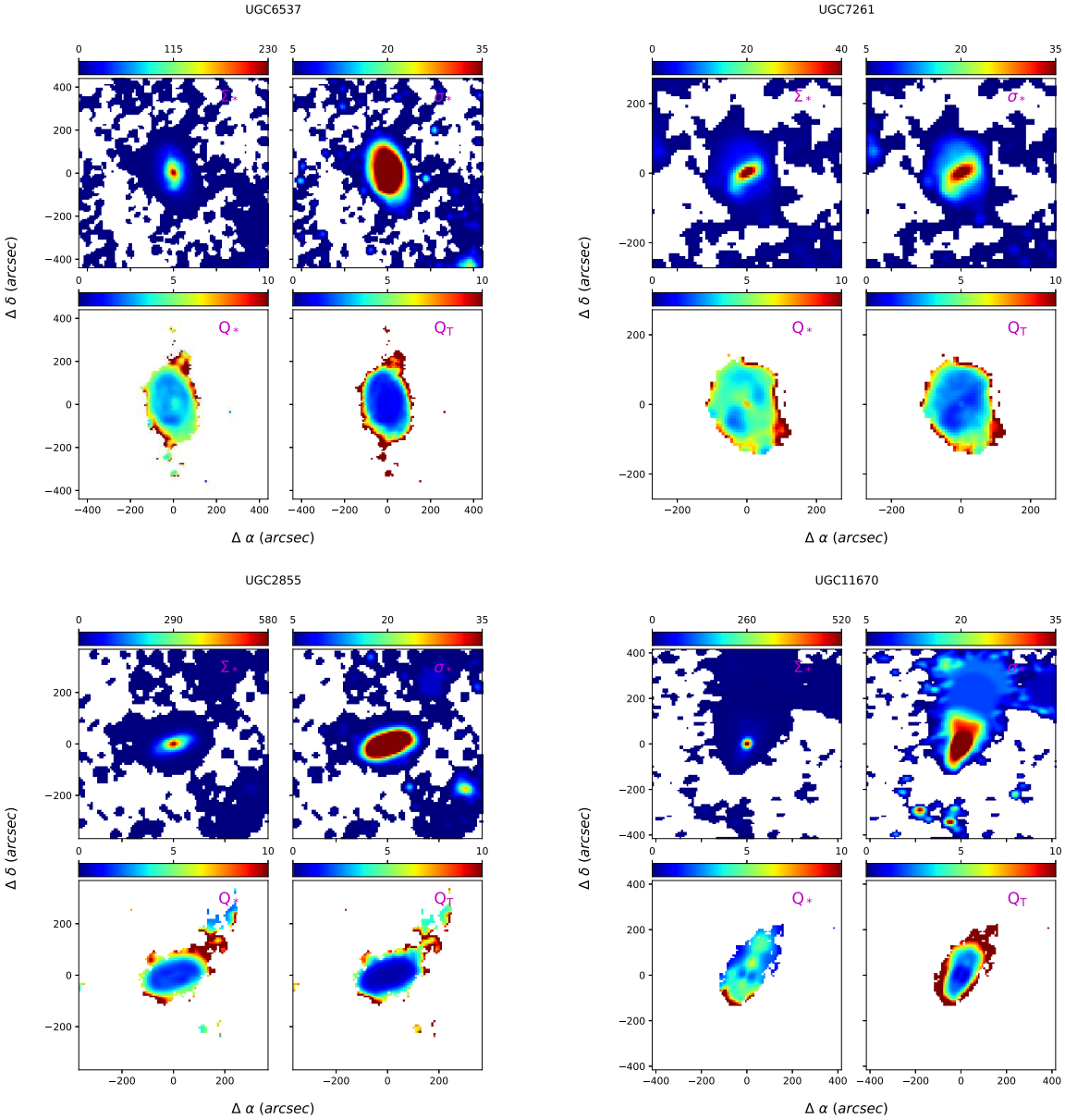

Figure C.20: Two-fluid disk stability derivations

C.3.3 Error Analysis

Single-fluid disk

From the single-fluid disk Toomre criterion,

$$Q_g \;=\; \frac{\sigma_g \kappa}{\pi G \Sigma}, \tag{C.3}$$

the dominant sources of uncertainty are the gas velocity dispersion σ_g and the gas surface density Σ_g such that,

$$\frac{\Delta Q_g}{Q_g} \;=\; \sqrt{(\frac{\Delta \sigma_g}{\sigma_g})^2 \;+\; (\frac{\Delta \Sigma_g}{\Sigma_g})^2} \tag{C.4}$$

We thus propagated the uncertainties in these two quantities. The uncertainty on σ_g is 3.6 km/s (see Section 4.2.1), while the uncertainty on Σ_g propagates from the uncertainty in inclination ($\cos\ i$) through the cosine of the inclination during the de-projection process (see Equation 4.10).

$$\Delta \cos\ i \;=\; \sin\ i\, \Delta i, \tag{C.5}$$

where Δi is the uncertainty on the inclination, and for this we assumed a 5% error. The 2D maps of the uncertainty in Q_g are shown in Figure C.21.

Two-fluid disk

Calculating the uncertainty on Q_T was slightly more complex than in the case of Q_g. The dominant sources of error were from the gas and stellar velocity dispersions (σ_g and σ_*) as well as the gas and stellar surface densities (Σ_g and Σ_*) . But first, we expanded the Q_T equation,

$$Q_T \;=\; \left(\frac{2q}{Q_*(1+q^2)} \;+\; \frac{2qR}{Q_g(1+q^2R^2)}\right)^{-1}, \tag{C.6}$$

where $q = \frac{k\sigma_*}{\kappa}$ and $R = \frac{\sigma_g}{\sigma_*}$, to

$$Q_T \;=\; \frac{\frac{\sigma_*\sigma_g}{G^2\ \Sigma_*\Sigma_g}\left(\frac{\kappa^2}{\pi^2} \;+\; \sigma_g^2 \;+\; \frac{\sigma_*^2}{K} \;+\; \frac{\sigma_*^2\sigma_g^2\pi^2}{\kappa^3}\right)}{\frac{2\sigma_*\sigma_g}{G}\left(\frac{1}{\Sigma_*} \;+\; \frac{1}{\Sigma_g}\right) \;+\; \frac{2\pi^2\sigma_*\sigma_g}{G\kappa^2}\left(\frac{\sigma_*^2}{\Sigma_*} \;+\; \frac{\sigma_g^2}{\Sigma_g}\right)}, \tag{C.7}$$

having substituted wave number $k = \pi$, in keeping with the scale of instabilities investigated in Chapter 4. When we choose the dominant terms in both the numerator and denominator as contributing most to the error, we have;

$$Q_T \;\approx\; \frac{\frac{\sigma_*^3\sigma_g^3\pi^2}{G^2\Sigma_*\Sigma_g\kappa^3}}{\frac{2\pi^2\sigma_*\sigma_g}{G\kappa^2}\left(\frac{\sigma_*^2}{\Sigma_*} \;+\; \frac{\sigma_g^2}{\Sigma_g}\right)}, \tag{C.8}$$

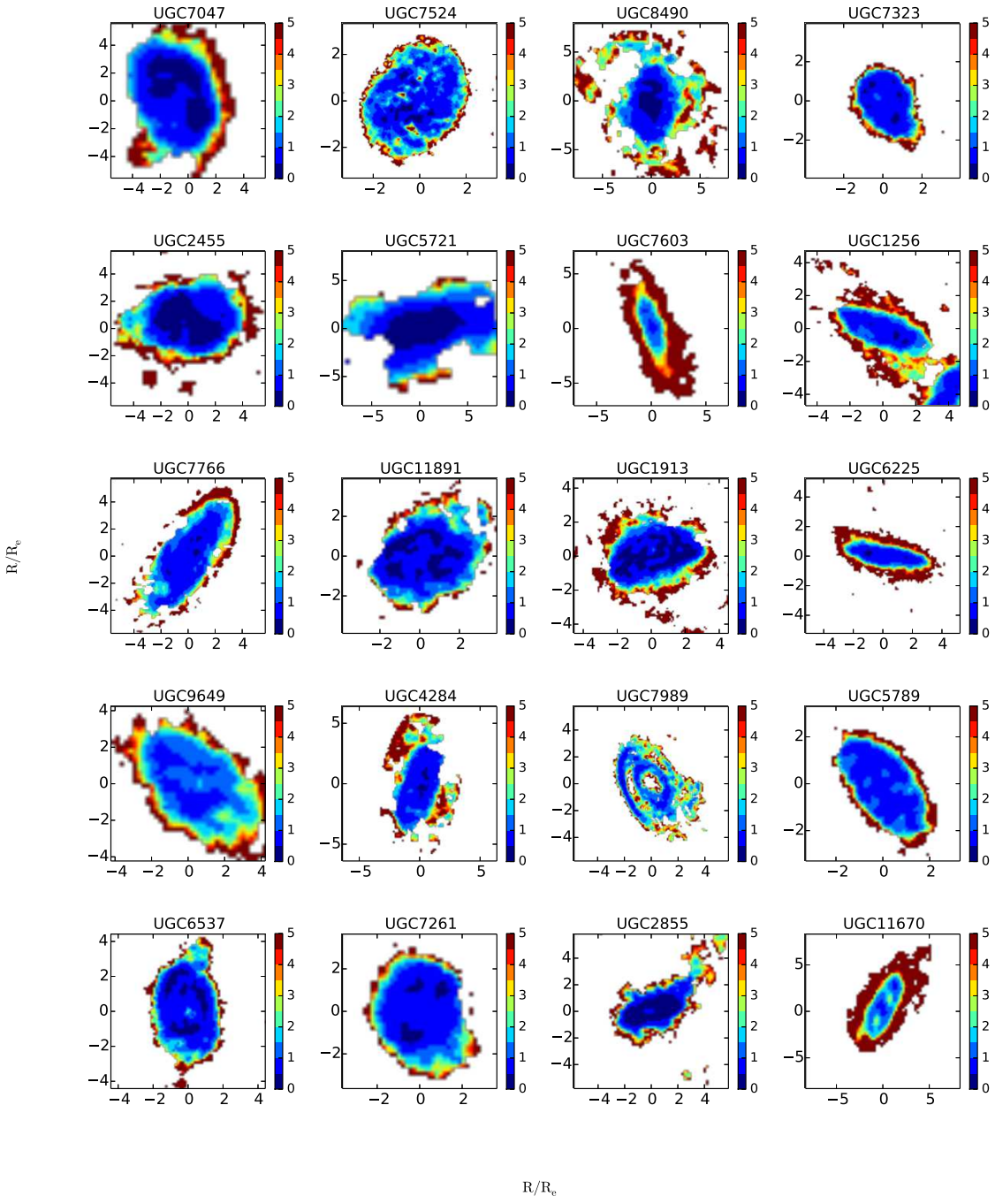

Figure C.21: Maps of the uncertainty on the Q_g maps. These were derived by propagating the dominant uncertainties on the gas velocity dispersion and gas surface density.

which reduces to;

$$Q_T \approx \frac{\sigma_*^2 \sigma_g^2}{2G\kappa \left(\sigma_g^2 \Sigma_* + \sigma_*^2 \Sigma_g\right)}. \tag{C.9}$$

The uncertainties on σ_g and Σ_g are the same as in Section C.3.3. The uncertainty on Σ_* was propagated from $\Delta \cos\ i$ due to de-projection (see Equation 4.25). Since the stellar velocity dispersion was derived from the stellar surface density, the uncertainty in Σ_* was propagated further into the σ_* (see Equation 4.27). Having calculated the uncertainty on the dominant sources, further propagation of these uncertainties into Q_T was done by applying the Python *uncertainties*[*] module to Equation C.9.
The maps of the uncertainty in Q_T are shown in Figure C.22.

[*]https://pypi.org/project/uncertainties/

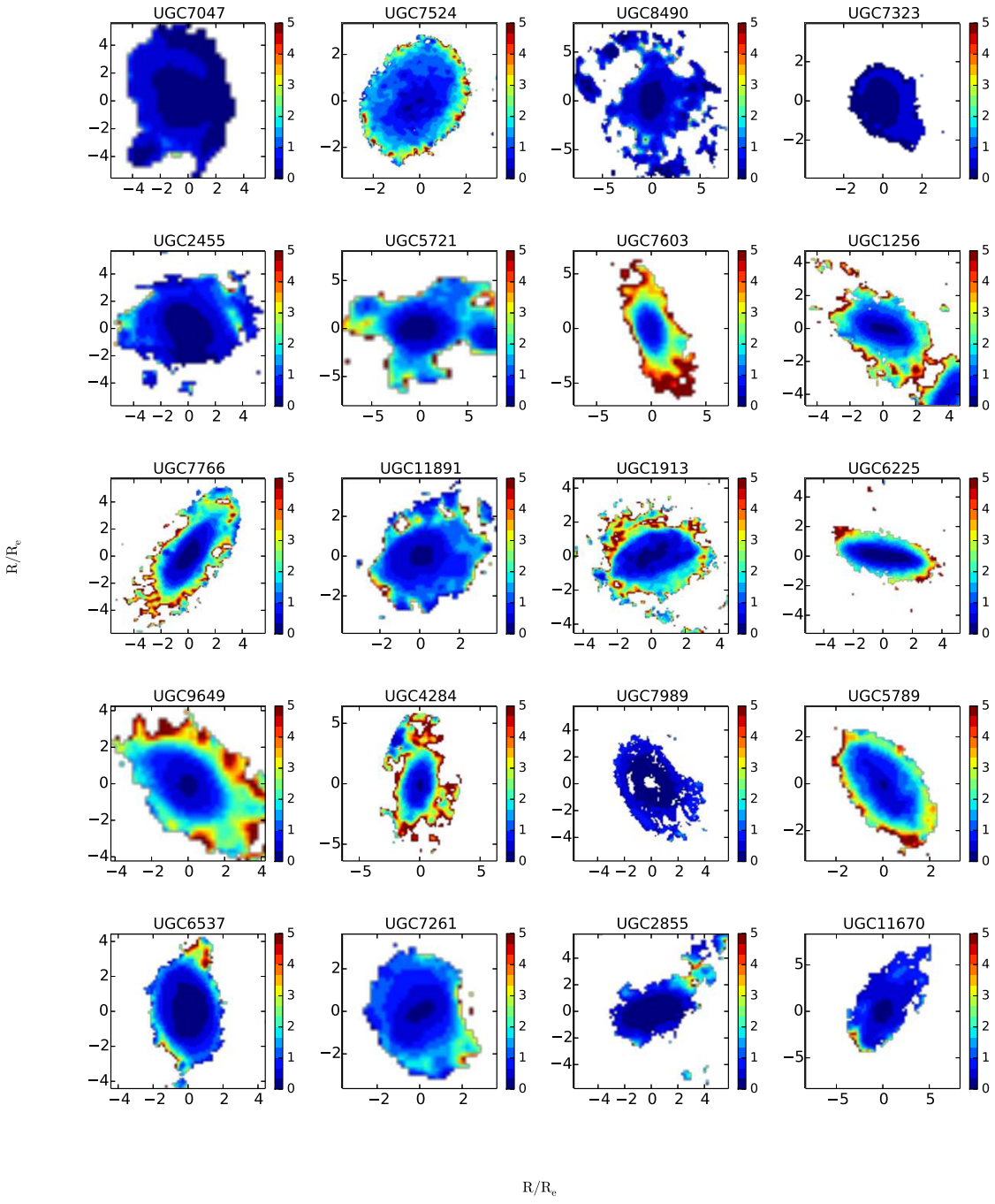

Figure C.22: Maps of the uncertainty on the Q_T maps. These were derived by propagating the dominant uncertainties on the gas and stellar velocity dispersions, and the gas and stellar surface densities.

C.4 The Wang and Silk Formulation

The Wang & Silk (1994) formulation (Equation 1.10) for two-fluid instabilities is often used in the literature owing to its simplicity (see Chapter 1.2.2). However, it is also known to yield much lower values of the stability parameter, and has been criticized by Jog (1996) for not considering the combined two-fluid dynamics of the stellar and gaseous disks. For general comparison, we derived the Wang and Silk stability parameter (Q_{WS}) for our sample. We find that indeed the disks have lower values for Q_{WS}. The formulation renders large areas of the disks unstable in 30% of the sample according to the $Q_T \leq 1$ criterion. When we consider the observed threshold of $Q_T \leq 2$, all the disks in the sample are rendered unstable. Maps of the Q_{WS} parameter are shown in Figure C.23 below.

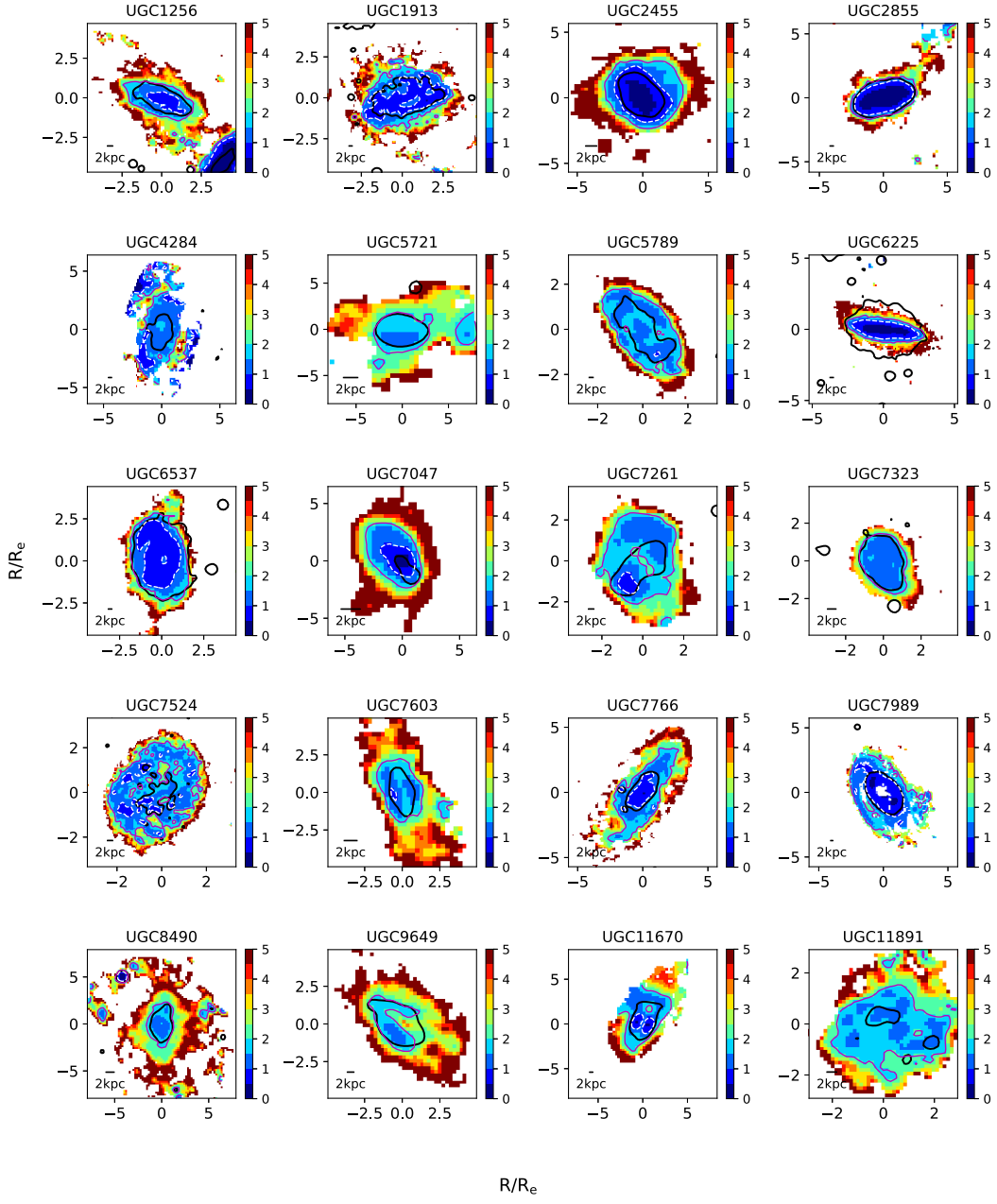

Figure C.23: The Wang and Silk stability parameter derived for our sample. White and Magenta contours mark regions of $Q_{WS} \leq 1$ and $Q_{WS} \leq 2$ respectively. Black contours mark the edge of the 'star forming disk' defined by an isophote in surface brightness which roughly matches the 5σ (in most cases, $\sim$ 18.8mag arcsec^{-2}) level in the W3 maps (see Chapter 4.1). The Q_{WS} formulation returns much lower values of the stability parameter and renders large areas of the disks unstable.

Bibliography

Abramova, O. V. 2012, Astronomy Letters, 38, 222

Alatalo, K., Davis, T. A., Bureau, M., Young, L. M., Blitz, L., Crocker, A. F., Bayet, E., Bois, M., Bournaud, F., Cappellari, M., et al. 2013, Monthly Notices of the Royal Astronomical Society, 432, 1796

Bacchini, C., Fraternali, F., Iorio, G., & Pezzulli, G. 2018, ArXiv e-prints

Begeman, K. G. 1987, PhD thesis, , Kapteyn Institute, (1987)

—. 1989, A&A, 223, 47

Begum, A., Chengalur, J. N., Karachentsev, I. D., Sharina, M. E., & Kaisin, S. S. 2008, MNRAS, 386, 1667

Behroozi, P. S., Wechsler, R. H., & Conroy, C. 2013, ApJ, 770, 57

Bekki, K., Couch, W. J., & Shioya, Y. 2002, ApJ, 577, 651

Bel, N. & Schatzman, E. 1958, Reviews of Modern Physics, 30, 1015

Bell, E. F. & de Jong, R. S. 2001, ApJ, 550, 212

Bell, E. F., McIntosh, D. H., Katz, N., & Weinberg, M. D. 2003, ApJS, 149, 289

Bigiel, F., Leroy, A., Walter, F., Blitz, L., Brinks, E., de Blok, W. J. G., & Madore, B. 2010, AJ, 140, 1194

Bigiel, F., Leroy, A., Walter, F., Brinks, E., de Blok, W. J. G., Madore, B., & Thornley, M. D. 2008, AJ, 136, 2846

Boissier, S. & Prantzos, N. 1999, MNRAS, 307, 857

Boissier, S., Prantzos, N., Boselli, A., & Gavazzi, G. 2003, MNRAS, 346, 1215

Bolatto, A. D., Leroy, A. K., Jameson, K., Ostriker, E., Gordon, K., Lawton, B., Stanimirović, S., Israel, F. P., Madden, S. C., Hony, S., Sandstrom, K. M., Bot, C., Rubio, M., Winkler, P. F., Roman-Duval, J., van Loon, J. T., Oliveira, J. M., & Indebetouw, R. 2011, ApJ, 741, 12

Bolatto, A. D., Wolfire, M., & Leroy, A. K. 2013, ARA&A, 51, 207

Booth, R. S., de Blok, W. J. G., Jonas, J. L., & Fanaroff, B. 2009, arXiv e-prints, arXiv:0910.2935

Booth, R. S. & Jonas, J. L. 2012, African Skies, 16, 101

Bosma, A. 1981, AJ, 86, 1825

Brinchmann, J., Charlot, S., White, S. D. M., Tremonti, C., Kauffmann, G., Heckman, T., & Brinkmann, J. 2004, \mnras, 351, 1151

Brinks, E. 2006, The Definitive Guide to Calculating HI Masses

Broeils, A. H. & Rhee, M.-H. 1997, A&A, 324, 877

Bullock, J. S. & Boylan-Kolchin, M. 2017, ARA&A, 55, 343

Calzetti, D. 2013, Star Formation Rate Indicators, ed. J. Falcón-Barroso & J. H. Knapen, 419

Calzetti, D., Kennicutt, R. C., Engelbracht, C. W., Leitherer, C., Draine, B. T., Kewley, L., Moustakas, J., Sosey, M., Dale, D. A., Gordon, K. D., Helou, G. X., Hollenbach, D. J., Armus, L., Bendo, G., Bot, C., Buckalew, B., Jarrett, T., Li, A., Meyer, M., Murphy, E. J., Prescott, M., Regan, M. W., Rieke, G. H., Roussel, H., Sheth, K., Smith, J. D. T., Thornley, M. D., & Walter, F. 2007, ApJ, 666, 870

Calzetti, D., Wilson, G. W., Draine, B. T., Roussel, H., Johnson, K. E., Heyer, M. H., Wall, W. F., Grasha, K., Battisti, A., Andrews, J. E., Kirkpatrick, A., Rosa González, D., Vega, O., Puschnig, J., Yun, M., Östlin, G., Evans, A. S., Tang, Y., Lowenthal, J., & Sánchez-Arguelles, D. 2018, ApJ, 852, 106

Cayatte, V., Kotanyi, C., Balkowski, C., & van Gorkom, J. H. 1994, AJ, 107, 1003

Chandrasekhar, S. 1955, Vistas in Astronomy, 1, 344

Cluver, M. E., Jarrett, T. H., Dale, D. A., Smith, J.-D. T., August, T., & Brown, M. J. I. 2017, ApJ, 850, 68

Cluver, M. E., Jarrett, T. H., Hopkins, A. M., Driver, S. P., Liske, J., Gunawardhana, M. L. P., Taylor, E. N., Robotham, A. S. G., Alpaslan, M., Baldry, I., Brown, M. J. I., Peacock, J. A., Popescu, C. C., Tuffs, R. J., Bauer, A. E., Bland-Hawthorn, J., Colless, M., Holwerda, B. W., Lara-López, M. A., Leschinski, K., López-Sánchez, A. R., Norberg, P., Owers, M. S., Wang, L., & Wilkins, S. M. 2014, ApJ, 782, 90

Cluver, M. E., Jarrett, T. H., Kraan-Korteweg, R. C., Koribalski, B. S., Appleton, P. N., Melbourne, J., Emonts, B., & Woudt, P. A. 2010, ApJ, 725, 1550

Cutri, R. M. & et al. 2012, VizieR Online Data Catalog, 2311

Daddi, E., Dickinson, M., Morrison, G., Chary, R., Cimatti, A., Elbaz, D., Frayer, D., Renzini, A., Pope, A., Alexander, D. M., Bauer, F. E., Giavalisco, M., Huynh, M., Kurk, J., & Mignoli, M. 2007, ApJ, 670, 156

Davé, R., Rafieferantsoa, M. H., Thompson, R. J., & Hopkins, P. F. 2017, MNRAS, 467, 115

Davis, M., Efstathiou, G., Frenk, C. S., & White, S. D. M. 1985, ApJ, 292, 371

de Blok, E., Fraternali, F., Heald, G., Adams, B., Bosma, A., & Koribalski, B. 2015, Advancing Astrophysics with the Square Kilometre Array (AASKA14), 129

de Blok, W. J. G., Adams, E. A. K., Amram, P., Athanassoula, E., Bagetakos, I., Balkowski, C., Bershady, M. A., Beswick, R. J., Bigiel, F., Blyth, S. L., Bosma, A., Booth, R. S., Bouchard, A., Brinks, E., Carignan, C., Chemin, L., Combes, F., Conway, J., Elson, E. C., English, J., Epinat, B., Frank, B. S., Fiege, J., Fraternali, F., Gallagher, J. S., Gibson, B. K., Heald, G., Henning, P. A., Holwerda, B. W., Jarrett, T. H., Jerjen, H., Józsa, G. I., Kapala, M., Klöckner, H. R., Koribalski, B. S., Kraan-Korteweg, R. C., Leon, S., Leroy, A., Loubser, S. I., Lucero, D. M., McGaugh, S. S., Meurer, G. R., Meyer, M., Mogotsi, M., Namumba, B., Oh, S. H., Oosterloo, T. A., Pisano, D. J., Popping, A., Ratcliffe, S., Sellwood, J. A., Schinnerer, E., Schröder, A. C., Sheth, K., Smith, M. W. L., Sorgho, A., Spekkens, K., Stanimirovic, S., van der Heyden, K. J., Verdes-Montenegro, L., van Driel, W., Walter, F., Westmeier, T., Wilcots, E., Williams, T., Wong, O. I., Woudt, P. A., & Zijlstra, A. 2016, in Proceedings of MeerKAT Science: On the Pathway to the SKA. 25-27 May, 2016 Stellenbosch, South Africa (MeerKAT2016). Online at <A href="href=">href="https://pos.sissa.it/cgi-bin/reader/conf.cgi?confid=277</A>, id.7, 7

de Blok, W. J. G. & Walter, F. 2006, AJ, 131, 363

de Blok, W. J. G., Walter, F., Brinks, E., Trachternach, C., Oh, S.-H., & Kennicutt Jr., R. C. 2008, \aj, 136, 2648

de Vaucouleurs, G., de Vaucouleurs, A., Corwin, Jr., H. G., Buta, R. J., Paturel, G., & Fouqué, P. 1991, Third Reference Catalogue of Bright Galaxies. Volume I: Explanations and references. Volume II: Data for galaxies between 0^h and 12^h. Volume III: Data for galaxies between 12^h and 24^h.

DES Collaboration, Abbott, T. M. C., Abdalla, F. B., Alarcon, A., Aleksić, J., Allam, S., Allen, S., Amara, A., Annis, J., Asorey, J., Avila, S., Bacon, D., Balbinot, E., Banerji, M., Banik, N., Barkhouse, W., Baumer, M., Baxter, E., Bechtol, K., Becker, M. R., Benoit-Lévy, A., Benson, B. A., Bernstein, G. M., Bertin, E., Blazek, J., Bridle, S. L., Brooks, D., Brout, D., Buckley-Geer, E., Burke, D. L., Busha, M. T., Capozzi, D., Carnero Rosell, A., Carrasco Kind, M., Carretero, J., Castander, F. J., Cawthon, R., Chang, C., Chen, N., Childress, M., Choi, A., Conselice, C., Crittenden, R., Crocce, M., Cunha,

C. E., D'Andrea, C. B., da Costa, L. N., Das, R., Davis, T. M., Davis, C., De Vicente, J., DePoy, D. L., DeRose, J., Desai, S., Diehl, H. T., Dietrich, J. P., Dodelson, S., Doel, P., Drlica-Wagner, A., Eifler, T. F., Elliott, A. E., Elsner, F., Elvin-Poole, J., Estrada, J., Evrard, A. E., Fang, Y., Fernandez, E., Ferté, A., Finley, D. A., Flaugher, B., Fosalba, P., Friedrich, O., Frieman, J., García-Bellido, J., Garcia-Fernandez, M., Gatti, M., Gaztanaga, E., Gerdes, D. W., Giannantonio, T., Gill, M. S. S., Glazebrook, K., Goldstein, D. A., Gruen, D., Gruendl, R. A., Gschwend, J., Gutierrez, G., Hamilton, S., Hartley, W. G., Hinton, S. R., Honscheid, K., Hoyle, B., Huterer, D., Jain, B., James, D. J., Jarvis, M., Jeltema, T., Johnson, M. D., Johnson, M. W. G., Kacprzak, T., Kent, S., Kim, A. G., King, A., Kirk, D., Kokron, N., Kovacs, A., Krause, E., Krawiec, C., Kremin, A., Kuehn, K., Kuhlmann, S., Kuropatkin, N., Lacasa, F., Lahav, O., Li, T. S., Liddle, A. R., Lidman, C., Lima, M., Lin, H., MacCrann, N., Maia, M. A. G., Makler, M., Manera, M., March, M., Marshall, J. L., Martini, P., McMahon, R. G., Melchior, P., Menanteau, F., Miquel, R., Miranda, V., Mudd, D., Muir, J., Möller, A., Neilsen, E., Nichol, R. C., Nord, B., Nugent, P., Ogando, R. L. C., Palmese, A., Peacock, J., Peiris, H. V., Peoples, J., Percival, W. J., Petravick, D., Plazas, A. A., Porredon, A., Prat, J., Pujol, A., Rau, M. M., Refregier, A., Ricker, P. M., Roe, N., Rollins, R. P., Romer, A. K., Roodman, A., Rosenfeld, R., Ross, A. J., Rozo, E., Rykoff, E. S., Sako, M., Salvador, A. I., Samuroff, S., Sánchez, C., Sanchez, E., Santiago, B., Scarpine, V., Schindler, R., Scolnic, D., Secco, L. F., Serrano, S., Sevilla-Noarbe, I., Sheldon, E., Smith, R. C., Smith, M., Smith, J., Soares-Santos, M., Sobreira, F., Suchyta, E., Tarle, G., Thomas, D., Troxel, M. A., Tucker, D. L., Tucker, B. E., Uddin, S. A., Varga, T. N., Vielzeuf, P., Vikram, V., Vivas, A. K., Walker, A. R., Wang, M., Wechsler, R. H., Weller, J., Wester, W., Wolf, R. C., Yanny, B., Yuan, F., Zenteno, A., Zhang, B., Zhang, Y., & Zuntz, J. 2017, ArXiv e-prints

Dessauges-Zavadsky, M., Verdugo, C., Combes, F., & Pfenniger, D. 2014, A&A, 566, A147

Di Matteo, P., Combes, F., Melchior, A.-L., & Semelin, B. 2007, \aap, 468, 61

Drew, J. E., Greimel, R., Irwin, M. J., Aungwerojwit, A., Barlow, M. J., Corradi, R. L. M., Drake, J. J., Gänsicke, B. T., Groot, P., Hales, A., Hopewell, E. C., Irwin, J., Knigge, C., Leisy, P., Lennon, D. J., Mampaso, A., Masheder, M. R. W., Matsuura, M., Morales-Rueda, L., Morris, R. A. H., Parker, Q. A., Phillipps, S., Rodriguez-Gil, P., Roelofs, G., Skillen, I., Sokoloski, J. L., Steeghs, D., Unruh, Y. C., Viironen, K., Vink, J. S., Walton, N. A., Witham, A., Wright, N., Zijlstra, A. A., & Zurita, A. 2005, MNRAS, 362, 753

Duffy, A. R., Meyer, M. J., Staveley-Smith, L., Bernyk, M., Croton, D. J., Koribalski, B. S., Gerstmann, D., & Westerlund, S. 2012, Mon. Not. R. Astron. Soc, 426, 3385

Egusa, F., Koda, J., & Scoville, N. 2011, ApJ, 726, 85

Ellison, S. L., Mendel, J. T., Patton, D. R., & Scudder, J. M. 2013, MNRAS, 435, 3627

Elmegreen, B. G. 2011, ApJ, 737, 10

Elmegreen, B. G. & Hunter, D. A. 2015, ApJ, 805, 145

Elson, E. C., de Blok, W. J. G., & Kraan-Korteweg, R. C. 2012, AJ, 143, 1

Epinat, B., Amram, P., Marcelin, M., Balkowski, C., Daigle, O., Hernandez, O., Chemin, L., Carignan, C., Gach, J.-L., & Balard, P. 2008, MNRAS, 388, 500

Evans, II, N. J., Heiderman, A., & Vutisalchavakul, N. 2014, ApJ, 782, 114

Ewen, H. I. & Purcell, E. M. 1951, Nature, 168, 356

Firmani, C. & Avila-Reese, V. 2000, MNRAS, 315, 457

Flores, R. A. & Primack, J. R. 1994, ApJ, 427, L1

Fumagalli, M. & Gavazzi, G. 2008, A&A, 490, 571

Garrido, O., Marcelin, M., Amram, P., & Boulesteix, J. 2002, A&A, 387, 821

Giovanelli, R. & Haynes, M. P. 2002, ApJ, 571, L107

Griv, E. & Gedalin, M. 2012, MNRAS, 422, 600

Grootes, M. W., Tuffs, R. J., Popescu, C. C., Pastrav, B., Andrae, E., Gunawardhana, M., Kelvin, L. S., Liske, J., Seibert, M., Taylor, E. N., Graham, A. W., Baes, M., Baldry, I. K., Bourne, N., Brough, S., Cooray, A., Dariush, A., De Zotti, G., Driver, S. P., Dunne, L., Gomez, H., Hopkins, A. M., Hopwood, R., Jarvis, M., Loveday, J., Maddox, S., Madore, B. F., Michałowski, M. J., Norberg, P., Parkinson, H. R., Prescott, M., Robotham, A. S. G., Smith, D. J. B., Thomas, D., & Valiante, E. 2013, ApJ, 766, 59

Guo, K., Zheng, X. Z., Wang, T., & Fu, H. 2015, ApJ, 808, L49

Hao, C.-N., Kennicutt, R. C., Johnson, B. D., Calzetti, D., Dale, D. A., & Moustakas, J. 2011, ApJ, 741, 124

Hatton, S., Devriendt, J. E. G., Ninin, S., Bouchet, F. R., Guiderdoni, B., & Vibert, D. 2003, MNRAS, 343, 75

Heald, G., Józsa, G., Serra, P., Zschaechner, L., Rand, R., Fraternali, F., Oosterloo, T., Walterbos, R., Jütte, E., & Gentile, G. 2011, A&A, 526, A118

Helfer, T. T., Thornley, M. D., Regan, M. W., Wong, T., Sheth, K., Vogel, S. N., Blitz, L., & Bock, D. C.-J. 2003, ApJS, 145, 259

Henriques, B. M. B., White, S. D. M., Thomas, P. A., Angulo, R., Guo, Q., Lemson, G., Springel, V., & Overzier, R. 2015, MNRAS, 451, 2663

Heyer, M. H., Corbelli, E., Schneider, S. E., & Young, J. S. 2004, ApJ, 602, 723

Huchra, J., Jarrett, T., Skrutskie, M., Cutri, R., Schneider, S., Macri, L., Steining, R., Mader, J., Martimbeau, N., & George, T. 2005, in Astronomical Society of the Pacific Conference Series, Vol. 329, Nearby Large-Scale Structures and the Zone of Avoidance, ed. A. P. Fairall & P. A. Woudt, Fairall

Hunter, D. A., Elmegreen, B. G., & Baker, A. L. 1998, ApJ, 493, 595

Ianjamasimanana, R., de Blok, W. J. G., Walter, F., & Heald, G. H. 2012, AJ, 144, 96

Ilbert, O., Arnouts, S., Le Floc'h, E., Aussel, H., Bethermin, M., Capak, P., Hsieh, B.-C., Kajisawa, M., Karim, A., Le Fèvre, O., Lee, N., Lilly, S., McCracken, H. J., Michel-Dansac, L., Moutard, T., Renzini, M. A., Salvato, M., Sanders, D. B., Scoville, N., Sheth, K., Silverman, J. D., Smolčić, V., Taniguchi, Y., & Tresse, L. 2015, A&A, 579, A2

Jameson, K. E., Bolatto, A. D., Leroy, A. K., Meixner, M., Roman-Duval, J., Gordon, K., Hughes, A., Israel, F. P., Rubio, M., Indebetouw, R., Madden, S. C., Bot, C., Hony, S., Cormier, D., Pellegrini, E. W., Galametz, M., & Sonneborn, G. 2016, ApJ, 825, 12

Jarrett, T. H., Chester, T., Cutri, R., Schneider, S., Skrutskie, M., & Huchra, J. P. 2000, AJ, 119, 2498

Jarrett, T. H., Cluver, M. E., Magoulas, C., Bilicki, M., Alpaslan, M., Bland-Hawthorn, J., Brough, S., Brown, M. J. I., Croom, S., Driver, S., Holwerda, B. W., Hopkins, A. M., Loveday, J., Norberg, P., Peacock, J. A., Popescu, C. C., Sadler, E. M., Taylor, E. N., Tuffs, R. J., & Wang, L. 2017, ApJ, 836, 182

Jarrett, T. H., Masci, F., Tsai, C. W., Petty, S., Cluver, M., Assef, R. J., Benford, D., Blain, A., Bridge, C., Donoso, E., Eisenhardt, P., Fowler, J., Koribalski, B., Lake, S., Neill, J. D., Seibert, M., Sheth, K., Stanford, S., & Wright, E. 2012, AJ, 144, 68

Jarrett, T. H., Masci, F., Tsai, C. W., Petty, S., Cluver, M. E., Assef, R. J., Benford, D., Blain, A., Bridge, C., Donoso, E., Eisenhardt, P., Koribalski, B., Lake, S., Neill, J. D., Seibert, M., Sheth, K., Stanford, S., & Wright, E. 2013, AJ, 145, 6

Jeans, J. H. 1902, Philosophical Transactions of the Royal Society of London Series A, 199, 1

Jog, C. J. 1996, MNRAS, 278, 209

Jog, C. J. & Solomon, P. M. 1984a, ApJ, 276, 127

—. 1984b, ApJ, 276, 114

Johnston, S., Taylor, R., Bailes, M., Bartel, N., Baugh, C., Bietenholz, M., Blake, C., Braun, R., Brown, J., Chatterjee, S., Darling, J., Deller, A., Dodson, R., Edwards, P., Ekers, R., Ellingsen, S., Feain, I., Gaensler, B., Haverkorn, M., Hobbs, G., Hopkins, A., Jackson, C., James, C., Joncas, G., Kaspi, V., Kilborn, V., Koribalski, B., Kothes, R., Landecker, T.,

Lenc, E., Lovell, J., Macquart, J.-P., Manchester, R., Matthews, D., McClure-Griffiths, N., Norris, R., Pen, U.-L., Phillips, C., Power, C., Protheroe, R., Sadler, E., Schmidt, B., Stairs, I., Staveley-Smith, L., Stil, J., Tingay, S., Tzioumis, A., Walker, M., Wall, J., & Wolleben, M. 2008, Experimental Astronomy, 22, 151

Kamphuis, J. J., Sijbring, D., & van Albada, T. S. 1996, A&AS, 116, 15

Karachentsev, I. D., Karachentseva, V. E., Huchtmeier, W. K., & Makarov, D. I. 2004, AJ, 127, 2031

Kennicutt, R. C. & Evans, N. J. 2012, \araa, 50, 531

Kennicutt, Jr., R. C. 1989, ApJ, 344, 685

—. 1998a, ARA&A, 36, 189

—. 1998b, ApJ, 498, 541

Kennicutt, Jr., R. C., Calzetti, D., Walter, F., Helou, G., Hollenbach, D. J., Armus, L., Bendo, G., Dale, D. A., Draine, B. T., Engelbracht, C. W., Gordon, K. D., Prescott, M. K. M., Regan, M. W., Thornley, M. D., Bot, C., Brinks, E., de Blok, E., de Mello, D., Meyer, M., Moustakas, J., Murphy, E. J., Sheth, K., & Smith, J. D. T. 2007, ApJ, 671, 333

Kessler, M. F., Mueller, T. G., Leech, K., Arviset, C., Garcia-Lario, P., Metcalfe, L., Pollock, A., Prusti, T., & Salama, A. 2003, The ISO Handbook, Volume I - Mission & Satellite Overview

Kim, J.-h., Krumholz, M. R., Wise, J. H., Turk, M. J., Goldbaum, N. J., & Abel, T. 2013, ApJ, 779, 8

Klypin, A. A., Trujillo-Gomez, S., & Primack, J. 2011, ApJ, 740, 102

Knapp, G. R., van Driel, W., Schwarz, U. J., van Woerden, H., & Gallagher, III, J. S. 1984, A&A, 133, 127

Koribalski, B. & Staveley-Smith, L. 2009, WALLABY: Widefield ASKAP L-band Legacy All-sky Blind surveY, ASKAP Survey Science Proposal

Koribalski, B. S., Wang, J., Kamphuis, P., Westmeier, T., Staveley-Smith, L., Oh, S.-H., López-Sánchez, Á. R., Wong, O. I., Ott, J., de Blok, W. J. G., & Shao, L. 2018, MNRAS, 478, 1611

Kregel, M., van der Kruit, P. C., & de Grijs, R. 2002, MNRAS, 334, 646

Kroupa, P., Famaey, B., de Boer, K. S., Dabringhausen, J., Pawlowski, M. S., Boily, C. M., Jerjen, H., Forbes, D., Hensler, G., & Metz, M. 2010, A&A, 523, A32

Krumholz, M. R. 2012, ApJ, 759, 9

Krumholz, M. R., Dekel, A., & McKee, C. F. 2012, ApJ, 745, 69

Krumholz, M. R., McKee, C. F., & Tumlinson, J. 2009a, ApJ, 693, 216

—. 2009b, ApJ, 699, 850

Lambas, D. G., Tissera, P. B., Alonso, M. S., & Coldwell, G. 2003, MNRAS, 346, 1189

Lebrun, F., Bennett, K., Bignami, G. F., Bloemen, J. B. G. M., Buccheri, R., Caraveo, P. A., Gottwald, M., Hermsen, W., Kanbach, G., Mayer-Hasselwander, H. A., Montmerle, T., Paul, J. A., Sacco, B., Strong, A. W., Wills, R. D., Dame, T. M., Cohen R. S., & Thaddeus, P. 1983, ApJ, 274, 231

Leisawitz, D., Bash, F. N., & Thaddeus, P. 1989, ApJS, 70, 731

Leitner, S. N. 2012, ApJ, 745, 149

Leroy, A. K., Walter, F., Bigiel, F., Usero, A., Weiss, A., Brinks, E., de Blok, W. J. G., Kennicutt, R. C., Schuster, K.-F., Kramer, C., Wiesemeyer, H. W., & Roussel, H. 2009, AJ, 137, 4670

Leroy, A. K., Walter, F., Brinks, E., Bigiel, F., de Blok, W. J. G., Madore, B., & Thornley, M. D. 2008, AJ, 136, 2782

Leroy, A. K., Walter, F., Sandstrom, K., Schruba, A., Munoz-Mateos, J.-C., Bigiel, F., Bolatto, A., Brinks, E., de Blok, W. J. G., Meidt, S., Rix, H.-W., Rosolowsky, E., Schinnerer, E., Schuster, K.-F., & Usero, A. 2013, AJ, 146, 19

Li, H., Gnedin, O. Y., Gnedin, N. Y., Meng, X., Semenov, V. A., & Kravtsov, A. V. 2017, ApJ, 834, 69

Lia, C., Portinari, L., & Carraro, G. 2002, MNRAS, 330, 821

Liu, G., Koda, J., Calzetti, D., Fukuhara, M., & Momose, R. 2011, ApJ, 735, 63

Liu, L., Gao, Y., & Greve, T. R. 2015, ApJ, 805, 31

López-Sánchez, Á. R., Lagos, C. D. P., Young, T., & Jerjen, H. 2018, MNRAS, 480, 210

Louie, M., Koda, J., & Egusa, F. 2013, ApJ, 763, 94

Maoz, D., Filippenko, A. V., Ho, L. C., Macchetto, F. D., Rix, H.-W., & Schneider, D. P. 1996, ApJS, 107, 215

Marchuk, A. A. 2018, MNRAS, 476, 3591

Martin, C. L. & Kennicutt Jr., R. C. 2001, \apj, 555, 301

Martinsson, T. P. K. 2011, PhD thesis, University of Groningen

McGaugh, S. S. & Schombert, J. M. 2014, AJ, 148, 77

Meidt, S. E., Schinnerer, E., Knapen, J. H., Bosma, A., Athanassoula, E., Sheth, K., Buta, R. J., Zaritsky, D., Laurikainen, E., Elmegreen, D., Elmegreen, B. G., Gadotti, D. A., Salo, H., Regan, M., Ho, L. C., Madore, B. F., Hinz, J. L., Skibba, R. A., Gil de Paz, A., Muñoz-Mateos, J.-C., Menéndez-Delmestre, K., Seibert, M., Kim, T., Mizusawa, T., Laine, J., & Comerón, S. 2012, ApJ, 744, 17

Meidt, S. E., Schinnerer, E., van de Ven, G., Zaritsky, D., Peletier, R., Knapen, J. H., Sheth, K., Regan, M., Querejeta, M., Muñoz-Mateos, J.-C., Kim, T., Hinz, J. L., Gil de Paz, A., Athanassoula, E., Bosma, A., Buta, R. J., Cisternas, M., Ho, L. C., Holwerda, B., Skibba, R., Laurikainen, E., Salo, H., Gadotti, D. A., Laine, J., Erroz-Ferrer, S., Comerón, S., Menéndez-Delmestre, K., Seibert, M., & Mizusawa, T. 2014, ApJ, 788, 144

Meurer, G. R., Heckman, T. M., Leitherer, C., Kinney, A., Robert, C., & Garnett, D. R. 1995, AJ, 110, 2665

Michałowski, M. J., Gentile, G., Hjorth, J., Krumholz, M. R., Tanvir, N. R., Kamphuis, P., Burlon, D., Baes, M., Basa, S., Berta, S., Castro Cerón, J. M., Crosby, D., D'Elia, V., Elliott, J., Greiner, J., Hunt, L. K., Klose, S., Koprowski, M. P., Le Floc'h, E., Malesani, D., Murphy, T., Nicuesa Guelbenzu, A., Palazzi, E., Rasmussen, J., Rossi, A., Savaglio, S., Schady, P., Sollerman, J., de Ugarte Postigo, A., Watson, D., van der Werf, P., Vergani, S. D., & Xu, D. 2015, A&A, 582, A78

Miura, R., Okumura, S. K., Tosaki, T., Tamura, Y., Kurono, Y., Kuno, N., Nakanishi, K., Sakamoto, S., Hasegawa, T., & Kawabe, R. 2010, ApJ, 724, 1120

Mogotsi, K. M., de Blok, W. J. G., Caldú-Primo, A., Walter, F., Ianjamasimanana, R., & Leroy, A. K. 2016, AJ, 151, 15

Mould, J. R., Huchra, J. P., Freedman, W. L., Kennicutt, Jr., R. C., Ferrarese, L., Ford, H. C., Gibson, B. K., Graham, J. A., Hughes, S. M. G., Illingworth, G. D., Kelson, D. D., Macri, L. M., Madore, B. F., Sakai, S., Sebo, K. M., Silbermann, N. A., & Stetson, P. B. 2000, ApJ, 529, 786

Nan, R., Li, D., Jin, C., Wang, Q., Zhu, L., Zhu, W., Zhang, H., Yue, Y., & Qian, L. 2011, International Journal of Modern Physics D, 20, 989

Navarro, J. F., Frenk, C. S., & White, S. D. M. 1996, ApJ, 462, 563

Neugebauer, G., Habing, H. J., van Duinen, R., Aumann, H. H., Baud, B., Beichman, C. A., Beintema, D. A., Boggess, N., Clegg, P. E., de Jong, T., Emerson, J. P., Gautier, T. N., Gillett, F. C., Harris, S., Hauser, M. G., Houck, J. R., Jennings, R. E., Low, F. J., Marsden, P. L., Miley, G., Olnon, F. M., Pottasch, S. R., Raimond, E., Rowan-Robinson, M., Soifer, B. T., Walker, R. G., Wesselius, P. R., & Young, E. 1984, ApJ, 278, L1

Nilson, P. 1973, Uppsala general catalogue of galaxies

Noeske, K. G., Faber, S. M., Weiner, B. J., Koo, D. C., Primack, J. R., Dekel, A., Papovich, C., Conselice, C. J., Le Floc'h, E., Rieke, G. H., Coil, A. L., Lotz, J. M., Somerville, R. S., & Bundy, K. 2007, ApJ, 660, L47

Noordermeer, E., van der Hulst, J. M., Sancisi, R., Swaters, R. A., & van Albada, T. S. 2005, A&A, 442, 137

Norris, R. P., Hopkins, A., Afonso, J., Brown, S., Condon, J., Dunne, L., Feain, I., Hollow, R., Jarvis, M., Johnston-Hollitt, M., et al. 2011, Publications of the Astronomical Society of Australia, 28, 215

Oh, S.-H., de Blok, W. J. G., Walter, F., Brinks, E., & Kennicutt, Jr., R. C. 2008, AJ, 136, 2761

Onodera, S., Kuno, N., Tosaki, T., Kohno, K., Nakanishi, K., Sawada, T., Muraoka, K., Komugi, S., Miura, R., Kaneko, H., Hirota, A., & Kawabe, R. 2010, ApJ, 722, L127

Parkash, V., Brown, M. J. I., Jarrett, T. H., & Bonne, N. J. 2018, ApJ, 864, 40

Peng, Y.-j., Lilly, S. J., Kovač, K., Bolzonella, M., Pozzetti, L., Renzini, A., Zamorani, G., Ilbert, O., Knobel, C., Iovino, A., Maier, C., Cucciati, O., Tasca, L., Carollo, C. M., Silverman, J., Kampczyk, P., de Ravel, L., Sanders, D., Scoville, N., Contini, T., Mainieri, V., Scodeggio, M., Kneib, J.-P., Le Fèvre, O., Bardelli, S., Bongiorno, A., Caputi, K., Coppa, G., de la Torre, S., Franzetti, P., Garilli, B., Lamareille, F., Le Borgne, J.-F., Le Brun, V., Mignoli, M., Perez Montero, E., Pello, R., Ricciardelli, E., Tanaka, M., Tresse, L., Vergani, D., Welikala, N., Zucca, E., Oesch, P., Abbas, U., Barnes, L., Bordoloi, R., Bottini, D., Cappi, A., Cassata, P., Cimatti, A., Fumana, M., Hasinger, G., Koekemoer, A., Leauthaud, A., Maccagni, D., Marinoni, C., McCracken, H., Memeo, P., Meneux, B., Nair, P., Porciani, C., Presotto, V., & Scaramella, R. 2010, ApJ, 721, 193

Pilbratt, G. L., Riedinger, J. R., Passvogel, T., Crone, G., Doyle, D., Gageur, U., Heras, A. M., Jewell, C., Metcalfe, L., Ott, S., & Schmidt, M. 2010, A&A, 518, L1

Ponomareva, A. A., Verheijen, M. A. W., & Bosma, A. 2016, MNRAS, 463, 4052

Quirk, W. J. 1972, ApJ, 176, L9

Rafikov, R. R. 2001, MNRAS, 323, 445

Roberts, M. S. 1969, AJ, 74, 859

Rodighiero, G., Cimatti, A., Gruppioni, C., Popesso, P., Andreani, P., Altieri, B., Aussel, H., Berta, S., Bongiovanni, A., Brisbin, D., Cava, A., Cepa, J., Daddi, E., Dominguez-Sanchez, H., Elbaz, D., Fontana, A., Förster Schreiber, N., Franceschini, A., Genzel, R., Grazian, A., Lutz, D., Magdis, G., Magliocchetti, M., Magnelli, B., Maiolino, R., Mancini, C., Nordon, R., Perez Garcia, A. M., Poglitsch, A., Santini, P., Sanchez-Portal, M., Pozzi, F., Riguccini, L., Saintonge, A., Shao, L., Sturm, E., Tacconi, L., Valtchanov, I., Wetzstein, M., & Wieprecht, E. 2010, A&A, 518, L25

Romeo, A. B. & Falstad, N. 2013, MNRAS, 433, 1389

Romeo, A. B. & Mogotsi, K. M. 2017, MNRAS, 469, 286

Romeo, A. B. & Wiegert, J. 2011, MNRAS, 416, 1191

Rownd, B. K. & Young, J. S. 1999, AJ, 118, 670

Roychowdhury, S., Huang, M.-L., Kauffmann, G., Wang, J., & Chengalur, J. N. 2015, MNRAS, 449, 3700

Safronov, V. S. 1960, Annales d'Astrophysique, 23, 979

Salmi, F., Daddi, E., Elbaz, D., Sargent, M. T., Dickinson, M., Renzini, A., Bethermin, M., & Le Borgne, D. 2012, ApJ, 754, L14

Schaye, J. 2004, ApJ, 609, 667

Schaye, J., Crain, R. A., Bower, R. G., Furlong, M., Schaller, M., Theuns, T., Dalla Vecchia, C., Frenk, C. S., McCarthy, I. G., Helly, J. C., Jenkins, A., Rosas-Guevara, Y. M., White, S. D. M., Baes, M., Booth, C. M., Camps, P., Navarro, J. F., Qu, Y., Rahmati, A., Sawala, T., Thomas, P. A., & Trayford, J. 2015, MNRAS, 446, 521

Schmidt, M. 1959, ApJ, 129, 243

Schruba, A., Leroy, A. K., Walter, F., Bigiel, F., Brinks, E., de Blok, W. J. G., Dumas, G., Kramer, C., Rosolowsky, E., Sandstrom, K., Schuster, K., Usero, A., Weiss, A., & Wiesemeyer, H. 2011, AJ, 142, 37

Sheth, K., Vogel, S. N., Regan, M. W., Teuben, P. J., Harris, A. I., & Thornley, M. D. 2002, AJ, 124, 2581

Sicotte, V. & Carignan, C. 1997, AJ, 113, 609

Silk, J. 1997, ApJ, 481, 703

Sofue, Y. 2017, MNRAS, 469, 1647

Sofue, Y. & Rubin, V. 2001, \araa, 39, 137

Somerville, R. S. & Davé, R. 2015, ARA&A, 53, 51

Sparre, M., Hayward, C. C., Springel, V., Vogelsberger, M., Genel, S., Torrey, P., Nelson, D., Sijacki, D., & Hernquist, L. 2015, MNRAS, 447, 3548

Speagle, J. S., Steinhardt, C. L., Capak, P. L., & Silverman, J. D. 2014, ApJS, 214, 15

Spekkens, K. & Sellwood, J. A. 2007, \apj, 664, 204

Spitzer, L. 1968, Diffuse matter in space

Springel, V., White, S. D. M., Jenkins, A., Frenk, C. S., Yoshida, N., Gao, L., Navarro, J., Thacker, R., Croton, D., Helly, J., Peacock, J. A., Cole, S., Thomas, P., Couchman, H., Evrard, A., Colberg, J., & Pearce, F. 2005, Nature, 435, 629

Swaters, R. A. 1999, PhD thesis, , Rijksuniversiteit Groningen, (1999)

Swaters, R. A., Sancisi, R., van Albada, T. S., & van der Hulst, J. M. 2009, \aap, 493, 871

Swaters, R. A., van Albada, T. S., van der Hulst, J. M., & Sancisi, R. 2002, \aap, 390, 829

Tamburro, D., Rix, H.-W., Leroy, A. K., Mac Low, M.-M., Walter, F., Kennicutt, R. C., Brinks, E., & de Blok, W. J. G. 2009, AJ, 137, 4424

Taylor, A. R. & Jarvis, M. 2016, in 2016 IEEE Radio and Antenna Days of the Indian Ocean (RADIO), 1–2

Thornley, M. D. & Wilson, C. D. 1995, ApJ, 447, 616

Tielens, A. G. G. M. 2008, ARA&A, 46, 289

Tilanus, R. P. J. & Allen, R. J. 1993, A&A, 274, 707

Tody, D. 1986, in Proc. SPIE, Vol. 627, Instrumentation in astronomy VI, ed. D. L. Crawford, 733

Toomre, A. 1964, ApJ, 139, 1217

Tully, R. B., Courtois, H. M., Dolphin, A. E., Fisher, J. R., Héraudeau, P., Jacobs, B. A., Karachentsev, I. D., Makarov, D., Makarova, L., Mitronova, S., Rizzi, L., Shaya, E. J., Sorce, J. G., & Wu, P.-F. 2013, AJ, 146, 86

Tully, R. B., Rizzi, L., Shaya, E. J., Courtois, H. M., Makarov, D. I., & Jacobs, B. A. 2009, AJ, 138, 323

van de Hulst, H. C. 1951, AJ, 56, 144

van der Hulst, J. M., Skillman, E. D., Smith, T. R., Bothun, G. D., McGaugh, S. S., & de Blok, W. J. G. 1993, AJ, 106, 548

van der Hulst, J. M., Terlouw, J. P., Begeman, K. G., Zwitser, W., & Roelfsema, P. R. 1992, in Astronomical Society of the Pacific Conference Series, Vol. 25, Astronomical Data Analysis Software and Systems I, ed. D. M. Worrall, C. Biemesderfer, & J. Barnes, 131

van der Hulst, J. M., van Albada, T. S., & Sancisi, R. 2001, in Astronomical Society of the Pacific Conference Series, Vol. 240, Gas and Galaxy Evolution, ed. J. E. Hibbard, M. Rupen, & J. H. van Gorkom, 451

van der Kruit, P. C. 1988, A&A, 192, 117

van der Kruit, P. C. & Searle, L. 1981, A&A, 95, 105

van der Marel, R. P. & Franx, M. 1993, ApJ, 407, 525

van Eymeren, J., Jütte, E., Jog, C. J., Stein, Y., & Dettmar, R.-J. 2011, A&A, 530, A29

Verheijen, M. A., Oosterloo, T., Heald, G., & van Cappellen, W. 2010, in Panoramic Radio Astronomy: Wide-field 1-2 GHz research on galaxy evolution, Vol. 89, SISSA Medialab, 010

Verheijen, M. A. W. 1997, PhD thesis, University of Groningen

Verheijen, M. A. W., Oosterloo, T. A., van Cappellen, W. A., Bakker, L., Ivashina, M. V., & van der Hulst, J. M. 2008, in American Institute of Physics Conference Series, Vol. 1035, The Evolution of Galaxies Through the Neutral Hydrogen Window, ed. R. Minchin & E. Momjian, 265–271

Verheijen, M. A. W. & Sancisi, R. 2001, A&A, 370, 765

Vogelaar, M. G. R. & Terlouw, J. P. 2001, in Astronomical Society of the Pacific Conference Series, Vol. 238, Astronomical Data Analysis Software and Systems X, ed. F. R. Harnden, Jr., F. A. Primini, & H. E. Payne, 358

Voigtländer, P., Kamphuis, P., Marcelin, M., Bomans, D. J., & Dettmar, R.-J. 2013, A&A, 554, A133

Walter, F., Brinks, E., de Blok, W. J. G., Bigiel, F., Kennicutt, Jr., R. C., Thornley, M. D., & Leroy, A. 2008, AJ, 136, 2563

Wang, B. & Silk, J. 1994, ApJ, 427, 759

Wang, J., Fu, J., Aumer, M., Kauffmann, G., Józsa, G. I. G., Serra, P., Huang, M.-l., Brinchmann, J., van der Hulst, T., & Bigiel, F. 2014, MNRAS, 441, 2159

Wang, J., Koribalski, B. S., Serra, P., van der Hulst, T., Roychowdhury, S., Kamphuis, P., & Chengalur, J. N. 2016, MNRAS, 460, 2143

Wang, Z. 1990, ApJ, 360, 529

Werner, M. W., Roellig, T. L., Low, F. J., Rieke, G. H., Rieke, M., Hoffmann, W. F., Young, E., Houck, J. R., Brandl, B., Fazio, G. G., Hora, J. L., Gehrz, R. D., Helou, G., Soifer, B. T., Stauffer, J., Keene, J., Eisenhardt, P., Gallagher, D., Gautier, T. N., Irace, W., Lawrence, C. R., Simmons, L., Van Cleve, J. E., Jura, M., Wright, E. L., & Cruikshank, D. P. 2004, ApJS, 154, 1

Wilcots, E. M. & Miller, B. W. 1998, AJ, 116, 2363

Williams, J., Blitz, L., & McKee, C. 2000, Protostars and Planets IV, 97

Williams, T. G., Gear, W. K., & Smith, M. W. L. 2018, MNRAS, 479, 297

Wong, O. I., Meurer, G. R., Zheng, Z., Heckman, T. M., Thilker, D. A., & Zwaan, M. A. 2016, MNRAS, 460, 1106

Wong, T. & Blitz, L. 2002, ApJ, 569, 157

Wright, E. L., Eisenhardt, P. R. M., Mainzer, A. K., Ressler, M. E., Cutri, R. M., Jarrett, T., Kirkpatrick, J. D., Padgett, D., McMillan, R. S., Skrutskie, M., Stanford, S. A., Cohen, M., Walker, R. G., Mather, J. C., Leisawitz, D., Gautier, III, T. N., McLean, I., Benford, D., Lonsdale, C. J., Blain, A., Mendez, B., Irace, W. R., Duval, V., Liu, F., Royer, D., Heinrichsen, I., Howard, J., Shannon, M., Kendall, M., Walsh, A. L., Larsen, M., Cardon, J. G., Schick, S., Schwalm, M., Abid, M., Fabinsky, B., Naes, L., & Tsai, C.-W. 2010, AJ, 140, 1868

Wu, H., Cao, C., Hao, C.-N., Liu, F.-S., Wang, J.-L., Xia, X.-Y., Deng, Z.-G., & Young, C. K.-S. 2005, ApJ, 632, L79

Wuyts, S., Förster Schreiber, N. M., van der Wel, A., Magnelli, B., Guo, Y., Genzel, R., Lutz, D., Aussel, H., Barro, G., Berta, S., Cava, A., Graciá-Carpio, J., Hathi, N. P., Huang, K.-H., Kocevski, D. D., Koekemoer, A. M., Lee, K.-S., Le Floc'h, E., McGrath, E. J., Nordon, R., Popesso, P., Pozzi, F., Riguccini, L., Rodighiero, G., Saintonge, A., & Tacconi, L. 2011, ApJ, 742, 96

Wyder, T. K., Martin, D. C., Barlow, T. A., Foster, K., Friedman, P. G., Morrissey, P., Neff, S. G., Neill, J. D., Schiminovich, D., Seibert, M., Bianchi, L., Donas, J., Heckman, T. M., Lee, Y.-W., Madore, B. F., Milliard, B., Rich, R. M., Szalay, A. S., & Yi, S. K. 2009, ApJ, 696, 1834

Yang, C.-C., Gruendl, R. A., Chu, Y.-H., Mac Low, M.-M., & Fukui, Y. 2007, ApJ, 671, 374

Yim, K. & van der Hulst, J. M. 2016, MNRAS, 463, 2092

Young, J. S., Xie, S., Tacconi, L., Knezek, P., Viscuso, P., Tacconi-Garman, L., Scoville, N., Schneider, S., Schloerb, F. P., Lord, S., Lesser, A., Kenney, J., Huang, Y.-L., Devereux, N., Claussen, M., Case, J., Carpenter, J., Berry, M., & Allen, L. 1995, ApJS, 98, 219

Young, L. M., Bureau, M., Davis, T. A., Combes, F., McDermid, R. M., Alatalo, K., Blitz, L., Bois, M., Bournaud, F., Cappellari, M., Davies, R. L., de Zeeuw, P. T., Emsellem, E., Khochfar, S., Krajnović, D., Kuntschner, H., Lablanche, P.-Y., Morganti, R., Naab, T., Oosterloo, T., Sarzi, M., Scott, N., Serra, P., & Weijmans, A.-M. 2011, \mnras, 414, 940